THE HETEROGENEITY AND VOLATILE CONTENT OF EARTH'S MANTLE, MAGMAS AND CRUST

by

Benjamin M. Urann
B.S., University of Massachusetts Amherst (2014)

Submitted to the Department of Earth, Atmospheric, and Planetary Sciences in partial fulfilment of the requirements for the degree of

Doctor of Philosophy

at the

MASSACHUSETTS INSTITUTE OF TECHNOLOGY

and the

WOODS HOLE OCEANOGRAPHIC INSTITUTION

February 2021

Signature of Author _____
Joint Program in Oceanography and Applied Ocean Science & Engineering
Massachusetts Institute of Technology & Woods Hole Oceanographic Institution
January 12, 2021

Certified by_____
Henry J.B. Dick
Senior Scientist in Geology and Geophysics, Woods Hole Oceanographic Institution
Thesis Co-Supervisor

Certified by _____
Veronique Le Roux
Assistant Scientist in Geology and Geophysics, Woods Hole Oceanographic Institution
Thesis Co-Supervisor

Accepted by _____
Oliver Jagoutz
Associate Professor of Geology, Massachusetts Institute of Technology
Chair, Joint Committee for Marine Geology and Geophysics
January 12, 2021

THE HETEROGENEITY AND VOLATILE CONTENT OF EARTH'S MANTLE, MAGMAS AND CRUST

by

Benjamin M. Urann

Submitted to the Department of Earth, Atmospheric, and Planetary Sciences on January 12, 2021 in partial fulfillment of the requirements for the degree of Doctor of Philosophy in Marine Geology.

Abstract

This thesis explores the volatile content of the mantle, subducted oceanic crust, and arc magmas as well as the structure of slow spreading ocean crust and the heterogeneity of Earth's upper mantle. In Chapter 2, I directly explore the halogen (F and Cl) content of mantle minerals in situ, then use these measurements to assess the halogen content of the upper mantle. In Chapter 3, I investigate the volatile content of Raspas eclogites (SW Ecuador), a proxy for deeply subducted oceanic crust, to evaluate volatile transfer from crustal generation at divergent plate boundaries (e.g., mid-ocean ridges) to recycling of ocean crust at subduction zones. In Chapter 4, I use the H_2O content of nominally anhydrous minerals in plutonic arc cumulates to elucidate the H_2O content of the melts from which the rocks crystallized. In this way, I assert that primitive arc magmas may contain 4–10 wt.% H_2O and through fractional crystallization up to ~20 wt.% H_2O, making them far more hydrous than traditional methods (i.e., olivine-hosted melt inclusions) surmise. In Chapter 5, I show that mantle peridotite exposed along the 16°N region of the Mid-Atlantic Ridge originated in an arc setting and has been remixed into sub-ridge mantle, indicating that the sub-ridge mantle is more heterogeneous and depleted than inferences made from mid-ocean ridge basalts suggest. Chapter 6 surveys the life cycle of oceanic core complexes through zircon geochronology and posits an updated framework for understanding the termination of oceanic core complexes, and more broadly oceanic detachment faults. Together, this contribution highlights the chemical heterogeneity of the mantle, and quantifies the full extent of volatiles hosted by mantle and crustal reservoirs.

Thesis Co-Supervisor: Dr. **Veronique Le Roux**
Title: Associate Scientist in Geology & Geophysics
Woods Hole Oceanographic Institution

Thesis Co-Supervisor: Dr. **Henry J.B. Dick**
Title: Senior Scientist in Geology & Geophysics
Woods Hole Oceanographic Institution

Acknowledgments

Having read the abstract, one might be struck by the notion that this thesis is a meandering body. That would be true; the path to this point in time was constructed by innumerable oxbows, each of which added a novel aspect to my matriculation as a scientist.

First, I must thank my wife Haley, without whom I would be rudderless and after whom all else follows. Your patience, kindness, and sage advice have kept me motivated and moving forward the past five years. Also, to my family, who satiated my curiosity and entertained my pursuit of geology. My father impressed upon me what a special place Woods Hole was; I grew up looking at his maps of the Scotian Shelf plotted during his time aboard the Albatross IV (after spending a few summers there himself), A dozen years later, I was able to recount to him my own experiences at sea.

In chronological order, my first foray into geology began at UMass Amherst as a nascent biology major, where I took an excellent introductory geology class with Richard Yuretich. This spawned another (with Mark Leckie), then another, and before I knew it, I'd switched majors and started anew. I was fortunate to be taken under the wings of Isla Castaneda, who provided guidance as a thesis advisor and employment during my undergraduate studies, and who first suggested that I consider graduate school. Sheila Seaman and Mike Williams were incredibly influential in fostering my passion for structural geology, field work, and petrology. For those who knew Sheila, she was an incredible individual who inspired countless students to pursue their passion and to leave the world better than they found it. She is sorely missed; I hope my work on the water content of minerals (Chapter 4), a subject she was keen to explore, would make her proud.

I must thank Henry Dick for taking a chance on an unknown undergraduate as a Summer Student Fellow; Debbie Smith, who willingly brought said unknown undergraduate to sea for six weeks on her cruise; to the science party, captain, and crew aboard the R/V Knorr, who were as kind and welcoming as one could wish; and finally, the lot of them for fostering my curiosity on the structure and composition of ocean crust.

Debbie Smith and Henry generously provided salary for me as a research assistant after I finished at UMass, without which I might very well have skipped graduate school all together.

This research assistantship introduced me to my future co-advisor, Veronique Le Roux, who knew me as the guy who toiled picking chromian spinel all day in her shared lab space. She took a chance on me, and for that I am grateful. We've done some great science together.

The staff at Academic Programs Office has been helpful in all aspects of my graduate experience. Special thanks to Dean Meg Tivey, Lea Fraser, and Julia Westwater. As I've told countless prospective students over the years, the Joint Program is the best graduate program in the world, bar none.

This research benefited from the world class individuals brought together at WHOI. Without their insights and comradery, this work would not have been possible. Conversations with Brian Monteleone, Frieder Klein, Forest Horton, Glenn Gaetani, Horst Marschall, Brian Tocholke, Jim Broda, Mark Kurz, Adam Soule, Pablo Canales, Maurice Tivey, Mark Behn, Dan Lizarralde, David Glover, and others have expanded my horizons and enriched my time in graduate school. Not to be forgotten, Greg Hirth was kind enough to allow me to take his rock mechanics class at Brown, which was both useful and enlightening. Finally, I would be remiss to forget mentioning Jim Broda, whose stories kept me in rapture many an afternoon, and whose vehicles are most often driven on two wheels around campus.

This thesis brought together a diverse group of scientists, who I've been fortunate enough to learn from and collaborate with: Horst Marschall (Uni. Frankfurt), Brian Monteleone (WHOI), Keiji Hammond (SMNH), Cin-Ty Lee (Rice), Timm John (Uni. Berlin), Grace Beaudoin (UT Austin), Jaime Barnes (UT Austin), Jack Casey (U. Houston), Ross Parnell-Turner (Scripps), Oliver Jagoutz (MIT), Othmar Müntener (U. Lausanne), Mark Behn (Boston College), Emily Chin (Scripps), Barbara John (UWyoming) and Mike Cheadle (UWyoming).

I've been fortunate to partake in two additional cruises aboard the R/V Sikuliaq and R/V Thomas Thompson. The friends and connections I made then reverberate now: Dan Brunelli, John Greene, Vincent Salters, Jurgen Koepke, Dominik Woelki, John Zayac, Bernie Coakley, Rob Pockalny.

The friendship of many past and present students over the years has been a source of inspiration and moderating force for sanity. Thanks to Emmanuel Codillo, Adam Sarafian, Emily Sarafian, Ma, Weiqi Zhou and Billy Shinevar. G&G student numbers were lean for a few years, but that certainly brought us closer.

Chapter 6 was a product of the generosity of Bobbie John and Mike Cheadle, who opened their home in Laramie to me for a month and brought me along to Stanford to analyze gabbroic zircons in 2016. This experience broadened my horizons immensely and fostered two close friendships which I will carry forward long after graduate school.

This work was supported by a series of grants, both internal and external. The Stanley Watson Fellowship (WHOI) provided financial support during my first year of graduate school. The Academic Programs Office Ocean Venture Fund (WHOI) provided seed funding which initiated Chapters 3 and 4, and ultimately led to two funded NSF proposals. These resources are vital to JP students, and I am incredibly grateful for them. Primary support was provided by the National Science Foundation grants to Veronique Le Roux (EAR P&G #1524311, #1839128, #1855302) and Henry Dick (MG&G #1637130, #1657983).

Contents

List of Figures

List of Tables

Chapter 1

Introduction

This introduction is written for a general audience. Citations for relevant topics may be found in individual chapters.

Earth is unique in our solar system as the only planet to display active plate tectonics. Plate tectonics, in turn, relies on heat dissipated from the core and mantle to allow plates to continue their slow dance across Earth's surface. Critical to the continuation of plate tectonics are volatiles such as H_2O, CO_2, F and Cl which affect the physical and chemical properties of both rocks and magmas. Despite their relative importance, much remains to be learned about the absolute abundances and behavior of these species in the mantle and crust.

To the casual observer, volcanic eruptions are infrequent occurrences. Yet, the overwhelming majority of volcanic activity on Earth occurs regularly under the sea surface at mid-ocean ridges, where two plates diverge. As the plate pull apart, mantle rock (i.e. olivine-rich peridotite) upwells beneath the ridge and melts to form mid-ocean ridge basalt (MORB). Melts are more buoyant than their mantle source and will rise to the surface to generate new basaltic crust, the most voluminous crustal rock on Earth. As this new basaltic crust cools, it will eventually become dense and sink back into the underlying mantle at subduction zones. The sinking plate, having been hydrated by interaction with seawater, will dewater and expel these fluids into the overlying arc mantle where melting under hydrous conditions generates arc volcanism. Hydrous arc magmas will begin to crystallize upon ascent at the base of the crust. Depending on the pressure at which this crystallization occurs, deeply crystallized magmas (lower crustal igneous cumulates, or arclogites) may be denser than the underlying peridotite and sink back into mantle in a process known as delamination. Subduction and delamination, then, are the fundamental means of geochemical cycling between the crust and mantle. Over the course of Earth's history, the mantle has been mixed with various subducted lithologies (ocean crust, sediments, carbonates) to generate a witch's brew of isotopic, chemical, and lithologic heterogeneities. Documenting the composition and occurrence of these heterogeneities remains an important subject of research.

To better understand the composition and behavior of volatiles in the crust-mantle system, I performed a systematic series of investigations. First, I develop and refine a technique to measure in situ volatile abundances in nominally dry (no structurally bound H_2O) minerals, which are the primary constituents of the mantle. I use these techniques to conduct an inventory of the volatile (F and Cl) content of mantle peridotite (Chapter 2) from a global suite of samples. Next, I explore the volatile (H_2O, F, Cl, S) content of deeply subducted ocean crust using mid-ocean ridge basalt-like eclogite as a proxy (Chapter 3), to quantify the volatile carrying capacity of subducted oceanic crust in the broader context of crust-mantle geochemical cycling. Next, I use these techniques to evaluate the volatile abundances of lower crustal igneous cumulates to ascertain both the water content of the magmas from which the cumulates crystallized and the contribution of delaminated lower crust to volatile cycling between the crust and mantle (Chapter 4).

To explore the compositional heterogeneity of the mantle, I document the 16°N region of the Mid-Atlantic Ridge where chemically anomalous mantle peridotite is exposed on the seafloor (Chapter 5). I posit that this mantle parcel was once arc mantle in an ancient subduction zone complex that underwent extreme extents of hydrous melting and has subsequently been remixed into the ambient mantle where it is now exposed along the Mid-Atlantic Ridge.

Although idealized cartoons often depict ocean crust as a simple layer cake model capped by basalt, nearly 40% of the seafloor fits no such model. These regions, slow and ultra-slow spreading ridges, may expose mantle and lower crust directly on the seafloor via long-lived faults. Chapter 6 explores the crustal structure of these regions, using the 16°N locality of the Mid-Atlantic Ridge as a case study. To do this, I apply zircon geochronology to assess the process of lower crust and mantle exposures by detachment faulting. By evaluating the timing and tempo of faulting via zircon ages, I reevaluate the life cycle of detachment faults, and show the utility of combining zircon dating with geophysical data (e.g. magnetics).

Taken together, this thesis provides novel insights on longstanding uncertainties within the Earth system. Fundamentally, the contribution lays the groundwork for numerous avenues of future work, which I discuss in Chapter 7.

Chapter *2*

Fluorine and chlorine in mantle minerals and the halogen budget of the Earth's mantle

This chapter was originally published in *Contributions to Mineralogy and Petrology* (2017) as:

Urann, B. M., Le Roux, V., Hammond, K., Marschall, H. R., Lee, C. T., & Monteleone, B. D. (2017). Fluorine and chlorine in mantle minerals and the halogen budget of the Earth's mantle. *Contributions to Mineralogy and Petrology*, *172*(7), 51.

2.1 Abstract

The fluorine (F) and chlorine (Cl) contents of arc magmas have been used to track the composition of subducted components, and the F and Cl contents of MORB have been used to estimate the halogen content of depleted MORB mantle (DMM). Yet, the F and Cl budget of the Earth's upper mantle and their distribution in peridotite minerals remain to be constrained. Here, we developed a method to measure low concentrations of halogens (≥0.4 μg/g F and ≥0.3 μg/g Cl) in minerals by secondary ion mass spectroscopy. We present a comprehensive study of F and Cl in co-existing natural olivine, orthopyroxene, clinopyroxene, and amphibole in seventeen samples from different tectonic settings. We support the hypothesis that F in olivine is controlled by melt polymerization, and that F in pyroxene is controlled by their Na and Al contents, with some effect of melt polymerization. We infer that Cl compatibility ranks as follows: amphibole > clinopyroxene > olivine ~ orthopyroxene, while F compatibility ranks as follows: amphibole > clinopyroxene > orthopyroxene ≥ olivine, depending on the tectonic context. In addition, we show that F, Cl, Be and B are correlated in pyroxenes and amphibole. F and Cl variations suggest that interaction with slab melts and fluids can significantly alter the halogen content of mantle minerals. In particular, F in oceanic peridotites is mostly hosted in pyroxenes, and proportionally increases in olivine in subduction-related peridotites. The mantle wedge is likely enriched in F com- pared to un-metasomatized mantle, while Cl is always low (<1 μg/g) in all tectonic settings studied here. The bulk anhydrous peridotite mantle contains 1.4–31 μg/g F and 0.14–0.38 μg/g Cl. The bulk F content of oceanic-like peridotites (2.1–9.4 μg/g) is lower than DMM estimates, consistent with F-rich eclogite in the source of MORB. Furthermore, the bulk Cl budget of all anhydrous peridotites studied here is lower than previous DMM estimates. Our results indicate that nearly all MORB may be somewhat contaminated by seawater-rich material and that the Cl content of DMM could be overestimated. With this study, we demonstrate that the halogen contents of natural peridotite minerals are a unique tool to understand the cycling of halogens, from ridge settings to subduction zones.

2.2 Introduction

Fluorine and chlorine concentrations in arc-derived melts have been used to track the composition of subducted components transported from the slab to the hot corner of the mantle wedge (Straub and Layne 2003, Dalou, Koga et al. 2014, Le Voyer, Cottrell et al. 2015, Van den Bleeken and Koga 2015), and the F and Cl contents of MORB have been used to estimate the halogen content of the Depleted MORB Mantle (Michael and Schilling 1989, Saal, Hauri et al. 2002, Salters and Stracke 2004, Shaw, Behn et al. 2010, Shimizu, Saal et al. 2016). Unlike H_2O or CO_2, the F and Cl content of mantle melts do not vary significantly during their ascent to the surface, as they only degas at shallow pressures (< 20 MPa and 100 MPa, respectively; (Spilliaert, Métrich et al. 2006). Thus, the F and Cl contents of primitive mantle melts should reflect the halogen content of the mantle source at the time of magma genesis. Studies of arc melt inclusions have shown that incompatible elements F and Cl are enriched in arc magmas relative to MORB. F concentrations are 1 to 16 times higher in arcs than in N-MORB (Le Voyer, Rose-Koga et al. 2010, Wu and Koga 2013). It has been suggested that F transport from the subducted slab to the overlying mantle wedge must be achieved by percolation of silicate melts (Wu and Koga 2013), as F solubility in silicate melts is high (Dingwell 1989), and increases with increasing H_2O content dissolved in the melt (Dalou, Koga et al. 2014, Dalou and Mysen 2015). Similarly, Cl concentrations may be up to 20 times higher in arcs than in N-MORB (Jenner and O'Neill 2012, Dalou, Koga et al. 2014) because Cl is highly soluble in slab aqueous fluids (Brenan, Ryerson et al. 1998) and effectively lost from the slab during subduction process (Philippot, Agrinier et al. 1998, Straub and Layne 2003, Scambelluri, Müntener et al. 2004, Bonifacie, Busigny et al. 2008, Marschall, Altherr et al. 2009, John, Scambelluri et al. 2011). During subduction, Cl may be directly added to the mantle wedge via fluids or fluid-rich rocks. However, although Cl/F of seawater is 15,000-20,000, the Cl/F ratio of aqueous fluids in arcs is usually < 10, depending on the location of the arc (Straub and Layne 2003, Le Voyer, Rose-Koga et al. 2010). Thus, although previous studies suggest that F and Cl should be enriched in the mantle wedge compared to the depleted MORB mantle (DMM), the distribution of F and Cl in peridotite minerals from ridge and convergent settings, and their cycling throughout the subduction process, are yet to be determined (Debret, Koga et al. 2014).

Literature data for F and Cl in natural peridotite minerals are limited. Benard et al. (2017), Debret et al. (2014) and Beyer et al. (2012) have reported a range of 2–33 μg/g Cl, 4–17 μg/g Cl, and 14–20 μg/g Cl for olivine (Ol), orthopyroxene (Opx), and clinopyroxene (Cpx), respectively. Previous studies on F in natural peridotite minerals (Peslier and Luhr 2006, Bromiley and Kohn 2007, Beyer, Klemme et al. 2012, Guggino 2012, Guggino and Hervig 2012, Fabbrizio, Stalder et al. 2013, Mosenfelder and Rossman 2013, Mosenfelder and Rossman 2013, Debret, Koga et al. 2014, Warren and Hauri 2014, Bénard, Koga et al. 2017) have suggested that olivine, orthopyroxene and clinopyroxene contain non negligible amounts of F (1–51 μg/g, <1–41 μg/g, and 8-46 μg/g, respectively), most likely incorporated into oxygen sites. In particular, Mosenfelder and Rossman (2013b) have proposed that F^- is incorporated into

clinopyroxenes on the oxygen site, charge balanced by substitution of Si^{4+} with Al^{3+} and/or Fe^{3+} or coupled substitution with monovalent cations in the M2 site. These studies support the idea that olivine and pyroxene, the main constituents of the Earth's upper mantle, can accommodate most if not all of the F budget of the mantle (Beyer, Klemme et al. 2012, Mosenfelder and Rossman 2013), assuming that apatite is not stable in the asthenospheric source of MORB (Konzett and Frost 2009).

Here we present the first extensive study of F and Cl in natural and co-existing mantle minerals olivine, orthopyroxene, and clinopyroxene, and amphibole. First, we describe the analytical developments that were required to measure low concentrations of halogens (≥ 0.4 μg/g F and ≥ 0.3 μg/g Cl) in mantle minerals by secondary-ion mass spectrometry (SIMS), and we present the recommended analytical settings used on the IMS 1280 hosted at the NENIMF facility (Woods Hole Oceanographic Institution, USA). Second, we present our results on the distribution of F and Cl in natural peridotite minerals and compare them to the limited literature available for natural peridotite minerals and experimental runs. Then, we discuss the incorporation mechanisms of F and Cl into mantle minerals and we identify the key parameters that control the abundances of F and Cl in mantle minerals. We also compare the F and Cl contents obtained in this study with Li, Be, and B values for pyroxene and amphibole from the Finero massif (Italy). Finally, we discuss the implications of this work for halogen cycling during subduction and the halogen budget of the peridotite mantle.

2.3 Sample description

We selected a total of seventeen natural peridotite samples for study. Eleven olivine grains, seventeen orthopyroxene grains, fifteen clinopyroxene grains, and two amphibole grains were analyzed for F and Cl. In addition, one clinopyroxene grain, one orthopyroxene grain and one amphibole were profiled for Li, Be, and B. The samples were chosen to represent a variety of tectonic environments including supra-subduction ophiolites (Josephine Peridotite, USA), subduction-metasomatized subcontinental lithospheric mantle (Finero, Ivrea Zone, Italy), unmetasomatized subcontinental lithospheric mantle (Balmuccia, Ivrea Zone, Italy), metasomatized mantle-derived xenoliths (Colorado Plateau, USA), and fresh abyssal peridotites from the Mid Atlantic Ridge spreading center (MAR). Sample descriptions and mineral modes are available in Tables 1 and 5, respectively. Below we provide a brief description of the geological contexts of our samples.

The Josephine Peridotite (USA) is a ~ 640 km^2 ultramafic massif located in southern Oregon and consists mostly of depleted harzburgites and lherzolites, with subordinate dunites and pyroxenites. It is part of a supra-subduction ophiolite that was emplaced ~157 Ma ago. Previous studies have revealed that the compositional variability of the mantle there occurs at two scales (Le Roux, Dick et al. 2014). Large compositional variations occur at kilometer scales and are consistent with a model where variable degrees of melt extraction (10 to > 23 %) occurred while the mantle was continuously re-supplied with small amounts (< 0.1 wt.%) of seawater-like

fluids derived from the underlying subducting plate (Le Roux, Dick et al. 2014). Areas where fluid-rich materials were focused experienced significantly greater degrees of melting compared to a typical MORB mantle. Single outcrops display sharp compositional transitions attributed to local melt-rock reactions, where partial re-equilibration of harzburgites with boninite melts is recorded. Our samples feature harzburgites (J127-19, J127-17) and lherzolites (J98-10, J127-09) that reflect the km-scale compositional variations observed in the Josephine peridotite.

The Finero and Balmuccia Massifs (Italy) are part of the Ivrea Zone, a region of exposed lower crust and mantle tectonically emplaced after mantle metasomatism occurred during Triassic subduction. The Balmuccia peridotite consists largely of lherzolites, with minor harzburgites (sample BM5) and dunites (Selverstone and Sharp 2011). The Balmuccia lherzolites underwent minor melt depletion (~5%), little to no enrichment, and thus are relatively pristine (Selverstone and Sharp 2011). The Finero peridotite is compositionally more variable, and may have undergone substantial metasomatic enrichment from at least two metasomatic agents including a hydrated clinopyroxenite component and an isotopically heavy component, enriched in large ion lithophile elements (LILE), high field strength elements (HFSE) and Cl (Selverstone and Sharp 2011). Finero samples (Fin10, Fin1b) contain abundant olivine, orthopyroxene, clinopyroxene, amphibole and phlogopite, and provide a unique opportunity to study the distribution of halogens and other volatile elements in coexisting hydrous and anhydrous phases.

Mantle-derived xenoliths presented in this study define a transect from the Basin and range to the Colorado Plateau (USA) (Li, Lee et al. 2008). Samples were selected to include sub-continental lithospheric mantle samples thought to have undergone varying degrees of hydration/metasomatism from the subduction of the Farallon plate during the early Cenozoic (Dixon, Dixon et al. 2004, Lee 2005, Humphreys and Niu 2009). Dish Hill lherzolites (DHS02;07;18) are from the Pliocene alkali basalt cinder cone in the Basin and Range (westernmost), and displayed equigranular to porphyroclastic textures (Luffi, Saleeby et al. 2009). Sample GC2b is a spinel harzburgite from the Grand Canyon Uinkaret volcanic field on the western edge of the Colorado Plateau (Li, Lee et al. 2008). San Carlos xenolith sample (SC-99) comes from a Pliocene alkali basalt lava flow in the Basin and Range province, south of the Colorado Plateau. Sample KLB1, a lherzolite, was collected from ejecta deposits of the basanitic maar volcano that created Kilbourne Hole, at the southern edge of the Rio Grande Rift. Sample TH2, a spinel harzburgite, was recovered at the Thumb, an ultra-potassic minette diatreme of the Eocene Navajo Volcanic Field (Roden 1981, Lee 2005). Detailed sample descriptions can be found in Li et al. (2008).

MAR sample KNR210-05 D41-24 is a spinel harzburgite with a proto-granular texture and grain size ~1–5mm. The sample was collected from the 16˚30'N region of the Mid Atlantic Ridge, a region of slow spreading (S.R. 25km/Ma) and active detachment faulting where abundant mantle peridotite is exposed on the seafloor, with limited axial volcanism (Smith,

Schouten et al. 2014). This region consists primarily of depleted/ ultra-depleted harzburgite (Silantyev, Bortnikov et al. 2016).

Nine samples were analyzed as thin sections (Josephine series, MAR, Fin1b, Fin10), and eight samples were mounted as individual grains in indium (KLB-1, SC99, GC2B, TH2, DHS2, DHS7, DHS18, BM5).

2.4 Methods

All F and Cl measurements were conducted on a Cameca IMS 1280 at the Northeast National Ion Microprobe Facility (Woods Hole Oceanographic Institution). Details on sample preparation procedures and technical developments can be found in the Supplementary Material section. We utilized a primary Cs^+ beam of 5.0–7.5nA to sputter through the sample surface. A 30 x 30 μm^2 raster and a 400 μm field aperture were used, which only allowed transmission of ions from the innermost 3.8 μm diameter of the beam crater. Secondary magnet mass calibration was done before each measurement, and mass resolving power was > 6000 (m/dm at 10 % peak height). We measured $^{19}F/^{30}Si$ and $^{35}Cl/^{30}Si$ ratios in glass standards D51-3, D52-5, 519-4-1, 46D, 1649-3, 1654-3 to produce a calibration curve for each session. Glass standard F and Cl concentrations are available in Rose-Koga (2008). Matrix effects were considered negligible, following the conclusions of Hauri et al. (2002). No nominally anhydrous mineral standards currently exist for F and Cl. However, the F and Cl contents of Herasil® 102, an optical quality glass, and Synthetic Forsterite were measured in each of the six sessions over the course of one year (Figure 2.1a and b) and are believed to be very low (E. Hauri, *pers. comm*). Herasil® systematically displayed the lowest F contents, and synthetic forsterite the lowest Cl contents. We conservatively assumed that Herasil® contains no F and synthetic forsterite contains no Cl, such that measured F in Herasil® and measured Cl in Synthetic Forsterite represent our maximum background values for F and Cl respectively, for each session (Table 2.1). This step was critical to conservatively estimate our errors, especially for very low F and Cl concentrations. The decrease of our background values from session 1 to session 4 (Figs. 2.1A and 2.1B) reflects the technical developments associated with this work. In Figure 2.1C and 2.1D, we illustrate a typical week of measurements, where machine tuning is essential to reach the lowest possible background values. Analytical uncertainties over ten counting cycles (internal precision: typical standard error (SE) <1 % F, <2% Cl) were combined with calibration curve regression uncertainties (accuracy: typical error 5% F, <10% Cl) to yield no more than 10 % error for F measurements, and 12 % error for Cl measurements. Measurements where the standard deviation over ten counting cycles was greater than 20% were excluded from the data set. The combination of those two errors (2SE plus error on calibration curve) corresponds to the positive error bar on all of our figures. The negative error bars are larger because, in addition to those two errors, we have added the conservative uncertainty on the maximum background defined by Herasil® and Synthetic Forsterite measurements (Fig. 2.1).

Lithium, Be, and B measurement details, along with electron microprobe methods for major element analyses, can be found in the supplementary materials.

2.5 Results

2.5.1 F, Cl, Li, Be, and B variability in mantle minerals

Measuring the primary F and Cl contents of mantle minerals

The peridotite samples selected for this study are all relatively fresh rocks that display less than 20% alteration and minimal weathering features. Individual spot measurements and profiles were conducted on the least altered grains in order to minimize the potential disturbance of primary F and Cl contents of minerals by secondary processes. Individual measurements can be found in Table 2.1. F and Cl concentration profiles were measured in orthopyroxene for samples Fin1b (Fig. 2.2), Fin10 (Fig. 2.3), and J98-10 (Fig. 2.S1), in clinopyroxene for samples Fin1b (Fig. 2.4), Fin10 (Fig. 2.5), and J127-09 (Fig. 2.S2), and in amphibole for sample Fin1b (Fig. 2.6). For the Finero samples, F and Cl profiles followed the same path as Li, Be, and B profiles. Other analyses consisted of individual spots. All of our analyses were performed on surfaces devoid of cracks or other alteration features. Still, Cl concentrations showed local enrichments within the same grain, even on surfaces that appear to be pristine under reflected light (Fig. 2.S2A). Petrographic observations using high magnification in transmitted light revealed that small fractures (μm-wide) located below the grain's surface and not visible in reflected light locally cause elevated Cl signals (Fig. 2.S2C). These range from two to ten times the average Cl concentration of the grain, suggesting local Cl enrichment through secondary processes. Thus, incipient alteration can significantly affect the apparent Cl content of primary minerals. Therefore, we discarded data that were acquired within 30 μm or less of an alteration feature present at depth (~10% of our total dataset). Fluorine concentrations were not affected by the presence of these micro-cracks (Fig. 2.S2B).

F, Cl, Li, Be, B variability along intra-grain profiles in clinopyroxene

Apart from four high Cl values linked to the presence of micro-cracks, Cl concentrations in J127-09 clinopyroxene show limited variability across the grain (Fig. 2.S2c). Likewise, Cl concentrations in Fin1b (Fig. 2.4) and Fin10 (Fig. 2.5) clinopyroxene are indistinguishable from core to rim. With respect to F, elevated concentrations are observed in the core of Fin1b clinopyroxene (Figure 2.4). The F content of clinopyroxene can significantly vary between samples. For example, J127-09 clinopyroxene displays a restricted F content from core to rim, averaging 2.3 μg/g (Fig. 2.S2b). Although lower F contents are observed in the core of the grain if we only consider 2SE uncertainty, variations are indistinguishable within our conservative background values. However, in Fin10, F ranges from 18 μg/g in the core to 6 μg/g at the rim (Fig. 2.5b). In Fin1b, F is even more variable, ranging from 44 μg/g in the core to 4 μg/g at the

rim (Figure 2.4). Boron and Be concentrations in Fin1b are slightly higher in the core, while Li is slightly depleted in the core and directly adjacent to the rim. To summarize, the F contents of Josephine clinopyroxene are low and display limited variability, while the cores of Finero clinopyroxenes are highly enriched in F (core concentrations up to ten times the rim). Also, profiles in Finero clinopyroxene indicate that B and Be correlate with F, while Li does not correlate with other elements.

F, Cl, Li, Be, B variability along intra-grain profiles in orthopyroxene

Cl concentrations in orthopyroxene are low and have limited variability (Figures 2.2, 2.3, 2.S1). Although lower F contents are observed in the core of J98-10 orthopyroxene if we only consider 2SE uncertainty (Fig. 2.S1), we cannot distinguish variations within our conservative background values. In Fin1b orthopyroxene profile (Fig. 2.2), F, Be, B and Li are slightly depleted at the edges. Similar to Fin1b clinopyroxene, the core of Fin1b orthopyroxene is depleted in Li, and that depletion is not reflected in any other elements. Fluorine in Fin10 orthopyroxene is more variable (Fig. 2.3), ranging from 3.8 μg/g in the core to 1.8 μg/g at the rim. To summarize, the F contents of Josephine orthopyroxene are low and display limited variability, while the cores of Finero orthopyroxenes tend to be slightly enriched in F compared to the rims. Also, profiles in Finero orthopyroxene indicate that B and Be may correlate with F, but higher precision would be needed to determine this.

F, Cl, Li, Be, B variability along intra-grain profile in amphibole

A hornblende from sample Fin1b was also analyzed for F, Cl, Li, Be, and B along a 2-mm profile (Fig. 2.6). Measurements yielded an average F and Cl content of 916 μg/g and 10.2 μg/g respectively, significantly higher than in pyroxenes. Here, F, Cl, B and Be are clearly correlated along the grain profile. As for the pyroxenes, no clear correlation is observed between Li and the other elements.

2.5.2 Fluorine and chlorine inter-mineral partition coefficients

Here we evaluate the inter-mineral partition coefficients ($D_{element}^{mineral\ A/mineral\ B}$) of F and Cl between orthopyroxene-clinopyroxene, olivine-orthopyroxene, and olivine-clinopyroxene (Figures 2.7 and 2.8). In Figure 2.8, inter-mineral partition coefficients for Cl between olivine, orthopyroxene and clinopyroxene are near unity (between 0.94 and 1.3) within our conservative errors. Chlorine appears to be more compatible in clinopyroxene compared to both olivine and orthopyroxene if we only consider 2SE uncertainty, however there are still large uncertainties on low Cl concentrations if one considers a conservative background error. A linear inter-mineral partitioning trend for each mineral pair indicates that Cl partitioning may be controlled by similar processes in those three phases. In Figure 2.7A, inter-pyroxene partitioning data from this study yield a $D_F^{Cpx/Opx}$ of 2.40 with an r^2 value of 0.95. In pyroxenes with low F

concentrations (inset in Figure 2.7b), the trend holds within error, except for one MAR analysis. A linear inter-mineral partitioning trend between orthopyroxene and clinopyroxene indicates that F partitioning may be controlled by similar processes in pyroxenes. The trend defined by our study is also in agreement with limited previous literature data on natural pyroxenes, but differs from experimental studies, which show more scattering. In contrast, olivine-clinopyroxene (Figures 2.7C and 2.7D) and olivine-orthopyroxene (Figures 2.7E and 2.7F) inter-mineral partition coefficients define a wide array of values. F is systematically more compatible in clinopyroxene compared to olivine (range of slope 3–50) and orthopyroxene (slope equal to 2.40), but F compatibility between olivine and orthopyroxene can approach unity in some samples (range of slope 1.19–16.67). Dish Hill and San Carlos samples plot near a steep trend defined by previously published values for abyssal samples (Warren and Hauri 2014). Alternatively, samples from Kilbourne Hole, Grand Canyon, the Thumb and Finero proportionally contain more F in olivine. An array of inter-mineral partitioning trends between pyroxenes and olivine indicates that controls on F partitioning are different for those minerals. Based on inter-mineral partitioning data, we infer that Cl compatibility ranks as follows: amphibole > cpx > olivine ~ opx, while for F compatibility ranks as follows: amphibole > cpx > opx ≥ olivine, depending on the tectonic context of the samples. For comparison, Hauri (2006) and Dalou (2012) concluded that F compatibility is arranged as cpx > opx > garnet >olivine, while Mosenfelder (2013) concluded that cpx > olivine > opx > garnet. Our new inter-mineral partitioning data reconcile previous discrepancies as they illustrate how orthopyroxene and olivine from different tectonic environments can accommodate variable amounts of F, leading to variable halogen compatibility as a function of mineral chemical composition, melt/fluid composition, and potentially extrinsic variables such as pressure and temperature.

2.5.3 Correlation between F, Cl and major elements

Major element data for all olivine, orthopyroxene, and clinopyroxene are presented in Table 2.4. Major element data for Fin1b profiles in clinopyroxene (Fig. 2.4), orthopyroxene (Fig. 2.2), and amphibole (Fig. 2.6) can be found in Table 2.5. We plotted the major element content of mantle minerals versus F and Cl to investigate the incorporation mechanisms of F and Cl in the crystal structure of minerals. The F and Cl contents of olivine do not correlate with any major element. The F content of orthopyroxene in this study displays a robust correlation (r^2=0.95) with Na (Figures 2.9A and 2.9B). Although no correlation is observed between Al and F in orthopyroxene from different samples (Figure 2.S3B), Al content and F-Be-B in Fin1b orthopyroxene are consistently depleted at the rims (Figure 2.2), which could indicate that they broadly correlate. Na is too low to show any correlation. The F content of clinopyroxene analyzed in this study also displays a broad correlation (r^2=0.84) with Na (Figures 2.9C and 2.9D). Although no relationship is observed between Al and F in clinopyroxene from different samples (Figure 2.S3A), we observe a correlation between Na and Al content and F-Be-B in Fin1b clinopyroxene, where all those elements are enriched in the core of the grain (Fig. 2.4).

Recasting clinopyroxene chemical compositions into end-member pyroxene compositions (En, Fs, Wo) showed no relationship with F concentration, nor with $D_F^{cpx/melt}$ beyond the negative En vs. $D_F^{cpx/melt}$ correlation shown by Guggino (2012). In addition, Na and Al clearly correlate with F-Cl-Be-B in amphibole (Fig. 2.6).

2.6 Discussion

2.6.1 Incorporation mechanisms of F and Cl in olivine

Major element data from this study do not correlate with F and Cl concentrations in olivine, indicating that their incorporation may not be primarily controlled by crystal chemistry. That being said, trends between major elements (weight %) and halogens (μg/g) in olivine are difficult to discern and we leave open the possibility of coupled exchanges between species at low concentrations. To our knowledge, no incorporation mechanism has been proposed for Cl in olivine, and the lack of experimental data for Cl partitioning between olivine and melt prevent us from investigating the effect of melt composition on the Cl content of olivine.

A limited number of experimental studies provide information on the partitioning of F between olivine and mantle-derived melts (Hauri, Gaetani et al. 2006, O'Leary, Gaetani et al. 2010, Beyer, Klemme et al. 2012, Guggino 2012, Bernini, Wiedenbeck et al. 2013, Dalou, Koga et al. 2014). Guggino (2012) suggests that F partitioning is controlled primarily by the ratio of non-bridging oxygen (NBO) atoms to tetrahedrally coordinated cations (NBO/T) in the melt, where NBO/T decreases with increasing degree of polymerization in the silicate melt (Mysen and Cody 2004, Mysen 2007). We compiled experimental studies that provide partition coefficients of F between olivine and silicate melt ($D_F^{olivine/melt}$) at T ≈ 1000–1360°C and P ≈ 0.1–3 GPa, and calculated the NBO/T of mantle-like melts in those experiments (Fig. 2.10). We included both hydrous and anhydrous experimental data due to limited available data; therefore, the water content of the mineral phases could be an additional variable, which cannot be addressed at present. We incorporated the depolymerizing effects of H_2O (Mysen 2007) and F (Dalou, Koga et al. 2014) on the NBO/T values, assuming equivalent effects of H_2O and F on melt polymerization (Dalou, Koga et al. 2014). The combined H_2O and F corrections improve the fit slightly (r^2 from 0.89 to 0.92). The robust positive correlation between $D_F^{olivine/melt}$ and the degree of melt polymerization indicates that if melting or melt-rock reaction produces more polymerized melts, increasing amounts of F are accommodated in the crystal structure of olivine, as originally suggested by Guggino (2012) and confirmed by this compilation. F compatibility in olivine increases by an order of magnitude with increasing melt polymerization (Figure 2.10A). Mysen (2007) found similar melt polymerization effects on the partitioning of Ca, Mg, and transition metals between olivine and melt, where mineral-melt partition coefficients exponentially increased with melt polymerization. We note that oxygen fugacity could also play a

role in the incorporation of halogens into the crystal structure by charge balancing with Fe^{3+} (Guggino 2012). However, using the calculated ferric iron content of our samples, we did not observe an obvious correlation between ferric iron and halogen content. Olivine mineral-melt partition coefficients from available literature show a slight temperature dependence, however this effect does not appear to be the dominant control on the NBO/T trend. Thus, the data indicate that the effect of melt polymerization plays a larger role than does temperature on the partitioning of F between olivine and melt.

2.6.2 Incorporation mechanism of F and Cl in orthopyroxene

The F content of orthopyroxene is strongly controlled by Na content (r^2=0.95; Fig. 2.9B). Thus, our measurements from natural samples support an incorporation mechanism where Na^+ in the M2 octahedral site charge balances F in the O sites. We also found that Al may correlate with F-Be-B in orthopyroxene, in agreement with Mosenfelder who suggested that Al might play a limited role in F incorporation in orthopyroxene. Experimental datasets that provide $D_F^{opx/melt}$ and NBO/T of melts (Fig. 2.10B) are more limited than for clinopyroxene and olivine. However, given the strong correlation that we obtain between F and Al-Na contents in our natural orthopyroxene, crystal chemistry is likely the primary control on F incorporation into natural orthopyroxene. The variability observed in inter-mineral partitioning values of F between orthopyroxene and olivine (Figures 2.7E and 2.7F) is linked to the fact that F in olivine is controlled by the NBO/T of melts, while F in orthopyroxene is primarily controlled by the Na and Al content of orthopyroxene.

2.6.3 Incorporation mechanism of F and Cl in clinopyroxene

Experimental literature data for water content and fluorine content of cpx show a broad correlation (r^2 =0.64) that implies similar incorporation mechanisms for those two elements, e.g. tetrahedral Al^{3+} charge balancing F. Our data, aggregated with literature data, show a broad positive correlation between Na and F contents of clinopyroxene (Figures 2.9C and 2.9D), indicating that crystal chemistry exerts influence on the incorporation of F into clinopyroxene. In Finero samples (Fig. 2.4), both Na and Al correlate with F-Be-B, confirming that Al should also play a role in the incorporation of F into clinopyroxene. K_2O data is unavailable but it has also been suggested that coupled K^+ substitution in the pyroxene M sites may be another mechanism for F incorporation into clinopyroxene (Mosenfelder and Rossman 2013). Melt composition can also play a role in halogen partitioning between clinopyroxene and melt (Dalou, Koga et al. 2012, Guggino 2012, Dalou, Koga et al. 2014, Bénard, Koga et al. 2017). We compiled available experimental data on halogen partitioning between cpx and melt (Hauri, Gaetani et al. 2006, O'Leary, Gaetani et al. 2010, Guggino 2012, Dalou, Koga et al. 2014), in experiments performed at T ≈ 1000–1360°C and P ≈ 0.1–3GPa. We used both anhydrous and hydrous experimental data due to the limited literature data available, and corrected NBO/T for the depolymerizing effects of H_2O and F as outlined in Dalou (2014). We note that the water

content of mineral phases could be an additional variable, which cannot be addressed with the current data. In Figure 2.10C, a broad correlation exists between NBO/T of experimental melts and F concentrations in clinopyroxene where the amount of F incorporated in clinopyroxene increases with increasing melt polymerization ($r^2 = 0.70$). Similar effects have been found for trace elements in clinopyroxene, where the mineral melt partition coefficient increases exponentially with increasing melt polymerization (Gaetani 2004). Our data, combined with previous experimental studies, support the hypothesis that there are various means by which halogens can be incorporated into the crystal lattice of Cpx. We conclude that the F content of clinopyroxene is a function of both crystal chemistry (e.g. Na and Al contents) and melt structure (NBO/T). We note that oxygen fugacity, and thereby ferric iron content could also play a role in the accommodation of F in Cpx, however we did not find a correlation between ferric iron content (calculated by stoichiometry) and F concentration in our samples. Further work would be needed to better constrain the role of ferric iron in the accommodation of crystal site defects. The variability observed in inter-mineral partitioning values of F between clinopyroxene and olivine (Figures 2.7C and 2.7D) is linked to the fact that F in olivine is primarily controlled by the NBO/T of melts, while F in Cpx is controlled by a combination of crystal chemistry and melt structure.

2.6.4 Halogens as tracers of fluid/melt percolation in mantle minerals

Samples from our study come from a variety of tectonic environments and provide valuable information on the cycling of halogens during various mantle processes.

Josephine samples have the highest Cl concentrations in clinopyroxene (> 0.6 μg/g) and olivine (> 0.4 μg/g), and one of the highest Cl concentrations in orthopyroxene (> 0.4 μg/g). Although those values are conservatively considered as maximum values, the most depleted samples in our study contain the highest Cl contents (Fig. 2.8), and the lowest F values (< 3 μg/g F; Fig. 2.7). Low F contents in the Josephine samples are consistent with high degrees of flux melting in the Josephine peridotite (Le Roux, Dick et al. 2014), whereas slight enrichment in Cl and F at the edges of pyroxene grains (Figures 2.S1 and 2.S2) are consistent with late percolation of Cl-F-fluids/hydrous melts (e.g., boninite; (Le Roux, Dick et al. 2014)).

Cl concentrations in minerals from Dish Hill, Kilbourne Hole, San Carlos and Grand Canyon are the lowest of our sample selection and do not record the percolation of Cl-rich fluids. F contents in samples from Dish Hill and San Carlos plot near a steep trend defined by previously published values for abyssal samples (Fig. 2.7) (Warren and Hauri 2014). The fact that the Dish Hill samples follow a similar trend as abyssal peridotites is consistent with a process where Dish Hill lherzolites formed by melting and refertilization beneath mid-ocean ridges (Luffi, Saleeby et al. 2009). The same authors suggest that the mantle underneath Dish Hill has been rejuvenated by the emplacement of flat-subducted young oceanic peridotites. In contrast, samples from Grand Canyon, Kilbourne Hole, and the Thumb define a distinct trend (Figs. 2.7C–2.7F). Those samples contain proportionally more F in olivine, which we ascribe to

increased compatibility of F in olivine during melt-rock reactions with polymerized (siliceous) and hydrous melts. This interpretation supports the findings of Lee (2005) who postulated that the REE patterns found in Thumb xenoliths require interaction with a slab melt. This is also in agreement with previous work that showed that flat slab subduction of the Farallon plate during the early Cenozoic hydrated the sub-continental lithospheric mantle (Dixon, Dixon et al. 2004, Lee 2005, Humphreys and Niu 2009), and with the fact that the Thumb minerals contains the highest water content of any Colorado Plateau xenoliths (Li, Lee et al. 2008).

Core to rim variations are nearly ubiquitous in the Finero samples analyzed. The cores of Finero clinopyroxenes are enriched in F, while Finero orthopyroxenes show no such enrichments. The correlation between major elements and volatile elements likely reflects re-equilibration with several generations of fluids/melts. Finero samples plot on a similar trend defined by Grand Canyon, Kilbourne Hole and Thumb samples (Fig. 2.7). Thus, similar to those samples, we attribute F enrichment in olivine to interaction of the mantle with hydrous siliceous melts. Our data are consistent with previous studies that suggest that several episodes of pervasive metasomatism occurred in Finero (Zanetti, Mazzucchelli et al. 1999, Giovanardi, Morishita et al. 2013), which would be reflected in the core to rim variability that we observe. In particular, Selverstone and Sharp (2011) suggested that both Cl-rich fluids and an evolved hydrous melt had percolated the Finero mantle, which would explain why those samples show various generations of Cl and F enrichments. The single amphibole measured in this study (Finero 1b) shows F to be 100x more abundant than Cl, lending support to the suggestion of Bénard et al. (2017) that amphibole crystallization effectively depletes metasomatic melts in F relative to Cl due to the compatible nature of F in amphibole. Although rapid diffusion of Li may have erased correlations between Li and other elements, a multi-phase process would also explain the depletions in F, Li, Be and B in the rims of mantle minerals. It is not clear whether Cl is enriched or depleted at the grain edges. The late percolation of fluids could have leached F, B, Be and Li out of the pyroxene grains, resulting in the rim depletions. Such rim depletions are observed in all grains, hence those elements must have been lost from the rock when a fluid phase migrated along the grain boundaries Taken together, the F, Cl (and Li-Be-B) variations in pyroxenes and amphibole depict a multi-stage history in Finero that involves diffusive re-equilibration and interaction with several generations of fluids/melts.

Finally, F in the MAR pyroxenes and olivine does not follow the trend defined by the limited number of abyssal samples (Warren and Hauri 2014). Further work is needed to identify the reason for inter-oceanic variability. Also noteworthy, the minerals from Balmuccia (BM5) plot between the two extreme trends defined by Dish Hill and Thumb (Figure 2.7C–2.7D), showing no specific enrichment from Cl-rich fluids or F-rich hydrous melts, consistent with a mantle that experienced limited amounts of metasomatism.

2.6.5 Fluorine and chlorine budget of the upper mantle

Previous studies have indirectly estimated the F-Cl budget of the MORB mantle by using the halogen content of primitive basalts (Salters and Stracke 2004) and olivine hosted melt inclusions (Saal, Hauri et al. 2002). In particular, these studies have relied on elemental ratios that are minimally fractionated during mantle melting, (e.g., F/P, F/Nd, Cl/K, and Cl/P) and/or on elemental correlations (e.g., CO_2 vs Cl) to estimate the halogen budget of the MORB mantle. Estimates range from 11–17 μg/g F and 0.38–5 μg/g Cl for depleted MORB mantle (Saal, Hauri et al. 2002, Salters and Stracke 2004, Workman and Hart 2005, le Roux, Shirey et al. 2006, Shaw, Behn et al. 2010, Beyer, Klemme et al. 2012, Le Voyer, Cottrell et al. 2015) to 8–31 μg/g F and 0.4–22 μg/g Cl (Shimizu, Saal et al. 2016) if ultra-depleted (D-DMM) and enriched MORB mantle (E-DMM) are accounted for (Table 2.6). Based on results from this study, we provide two independent methods to estimate the F and Cl budget of the upper mantle.

First, we use a compilation of published partition coefficients (Fig. 2.10) and inter-mineral partition coefficients from this study (Figure 2.7a and 2.7b) to estimate the bulk partition coefficients for F and Cl applicable to DMM melting. Experimental literature provides highly variable data for halogen partitioning between olivine, pyroxene, and silicate melts. $D_F^{olivine/melt}$ ranges from 0.007 to 0.146 (Hauri, Gaetani et al. 2006, Dalou, Koga et al. 2012, Guggino 2012, Dalou, Koga et al. 2014), $D_F^{opx/melt}$ ranges from 0.016 to 0.139 (Hauri, Gaetani et al. 2006, Dalou, Koga et al. 2012, Dalou, Koga et al. 2014), and $D_F^{cpx/melt}$ ranges from 0.005 to 0.219 (Hauri, Gaetani et al. 2006, O'Leary, Gaetani et al. 2010, Dalou, Koga et al. 2012, Guggino 2012, Dalou, Koga et al. 2014). In order to estimate the bulk partition coefficients of F and Cl during DMM melting, we use the correlation between $D_F^{olivine/melt}$, $D_F^{cpx/melt}$ and NBO/T (Figure 2.10a and 10c) of average N-MORB (0.81; (Gale, Dalton et al. 2013)). For DMM melting, $D_F^{olivine/melt}$ = 0.005 and $D_F^{cpx/melt}$ = 0.051. We then utilize the robust correlation of F in coexisting pyroxenes (slope of 2.40 in Figure 2.7B), to calculate $D_F^{opx/melt}$ = 0.02. Based on the modal abundances of DMM (Workman and Hart 2005), these calculations together yield $D_F^{mantle/melt}$ = 0.017. Experimental data for Cl partitioning is very limited. Here we use $D_{Cl}^{opx/melt}$ of 0.002±0.001 from the anhydrous experiment CD1H0 (Dalou, Koga et al. 2014) and use inter-mineral partitioning data to calculate a $D_{Cl}^{cpx/melt}$ = 0.003 based on the inter-mineral partition slope of our data of 1.3. Our data show that olivine and orthopyroxene have similar partition coefficients for Cl, thus we use the same value for olivine as orthopyroxene of 0.002. These calculations together yield $D_{Cl}^{mantle/melt}$ = 0.002±0.001, an order of magnitude lower than the bulk partition coefficient for F. MORB contain on average 250±50 μg/g F and 2–400 μg/g Cl for MORB unaffected by hydrothermal alteration (Saal, Hauri et al. 2002). We assume a batch melting model using the above bulk partition coefficients for F and Cl and average literature F-Cl values in MORB. This procedure yields oceanic peridotitic mantle values

of 4.3±0.9 μg/g for F and 0.004–0.82 μg/g for Cl, which is lower than most previous studies have proposed (Table 2.6) but within the range proposed by Shimizu et al. (2016) and Saal et al. (2002).

Second, we use the F and Cl contents and modal proportions of olivine, orthopyroxene and clinopyroxene from this study to estimate the F and Cl variability of anhydrous peridotite mantle, assuming that all F and Cl is contained in those three minerals and that apatite is not stable in the source of MORB (Konzett and Frost 2009). Our bulk anhydrous peridotite values (excluding hydrous samples from Ivrea Zone) define a range from 1.39 μg/g to 31.1 μg/g for F and from 0.14 μg/g to 0.38 μg/g for Cl (Table 2.6). Our Cl values are in good agreement with Workman and Hart's (2005) estimate of 0.38 ± 0.25 μg/g. Samples believed to be derived from the oceanic mantle (e.g., MAR, Dish Hill) yield more restricted bulk F contents (2.1–9.4 μg/g) that are within the range of the estimate based on bulk partitioning for DMM melting (~ 4 μg/g), and within the lower range of previously published values (e.g., 11 ± 4.5 μg/g; (Salters and Stracke 2004)). The range of F content observed in bulk anhydrous peridotite (Table 2.6) strongly reflects the heterogeneous distribution of F in the Earth's upper mantle and indicates that F is likely enriched in the mantle wedge of subduction zones, as observed in xenoliths from the Colorado Plateau. The presence of F-rich subduction-derived components in the source of MORB could explain why bulk mantle F calculated in oceanic peridotites in this study (2.1–9.4 μg/g) is lower than bulk mantle F previously calculated from MORB (11–17 μg/g). Consistent with this hypothesis, Beyer (2016) suggested that eclogitized oceanic crust could host more F (in omphacitic cpx) per mass unit than the depleted oceanic mantle which is typically cpx poor. In this case, F is transported in the down-going slab via serpentine and amphibole (often tens to thousands of μg/g F), then is partitioned into omphacite upon phase changes as the slab thermally equilibrates, dehydrates, and forms eclogite, effectively returning F to the mantle (Van den Bleeken and Koga 2015). Later melting of such halogen rich lithologies (cpx in particular) could then account for halogen enrichments found in ocean island basalts.

All peridotite samples, regardless of their tectonic setting, yield bulk Cl values (0.14–0.38 μg/g) that are lower than previously published values for DMM (0.4–5 μg/g; (Saal, Hauri et al. 2002, Shaw, Behn et al. 2010, Shimizu, Saal et al. 2016)) and more restricted than our estimate of DMM based on bulk partitioning (0.004–0.82 μg/g) (Figure 2.11). Two scenarios can explain the fact that measured bulk Cl in all mantle peridotites (olivine and pyroxenes combined) is lower than the estimated bulk Cl content of DMM. First, the presence of Cl-rich recycled components in the source of MORB could explain the discrepancy, although there are no constraints on the Cl content of recycled oceanic crust. Second, N-MORB are considered to be uncontaminated by seawater if their Cl/K ratio is 0.01–0.02 or less. However, Cl contamination in MORB by assimilation of hydrothermally altered rock could occur (Michael and Schilling 1989). A very minor contribution of seawater to melts (one to ten parts per thousand) can drastically alter the Cl content of the composite melt. Thus, if all MORB actually experienced some degree of Cl contamination from interaction with seawater or contamination from

seawater-rich material at depth, Cl DMM estimates calculated from MORB and olivine-hosted melt inclusions could be overestimated. To illustrate this, we plotted previous MORB mantle estimates and olivine-hosted melt inclusion (MI) data from various tectonic settings (Table 2.7) along with measurements from this study (Fig. 2.11). Interestingly, our peridotitic MORB mantle F and Cl values used to calculate the melting trends shown in Figure 2.11 agree well with the primary melt inclusion data of Saal et al. (2002). This could indicate that the source of the Siquieros MIs is composed of pure peridotite mantle, (i.e. no enriched component) and that MI Cl contamination is nil.

2.7 Conclusions

We have developed a technique to reliably measure the F and Cl contents of natural peridotite minerals by SIMS down to ≥ 0.4 μg/g F and ≥ 0.3 μg/g Cl. This work is the first extensive study of the distribution of F and Cl in co-existing natural peridotite minerals (olivine, orthopyroxene, clinopyroxene, amphibole). Halogen intra-grain variation can be significant, and the utilization of profiles as opposed to single spots when measuring grains is important to properly characterize minerals. Using previously published experimental studies, we argue that the F content of olivine is strongly controlled by NBO/T of silicate melts, which reflects melt polymerization, and we provide mineral/melt partition coefficients for F and Cl applicable to mantle melting. We propose that the F content of orthopyroxene is strongly controlled by Na and Al content. In addition, the F (and potentially Cl) content of clinopyroxene is controlled by a combination of crystal chemistry (Al, Na) and melt polymerization. In amphibole, F and Cl also correlate with major elements Al and Na. Finally, we show that F, Cl, Be and B concentrations along grain profiles are correlated in both pyroxenes and amphibole. Using F and Cl inter-mineral partition coefficients determined in this study, we show that F and Cl distribution between olivine and pyroxenes in oceanic peridotites and subduction-related peridotites is drastically different. F in oceanic peridotites is mostly hosted in pyroxenes, while the F content of olivine significantly increases in subduction-related peridotites. Further, olivine and pyroxenes from the mantle wedge can be significantly enriched in F compared to un-metasomatized mantle, while Cl contents are consistently low (< 1 μg/g) in all tectonic environments. Finally, assuming that F and Cl in the anhydrous peridotite mantle is entirely contained in olivine and pyroxenes, the bulk F and Cl content of oceanic mantle (2.1–9.4 μg/g F; 0.15–0.32 μg/g Cl) is lower than previous estimates for DMM. These results support the hypothesis that the source of MORB contains F-rich recycled oceanic crust. The bulk Cl budget of all anhydrous peridotites analyzed in this study (0.14–0.38 μg/g Cl) is lower than most previous estimates for DMM. These results suggest that virtually all MORB, including many olivine-hosted melt inclusions, could be variably contaminated by seawater-rich material at depth and that the Cl content of DMM could be overestimated. The halogen contents of mantle

minerals are a unique tool to understand the distribution and cycling of halogens, from ridge settings to subduction zones.

2.8 Acknowledgments

This research was supported by grant NSF EAR-P&G 1524311 and DOEI award 18563 to VLR. We thank two anonymous reviewers for their insights, which improved the manuscript. We also thank Erik Hauri for providing the Herasil® glasses, Henry Dick for providing the MAR sample, and Nobumichi Shimizu for providing the Synthetic Forsterite grains. Urann was supported by the Stanley W. Watson Student Fellowship Fund based at WHOI.

2.9 Figures

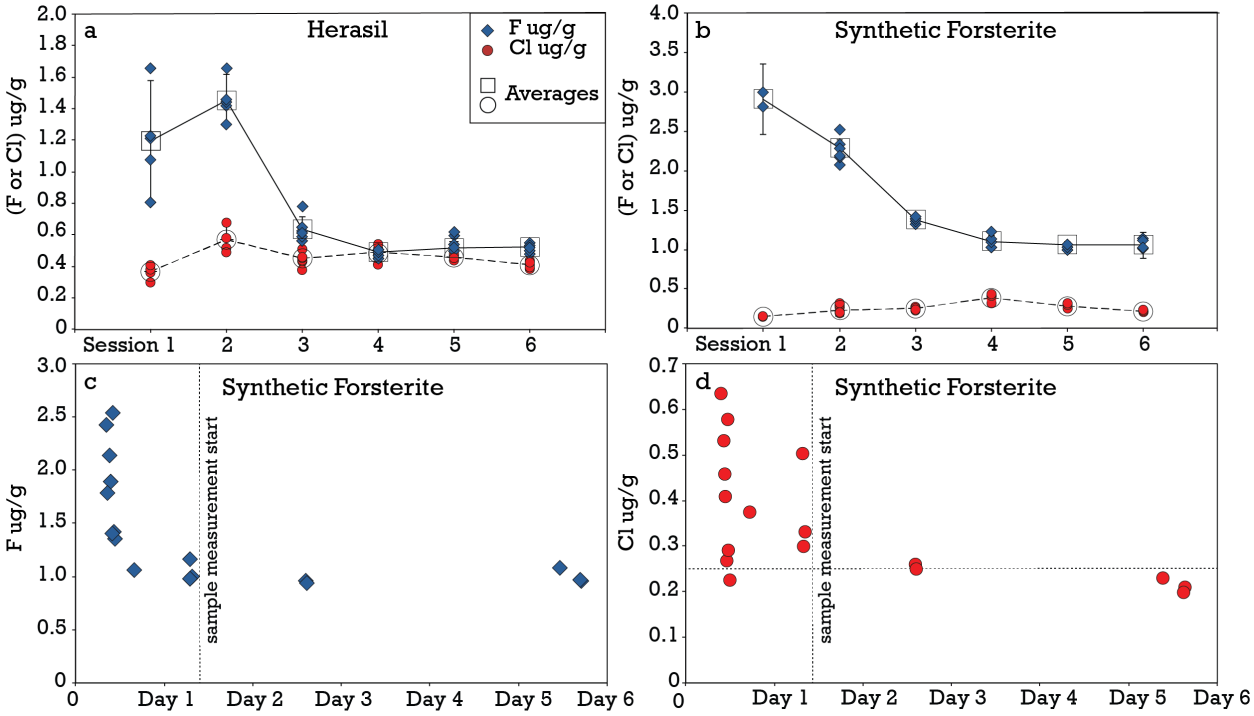

Fig. 2.1 a. F and Cl concentrations in Herasil® glass over six analytical sessions, with 95% confidence standard error. b. F and Cl concentrations in Synthetic Forsterite over six analytical sessions, with 95% confidence standard error. F (c) and Cl (d) concentrations in Synthetic Forsterite over a 6-day SIMS session showing the setting optimization at the beginning of each session, after which natural samples measurements started (vertical line) once Synthetic Forsterite stabilized at its lowest F and Cl value (horizontal line shows the maximum Cl background value for that particular session). Session measurements can be found in Table 1.

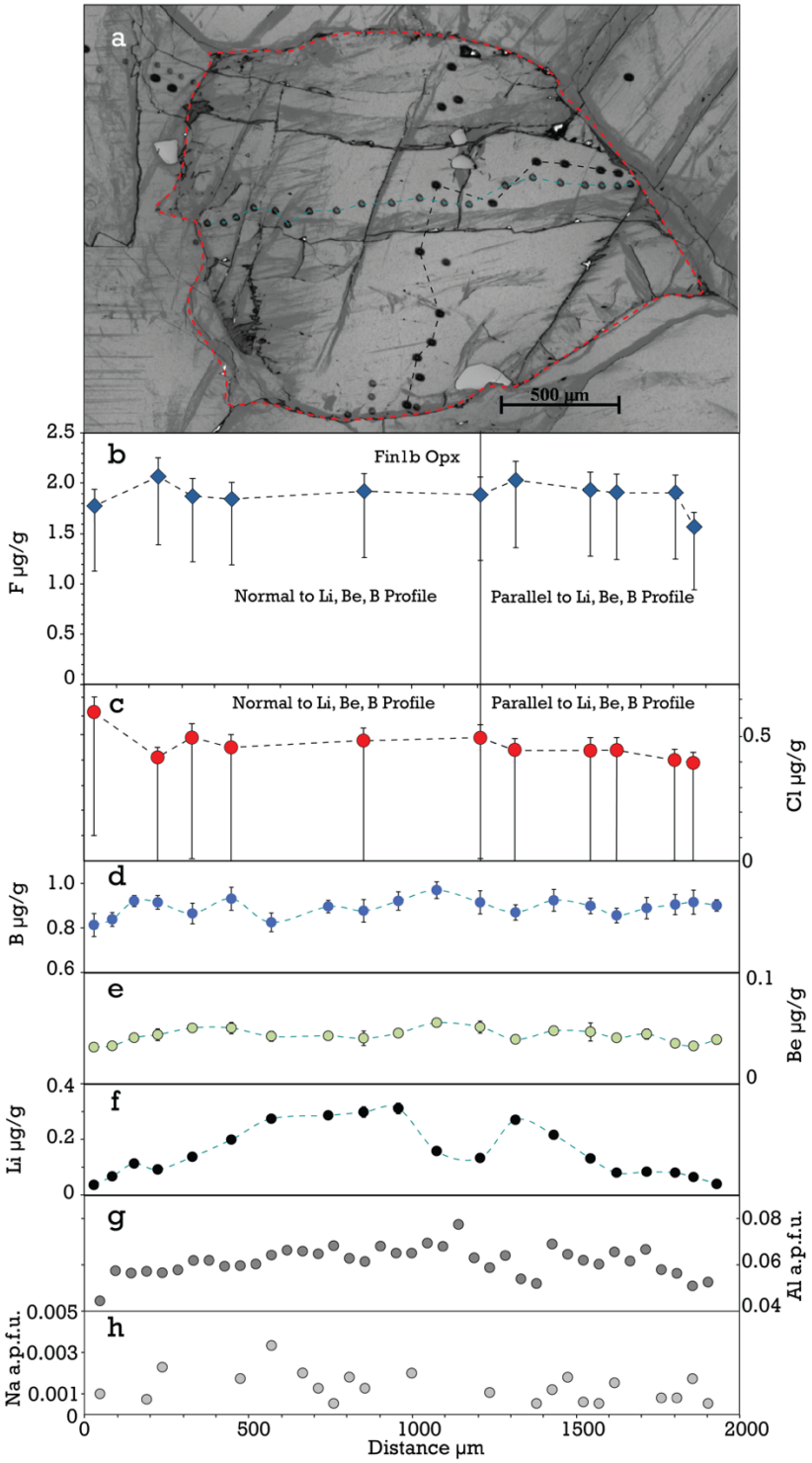

Fig. 2.2 Concentration profiles in Fin1b orthopyroxene. Two F and Cl core to rim profiles were conducted, one parallel to B, Be, Li. Al, Na profiles and the other normal to it. Positive error bars are internal errors propagated with calibration curve errors. Negative error bars are internal errors propagated with calibration curve errors and maximum background errors monitored by Cl measurements in Synthetic Forsterite and F measurements in Herasil® glass.

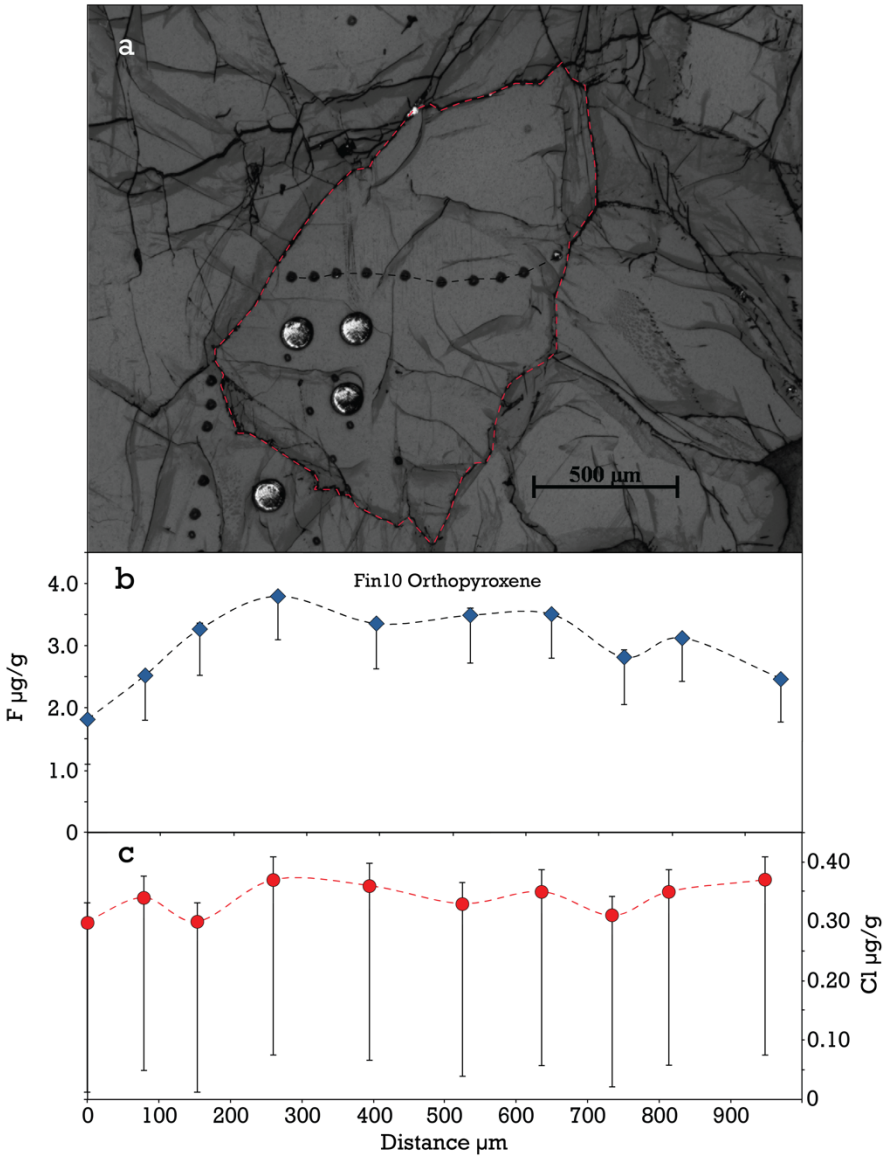

Fig. 2.3 F and Cl profile across Fin10 orthopyroxene. Positive error bars are internal errors propagated with calibration curve errors. Negative error bars are internal errors propagated with calibration curve errors and maximum background errors monitored by Cl measurements in Synthetic Forsterite and F measurements in Herasil® glass. Individual measurements are reported in Table 3.

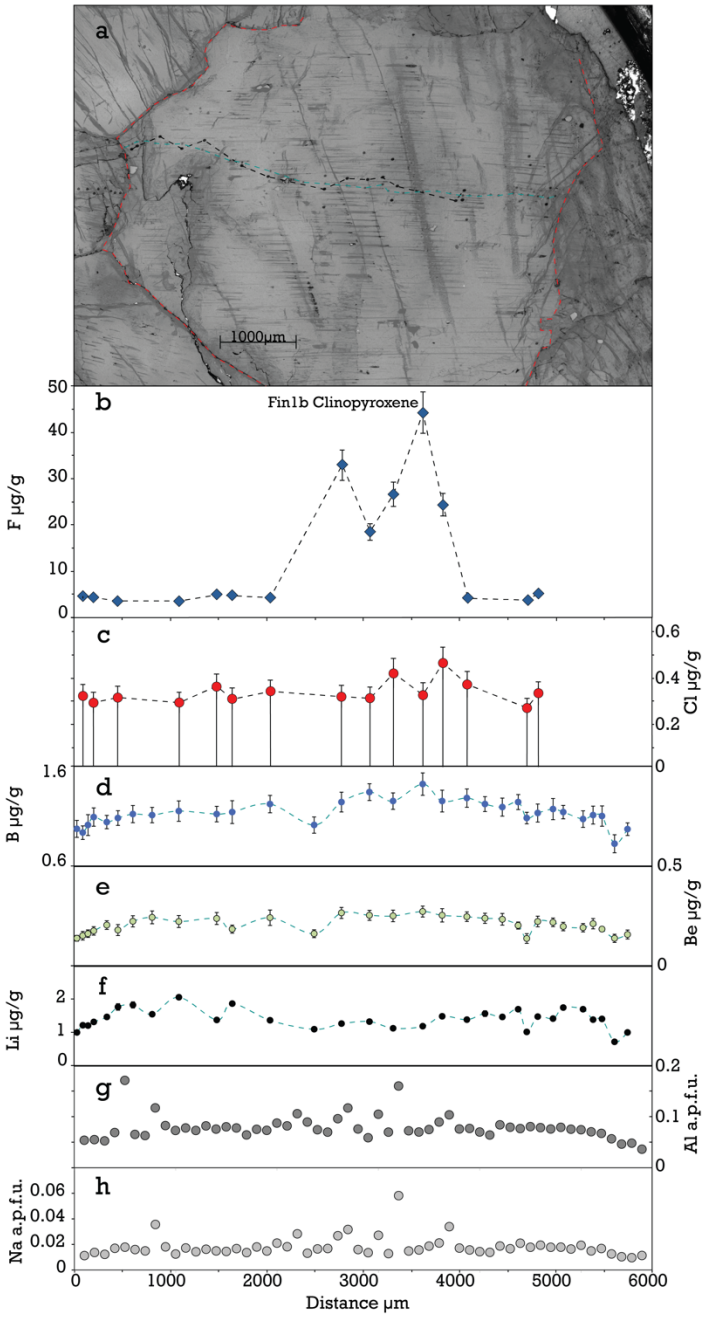

Fig. 2.4 Concentration profiles for Fin1b clinopyroxene. F and Cl profiles were conducted parallel to B, Be, Li, Al, Na profiles. Positive error bars are internal errors propagated with calibration curve errors. Negative error bars are internal errors propagated with calibration curve errors and maximum background errors monitored by Cl measurements in Synthetic Forsterite and F measurements in Herasil® glass. Individual measurements are reported in Tables 3 and 4.

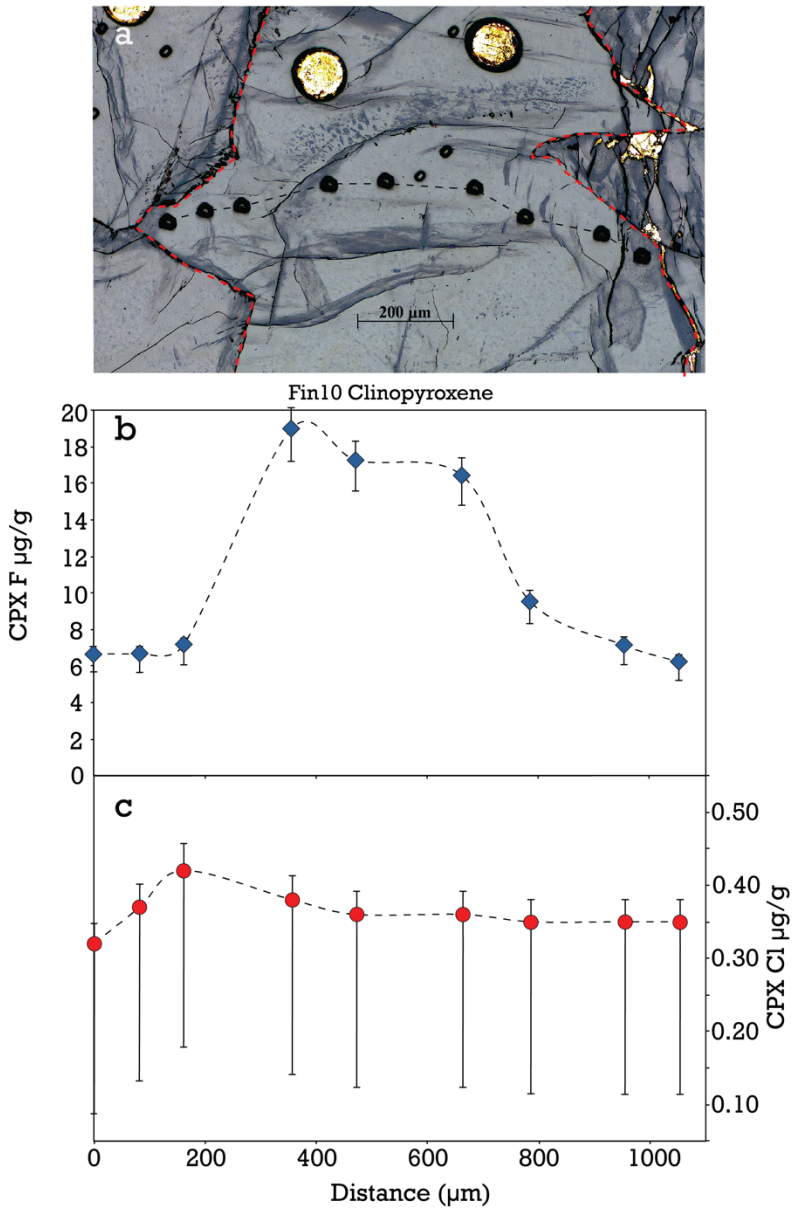

Fig. 2.5 a. Reflected light photomicrograph of Fin 10 clinopyroxene, with grain boundary outlined with red dashed line and SIMS profile denoted with black dashed line. **b.** F profile and **c.** Cl profile across Fin10 clinopyroxene. Positive error bars are internal errors propagated with calibration curve errors. Negative error bars are internal errors propagated with calibration curve errors and maximum background errors monitored by Cl measurements in Synthetic Forsterite and F measurements in Herasil® glass. Individual measurements are reported in Table 3.

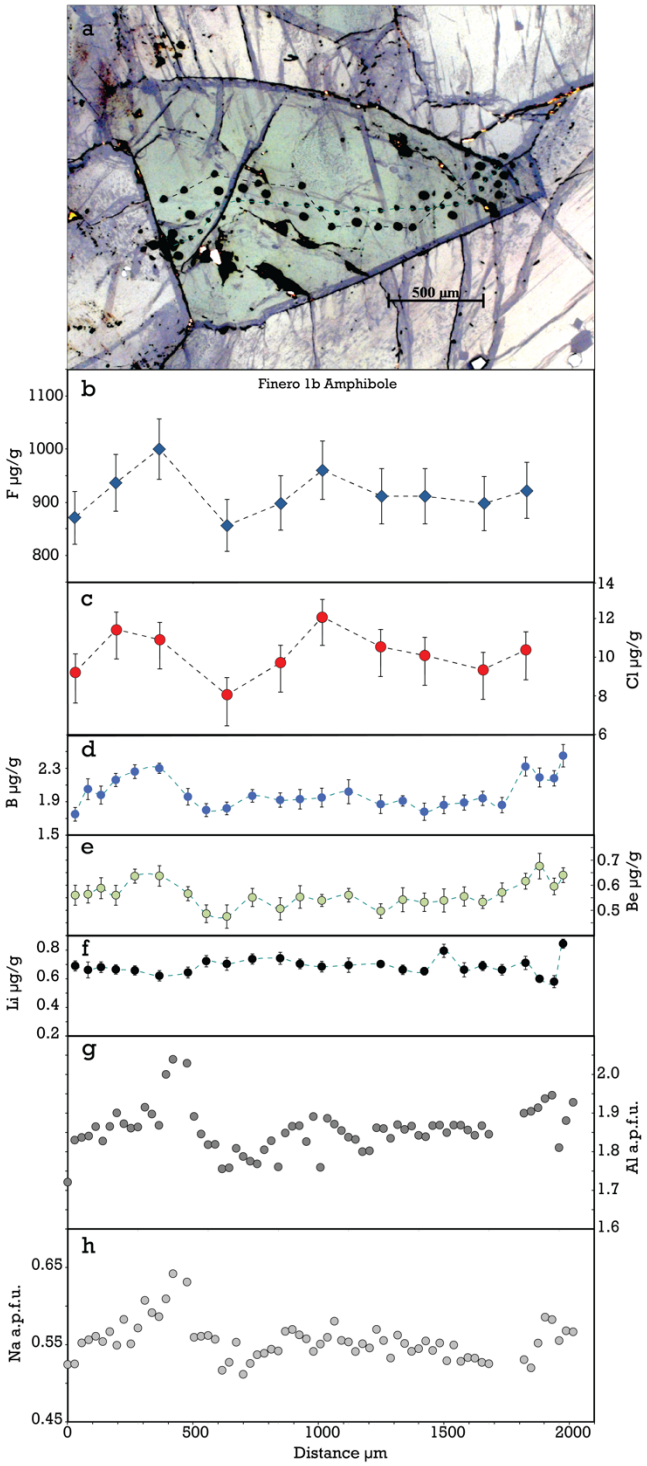

Fig. 2.6 Concentration profiles in Fin1b amphibole. F and Cl profiles were conducted parallel to B, Be, Li, Al, Na profiles. Positive error bars are internal errors propagated with calibration curve errors. Negative error bars are internal errors propagated with calibration curve errors and maximum background errors monitored by Cl measurements in Synthetic Forsterite and F measurements in Herasil® glass. Individual measurements are reported in Tables 3 and 4.

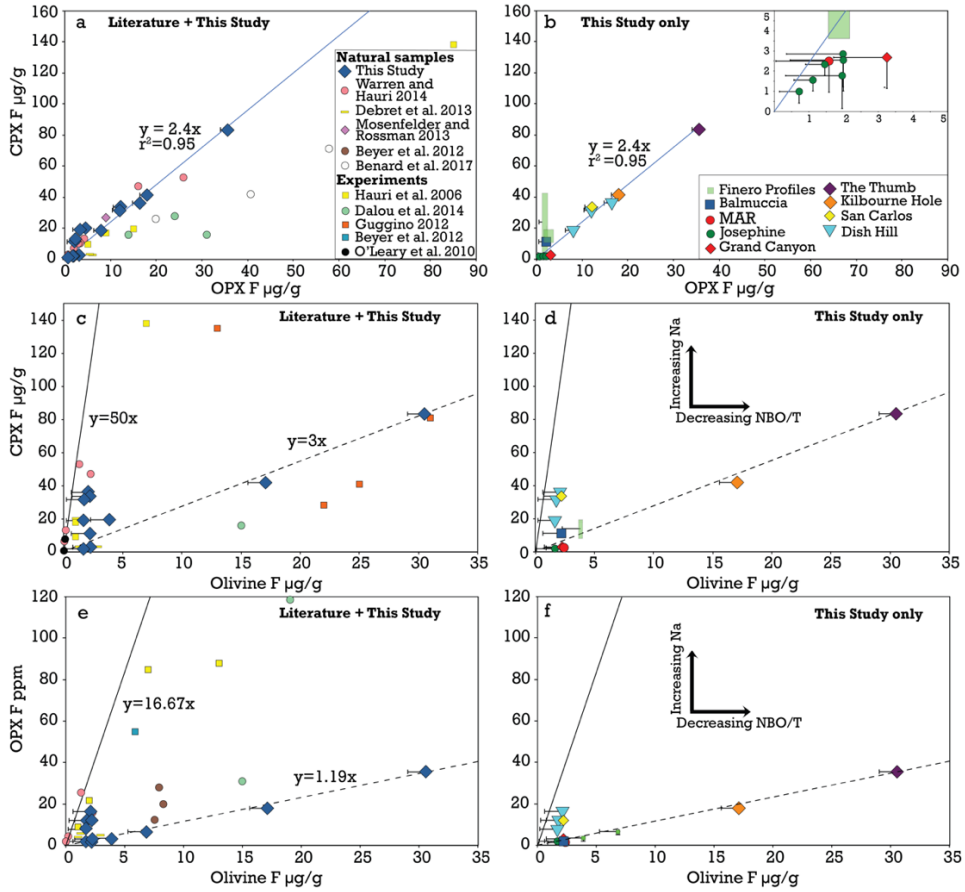

Fig. 2.7 Inter-mineral partition coefficients for F between coexisting olivine, orthopyroxene and clinopyroxene. Since Finero samples have the largest intra-grain range of concentrations, profiles are identified by rectangles. **a.** Opx-Cpx inter-mineral partition coefficients from literature and this study. Blue solid line denotes linear best fit (this study only) where the slope of the line equals the inter-mineral partition coefficient. **b.** Opx-Cpx inter-mineral partition coefficients from this study only. Inset expands low (sub-5µg/g) F concentrations. Blue solid line denotes linear best fit (this study only) where the slope of the line equals the inter-mineral partition coefficient. **c**. Ol-Cpx inter-mineral partition coefficients from literature and this study. **d.** Ol-Cpx inter-mineral partition coefficients from this study only. **e.** Ol-Opx inter-mineral partition coefficients from literature and this study. **f.** Ol-Opx inter-mineral partition coefficients from this study only. Black solid lines in **c**, **d**, **e**, and **f** denote inter-mineral partition coefficients using data from Warren and Hauri (2014). Black dashed lines denote trends for a sub-set of samples from this study. Positive error bars are internal errors propagated with calibration curve errors. Negative error bars are internal errors propagated with calibration curve errors and maximum background errors monitored by Cl measurements in Synthetic Forsterite and F measurements in Herasil® glass. Error bars not visible are smaller than symbols. Individual measurements are reported in Table 1.

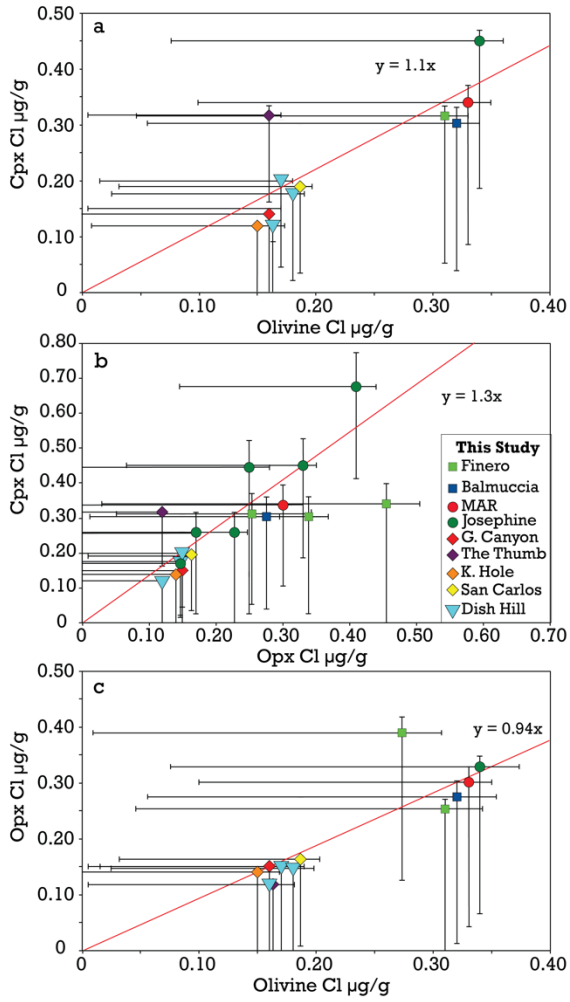

Fig. 2.8 Inter-mineral partition coefficients for Cl between coexisting olivine, orthopyroxene and clinopyroxene from this study. **a.** Ol-Cpx intermineral partition coefficients. Red line denotes linear best fit **b.** Opx-Cpx intermineral partition coefficients. Red line linear best fit. **c.** Ol-Opx intermineral partition coefficients. In **a**, **b**, and **c**, red line denotes linear best fit. Positive error bars are internal errors propagated with calibration curve errors. Negative error bars are internal errors propagated with calibration curve errors and maximum background errors monitored by Cl measurements in Synthetic Forsterite and F measurements in Herasil® glass. Individual measurements are reported in Table 1.

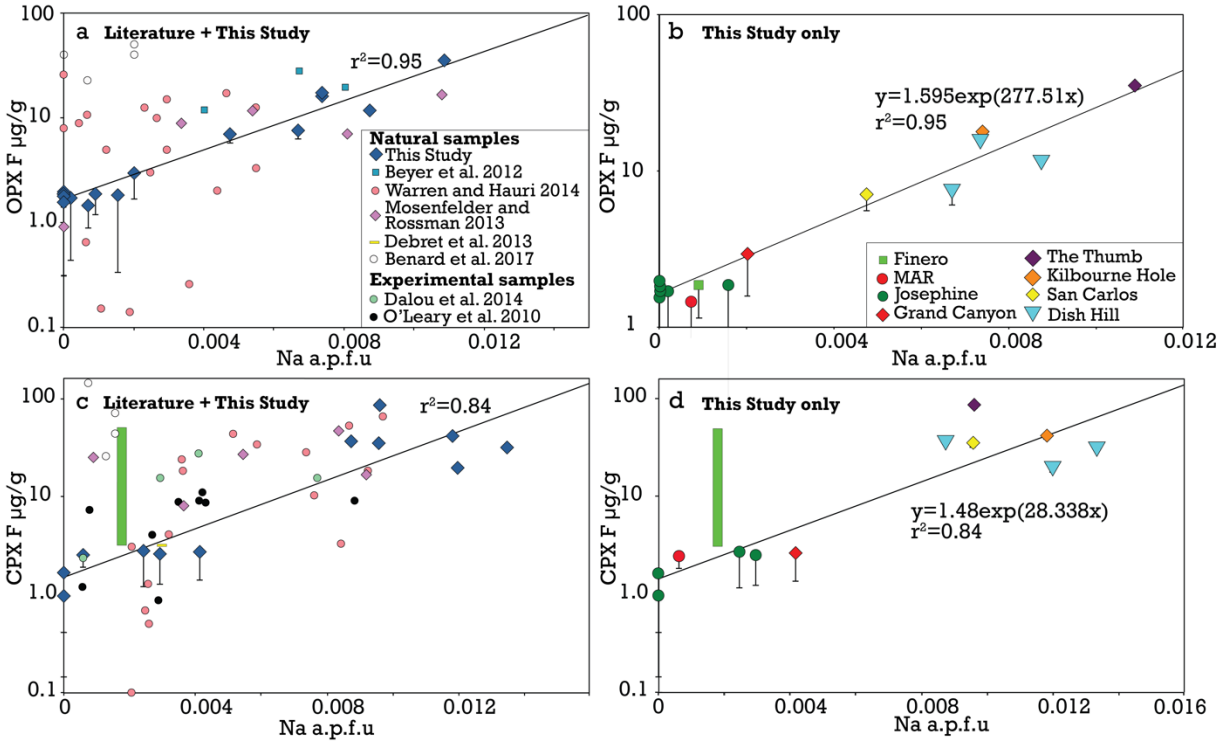

Figure 2.9 a. Orthopyroxene Na content in atoms per formula unit (a.p.f.u) versus F µg/g for all available experimental and natural data, including this study. **b.** Orthopyroxene Na content in a.p.f.u. versus F µg/g for all natural samples from this study only. **c.** Clinopyroxene Na content in a.p.f.u. versus F µg/g for all available experimental and natural data, including this study. **d.** Clinopyroxene Na content in a.p.f.u. versus F µg/g for all natural samples from this study only. In **a**, **b**, **c**, and **d**, the solid black line denotes best fit. For Finero sample, green bars show range of values along profiles. Positive error bars are internal errors propagated with calibration curve errors. Negative error bars are internal errors propagated with calibration curve errors and background errors monitored by F measurements in Herasil® glass. Error bars not visible are smaller than symbols. Individual measurements are reported in Tables 2, 3 and 4.

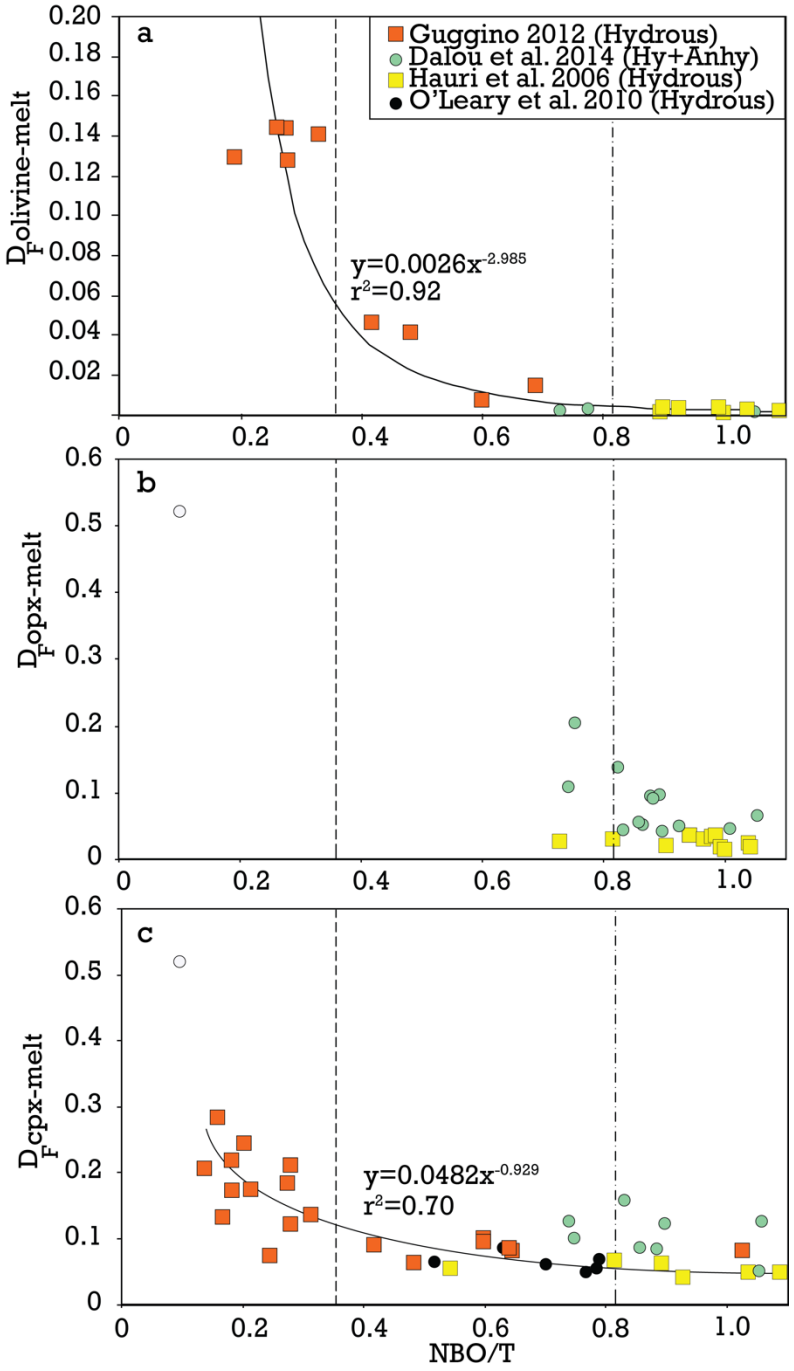

Fig. 2.10 Mineral-melt partition coefficients for F plotted against NBO/T of mantle melts, corrected for the depolymerizing effects of F and H_2O. **a.** olivine-melt, **b.** orthopyroxene-melt, and **c.** clinopyroxene-melt. Published experiments have been performed at T ≈ 1000–1360°C and P ≈ 0.1–3 GPa. Vertical dashed lines represent the NBO/T for an average basaltic-andesite composition from GeoRoc database (0.358), and the NBO/T for average MORB composition (0.81) from Gale et al. (2013).

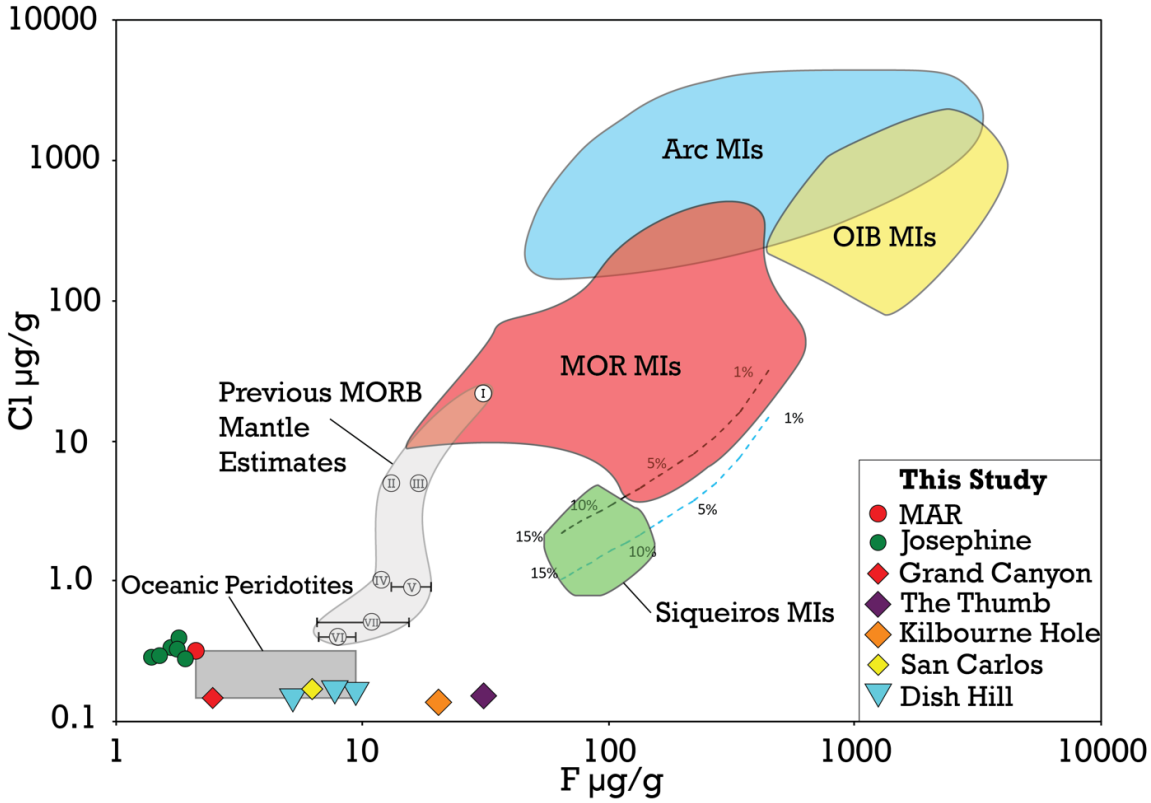

Fig. 2.11 Halogen budget of the mantle as inferred from this study. Hollow circles with Roman numerals denote previous DMM estimates. Error bars shown are those provided (if any) by literature source. I. E-DMM, (Shimizu, Saal et al. 2016). II. Pacific Mantle, (Shimizu, Saal et al. 2016). III. Gakkel Ridge Mantle, (Shaw, Behn et al. 2010). IV. DMM, (Le Voyer, Cottrell et al. 2015). V. DMM, (Saal, Hauri et al. 2002). VI. D-DMM, (Shimizu, Saal et al. 2016). VII. DMM,(Salters and Stracke 2004). Dashed box denotes DMM estimate from this study, as collected from in-situ measurements of oceanic peridotites. Melting trends reflect non-modal fractional melting in the spinel stability field with calculated bulk F content of sample DHS02 (9.4 µg/g), and a bulk Cl content of 0.15µg/g (blue dashed line) and 0.32µg/g (black dashed line). Partition coefficients for this melting model use the NBO/T parameterization of MORB melts for F (see text) and sample CD1H0 for Cl from Dalou (2014). Mantle mineral modal composition of Workman and Hart (2005). Individual measurements from this study use the same symbols are Figure 7. Opaque fields denote olivine-hosted melt inclusion data from various tectonic settings. Siqueiros measurements (East Pacific Rise, Siqueros Transform) from Saal et al. (2002). Mid-ocean ridge MI data from various sources (Shaw, Behn et al. 2010, Wanless and Shaw 2012, Wanless, Behn et al. 2014, Le Voyer, Cottrell et al. 2015, Wanless, Shaw et al. 2015). Ocean island basalt MI data aggregated from literature (Cabral, Jackson et al. 2014, Kendrick, Jackson et al. 2014, Rose-Koga, Koga et al. 2017). Arc olivine-hosted melt inclusion data from literature (Portnyagin, Hoernle et al. 2007, Bouvier, Metrich et al. 2008, Sadofsky, Portnyagin et al. 2008, Bouvier, Deloule et al. 2010, Rose-Koga, Koga et al. 2012, Rose-Koga, Koga et al. 2014).

2.10 Tables

Table 2.1. Background F-Cl monitoring using Herasil® and Synthetic Forsterite.

	Herasil					Synthetic Forsterite				
Session	No. Analyses	F µg/g	% (2SE Internal + Calibratio	Cl µg/g	% (2SE Internal + Calibratio	No. Analyses	F µg/g	% (2SE Internal + Calibratio	Cl µg/g	% (2SE Internal + Calibratio
Mar-15	5	1.20	3.30	0.37	7.3	2	2.91	2.60%	0.15	8.20
May-15	5	1.45	2.90	0.57	6.5	6	2.28	2.50%	0.23	6.70
Jan-16	6	0.64	6.00	0.44	9.9	4	1.38	5.70%	0.26	10.4
Feb-16	10	0.49	9.20	0.49	10.4	6	1.10	9.20%	0.39	10.6
Apr-16	13	0.52	3.60	0.46	9.4	5	1.06	3.48%	0.29	9.59
May-16	5	0.52	3.30	0.41	9.4	3	1.06	3.25%	0.21	9.70

Table 2.2. F and Cl concentrations and sample descriptions.

Clinopyroxene

Sample	Description	No. Analyses	F (ppm)	F Error % (2SE Internal + Calibration Curve)	F Error % (2SE Internal, Calibration, Background)	Cl (ppm)	Cl Error % (2SE Internal + Calibration Curve)	Cl Error % (2SE Internal, Calibration, Background)
Fin 10	Amphibole-bearing Cpx-rich Harzburgite	3	19.4	2.86	11.6	0.317	6.62	82.0
Fin1b (core)	Amphibole-bearing Cpx-rich Harzburgite	1	44.2	9.05	12.3	0.330	10.6	118.0
BM5	Harzburgite	3	11.0	2.47	16.9	0.303	6.33	85.0
J127-19	Harzburgite	3	1.66	2.75	91.5	0.450	6.20	60.2
J127-9	Cpx-rich Harzburgite/lherzolite	2	2.55	2.62	51.4	0.170	7.25	99.1
J98-10	Cpx-rich Harzburgite/lherzolite	3	1.57	3.18	38.2	0.259	14.1	105.8
J127-17	Harzburgite	3	0.984	3.30	58.2	0.256	9.75	111.4
J137-14	Harzburgite							
J127-16	Harzburgite							
GC2b	Harzburgite	4	2.68	2.68	49.0	0.150	7.47	111.1
SC99-2	Harzburgite	3	33.6	2.58	7.77	0.190	7.52	90.0
KLB-1	Lherzolite	2	41.7	2.64	7.08	0.140	7.76	118.4
DHS18	Lherzolite	4	31.7	2.67	7.98	0.200	7.16	85.9
DHS2	Lherzolite	3	36.1	2.58	7.52	0.177	6.84	95.6
DHS7	Lherzolite	4	18.8	2.56	10.5	0.120	7.66	136.2
TH2	Harzburgite	2	83.4	2.55	5.54	0.317	7.17	58.2
MAR D41-24	Harzburgite	2	2.50	3.12	25.7	0.339	9.42	87.2

Orthopyroxene

Sample	No. Analyses	F (ppm)	F Error % (2SE Internal + Calibration Curve)	F Error % (2SE Internal, Calibration, Background)	Cl (ppm)	Cl Error % (2SE Internal + Calibration Curve)	Cl Error % (2SE Internal, Calibration, Background)
Fin 10	3	3.02	2.65	25.1	0.253	6.64	112
Fin1b	13	1.87	9.12	37.1	0.455	10.7	101
BM5	5	2.01	2.70	76.0	0.276	6.72	92.8
J127-19	2	1.84	2.54	82.8	0.330	6.08	78.7
J127-09	3	1.71	2.63	74.2	0.147	7.12	113
J98-10	3	1.86	2.64	81.9	0.410	6.24	65.2
J127-17	4	0.719	3.27	76.8	0.171	10.1	156
J137-14	3	1.56	2.75	96.9	0.300	7.16	86.5
J127-16	3	1.72	2.66	88.2	0.287	7.00	89.9
GC2b	3	2.97	2.59	44.6	0.150	8.42	112
SC99-2	4	7.07	2.68	21.2	0.159	7.36	105
KLB-1	2	17.8	2.63	11.0	0.140	7.56	118
DHS18	6	11.7	2.78	14.5	0.150	7.19	111
DHS2	3	16.1	2.56	11.6	0.147	7.10	113
DHS7	3	7.69	2.57	19.7	0.120	7.24	136
TH2	3	35.3	2.57	7.60	0.118	7.02	138
MAR D41-24	2	1.47	3.04	40.3	0.301	9.58	96.7

Table 2.2. (cont.)

Olivine

Sample	No. Analyses	F (ppm)	F Error % (2SE Internal + Calibration Curve)	F Error % (2SE Internal, Calibration, Background)	Cl (ppm)	Cl Error % (2SE Internal + Calibration Curve)	Cl Error % (2SE Internal, Calibration, Background)
Fin10	3	3.87	2.86	41.6	0.310	7.03	83.9
BM5	4	2.19	2.57	70.1	0.320	6.98	81.6
J127-19	1	1.67	2.64	90.7	0.340	6.96	77.0
GC2b	3	2.25	2.77	57.6	0.160	7.47	105
SC99-2	3	2.20	2.67	58.7	0.187	7.15	91.3
KLB-1	3	17.1	2.56	11.1	0.150	7.64	111
DHS18	4	1.74	2.72	73.2	0.170	7.30	99.2
DHS2	3	1.82	2.66	70.0	0.180	7.32	94.3
DHS7	3	1.70	2.66	74.8	0.163	7.37	103
TH2	4	30.5	2.65	8.13	0.160	6.99	105
MAR D41-24	1	2.35	2.99	26.8	0.330	9.48	89.2

Amphibole

Sample	# of Analyses	F (ppm)	F Error % (2SE Internal + Calibration Curve)	F Error % (2SE Internal, Calibration, Background)	Cl (ppm)	Cl Error % (2SE Internal + Calibration Curve)	Cl Error % (2SE Internal, Calibration, Background)
Fin 10	3	1787	2.94	4.18	14.5	6.15	10.7
Fin 1b	10	917	5.57	8.25	10.3	9.75	17.6

Table 2.3. Intra-grain variations in F, Cl, Li, Be, B

Finero 1b											
Clinopyroxene											
Cpx1											
F [ppm]	4.60	4.35	3.60	3.54	4.98	4.77	4.32	32.9	18.5	26.6	44.2
F Error % (2SE Int+Calib)	9.83	9.13	9.11	9.13	9.23	9.92	9.46	9.17	10.1	10.1	9.05
F Error % (2SE Int+Calib+Background)	22.2	22.2	24.5	24.7	20.8	21.8	22.5	12.4	14.4	13.6	12.0
Cl [ppm]	0.320	0.290	0.320	0.290	0.360	0.310	0.340	0.320	0.310	0.420	0.330
Cl Error % (2SE Int+Calib)	10.7	10.6	10.7	10.5	10.4	10.4	10.7	10.4	10.4	10.5	10.6
Cl Error % (2SE Int+Calib+Background)	137	150	137	149	123	141	130	137	141	108	133
Distance [µm]	0.0	138	408	791	1080	1712	2027	2837	3158	3406	3637
	Rim										**Core**
Li [ppm]	1.00	1.21	1.20	1.31	1.46	1.76	1.82	1.54	2.05	1.37	1.86
2SE Int	0.062	0.052	0.060	0.036	0.073	0.099	0.093	0.052	0.046	0.066	0.046
Be [ppm]	0.138	0.151	0.161	0.175	0.204	0.179	0.223	0.243	0.222	0.237	0.184
2SE Int	0.014	0.021	0.019	0.021	0.022	0.027	0.028	0.032	0.030	0.030	0.020
B [ppm]	0.972	0.934	1.01	1.09	1.04	1.08	1.12	1.11	1.15	1.12	1.14
2SE Int	0.085	0.067	0.104	0.092	0.066	0.073	0.086	0.077	0.102	0.078	0.114
Distance [µm]	30.0	91.0	146	205	341	457	612	812	1089	1483	1644
	Rim										
Orthopyroxene											
Opx1											
F [ppm]	1.78	2.07	1.88	1.85	1.93	1.89	1.74	1.85			
F Error % (2SE Int+Calib)	9.12	9.16	9.10	9.13	9.07	9.07	9.08	9.09			
F Error % (2SE Int+Calib+Background)	38.4	34.6	36.9	37.4	36.2	36.8	39.0	37.4			
Cl [ppm]	0.590	0.410	0.490	0.450	0.480	0.490	0.460	0.430			
Cl Error % (2SE Int+Calib)	10.3	10.4	10.7	11.1	10.6	10.6	10.5	10.6			
Cl Error % (2SE Int+Calib+Background)	80.9	110	94.7	102	96.3	94.6	99.8	106			
Distance [µm]	0.0	210	301	430	704	997	1331	1509			
	Rim					**Core**		**Rim**			

Table 2.3. (cont.)

Finero 1b											
Clinopyroxene											
Cpx1											
F [ppm]	24.4	4.10	3.81	5.22							
F Error % (2SE Int+Calib)	10.4	9.09	9.13	9.07							
F Error % (2SE Int+Calib+Background)	14.0	22.8	23.8	20.2							
Cl [ppm]	0.460	0.370	0.270	0.330							
Cl Error % (2SE Int+Calib)	10.5	10.5	10.7	11.0							
Cl Error % (2SE Int+Calib+Background)	99.7	120	160	133							
Distance [µm]	3938	4161	4982	5137							
				Rim							
Li [ppm]	1.36	1.09	1.26	1.32	1.12	1.18	1.48	1.38	1.56	1.46	1.69
2SE Int	0.074	0.063	0.044	0.066	0.044	0.057	0.076	0.049	0.087	0.076	0.046
Be [ppm]	0.241	0.161	0.265	0.253	0.250	0.272	0.253	0.246	0.238	0.233	0.202
2SE Int	0.039	0.020	0.027	0.025	0.029	0.027	0.033	0.024	0.025	0.029	0.018
B [ppm]	1.22	1.01	1.24	1.34	1.25	1.42	1.25	1.28	1.22	1.19	1.24
2SE Int	0.087	0.082	0.099	0.084	0.083	0.112	0.109	0.091	0.074	0.090	0.075
Distance [µm]	2037	2495	2779	3070	3315	3623	3825	4082	4270	4450	4615
Orthopyroxene											
Opx1											
F [ppm]											
F Error % (2SE Int+Calib)											
F Error % (2SE Int+Calib+Background)											
Cl [ppm]											
Cl Error % (2SE Int+Calib)											
Cl Error % (2SE Int+Calib+Background)											
Distance [µm]											

Table 2.3. (cont.)

Finero 1b									
Clinopyroxene									
Cpx1									
F [ppm]									
F Error % (2SE Int+Calib)									
F Error % (2SE Int+Calib+Background)									
Cl [ppm]									
Cl Error % (2SE Int+Calib)									
Cl Error % (2SE Int+Calib+Background)									
Distance [µm]									
Li [ppm]	1.01	1.47	1.41	1.74	1.69	1.38	1.40	0.71	0.99
2SE Int	0.036	0.054	0.059	0.053	0.065	0.055	0.067	0.039	0.069
Be [ppm]	0.137	0.222	0.218	0.197	0.191	0.211	0.184	0.138	0.157
2SE Int	0.024	0.027	0.021	0.021	0.021	0.026	0.009	0.020	0.022
B [ppm]	1.08	1.13	1.17	1.14	1.07	1.11	1.10	0.823	0.969
2SE Int	0.058	0.090	0.106	0.067	0.082	0.089	0.102	0.090	0.063
Distance [µm]	4704	4818	4977	5083	5289	5393	5486	5616	5751
									Rim
Orthopyroxene									
Opx1									
F [ppm]									
F Error % (2SE Int+Calib)									
F Error % (2SE Int+Calib+Background)									
Cl [ppm]									
Cl Error % (2SE Int+Calib)									
Cl Error % (2SE Int+Calib+Background)									
Distance [µm]									

Table 2.3. (cont.)

Li [ppm]	0.036	0.067	0.113	0.092	0.137	0.199	0.274	0.286	0.298	0.311	0.158
2SE Int	0.006	0.009	0.007	0.009	0.012	0.015	0.009	0.011	0.019	0.019	0.011
Be [ppm]	0.033	0.034	0.041	0.044	0.050	0.050	0.043	0.043	0.041	0.045	0.055
2SE Int	0.004	0.004	0.004	0.005	0.003	0.005	0.004	0.003	0.007	0.004	0.004
B [ppm]	0.813	0.838	0.921	0.915	0.865	0.931	0.825	0.896	0.877	0.921	0.970
2SE Int	0.051	0.031	0.025	0.031	0.047	0.052	0.042	0.028	0.051	0.042	0.037
Distance [μm]	30.0	86.0	153	225	331	450	572	746	854	960	1077
	Rim										
Amphibole											
Amphibole 1											
F [ppm]	871	936	1000	857	899	960	911	911	898	922	
F Error % (2SE Int+Calib)	5.51	5.64	5.72	5.54	5.52	5.64	5.55	5.55	5.53	5.54	
F Error % (2SE Int+Calib+Background)	8.20	8.28	8.33	8.22	8.20	8.28	8.22	8.22	8.21	8.21	
Cl [ppm]	9.23	11.6	11.0	8.13	9.69	12.4	10.6	10.1	9.33	10.4	
Cl Error % (2SE Int+Calib)	9.72	10.01	9.69	9.74	9.70	9.71	9.72	9.71	9.73	9.74	
Cl Error % (2SE Int+Calib+Background)	17.1	16.7	16.6	17.5	16.9	16.3	16.7	16.8	17.0	16.8	
Distance [μm]	0.0	118	302	538	770	1041	1285	1466	1903	2060	
	Rim				**Core**					**Rim**	
Li [ppm]	0.690	0.662	0.681	0.665	0.658	0.621	0.644	0.723	0.704	0.738	0.743
2SE Int	0.035	0.055	0.037	0.033	0.032	0.036	0.038	0.040	0.044	0.036	0.042
Be [ppm]	0.560	0.564	0.588	0.560	0.636	0.637	0.566	0.486	0.475	0.551	0.506
2SE Int	0.040	0.035	0.042	0.040	0.028	0.041	0.028	0.035	0.046	0.036	0.044
B [ppm]	1.75	2.05	1.98	2.16	2.26	2.30	1.96	1.80	1.82	1.97	1.92
2SE Int	0.082	0.125	0.108	0.079	0.082	0.061	0.099	0.078	0.075	0.075	0.086
Distance [μm]	30.0	81.0	133	192	268	366	480	553	635	737	848
	Rim										

Table 2.3. (cont.)

Li [ppm]	0.133	0.270	0.216	0.131	0.080	0.083	0.080	0.064	0.039		
2SE Int	0.010	0.012	0.013	0.012	0.006	0.006	0.010	0.007	0.005		
Be [ppm]	0.051	0.040	0.048	0.047	0.041	0.045	0.036	0.034	0.040		
2SE Int	0.005	0.003	0.003	0.008	0.004	0.005	0.004	0.004	0.004		
B [ppm]	0.915	0.870	0.924	0.899	0.856	0.889	0.905	0.916	0.901		
2SE Int	0.052	0.035	0.049	0.035	0.033	0.048	0.045	0.054	0.026		
Distance [μm]	1210	1318	1435	1547	1627	1719	1806	1862	1933		
									Rim		
Amphibole											
Amphibole 1											
F [ppm]											
F Error % (2SE Int+Calib)											
F Error % (2SE Int+Calib+Background)											
Cl [ppm]											
Cl Error % (2SE Int+Calib)											
Cl Error % (2SE Int+Calib+Background)											
Distance [μm]											
Li [ppm]	0.704	0.685	0.695	0.703	0.663	0.653	0.795	0.663	0.690	0.663	0.711
2SE Int	0.034	0.037	0.050	0.017	0.033	0.027	0.046	0.050	0.033	0.037	0.046
Be [ppm]	0.553	0.539	0.560	0.497	0.542	0.532	0.539	0.555	0.533	0.571	0.616
2SE Int	0.045	0.024	0.027	0.029	0.048	0.037	0.046	0.038	0.026	0.038	0.032
B [ppm]	1.93	1.95	2.02	1.87	1.91	1.78	1.86	1.89	1.94	1.86	2.32
2SE Int	0.117	0.113	0.144	0.112	0.062	0.103	0.103	0.090	0.084	0.092	0.112
Distance [μm]	927	1014	1121	1249	1337	1423	1501	1582	1656	1733	1827

Table 2.3. (cont.)

Li [ppm]									
2SE Int									
Be [ppm]									
2SE Int									
B [ppm]									
2SE Int									
Distance [µm]									
Amphibole									
Amphibole 1									
F [ppm]									
F Error % (2SE Int+Calib)									
F Error % (2SE Int+Calib+Background)									
Cl [ppm]									
Cl Error % (2SE Int+Calib)									
Cl Error % (2SE Int+Calib+Background)									
Distance [µm]									
Li [ppm]	0.600	0.580	0.845	0.276					
2SE Int	0.012	0.042	0.032	0.037					
Be [ppm]	0.676	0.595	0.640	0.659					
2SE Int	0.051	0.033	0.030	0.046					
B [ppm]	2.19	2.18	2.45	2.46					
2SE Int	0.113	0.091	0.134	0.078					
Distance [µm]	1883	1941	1977	1987					
				Rim					

Table 2.3. (cont.)

Finero 10											
Cpx1											
F [ppm]	6.66	6.7	7.13	19.0	17.3	16.4	9.54	7.14	6.23		
F Error % (2SE Int+Calib)	5.55	5.79	5.86	6.15	6.21	5.78	5.74	5.57	5.60		
F Error % (2SE Int+Calib+Background)	17.8	17.9	17.3	11.9	12.3	12.2	15.0	17.1	18.5		
Cl [ppm]	0.270	0.320	0.370	0.330	0.310	0.310	0.300	0.300	0.300		
Cl Error % (2SE Int+Calib)	9.85	10.4	10.2	10.2	10.5	9.85	10.2	10.0	10.1		
Cl Error % (2SE Int+Calib+Background)	111	96.0	84.9	93.4	98.6	98.2	101	101	101		
Distance [μm]	0.0	82.6	161	357	472	663	786	955	1054		
	Rim				**Core**				**Rim**		
Opx1											
F [ppm]	1.81	2.52	3.27	3.8	3.36	3.49	3.5	2.82	3.13	2.48	
F Error % (2SE Int+Calib)	5.55	5.59	5.68	5.71	5.57	5.69	5.93	5.65	5.95	5.56	
F Error % (2SE Int+Calib+Background)	43.5	33.6	27.8	25.1	27.2	26.6	26.7	30.9	28.9	34.0	
Cl [ppm]	0.300	0.340	0.300	0.370	0.360	0.330	0.350	0.310	0.350	0.370	
Cl Error % (2SE Int+Calib)	9.74	9.78	10.5	10.3	10.2	9.88	10.1	10.4	10.2	10.0	
Cl Error % (2SE Int+Calib+Background)	101	90.8	101	84.9	86.8	93.1	88.8	98.6	88.9	84.7	
Distance [μm]	0.0	78.4	154	260	395	524	636	734	814	948	
	Rim				**Core**					**Rim**	
J127-09											
Cpx1											
F [ppm]	2.31	2.40	2.34	2.50	2.00						
F Error % (2SE Int+Calib)	2.98	3.08	3.14	3.00	3.09						
F Error % (2SE Int+Calib+Background)	27.3	26.5	27.1	25.6	30.9						
Cl [ppm]	0.669	0.400	0.303	0.721	0.280						
Cl Error % (2SE Int+Calib)	11.8	9.95	9.39	9.64	9.54						
Cl Error % (2SE Int+Calib+Background)	52.6	76.3	96.0	48.3	102.7						

Table 2.3. (cont.)

Opx1											
F [ppm]	1.57	1.39	1.37	1.45	1.44						
F Error % (2SE Int+Calib)	3.01	3.06	3.44	3.01	3.01						
F Error % (2SE Int+Calib+Background)	38.1	42.5	43.2	40.9	41.1						
Cl [ppm]	0.239	0.244	0.231	0.290	0.247						
Cl Error % (2SE Int+Calib)	9.84	9.69	9.54	10.8	10.1						
Cl Error % (2SE Int+Calib+Background)	118	116	122	101	115						
Distance [μm]	0.0	88.6	323	632	703						
	Rim		**Core**								
J98-10											
Opx1											
F [ppm]	1.07	1.09	1.10	1.12	0.98	1.05	1.01	1.09	1.15		
F Error % (2SE Int+Calib)	3.33	3.25	3.16	3.31	3.36	3.01	3.23	3.07	3.04		
F Error % (2SE Int+Calib+Background)	53.7	53.1	52.3	51.8	58.5	54.7	56.8	52.8	50.5		
Cl [ppm]	0.230	0.225	0.224	0.213	0.190	0.212	0.197	0.239	0.241		
Cl Error % (2SE Int+Calib)	9.55	9.57	9.60	9.72	9.54	9.29	9.73	9.66	9.49		
Cl Error % (2SE Int+Calib+Background)	106	104	103	99.0	89.6	98.0	92.4	109	110		
Distance [μm]	0	221	283	427	810	1136	1329	1461	1666		
	Rim				**Core**				**Rim**		
Title:											
Intra-Grain Variations in F, Cl, Li, Be, B											

Table 2.4. Major element data, this study and literature. * Major elements are an average of entire profile for opx and cpx. Major element profiles in Table 5.

Major element concentrations of olivine obtained by EPMA

Literature Source	Sample	SiO2	TiO2	Al2O3	Cr2O3	Fe3+ (Blank)	FeO	MnO	MgO	CaO	NiO	Si	Ti	Al	Cr	Fe-3	Fe-2	Mn	Mg	Ca	Fetotal	F ppm	H2O ppm	Cl ppm
Le Roux et al. 2014	P98-10	40.9					9.96	0.100	49.6	0.020	0.350	1.002					0.186	0.002	1.810	0.001	0.186			
	J127-9	40.6					8.72	0.160	50.1	0.040	0.340	0.993				0.015	0.164	0.003	1.825	0.001	0.178			
	J127-16	40.6					8.81	0.150	50.0	0.050	0.370	0.993				0.014	0.166	0.003	1.823	0.001	0.180			
	J127-17	40.6					8.94	0.150	49.9	0.030	0.380	0.993				0.015	0.168	0.003	1.821	0.001	0.183			
	J127-19	40.7					8.71	0.150	50.1	0.030	0.360	0.994				0.012	0.166	0.003	1.824	0.001	0.178	1.67		0.340
	J134-3	40.6					9.27	0.170	49.6	0.040	0.350	0.995				0.010	0.180	0.004	1.810	0.001	0.196			
	J134-14	40.5					8.63	0.160	50.3	0.040	0.360	0.994				0.020	0.156	0.003	1.829	0.001	0.174			
Luffi et al. 2009	DHS07	40.3					9.09	0.140	49.3	0.030	0.370	1.002					0.166	0.003	1.806	0.003	0.186	1.82		0.180
	DHS07	40.3					9.70	0.120	48.8	0.070	0.360	0.996				0.007	0.193	0.003	1.799	0.002	0.200	1.70		0.160
	DHS18	40.2	0.010		0.010		9.58	0.120	49.0	0.070	0.410	0.993	0.000		0.000	0.013	0.185	0.003	1.804	0.002	0.198	1.74		0.170
Li et al 2008	GC2B	40.2					9.54	0.140	49.2	0.050	0.400	0.992				0.017	0.180	0.003	1.808	0.001	0.197	2.25		0.160
	TH2	41.1			0.050		7.83	0.120	50.7	0.050	0.430	0.999				0.001	0.158	0.002	1.837	0.001	0.159	30.5		0.160
	SC99-2	40.1					10.2	0.160	48.3	0.070	0.410	0.996				0.008	0.204	0.003	1.787	0.002	0.212	2.20		0.190
Fred Davis, 2009 Composition of K	KLB-1	40.6			0.010		10.1	0.150	48.4	0.090		1.003				0.000	0.208	0.003	1.783	0.002	0.208	17.1		0.150
This Study	Tm1*																							
	MARKNR219-05	40.4	0.017		0.022		8.85	0.147	50.6	0.094	0.396	0.982	0.000		0.000	0.036	0.144	0.003	1.832	0.002	0.180	2.35		0.330
Dalou et al. 2014	CD2H3	40.4		0.090	0.040		13.6	0.160	45.8	0.240												33.0		9.0
	CD2H4																							
	CD2H5																							
	CD2H6																							
	P2gal2a	40.5		0.120	0.160		10.0	0.130	48.9	0.200												19.0	ND	20.0
	P4gal3a																							
	P1gal3a																							
	P5gal3a																							
	C4gal2b	40.8	0.040	0.130	0.040		10.1	0.130	48.6	0.210	0.030											ND	ND	ND
	C3gal2b	40.8	0.010	0.110	0.130		9.76	0.120	48.4	0.200	0.150											ND	ND	ND
	C3gal3a	40.8	0.010	0.110	0.070		10.3	0.140	48.7	0.250	ND											ND	ND	ND
	C4gal4a																							
	CC01gal3b4	40.4	0.010	0.070	0.150		11.7	0.150	46.8	0.290	0.010											15	1697	2.0
	CP1gal3a5	40.4	0.040	0.080	0.220		11.1	0.190	48.0	0.290	ND											ND	ND	ND
	CC4gal7b, CD1H6																							
	CP3gal5c																							
	CD1gal4a1																							
	Cap425a1																							
Debret et al. 2013, Lanzo Massif	LZC02																					1.04-2.9		2.4-33.1
Beyer 2012	Natural																							
	LANZ1 (2/5)	41.3			0.010		8.40	0.130	50.1	0.040												7.50		5.8
	LEU1 (2/4)	40.9	0.010		0.030		9.43	0.130	49.4	0.070												7.90		5.0
	MPM1 (2/5)	40.9	0.020		0.050		8.50	0.130	49.3	0.130												8.30		6.1
	Experimental																							
	Sample (4/9)**																							
	PC561-m (4/7)																							
	PC562-m (4/6)																							
	PC563-m (2/7)	42.2		0.200					56.6	0.300												5.90		
	PC566-m (3/7)*	41.4	0.020	0.030	0.060		5.80	0.170	52.4	0.420												6.50		
Warren and Hauri 2014	PS86-6-38																							
	Va07-85-20																							
	Va07-85-42																							
	Va07-85-47																							
	Va07-85-49																							
	Va07-86-27																							
	Va07-96-09W																							
	Va07-96-11T																							
	Va07-96-18M																							
	Va07-96-18W																							
	Va07-96-21M																							
	Va07-96-21Y																							
	Va07-96-25																							
	Va07-96-28																							
	Va07-96-35																							
	Va07-96-38																							
	LS-31																							
	LS-33																							
	SAA3-9																							
	SAV-1-28																							
	SAV-1-01																							
	TK40																					2.280		
	SAV-AS1																							
	SAV-AS2																							

Table 2.4. (cont.)

Major element concentrations of orthopyroxene obtained by EPMA

Literature Source	Sample	SiO2	TiO2	Al2O3	Cr2O3	Fe2O3	FeO Tot	MnO	MgO	CaO	Na2O	Si	Ti	Al	AlIV	AlVI	Cr	Fe+3	Fe+2	Mn	Mg	Ca	Na	Fe/Tot	F ppm	H2O ppm	Cl ppm
Le Roux et al. 2014	J98-30	54.9	0.057	4.16	0.544		6.19	0.153	32.2	1.81	0.021	1.90	0.001	0.170	0.071	0.099	0.015	0.011	0.168	0.004	1.66	0.067	0.002	0.179	1.86		0.210
	J127-9	54.7	0.053	4.26	0.760		5.83	0.106	32.7	1.52	0.003	1.89	0.001	0.173	0.064	0.109	0.021	0.022	0.147	0.003	1.69	0.056	0.000	0.169	1.71		0.200
	J127-16	57.3	0.015	0.89	0.446		6.01	0.111	34.1	0.983		1.98	0.000	0.036	0.012	0.024	0.012		0.174	0.003	1.76	0.036		0.174	1.72		0.290
	J127-17	55.8	0.021	2.51	0.760		6.03	0.120	33.6	1.21		1.93	0.001	0.102	0.028	0.075	0.021	0.025	0.149	0.004	1.73	0.045		0.174	1.98		0.170
	J127-19	56.1	0.020	2.45	0.679		6.00	0.119	33.8	0.84		1.94	0.001	0.100	0.037	0.063	0.019	0.006	0.167	0.003	1.74	0.031		0.173	1.84		0.310
	J134-1	55.3	0.045	3.44	0.794		6.11	0.122	32.6	1.64		1.92	0.001	0.140	0.054	0.085	0.022	0.005	0.172	0.004	1.68	0.061		0.177			
	J137-14	56.4	0.011	1.70	0.713		5.69	0.120	33.6	1.73		1.95	0.000	0.069	0.017	0.053	0.019	0.016	0.148	0.003	1.73	0.064		0.164	1.56		0.300
Luffi et al. 2009	DHS02 (core)	55.2	0.090	4.74	0.640		5.85	0.150	32.4	1.08	0.130	1.90	0.002	0.193	0.095	0.097	0.017		0.169	0.004	1.66	0.040	0.007	0.169	16.1		0.350
	DHS02 (core)	54.9	0.100	4.84	0.350		6.45	0.130	32.4	0.870	0.100	1.90	0.003	0.197	0.092	0.104	0.010	0.004	0.182	0.004	1.67	0.032	0.007	0.186	7.69		0.320
	DHS18 (core)	53.6	0.160	5.22	0.450		6.32	0.160	32.5	0.830	0.130	1.86	0.004	0.213	0.074	0.139	0.012	0.054	0.150	0.003	1.68	0.031	0.009	0.183	11.7		0.350
Li et al 2008	GC2B	55.1	0.030	3.81	0.360		5.96	0.150	33.2	0.660	0.030	1.91	0.001	0.156	0.069	0.087	0.010	0.008	0.163	0.004	1.72	0.025	0.002	0.173	2.97		0.350
	TH2	55.9	0.100	1.53	0.650		4.75	0.120	33.8	0.900	0.160	1.96	0.003	0.063	0.026	0.037	0.018		0.139	0.004	1.77	0.034	0.013	0.139	35.3		0.120
	SC99-2	54.6	0.120	6.15	0.310		6.67	0.160	30.6	0.840	0.070	1.91	0.003	0.253	0.159	0.094	0.009		0.193	0.003	1.59	0.031	0.005	0.193	7.07		0.360
Fred Davis, 2009 Composition of K	KLB-1	54.2	0.100	5.35	0.350		6.35	0.130	32.1	0.820	0.130	1.88	0.003	0.219	0.101	0.118	0.010	0.010	0.174	0.004	1.66	0.031	0.007	0.184	17.8		0.340
This Study	Hasib	57.0	0.032	1.52	0.353		6.41	0.155	34.5	0.327	0.031	1.96	0.001	0.061	0.020	0.041	0.010	0.011	0.174	0.005	1.77	0.012	0.001	0.184	1.87		
	MARKNR230-05	56.0	0.013	2.42	0.858		5.52	0.133	32.6	2.36	0.030	1.94	0.000	0.099	0.040	0.059	0.024		0.160	0.004	1.68	0.088	0.001	0.160	1.47		0.300
Dalou et al. 2014	CD2H1	53.7	0.110	5.25	0.860		7.50	0.160	30.8	1.74	0.070														1203		83.0
	CD2H4	53.5	0.080	3.70	0.490		12.2	0.240	27.7	1.87	0.130																
	CD2H5	54.4	0.060	4.93	0.230		4.53	0.180	34.4	1.29	0.040														668		98.0
	CD2H6	54.6	0.050	3.83	0.890		8.42	0.210	31.0	1.25	0.050														2003		35.0
	F3@2a	53.7	0.070	6.53	0.780		6.08	0.110	31.6	1.39	0.020														119	172	26.0
	F4@3a	52.1	0.120	9.11	0.630		7.17	0.140	29.5	1.72	0.070														268	348	15.0
	F1@1b	53.7	0.060	6.19	0.760		6.14	0.110	31.1	1.27	0.120														538		29.0
	F5@1b	53.9	0.090	5.79	0.740		6.42	0.120	31.2	1.40	0.040														336		43.0
	C4@2b	53.5	0.080	7.10	0.860		6.08	0.110	31.4	1.45	0.090																40.0
	C3@2b	53.5	0.120	6.77	0.790		6.09	0.120	31.2	1.39	0.030														2.00	N D	43.0
	O1@1a	52.8	0.010	7.88	0.610		6.53	0.120	30.3	2.00	0.150														5.00	2138	39.0
	C4@4a	52.2	0.110	8.11	0.150		7.40	0.150	29.1	1.78	0.030																148
	CC01@8b3-4	53.5	0.130	5.82	1.03		6.82	0.140	29.9	2.09	0.090														31.0	973	4.00
	CF1@8b5	55.3	0.100	3.85	1.09		6.37	0.100	31.0	2.66	0.020														571	1296	4.00
	CC4@7a, CC01@8	54.0	0.080	5.93	0.940		6.73	0.150	30.5	2.14	0.080														14.0	1039	19.0
	CF5@7c	54.3	0.110	5.97	0.960		6.69	0.130	30.4	2.20	0.100														526	1351	5.00
	CF01@6b3-1	52.7	0.720	8.31	0.720		7.29	0.170	28.9	2.33	0.120														24.0		5.00
	C4@4234b	54.1	0.090	6.74	0.260		7.12	0.110	29.3	1.97	0.430														1.21	4856	13.0
Debiet et al. 2013, Lamo Massif	LZC02																								3.9-6.0			
Beyer 2012	LANZ1 (3/2)	56.3	0.030	2.20	0.710		5.42	0.130	33.6	1.50	0.060														12.0		
	LEU1 (2/4)	55.5	0.090	3.90	0.560		5.91	0.120	32.8	0.810	0.100														28.0		
	MEM1 (2/5)	55.8	0.070	3.10	0.990		5.30	0.130	33.0	1.40	0.120														20.0		
	Sample (#/#)**																										
	PC554-m (4/7)	50.7		13.6					32.2	2.40															392		
	PC561-m (4/7)	51.9		12.7					32.9	2.20															350		
	PC562-m (4/6)	51.9		13.6					33.1	2.40															432		
	PC563-m (2/7)	55.1		7.60					35.7	1.40															55.0		
Warren and Hauri 2014	PS86-6-18	53.8	0.138	6.12	0.611		6.31	0.154	30.7	1.76	0.081														3.35464.9103		
	Vm07-85-30	55.4	0.065	3.91	0.506		6.11	0.116	32.1	1.59	0.036														0.150		
	Vm07-85-42	55.1	0.082	5.20	0.719		6.23	0.116	31.5	2.03	0.028														0.140		
	Vm07-85-47	54.8	0.097	5.24	0.759		6.18	0.136	31.0	2.53	0.054														0.260		
	Vm07-85-49	54.6	0.045	4.48	0.641	0.236	5.94	0.105	32.0	1.72	0.030														0.670		
	Vm07-86-27	54.9	0.084	4.65	0.691		6.16	0.129	31.6	1.88	0.051																
	Vm07-96-09V	54.2	0.149	4.69	0.275		6.49	0.178	31.1	1.69	0.039														5.00		
	Vm07-96-16V	54.5	0.232	5.03	0.568	0.275	6.69	0.154	31.8	1.28	0.037														3.00		
	Vm07-96-18M	54.3	0.137	5.28		1.66	5.50	0.138	32.4	1.46	0.007														9.00		
	Vm07-96-18V	54.9	0.164	3.42		1.60	5.74	0.158	32.6	1.42															8.00		
	Vm07-96-21M	53.9	0.147	6.02	0.619		6.42	0.141	31.3	1.14	0.044														15.00		
	Vm07-96-21V	55.1	0.193	3.97	0.537		6.23	0.137	32.0	1.23	0.034														12.60		
	Vm07-96-23	53.3	0.112	5.58		1.31	5.68	0.109	31.5	1.48	0.041														5.00		
	Vm07-96-28	53.8	0.142	5.38		1.03	5.07	0.098	31.4	2.44	0.039														10.0		
	Vm07-96-35	55.2	0.101	3.93	0.923		5.55	0.115	32.0	1.59	0.081														12.60		
	Vm07-96-38	53.6	0.137	6.36	0.568		6.45	0.130	30.3	1.36	0.005														2.00		
	LS-33	55.4	0.140	4.20	0.500		7.07	0.070	30.2	1.36															25.0		
	SA-3-9	56.2	0.010	2.55	0.693	0.790	4.84	0.100	34.2	1.00	0.010														10.00		
	SAV-1-28	56.3	0.020	2.66	0.740	0.477	5.02	0.110	34.3	0.730	0.070														17.2		
	3SJ-G01	56.8	0.010	2.14	0.360		5.68	0.130	34.0	0.940																	
	TMO																										
	SAV-AS1																								4.21		
	SAV-AS2																								1.90		

Table 2.4. (cont.)

Literature Source		Major element concentrations of clinopyroxene obtained by EPMA																												
	Sample	SiO2	TiO 2	Al2O3	Cr2O3	Fe2O3	FeO	MnO	MgO	CaO	Na2O	Si	Ti	Al	Cr	Fe+3	Fe+2	Mn	Mg	Ca	Na	AlIV	AlVI	F ppm	H2O ppm	Cl ppm
Le Roux et al. 2014	J98-10	51.3	0.200	5.29	0.919		3.05	0.116	17.4	21.5	0.350	1.86	0.005	0.227	0.026		0.093	0.004	0.941	0.835	0.025	0.089	0.138	2.73		0.260
	J127-9	51.2	0.160	5.61	1.24		2.61	0.079	16.2	22.4	0.420	1.86	0.004	0.240	0.036		0.080	0.002	0.881	0.873	0.030	0.104	0.137	2.55		0.450
	J127-16	54.3	0.045	1.11	0.75		2.08	0.066	18.1	23.5	0.126	1.97	0.001	0.048	0.022	0.003	0.060	0.002	0.978	0.911	0.009	0.014	0.033			
	J127-17	52.7	0.069	2.92	1.21		2.21	0.070	17.1	23.8		1.92	0.002	0.125	0.035	0.004	0.063	0.002	0.927	0.926		0.041	0.084	0.980		0.260
	J127-19	52.3	0.068	3.35	1.37		2.27	0.077	16.9	23.7		1.90	0.002	0.144	0.039	0.009	0.060	0.002	0.918	0.924		0.046	0.098	1.66		0.450
	J134-3	52.2	0.104	3.94	1.10		2.74	0.080	17.2	22.6	0.059	1.90	0.003	0.169	0.032		0.083	0.002	0.932	0.882	0.004	0.065	0.104			
	J137-14	53.2	0.024	2.12	1.14		2.43	0.079	18.1	22.9		1.93	0.001	0.091	0.033	0.012	0.062	0.002	0.977	0.891		0.022	0.069			
Luffi et al. 2009	DHS02	52.0	0.370	6.20	1.23		3.21	0.100	16.2	20.2	1.25	1.87	0.010	0.263	0.035		0.097	0.003	0.868	0.778	0.087	0.135	0.128	37.2		0.180
	DHS07	51.5	0.540	7.34	0.760		3.30	0.080	15.2	19.9	1.71	1.86	0.015	0.312	0.022		0.100	0.002	0.818	0.768	0.120	0.173	0.139	19.8		0.120
	DHS18	50.6	0.520	7.53	0.830		2.83	0.110	15.3	19.4	1.90	1.85	0.014	0.324	0.024		0.086	0.003	0.835	0.759	0.135	0.173	0.151	31.7		0.200
Li et al. 2008	GC 2B	52.2	0.110	3.98	0.440		2.46	0.090	16.8	23.6	0.590	1.90	0.003	0.171	0.013		0.075	0.003	0.908	0.919	0.042	0.067	0.103	2.68		0.150
	TH2	52.6	0.400	1.81	1.87		2.50	0.090	17.3	20.3	1.34	1.95	0.011	0.079	0.055		0.077	0.003	0.952	0.804	0.096	0.026	0.053	84.5		0.320
	SC99-2	51.0	0.550	8.76	0.650		3.12	0.090	14.4	20.6	1.37	1.84	0.015	0.372	0.019		0.094	0.003	0.772	0.795	0.096	0.208	0.164	34.7		0.190
Fred Davis, 2009 Composition of K	KLB-1	51.3	0.550	7.83	0.690		3.18	0.070	14.8	19.5	1.68	1.86	0.015	0.335	0.020		0.096	0.002	0.802	0.757	0.118	0.196	0.139	41.7		0.140
This Study	Fin1b	53.6	0.065	1.83	0.690		2.21	0.080	17.1	23.8	0.256	1.95	0.002	0.078	0.020	0.011	0.056	0.002	0.930	0.930	0.018	0.031	0.047	12.7		0.340
	MAR K NR210-05 D 41-24	52.9	0.011	3.20	1.30		3.13	0.099	19.8	20.0	0.087	1.90	0.000	0.136	0.037		0.094	0.003	1.060	0.771	0.006	0.040	0.096	2.50		0.340
Dalou et al. 2014	CD2H3	51.0	0.220	6.36	0.940		5.07	0.140	17.3	18.6	0.620													2.319		44.0
	CD2H4																									
	CD2H5	49.4	0.200	6.01	0.300		6.80	0.140	15.7	20.2	0.880													1.185		35.0
	CD2H6																									
	E2:pl2a																									
	E4:pl3a																									
	F1#3b																									
	F5#3b																									
	C4pl#2b																									
	C5pl#2b																									
	C04#3a																									
	C 48#4a																									
	CC01#8kb4	53.0	0.580	5.29	1.06		3.40	0.080	16.4	19.2	1.10													16.0	3.18	26.0
	CF1#8kb5	53.6	0.190	4.29	0.860		4.71	0.140	20.7	15.8	0.330													472	89.0	37.0
	CC4#7b, CD1H0	52.3	0.200	5.96	1.09		4.80	0.130	20.3	14.8	0.420													16.0	5.50	77.0
	CF5#7c	52.6	0.140	6.10	1.10		4.93	0.150	20.6	14.7	0.400													6.26		12.0
	CF01#16kb1	50.5	0.720	9.73	0.710		5.36	0.160	19.0	14.1	0.590													28.0		2.00
	C4pl#25kb	53.4	0.170	8.23	0.130		6.52	0.130	21.2	8.76	1.64													319	39.36	10.0
Debret et al. 2013, Lanzo Massif	LZC02	50.8	0.610	5.54	1.24		2.82	0.070	15.1	23.3	0.440													3.2-20.6		13.5-19.9
Beyer 2012	LANZI (3/2)																									
	LEU1 (2/4)																									
	MPM1 (2/5)																									
	PC554-m (4/7)																									
	PC561-m (4/7)																									
	PC562-m (4/6)																									
	PC563-m (2/7)																									
Warren and Hauri 2014	PS86-6-38	51.2	0.410	7.23	0.929	1.06	2.17	0.121	15.4	21.0	1.09													10.3		
	Van7-85-30	51.0	0.219	6.22	1.09	0.34	2.70	0.088	16.3	21.6	0.370													0.500		
	Van7-85-42	51.7	0.222	6.28	1.08	0.54	2.79	0.095	17.1	21.1	0.357													0.700		
	Van7-85-47	51.5	0.221	6.31	1.07	0.42	2.83	0.099	17.1	20.9	0.368													1.30		
	Van7-85-49	51.3	0.173	6.08	1.08	0.28	2.98	0.066	17.5	20.3	0.294													3.10		
	Van7-86-27	51.6	0.239	5.80	1.03	0.17	2.83	0.091	16.8	21.6	0.292													0.100		
	Van7-96-09V	50.5	0.445	6.75	0.602	0.81	2.69	0.122	16.5	20.5	0.512													18.5		
	Van7-96-16V	51.0	0.741	6.50	0.511	0.53	2.93	0.126	16.4	21.2	0.456													4.10		
	Van7-96-18M	50.2	0.493	7.60		2.99	0.93	0.093	15.6	20.8	1.07															
	Van7-96-18V	50.1	0.500	6.87		2.44	1.77	0.112	16.5	20.9	0.530													23.6		
	Van7-96-21M	50.4	0.548	7.58	0.97	0.98	2.31	0.095	15.7	21.0	0.734													43.9		
	Van7-96-21V	50.7	0.491	7.70	0.96	0.83	2.83	0.099	16.8	19.0	0.837													34.1		
	Van7-96-25	51.1	0.361	7.06	1.05	0.30	3.08	0.069	14.8	20.2	1.31													18.5		
	Van7-96-28	51.2	0.347	6.75	1.32	0.66	2.61	0.068	16.0	20.0	1.05													28.1		
	Van7-96-35	52.2	0.323	5.33	1.69	1.03	1.66	0.084	16.0	20.3	1.38													66.2		
	Van7-96-38	51.0	0.451	7.83	0.875	0.22	3.36	0.093	16.0	18.7	1.20													3.30		
	LS-33	52.1	0.400	5.30	1.11		3.45	0.070	16.7	17.9	1.22													52.6		
	SA-3-9	53.5	0.020	2.54	0.850	0.15	2.02	0.020	18.1	22.5	0.160															
	SAV-1-28	53.7	0.170	2.09	2.03	1.84	0.793	0.100	16.8	22.5	1.02															
	3925G01	53.1	0.060	3.02	1.00		2.38	0.080	17.7	23.0																
	TMO																								350.00	
	SAV-AS1																							13.30	301.00	
	SAV-AS2																							6.90		

Table 2.4. (cont.)

Literature Source	Major element concentrations of MELTs obtained by EPMA														
	Sample	SiO2	TiO2	Al2O3	Cr2O3	FeO	MnO	MgO	CaO	Na2O	K2O	P2O5	H2O ppm	F ppm	Cl ppm
Le Roux et al. 2014	J98-10														
	J127-9														
	J127-16														
	J127-17														
	J127-19														
	J134-3														
	J137-14														
Luffi et al. 2009	DHS02														
	DHS07														
	DHS18														
Li et al 2008	GC2B														
	TH2														
	SC99-2														
Fred Davis, 2009 Composition of K	KLB-1														
This Study	Fin1b														
	MAR KNR210-05 D41-24														
Dalou et al. 2014	CD2H3	45.9	0.710	15.6	0.040	10.1	0.140	10.3	10.9	2.69	0.130		1439	18241	3491
	CD2H4	45.0	0.580	13.4	0.040	7.87	0.180	12.8	13.4	1.46	0.090		2406	146867	405.0
	CD2H5	50.9	0.600	14.6	0.040	6.73	0.140	9.30	9.56	2.79	0.170		2717	14765	2491
	CD2H6	43.7	0.590	12.4	0.110	7.71	0.130	14.8	12.7	1.81	0.090		3267	119267	640.0
	F2p#2a	48.5	0.600	16.4	0.170	8.29	0.150	13.2	9.66	1.79	0.130		2904	2775	2009
	F4p#3a	47.6	0.630	17.5	0.060	8.49	0.150	11.2	10.5	2.45	0.160		4524	4807	1560
	F1#3b	47.4	0.560	16.1	0.140	8.25	0.130	13.3	10.0	1.75	0.150		3661	11985	1939
	F5#3b	48.1	0.620	16.6	0.110	8.30	0.150	12.7	10.2	1.69	0.190		4577	6721	1537
	C4p#2b	48.2	0.570	16.7	0.180	8.19	0.160	12.9	10.0	1.90	0.100		2778	41.0	2362
	C8p#2b	48.1	0.570	16.5	0.210	8.41	0.180	13.2	9.21	1.79	0.150		2526	38.0	3102
	C04#3a	46.6	0.530	17.2	0.150	7.70	0.170	12.0	11.3	2.39	0.200		4981	54.0	1352
	C4#4a	49.3	0.610	16.6	0.110	8.12	0.140	10.6	10.5	2.04	0.150		3043	35.0	4965
	CC01#8kb4	49.3	0.590	16.8	0.170	7.63	0.110	9.60	11.7	2.11	0.180		2127	151.0	2035
	CF1#8kb5	49.5	0.640	16.3	0.180	7.18	0.200	10.8	12.4	2.10	0.160		1807	6011	1860
	CC4#7b, CI	49.6	0.670	15.9	0.150	8.03	0.130	10.5	11.8	2.11	0.150		1712	101.0	8515
	CF5#7c	49.0	0.610	16.0	0.160	7.76	0.130	11.2	11.8	1.97	0.130		2222	5336	2386
	CF01#16kb1	49.0	0.670	17.7	0.080	8.27	0.100	10.0	10.9	2.32	0.190		1982	222.0	2502
	C4p#25kb	45.8	1.08	13.9	0.080	9.25	0.090	11.2	8.70	4.32	0.350		7839	6406	4772
Debret et al. 2013, Lanzo Massif	LZC02														
Beyer 2012															
	LANZ1 (2/5)														
	LEU1 (2/4)														
	MFM1 (2/5)														
	PC554-m (4	47.4		18.0				18.2	14.7					10595	
	PC561-m (4	47.4		18.1				18.6	14.1					10294	
	PC562-m (4	47.2		18.4				17.4	14.6					12000	
	PC563-m (2	50.6		19.3				15.9	12.3	0.600				1788	
	PC566-m (3	47.3	1.68	8.7	0.160	7.80	0.170	14.1	14.5	2.10				9286	
Warren and Hauri 2014															

Table 2.4. (cont.)

	Sample	SrO2	TiO2	ADO3	Cr2O3	Fe3+ (Blank)	FeO	MnO	MgO	CaO	NiO	Si	Ti	Al	Cr	Fe+3	Fe+2	Mn	Mg	Ca	Fcount	F ppm	H2O ppm	Cl ppm
O'Leary et al. 2010	8272FH-11																							
	8272RH-19																							
	8272FH-18																							
	8272FH-22																							
	8272FH-23																							
	8272FH-17																							
	ALFB-7	40.2					9.80		47.8	1.500											0.16		20.0	
	ALFB-20	40.3					10.4		47.7	1.440											0.04		23.0	
	ALFB-21	40.4					9.60		49.0	1.110											0.04		23.0	
	ALFB-17	40.5					9.21		48.9	1.300											0.04		33.0	
Van der Bleeken and Kogga, 2015	GBC05_RRO buffered																							
	GBC06 RRO buffered																							
	GBC07																							
	GBC08																							
	GBC09(c)																							
	GBC12																							
	GBC13																							
Hauri and Gaetani 2006	B330	40.5	0.020	0.060	0.120		11.3	0.130	48.3	0.170											1.00		65.0	
	B333	40.4	0.010	0.070	0.040		10.0	0.130	49.9	0.180											1.00		63.0	
	B359	40.0	0.020	0.070	0.040		10.4	0.100	49.1	0.180											1.00		89.0	
	B366	40.3	0.060	0.040	0.040		11.7	0.130	48.3	0.170											7.00		94.0	
	B384	40.4	0.020	0.080	0.150		11.6	0.150	48.6	0.150											2.00		72.0	
	B388	41.1	0.010	0.080	0.030		11.1	0.100	48.7	0.130											13.0		82.0	
	B394																						36.0	
	B408	40.3	0.050	0.050	0.100		11.5	0.130	48.9	0.170													62.0	
	B412	40.4	0.100	0.050	0.070		12.0	0.150	48.3	0.150													66.0	
	#1799																							
	#1833																							
	#1450																				2.00		72.0	
	#1802																							
Moscatelder and Rossman 2013	JLM-50																							
	BPcmA																							
	CTT7210																							
	ROM271-D110																							
	KBH-2																							
	DI2.1																							
	PMR-54																							
	GRR1650B																							
	ZM1_pdHT																							
Gaggino 2012	MIW-6	38.9					16.1		42.3	0.300											13.0			
	MIW-20	39.3					15.3		43.5	0.200	0.100										31.0			
	MIW-23																							
	MIW-26																							
	MIW-12																							
	MOA-2	38.6					17.3		42.6	0.300											96.0			
	MO-14																							
	LIW-39																							
	LIW-37																							
	LIW-40																							
	LIW-51																							
	PEM22-1	39.5					16.3		45.7	0.100											25.0			
	PEM22-18	40.1		0.800			15.6		42.4	0.400	0.100										22.0			
	MIW18	39.1					15.8		43.0	0.200											83.0			
	PEM22-19	39.4					15.8		43.8												17.0			
	PEM22-12	41.5		0.100			3.70		53.9	0.200											17.0			
	PEM22-17																							
	PEM22-6	39.9					15.3		44.1	0.020											21.0			
	PEM22-5	40.4					10.8		49.0	0.200											25.0			
	PEM22-4	40.6					11.2		47.7	0.200											26.0			
	56B																							
	LOA-15																							
	LOA-18																							
	LOA-8																							
	LOA-13																							

Table 2.4. (cont.)

	Sample	SiO2	TiO2	Al2O3	Cr2O3	Fe2O3	FeO/Vol.	MnO	MgO	CaO	Na2O	Sr	Fl	Jd	MV	AVI	Cr	Jn+1	Jn+2	Mn	Mg	Ca	Na	Pr1/et	P gpm	HiO gpm	Cl ppm
O'Leary et al. 2010	EP2H1-71																										
	EP2H1-119																										
	EP2H1-88																										
	EP2H1-22																										
	EP2H1-87																										
	ALH1-20																										
	ALH1-31																										
	ALH1-37																										
Vicedo Blaclaes and Kogo, 2015	GRC/9_HKO buffered																										
	GRC/9_HKO buffered																										
	GRC/06																										
	GRC/06(2)																										
	GRC/21																										
Hunt and Gurnis 2006	B3/10	55.0	0.098	5.40	0.750		7.00	0.130	2.11	130	0.060																
	B1/11	55.0	0.098	6.05	0.900		6.40	0.130	1.12	170	0.080																
	B1/07	55.0	0.098	6.05	0.900		6.70	0.130	1.57	170	0.080																
	B1/02	54.6	0.130	7.13	0.130		7.20	0.130	3.07	135	0.080																
	B1/04	55.4	0.100	4.05	0.600		7.20	0.130	3.03	143	0.060																
	B1/06	55.7	0.130	4.20	0.750		7.00	0.160	3.20	133	0.080																
	B4/08	55.1	0.130	4.40	0.750		7.08	0.130	3.18	133	0.070																
	B4/42	54.4	0.200	7.05	0.480		6.90	0.160	3.07	143	0.080																
	#3/99																										
	#3/83																										
	#3/65																										
Mouchrifder and Rozman 2013	BA8 3/0	47.5	0.300	9.33	0.085		177	0.200	2.65	1.23	0.380														1510	1460	
	BA8 3/5	59.5		0.47			0.76		3.93	0.390															280		
	CO17/210																										
	BON27/1-1930																										
	GRH1-1	54.5	0.110	4.67	0.530		6.03	0.130	3.13	0.480	0.320														720		
	DG1-4	57.1	0.370	0.53	0.090		8.34	0.130	3.24	0.620	0.080														121		
	GRH1-4	57.0	0.360	0.55	0.100		8.40	0.130	3.31	0.600	0.060														1210		
	GRH1-92B	55.5	0.064	0.73	0.020		13.36	0.280	2.89	0.320	0.050														0.920		
	ZM1_mHT	45.8	0.060	2.81	0.600		6.31	0.130	3.11	0.670	0.080														900		
Guggino 2012	MIW-6																										
	MIW-20																										
	MIW-23																										
	MIW-26																										
	MIW-23																										
	MVA-4																										
	LIW-39																										
	LIW-47																										
	LIW-49																										
	LIW-51																										
	LIW-31																										
	PVA12-13																										
	PVA12-18																										
	MIW9-8																										
	PVA12-19																										
	PVA12-13																										
	PVA12-17																										
	PVA12-6																										
	PVA12-5																										
	PVA12-4																										
	9-8																										
	LOA-15																										
	LOA-38																										
	LOA-4																										
	LOA-13																										

Table 2.4. (cont.)

	Sample	SiO2	TiO2	Al2O3	Cr2O3	Fe2O3	FeO	MnO	MgO	CaO	Na2O	Si	Ti	Al	Cr	Fe+3	Fe+2	Mn	Mg	Ca	Na	AlIV	AlVI	F ppm	H2O ppm	Cl ppm	
O'Leary et al. 2010	8272FH-11	47.0	0.480	14.50	0.050		6.00		15.0	16.4	0.110													7.30	558		
	8272RH-19	48.8	0.480	0.120	0.050		7.60		14.6	15.8	1.100													9.00	370		
	8272FH-18	49.2	0.270	10.80	0.290		4.94		18.1	15.7	0.500													8.90	680		
	8272FH-22	48.2	0.300	12.40	0.150		5.40		16.9	16.1	0.590													9.00	712		
	8272FH-23	50.0	0.260	10.30	0.120		5.70		18.8	14.8	0.610													11.0	520		
	8272FH-17	48.1	0.330	12.50	0.130		5.34		16.2	17.2	0.620													8.60	506		
	ALFB-7	53.3		0.900			4.30		16.6	24.6	0.380													4.10	410		
	ALFB-20	53.9		0.060			4.30		16.5	24.0	0.080													1.20	118		
	ALFB-21	54.7		0.050			3.23		17.8	24.2	0.410													0.87	122		
	ALFB-17																										
Van der Bleeken and Koga, 2015	GBC05, RRO buffered	50.9	0.340	5.05	0.060		9.29	0.070	11.3	19.1	2.64													1980			
	GBC06 RRO buffered	51.1	0.630	7.21	0.190		10.9	0.200	8.6	16.3	3.98													1715			
	GBC07	48.9	0.720	6.90	0.010		11.3	0.120	9.1	19.5	2.69													282			
	GBC08	50.7	0.570	7.45	0.070		10.7	0.090	8.5	16.4	3.81													599			
	GBC09(c)	52.4	0.680	8.49	0.040		8.27	0.080	8.6	16.0	4.15													1076			
	GBC12	54.2	0.350	5.99	0.210		6.11		12.9	16.9	2.93													1201			
	GBC13	48.9	0.720	6.90	0.010		11.3	0.120	9.1	19.5	2.69													303			
Hauri and Gaetani 2006	B330	52.0	0.180	6.20	0.800		3.90	0.090	18.0	18.9	0.430													9.00	910		
	B333	52.4	0.140	6.00	0.900		4.10	0.080	19.4	17.6	0.490																
	B359	51.0	0.170	8.00	0.370		3.90	0.100	17.8	18.1	0.660													18.0	1250		
	B366	51.6	0.190	7.10	0.320		4.10	0.060	18.2	18.4	0.450													138	2000		
	B384																										
	B388																										
	B394																								332		
	B408																										
	B432	51.6	0.530	7.70	0.610		3.80	0.060	17.2	18.9	0.800													11.0	829		
	#1799																										
	#1833																										
	#1450	49.6	1.11	3.59	0.030		6.62	0.170	15.1	22.4	0.350													62.0	1350		
	#1802	47.1	1.14	10.22	0.090		10.9	0.190	12.1	15.5	1.71													20.0	1850		
Mosenfelder and Rossman 2013	ILM-50																										
	BPcpxA	55.2	0.040	0.77	0.480		2.16	0.050	17.0	24.4	0.520													8.00			
	CITI7210	55.5		0.830			0.090	0.260	18.0	26.2	0.130													25.0			
	ROM271-DI10	54.7	0.150	0.500	0.300		5.25	0.100	15.9	21.9	1.30													16.6			
	KBH-2	48.2	1.34	8.81			6.75	0.140	13.6	19.2	1.17													46.4			
	KBH-1																										
	DE2-1																										
	PMR-54																										
	GRR1650B																										
	ZM1_pxHT	52.9	0.170	3.65	1.15		2.68		17.0	21.9	0.780													27.0			
Guggino 2012	MIW-6	54.1	0.500	1.00			3.50		17.5	23.1	0.500													135			
	MIW-20	53.7	0.500	1.10			4.30		18.1	21.6	0.400													81.0			
	MIW-23	53.2	0.600	1.10			4.40		17.2	22.3	0.400													117			
	MIW-26	53.3	0.600	0.80			4.20		17.0	23.2	0.400													99.0			
	MIW-12	53.8	0.500	1.00			3.80		17.8	22.3	0.500													142			
	MOA-2	53.8	0.500	0.900			4.00		17.6	22.4	0.400													140			
	MOA-4	53.3	0.500	0.900			3.80		17.3	22.5	0.300													114			
	LIW-39	51.8	0.400	2.80			7.60		14.0	22.2	0.900													176			
	LIW-37	53.6	0.400	1.40			5.90		17.4	20.5	0.300													101			
	LIW-40	52.8	0.600	2.30			6.90		16.2	20.8	0.400													150			
	LIW-51	52.0	0.700	3.10			6.80		15.7	20.2	0.600													98.0			
	PEM22-1	50.6	0.900	5.10			7.50		15.1	21.4	0.300													41.0			
	PEM22-18	50.5	0.700	4.20			6.30		15.4	22.0	0.300													28.0			
	MIW18	53.7	0.700	0.90			4.00		17.0	22.9	0.300													154			
	PEM22-19																										
	PEM22-12																										
	PEM22-17	50.1	0.800	4.20			6.90		15.4	21.5	0.400													29.0			
	PEM22-6																										
	PEM22-5																										
	PEM22-4																										
	56B	53.7	0.700	1.40			4.70		17.0	22.3	0.300													145			
	LOA-15	51.5	0.400	2.70			8.30		13.6	22.6	0.800													221			
	LOA-18	53.0	0.400	1.90			7.60		16.6	19.7	0.500													70.0			
	LOA-8	51.6	0.400	2.60			8.30		15.1	20.3	0.600													218			
	LOA-13	51.9	0.400	1.90			7.00		14.9	22.9	0.600													211			

Table 2.4. (cont.)

	Sample	SiO2	TiO2	Al2O3	Cr2O3	FeO	MnO	MgO	CaO	Na2O	K2O	P2O5	H2O ppm	F ppm	Cl ppm
O'Leary et al. 2010	8272FH-11	49.1	0.720	19.7		8.95		7.89	9.50	3.54	0.160	0.080	11700	84.0	14.9
	8272RH-19	49.8	0.760	20.5		8.65		6.40	8.61	3.80	0.200	0.100	10940	137	15.5
	8272FH-18	47.5	0.650	19.3		8.11		9.74	10.5	2.73	0.140	0.060	23200	176	18.4
	8272FH-22	46.5	0.820	18.7		7.93		10.1	10.5	2.79	0.120	0.060	18700	131	20.7
	8272FH-23	46.4	0.660	18.7		7.92		9.50	10.3	3.17	0.150	0.050	22760	199	19.6
	8272FH-17	47.6	0.840	18.9		8.64		8.56	8.77	4.18	0.170	0.080	16400	141	16.8
	ALFB-7	39.1		0.37		14.3		12.9	23.2	4.43			57800	298	72.4
	ALFB-20	43.4		0.42		14.0		14.9	21.9	4.14			26660	226	63.6
	ALFB-21	43.3		0.22		13.1		14.9	19.4	4.60			27500	168	56.7
	ALFB-17	43.8		0.26		12.2		15.7	19.9	4.49			26400	156	53.0
Van der Bleeken and Koga, 2015	GBC05, RR(	63.9	0.250	16.1	0.010	1.26	0.050	0.090	2.04	5.48	1.11			3920	
	GBC06 RR(	62.7	0.250	15.5		1.27	0.030	0.280	1.71	6.17	1.14			2978	
	GBC07	63.6	0.140	15.8		0.99	0.060	0.110	2.18	6.14	1.14			3579	
	GBC08	61.1	0.200	15.0	0.040	0.77	0.010	0.070	1.50	6.86	1.18			4906	
	GBC09(c)	60.0	0.300	14.9	0.050	1.26	0.030	0.420	1.61	6.65	1.04			4431	
	GBC12	65.0	0.460	14.6		0.49	0.100	0.220	2.08	5.91	1.67			5165	
	GBC13	63.6	0.140	15.8		0.99	0.060	0.110	2.18	6.14	1.14			5175	
Hauri and Gaetani 2006	B330	45.1	0.600	17.6	0.110	6.92	0.120	10.3	10.2	2.15	0.10	0.100	51410	213	
	B333	45.8	0.610	17.1	0.090	6.87	0.140	11.4	10.9	2.03	0.13	0.090	40600	99.0	
	B359	43.9	0.660	17.2	0.080	7.36	0.080	11.8	10.4	2.37	0.12	0.150	49600	365	
	B366	44.2	0.660	16.8	0.120	7.77	0.130	11.4	9.86	2.42	0.11	0.160	60700	2820	
	B384	45.9	0.570	15.8	0.120	7.39	0.110	10.3	9.47	2.71	0.35	0.210	53900	1400	
	B388	45.8	0.570	15.6	0.150	6.65	0.100	10.4	9.55	2.66	0.35	0.150	45600	4740	
	B394												17500		
	B408	46.8	1.20	16.2	0.120	6.97	0.100	9.74	8.90	3.06	0.70	0.320	49200	381	
	B432	45.8	1.26	18.1	0.020	6.97	0.170	8.76	8.91	3.59	0.48		44000	164	
	#1799														
	#1833														
	#1450	44.5	2.18	14.9		8.80	0.160	5.15	9.14	3.75	2.01		55400	965	
	#1802	50.3	2.15	16.2		7.96	0.120	3.16	5.66	3.64	0.690	0.390	54500	357	
Mosenfelder and Rossman 2013															
Guggino 2012	MIW-6	52.5	2.50	14.5		9.90		5.10	7.00	2.60	5.70			1391	
	MIW-20	50.5	2.80	13.2		8.80		7.10	7.70	2.60	6.20	1.30		1820	
	MIW-23	52.5	2.70	13.8		9.50		6.50	6.70	4.90	1.50			1411	
	MIW-26	53.2	2.30	14.9		9.30		5.10	6.10	2.30	5.10	1.70			
	MIW-12	47.5	2.50	11.2		16.8		7.20	8.20	1.70	4.70			1707	
	MOA-2	53.3	3.10	16.0		8.40		5.10	6.10	1.70	6.10			2237	
	MOA-4	55.0	2.30	13.6		8.00		7.60	9.40	0.70	3.30			1302	
	LIW-39	62.0	1.20	17.5		5.00		2.60	4.30	2.10	5.10	0.300		802	
	LIW-37	60.0	1.10	16.1		5.30		3.30	5.40	2.70	6.20			733	
	LIW-40	62.0	1.20	17.1		5.10		2.00	4.10	2.50	5.70	0.300		862	
	LIW-51	60.5	1.10	16.6		5.40		3.20	5.70	2.20	5.50	0.200		800	
	PEM22-1	56.1	0.900	17.0		5.00		3.10	5.40	5.10	1.80			193	
	PEM22-18	53.2	1.00	17.6		4.90		3.30	6.50	3.90	1.20			151	
	MIW18	51.1	2.50	11.1		8.10		8.90	9.80	2.30	5.20			1708	
	PEM22-19	53.0	0.500	16.7		4.80		3.40	5.20	3.80	1.30			116	
	PEM22-12	51.8	0.600	17.5		4.50		5.20	6.40	3.10	1.30			119	
	PEM22-17	55.7	0.800	17.4		3.30		3.10	5.60	4.20	1.50			165	
	PEM22-6	58.5	0.900	16.9		5.00		2.80	5.40	2.20	1.70			175	
	PEM22-5													192	
	PEM22-4														
	56B	58.8	1.10	16.0		3.00		1.40	2.50	3.90	7.10			1092	
	LOA-15	64.2	1.00	16.7		5.10		2.00	4.90	0.80	4.80			780	
	LOA-18	62.5	1.20	15.8		5.00		2.80	5.30	1.50	5.60			963	
	LOA-8	62.8	1.00	16.6		5.20		2.10	4.30	2.20	5.80			888	
	LOA-13	66.6	1.10	16.4		4.30		2.50	4.30	0.80	3.90			1021	

Table 2.5. Intra-grain variability: electron microprobe profiles of major elements.

Fin1b Cpx

Number	177	178	179	180	181	182	183
Comment	Fin1b-Cpx1	Fin1b-Cpx1	Fin1b-Cpx1	Fin1b-Cpx1	Fin1b-Cpx1	Fin1b-Cpx1	Fin1b-Cpx1
Type	Cpx	Cpx	Cpx	Cpx	Cpx	Cpx	Cpx
	Rim						
SiO2	54.2	54.3	54.1	54.1	52.3	53.9	53.6
TiO2	.080	.040	.040	.110	.060	.050	.100
Al2O3	1.26	1.28	1.22	1.61	3.96	1.52	1.46
Cr2O3	.400	.470	.500	.700	.870	.720	.550
Fe2O3	.560	.000	.480	.120	.000	.570	.610
FeO	1.16	1.70	1.59	1.93	2.57	1.58	1.77
MnO	.060	.100	.140	.090	.130	.060	.030
NiO	.020	.080	.040	.020	.080	.030	.060
MgO	17.5	17.3	17.2	17.1	17.4	17.1	17.1
CaO	24.8	24.4	24.5	24.3	21.2	24.4	24.1
Na2O	.160	.190	.170	.240	.250	.230	.210
K2O			.020		.010		
H2O							
Sum	100.14	99.79	100.00	100.27	98.82	100.12	99.63

Si	1.96	1.97	1.97	1.96	1.91	1.96	1.96
Ti	0.002	0.001	0.001	0.003	0.002	0.001	0.003
Al	0.054	0.055	0.052	0.069	0.171	0.065	0.063
Cr	0.011	0.013	0.014	0.020	0.025	0.021	0.016
Fe3	0.015	0.000	0.013	0.003	0.000	0.015	0.017
Fe2	0.035	0.052	0.048	0.058	0.079	0.048	0.054
Mn	0.002	0.003	0.004	0.003	0.004	0.002	0.001
Ni	0.001	0.002	0.001	0.001	0.002	0.001	0.002
Mg	0.943	0.936	0.934	0.923	0.949	0.924	0.932
Ca	0.963	0.949	0.953	0.944	0.833	0.950	0.942
Na	0.011	0.014	0.012	0.017	0.018	0.016	0.015
K	0.000	0.000	0.001	0.000	0.000	0.000	0.000
OH							
*H2O							

Table 2.5. (cont.)

Fin1b Cpx

Number	184	185	186	187	188	189	190	191
Comment	Fin1b-Cpx1	Fin1b-Cpx1	Fin1b-Cpx1	Fin1b-Cpx1	Fin1b-Cpx1	Fin1b-Cpx1	Fin1b-Cpx1	Fin1b-Cpx1
Type	Cpx	Cpx	Cpx	Cpx	Cpx	Cpx	Cpx	Cpx
SiO2	52.9	53.5	53.6	53.8	53.9	53.5	53.7	53.5
TiO2	.150	.070	.070	.060	.080	.060	.080	.050
Al2O3	2.73	1.92	1.69	1.82	1.70	1.90	1.75	1.86
Cr2O3	.890	.690	.680	.730	.810	.700	.740	.700
Fe2O3	1.230	.550	.000	.670	.000	.120	.000	.000
FeO	1.11	1.61	2.05	1.62	2.08	2.06	1.94	2.18
MnO	.080	.080	.040	.070	.080	.090	.100	.140
NiO	.040	.060	.030	.020	.050	.040	.030	.040
MgO	17.5	17.2	16.8	17.1	17.0	16.8	16.9	16.8
CaO	22.4	23.7	24.3	24.3	23.9	24.1	24.1	24.1
Na2O	.500	.260	.180	.240	.200	.230	.210	.200
K2O				.010	.020			.010
H2O								
Sum	99.41	99.62	99.41	100.44	99.85	99.65	99.51	99.51
Si	1.93	1.95	1.96	1.95	1.96	1.95	1.96	1.96
Ti	0.004	0.002	0.002	0.002	0.002	0.002	0.002	0.001
Al	0.117	0.082	0.073	0.078	0.073	0.082	0.075	0.080
Cr	0.026	0.020	0.020	0.021	0.023	0.020	0.021	0.020
Fe3	0.034	0.015	0.000	0.018	0.000	0.003	0.000	0.000
Fe2	0.034	0.049	0.063	0.049	0.063	0.063	0.059	0.067
Mn	0.003	0.002	0.001	0.002	0.002	0.003	0.003	0.004
Ni	0.001	0.002	0.001	0.000	0.001	0.001	0.001	0.001
Mg	0.949	0.935	0.918	0.920	0.921	0.912	0.917	0.914
Ca	0.872	0.925	0.952	0.944	0.933	0.944	0.943	0.942
Na	0.036	0.018	0.012	0.017	0.014	0.016	0.015	0.014
K	0.000	0.000	0.000	0.000	0.001	0.000	0.000	0.000
OH								
*H2O								

Table 2.5. (cont.)

Fin1b Cpx

Number	192	193	194	195	196	197	198	199	200
Comment	Fin1b-Cpx1	Fin1b-Cpx1	Fin1b-Cpx1	Fin1b-Cpx1	Fin1b-Cpx1	Fin1b-Cpx1	Fin1b-Cpx1	Fin1b-Cpx1	Fin1b-Cpx1
Type	Cpx	Cpx	Cpx	Cpx	Cpx	Cpx	Cpx	Cpx	Cpx
SiO2	53.5	54.6	54.0	53.6	53.4	53.7	53.3	53.2	53.7
TiO2	.040	.070	.050	.040	.100	.060	.060	.020	.090
Al2O3	1.81	1.48	1.75	1.70	2.04	1.91	2.46	2.08	1.74
Cr2O3	.780	.610	.750	.700	.640	.750	.860	.750	.700
Fe2O3	.790	.000	.000	.660	1.110	.500	.650	.700	.690
FeO	1.50	3.61	2.09	1.65	1.27	1.89	1.53	1.56	1.70
MnO	.100	.050	.050	.070	.100	.000	.130	.020	.130
NiO	.000	.080	.050	.060	.060	.070	.030	.070	.040
MgO	17.0	18.7	16.7	17.0	16.9	17.0	17.0	17.1	17.2
CaO	24.1	18.9	24.0	24.2	24.2	24.0	23.3	23.9	24.1
Na2O	.240	.190	.260	.210	.300	.260	.400	.190	.230
K2O				.010			.010		
H2O									
Sum	99.85	98.26	99.79	99.95	100.08	100.11	99.76	99.59	100.27

Si	1.95	2.00	1.97	1.95	1.94	1.95	1.94	1.94	1.95
Ti	0.001	0.002	0.001	0.001	0.003	0.002	0.002	0.001	0.002
Al	0.078	0.064	0.075	0.073	0.087	0.082	0.106	0.089	0.074
Cr	0.023	0.018	0.022	0.020	0.018	0.022	0.025	0.022	0.020
Fe3	0.022	0.000	0.000	0.018	0.030	0.014	0.018	0.019	0.019
Fe2	0.046	0.111	0.064	0.050	0.039	0.058	0.047	0.047	0.052
Mn	0.003	0.001	0.001	0.002	0.003	0.000	0.004	0.001	0.004
Ni	0.000	0.002	0.001	0.002	0.002	0.002	0.001	0.002	0.001
Mg	0.925	1.02	0.908	0.924	0.913	0.921	0.924	0.932	0.927
Ca	0.940	0.742	0.936	0.944	0.944	0.934	0.908	0.933	0.935
Na	0.017	0.014	0.018	0.015	0.021	0.018	0.028	0.013	0.016
K	0.000	0.000	0.000	0.000	0.000	0.000	0.000	0.000	0.000
OH									
*H2O									

Table 2.5. (cont.)

Fin1b Cpx

Number	201	202	203	204	205	206	207	208
Comment	Fin1b-Cpx1	Fin1b-Cpx1	Fin1b-Cpx1	Fin1b-Cpx1	Fin1b-Cpx1	Fin1b-Cpx1	Fin1b-Cpx1	Fin1b-Cpx1
Type	Cpx	Cpx	Cpx	Cpx	Cpx	Cpx	Cpx	Cpx
SiO2	53.7	53.3	52.8	53.7	54.0	52.9	53.7	52.6
TiO2	.050	.090	.080	.040	.070	.060	.050	.120
Al2O3	1.62	2.24	2.72	1.77	1.36	2.43	1.62	3.74
Cr2O3	.600	.790	.900	.690	.550	.740	.690	.920
Fe2O3	.700	1.280	1.310	.340	.000	1.500	.520	1.820
FeO	1.47	1.04	1.21	1.82	1.99	.85	1.78	.72
MnO	.120	.130	.020	.080	.070	.080	.090	.080
NiO	.070	.000	.070	.030	.090	.050	.040	.070
MgO	17.0	17.3	17.5	17.0	17.0	17.3	17.0	17.4
CaO	24.4	23.4	22.3	24.2	24.3	23.2	24.4	21.3
Na2O	.240	.380	.450	.230	.190	.380	.180	.830
K2O								.010
H2O								
Sum	99.94	99.93	99.44	99.94	99.63	99.46	100.06	99.50
Si	1.95	1.93	1.93	1.95	1.97	1.93	1.95	1.91
Ti	0.001	0.002	0.002	0.001	0.002	0.002	0.001	0.003
Al	0.070	0.096	0.117	0.076	0.058	0.105	0.070	0.160
Cr	0.017	0.023	0.026	0.020	0.016	0.021	0.020	0.026
Fe3	0.019	0.035	0.036	0.009	0.000	0.041	0.014	0.050
Fe2	0.045	0.032	0.037	0.055	0.061	0.026	0.054	0.022
Mn	0.004	0.004	0.001	0.002	0.002	0.002	0.003	0.002
Ni	0.002	0.000	0.002	0.001	0.003	0.001	0.001	0.002
Mg	0.922	0.938	0.953	0.922	0.925	0.939	0.921	0.940
Ca	0.950	0.909	0.871	0.943	0.951	0.907	0.950	0.828
Na	0.017	0.027	0.032	0.016	0.014	0.027	0.013	0.058
K	0.000	0.000	0.000	0.000	0.000	0.000	0.000	0.000
OH								
*H2O								

Table 2.5. (cont.)

Fin1b Cpx

Number	209	210	211	212	213	214	215	216
Comment	Fin1b-Cpx1	Fin1b-Cpx1	Fin1b-Cpx1	Fin1b-Cpx1	Fin1b-Cpx1	Fin1b-Cpx1	Fin1b-Cpx1	Fin1b-Cpx1
Type	Cpx	Cpx	Cpx	Cpx	Cpx	Cpx	Cpx	Cpx
SiO2	53.7	53.8	53.6	53.3	53.3	53.8	53.6	53.6
TiO2	.060	.070	.040	.090	.100	.030	.090	.080
Al2O3	1.68	1.63	1.74	2.08	2.41	1.77	1.79	1.61
Cr2O3	.740	.720	.660	.700	.850	.670	.750	.610
Fe2O3	.260	.190	.660	.680	.910	.680	.690	.000
FeO	1.77	1.93	1.57	1.66	1.26	1.36	1.63	1.97
MnO	.130	.020	.100	.050	.110	.070	.040	.120
NiO	.020	.070	.070	.050	.040	.030	.050	.030
MgO	17.0	17.0	17.0	17.1	17.3	17.1	17.1	17.1
CaO	24.3	24.3	24.1	23.6	22.8	24.4	24.2	23.8
Na2O	.210	.220	.260	.300	.480	.240	.220	.200
K2O	.010			.010	.010	.010	.010	
H2O								
Sum	99.80	99.88	99.75	99.56	99.55	100.11	100.18	99.14
Si	1.96	1.96	1.95	1.94	1.94	1.95	1.95	1.96
Ti	0.002	0.002	0.001	0.002	0.003	0.001	0.003	0.002
Al	0.072	0.070	0.075	0.089	0.103	0.076	0.077	0.070
Cr	0.021	0.021	0.019	0.020	0.024	0.019	0.022	0.018
Fe3	0.007	0.005	0.018	0.019	0.025	0.019	0.019	0.000
Fe2	0.054	0.059	0.048	0.051	0.038	0.041	0.050	0.060
Mn	0.004	0.001	0.003	0.002	0.003	0.002	0.001	0.004
Ni	0.001	0.002	0.002	0.001	0.001	0.001	0.001	0.001
Mg	0.922	0.920	0.921	0.929	0.940	0.924	0.924	0.935
Ca	0.947	0.947	0.943	0.921	0.890	0.949	0.941	0.935
Na	0.015	0.016	0.019	0.021	0.034	0.017	0.016	0.014
K	0.000	0.000	0.000	0.000	0.000	0.000	0.000	0.000
OH								
*H2O								

Table 2.5. (cont.)

Fin1b Cpx

Number	217	218	219	220	221	222	223	224	225
Comment	Fin1b-Cpx1	Fin1b-Cpx1	Fin1b-Cpx1	Fin1b-Cpx1	Fin1b-Cpx1	Fin1b-Cpx1	Fin1b-Cpx1	Fin1b-Cpx1	Fin1b-Cpx1
Type	Cpx	Cpx	Cpx	Cpx	Cpx	Cpx	Cpx	Cpx	Cpx
SiO2	53.9	53.6	53.7	53.7	53.4	53.5	53.8	53.7	53.6
TiO2	.050	.050	.040	.060	.070	.080	.060	.050	.060
Al2O3	1.49	1.95	1.85	1.79	1.88	1.82	1.76	1.84	1.76
Cr2O3	.600	.770	.770	.780	.700	.740	.740	.730	.770
Fe2O3	.230	.000	.330	.740	1.410	.560	.000	.140	.730
FeO	1.90	2.11	1.93	1.30	.78	1.62	2.07	1.96	1.71
MnO	.070	.040	.070	.080	.070	.050	.060	.130	.080
NiO	.040	.020	.010	.080	.030	.030	.080	.030	.030
MgO	17.2	17.0	17.0	17.1	17.0	16.9	17.0	16.8	17.0
CaO	24.1	23.8	24.1	24.2	24.6	24.1	23.9	24.2	24.1
Na2O	.190	.260	.240	.300	.250	.270	.250	.250	.230
K2O					.010		.020		
H2O									
Sum	99.83	99.60	100.06	100.14	100.12	99.65	99.73	99.82	100.06
Si	1.96	1.96	1.95	1.95	1.94	1.95	1.96	1.96	1.95
Ti	0.001	0.001	0.001	0.002	0.002	0.002	0.002	0.001	0.002
Al	0.064	0.084	0.079	0.076	0.080	0.078	0.076	0.079	0.075
Cr	0.017	0.022	0.022	0.022	0.020	0.021	0.021	0.021	0.022
Fe3	0.006	0.000	0.009	0.020	0.039	0.015	0.000	0.004	0.020
Fe2	0.058	0.064	0.059	0.040	0.024	0.049	0.063	0.060	0.052
Mn	0.002	0.001	0.002	0.003	0.002	0.001	0.002	0.004	0.002
Ni	0.001	0.001	0.000	0.002	0.001	0.001	0.002	0.001	0.001
Mg	0.933	0.923	0.922	0.927	0.921	0.918	0.925	0.913	0.923
Ca	0.941	0.930	0.937	0.938	0.955	0.944	0.932	0.944	0.938
Na	0.014	0.019	0.017	0.021	0.018	0.019	0.018	0.018	0.016
K	0.000	0.000	0.000	0.000	0.000	0.000	0.001	0.000	0.000
OH									
*H2O									

Table 2.5. (cont.)

Fin1b Cpx

Number	226	227	228	229	230	231	232
Comment	Fin1b-Cpx1	Fin1b-Cpx1	Fin1b-Cpx1	Fin1b-Cpx1	Fin1b-Cpx1	Fin1b-Cpx1	Fin1b-Cpx1
Type	Cpx	Cpx	Cpx	Cpx	Cpx	Cpx	Cpx
							Rim
SiO2	54.0	53.7	53.7	53.7	54.3	54.3	53.9
TiO2	.040	.060	.070	.040	.100	.050	.010
Al2O3	1.73	1.63	1.56	1.32	1.08	1.12	.84
Cr2O3	.650	.700	.650	.580	.540	.380	.300
Fe2O3	.300	.350	.800	.570			1.07
FeO	1.82	1.92	1.31	1.47	2.11	1.96	.940
MnO	.070	.120	.120	.080	.050	.080	.100
NiO	.080	.040	.000	.030	.080	.090	.060
MgO	17.1	17.1	17.2	17.3	17.4	17.3	17.5
CaO	24.0	24.1	24.1	24.3	24.1	24.3	24.5
Na2O	.270	.210	.240	.180	.150	.140	.160
K2O	.010		.020		.010		
H2O							
Sum	100.06	99.89	99.76	99.53	99.99	99.79	99.38
Si	1.96	1.96	1.95	1.96	1.97	1.98	1.97
Ti	0.001	0.002	0.002	0.001	0.003	0.001	0.000
Al	0.074	0.070	0.067	0.057	0.046	0.048	0.036
Cr	0.019	0.020	0.019	0.017	0.016	0.011	0.009
Fe3	0.008	0.009	0.022	0.016	0.000	0.000	0.030
Fe2	0.055	0.058	0.040	0.045	0.064	0.060	0.029
Mn	0.002	0.004	0.004	0.002	0.002	0.002	0.003
Ni	0.002	0.001	0.000	0.001	0.002	0.003	0.002
Mg	0.927	0.926	0.935	0.940	0.944	0.939	0.953
Ca	0.934	0.939	0.941	0.948	0.938	0.947	0.959
Na	0.019	0.015	0.017	0.013	0.010	0.010	0.011
K	0.000	0.000	0.001	0.000	0.001	0.000	0.000
OH							
*H2O							

Table 2.5. (cont.)

Fin1b Amph

Number	52	53	54	55	56	57	58
Comment	Fin1b-Am1	Fin1b-Am1	Fin1b-Am1	Fin1b-Am1	Fin1b-Am1	Fin1b-Am1	Fin1b-Am1
Type	Am	Am	Am	Am	Am	Am	Am
	Rim						
SiO2	46.8	47.6	46.5	45.9	45.9	45.9	46.0
TiO2	.305	.254	.322	.334	.339	.300	.352
Al2O3	10.6	10.5	11.1	11.0	11.0	11.2	11.0
Cr2O3	1.99	1.96	1.92	2.02	1.98	1.91	1.92
Fe2O3	3.67	3.67	4.06	3.61	4.11	4.13	4.10
FeO	.00	.31	.00	.39	.00	.00	.13
MnO	.02	.06	.01	.05	.07	.07	.04
NiO	.07	.11	.13	.15	.17	.13	.09
MgO	19.0	19.1	18.9	18.7	18.6	18.6	18.9
CaO	12.4	12.5	12.5	12.5	12.3	12.2	12.6
Na2O	1.91	1.94	1.93	2.01	2.03	2.04	2.03
K2O	.614	.650	.699	.679	.711	.713	.675
H2O	2.13	2.15	2.14	2.12	2.12	2.12	2.13
Summe	99.42	100.71	100.14	99.48	99.37	99.30	99.88
Si	6.60	6.63	6.53	6.51	6.50	6.50	6.48
Ti	0.032	0.027	0.034	0.036	0.036	0.032	0.037
Al	1.76	1.72	1.83	1.84	1.84	1.86	1.83
Cr	0.222	0.216	0.213	0.226	0.222	0.214	0.214
Fe3	0.389	0.385	0.429	0.385	0.439	0.441	0.435
Fe2		0.036		0.046			0.015
Mn	0.002	0.007	0.001	0.006	0.009	0.008	0.004
Ni	0.007	0.013	0.015	0.018	0.019	0.015	0.010
Mg	3.99	3.97	3.95	3.94	3.94	3.93	3.97
Ca	1.87	1.86	1.88	1.90	1.87	1.85	1.90
Na	0.521	0.524	0.525	0.552	0.556	0.561	0.554
K	0.110	0.116	0.125	0.123	0.129	0.129	0.121
OH	2.00	2.00	2.00	2.00	2.00	2.00	2.00
*H2O							

Table 2.5. (cont.)

Fin1b Amph

Number	59	60	61	62	63	64	65	66
Comment	Fin1b-Am1	Fin1b-Am1	Fin1b-Am1	Fin1b-Am1	Fin1b-Am1	Fin1b-Am1	Fin1b-Am1	Fin1b-Am1
Type	Am	Am	Am	Am	Am	Am	Am	Am
SiO2	45.9	45.7	45.9	45.8	45.8	45.6	45.7	45.9
TiO2	.332	.354	.357	.339	.254	.272	.315	.312
Al2O3	11.2	11.4	11.3	11.2	11.2	11.5	11.4	11.2
Cr2O3	1.87	1.94	1.84	1.87	1.84	1.87	1.76	1.78
Fe2O3	4.11	4.05	4.31	4.30	4.31	4.25	3.80	4.20
FeO	.00	.08	.00	.00	.00	.00	.40	.00
MnO	.06	.04	.07	.01	.04	.10	.01	.04
NiO	.13	.09	.12	.12	.14	.11	.05	.11
MgO	18.6	18.7	18.7	18.8	18.9	18.7	18.6	18.8
CaO	12.2	12.5	12.3	12.5	12.4	12.4	12.4	12.4
Na2O	2.06	2.00	2.13	2.01	2.09	2.22	2.15	2.14
K2O	.678	.724	.712	.700	.693	.701	.669	.725
H2O	2.11	2.12	2.13	2.12	2.12	2.12	2.11	2.13
Summe	99.19	99.65	99.86	99.68	99.81	99.86	99.29	99.80
Si	6.50	6.45	6.48	6.47	6.47	6.44	6.48	6.48
Ti	0.035	0.038	0.038	0.036	0.027	0.029	0.034	0.033
Al	1.87	1.90	1.87	1.86	1.86	1.92	1.90	1.87
Cr	0.210	0.217	0.205	0.208	0.206	0.209	0.197	0.199
Fe3	0.439	0.431	0.457	0.457	0.458	0.452	0.405	0.446
Fe2		0.009					0.047	
Mn	0.007	0.005	0.008	0.001	0.005	0.012	0.002	0.005
Ni	0.014	0.010	0.013	0.014	0.015	0.013	0.006	0.012
Mg	3.93	3.93	3.94	3.96	3.97	3.93	3.93	3.96
Ca	1.85	1.89	1.86	1.89	1.88	1.87	1.88	1.87
Na	0.567	0.549	0.583	0.551	0.572	0.607	0.591	0.586
K	0.123	0.131	0.128	0.126	0.125	0.126	0.121	0.130
OH	2.00	2.00	2.00	2.00	2.00	2.00	2.00	2.00
*H2O								

Table 2.5. (cont.)

Fin1b Amph

Number	67	68		70	71	72	73	74	75
Comment	Fin1b-Am1	Fin1b-Am1	Fin1b-Am1	Fin1b-Am1	Fin1b-Am1	Fin1b-Am1	Fin1b-Am1	Fin1b-Am1	Fin1b-Am1
Type	Am	Am	Chl	Am	Am	Am	Am	Am	Am
SiO2	45.1	44.8	40.2	44.5	45.5	45.9	45.9	46.1	46.6
TiO2	.362	.397	.062	.362	.292	.349	.299	.254	.377
Al2O3	12.0	12.2	4.8	12.0	11.3	11.0	10.9	10.9	10.6
Cr2O3	1.94	1.97	.49	2.09	1.94	1.90	2.00	1.77	1.95
Fe2O3	4.14	3.53	.00	3.27	4.43	3.27	3.86	3.47	3.82
FeO	.15	1.04	4.24	1.11	.00	.83	.40	.57	.07
MnO	.02	.05	.04	.08	.00	.06	.00	.07	.08
NiO	.11	.12	.11	.12	.07	.09	.12	.09	.12
MgO	18.5	18.1	33.8	17.9	18.7	18.4	18.7	18.8	19.0
CaO	12.5	12.4	1.0	12.4	12.4	12.4	12.5	12.5	12.5
Na2O	2.23	2.33	.07	2.27	2.04	2.03	2.05	2.03	1.89
K2O	.725	.760	.022	.748	.716	.740	.709	.712	.644
H2O	2.12	2.11	12.40	2.09	2.12	2.11	2.12	2.11	2.13
Summe	99.96	99.80	97.20	98.98	99.50	99.07	99.55	99.30	99.86
Si	6.37	6.36	3.89	6.36	6.44	6.52	6.50	6.53	6.56
Ti	0.038	0.042	0.005	0.039	0.031	0.037	0.032	0.027	0.040
Al	2.00	2.04	0.55	2.03	1.89	1.85	1.82	1.82	1.76
Cr	0.217	0.221	0.037	0.236	0.218	0.214	0.223	0.199	0.217
Fe3	0.440	0.377	0.000	0.352	0.472	0.350	0.412	0.370	0.404
Fe2	0.017	0.123	0.343	0.133		0.099	0.048	0.068	0.008
Mn	0.003	0.006	0.003	0.010	0.000	0.008	0.000	0.009	0.010
Ni	0.013	0.013	0.009	0.013	0.008	0.011	0.014	0.010	0.014
Mg	3.90	3.82	4.88	3.83	3.95	3.91	3.95	3.97	3.99
Ca	1.89	1.89	0.11	1.91	1.88	1.89	1.89	1.90	1.89
Na	0.609	0.642	0.013	0.631	0.560	0.561	0.562	0.557	0.517
K	0.131	0.138	0.003	0.137	0.129	0.134	0.128	0.129	0.116
OH	2.00	2.00	8.00	2.00	2.00	2.00	2.00	2.00	2.00
*H2O									

Table 2.5. (cont.)

Fin1b Amph

Number	76	77	78	79	80	81	82	83
Comment	Fin1b-Am1	Fin1b-Am1	Fin1b-Am1	Fin1b-Am1	Fin1b-Am1	Fin1b-Am1	Fin1b-Am1	Fin1b-Am1
Type	Am	Am	Am	Am	Am	Am	Am	Am
SiO2	46.6	46.4	46.4	46.6	46.3	46.3	46.3	46.6
TiO2	.320	.297	.297	.304	.224	.354	.280	.319
Al2O3	10.6	10.9	10.7	10.7	10.6	10.9	11.0	10.6
Cr2O3	1.93	1.94	1.87	1.94	1.85	1.89	1.85	1.86
Fe2O3	4.07	4.06	3.30	3.42	3.53	3.87	3.28	4.39
FeO	.00	.00	.41	.40	.43	.00	.59	.00
MnO	.03	.07	.08	.04	.08	.02	.05	.05
NiO	.12	.16	.09	.14	.13	.10	.13	.14
MgO	19.1	18.7	18.7	18.8	18.7	19.1	18.7	19.0
CaO	12.5	12.3	12.4	12.4	12.4	12.4	12.5	12.4
Na2O	1.93	2.02	1.86	1.92	1.95	1.97	1.98	1.99
K2O	.625	.664	.675	.647	.653	.620	.660	.708
H2O	2.13	2.12	2.11	2.12	2.11	2.13	2.12	2.14
Summe	100.01	99.59	98.86	99.40	99.03	99.61	99.31	100.29
Si	6.55	6.55	6.59	6.58	6.58	6.53	6.55	6.54
Ti	0.034	0.032	0.032	0.032	0.024	0.038	0.030	0.034
Al	1.76	1.81	1.79	1.78	1.77	1.81	1.83	1.76
Cr	0.215	0.216	0.210	0.217	0.207	0.211	0.207	0.206
Fe3	0.431	0.431	0.353	0.364	0.377	0.411	0.349	0.464
Fe2			0.049	0.048	0.051		0.070	
Mn	0.004	0.008	0.010	0.004	0.010	0.002	0.006	0.006
Ni	0.013	0.018	0.010	0.016	0.014	0.011	0.015	0.015
Mg	4.01	3.94	3.96	3.96	3.97	4.00	3.94	3.97
Ca	1.88	1.85	1.89	1.88	1.89	1.87	1.89	1.87
Na	0.527	0.553	0.511	0.526	0.537	0.539	0.544	0.542
K	0.112	0.120	0.122	0.117	0.118	0.112	0.119	0.127
OH	2.00	2.00	2.00	2.00	2.00	2.00	2.00	2.00
*H2O								

Table 2.5. (cont.)

Fin1b Amph

Number	84	85	86	87	88	89	90	91
Comment	Fin1b-Am1	Fin1b-Am1	Fin1b-Am1	Fin1b-Am1	Fin1b-Am1	Fin1b-Am1	Fin1b-Am1	Fin1b-Am1
Type	Am	Am	Am	Am	Am	Am	Am	Am
SiO2	45.7	45.9	45.8	45.9	45.8	46.4	46.2	45.7
TiO2	.322	.364	.314	.305	.324	.324	.312	.332
Al2O3	11.0	11.2	11.2	11.0	11.3	10.5	11.4	11.2
Cr2O3	1.84	1.83	1.80	1.79	1.89	1.94	1.81	1.83
Fe2O3	3.52	3.78	3.97	4.04	4.07	3.27	4.01	3.31
FeO	.43	.28	.00	.13	.00	.74	.00	.71
MnO	.00	.05	.08	.07	.05	.06	.08	.01
NiO	.12	.11	.09	.09	.16	.12	.12	.11
MgO	18.8	18.7	18.7	18.9	18.6	18.7	18.9	18.6
CaO	12.6	12.4	12.3	12.6	12.3	12.4	12.5	12.5
Na2O	2.06	2.08	2.05	2.03	1.97	2.00	2.05	2.11
K2O	.656	.743	.734	.697	.703	.667	.699	.711
H2O	2.11	2.12	2.11	2.12	2.12	2.12	2.13	2.11
Summe	99.08	99.52	99.11	99.65	99.38	99.30	100.14	99.18
Si	6.50	6.49	6.50	6.49	6.49	6.58	6.49	6.49
Ti	0.034	0.039	0.034	0.032	0.034	0.035	0.033	0.035
Al	1.85	1.87	1.87	1.83	1.89	1.76	1.89	1.87
Cr	0.206	0.205	0.202	0.200	0.212	0.217	0.201	0.206
Fe3	0.376	0.402	0.424	0.430	0.434	0.348	0.424	0.354
Fe2	0.051	0.033		0.016		0.088		0.085
Mn	0.000	0.006	0.010	0.008	0.006	0.008	0.010	0.002
Ni	0.013	0.012	0.010	0.010	0.018	0.014	0.014	0.012
Mg	3.97	3.95	3.96	3.98	3.92	3.95	3.95	3.94
Ca	1.91	1.88	1.87	1.90	1.87	1.88	1.88	1.90
Na	0.567	0.570	0.563	0.558	0.541	0.551	0.559	0.580
K	0.119	0.134	0.133	0.126	0.127	0.121	0.125	0.129
OH	2.00	2.00	2.00	2.00	2.00	2.00	2.00	2.00
*H2O								

Table 2.5. (cont.)

Fin1b Amph

Number	92	93	94	95	96	97	98	99	100
Comment	Fin1b-Am1	Fin1b-Am1	Fin1b-Am1	Fin1b-Am1	Fin1b-Am1	Fin1b-Am1	Fin1b-Am1	Fin1b-Am1	Fin1b-Am1
Type	Am	Am	Am	Am	Am	Am	Am	Am	Am
SiO2	46.0	46.0	46.1	46.0	46.3	45.9	46.1	45.9	46.1
TiO2	.277	.304	.307	.330	.332	.327	.279	.274	.335
Al2O3	11.1	11.0	11.0	10.8	10.8	11.2	11.2	11.0	11.2
Cr2O3	1.98	1.99	1.94	1.86	1.97	1.95	2.00	1.98	1.95
Fe2O3	4.09	3.67	3.94	3.51	3.80	4.08	3.96	3.78	3.52
FeO	.00	.25	.07	.49	.00	.12	.00	.06	.26
MnO	.05	.03	.01	.04	.00	.04	.03	.08	.05
NiO	.11	.10	.07	.15	.11	.10	.13	.14	.11
MgO	18.7	18.7	18.8	18.7	19.0	18.7	18.8	18.6	18.7
CaO	12.2	12.4	12.4	12.5	12.2	12.4	12.4	12.4	12.4
Na2O	2.03	2.01	1.97	2.00	1.99	2.08	2.03	1.93	2.05
K2O	.701	.719	.732	.667	.748	.711	.723	.699	.747
H2O	2.12	2.11	2.12	2.11	2.12	2.12	2.13	2.11	2.12
Summe	99.50	99.17	99.31	99.18	99.32	99.64	99.71	98.93	99.59
Si	6.51	6.52	6.52	6.53	6.55	6.49	6.50	6.53	6.51
Ti	0.029	0.032	0.033	0.035	0.035	0.035	0.030	0.029	0.036
Al	1.85	1.84	1.83	1.80	1.80	1.86	1.86	1.83	1.87
Cr	0.221	0.223	0.217	0.208	0.220	0.218	0.223	0.222	0.218
Fe3	0.435	0.392	0.419	0.375	0.404	0.434	0.421	0.404	0.375
Fe2		0.029	0.008	0.058		0.014		0.007	0.030
Mn	0.006	0.003	0.002	0.004		0.005	0.003	0.010	0.006
Ni	0.013	0.011	0.008	0.017	0.013	0.011	0.015	0.016	0.012
Mg	3.95	3.95	3.96	3.97	4.00	3.93	3.96	3.95	3.94
Ca	1.85	1.88	1.87	1.90	1.84	1.87	1.87	1.88	1.88
Na	0.555	0.553	0.541	0.551	0.546	0.570	0.555	0.533	0.562
K	0.126	0.130	0.132	0.121	0.135	0.128	0.130	0.127	0.135
OH	2.00	2.00	2.00	2.00	2.00	2.00	2.00	2.00	2.00
*H2O									

Table 2.5. (cont.)

Fin1b Amph

Number	101	102	103	104	105	106	107
Comment	Fin1b-Am1	Fin1b-Am1	Fin1b-Am1	Fin1b-Am1	Fin1b-Am1	Fin1b-Am1	Fin1b-Am1
Type	Am	Am	Am	Am	Am	Am	Am
SiO2	45.7	45.7	45.7	45.9	46.1	46.0	46.1
TiO2	.392	.342	.292	.317	.280	.314	.290
Al2O3	11.1	11.2	11.0	11.0	11.2	11.2	11.1
Cr2O3	1.88	1.91	1.87	1.92	1.91	2.00	1.94
Fe2O3	3.80	4.30	4.29	3.46	4.19	3.59	3.91
FeO	.26	.00	.00	.54	.00	.50	.28
MnO	.08	.07	.10	.05	.02	.05	.10
NiO	.07	.09	.12	.14	.10	.11	.19
MgO	18.7	18.7	18.7	18.8	18.7	18.6	18.5
CaO	12.5	12.4	12.4	12.6	12.3	12.4	12.4
Na2O	2.00	1.97	1.98	2.02	1.98	2.02	1.93
K2O	.734	.689	.736	.762	.732	.724	.758
H2O	2.11	2.12	2.11	2.12	2.13	2.12	2.12
Summe	99.20	99.46	99.30	99.63	99.74	99.68	99.65
Si	6.48	6.47	6.48	6.49	6.50	6.50	6.51
Ti	0.042	0.036	0.031	0.034	0.030	0.033	0.031
Al	1.86	1.87	1.84	1.84	1.87	1.87	1.85
Cr	0.211	0.213	0.210	0.215	0.213	0.223	0.217
Fe3	0.406	0.458	0.458	0.368	0.444	0.382	0.416
Fe2	0.030			0.063		0.059	0.033
Mn	0.009	0.009	0.012	0.006	0.003	0.006	0.012
Ni	0.008	0.010	0.013	0.015	0.012	0.012	0.021
Mg	3.95	3.94	3.95	3.97	3.93	3.91	3.91
Ca	1.90	1.87	1.89	1.91	1.86	1.88	1.88
Na	0.552	0.541	0.545	0.555	0.542	0.552	0.529
K	0.133	0.124	0.133	0.138	0.132	0.131	0.137
OH	2.00	2.00	2.00	2.00	2.00	2.00	2.00
*H2O							

Table 2.5. (cont.)

Fin1b Amph

Number	108	109	110	111	112	113	118
Comment	Fin1b-Am1	Fin1b-Am1	Fin1b-Am1	Fin1b-Am1	Fin1b-Am1	Fin1b-Am1	Fin1b-Am1
Type	Am	Am	Am	Am	Am	Am	Am
SiO2	46.0	45.9	45.7	46.4	46.0	46.0	46.1
TiO2	.292	.292	.340	.272	.284	.272	.314
Al2O3	11.2	11.2	11.1	11.1	11.2	11.0	11.4
Cr2O3	2.04	1.89	2.03	1.90	1.91	1.93	1.97
Fe2O3	4.21	4.02	3.89	3.48	3.89	3.23	3.46
FeO	.14	.00	.00	.65	.00	.76	.34
MnO	.03	.04	.08	.08	.02	.08	.07
NiO	.09	.12	.11	.13	.15	.10	.12
MgO	18.6	18.7	18.8	18.5	18.6	18.6	18.6
CaO	12.3	12.3	12.3	12.4	12.3	12.6	12.5
Na2O	2.01	1.92	1.94	1.95	1.92	1.91	1.94
K2O	.762	.723	.744	.743	.738	.707	.654
H2O	2.12	2.12	2.11	2.12	2.12	2.11	2.12
Summe	99.80	99.30	99.13	99.76	99.15	99.30	99.58
Si	6.49	6.50	6.49	6.55	6.52	6.52	6.50
Ti	0.031	0.031	0.036	0.029	0.030	0.029	0.033
Al	1.87	1.87	1.86	1.84	1.87	1.85	1.90
Cr	0.227	0.211	0.228	0.212	0.214	0.217	0.220
Fe3	0.447	0.429	0.416	0.369	0.415	0.345	0.367
Fe2	0.017			0.077		0.090	0.040
Mn	0.003	0.004	0.010	0.010	0.003	0.009	0.008
Ni	0.011	0.014	0.012	0.015	0.017	0.012	0.013
Mg	3.91	3.96	3.97	3.90	3.94	3.93	3.91
Ca	1.87	1.87	1.86	1.88	1.86	1.92	1.90
Na	0.550	0.528	0.533	0.532	0.527	0.525	0.531
K	0.137	0.131	0.135	0.134	0.133	0.128	0.118
OH	2.00	2.00	2.00	2.00	2.00	2.00	2.00
*H2O							

Table 2.5. (cont.)

Fin1b Amph

Number	119	120	121	122	123	124	125
Comment	Fin1b-Am1	Fin1b-Am1	Fin1b-Am1	Fin1b-Am1	Fin1b-Am1	Fin1b-Am1	Fin1b-Am1
Type	Am	Am	Am	Am	Am	Am	Am
							Rim
SiO2	46.3	45.7	45.6	45.6	46.4	45.9	46.0
TiO2	.352	.369	.360	.377	.372	.350	.359
Al2O3	11.6	11.4	11.6	11.7	10.9	11.3	11.5
Cr2O3	2.03	1.84	1.95	1.96	1.86	1.89	1.95
Fe2O3	4.00	3.28	4.30	3.82	3.51	3.10	2.65
FeO	.00	.62	.00	.39	.61	.85	1.08
MnO	.10	.07	.04	.08	.02	.07	.05
NiO	.10	.12	.11	.08	.11	.06	.14
MgO	19.0	18.3	18.5	18.5	18.6	18.5	18.3
CaO	12.4	12.3	12.2	12.5	12.3	12.5	12.4
Na2O	1.92	2.00	2.14	2.13	2.03	2.07	2.06
K2O	.676	.728	.670	.696	.701	.658	.683
H2O	2.14	2.11	2.12	2.13	2.12	2.11	2.12
Summe	100.57	98.82	99.62	100.05	99.46	99.36	99.32
Si	6.47	6.51	6.44	6.43	6.57	6.51	6.52
Ti	0.037	0.040	0.038	0.040	0.040	0.037	0.038
Al	1.90	1.91	1.94	1.95	1.81	1.88	1.93
Cr	0.225	0.207	0.218	0.218	0.208	0.211	0.218
Fe3	0.421	0.351	0.457	0.405	0.374	0.331	0.282
Fe2		0.074		0.046	0.072	0.100	0.127
Mn	0.012	0.008	0.004	0.009	0.002	0.008	0.006
Ni	0.012	0.014	0.012	0.009	0.013	0.007	0.016
Mg	3.96	3.89	3.90	3.89	3.92	3.92	3.87
Ca	1.86	1.88	1.85	1.89	1.86	1.90	1.88
Na	0.520	0.552	0.586	0.582	0.555	0.568	0.567
K	0.121	0.132	0.121	0.125	0.126	0.119	0.123
OH	2.00	2.00	2.00	2.00	2.00	2.00	2.00
*H2O							

Table 2.5. (cont.)

Fin1b Opx

Number	131	132	133	134	135	136	137
Comment	Fin1b-Opx1	Fin1b-Opx1	Fin1b-Opx1	Fin1b-Opx1	Fin1b-Opx1	Fin1b-Opx1	Fin1b-Opx1
Type	Opx	Opx	Opx	Opx	Opx	Opx	Opx
	Rim						
SiO2	57.4	57.3	57.1	56.8	56.5	56.9	56.9
TiO2	.023	.010	.038	.000	.022	.048	.020
Al2O3	1.09	1.42	1.39	1.41	1.38	1.43	1.53
Cr2O3	.209	.276	.354	.311	.339	.295	.308
Fe2O3	.000	.274	.086	.954	.501	.651	1.06
FeO	6.56	6.25	6.32	5.65	5.65	5.88	5.70
MnO	.11	.20	.15	.18	.08	.19	.14
NiO	.08	.08	.07	.10	.08	.09	.10
MgO	34.43	34.55	34.44	34.51	34.32	34.42	34.55
CaO	.291	.294	.302	.362	.360	.416	.379
Na2O	.015	.000	.000	.011	.034	.000	.005
K2O		.002	.001		.002	.014	
H2O							
Sum	100.23	100.62	100.25	100.32	99.30	100.31	100.69

Si	1.98	1.96	1.96	1.96	1.96	1.96	1.95
Ti	0.001	0.000	0.001	0.000	0.001	0.001	0.001
Al	0.044	0.057	0.056	0.057	0.057	0.058	0.062
Cr	0.006	0.007	0.010	0.008	0.009	0.008	0.008
Fe3	0.000	0.007	0.002	0.025	0.013	0.017	0.027
Fe2	0.189	0.179	0.182	0.163	0.164	0.169	0.164
Mn	0.003	0.006	0.004	0.005	0.002	0.005	0.004
Ni	0.002	0.002	0.002	0.003	0.002	0.002	0.003
Mg	1.77	1.77	1.77	1.77	1.78	1.77	1.77
Ca	0.011	0.011	0.011	0.013	0.013	0.015	0.014
Na	0.001			0.001	0.002		
K						0.001	
OH							
*H2O							

Table 2.5. (cont.)

Fin1b Opx

Number	138	139	140	141	142	143	144	145
Comment	Fin1b-Opx1	Fin1b-Opx1	Fin1b-Opx1	Fin1b-Opx1	Fin1b-Opx1	Fin1b-Opx1	Fin1b-Opx1	Fin1b-Opx1
Type	Opx	Opx	Opx	Opx	Opx	Opx	Opx	Opx
SiO2	57.1	56.7	57.0	57.0	57.1	57.1	56.9	57.0
TiO2	.038	.013	.052	.043	.063	.037	.048	.057
Al2O3	1.53	1.46	1.47	1.49	1.59	1.64	1.63	1.60
Cr2O3	.348	.373	.402	.400	.390	.383	.387	.383
Fe2O3	.538	.625	.195	.504		.701	.476	.469
FeO	5.99	5.70	6.04	6.00	6.12	5.72	6.08	5.94
MnO	.12	.08	.17	.18	.17	.17	.17	.18
NiO	.07	.10	.11	.06	.12	.06	.03	.06
MgO	34.57	34.45	34.42	34.48	34.35	34.61	34.29	34.50
CaO	.364	.318	.311	.343	.305	.427	.348	.302
Na2O	.000	.005	.026	.001	.050	.000	.030	.019
K2O		.017	.005	.011	.001	.019	.019	.005
H2O								
Sum	100.64	99.82	100.22	100.50	100.30	100.83	100.38	100.47

Si	1.96	1.96	1.96	1.96	1.96	1.95	1.96	1.96
Ti	0.001	0.000	0.001	0.001	0.002	0.001	0.001	0.001
Al	0.062	0.059	0.060	0.060	0.064	0.066	0.066	0.065
Cr	0.009	0.010	0.011	0.011	0.011	0.010	0.011	0.010
Fe3	0.014	0.016	0.005	0.013	0.000	0.018	0.012	0.012
Fe2	0.172	0.165	0.174	0.172	0.176	0.164	0.175	0.170
Mn	0.004	0.002	0.005	0.005	0.005	0.005	0.005	0.005
Ni	0.002	0.003	0.003	0.002	0.003	0.002	0.001	0.002
Mg	1.77	1.77	1.77	1.77	1.76	1.77	1.76	1.77
Ca	0.013	0.012	0.011	0.013	0.011	0.016	0.013	0.011
Na			0.002		0.003		0.002	0.001
K		0.001				0.001	0.001	
OH								
*H2O								

Table 2.5. (cont.)

Fin1b Opx

Number	146	147	148	149	150	151	152	153	154
Comment	Fin1b-Opx1	Fin1b-Opx1	Fin1b-Opx1	Fin1b-Opx1	Fin1b-Opx1	Fin1b-Opx1	Fin1b-Opx1	Fin1b-Opx1	Fin1b-Opx1
Type	Opx	Opx	Opx	Opx	Opx	Opx	Opx	Opx	Opx
SiO2	57.2	57.0	56.9	57.2	56.8	57.1	56.8	56.8	56.6
TiO2	.023	.010	.052	.068	.047	.020	.048	.005	.067
Al2O3	1.69	1.55	1.52	1.69	1.60	1.61	1.71	1.67	1.91
Cr2O3	.419	.368	.428	.398	.313	.339	.415	.392	.379
Fe2O3		.009	.750	.164	.297	.239	.039	.271	.746
FeO	6.17	6.36	5.75	6.38	6.03	6.09	6.40	6.19	5.97
MnO	.17	.04	.19	.20	.20	.16	.15	.18	.21
NiO	.11	.05	.09	.07	.06	.14	.19	.10	.08
MgO	34.45	34.30	34.52	34.48	34.29	34.39	34.15	34.20	34.28
CaO	.318	.382	.304	.270	.327	.329	.316	.339	.280
Na2O	.008	.027	.019	.005	.000	.030	.000	.007	.000
K2O			.004		.025	.017		.004	
H2O									
Sum	100.52	100.12	100.49	100.95	99.94	100.45	100.25	100.17	100.50

Si	1.96	1.96	1.95	1.96	1.96	1.96	1.96	1.96	1.94
Ti	0.001	0.000	0.001	0.002	0.001	0.001	0.001	0.000	0.002
Al	0.068	0.063	0.061	0.068	0.065	0.065	0.069	0.068	0.077
Cr	0.011	0.010	0.012	0.011	0.009	0.009	0.011	0.011	0.010
Fe3	0.000	0.000	0.019	0.004	0.008	0.006	0.001	0.007	0.019
Fe2	0.177	0.183	0.165	0.183	0.174	0.175	0.184	0.178	0.171
Mn	0.005	0.001	0.006	0.006	0.006	0.005	0.004	0.005	0.006
Ni	0.003	0.001	0.003	0.002	0.002	0.004	0.005	0.003	0.002
Mg	1.76	1.76	1.77	1.76	1.76	1.76	1.75	1.76	1.76
Ca	0.012	0.014	0.011	0.010	0.012	0.012	0.012	0.013	0.010
Na	0.001	0.002	0.001			0.002			
K					0.001	0.001			
OH									
*H2O									

Table 2.5. (cont.)

Fin1b Opx

Number	155	156	157	158	159	160	161	162
Comment	Fin1b-Opx1	Fin1b-Opx1	Fin1b-Opx1	Fin1b-Opx1	Fin1b-Opx1	Fin1b-Opx1	Fin1b-Opx1	Fin1b-Opx1
Type	Opx	Opx	Opx	Opx	Opx	Opx	Opx	Opx
SiO2	57.1	57.1	57.1	57.4	57.4	56.9	57.1	56.9
TiO2	.052	.005	.042	.022	.037	.000	.033	.065
Al2O3	1.56	1.46	1.59	1.34	1.29	1.70	1.60	1.53
Cr2O3	.338	.364	.361	.376	.364	.387	.373	.349
Fe2O3	.611	.750	.633	.601	.869	.368	.402	.637
FeO	5.94	5.88	5.98	5.75	5.59	6.03	6.07	5.82
MnO	.13	.14	.14	.12	.17	.17	.18	.15
NiO	.09	.07	.09	.11	.11	.09	.11	.10
MgO	34.52	34.63	34.63	34.93	34.85	34.35	34.44	34.50
CaO	.407	.295	.301	.298	.472	.322	.326	.337
Na2O	.005	.016	.000	.000	.008	.018	.027	.009
K2O	.005	.005	.001		.010		.001	.013
H2O								
Sum	100.72	100.73	100.87	100.93	101.16	100.32	100.64	100.39

Si	1.95	1.96	1.95	1.96	1.96	1.96	1.96	1.95
Ti	0.001	0.000	0.001	0.001	0.001	0.000	0.001	0.002
Al	0.063	0.059	0.064	0.054	0.052	0.069	0.065	0.062
Cr	0.009	0.010	0.010	0.010	0.010	0.011	0.010	0.009
Fe3	0.016	0.019	0.016	0.015	0.022	0.010	0.010	0.016
Fe2	0.170	0.169	0.171	0.164	0.159	0.173	0.174	0.167
Mn	0.004	0.004	0.004	0.004	0.005	0.005	0.005	0.004
Ni	0.003	0.002	0.002	0.003	0.003	0.003	0.003	0.003
Mg	1.76	1.77	1.77	1.78	1.77	1.76	1.76	1.77
Ca	0.015	0.011	0.011	0.011	0.017	0.012	0.012	0.012
Na		0.001			0.001	0.001	0.002	0.001
K								0.001
OH								
*H2O								

Table 2.5. (cont.)

Fin1b Opx

Number	163	164	165	166	167	168	169	170
Comment	Fin1b-Opx1	Fin1b-Opx1	Fin1b-Opx1	Fin1b-Opx1	Fin1b-Opx1	Fin1b-Opx1	Fin1b-Opx1	Fin1b-Opx1
Type	Opx	Opx	Opx	bad	Opx	Opx	Opx	Opx
								Rim
SiO2	57.0	57.1	57.1	54.7	57.2	57.2	57.2	57.2
TiO2	.000	.020	.033	.042	.027	.005	.028	.000
Al2O3	1.49	1.63	1.53	1.60	1.43	1.39	1.26	1.30
Cr2O3	.317	.376	.357	.395	.276	.303	.270	.225
Fe2O3	.508	.680	.516	2.08	.521		.765	.243
FeO	5.77	5.99	6.11	2.56	6.11	6.25	5.59	6.46
MnO	.11	.21	.13	.15	.13	.16	.19	.16
NiO	.11	.06	.06	.08	.09	.09	.11	.06
MgO	34.59	34.50	34.54	34.75	34.57	34.34	34.74	34.46
CaO	.341	.340	.326	.203	.318	.299	.302	.208
Na2O	.008	.023	.000	.074	.012	.012	.026	.008
K2O			.010	.047	.012		.017	.011
H2O								
Sum	100.22	100.93	100.71	96.70	100.72	100.03	100.44	100.35

Si	1.96	1.95	1.96	1.94	1.96	1.97	1.96	1.97
Ti	0.000	0.001	0.001	0.001	0.001	0.000	0.001	0.000
Al	0.060	0.066	0.062	0.067	0.058	0.056	0.051	0.053
Cr	0.009	0.010	0.010	0.011	0.007	0.008	0.007	0.006
Fe3	0.013	0.018	0.013	0.055	0.013	0.000	0.020	0.006
Fe2	0.166	0.171	0.175	0.076	0.175	0.180	0.160	0.186
Mn	0.003	0.006	0.004	0.004	0.004	0.005	0.005	0.005
Ni	0.003	0.002	0.002	0.002	0.003	0.002	0.003	0.002
Mg	1.77	1.76	1.76	1.83	1.77	1.76	1.78	1.77
Ca	0.013	0.012	0.012	0.008	0.012	0.011	0.011	0.008
Na	0.001	0.002		0.005	0.001	0.001	0.002	0.001
K				0.002	0.001		0.001	
OH								
*H2O								

Table 2.6. Estimated halogen content of bulk peridotite (this study) and DMM (literature)

Sample ID	Bulk F Budget (ppm)	Bulk Cl Budget (ppm)	Modal Proportions			References
			Olivine	Opx	Cpx	
J127-19	1.69	0.340	0.77	0.19	0.04	Le Roux et al. 2014
J98-10**	1.79	0.384	0.65	0.24	0.10	Le Roux et al. 2014
J127-17**	1.39	0.291	0.70	0.27	0.03	Le Roux et al. 2014
J98-10**	1.50	0.300	0.65	0.24	0.10	Le Roux et al. 2014
J127-09** I	1.92	0.282	0.69	0.18	0.13	Le Roux et al. 2014
J127-09** II	1.70	0.336	0.69	0.18	0.13	Le Roux et al. 2014
GC2b	2.47	0.148	0.55	0.35	0.05	Li 2008
SC99-2	6.22	0.176	0.60	0.30	0.08	Li 2008
KLB-1	20.3	0.140	0.60	0.23	0.14	Davis 2009
TH2	31.1	0.156	0.90	0.10	0.001	Li 2008
DHS18	7.76	0.166	0.63	0.23	0.12	Luffi 2009
DHS2*	9.35	0.169	0.63	0.23	0.12	Luffi 2009
DHS7*	5.24	0.145	0.63	0.23	0.12	Luffi 2009
MAR	2.07	0.318	0.68	0.28	0.02	This Study
	Literature Estimates					
	Saal et al 2002		16±3	0.9		
	Salters and Stracke 2004		11±4.5	0.51		
	Le Roux 2006		16.7±1.0	-		
	Shaw 2010		17	5		
	Beyer 2012		12	-		
	Le Voyer 2015		12	1		
	Shimizu 2016 D-DMM		8±1.4	0.4		
	Shimizu 2016 E-DMM		31	22		
	Shimizu 2016 Pacific Mantle		13	5		
		* Mineral modes from DHS18				
		** Olivine F concentratiom is taken from J127-19				

Table 2.6. (cont.)

Sample ID	F ppm	Cl ppm	F Background (ppm)	Cl Background ppm		F ppm	Cl ppm	F Background ppm	Cl Background ppm
	CPX					OPX			
J127-19	1.66	0.450	1.45	0.230	J127-19	1.84	0.330	1.45	0.230
J98-10**	2.73	0.677	1.45	0.230	J98-10	1.86	0.410	1.45	0.230
J127-17**	0.98	0.256	0.510	0.170	J127-17	0.72	0.170	0.51	0.170
J98-10**	1.57	0.259	0.510	0.170	J98-10	1.10	0.228	0.51	0.170
J127-09** I	3.63	0.170	1.20	0.120	J127-9	1.71	0.147	1.20	0.120
J127-09** II	2.28	0.445	0.510	0.170	J127-09	1.44	0.250	0.51	0.170
GC2b	3.76	0.150	1.20	0.120	GC2b	2.97	0.150	1.20	0.120
SC99-2	34.7	0.190	1.20	0.120	SC99-2	7.07	0.163	1.20	0.120
KLB-1	42.8	0.135	1.20	0.120	KLB-1	17.8	0.135	1.20	0.120
TH2	84.5	0.317	1.20	0.120	TH2	35.3	0.120	1.20	0.120
DHS18	32.8	0.200	1.20	0.120	DHS18	11.7	0.150	1.20	0.120
DHS2*	37.2	0.177	1.20	0.120	DHS2	16.1	0.147	1.20	0.120
DHS7*	19.8	0.120	1.20	0.120	DHS7	7.69	0.120	1.20	0.120
MAR	2.50	0.339	0.510	0.170	MAR	1.47	0.301	0.510	0.170
Sa									
Sh									
Sh									
Shin									

Table 2.6. (cont.)

Sample ID		F ppm	Cl ppm	F Background ppm	Cl Background ppm
		OL			
J127-19	J127-19	1.67	0.340	1.45	0.230
J98-10**					
J127-17**					
J98-10**					
J127-09** I					
J127-09** II					
GC2b	GC2b	2.25	0.160	1.20	0.120
SC99-2	SC99-2	2.20	0.187	1.20	0.120
KLB-1	KLB-1	17.1	0.150	1.20	0.120
TH2	TH2	30.5	0.160	1.20	0.120
DHS18	DHS18	1.74	0.170	1.20	0.120
DHS2*	DHS2	1.82	0.180	1.20	0.120
DHS7*	DHS7	1.70	0.163	1.20	0.120
MAR	MAR	2.35	0.330	0.51	0.170
Sa					
Sh					
Sh					
Shin					

Table 2.7. See Citations. Full dataset available from Contributions to Mineralogy and Petrology website (https://link.springer.com/article/10.1007/s00410-017-1368-7).

Chapter 3

The distribution and abundance of halogens in eclogites: An in situ SIMS perspective of the Raspas Complex (Ecuador)

This chapter was originally published in *American Mineralogist* (2020) as:

Urann, B. M., Le Roux, V., John, T., Beaudoin, G. M. & Barnes, J. D. The distribution and abundance of halogens in eclogites: An in situ SIMS perspective of the Raspas Complex (Ecuador). *American Mineralogist: Journal of Earth and Planetary Materials* **105**, 307-318 (2020).

This paper has been reprinted with permissions granted in the original copyright agreement.

3.1 Abstract

We present in situ secondary ion mass spectrometry and electron microprobe analyses of coexisting garnet, omphacite, phengite, amphibole, and apatite, combined with pyrohydrolysis bulk-rock analyses to constrain the distribution, abundance, and behavior of halogens (F and Cl) in six MORB-like eclogites from the Raspas Complex (Southern Ecuador). In all cases concerning lattice-hosted halogens, F compatibility decreases from apatite (1.47–3.25 wt%), to amphibole (563–4727 μg/g), phengite (610–1822 μg/g), omphacite (6.5–54.1 μg/g), and garnet (1.7–8.9 μg/g). The relative compatibility of Cl in the assemblage is greatest for apatite (192–515 μg/g), followed by amphibole (0.64–82.7 μg/g), phengite (1.2–2.1 μg/g), omphacite (<0.05–1.0 μg/g), and garnet (<0.05 μg/g). Congruence between SIMS-reconstructed F bulk abundances and yield-corrected bulk pyrohydrolysis analyses indicates that F is primarily hosted within the crystal lattice of eclogitic minerals. However, SIMS-reconstructed Cl abundances are a factor of five lower, on average, than pyrohydrolysis-derived bulk concentrations. This discrepancy results from the contribution of fluid inclusions, which may host at least 80% of the bulk rock Cl. The combination of SIMS and pyrohydrolysis is highly complementary. Whereas SIMS is well suited to determine bulk F abundances, pyrohydrolysis better quantifies bulk Cl concentrations, which include the contribution of fluid inclusion-hosted Cl. Raspas eclogites contain 145–258 μg/g F and at least 7–11 μg/g Cl. We estimate that ~95% of F is retained in the slab through eclogitization and returned to the upper mantle during subduction, whereas at least 95% of subducted Cl is removed from the rock by the time the slab equilibrates at eclogite facies conditions. Our calculations provide further evidence for the fractionation of F from Cl during high-pressure metamorphism in subduction zones. Although the HIMU (high U/Pb) mantle source (dehydrated oceanic crust) is often associated with enrichments in Cl/K and F/Nd, Raspas eclogites show relatively low halogen ratios identical within uncertainty to depleted MORB mantle (DMM). Thus, the observed halogen enrichments in HIMU ocean island basalts require either further fractionation during mantle processing or recycling of a halogen-enriched carrier lithology such as serpentinite into the mantle.

3.2 Introduction

Our understanding of the abundance and distribution of halogens in subducted slabs is limited. Hydrothermally altered oceanic crust (AOC) is thought to be a major halogen carrier during subduction, where F and Cl substitute into the hydroxyl sites of hydrous minerals such as amphibole and mica (Ito et al. 1983; Philippot et al. 1998; Van den Bleeken and Koga 2015; Barnes et al. 2018). Bulk estimates of pre-subduction AOC vary from 50–253 μg/g Cl and 216–400 μg/g F (Ito et al. 1983; Straub and Layne 2003; Barnes and Cisneros 2012; Van den Bleeken and Koga 2015; Chavrit et al. 2016). More recently, primary halogen measurements of AOC from the East Pacific Rise (Penrose-type oceanic crust) and Atlantis Bank (SWIR, ultra-slow spreading) have shown extreme variability with both stratigraphic depth and lithology (Kendrick 2019a; 2019b). Bulk halogen measurements of blueschists and eclogites thought to represent high-pressure metamorphic AOC are also sparse. In a study of mélange rocks from Syros, Greece, Marschall et al. (2009) measured the bulk Cl content of eclogites (28–60 μg/g) and called into question previous estimates of eclogitized AOC Cl abundances, e.g. 100–200 μg/g Cl of Philippot et al. (1998), speculating that they may be overestimated. Pagé et al. (2016) analyzed a suite of blueschists from northwest Turkey; their results (8–22 μg/g Cl) also indicate that bulk eclogitized AOC could host less Cl than previously thought. Debret et al. (2016) reconstructed bulk halogen concentrations (57–79 μg/g Cl and 10–62 μg/g F) from in situ secondary ion mass spectrometry (SIMS) analyses for both blueschists and eclogites from the Western Alps, cautioning that typical bulk halogen measurements are not representative of prograde conditions due to potential retrogression during exhumation.

In situ halogen data in eclogitized AOC are also limited to a handful of studies, yet provide important first order observations. Debret et al. (2016) suggested that approximately 50% of F and 90% of Cl in the initial bulk-rock are lost to fluids during the first 80 km of subduction. Hughes et al. (2018) analyzed in situ halogen abundances of eclogites from the Western and Central Alps, and provided eclogitized AOC estimates of as low as 3 μg/g Cl. Finally, Pagé et al. (2016) reported low Cl and high F abundances in blueschist-hosted minerals, and concluded that Cl is primarily expelled at shallow depths, whereas F is retained to at least 80 km depth.

Estimates of halogen fluxes in subduction zones are typically derived from the difference between the trench inputs and extrusive products of arc magmatism (e.g. (Mather et al. 2006; Sadofsky et al. 2008; Pyle and Mather 2009; Freundt et al. 2014). Straub and Layne (2003) inferred a global arc recycling efficiency of 77–103% (Cl), and ~4–5% (F), implying near-total return of Cl to surface reservoirs whereas most F is returned to the mantle. John et al. (2011) reached similar conclusions based on Cl mass balance constraints regarding in- and out-fluxes from the subducted slab perspective. Barnes et al. (2018) also concluded that F is efficiently returned to the mantle, however their estimated Cl fluxes are more variable, indicating that some

Cl could be delivered back into the mantle by serpentinites (John et al. 2011; Kendrick et al. 2017). In a recent study, Pagé et al. (2018) found that Himalayan antigorite serpentinites host significant quantities of F (50–650 μg/g) and are enriched in Cl (8.8–35 μg/g) with respect to depleted mantle (11.0 μg/g F and 0.51 μg/g Cl, Salters and Stracke (2004)). Taken together, these studies illustrate the challenge of estimating halogen input fluxes. A better understanding of the inherent variability within different lithologies used in flux calculations could help to refine such estimates.

In particular, the halogen content of eclogitized AOC remains largely unconstrained. Here we discuss the F and Cl abundances of Raspas Complex eclogites, a Cretaceous eclogite suite that we consider to be an ideal analog for subducted AOC. We combine in situ SIMS and EMP analyses of minerals with pyrohydrolysis-derived bulk halogen abundances and discuss the relative contribution of minerals, grain boundaries and fluid inclusions to the total budget of halogens in subducted eclogites. Finally, we present new constraints on slab halogen fluxes and discuss the implications for the signature of eclogitized AOC in the HIMU mantle source.

3.3 Geologic Context

An accreted parcel of oceanic lithosphere, the early Cretaceous Raspas Complex consists of blueschist- and eclogite-facies rocks (Feininger 1980; 1987; Maruyama et al. 1996). The high-pressure metamorphic suite is bound by the La Palma-El Guayabo Shear Zone to the north and lower grade greenschists and amphibolites to the south (Gabriele 2002). While no pillow structures or sheeted dikes were observed in the field, fluid-immobile REE and HFSE abundances, Nb/Zr and Hf/Yb systematics, TiO_2/Yb ratios, and Nd isotope systematics provide a well-reasoned rationale for inferred protoliths (John et al. 2010; Halama et al. 2011). Based on these characteristics, the blueschists and eclogites were derived from seamount-like basalt and normal mid-ocean ridge basalt (MORB) protoliths, respectively. Both underwent similar peak metamorphic conditions (based on major element thermobarometry) of ~600°C to a maximum burial depth of approximately 60 km (John et al. 2010). Raspas eclogites show evidence for low-temperature seafloor alteration typical of basalts based on O isotopic compositions, and occur as two geochemically distinct groups: a MORB-type group (this study) with LREE depleted patterns, and a zoisite eclogite group characterized by significant incompatible trace-element enrichments which are interpreted to have been derived from serpentinite-derived dehydration fluids, and which also display a fluid component indicative of some minor sediment contribution (Halama et al. 2011; Herms et al. 2012). Thus, the Raspas MORB-type group provides an excellent analog to study the in situ distribution of halogens in eclogitized AOC processed through subduction systems globally.

3.4 Sample Description

We chose a set of six minimally retrogressed MORB-type eclogites which have been previously described by John et al. (2010). Samples consist of omphacite + garnet + rutile +

apatite ± amphibole ± phengite ± quartz with minor secondary titanite. Subhedral to euhedral garnet porphyroblasts vary in size from <100 μm to 4mm, commonly hosting inclusions of rutile and quartz. Some samples exhibit weakly deformed fabrics characterized by lineated omphacite. A single sample, SEC42-06, shows a strongly foliated texture with alternating layers of nearly monomineralic garnet and omphacite domains. Modal mineralogy varies significantly between samples, from nearly bimineralic garnet + omphacite to ~30% modal amphibole; such variability at similar P-T conditions is likely the result of bulk chemical compositional effects (Beinlich et al. 2010; John et al. 2010; Rebay et al. 2010). Representative photomicrographs of sample textures are presented in Fig. 3.1 and 3.S1. Petrographic observations reveal near-ubiquitous fluid inclusions (FI). All samples contain variable quantities of FI hosted in omphacite and garnet, typically located in mineral cores (Fig. 3.1; see also Herms et al. (2012)). In SEC46-02, monomineralic amphibole veinlets crosscut eclogite textures and contain secondary titanite overgrowths rimming rutile. Directly adjacent to these veinlets, FI-rich omphacite appears opaque in thin section (Fig. 3.1), which is unique to this sample and appears to reflect fluid infiltration.

3.5 Methods

3.5.1 SIMS

SIMS analyses were conducted at the Northeast National Ion Microprobe Facility (NENIMF) at the Woods Hole Oceanographic Institution using a Cameca IMS 1280. We follow the methods outlined in Urann et al. (2017), adding OH and S measurements to the protocol. Polished thick-sections (150 μm) were used for all analyses. Samples were cleaned with ethanol and deionized water to remove surface contamination, then placed in a vacuum oven at 50°C to dry. Samples were gold coated to ~160 nm thickness and placed into a vacuum chamber for storage until analysis. Samples were loaded into the instrument sample chamber at least 12 hours prior to analysis, to allow adequate pump down time and achieve chamber pressures of no more than ~$5x10^{-9}$ torr. Each spot location was chosen to avoid surface cracks, which are known to influence analyses (Urann et al. 2017). A primary Cs^+ beam of 5.0–7.5 nA was sputtered through the sample surface with a 30 x 30 μm^2 raster and a 400 μm field aperture, allowing only transmission of ions from the innermost 5 x 5 μm^2 of the beam crater. Secondary magnet mass calibration was done before each measurement with mass resolving power of > 6000 (m/Δm at 10 % peak height). We measured $^{19}F/^{30}Si$, $^{16}O^1H/^{30}Si$, $^{32}S/^{30}Si$, and $^{35}Cl/^{30}Si$ ratios in glass reference materials D51-3, D52-5, ALV519-4-1, 46D, 1649-3, 1654-3 6001, and AII107-D20 to produce a calibration slope for each one-week analytical session (Fig. 3.S2). Calibration slopes (m) were obtained by plotting measured isotope ratios (x) against known reference material concentrations (y) of the form $y = mx$ for each element of interest. Sample unknowns were then calculated by multiplying measured ratios by m. Calibration slope uncertainties were assessed utilizing a bootstrapping technique (5000 iterations) to derive confidence intervals. Measurements where the internal precision (one standard deviation) was greater than 20% were

screened and excluded from the data set; these low precision measurements (less than ten in total) were associated with elevated C (not reported) and Cl concentrations, and are likely the result of analyses conducted on micro-fractures. After screening, analytical uncertainties over five counting cycles (internal precision: typical standard error ~1 % OH, <1.5 % F, <3% Cl) were combined with calibration slope uncertainties (accuracy: typical uncertainty 6% OH, 5% F, <10% Cl, 95% confidence intervals) to yield no more than 8%, 6% and 16% total uncertainty (2SE, 95% confidence intervals) for OH, F and Cl measurements, respectively. Since mineral-specific calibrations are not well constrained and/or not available for halogens in most eclogitic phases, we used a basaltic glass calibration to present a unified dataset that is self-consistent. This may introduce crystal-specific matrix effects, although preliminary calibrations of F in pyroxene and glass (Kumamoto et al. 2017) show slopes indistinguishable within uncertainty. Continuous measurements of ALV519-4-1 were used throughout the session to monitor instrument drift, which was found to be negligible. The OH, F, and Cl concentrations of Suprasil and Herasil® 102, both optical-quality glasses, along with Synthetic Forsterite, were measured regularly in each session. There are no published values for the OH, F, and Cl content of Suprasil, Herasil® 102 and Synthetic Forsterite, but those samples are believed to have very low OH, F, and Cl concentrations (less than 0.1 μg/g), respectively (E. Hauri, *pers. comm.*). To quantify our maximum backgrounds, we assume that Suprasil contains no OH, Herasil® contains no F, and Synthetic Forsterite contains no Cl. Background OH, F, and Cl values were less than 7.3 μg/g, 0.19 μg/g, and 0.15 μg/g, respectively, for all sessions. Individual mineral analyses were not corrected for background when background values were less than propagated 2SE uncertainty; otherwise, measurements are corrected to remove backgrounds (Table 1). Chlorine measurement uncertainties on omphacite, garnet, and phengite are near parity with Synthetic Forsterite Cl values. We therefore subtracted our background Cl values from measured values for all bulk calculations.

3.9.2 Electron microprobe analysis

All mineral phases were analyzed using JEOL JXA–8200 electron microprobe (EMP) at the Massachusetts Institute of Technology. A 1nA beam current and 15kV accelerating potential were used for all analyses except apatite which utilized a 10 nA beam current. Beam diameter was <1 micron for garnet and omphacite, and 10 μm for amphibole and phengite. Data reduction was done using CITZAF software (Armstrong 1995). The counting times used for phase analysis was 40s on peak, and 20s on background. With respect to halogen abundances in amphibole and phengite, detection limits based on counting statistics were ~470 μg/g for F and ~60 μg/g for Cl. For apatite, care was taken to address known issues pertaining to fluorine excitation by electron microprobe analysis (Stormer and Pierson 1993). Peak searches were conducted only on the standard, and background was only measured on the first point for each grain. In addition, the LDE1 (W/Si) crystal was used for F measurements, which suppresses elemental interferences. Counting times for F were abbreviated to 10s on peak and 40 s for P,

Ca, and Cl while background counts were 5s for F and 20s for Ca, P, and Cl. Analytical uncertainties including background for F and Cl in apatite based on counting statistics were 3.4–4.4% and 7.2–11.6% (1σ), respectively, at concentrations of 1.47–3.25 wt % F and 192–515 μg/g Cl.

3.9.3 Bulk halogen measurements

Sample powders were washed in ultra-pure (18.2 mega ohm) deionized water and oven-dried overnight to avoid surficial Cl contamination by adsorption. This may have removed a portion of halogens along grain boundaries or in fluid inclusions; therefore we report Cl concentrations as minimums. We note that fluid inclusion dimensions (~1μm to 10 μm, on average) are smaller than estimated powder grain size (<100 μm), and were likely retained, as demonstrated in a subsequent section. Halogens were extracted from approximately 2 grams of sample powder by pyrohydrolysis, in which a stream of water vapor captures volatiles as they are released from the sample during fusion by a gas torch. The vapor is condensed to produce an aqueous solution (Schnetger and Muramatsu 1996). From this solution, F and Cl concentrations are measured via ion chromatography (IC) using a Dionex Integrion HPIC System at the University of Texas at Austin. Detection limits of the analyzed solution are 0.05 μg/g for both F and Cl. The halogen content of the whole rock is then calculated using solution concentration, solution volume, and the mass of the powder melted. Using the JB-2 basalt reference material (98.5 μg/g F and 281 μg/g Cl (Imai et al. 1995)), F and Cl yields are 75–83% and 68–95% (n = 5), respectively. Samples were analyzed with triple replicates in two batches. Since JB-2 yields are constrained within each contemporaneous batch, concentrations were yield-corrected by batch to the JB-2 reference material to more rigorously quantify absolute halogen concentrations. The yield correction assumes that standard yields and sample yields are similar. Although not perfect, this correction likely provides more accurate values. Both uncorrected and yield-corrected values are presented in this study for comparison. Reproducibility for each sample (precision) was combined with batch-specific JB-2 yield uncertainty (accuracy) to derive 1σ uncertainties. Replicate measurements of JB-2 and uncertainties are given in Table S9.

3.9.4 Modal mineralogy

We calculated the modal abundances of each phase by inverting the bulk-rock major element data of John et al. (2010) with EMP analyses of individual phases (Tables S1-S6). Although EMPA indicates zonation in some phases (e.g. TiO_2 and MnO), changes in modal proportions were negligible (often <1% difference) when varying mineral compositions were used. We performed our calculations by taking the mean composition for each phase. SiO_2, TiO_2, Al_2O_3, FeO, MnO, MgO, CaO, Na_2O, K_2O, and P_2O_5 were used in the minimization. P_2O_5 was assumed to reside entirely within apatite. Calculated modes agree well with independently estimated mineral modes based on optical microscopy. Calculated mineral modes and uncertainties are shown in Table 2.

All eclogite samples contain >35 modal % garnet. Omphacite modal proportions range from 23–53 vol.%, whereas phengite, when present, makes up 2–4 vol% of the bulk-rock modally. Samples contain varying modal proportions of amphibole, from 0.5 vol% to ~30 vol%. Quartz, when present, is up to 8 vol% of the bulk rock whereas rutile (1–2 vol%) and apatite (0.25–1.6 vol%) are omnipresent.

3.6 Results

3.6.1 Major element variability by EMPA

Major element profiles show garnet zonation with respect to end member components almandine, pyrope, grossular, and spessartine (Table S1). Garnet porphyroblast cores are often elevated in the spessartine component as well as TiO_2, with a gradual decrease towards the rim consistent with prograde garnet growth.

Omphacite (Cpx) Mg# (molar Mg/(Mg+Fe)) varies from 0.68 to 0.79 (Table S2) and correlates negatively with Cpx abundances, reflecting the influence of bulk-rock chemistry on mineral modes. Omphacite EMPA profiles show some intra-mineral zonation; in particular, SEC42-06 and SEC43-01 show increasing Si concentrations from core to rim, while SEC43-03 Si content decreases from core to rim. Mg# remain uniform within single grains.

Phengite was analyzed in samples SEC42-06, SEC43-01, and SEC47-01 (Table S5). SEC42-06 is relatively homogeneous, with slight Na enrichment approaching the rim. A full rim-to-rim profile in SEC43-01 shows strong zonation with increases in Na and Al from core to rim, and decreases in Si, K, Fe and Mg (Fig. 3.S3). SEC47-01 shows slight Si, K, and Mg rim depletions. Both phengite profiles are consistent with continued grain growth or partial recrystallization during decompression due to decreasing Si from core to rim (Massonne and Schreyer 1987).

Amphibole occurs as several different species which likely reflect bulk compositional variations; analyses are presented in Table S4, along with IMA 2012 recommended nomenclature calculated using the routine of Locock (2014). SEC42-06, SEC43-01, and SEC43-03 are Na-Ca subgroup katophorite, SEC46-01 and SEC46-02 are Ca subgroup pargasite, and SEC47-01 is classified as a Na-Ca subgroup winchite. Nearly all EMP analyses show Cl abundances at or below the detection limit of ~60 μg/g. However, F concentrations show significant intra-grain variability, differing by as much as a factor of two from core to rim (e.g., SEC42-06, 869–1834 μg/g).

Apatite halogen contents range from 1.47–3.25% wt% F and 0.019–0.051 wt% Cl (Table S5). The hydroxyl content of the apatite is taken as the oxide sum subtracted from one hundred, which classifies apatite in samples SEC43-03, SEC46-01, SEC46-02, and SEC47-01 as hydroxylapatite and apatite in sample SEC43-01 and SEC42-06 as fluoroapatite. Apatite halogen abundances are similar to apatite from other blueschist and eclogite metamorphic terranes with low Cl abundances (Pagé et al. 2016; Hughes et al. 2018) whereas some HP terranes developed from oceanic protoliths also contain Cl-rich apatite (John and Schenk 2003).

Typical MORB (0.164 wt% P_2O_5, Gale et al. (2013)) must undergo significant fractional crystallization (>70%) before reaching apatite saturation (~0.7 wt% P_2O_5); indeed, apatite-saturated MORB are few (Anderson and Greenland 1969; Watson 1979). Based on the bulk rock chemistry of Raspas provided by John et al. (2010) these conditions are unlikely to have been met. Therefore, interstitial grains most likely formed as new growth during progressive metamorphism.

3.6.2 Halogen and water variability

Bulk rock pyrohydrolysis analyses are presented in Table 3. As noted previously, we report both yield-corrected and uncorrected halogen abundances. Yield-corrected F and Cl concentrations for all samples were 115—199 μg/g and 6.7—19.9 μg/g, respectively. In situ halogen measurements are presented in Tables 1 and S5. Resolvable intra- and inter-grain heterogeneity is observed for F and OH in all phases both in single-grain SIMS profiles (Table S7) and in multiple grains from the same sample.

Halogen variability is notable in nominally anhydrous minerals (NAMs), particularly garnet with both inter- and intra-grain heterogeneity observed (Figure 3.S4, Tables 1 and S7). Grain-averaged sample values range from 1.7 to 8.9 μg/g F and 60 to 201 μg/g OH, while Cl is always at or near detection limits. Intra-sample garnet F and OH variability is up to 93% and 67%, respectively (1σ, Table 1). Variations from core to rim were not systematic, nor can they be attributed to analytical uncertainty; in some cases cores were enriched in F or OH relative to rims, while in other grains the case was reversed. Core and rim measurements for OH and F are presented in Fig. 3.2, illustrating that while some intragrain variability is present, most grains plot on or near 1:1 lines within uncertainty.

Omphacite has highly variable F abundances (6.5–54.1 μg/g) while OH range from 445 to 773 μg/g. Similar to garnet, Cl abundances are less than 0.1 μg/g for five of the six samples. However, SEC46-02 yields significantly higher mean Cl abundances of 1.05 μg/g. F and OH variability within a single sample was less than 24% and 14%, respectively. A profile of Cpx from SEC43-01 exemplifies core to rim variations, with F and OH concentrations of 42.1–69.7 μg/g and 362–557 μg/g, respectively (Fig. 3.S5). While these variations are discernable, heterogeneity in this grain is 15% or less for all three species; core to rim variations are modest and typically plot along a 1:1 line, within uncertainty (Fig. 3.2).

Amphibole occurs as both interstitial grains and monomineralic veinlets, with veins only occurring in SEC46-02. Interstitial amphibole yields F and Cl abundances of 747–4727 μg/g and 0.56–82.6 μg/g, respectively. Pargasite veins from SEC46-02 contain on average 563 μg/g F and 11.7 μg/g Cl. Single sample averaging produces variability of no more than 18% for F and 37% for Cl (1σ).

Phengite from three samples contains 610–1822 μg/g F and 1.01–1.98 μg/g Cl. Two of the three grains analyzed show no systematic core to rim halogen variations. Phengite is relatively homogeneous in terms of F and Cl, with 1σ sample variations of less than 20%. However, in a

rim to rim transect of SEC43-01 phengite (Fig. 3.S6), intra-grain variability is evident. F concentrations show a systematic decrease from core to rim, paralleling major element trends of decreasing K_2O, SiO_2, and MgO. Cl is enriched near grain boundaries by approximately 40% with respect to cores, following Al_2O_3 and Na_2O rim enrichments (Fig. 3.S3 and 3.S6). Finally, a single secondary titanite in SEC46-02 contains 1394 μg/g F, <0.1 μg/g Cl, and 4010 μg/g OH.

3.7 Discussion

3.7.1 Halogen redistribution during eclogitization

Halogen distribution between minerals during prograde metamorphism depends to a large extent on bulk-rock chemistry, which dictates the equilibrium mineral assemblage and phase proportions at any given pressure and temperature. Raspas eclogites show a strong positive correlation between the proportion of omphacite in the bulk-rock and the F content of omphacite (Fig. 3.S7), suggesting that F is repartitioned during eclogitization and progressive omphacite growth. In addition, we compare the modal proportion of nominally anhydrous minerals (omphacite + garnet + quartz) to the volatile content of analyzed phases (Fig. 3.S8). As the proportion of NAMs in the bulk assemblage increases, the F content of each phase shows a commensurate increase. Indeed, modal abundances of amphibole are negatively correlated with F concentrations in both omphacite and apatite, again suggesting effective redistribution of F during prograde metamorphism. Further, apatite Cl abundances increase as amphibole modes decrease and the mineral assemblage becomes dominated by garnet and omphacite. In all cases concerning lattice-hosted halogens, F is accommodated primarily in apatite (1.47–3.25 wt %), amphibole (563–4727 μg/g), and phengite (610–1822 μg/g) with lesser amounts in omphacite (6.5–54.1 μg/g) and garnet (1.7–8.9 μg/g). In addition, Cl is primarily hosted in apatite (192–515 μg/g), with lesser amounts in amphibole (0.64–82.7 μg/g), phengite (1.2–2.1 μg/g), omphacite (<0.05–1 μg/g) and garnet (<0.05 μg/g).

Our in situ measurements permit the calculation of distribution coefficients between various phases of interest (Figs. 3.3 and 3.4, Table S8). Given the scarcity of data, these new values provide important constraints on the distribution of F and Cl in eclogitic phases. A number of observations can made from the above distribution coefficients. First, F partitioning between mineral pairs defines a narrow range and appears to be insensitive to concentrations, which in some cases span nearly an order of magnitude. Second, as expected apatite will preferentially host crystal lattice-bound F and Cl when present in eclogitic assemblages, similar to apatite's halogen affinity in the presence of aqueous fluids (Kusebauch et al. 2015). Finally, F and Cl are preferentially partitioned into amphibole over phengite in all samples by a factor of 2.4 and 20, respectively. Interestingly, this observation is in contrast to blueschists studied by Pagé et al. (2016) who found $D_F^{Amph-Phen}$ was always less than unity whereas $D_{Cl}^{Amph-Phen}$ was approximately equal to one within error. Hence, blueschist to eclogite phase transformations may elicit changes in the relative compatibilities of halogens between coexisting phases, likely as a

function of changing modal proportions, mineral compositions (e.g. glaucophane to katophorite), and P-T conditions.

3.7.2 Comparison between measured and reconstructed bulk halogen abundances

Using mineral modes, in situ SIMS data, and EPMA halogen concentrations, we calculate a reconstructed bulk-rock F and Cl content for each eclogite sample, which can then be compared to bulk values measured by pyrohydrolysis (Table 3.3, Fig. 3.5). Both raw (not corrected for yield) and yield-corrected pyrohydrolysis halogen abundances are given in Table 3. We use yield-corrected concentrations in subsequent discussions.

Reconstructed concentrations and pyrohydrolysis measurements yield F concentrations of 168–415 μg/g and 115–199 μg/g, respectively. Reconstructed F abundances are broadly concordant with measured values; three of the six samples agree within uncertainty, whereas three samples display higher reconstructed values (Fig. 3.6; Table 3.3). The relative congruence between reconstructed and measured F values implies that F may be entirely hosted within the crystal lattice of eclogitic phase assemblages. The discrepancy observed for three of the six samples may be due to a combination of factors including uncertainties in pyrohydrolysis yields (Table S9) that are typically larger than SIMS analyses, inter-grain halogen heterogeneity, or uncertainties in the calculated modal proportions (Table 2). We note that uncertainties from calculated modal proportions as derived from whole rock analysis were assessed but found to be minor.

Bulk reconstructed and measured Cl concentrations for all samples are 0.8–8.2 μg/g and 6.7–19.9 μg/g, respectively. Unlike F, Cl shows very large and systematic discrepancies between reconstructed and measured values, with reconstructed values representing only 12–41% of the pyrohydrolysis-derived bulk values. We discuss these drastic differences below, in terms of uncertainties and possible means of reconciliation between the two methods. We consider three possible processes to explain the difference: retrograde alteration, grain boundary hosted Cl, and Cl-bearing fluid inclusions.

Bulk halogen analyses rely on the assumption that samples are perfectly preserved and have not been retrogressed along their exhumation path. Even minute amounts of alteration (e.g. chlorite or titanite) can drastically affect such bulk measurements (Debret et al. 2016). Most Raspas eclogites appear to be pristine with little to no visible alteration or retrogression, with the exception of SEC46-02 that contains titanite-on-rutile overgrowths and monomineralic amphibole veinlets adjacent to FI-rich omphacite, indicating possible fluid assimilation. This sample also displays elevated reconstructed (8.2 μg/g) and bulk (19.9 μg/g) Cl compared to the rest of the suite. In light of this suspected fluid assimilation, and the large F incongruity (~100%) between the two methods, we exclude this sample from subsequent bulk rock calculations. Minor retrogression may have contributed to the discrepancy for SEC46-02, however all other samples still show at least a factor of three difference between reconstructed and measured bulk Cl concentrations. Therefore, a factor other than late alteration is likely at play.

To further explore this discrepancy, we conducted additional SIMS analyses on grain boundaries of FI-free amphibole and garnet (Fig. 3.S9). Both profiles across grain boundaries display pronounced spikes in $^{35}Cl/^{30}Si$ signals within the immediate grain boundary at near constant ^{30}Si counts. These grain boundary measurements are equivalent to 7–18 μg/g Cl. Yet, the grain boundaries themselves are far smaller than the dimensions of our analysis spot (3.8x3.8 μm) and depending on their size, could contain > 1 wt% Cl assuming a grain boundary thickness of 5 nm or less. As grain boundary porosity values in eclogites are poorly constrained, we used equation 9.6 of Turcotte and Schubert (2002) to calculate grain boundary porosity values based on a simplified grain geometry over a range of grain boundary thicknesses (1–25 nm) with realistic grain sizes (500 μm) to yield values of $9x10^{-12}$ to $6x10^{-9}$ (Table S10). The Cl contribution from grain boundaries alone (<0.1 μg/g Cl in all cases, or <2% contribution compared to pyrohydrolysis Cl abundances), given the above parameters, is unable to reconcile the reconstructed versus measured Cl abundances.

Finally, we consider the possible role of fluid inclusions, as they could represent an important host for Cl (Philippot and Selverstone 1991; Herms et al. 2012; Kendrick 2018). FI (~1 μm to 10 μm on average) are found ubiquitously hosted in garnet (Fig. 3.S1C) and omphacite cores, both of which appear in textural equilibrium with adjacent phases and occur in all samples. FI are far more abundant in SEC46-02, in particular where omphacite is in contact with monomineralic pargasitic amphibole veinlets (Fig. 3.1B). Fluid inclusions appear cloudy in thin section owing to their prolific abundance. These features likely reflect crystallization in the presence of fluids, possibly during prograde conditions (e.g. John et al (2010) and Herms et al. (2012)); such features have also been noted elsewhere in previous studies (e.g. Massonne et al. (2012), Zack et al. (2001)). Although we cannot directly analyze fluid inclusions by SIMS, heterogeneous Cl enrichments in SEC46-02 FI–rich omphacite (44–94 μg/g Cl) indicate that each SIMS analysis may incorporate some Cl-rich FI material. FI-free (optically clear) omphacite from the same sample also contains an order of magnitude more Cl (1.05 μg/g) compared to omphacite from all other samples (<0.1 μg/g), which is consistent with assimilation of pervasive fluids during crystallization (Herms et al. 2012). FI may host significant quantities of Cl from hundreds of μg/g to >10 wt% NaCl equivalent (Philippot and Selverstone 1991; Philippot et al. 1998; Scambelluri and Philippot 2001; Svensen et al. 2001; Kendrick et al. 2015; Kendrick 2018). Herms et al. (2012) have shown that omphacite and garnet hosted FIs from Raspas contain ~2 wt% NaCl, congruent with the salinity of dehydration-related FI found in rocks that have undergone blueschist-to-eclogite conversion (Gao and Klemd 2001). Assuming that FI contain ~2 wt% NaCl and represent 0.05–0.1% of the total sample volume, one may reconcile the discrepancy between in situ and bulk Cl abundances. Thus, pyrohydrolysis appears to incorporate fluid inclusion contributions, whereas SIMS analyses do not. Our calculations imply that FI host the majority (at least 80%) of Cl in Raspas eclogites; whether these fluid inclusions are all primary in nature, and therefore should be considered in the halogen budget of recycled eclogites, remains to be determined.

Combining SIMS and pyrohydrolysis techniques affords unique insights on the distribution and abundance of halogens in subducted slabs. SIMS provides detailed constraints on crystal lattice hosted halogen abundances, and is well suited to determine bulk F concentrations, given the uncertainty that can be associated with pyrohydrolysis yields. Minimally retrogressed Raspas eclogites analyzed by SIMS contain between 145 and 258 μg/g F; F may be entirely hosted within the crystal lattice of eclogites, whereas only ~20% of Cl (at most), on average, is crystallographically hosted when FI are present. However, SIMS cannot accurately account for Cl abundances if primary fluid inclusions are present in the sample, which dominate the Cl budget of eclogites. Assuming that fluid inclusions observed here are primary features, pyrohydrolysis is the preferred method to measure the bulk Cl content of pristine FI-bearing rocks; minimally retrogressed Raspas eclogites analyzed by pyrohydrolysis contain between 6.7 and 11.3 μg/g Cl.

3.8 Implications

Previous studies have suggested that amphibole is the primary carrier of halogens to the upper mantle (Debret et al. 2016; Barnes et al. 2018). Our results suggest a more nuanced view when one takes into account the contributions from coexisting phases and FI; amphibole's contribution to mineral-hosted bulk F and Cl abundances range from 6–84% and 4–85%, respectively (Fig. 3.6, 3.S7). When amphibole modes are below ~5% (three of six samples), apatite is the most important carrier for mineral-hosted halogens, containing >80% of mineral–hosted Cl and 38–71% of mineral–hosted F. Apatite is thought to be stable to 7.5 GPa at 950º (Konzett and Frost 2009), and will act as an important halogen carrier in eclogitized ocean crust. The remaining F is distributed between amphibole (4–53%), phengite (6–32%), omphacite (4–16%), and garnet (up to 2.2%). The above calculations consider only crystal matrix hosted halogen abundances; our results further indicate that FI host the majority of Cl in the bulk rock (at least 80%, on average). The ultimate fate of Cl will be dictated by the redistribution of free fluid phases during subsequent phase transformations, diffusive re-equilibration, and dynamic recrystallization at higher pressures and temperatures.

Raspas reconstructed bulk F concentrations (145–258 μg/g) are similar to previous pre-subduction AOC estimates of 216 μg/g (Straub and Layne 2003), blueschist (457 ± 159 μg/g F) and eclogite-facies (283 ± 146 μg/g F) AOC (Pagé et al. 2016; Hughes et al. 2018), as well as mean N–MORB values of 183 ± 107 μg/g calculated from recent work from Le Voyer et al. (2018) (Fig. 3.7A). Therefore, F concentrations remain relatively unchanged during the progression from nascent MORB, to AOC, and finally eclogitized AOC. Our results indicate that F is efficiently returned (~95%, derived from SIMS) to the upper mantle during subduction (Straub and Layne 2003; John et al. 2011; Pagé et al. 2016). Conversely, bulk pyrohydrolysis Cl measurements (6.7–11.3 μg/g) are at least an order of magnitude lower than pre-subduction AOC estimates (e.g. 207 μg/g (Barnes and Cisneros 2012)). Yet, observed Raspas concentrations are quite similar to recent blueschist and eclogite-facies AOC estimates by Hughes et al. (2018)

of 3–23 μg/g Cl and Pagé et al. (2018) of 12 μg/g Cl, and well within the range observed in MORB (excluding Cl/K >0.1 after Shimizu and Saal (2016) and references therein) (Fig. 3.7A). Progression from initial MORB generation to seafloor alteration leads to an increase in Cl content, while subsequent eclogitization leads to a decrease in Cl abundances, returning to values similar to MORB. Using the pre-subduction AOC Cl bulk-rock estimate of Barnes and Cisneros (2012) of 207 μg/g Cl and data presented here, we calculate that the vast majority (>95%, derived from bulk pyrohydrolysis) of subducted Cl is expelled from the slab by the time the AOC parcel equilibrates at eclogite-facies conditions (Table 3), in agreement with previous workers (Straub and Layne 2003; John et al. 2011; Kendrick et al. 2014; Pagé et al. 2016). What little Cl remains will reside primarily in FI (at least 80%, on average). Thus, while most F is retained in the subducting slab at eclogite-facies conditions, most Cl previously added through hydrothermal alteration is expelled, fractionating F from Cl in eclogitized AOC. Yet, halogen abundances in Raspas are similar to unaltered MORB (Fig. 3.7A), while ratios of F and Cl with elements of similar compatibility during melting, Cl/K (0.0066 ± 0.0043), Cl/Nb (3.9 ± 1.0) and F/Nd (15.5 ± 4.8), are indistinguishable within uncertainty from DMM ratios of Salters and Stracke (2004) (Fig. 3.7B).

The HIMU (high U/Pb) mantle source is thought to contain ancient altered oceanic crust based on Pb isotope systematics (and more recently Tl, see Shu et al. (2019)), yielding enrichments in F/Nd, $^{35}Cl/^{37}Cl$, and often Cl/K and Cl/Nb ratios (Chase 1981; Hofmann and White 1982; Zindler et al. 1982; Stroncik and Haase 2004; John et al. 2011; Cabral et al. 2014; Jackson et al. 2015; Le Voyer et al. 2015; Kendrick et al. 2017; Rose-Koga et al. 2017; Hanyu et al. 2019). Our data indicate that halogen enrichments, and elevated F/Nd and Cl/K ratios, in the HIMU source cannot be produced by simple addition of recycled eclogitized AOC (Fig. 3.7B), but rather require delivery by an additional lithology, e.g. serpentinite as proposed by Kendrick et al. (2017), or an efficient fractionation mechanism to elevate halogen ratios during subsequent processing (e.g. Niu and O'Hara (2003)). The broad spectrum of F/Nd and Cl/K ratios observed in HIMU melts may then reflect variable contributions from subducted serpentinite (green line, Fig. 3.7B). However, antigorite serpentinite breakdown by the reaction: antigorite = olivine + orthopyroxene + H_2O requires geochemical transfer of halogens, likely into a fluid phase as both F and Cl are highly incompatible in olivine and orthopyroxene (Dalou et al. 2014; Joachim et al. 2015; Beyer et al. 2016); their ultimate host within the upper mantle remains unknown. Direct phase transformation from antigorite serpentinite to the dense hydrous magnesium silicate Phase A may occur along cold geothermal gradients (Schmidt and Poli 1998), or halogens may become more compatible in K-rich clinopyroxene at increasing pressures as K solubility in clinopyroxene increases to ~1 wt. % K_2O at 100 kbar (Schmidt and Poli 1998). Thus, subduction proceeds in returning to the upper mantle an eclogitized AOC parcel with halogen ratios quite similar to the MORB from which it was derived.

3.9 Acknowledgments
We thank two anonymous reviewers for their insights and suggestions, which improved the manuscript. This research was supported by NSF award EAR-P&G #1524311 and #1839128 to VLR. BMU acknowledges the support of the WHOI Ocean Venture Fund. This work was also supported by NSF-PIRE grant (OIA- 1545903) to JDB.

3.10 Figures

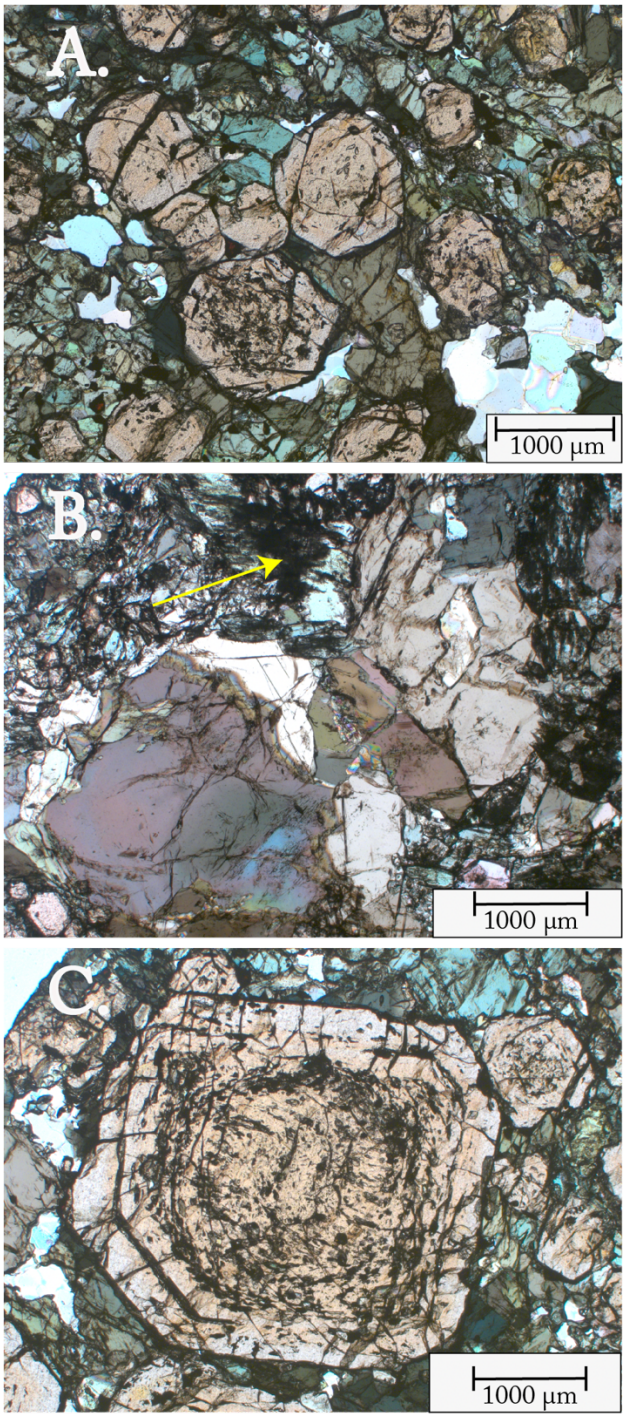

Figure 3.1. Representative photomicrographs of Raspas eclogite textures. A. SEC43-03 contains garnet porphyroblasts within a matrix of omphacite and lesser quartz. B. Amphibole veinlet in sample SEC46-02. Adjacent omphacite shows abundant fluid inclusions (yellow arrow). C. SEC43-03 Megacrystic, inclusion-rich garnet showing sector zoning.

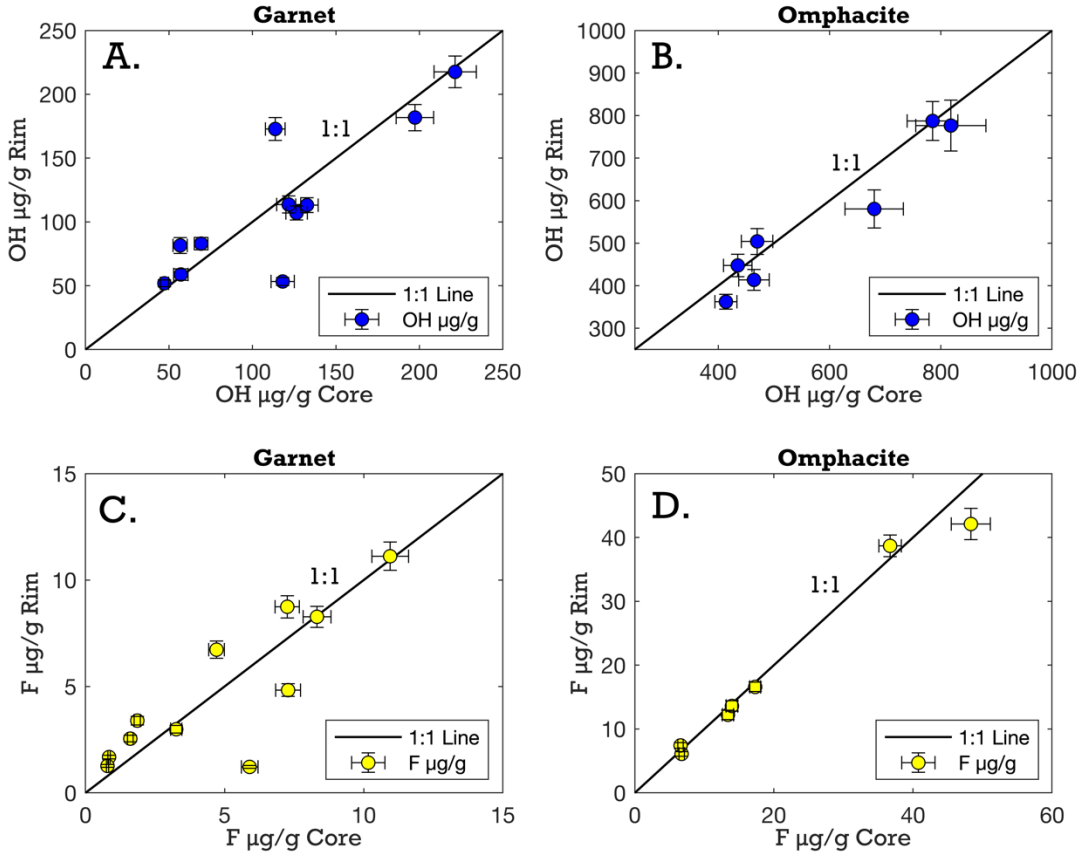

Figure 3.2. Core and rim measurements for OH (A. and B.) and F (C. and D.) in garnet and omphacite. The majority of samples show core and rim values that fall on a 1:1 line, within uncertainty, allowing a high degree of confidence in bulk rock calculations based on in situ measurements. Error bars are 2SE.

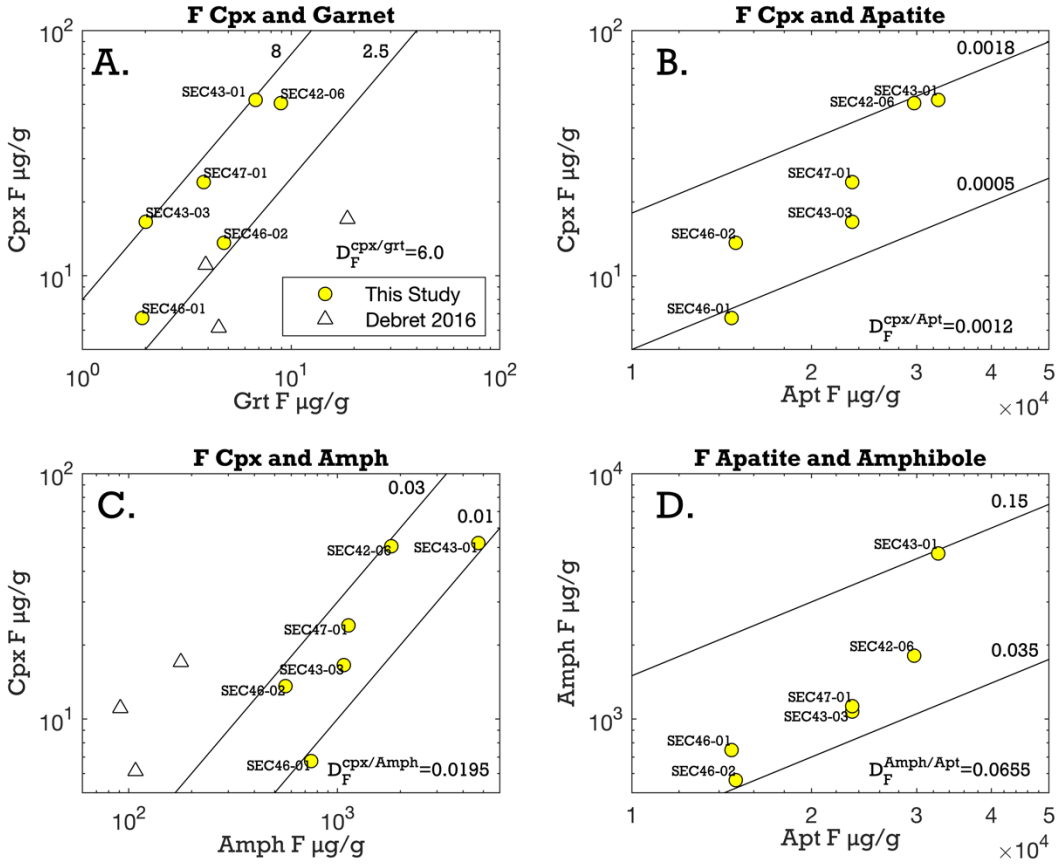

Figure 3.3. Inter-mineral F partitioning between A. omphacite and garnet, B. omphacite and apatite, C. omphacite and amphibole, and D. omphacite and phengite. White triangles are literature data from Debret et al. (2016). Solid lines show constant inter-mineral partition coefficients (labeled), while mean partition coefficients for each mineral pair are presented in the bottom right panel corner.

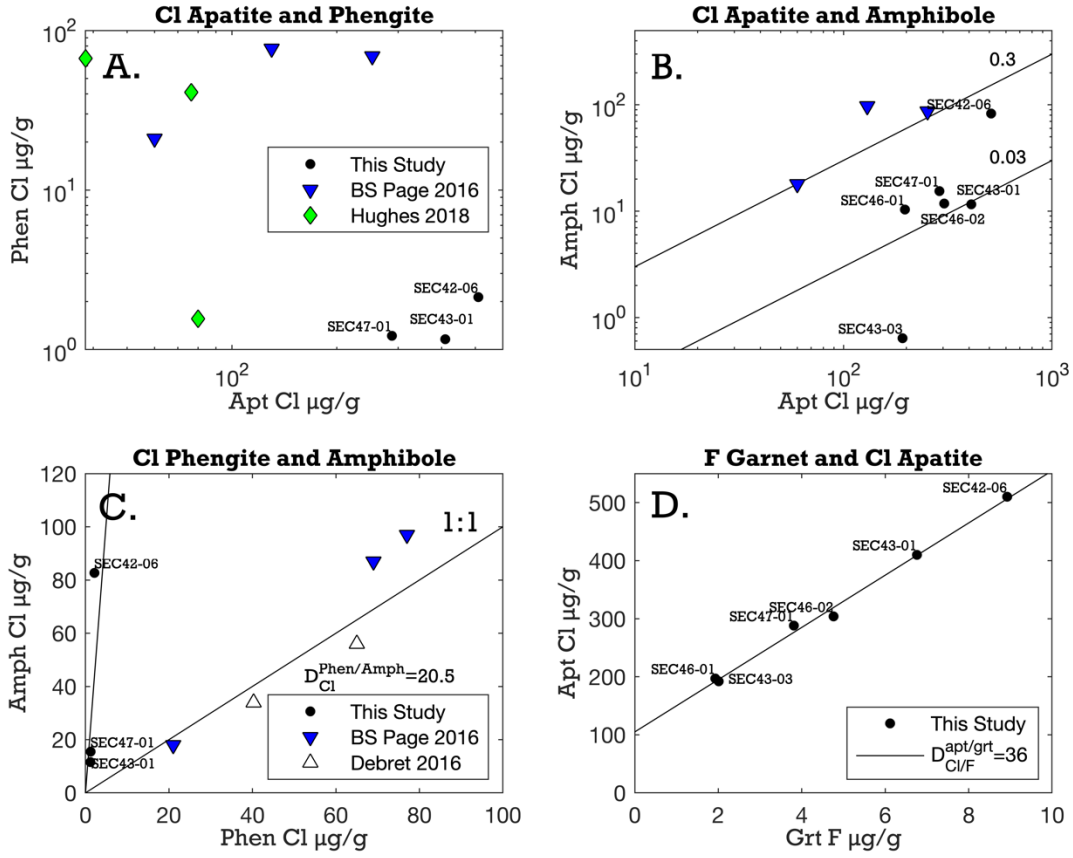

Figure 3.4. Inter-mineral Cl partitioning between A. phengite and apatite, B. apatite and amphibole, C. phengite and amphibole, and D. apatite Cl and garnet F concentrations. White triangles are literature data from Debret (2016), green diamonds from Hughes et al. (2018) and blue upside down triangles from Pagé et al. (2016). Solid lines denote constant inter-mineral partition coefficients as in Fig. 3.3.

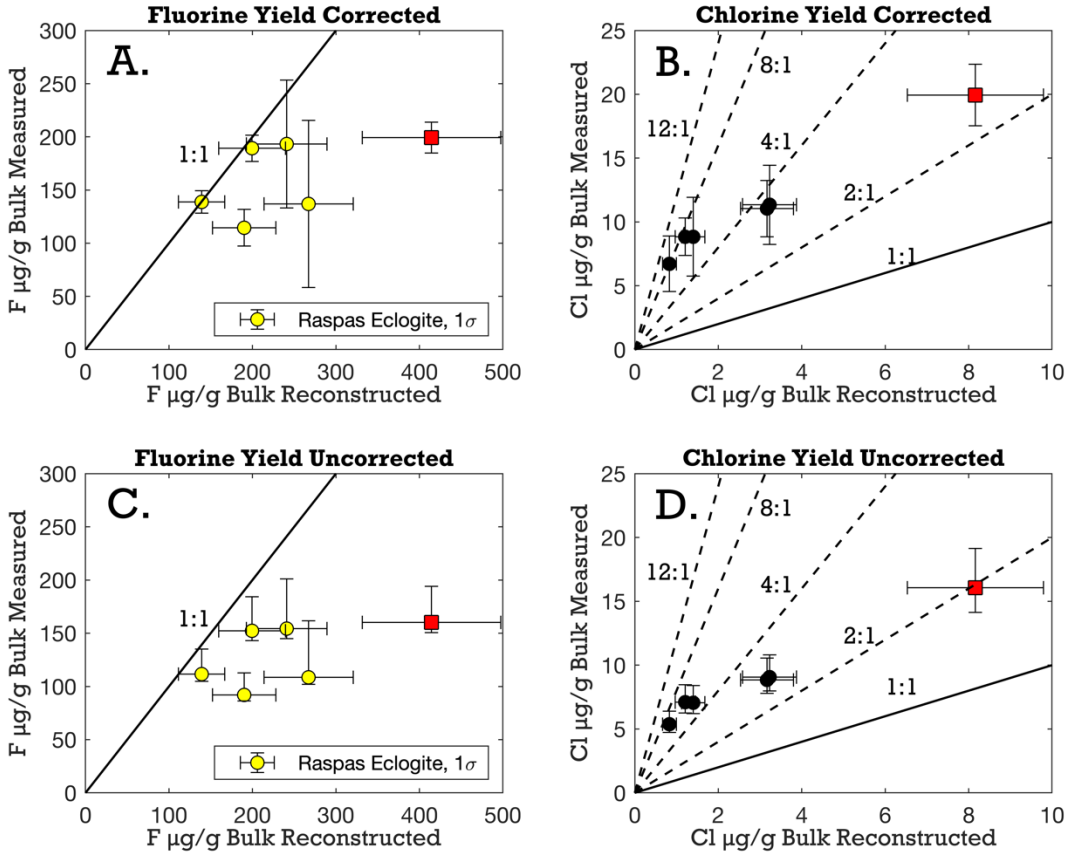

Figure 3.5. Bulk reconstructed and bulk measured (yield corrected) halogen abundances for F (A.) and Cl (B.). Y error bars show analytical reproducibility propagated with yield precision. Yield-uncorrected pyrohydrolysis values are shown in panels C and D, where positive Y error bars incorporate yield uncertainty. Red dots denote SEC46-02, which was not included in bulk calculations; see text for more information. Solid lines represent 1:1 lines; dashed lines plot various slopes, labeled accordingly.

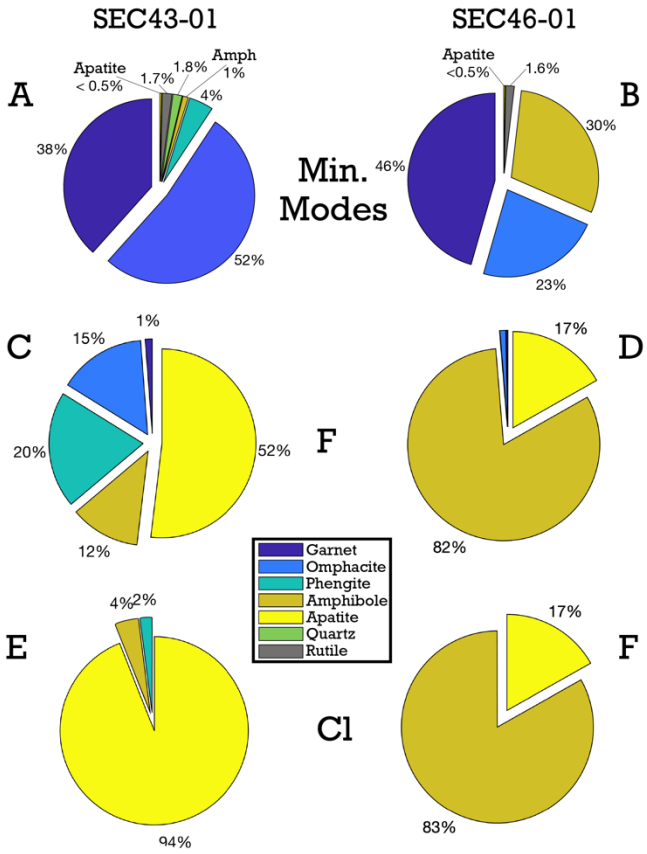

Figure 3.6. Pie diagrams show modal abundances (A. and B.), as well as the percent contribution from each phase to mineral-hosted halogen abundances as derived from SIMS analyses for F (C. and D.) and Cl (E. and F.) in two representative, yet mineralogically distinct, samples.

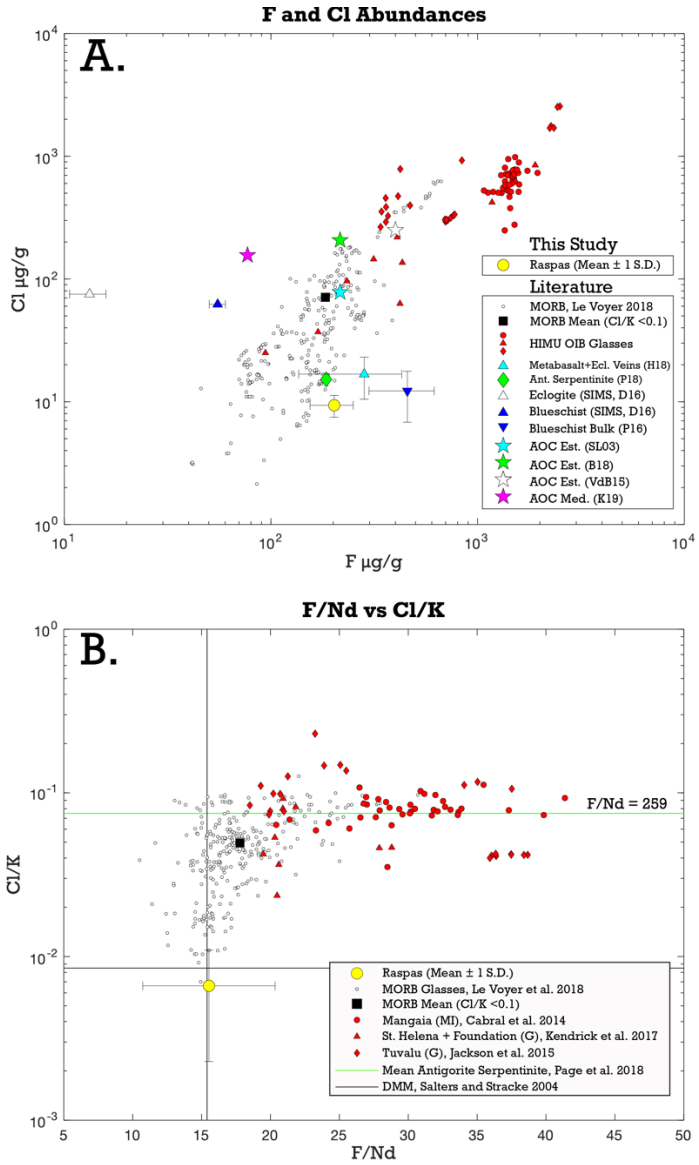

Figure 3.7. A. Fluorine and Cl abundances from this study in comparison to literature values for MORB glasses from Le Voyer et al. (2018), HIMU OIB (Cabral et al. 2014; Jackson et al. 2015; Kendrick et al. 2017), blueschist and eclogite (Debret et al. 2016; Pagé et al. 2016; Hughes et al. 2018), antigorite serpentinite (Pagé et al. 2018), and AOC estimates (Straub and Layne 2003; Van den Bleeken and Koga 2015; Barnes et al. 2018; Kendrick 2019a). MORB with Cl/K values in excess of 0.1 were screened out, due to possible seawater contamination after Shimizu and Saal (2016) and references therein. Peridotite mantle plots off the scale and would be 1.4–31 µg/g for F and from 0.14 to 0.38 µg/g for Cl (Urann et al. 2017). B. F/Nd and Cl/K ratios of Raspas samples (Nd and K from John et al. (2010)), MORB glasses from Le Voyer (2018), mean antigorite serpentinite halogen concentrations from Page et al. (2018) with DMM K (60 µg/g) and Nd (0.713 µg/g) values of Salters and Stracke (2004), and OIB MIs and glasses from the literature (Cabral et al. 2014; Jackson et al. 2015; Kendrick et al. 2017). We note that our eclogitized AOC samples indeed plot below the canonical F/Nd of 21, as posited by Rose-Koga et al. (2012) for deeply subducted oceanic crust.

3.11 Tables

Table 3.1. Volatile abundances by phase (SIMS). N.B. concentrations represent mean of each sample.

Table 1. Volatile abundances by phase (SIMS)		Clinopyroxene											
Sample	Description	No. grains analyzed	No. Analyses	H2O (µg/g)	H2O 2SE (µg/g)	F (µg/g)	F (2SE µg/g)	Cl (µg/g)	Cl (2SE µg/g)	P (µg/g)	P (2SE µg/g)	S (µg/g)	S (2SE µg/g)
C66	Olivine gabbronorite	2	9	152	8.2	0.633	0.048	0.020	0.019	17.44	3.88	0.024	0.015
C48	gabbronorite	3	4	638	141	4.16	1.49	0.140	0.027	-	-	0.017	0.009
C7	gabbronorite	2	6	1,061	399	13.0	7.83	0.277	0.298	17.05	4.99	0.132	0.085
KK5	Garnet Pyroxenite	2	7	1,770	204	5.68	1.87	0.040	0.065	9.13	0.709	0.019	0.004
KK8	Garnet Pyroxenite	3	8	1,842	126	3.40	0.328	0.049	0.027	8.90	0.818	0.023	0.004
P05-5A	Garnet Gabbro	2	5	3,900	1,000	54.8	16.3	3.09	2.25	-	-	0.063	0.047
		Garnet											
Sample	Description	No. grains analyzed	No. Analyses	H2O (µg/g)	H2O 2SE (µg/g)	F (µg/g)	F (2SE µg/g)	Cl (µg/g)	Cl (2SE µg/g)	P (µg/g)	P (2SE µg/g)	S (µg/g)	S (2SE µg/g)
C66	Olivine gabbronorite	-	-	-	-	-	-	-	-	-	-	-	-
C48	gabbronorite	-	-	-	-	-	-	-	-	-	-	-	-
C7	gabbronorite	-	-	-	-	-	-	-	-	-	-	-	-
KK5	Garnet Pyroxenite	2	3	167	21.5	1.46	0.12	-	-	48.6	3.07	0.02	0.00
KK8	Garnet Pyroxenite	3	6	153	10.0	3.41	0.27	0.18	0.10	57.9	12.4	0.02	0.00
P05-5A	Garnet Gabbro	2	4	94.3	22.5	3.39	0.22	0.04	0.00	-	-	-	-
		Opx											
Sample	Description	No. grains analyzed	No. Analyses	H2O (µg/g)	H2O 2SE (µg/g)	F (µg/g)	F (2SE µg/g)	Cl (µg/g)	Cl (2SE µg/g)	P (µg/g)	P (2SE µg/g)	S (µg/g)	S (2SE µg/g)
C66	Olivine gabbronorite	-	-	-	-	-	-	-	-	-	-	-	-
C48	gabbronorite	3	6	105	6.87	0.34	0.04	0.24	0.25	-	-	0.02	0.02
C7	gabbronorite	1	3	102	3.19	0.46	0.02	-	-	3.94	1.41	0.01	0.00
KK5	Garnet Pyroxenite	-	-	-	-	-	-	-	-	-	-	-	-
KK8	Garnet Pyroxenite	-	-	-	-	-	-	-	-	-	-	-	-
P05-5A	Garnet Gabbro	-	-	-	-	-	-	-	-	-	-	-	-
		Amphibole											
Sample	Description	No. grains analyzed	No. Analyses	H2O (µg/g)	H2O 2SE (µg/g)	F (µg/g)	F (2SE µg/g)	Cl (µg/g)	Cl (2SE µg/g)	P (µg/g)	P (2SE µg/g)	S (µg/g)	S (2SE µg/g)
C66	Olivine gabbronorite	-	-	-	-	-	-	-	-	-	-	-	-
C48	gabbronorite	2	3	20,686	462	479	15.3	84.1	16.9			6.62	1.51
C7	gabbronorite	-	-	-	-	-	-	-	-	-	-	-	-
KK5	Garnet Pyroxenite			18,592	435	295	11.0	108	5.53	35.2	0.96	0.26	0.04
KK8	Garnet Pyroxenite	-	-	-	-	-	-	-	-	-	-	-	-
P05-5A	Garnet Gabbro	1	1	18,154	173	44.0	0.49	0.02	0.02				

Table 3.2. Calculated mineral modes. Values in parenthesis represent 1 sigma uncertainties.

Table 2. Calculated mineral modes	Phase Fraction										
Est. Modal Abundances	Garnet	Omphacite	Phengite	Amphibole	Quartz	Rutile	Titanite	Apatite	SUM		NAMs (Grt+Cpx+Qtz)
SEC 42-06	0.421(32)	0.534(32)	0.015(2)	0.0050(5)	0	0.021(2)	0	0.0040(4)	1		0.96
SEC 43-01	0.384(30)	0.524(31)	0.045(4)	0.010(1)	0.017(2)	0.018(2)	0	0.0030(3)	1		0.92
SEC 43-03	0.378(28)	0.416(28)	0	0.099(10)	0.087(2)	0.016(2)	0	0.0040(4)	1		0.88
SEC46-01	0.456(28)	0.229(21)	0	0.297(25)	0	0.016(2)	0	0.0025(3)	1		0.68
SEC46-02	0.358(27)	0.346(27)	0	0.248(22)	0	0.010(1)	0.02(1)	0.016(2)	1		0.70
SEC47-01	0.406(31)	0.499(31)	0.044(4)	0.0050(5)	0.024	0.018(2)	0	0.0040(4)	1		0.93
Average Mineral Modes	0.41	0.43	0.011	0.107	0.023	0.000	0.018	0.006	1.000		

Table 3.3. Halogen bulk rock abundances and ratios.

Table 3. Halogen bulk rock abundances, ratios				Uncorrected for Yield		Corrected for Yield		Uncertainty (Yield Corrected)							
	Calculated Bulk (WHOI)			Pyrohydrolysis (UTA)		Pyrohydrolysis (UTA)		1SD Propogated		Calculated/Measured Bulk					Notes
Sample	OH µg/g	F µg/g	Cl µg/g	F µg/g	Cl µg/g	F µg/g	Cl µg/g	F (µg/g)	Cl (µg/g)	F %	Cl %	Cl/Nb**	Cl/K**	F/Nd**	
SEC42-06	901	168	2.5	92	8.9	115	11.0	15	2.2	146%	23%	3.03	0.0089	10.8	
SEC43-01	1783	258	1.4	109	7.1	137	8.9	68	3.1	189%	16%	4.34	0.0020	22.5	
SEC43-03	2342	200	0.8	152	5.4	189	6.7	11	2.2	105%	12%	2.80	0.0116	15.8	
SEC46-01	5123	241	3.2	154	9.1	193	11.3	52	3.1	125%	28%	5.18	0.0085	17.3	
SEC46-02	6836	415	8.2	160	16.1	199	19.9	12	2.4	208%	41%	4.68	0.0218	32.1	Evidence for fluid interaction, minor retrogression
SEC47-01	1663	145	1.3	112	7.1	139	8.8	9.1	1.5	104%	15%	4.23	0.0021	11.2	Table 1. Halogen abundances by phase (SIMS)
Average		237.7	2.9	129.8	8.9	162.0	11.1								
Standard Deviation		96.6	2.7	29.2	3.8	36.1	4.6								
Average*		202.3	1.85	123.7	7.5	154.5	9.4					3.9	0.0066	15.5	
Standard Deviation*		47.7	0.987	28.0	1.51	34.9	1.88					1.0	0.0043	4.8	
AOC (Barnes et al. 2018)		216	207												
Average Recycling Efficiency (to mantle)		93.7%	0.9%	57.3%	3.6%	71.5%	4.5%								

* Excludes SEC46-02 due to retrograde alteration

* Values used in bulk flux calculations

**Cl and F values from yield corrected pyrohydrolysis, K, Nb, Nd using bulk rock chemistry from John et al. 2010

Chapter 4

The root of the problem: a lower crustal perspective on water in subduction zones

This chapter was originally submitted to *Nature Geoscience* (Aug. 24th, 2020) and is currently under review:

Urann, B. M., Le Roux, V., Jagoutz, O., Muntener, O., Behn, M., & Chin, E. J. The root of the problem: a lower crustal perspective on water in subduction zones

4.1 Abstract

Water cycled between the crust and mantle affects the geophysical, rheological, and geochemical properties of minerals and melts, particularly at subduction zones where water is returned from surface reservoirs to the mantle. To constrain the water content of arc magmas, previous studies have relied on measuring extrusive products and mineral-hosted melt inclusions; yet these methods have inherent limitations, which may obfuscate the true water variability of arc magmas. Here we use secondary ion mass spectrometry to analyze H_2O concentrations in pyroxenes from two suites of lower arc cumulate rocks from the Kohistan paleo-arc (NW Pakistan) to evaluate the water content of the melts from which the cumulates crystallized. Pyroxenes were found to retain their primary water abundances and record two distinct parental melts: one water-poor (<1 wt.% H_2O), the other water-rich (>4 wt.% H_2O). Extensive crystal fractionation of the water-rich suite led to the formation of super-hydrous andesitic to dacitic melts (~12–20 wt.% H_2O), predicted petrologically yet rarely if ever observed. We calculate that foundering of water-rich lower arc roots can deliver water fluxes comparable to subducted oceanic crust, which underpins the importance of foundering in global volatile cycling.

4.2 Introduction

Subduction is the primary mechanism of volatile (H_2O, CO_2, F, Cl, S) transfer from Earth's surface reservoirs to the mantle. Dehydration of subducted material leads to melting of the overlying mantle, which generates volatile-rich arc magmas. The volatile content of arc magmas will dictate geochemical fluxes, explosivity of eruptions, and mineral phase stability, influencing both the rheology and density of arc crust. Our understanding of the volatile variability of arc magmas has relied primarily on analyses of minimally-degassed arc lavas and melt inclusions (MI) hosted in olivine and clinopyroxene (Cpx) phenocrysts (Sisson and Layne 1993, Dobson, Skogby et al. 1995, Straub and Layne 2003), which yield a range of 1.3–7.15 wt.% H_2O (melt Mg# 39–82) (Plank, Kelley et al. 2013). On the other hand, experimental and petrological studies have proposed that primitive arc melts may contain H_2O in excess of 12 wt.% (Anderson 1974, Carmichael 2002, Grove, Elkins-Tanton et al. 2003, Grove, Baker et al. 2005, Grove, Chatterjee et al. 2006, Krawczynski, Grove et al. 2012) as H_2O is highly soluble in basaltic melts, reaching >20 wt.% H_2O at 1 GPa and 1200°C (Mitchell, Gaetani et al. 2017). The apparent incongruence between direct volatile measurements and indirect assessments from phase petrology may come from physiochemical processes imposed during magma ascent such as degassing, rapid diffusive equilibration of volatiles during host magma ascent (Gaetani, O'Leary et al. 2012, Bucholz, Gaetani et al. 2013), and limits on the quenchability of hydrous melts (9 ± 1 wt.%. H_2O) (Gavrilenko, Krawczynski et al. 2019). To address these challenges and explore the maximum H_2O content of hydrous arc magmas, the H_2O content of intrusive crystallization products derived from arc melts may provide further clarity.

As hydrous magmas ascend through the upper mantle, crystal fractionation generates voluminous cumulates that lead to thickening of arc crust. As arc crust thickens, increased pressure leads to fractionation of garnet, clinopyroxene, amphibole (Müntener, Kelemen et al. 2001, Müntener and Ulmer 2006, Alonso Perez 2007, Alonso-Perez, Müntener et al. 2009, Müntener and Ulmer 2018, Ulmer, Kaegi et al. 2018). These Fe-rich lithologies are often more dense than underlying mantle peridotite, and may sink back into the mantle in a process known as lower crustal foundering (Arndt and Goldstein 1989, Kay and Mahlburg-Kay 1991). Consequently, full lower crustal exposures are rare (Behn and Kelemen 2006, Jagoutz and Behn 2013); however, lower crustal cumulates are sometimes exhumed in relict arc sections (e.g., Kohistan, Talkeetna) or as crustal xenoliths (Dodge, Lockwood et al. 1988, Ducea and Saleeby 1996, Bloch, Ibañez-Mejia et al. 2017). These samples could provide the means to circumvent issues surrounding melt inclusions and may hold unique insights into the nature and composition of primitive arc magmas at depth: in particular the H_2O content of the melts from which the cumulates crystallized. The utility of such information is myriad, as H_2O is known to influence the geophysical and rheological properties of minerals and aggregates (Hirth and Kohlstedt 1996, Karato 2003).

Here we use secondary ion mass spectrometry to determine the H_2O, F, Cl, S, C and P abundances of individual minerals from lower crustal rocks from the obducted Kohistan arc to

elucidate the water content of the melts from which the rocks crystallized. The Cretaceous Kohistan fossil arc terrane (NW Pakistan) is a near-complete section of volcanic, plutonic, and upper mantle rocks obducted 50 Ma ago as a consequence of northward subduction of the Indian plate during Himalayan orogenesis (Tahirkheli and Jan 1979). The Kohistan lower crust can be differentiated into two domains: the Southern Plutonic Complex at the stratigraphic base (1.5–0.8 GPa), and the Chilas Complex situated directly above (0.6–0.7 GPa) (Jagoutz and Schmidt 2012). The two Complexes are composed of a composite suite of plutonic rocks that have crystallized either from hydrous (Southern Plutonic Complex) or damp (Chilas) primitive melts, each following a distinct compositional sequence, or liquid line of descent (LLD), during differentiation (Jagoutz, Muntener et al. 2011). The Southern Plutonic Complex exemplifies a typical calc-alkaline (i.e., iron depletion trend) differentiation series, whereas Chilas is considered to represent a tholeiitic/calc-alkaline hybrid series. For this study, we selected three fresh (<5% alteration) gabbronorites from Chilas Complex (C7, C48, C66) that were studied in detail previously (Jagoutz, Müntener et al. 2007). These samples were shown to crystallize from a common parental magma along a single damp LLD with sample C66, an olivine gabbronorite, the most primitive of the suite compared to C48 and C7 (Jagoutz, Müntener et al. 2007). Similarly, three minimally altered samples were selected from the Southern Plutonic Complex, including two garnet pyroxenites (KK5 and KK8) and a garnet diorite (P05-5A). Experimental constraints and field data suggest that the Southern Plutonic Complex garnet pyroxenites and garnet diorite are also genetically related, with the former the result of earlier crystallization along a hydrous LLD, which eventually led to the formation of the latter through extensive fractional crystallization (Alonso Perez 2007, Jagoutz, Müntener et al. 2011, Müntener and Ulmer 2018, Ulmer, Kaegi et al. 2018). Detailed sample descriptions and locations are provided in the Supplement.

For each arc domain, we combine the volatile, major and trace element data on mineral phases with experimentally calibrated pyroxene partition coefficients (O'Leary, Gaetani et al. 2010) at relevant *P-T* conditions to evaluate the compositional evolution of the silicate melts from which the cumulates crystallized. Our results provide a novel avenue to determine the full variability of volatile contents of arc melts, from primitive to evolved, and shed new light on the role of density-unstable lower crust for volatile transfer between Earth's crust and mantle.

4.3 Volatile variability in lower crustal minerals

Measured H_2O abundances in Chilas clinopyroxenes increase from 152 ± 8 μg/g H_2O (2SE) in the most primitive sample (C66, Mg# 81.8) to 638 ± 141 μg/g H_2O and 1061 ± 399 μg/g H_2O in progressively more evolved C48 (Mg# 78.9) and C7 (Mg# 77.8), respectively (Table 4.1). Southern Plutonic Complex Cpx range from 1770 to 1842 μg/g H_2O in garnet pyroxenites KK5 (Mg# 76.2) and KK8 (Mg# 81.5) to 3900 μg/g H_2O in the more evolved garnet diorite (P05-5A, Mg# 70.7). These volatile variations are closely mirrored by mineral major and trace element chemistry (Table 4.S1). The Mg# (molar Mg/(Mg+Fe) of

clinopyroxene consistently decreases from more primitive, water-poor samples to more evolved, water-rich samples in both Chilas and Southern Plutonic Complex domains (Fig. 4.1). Similarly, Na positively correlates with water in Cpx, with the Chilas and Southern Plutonic Complex samples showing two distinct trends (Fig. 4.1). Finally, rare earth elements (REE, Table 4.S2), fluorine and chlorine exhibit systematic covariations with H_2O, particularly in Chilas (Fig. 4.2, Fig. 4.S2). Orthopyroxene (Chilas) and garnet (Southern Plutonic Complex) were also analyzed, yielding 102–105 μg/g and 94–167 μg/g H_2O, respectively.

The correlations observed between Cpx H_2O and other incompatible elements (e.g. F, Cl and REE), as well as indices of crystallization (e.g., decreasing Mg#) are striking and may reflect preservation of original water contents at the time of crystallization despite the fact that hydrogen diffusion in Cpx is known to be rapid (Demouchy, Jacobsen et al. 2006, Ferriss, Plank et al. 2016, Lloyd, Ferriss et al. 2016). Several lines of evidence suggest that measured H_2O here is primary in nature. Experimental studies have determined that hydrogen diffusivities tend to decrease with increasing Cpx Al content(Ferriss, Plank et al. 2016), consistent with hydrogen incorporation by a coupled substitution mechanism of H^+ and Al^{3+} for Si^{4+} (see O'Leary et al.(2010)). Diffusion of Al in Cpx is known to be slow (Sautter, Jaoul et al. 1988), and may then be a rate limiting step, impeding diffusive hydrogen loss or gain. In our samples, only minimal H_2O deviations are observed at the Cpx rims with respect to cores (Fig. 4.3). If one considers Cpx cores, H_2O abundances are well correlated with F and Cl, as well as slower diffusing elements like REE and major elements (Figs. 4.1 and 4.2); these covariations would have been erased had diffusion of hydrogen in Cpx been extensive. In addition, deep-seated intrusions have the potential to re-equilibrate during sub-solidus cooling; Chilas samples equilibrated from magmatic conditions to granulite facies (800–950°C), whereas for the more hydrous Southern Plutonic Complex, such temperatures were likely magmatic (e.g. T_{REE}, Table 4.2). Thus, hydrogen may have been redistributed during cooling. To evaluate this possibility, we compared our data to published inter-mineral partition coefficients (Figure 4. S3), finding broad consistency with experimental and natural samples. However, systematic chemical variations in coexisting minerals are not consistent with redistribution during cooling. For example, Ti abundances in coexisting pyroxenes (C48 and C7) show steady decreases from core to rim, inconsistent with redistribution during sub-solidus re-equilibration (Cherniak and Liang 2012). Finally, we did not observe reverse zoning in pyroxenes (e.g. Mg#), nor major or trace element rim enrichment, obviating appreciable post crystallization modification of pyroxene chemistry by late interstitial liquid. Therefore, measured Cpx volatile concentrations primarily reflect initial crystallization concentrations, with cores largely unaffected by diffusive reequilibration.

To validate our approach, two assumptions must be made: first, that measured H_2O concentrations were not disrupted by sub-solidus re-equilibration or open system processes (as indicated above), and second, that melts were undersaturated with respect to H_2O at relevant pressure and temperature conditions (which we evaluate below). To calculate an equilibrium melt H_2O content from an analyzed mineral, one must have well-defined distribution coefficients

between a given mineral and silicate melt, parameterized for pressure, temperature, and composition. A large number of experimental studies involving Cpx have permitted a rigorous assessment of H_2O partitioning between Cpx and melt (O'Leary, Gaetani et al. 2010). Therefore our calculations utilize Cpx H_2O concentrations with composition-dependent H_2O partition coefficients (O'Leary, Gaetani et al. 2010) between Cpx and silicate melt (Table 2).

4.4 The cumulate perspective on the water variability of arc magmas

The most primitive Chilas olivine gabbronorite, C66, yields equilibrium melt H_2O concentrations of 1.21 ± 0.09 wt.% H_2O (2SE, n=9). More differentiated samples C48 and C7 yield more hydrous equilibrium melt compositions of 6.38 ± 0.96 (2SE, n=3) and 10.95 ± 4.09 (2SE, n=6) wt.% H_2O, respectively. The solubility of H_2O in basaltic melts at 0.4–0.6 GPa is thought to be ~7–11 wt.% (Hamilton, Burnham et al. 1964, Khitarov, Kadik et al. 1968, Berndt, Liebske et al. 2002) and increases with increasing pressure to 20.6 ± 0.9 wt.% H_2O (2σ) at 1 GPa and 1200°C (Mitchell, Gaetani et al. 2017). Thus, melts from which the cumulates formed were likely undersaturated with respect to H_2O at high pressure and are unlikely to have degassed before the lower crustal cumulates crystallized at 0.6–0.7 GPa. Therefore, Cpx records the H_2O content of melts from which it crystallized. As H_2O is highly incompatible in nominally anhydrous minerals, crystallization leads to a reduction in melt mass (F) commensurate with an increase in H_2O in the remaining liquid, similar to other incompatible elements (e.g., Nd). Although the rare earth element Ce has a similar bulk partition coefficient to H_2O in mantle systems (Michael 1995, Saal, Hauri et al. 2002), Nd has a bulk partition coefficient closest to the calculated H_2O bulk partition coefficient based on a Cpx/Opx/Plag assemblage of 10/30/60 (Table 4.S3). We modeled the differentiation path of a melt in equilibrium with C66 using simple equilibrium and fractional crystallization models, the former of which appears to better reproduce the data as suggested by previous studies (Jagoutz, Müntener et al. 2007) (Fig. 4.4; see Methods and Supplementary Table 3 for details). In both models, prolonged crystallization leads to significant H_2O and incompatible element (e.g., Nd) enrichments in the evolving melt, genetically linking the gabbronorite suite from the most primitive sample (C66) to more evolved compositions (C48 and C7) (Jagoutz, Müntener et al. 2007). Evolved melts with H_2O abundances of >4 wt.% are also consistent with the presence of late magmatic amphibole (sometimes rimming Cpx) in some gabbronorites. In order to calculate the parental melt H_2O content, we consider that liquids in equilibrium with C66 were already moderately evolved, with an Mg# of ~53 and underwent 30–50% olivine and clinopyroxene fractionation prior to C66 crystallization (Jagoutz, Müntener et al. 2007). By applying an additional fractionation correction (see Methods), we estimate an initial parental melt H_2O content of 0.61–0.85 wt.% for Chilas primitive magmas. This is relatively H_2O-poor for subduction environments, but consistent with decompression melting in an intra-arc extensional setting and a damp basaltic parental magma with a minor slab contribution (Jagoutz, Müntener et al. 2006, Jagoutz, Müntener et al. 2007, Jagoutz, Müntener et al. 2011).

Using the above approach, garnet pyroxenites KK5 and KK8 yield equilibrium melt H_2O concentrations of 8.44 ± 0.39 (2SE, n=5) and 12.44 ± 0.34 (2SE, n=6) wt.% H_2O, respectively, whereas Southern Plutonic Complex garnet diorite Cpx (P05-5A) yields equilibrium melts containing 19.6 ± 1.5 wt.% H_2O (2SE, n=5) (Fig. 4.4). KK samples are well below H_2O saturation limits (Fig. 4.5C), while P05-5A appears to be at or near saturation at 1 GPa. Such water-rich melts are consistent with experimental H_2O solubility studies and petrologic constraints, yet to our knowledge have never been directly determined in natural samples. Like Chilas, Southern Plutonic Complex samples are relatively evolved and thus melts parental to these rocks have undergone prior crystallization. We use two independent approaches to evaluate H_2O concentrations of the initial parental magmas. First, we use a simplified fractionation model and assume that the melts parental to these garnet pyroxenites have undergone between 35 and 60% fractional crystallization of olivine + pyroxene prior to amphibole and garnet saturation (see Methods) (Müntener and Ulmer 2018, Ulmer, Kaegi et al. 2018). As H_2O is highly incompatible in both phases, this correction is rather insensitive to mineral modes and partition coefficients, and to a first order provides a reasonable range of primitive magma H_2O abundances. Applying this correction, we find that Southern Plutonic Complex parental magmas contained 3.4–5.5 wt.% H_2O (KK5) and 5.0–8.0 wt.% H_2O (KK8). We note that this method cannot be used to evaluate P05-5A, due to its evolved nature. In parallel, we apply a quantitative petrogenetic model of the Southern Plutonic Complex LLD (Jagoutz 2010), which permits us to explore a range of initial water abundances for each sample (Fig. 4.5). A melt H_2O content of 4 wt.% is required to stabilize amphibole (Cawthorn and O'Hara 1976); the presence of moderately fractionated amphibole-bearing garnet pyroxenites in the fractionation sequence (Jagoutz 2010) places a lower bound on initial melt H_2O abundances of ~3.25 wt.%. Modelling suggests parental melt H_2O abundances for Southern Plutonic Complex cumulates were ~4–5 wt.%. for P05-5A and 6–10 wt.% for KK5 and KK8 (Fig. 4.5), yielding broad consistency between both methods. Calculated initial melt H_2O contents suggest input from a hydrous slab component during flux melting in a mantle wedge (Jagoutz, Müntener et al. 2011), congruent with isotopic mixing models indicative of a modest slab fluid contribution (Jagoutz, Bouilhol et al. 2019). Fractionation of silica-poor garnet pyroxenites (± amphibole) leads to silica-enrichment in derivative liquids; thus, equilibrium melt compositions appear to reflect a range from basaltic (KK8) to dacitic (P05-5A). Southern Plutonic Complex samples were likely derived from different batches of melt based on trace element compositions (see Supplement for discussion) and field observations (Müntener and Ulmer 2018); therefore, a range of parental melts is given in Figure 4.4 (red rectangle).

Our results suggest that primitive arc magmas are far more H_2O-rich than indicated by the upper limit of ~7 wt.% H_2O recorded in melt inclusion studies (Figs. 4.4B, 4.5B). Southern Plutonic Complex cumulates are consistent with parental melts containing 4–10 wt.% H_2O, progressing to ~20 wt.% H_2O after extensive crystal fractionation (Fig. 4.5). Crustal filtering (e.g., degassing, CO_2 flushing (Caricchi, Sheldrake et al. 2018) and diffusive re-equilibration

(Gaetani, O'Leary et al. 2012) likely obfuscates the true heterogeneity of H_2O observed in melts that have made their way to the surface, either as crystal cargo bound in melt inclusions or as extrusives. Protracted crystallization will inevitably lead to H_2O enrichment (>10 wt.%), notwithstanding the onset of amphibole (~2 wt.% H_2O) fractionation. Upon magma ascent, the solubility of H_2O will decrease with decreasing pressure to ~7 wt.% at 0.5 GPa and 950°C for a basaltic composition (~12 wt.% for rhyolite) (Newman and Lowenstern 2002), leading to the exsolution of a free fluid phase. Coexisting silicate melts and aqueous fluids will partition Cl preferentially into the latter (up to a factor of ten) (Alletti, Baker et al. 2009), generating solute-rich brines. Our results indicate that these exsolved fluids, thought to be important in porphyry Cu, Mo and Au deposit formation (Hedenquist, Arribas et al. 1998, Richards 2003, Lee and Tang 2020), may be a natural consequence of H_2O exsolution in ascending, super-hydrous magmas at mid-crustal depths. Such a process is corroborated by mass balance estimates indicating H_2O-rich source melts (at least 10 wt.%) for the Questa porphyry Cu-Mo-deposit (New Mexico, USA) with exsolution initiating in the mid-crust (Klemm, Pettke et al. 2008). Further, the hydrous nature of Southern Plutonic Complex parental melts lies in stark contrast to the water-poor nature of Chilas, lending support to the classic interpretation of calc-alkaline differentiation (Southern Plutonic Complex) as a direct result of high (>4 wt.%) initial H_2O abundances, as opposed to the damp nature of the tholeiitic series (Sisson and Grove 1993).

4.5 Implications for volatile fluxes by lower crustal foundering

During juvenile arc maturation, crustal thickening leads to fractionation of hydrous arc magmas at pressure greater than ~1 GPa where clinopyroxene, amphibole, and garnet are stable liquidus phases (Alonso-Perez, Müntener et al. 2009). Continued fractionation may lead to a density-unstable configuration whereby the garnet-rich lower crust is negatively buoyant with respect to underlying mantle peridotite, as observed for Southern Plutonic Complex garnet diorite and garnet pyroxenites (Jagoutz, Müntener et al. 2011). This material may eventually founder and sink back into the mantle, until thermal equilibration leads to melting or the material reaches a depth of neutral buoyancy. Foundering fluxes are thought to be 6.4–8.1 km^3/yr over timescales of tens of Ma, or about one half that of oceanic crust subducted globally (~19 km^3/yr) (Jagoutz and Schmidt 2013), although the efficiency and frequency of such events will be dictated by arc thermal structure (Jagoutz and Behn 2013). Our results permit an evaluation of global mean volatile fluxes returned during lower crustal foundering. Using simplified Southern Plutonic Complex modal abundances of 50/30/20 (Cpx/Grt/Amph), we find that bulk H_2O abundances of 4500–5500 μg/g are nearly twice those observed for subducted oceanic eclogites (2360 ± 1600 μg/g), whereas Southern Plutonic Complex bulk F abundances (56 ± 11 μg/g) are significantly lower (202 ± 48 μg/g) (Urann, Le Roux et al. 2020). Recasting our samples to an anhydrous assemblage (50:50 Cpx:Grt, i.e. >3 GPa), the delaminate will contain 1000–2000 μg/g H_2O, nearly an order of magnitude more H_2O than typical depleted MORB mantle (~150 μg/g H_2O) (Saal, Hauri et al. 2002). Combining our bulk H_2O abundances with estimated

foundering fluxes (6.4–8.1 km^3/yr), we find that crustal foundering of an anhydrous (Cpx/Grt) delaminate may be capable of H_2O fluxes of 0.2–0.5x10^{11} $kg•yr^{-1}$, comparable to subduction fluxes (0.3–0.8x10^{11} $kg•yr^{-1}$) and approximately equal to estimates of annual ocean island basalt H_2O output (0.2–0.5x10^{11} $kg•yr^{-1}$) (Kendrick, Hémond et al. 2017) (Supplementary Table 4). As dense, amphibole-bearing garnet pyroxenites sink back into the mantle, the breakdown of amphibole is likely to release substantial quantities of H_2O back into the overlying mantle, which may promote further melting in the sub-arc region. Alternatively, liberated H_2O may diffusively equilibrate with surrounding lithologies, priming them for later melting. Therefore, in addition to subduction of eclogitized oceanic crust, lower crustal foundering is an important means of volatile transfer between the crust and mantle.

4.6 Acknowledgements
We thank Brian Monteleone for his diligence on the Cameca 1280 SIMS at WHOI. We also thank Neel Chatterjee for his assistance with electron microprobe analyses. We thank reviewers for their constructive reviews and the editor for expeditious handling of the manuscript.

4.7 Figures

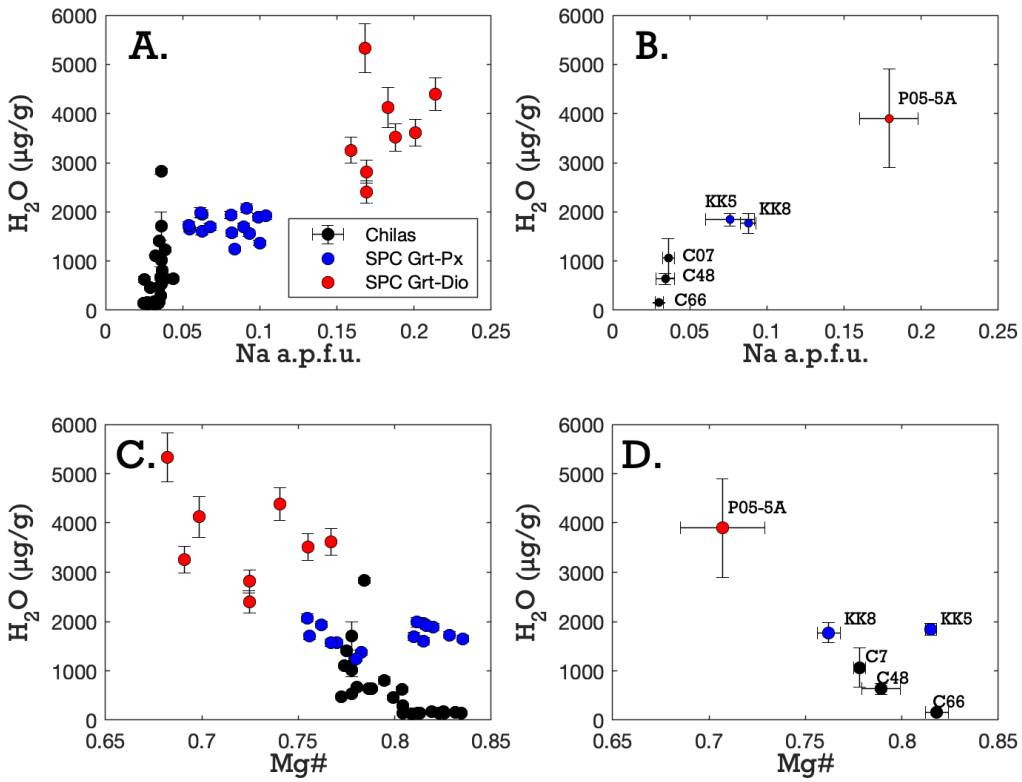

Figure 4.1. Individual analyses (A. and C.) and sample mean values (B. and D.) of clinopyroxene major element composition plotted against H_2O abundances. Octahedrally coordinated Na (A. and B.) in atoms per formula unit (a.p.f.u.), Mg# (C. and D.). H_2O error bars are propagated 2SE uncertainties for individual analyses (A. and C.); Panel B and D error bars are 2SE of the mean.

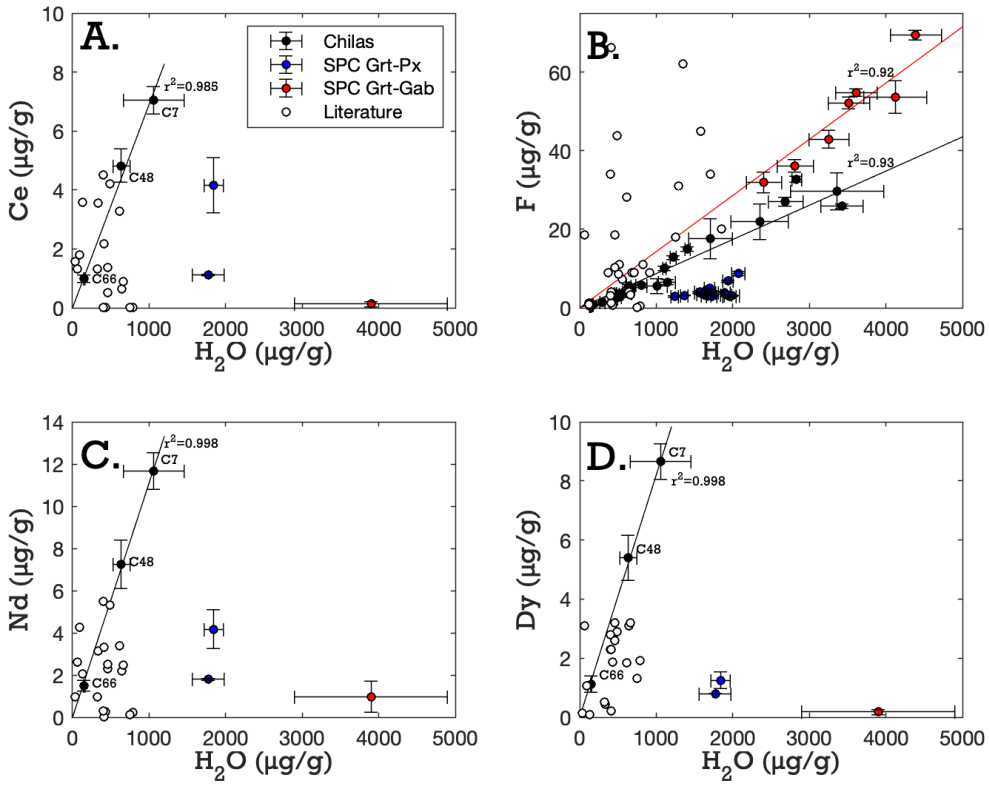

Figure 4.2. Clinopyroxene Ce (A.), F (B.), Nd (C.), Dy (D.) plotted against water concentrations. Values are the mean of each sample (Cpx cores only), except in Panel B where all volatiles analyses of Cpx are included. Nota bene: the vast majority of Cpx H_2O data are from peridotites; very little data exists on cumulate Cpx H_2O concentrations. Error bars are two standard error of the mean, except for panel B where propagated 2SE uncertainties for individual analyses are shown. White circles denote literature data (Hauri, Gaetani et al. 2006, O'Leary, Gaetani et al. 2010, Warren and Hauri 2014, Chin, Soustelle et al. 2016).

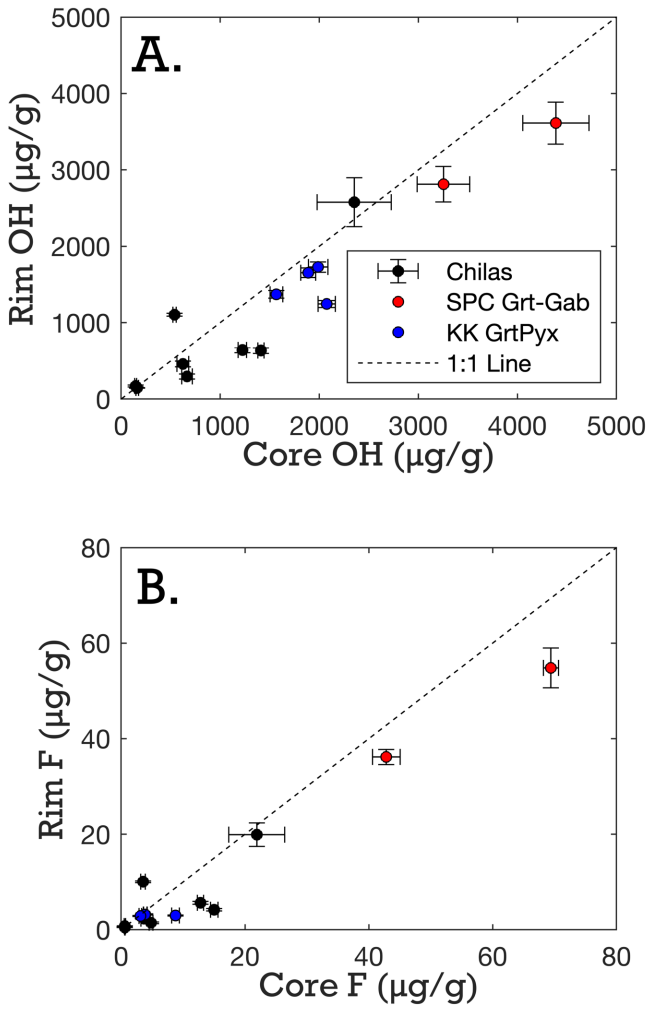

Figure 4.3. Clinopyroxene core and rim measurements for H_2O (A.) and F (B.). Error bars are two standard error propagated uncertainties for individual analyses.

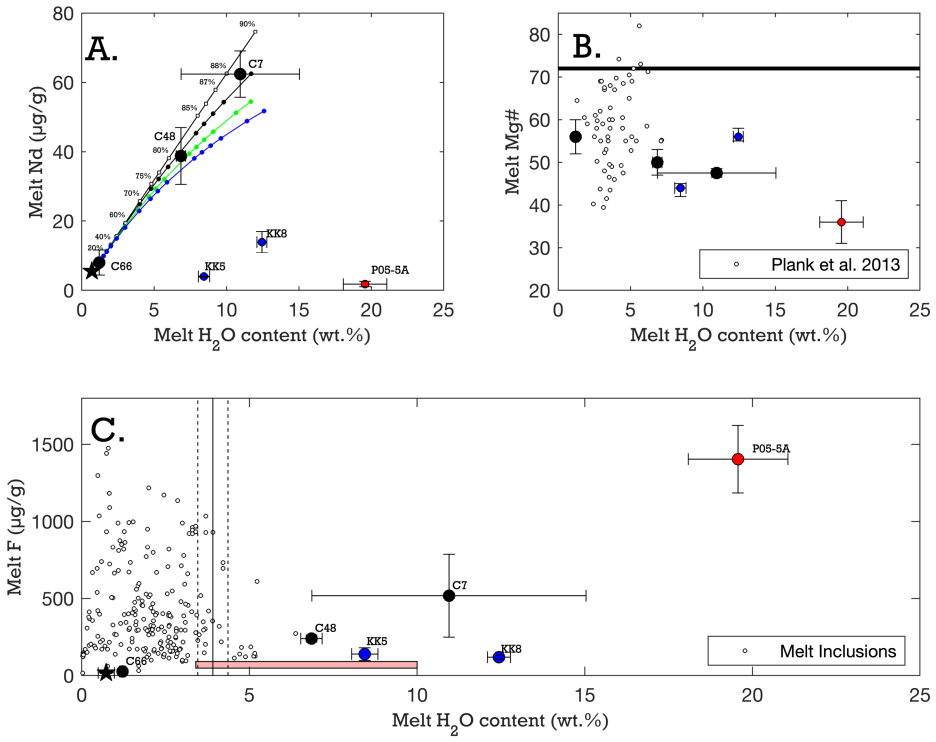

Figure 4.4. **A.** Equilibrium (black circles) and fractional (white squares) crystallization models for Chilas gabbronorites, individual samples labeled. Error bars are 2SE of the mean. Values along curve are percent crystallization. Starting composition from C66. Plag/Opx/Cpx mineral modes of 60/30/10 (black curve) after Jagoutz et al.(2007). For comparison, 5% amphibole in crystallization sequence shown in green curve. Blue curve uses 46/21/33 Plag/Opx/Opx, the highest Cpx modal abundances observed in gabbronorite sequence. Black star denotes Chilas parental melt. For model details, see Supplement. **B**. Calculated melt H_2O abundances plotted against mean melt Mg# from Cpx Mg# for Chilas and Southern Plutonic Complex samples. Mg# error bars denote highest and lowest measured Mg# for Cpx. Literature data (white circles) are maximum water abundances for individual arc volcanoes from Plank et al. (2013) converted from olivine forsterite content to melt Mg#. Thick black line denotes melts (Mg# 72) in equilibrium with mantle olivine Fo_{90}. **C**. Arc melt inclusions from the literature (Bown and White 1994, Portnyagin, Hoernle et al. 2007, Sadofsky, Portnyagin et al. 2008, Rose-Koga, Koga et al. 2012, Rose-Koga, Koga et al. 2014) shown as white circles, compared to equilibrium melts calculated for Kohistan. Black star denotes calculated Chilas parental melt. Red rectangle denotes range of SPC parental melts. Line signifies mean water content of arc melts with 1σ as dashed lines from Plank et al. (2013). Prolonged crystallization leads to water rich melts, which are unlikely to be sampled by melt inclusions due to degassing and re-equilibration. Fluorine content of equilibrium melts was calculated based on robust relationship between F and water in individual Cpx, with a D_F/D_{H2O} of 1.934 from experimental studies (Hauri, Gaetani et al. 2006, O'Leary, Gaetani et al. 2010).

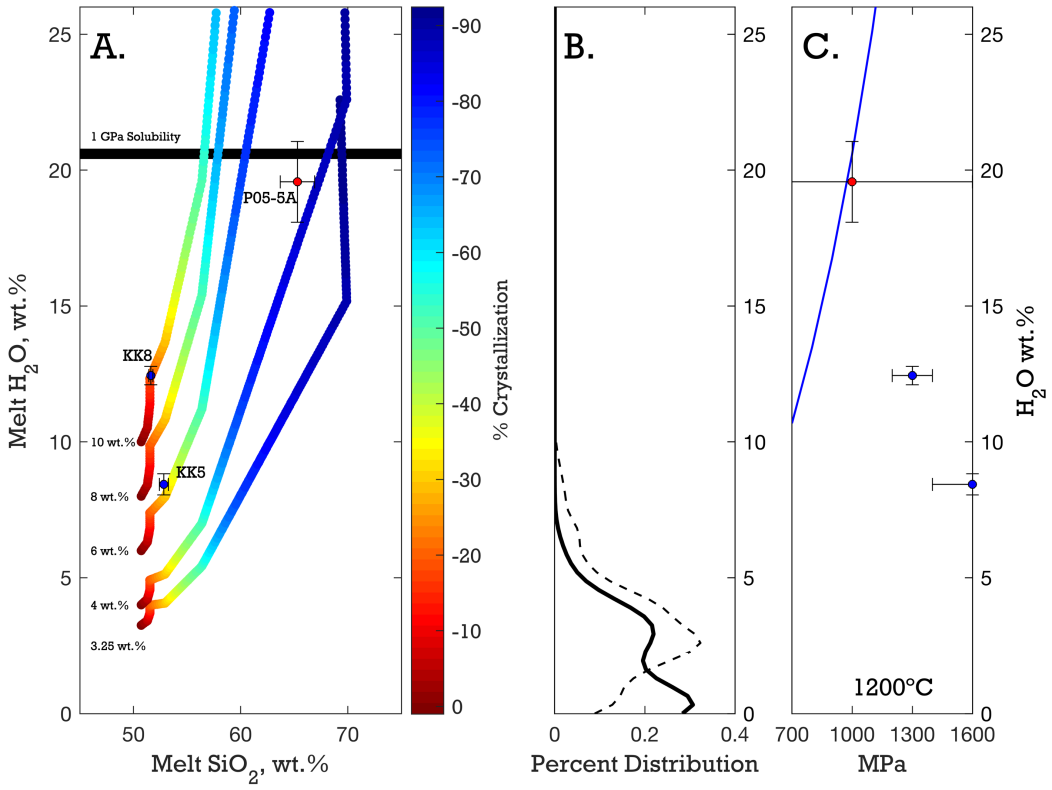

Figure 4.5. A. Southern Plutonic Complex melt crystallization model based on the petrogenetic model of Jagoutz (2010). Equilibrium melt SiO_2 content for each sample calculated based on Cpx Mg#, extrapolated to the equilibrium melt composition. Thick black line denotes 1 GPa H_2O solubility for a basaltic melt (Mitchell, Gaetani et al. 2017). We note that silicic magmas tend to have higher water solubilities than basalt, however constraints at relevant P-T conditions are lacking. $H_2O_{minimum}$ calculated as the minimum amount of water in the initial melt needed to crystallize amphibole (minimum 4 wt.% H_2O) in the fractionation sequence modeled by Jagoutz (2010). See Methods for details. B. Probability density function of olivine-hosted arc melt inclusions from the Georoc Database (http://georoc.mpch-mainz.gwdg.de/georoc/). Primitive (melt Mg#>65) shown as a solid back line, n=171. Melt Mg# of 35 to 65, comparable to Kohistan cumulates, shown as dashed black line, n=879. C. H_2O solubility curve for basaltic melts at 1200°C (Mitchell, Gaetani et al. 2017).

4.8 Tables

Table 4.1. Volatile abundances by mineral phase (SIMS)

Table 1. Volatile abundances by phase (SIMS)		Clinopyroxene											
Sample	Description	No. grains analyzed	No. Analyses	H2O (μg/g)	H2O 2SE (μg/g)	F (μg/g)	F (2SE μg/g)	Cl (μg/g)	Cl (2SE μg/g)	P (μg/g)	P (2SE μg/g)	S (μg/g)	S (2SE μg/g)
C66	Olivine gabbronorite	2	9	152	8.2	0.633	0.048	0.020	0.019	17.44	3.88	0.024	0.015
C48	gabbronorite	3	4	638	141	4.16	1.49	0.140	0.027	-	-	0.017	0.009
C7	gabbronorite	2	6	1,061	399	13.0	7.83	0.277	0.298	17.05	4.99	0.132	0.085
KK5	Garnet Pyroxenite	2	7	1,770	204	5.68	1.87	0.040	0.065	9.13	0.709	0.019	0.004
KK8	Garnet Pyroxenite	3	8	1,842	126	3.40	0.328	0.049	0.027	8.90	0.818	0.023	0.004
P05-5A	Garnet Gabbro	2	5	3,900	1,000	54.8	16.3	3.09	2.25	-	-	0.063	0.047
		Garnet											
Sample	Description	No. grains analyzed	No. Analyses	H2O (μg/g)	H2O 2SE (μg/g)	F (μg/g)	F (2SE μg/g)	Cl (μg/g)	Cl (2SE μg/g)	P (μg/g)	P (2SE μg/g)	S (μg/g)	S (2SE μg/g)
C66	Olivine gabbronorite	-	-	-	-	-	-	-	-	-	-	-	-
C48	gabbronorite	-	-	-	-	-	-	-	-	-	-	-	-
C7	gabbronorite	-	-	-	-	-	-	-	-	-	-	-	-
KK5	Garnet Pyroxenite	2	3	167	21.5	1.46	0.12	-	-	48.6	3.07	0.02	0.00
KK8	Garnet Pyroxenite	3	6	153	10.0	3.41	0.27	0.18	0.10	57.9	12.4	0.02	0.00
P05-5A	Garnet Gabbro	2	4	94.3	22.5	3.39	0.22	0.04	0.00	-	-	-	-
		Opx											
Sample	Description	No. grains analyzed	No. Analyses	H2O (μg/g)	H2O 2SE (μg/g)	F (μg/g)	F (2SE μg/g)	Cl (μg/g)	Cl (2SE μg/g)	P (μg/g)	P (2SE μg/g)	S (μg/g)	S (2SE μg/g)
C66	Olivine gabbronorite	-	-	-	-	-	-	-	-	-	-	-	-
C48	gabbronorite	3	6	105	6.87	0.34	0.04	0.24	0.25	-	-	0.02	0.02
C7	gabbronorite	1	3	102	3.19	0.46	0.02	-	-	3.94	1.41	0.01	0.00
KK5	Garnet Pyroxenite	-	-	-	-	-	-	-	-	-	-	-	-
KK8	Garnet Pyroxenite	-	-	-	-	-	-	-	-	-	-	-	-
P05-5A	Garnet Gabbro	-	-	-	-	-	-	-	-	-	-	-	-
		Amphibole											
Sample	Description	No. grains analyzed	No. Analyses	H2O (μg/g)	H2O 2SE (μg/g)	F (μg/g)	F (2SE μg/g)	Cl (μg/g)	Cl (2SE μg/g)	P (μg/g)	P (2SE μg/g)	S (μg/g)	S (2SE μg/g)
C66	Olivine gabbronorite	-	-	-	-	-	-	-	-	-	-	-	-
C48	gabbronorite	2	3	20,686	462	479	15.3	84.1	16.9			6.62	1.51
C7	gabbronorite	-	-	-	-	-	-	-	-	-	-	-	-
KK5	Garnet Pyroxenite			18,592	435	295	11.0	108	5.53	35.2	0.96	0.26	0.04
KK8	Garnet Pyroxenite	-	-	-	-	-	-	-	-	-	-	-	-
P05-5A	Garnet Gabbro	1	1	18,154	173	44.0	0.49	0.02	0.02				

N.B. 2SE corresponds to 2 standard error of the mean.

Table 4.2. Sample locations, rock types, pressure and temperature estimates

Sample	Latitude (°)	Longitude(°)	Description	Calculated Dcpx-melt	Calc. Equilbrium melt H2O (wt.%)	Calc. Equilbrium melt H2O 2SE (wt.%)	P Est. in GPa (REE Cpx-Grt, Sun and Liang 2015)	T Est. in °C (REE Cpx-Grt, Sun and Liang 2015)	T Est. in °C (Fe-Mg, Krogh (1988)
C66	35°19′20.9′′N	74°07′42′′E	Olivine gabbronorite	0.0123	1.21	0.09			
C48	35°24′10.3′′N	74°08′49.7′′	gabbronorite	0.0193	6.38	0.96			
C7	35°24′32.3′′N	74°08′59.7′′	gabbronorite	0.0096	10.95	4.09			
KK5	35°03'49.7"N	72°56'59.5"E	Garnet Pyroxenite	0.0148	8.44	0.39	1.6 ± 0.2	807 ± 23	1032
KK8	35°04'10.4"N	72°57'29.3"E	Garnet Pyroxenite	0.0123	12.44	0.34	1.3 ± 0.1	852 ± 14	1094
P05-5A	35°04'39.63" N	72°57'51.20"E	Garnet Gabbro	0.0199	19.57	1.49	1.0 ± 0.6	945 ± 63	913

Chapter 5

Recycled arc mantle recovered from the Mid-Atlantic Ridge

This chapter was originally published in *Nature Communications* (2020) as:

Urann, B., Dick, H., Parnell-Turner, R. & Casey, J. Recycled arc mantle recovered from the Mid-Atlantic Ridge. *Nature Communications* **11**, 1-9 (2020).

This chapter has been reprinted with permissions garnered from the original copyright agreement.

5.1 Abstract

Plate tectonics and mantle dynamics necessitate mantle recycling throughout Earth's history, yet direct geochemical evidence for mantle reprocessing remains elusive. Here we present evidence of recycled supra-subduction zone mantle wedge peridotite dredged from Mid- Atlantic Ridge near 16˚30′N. Peridotite trace-element characteristics are inconsistent with fractional anhydrous melting typically associated with a mid-ocean ridge setting. Instead, the samples are best explained by hydrous flux melting which changed the melting reactions such that clinopyroxene was not exhausted at high degrees of melting and was retained in the residuum. Based on along-axis ridge depth variations, this buoyant refractory arc mantle is likely compensated at depth by denser, likely garnet-rich, lithologies within the mantle column. Our results suggest that highly refractory arc mantle relicts are entrained in the upper mantle and may constitute >60% of the upper mantle by volume. These highly refractory mantle domains, which contribute little to mantle melting, are under-represented in compilations of mantle composition that rely on inverted basalt compositions alone.

5.2 Introduction

Mantle geochemistry involves the study of stochastic occurrences of peridotite from abyssal settings, xenoliths, and ophiolites. The random nature of sample acquisition requires certain assumptions and extrapolations to make meaningful interpretations of the mantle writ large. In classical theory, fertile mantle peridotite undergoes adiabatic melting during ascent beneath a divergent plate boundary; after melting, the restite will be depleted in FeO and incompatible elements, resulting in a refractory residue that is more buoyant than the primitive mantle from which it was derived (Niu and O'Hara 2008). While early studies relied on basalt compositions to infer source characteristics, and often assumed a homogeneous mantle, subsequent studies of mantle peridotites have shown unequivocally that the mantle is heterogeneous on length scales from meters to thousands of kilometers with respect to isotopes, major elements, and trace elements (e.g. Figs. 5.1 and 5.2) (Dosso, Bougault et al. 1999, Hauri 2002, Warren, Shimizu et al. 2009, Zhou and Dick 2013, Byerly and Lassiter 2014, Mallick, Dick et al. 2014, Dick and Zhou 2015, D'Errico, Warren et al. 2016). These heterogeneities reflect a time-integrated aggregate of inherited heterogeneity during Earth's accretion, dynamic advection of material, localized re-fertilization and re-equilibration, and mantle melting at both divergent and convergent plate margins over its history. Re–Os and Pb isotopic dating of abyssal peridotites has provided further insights into ancient (up to 2.0 Ga) melt depletion events (Harvey, Gannoun et al. 2006, Burton, Cenki-Tok et al. 2012), however relating peridotite trace element characteristics to previous melting events remains difficult and non-unique. If mantle advection is indeed robust, relicts of previous melting events are expected to occur in dissimilar tectonic settings: to date, evidence for this concept is scarce. In one instance, Simon et al. (2008) found that nearly two thirds of mantle xenoliths sampled from ocean island basalts represent ultra-refractory harzburgites (past clinopyroxene exhaustion) that resemble forearc peridotites. Gao et al. (2016) used Al-depleted peridotite bulk rock compositions to suggest that residues of hydrous melting could be entrained beneath the Southwest Indian Ridge, supporting the topographic relief observed along the Marion Rise. Nd and Hf isotope systematics in basalts and olivine hosted melt inclusions have provided additional evidence for ancient, ultra-depleted mantle domains beneath the Azores Rise (Hamelin, Bezos et al. 2013, Stracke, Genske et al. 2019.). These results show that our understanding of mantle composition and how it relates to basalt chemistry at slow and ultra-slow spreading mid-ocean ridges needs major modification, particularly where ultramafic samples appear to be uncorrelated to local basalt compositions (Zhou and Dick 2013, Dick and Zhou 2015).

The 14°–17° N region of the Mid-Atlantic Ridge (MAR) has long been an enigma for mantle geochemists. This slow-spreading region (~25 km•Ma^{-1} (DeMets, Gordon et al. 2010)) contains refractory, trace-element depleted peridotites (indicative of high degrees of melting) exposed directly on the seafloor, yet basalts recovered in the area display enrichments in incompatible and light rare earth elements with respect to normal mid-ocean ridge basalt (MORB) as well as high $Na_{8.0}$ values, suggesting low degrees of melting (Bonatti, Peyve et al. 1992, Cannat, Bideau et al. 1992, Dosso, Bougault et al. 1993, Dosso, Bougault et al. 1999, Seyler, Lorand et al.

2007, Casey, Gao et al. 2010, Wilson, Murton et al. 2013, Henrick, Dobrosavljevic et al. 2014, Silantyev, Bortnikov et al. 2016). The decoupling between peridotite and MORB major and trace element chemistry is likely a consequence of differential upwelling velocity between melt and the solid source, however recent workers have attributed to this to inherited mantle heterogeneity whereby more fertile (and radiogenic) domains contribute disproportionately large melt volumes to MORB compared to refractory mantle domains (Morgan 2001, Pertermann and Hirschmann 2003, Byerly and Lassiter 2014, Brunelli, Cipriani et al. 2018). The provenance of these highly refractory domains remains an open question, since melting at a mid-ocean ridge is generally limited by the thickness of the lithospheric lid and the clinopyroxene-out peritectic point (Dick and Fisher 1984), consequently restricting melting at slower spreading ridges (Reid and Jackson 1981, Bown and White 1994, Niu and Hekinian 1997, Dick, Lin et al. 2003). Here we use clinopyroxene (Cpx) from 16ºN abyssal peridotites to show that hydrous melting is required to explain their highly depleted heavy rare earth element (HREE) and Ti concentrations, suggesting that parcels of entrained mantle are in fact recycled from subduction zones to mid-ocean ridges and are likely a ubiquitous mantle component.

5.3 Results

Regional Synopsis and sample description

R/V Knorr Cruise 210 Leg 5 dredged residual mantle harzburgite, basalt, and gabbros along a 50–km long segment of the Mid-Atlantic Ridge between 16˚15'N and 16˚50'N that encompasses a southern fully magmatic, a central nearly amagmatic, and a northern weakly magmatic series of core complexes. Detailed bathymetry, descriptions, and dredge data can be found in Smith et al.(2014). Twenty harzburgite samples were selected for major element analysis of spinel, pyroxenes, and olivine. Samples have olivine Mg# (100 x Mg/[Mg+Fe^{2+}]) of 91 to 92.1 and chromian spinel Cr# (100 x Cr/[Cr+Al]) of 37 to 64 (Figs. 5.2 and 5.3, Table 5.S1). Point counting shows very low but discernable primary Cpx abundances, whereas some samples appear be devoid of Cpx irrespective of secondary alteration. Two particularly fresh (>95%), Cpx-bearing harzburgites were chosen for trace element analysis. Both samples (D41–24, D41–82) display protogranular textures with interstitial Cpx in textural equilibrium with olivine, orthopyroxene (Opx), and chromian spinel (Figure 5.S1). Cpx appears to be primary in origin based on textural observations, and not formed as an exsolution feature. Pyroxene grain sizes range from 500 to 3000 μm and were analyzed for trace elements using laser ablation inductively coupled plasma mass spectrometry (see Methods). Trace element concentrations are shown in Table 5.S2. Additional, previously unpublished Cpx REE data from the Fifteen-Twenty Fracture Zone is provided in the supplementary materials (Table 5.S2). Samples are ultra-depleted in HREE, middle rare earth elements, and high field strength elements (HFSE), whereas light rare earth elements (LREE) define a shallower slope than one would expect from fractional melting models based on lanthanide compatibility (Figure 5.S2). LREE decoupling from HREE and HFSE may be a result of partial

re-equilibration with migrating melt in the mantle column as it ascended (Navon and Stolper 1987), a product of disequilibrium melting (e.g. Liang and Liu (2016), Figure 5.S3), or have been generated by addition of an LREE-enriched subduction-derived fluid. Our study therefore focuses on HREE and Ti, which are fluid immobile and less susceptible to diffusive re-equilibration with passing melts during emplacement.

5.4 Discussion

5.4.1 Provenance of 16°N Peridotites

Cpx analyses presented here are more HREE and Ti depleted than any previously reported abyssal peridotites. These samples bear a striking geochemical resemblance to supra-subduction zone (SSZ) peridotites from convergent margins formed under hydrous conditions with respect to Cpx trace element concentrations (Supplementary Figures 4 and 5) and olivine and spinel major element compositions (Bizimis, Salters et al. 2000, Ishimaru, Arai et al. 2007, Jean, Shervais et al. 2010, Le Roux, Dick et al. 2014). In particular, 16°N peridotites display extreme Cr# spinel compositions greater than ~55 (Fig. 5.3), values that are normally restricted to supra-subduction zone settings (e.g., the Josephine Peridotite, Oregon, USA) (Dick and Bullen 1984). 16°N harzburgites also show similar Opx Al_2O_3 and spinel Cr# to highly refractory peridotite xenoliths sampled from ocean island basalts and described by Simon et al. (2008), as well as other SSZ peridotites (Jean, Shervais et al. 2010, Le Roux, Dick et al. 2014) (Figure 5.S6). To better understand the genesis of our samples, we modeled non-modal fractional melting of a depleted MORB mantle in the garnet and spinel stability field under anhydrous conditions typical of a mid-ocean ridge setting after Hellebrand et al. (2002) (and references therein, see Methods) and compared our results with published abyssal peridotite data (Fig. 5.4) (Warren 2016). Published data show a relatively narrow range of Cpx trace element concentrations in Yb–Ti space. Anhydrous melting alone is not sufficient to achieve the concentrations observed in our 16°N samples, as Cpx is exhausted before such depleted compositions are reached (Fig. 5.4, white circles and hexagons). Even if the peridotite were to undergo two distinct anhydrous events (e.g. 20% melting followed by a second anhydrous event), such concentrations would still not be attained before Cpx was exhausted from the residue by additional melting during the second event. Interestingly, EPR harzburgites from Hess Deep reported by Dick and Natland (1996) also appear to reside in the SSZ field, with Cr-spinel values (Cr#) of more than 50 and highly depleted Cpx trace element abundances, warranting further investigation.

Fractional melting under hydrous conditions is known to decrease the proportion of Cpx entering the melt with respect to Opx (Gaetani and Grove 1998, Bizimis, Salters et al. 2000). Hydrous melting therefore provides an efficient means of retaining Cpx in the residuum to higher extents of melting than anhydrous conditions allow, permitting higher degrees of depletion with respect to incompatible elements (e.g. HFSE). We model such a process in Fig. 5.4 (blue squares), where 16°N Ti and Yb systematics are reproduced by ~8% hydrous melting in the garnet stability field, followed by an additional high degree (>20%) of hydrous melting in the spinel field. 16°N

harzburgites may have melted further upon emplacement underneath the MAR, although mineral modal abundances suggest this would have been limited to retain any primary Cpx. Overall, their low HREE and HFSE incompatible element abundances, mineral modes and compositions make them the most refractory abyssal peridotites yet studied from a mid-ocean ridge setting. We also calculated melts in equilibrium with 16°N Opx based on published partition coefficients; the trace element characteristics, in particular their fluid-mobile element enriched and Ti depleted nature, are most consistent with a boninitic melt, similar to those found presently in the Bonin Archipelago (Figure 5.S5) (Umino, Kitamura et al. 2015). Boninites have characteristically low HFSE abundances coupled with fluid-mobile element and LREE enrichments; a boninite-like melt can reconcile both fluid-mobile element and LREE enrichments while maintaining Ti depletions as seen in 16°N Cpx and Opx (Figure 5.S5). It is notable then that our sample set includes several orthopyroxenite veins, always dredged along with dunite, but rare in other abyssal peridotite suites, yet consistent with an origin as late boninitic melts produced during the latter end of sub-arc melting as described in other SSZ mantle provinces (Shervais 1978, Choi, Shervais et al. 2008, Jean, Shervais et al. 2010).

Given the long history of subduction, accretion, and continental breakup, ultra-refractory harzburgitic parcels formed in arc-mantle wedge settings are likely entrained throughout the mantle; more detailed sampling could identify similar localities throughout the mid-ocean ridge system. To that end, we interpret the 14°–17°N MAR region as a parcel of buoyant arc mantle captured in the upwelling mantle column, similar to, but more refractory than peridotites described by Seyler et al. (2004) along the Southwest Indian Ridge. This refractory mantle province is likely a relict of a Proterozoic melting event as inferred by Re-Os isotope systematics at the 15°20'N region (Harvey, Gannoun et al. 2006); our results expand on this, and suggest a subduction zone setting. LREE-enriched basalts with relatively high $Na_{8.0}$ dredged in the region are therefore primarily sourced from more fertile components (e.g. lherzolite or pyroxenite veins), and are not representative of melting the modal or chemical composition of the shallow sub-ridge mantle (Henrick, Dobrosavljevic et al. 2014). Regional basalt compositions require a more fertile, possibly denser source mantle deeper in the melting column; a necessity required to explain the great depth of the ridge (Fig. 5.5). The incongruence between peridotite compositions (residues) and mantle melts (MORB) suggest that variable source contributions must be carefully considered when evaluating regional MORB geochemistry.

5.4.2 A Heterogeneous Atlantic Mantle

Although mantle peridotite at 14–16°N is highly refractory (and therefore buoyant), the region is not associated with a rifted bathymetric rise similar to Marion or the Azores (i.e. Zhou and Dick(2013)). Rifted rises such as Marion are a function of both compositional heterogeneity and to a lesser extent thermal variations; thermal variations are thought to be modest (<50°C) throughout the upper mantle (Mckenzie and Bickle 1988, Presnall, Gudfinnsson et al. 2002, Niu and O'Hara 2008, Zhou and Dick 2013). The density contrast due to chemical heterogeneity

between refractory (harzburgitic) and fertile (lherzolitic) mantle components is negligible in the spinel facies (< 70 km), however below ~70 km this density contrast increases markedly up to 1.2% within the garnet facies since bulk rock densities are sensitive to garnet modal proportions and hence, bulk Al_2O_3 content (Niu and O'Hara 2008). Our preferred interpretation is that the entire region, spanning ~3° of latitude (330 km), contains entrained parcels of buoyant arc mantle that is isostatically compensated at depth by more fertile, dense components (e.g. subducted ocean crust or fertile MORB mantle). At a given pressure and temperature, eclogite (subducted oceanic crust) will have a higher density and seismic shear wave velocity than peridotite (Anderson 2007), providing a means of assessing the feasibility of such a model. In fact, our hypothesis is consistent with tomographic observations, which show positive shear wave velocity (V_s) anomalies at 300 km depth beneath the ridge axis in the 14–17°N region and centered below the Vema Fracture Zone at 11°N (Fig. 5.5) (Ritsema and Allen 2003, Schaeffer and Lebedev 2013). The positive relationship observed between ridge depth and V_s observed along the Mid-Atlantic Ridge at 300 km depth (Fig. 5.5) may be explained by either thermal anomalies or compositional heterogeneities (e.g. Dalton et al. (2014)). However, the coefficient of thermal expansion for peridotite is modest; for a constant composition, a mantle potential temperature difference of 50°C (1320°C versus 1370°C) yields less than 500 m of relief in a 300 km column based on the parameterization of Abers and Hacker (2016). Thus, the anomalous ridge depths (~1 km) are likely the result of lithologic heterogeneities, manifested by significant density and compositional differences; the presence of buoyant arc mantle material in the 16°N region exemplifies the chemical diversity of the sub-ridge mantle. Here, density compensation at depth has effectively muted the ridge bathymetric high that would otherwise exist, as seen further north along the Azores rise, which is compensated by low-density refractory harzburgite (Fig. 5.5) (Dick and Zhou 2015).

Fertile material at depth, which is required to explain the elevated MORB $Na_{8.0}$ and LREE enrichments, provided the major contribution to melt genesis at 16°N due to lower solidus temperatures, while an overlying ultra-refractory component supplied a lesser amount. Isotopically, basalts in the region display extremely radiogenic εNd (8.6 to 11.3) and εHf (15.9 to 19.5) values, likely reflecting a small contribution from highly depleted mantle (Salters, Mallick et al. 2011, Henrick, Dobrosavljevic et al. 2014). Previous MORB studies have inferred a highly depleted source to reconcile decoupling of Nd and Hf isotopic systematics and extreme Hf values, e.g. the Residual Lithosphere (ReLish) component of Salters et al. (2011) or subduction-modified mantle of Janney et al.(2005). Our samples provide a likely candidate for such a ubiquitous mantle component, corroborating these studies. While isotopic analyses are beyond the scope of this work, we speculate that 16°N Cpx should possess highly radiogenic Hf isotopic compositions based on elevated Lu/Hf ratios (>1) of 16°N Cpx with respect to DMM (~0.37, (Workman and Hart 2005)) coupled with ancient Re-Os ages of nearby peridotites (Harvey, Gannoun et al. 2006).

5.5 Implications

Mantle heterogeneity likely plays an important role in the styles of oceanic crustal accretion, dictating the amount of melt available to generate new basaltic crust if ultra-refractory parcels are present in variable proportions in the melting column. However, the amount of ultra-refractory mantle residing in the mantle remains unknown. Based on estimates of the volume of mantle entering the sub-arc melting region per year (77 km^3 yr^{-1}, Jagoutz and Schmidt (2013)), and assuming this flux has been approximately constant over time, we estimate that ~67% of the mantle above the 660 km mantle discontinuity could have been processed through subduction zone environments, and thus could be considered ultra-refractory, over a period of ~2.5 Ga (Table 5.1). This is consistent with stochastic sampling of ocean island basalt-hosted xenoliths presented by Simon et al. (2008) where two thirds of samples were considered highly refractory (Figure 5.S6). We caution that our estimates represent upper bounds, as the influx of mantle entering the sub-arc region is not entirely melted under hydrous conditions. Cumulate rocks derived from both hydrous and nominally dry differentiation trends are commonly found in arc terranes, indicating both hydrous flux melting and adiabatic decompression melting (e.g., Jagoutz and Schmidt (2011)), the former of which would be responsible for generation of SSZ peridotite. However, our calculations square well with those of Salters et al. (2011) who estimated up to 50% ReLish in the MORB source to reconcile basalt Hf isotopic compositions. While recycled SSZ peridotite collected from mid-ocean ridges are limited to a handful of locations at present (14–17°N MAR and SWIR 53°E), we note that vast swaths of mid-ocean ridge system, including almost the entire southern Atlantic, have yet to be dredged off axis or studied in detail (see Warren (2016) Fig. 1 for map of current sample locations).

On a more local scale, a large proportion of refractory components will induce less adiabatic melting and generate lesser volumes of melt, leading to limited magmatically-accommodated spreading and inducing tectonic extension in the form of peridotite emplacement directly on the seafloor (e.g. significant portions of the Southwest Indian, Gakkel and Mid-Atlantic Ridges (Cannat, Lagabrielle et al. 1997, Dick, Lin et al. 2003, Sauter, Cannat et al. 2013)). This is the case at the 14–17°N region and represents an end-member mantle source composition dominated by ultra-refractory peridotite upwelling at the ridge axis.

The abundance of this refractory material will have implications for rheological and geophysical properties, as this material may have higher viscosities than more fertile mantle due to low water abundances, as well as higher shear wave velocities due to higher olivine forsterite contents (Hirth and Kohlstedt 1995, Lee 2003). Further study of mantle heterogeneity will require detailed sampling of mid-ocean ridges, while systematic peridotite geochemical characterization could lead to new insights as to the distribution of variably depleted source lithologies in the mantle. Buoyant, highly refractory melt residues are likely ubiquitous in the upper mantle, congruent with the hypotheses of previous workers (Anderson 2007); the former could comprise as much as 67% of the upper mantle, providing compelling evidence for ultra-depleted mantle (ReLish, subduction-modified mantle) throughout the MORB source. Mantle heterogeneity exerts a fundamental influence on melt generation, MORB composition, and plate tectonics, and

must be considered insofar as mantle geochemistry and dynamics are concerned. 16°N peridotites add to a growing body of evidence, which suggests that the upper mantle as a whole is more depleted than previously thought.

5.6 Acknowledgments:
We thank the science party for their dutiful collection and description of dredge samples, and in particular chief scientist Dr. Deborah K. Smith. Analysis work for this research was supported by an internal grant from the MIT EAPS Student Research Fund to BMU. Urann was supported by the Stanley W. Watson Student Fellowship Fund based at WHOI. Dick and Urann were supported by NSF OCE-1637130 and OCE-1155650. Dr. Yongjun Gao is thanked for conducting LA-ICP-MS trace elements analyses.

5.7 Tables

Table 5.1. Title: Mantle processing calculations
Mantle processing calculations based on mantle sub-arc melting region influx of 77 km^3 per year of Jagoutz and Schmidt (Jagoutz, Muntener et al. 2011) and a volume of mantle between 30 and 660 km depth.

Earth Radius (km)	Mantle subduction zone influx ($km^3 \bullet yr^{-1}$)	Earth volume below 30 km (km^3)	Mantle volume below 660 km (km^3)	Mantle volume 660 to 30 km depth (km^3)	Mantle processed since 2.5Ga (km^3)	Percent mantle processed since 2.5 Ga
6378	77	1.07E+12	7.83E+11	2.88E+11	1.93E+11	67%

5.8 Figures

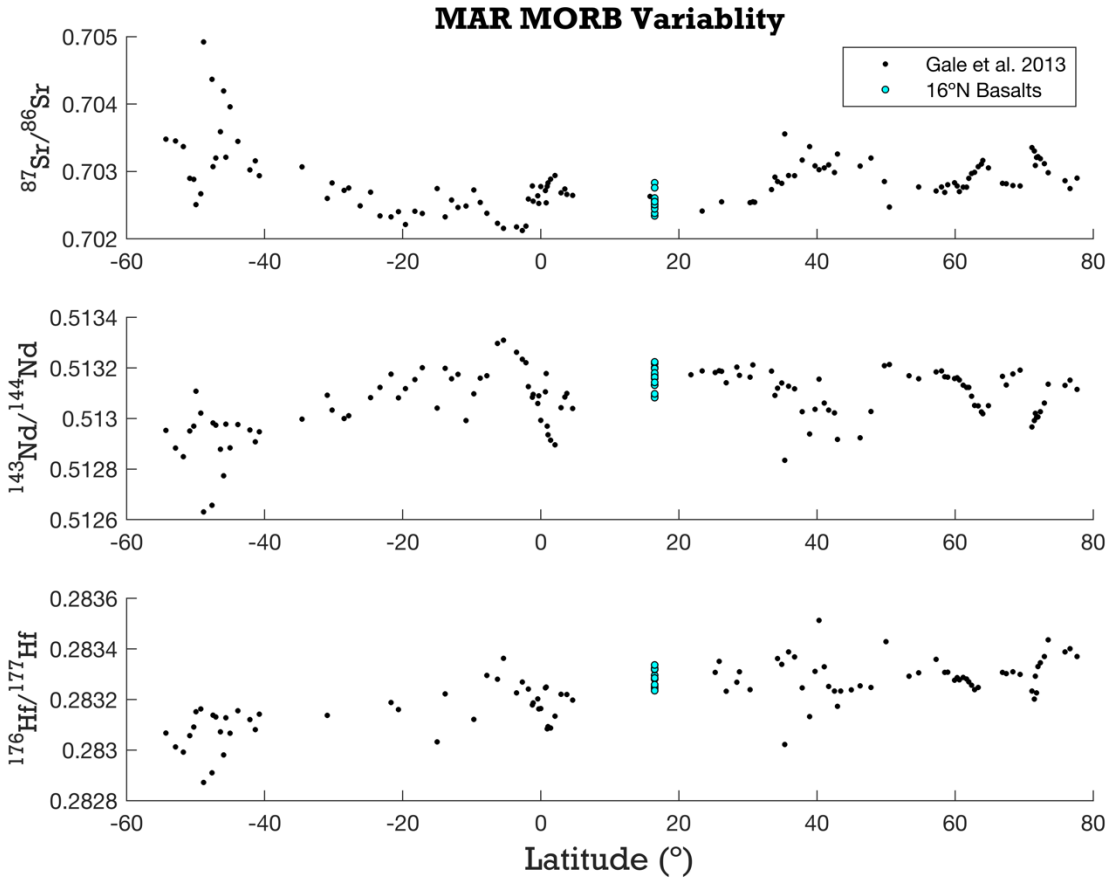

Figure 5.1. Title: Mid-ocean ridge basalt isotopic variability along the Mid-Atlantic Ridge MORB segment averages of $^{87}Sr/^{86}Sr$ (A.), $^{143}Nd/^{144}Nd$ (B.) and $^{176}Hf/^{177}Hf$ (C.) from Gale et al.(Gale, Dalton et al. 2013) exemplify the time-integrated source heterogeneity observed in Mid-Atlantic Ridge basalts. 16°N region, labeled, shows the heterogeneous nature of source material on scales of tens of kilometers, typical for Atlantic MORB. 16°N samples are given as a range with data from Henrick(Henrick 2016).

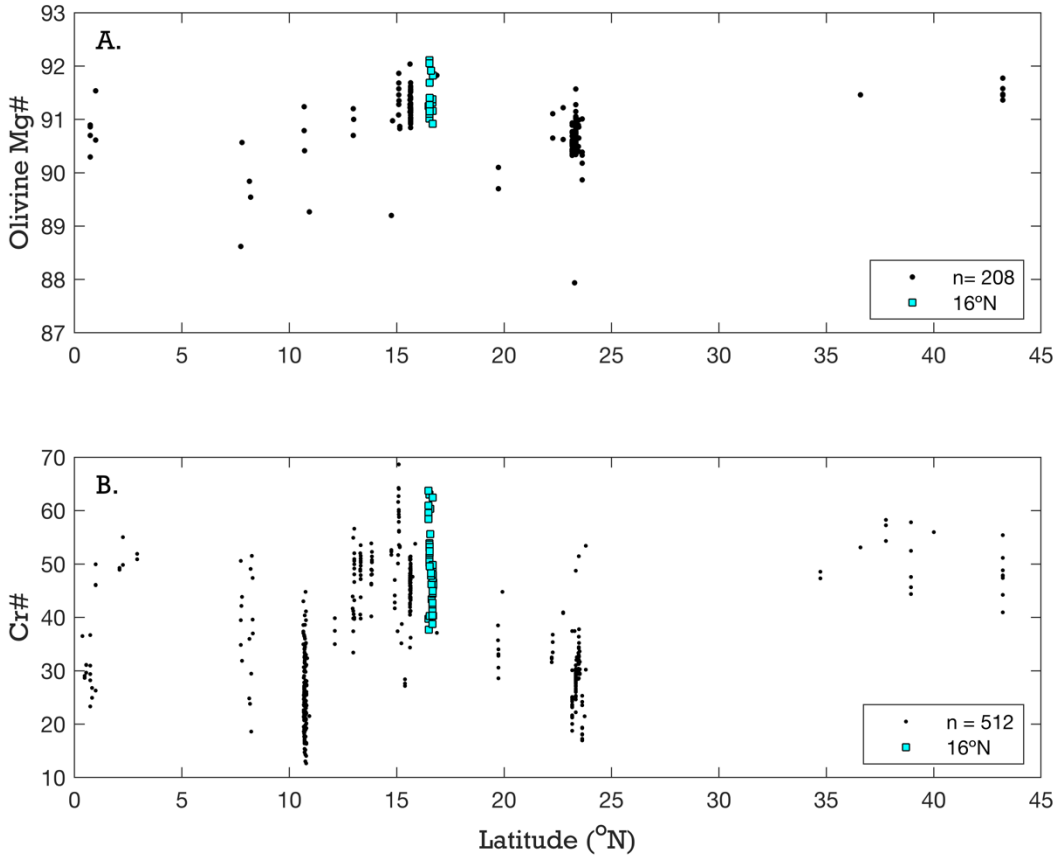

Figure 5.2. Title: Mid-Atlantic Ridge latitudinal variations in peridotite composition **A**. Olivine Mg# (molar Mg/(Mg+Fe^{2+})) along the Mid-Atlantic Ridge shows the anomalously refractory compositions present at the 14-17°N region. Additional data from 15°20'N FZ in Supplementary Data 4, previously unpublished. **B**. Peridotite spinel Cr# (molar Cr/(Cr+Al)) extend to very high values (>55) between 14° and 17°N, atypical of anhydrous melting at mid-ocean ridge settings. Black data points for both plots from the literature(Silantyev, Bortnikov et al. 2015, Silantyev, Bortnikov et al. 2016, Warren 2016). Analytical uncertainties smaller than symbols.

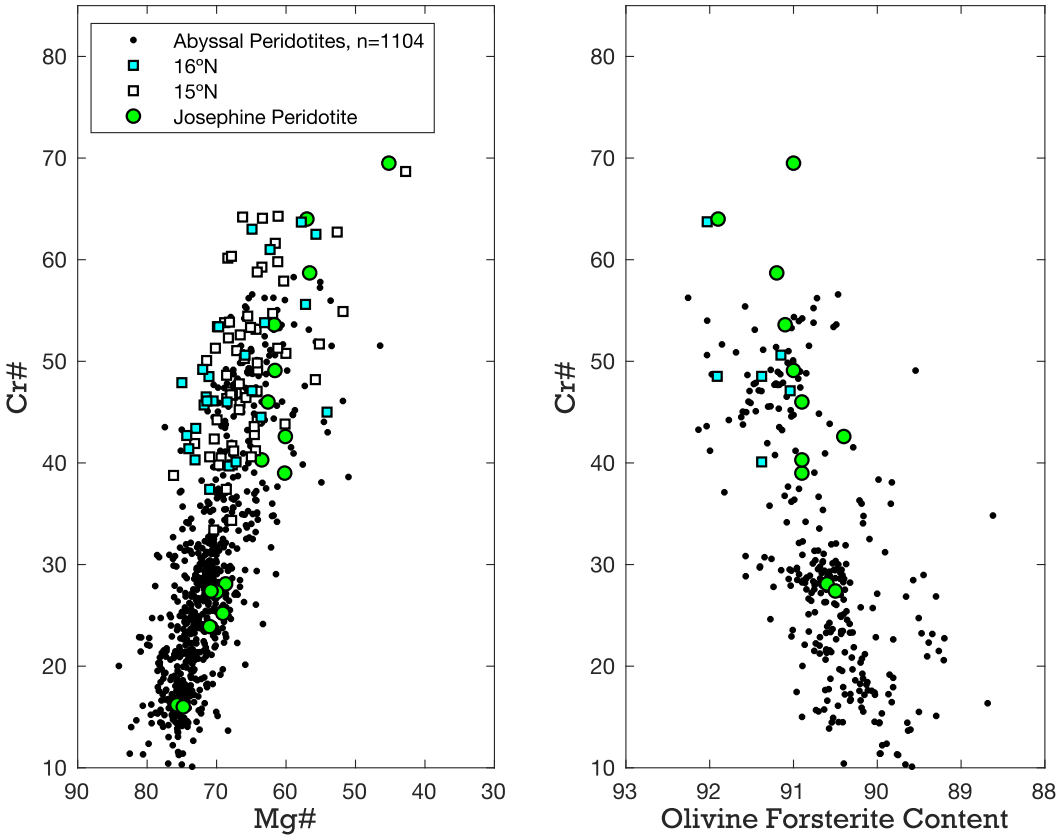

Figure 5.3. Title: Chromian spinel and olivine compositions of 14–16°N peridotites compared to abyssal peridotites

A. Cr# after Dick and Bullen(Dick and Bullen 1984). **B**. Spinel Cr# plotted against coexisting olivine forsterite content. Josephine peridotite, a well-known SSZ locality, plotted for comparison with data from Le Roux et al.(Le Roux, Dick et al. 2014). Abyssal peridotite data from the compilation of Warren (Warren 2016). Not all spinel–olivine pairs were analyzed due to alteration. Analytical uncertainties smaller than symbols.

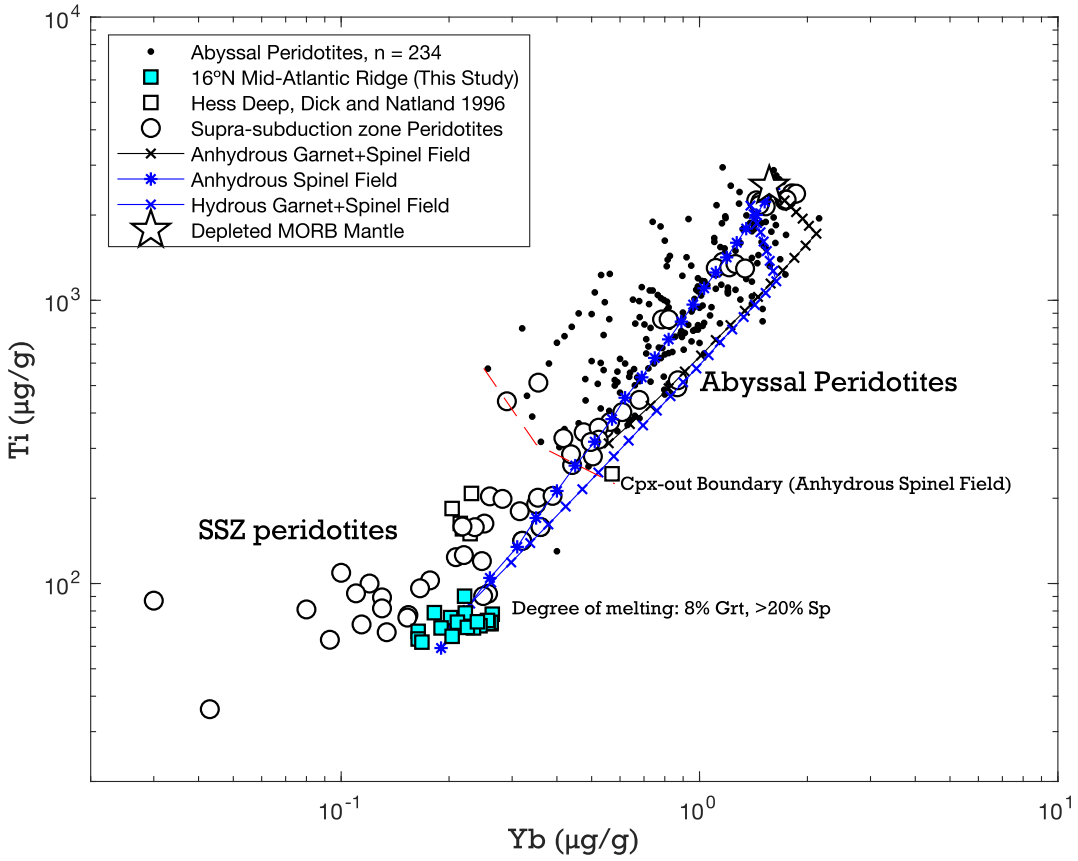

Figure 5.4. Title: Fractional melting model of incompatible elements titanium and ytterbium in clinopyroxene

Anhydrous melting alone cannot replicate the ultra-refractory Cpx compositions before Cpx is exhausted, whether one considers spinel field or garnet followed by spinel field (black ticked line) melting. However, changes in melting modes and partition coefficients in a hydrous melting environment permit extreme depletions in Ti, matching observations (blue lines). Cyan squares represent each individual measurement from 16°N Cpx (Supplementary Data 2). Red dashed line is approximate spinel-field Cpx-out boundary based on modeled anhydrous melting of DMM spinel bearing peridotite. Model details, including melting modes and partition coefficients, can be found in the Methods section and Supplementary Data 5. SSZ peridotites are thought to have undergone extreme degrees of melting in a mantle wedge setting, often resulting in the exhaustion of Cpx; SSZ Cpx Ti and Yb abundances are very similar to those observed in 16°N Cpx. Abyssal peridotite data from the literature as compiled by Warren(2016). SSZ peridotite data from the literature (Bizimis, Salters et al. 2000, Ishimaru, Arai et al. 2007, Jean, Shervais et al. 2010, Le Roux, Dick et al. 2014).

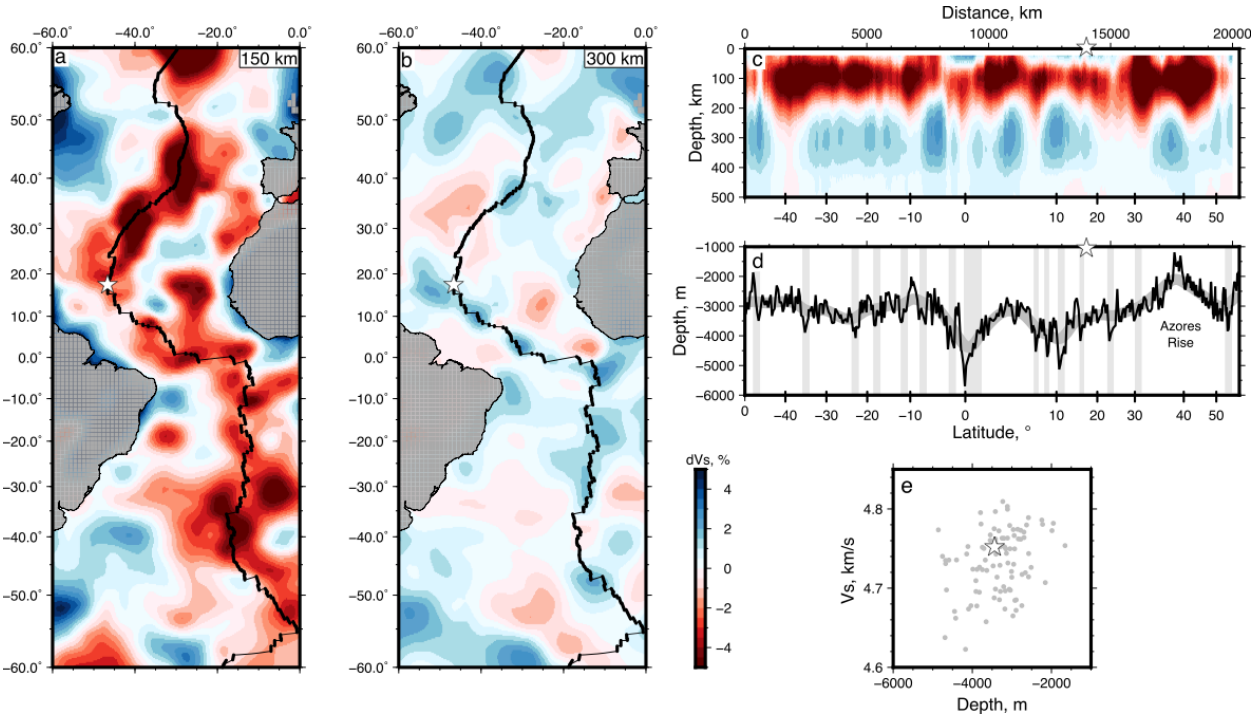

Figure 5.5. Title. Shear wave velocity structure beneath the Mid-Atlantic Ridge
a. and **b.**, horizontal slices through SL2013sv shear velocity tomographic model where percentage anomaly (dV_s) is with respect to AK135 model at 150 km and 300 km, respectively (Schaeffer and Lebedev 2013); thick/thin black lines are spreading segments/fracture zones, respectively(Gale, Dalton et al. 2013). Stars denote 16°N segment. **c**. Vertical slice along MAR shown in panels (a) and (b); gray bands are major fracture zones, star is 16°N segment. **d**. Black/gray line is ridge depth smoothed with 2000 km Gaussian filter. **e**. Ridge depth smoothed with a 280 km Gaussian filter, compared with V_s (gray dots) along the MAR between 50°S and 55°N; star is 16°N segment

Chapter 6

The Death of an Oceanic Core Complex: Evidence from Zircon U–Pb ages at 16°N, Mid-Atlantic Ridge

This chapter is being prepared for publication as:

Urann, B.M., John, B.E, Cheadle, M.J., and Dick, H.J.B. The Death of an Oceanic Core Complex: Evidence from Zircon U–Pb ages at 16°N, Mid-Atlantic Ridge

6.1 Abstract

Here we apply U-Pb dating to zircon-bearing gabbros from the footwall to an oceanic core complex footwall at 16º30'N, Mid-Atlantic Ridge to understand the spatial and temporal development and subsequent termination of detachment faulting. SIMS U–Pb zircon dating of widely distributed samples yields ^{230}Th-corrected zircon ^{206}Pb/^{238}U dates within error of one another. The two westernmost samples are separated by 14 km along strike (collected from the footwall of a high-angle normal fault), have dates of 1.112 ± 0.083 (2σ) Ma and 1.181 ± 0.074 Ma, lie 17–18km west of the present day axial volcanic ridge, and yield a time-integrated detachment fault slip and westward half spreading rate of 20 ± 0.5 km· Ma^{-1}, indicating significant asymmetric westward spreading. In contrast, two samples collected 6 km east nearer the ridge axis yield dates of 1.14±0.055 Ma and 1.221 ± 0.027 Ma, respectively, indistinguishable from samples to the west. Given the inferred spreading rate of 20.5 km·Ma^{-1}, these samples should be ~350 ka younger than those to the west and should deliver dates of ~0.8 Ma. To reconcile the observed age discrepancy, we posit that prolonged asymmetric detachment displacement led to migration of the detachment across the axial rift valley. Continued melt delivery to the ridge axis and coeval rifting then truncated the OCC, dropping the hanging wall into the axial rift valley. Concurrently, expeditious mass wasting carried gabbros from a nascent fault scarp into the rift valley, resulting in contemporaneous zircon U-Pb ages. Such mass wasting events obfuscate seafloor magnetic polarity boundaries, highlighting the need to consider secondary processes when evaluating seafloor (or sea surface) geophysical data. A global review indicates that the majority of oceanic core complexes are terminated by rifting induced truncation as asymmetric fault slip leads to the detachment fault system migrating over the ridge axis.

6.2 Introduction

Oceanic detachment faults are common at slow and ultra-slow spreading ridges (20-55 $km \cdot Ma^{-1}$) where magma supply can be insufficient to entirely accommodate plate separation (Cannat, Mevel et al. 1995, Tucholke, Lin et al. 1998, Buck, Lavier et al. 2005, Smith, Escartín et al. 2008, Escartín and Canales 2011). Lower crustal gabbro and upper mantle peridotite are typically exposed in the footwall of these low-angle faults. Oceanic core complexes (OCCs), the manifestation of prolonged slip and rollover of oceanic detachment faults, are common in slow and ultra-slow spreading regions and often display a characteristic inverted spoon shape (e.g. Mt. Dent, Mid-Cayman Rise, 13°20'N MAR) and corrugated fault surface. The life cycle of these structures has been described previously by MacLeod et al. (2009) and begins with initiation of a typical Andersonian normal fault in a low magma environment; with increasing fault slip, dip angles decrease to <30°. Continued fault displacement leads to asymmetric spreading (John and Cheadle 2010), which results in migration of the fault across the axial valley. Eventually, changes in magma supply or fault kinematics leave the detachment fault abandoned, as magma emplacement on the ridge axis overwhelms detachment displacement. High angle normal faults eventually cross cut the OCC during rifting, dropping the corrugated surface footwall into the rift valley and leaving a characteristic truncated nose morphology, e.g., 5°S MAR (Reston, Weinrebe et al. 2002) and Mt. Hudson along the Cayman Rise (Cheadle, John et al. 2012).

Large swaths of the MAR expose primarily peridotite and gabbro at the seafloor (Cannat, Bideau et al. 1992, Cannat, Mevel et al. 1995, Tucholke, Lin et al. 1998, Dick, Lin et al. 2003, Escartín, Mével et al. 2003, Kelemen, Kikawa et al. 2007, John, Cheadle et al. 2009). Such heterogeneous ocean crust, often with low intensity magnetization, presents numerous challenges to the interpretation of crustal magnetization data. Poorly constrained, low intensity magnetic signals are often attributed to alteration of peridotite during seawater interaction to form hydrous, low-density serpentine minerals and secondary magnetite (Dyment, Arkani-Hamed et al. 1997, Schroeder, John et al. 2002). The formation of secondary magnetite can weaken or enhance magnetization signals, complicating crustal magnetization interpretations (Schroeder, John et al. 2002, Bach, Garrido et al. 2004). Additionally, faulting may significantly alter the sequence of the lithologies. For example, Escartin et al. (2017) observed prolific mass wasting during early normal faulting (dips of ~60°) at 13°20'N MAR near the ridge axis, but found that mass wasting lessens as fault heave increases and fault dip decreases. Such complex ocean floor geology inevitably complicates the recognition of magnetic chrons and hence plate spreading rates (e.g., Atlantis Massif (30°N MAR) and Kane Megamullion (Williams 2007)).

Previous workers have used zircon sampled from evolved oceanic gabbros and felsic derivitives, to study crustal growth and plate spreading rates in various localities including the Southwest Indian Ridge, East Pacific Rise, and Mid-Atlantic Ridge (John, Foster et al. 2004, Schwartz, John et al. 2005, Baines, Cheadle et al. 2008, Baines, Cheadle et al. 2009, Grimes, John et al. 2009, John, Cheadle et al. 2009, Lissenberg, Rioux et al. 2009, Grimes, Cheadle et al. 2011,

Rioux, Cheadle et al. 2016). Zircon is an accessory phase formed during extensive fractional crystallization of MORB like melts, typically observed in plagiogranites, Fe-Ti oxide gabbros, and rarely in more primitive gabbronorites and olivine gabbros (Grimes, John et al. 2009). U–Pb zircon dating studies combined with trace element chemistry in zircon can provide critical information about crustal genesis and the timescales of lower crustal accretion. Further, U–Pb age derived spreading rates can be benchmarked against expected spreading rates from geomagnetic polarity boundary picks, to test the fidelity of each method and evaluate spreading rate asymmetry. For example, Baines et al. (2008) compared zircon U–Pb dates to magnetics ages at Atlantis Bank (Southwest Indian Ridge), finding remarkable congruence between the two methods.

Here we present zircon U–Pb zircon ages from a gabbroic core complex at 16°30'N (MAR) to elucidate the formation and termination of the OCC through time. Contemporaneous zircon ages provide evidence for magmatically-induced rifting, which truncated the core complex and generated 6 km of offset between the main detachment surface and its conjugate nose. Evidence for this process comes from high-resolution bathymetry, similarity of zircon U–Pb ages, trace element mineral chemistry kilometers apart along a flow-line and perturbed seafloor magnetic anomalies. We compare our findings with a global compilation of mapped OCCs, which suggest an addition to the conceptual life cycle of an OCC proposed by MacLeod et al. (2009). Surprisingly, the majority of OCCs are shown to have experienced a similar fate to 16°30'N, truncated by ongoing rifting and subsequent mass wasting. Thus, truncation of OCCs appears to be the rule, rather than the exception, at slow and ultra-slow spreading ridges.

6.3 Geological setting

The slow-spreading 16°30'N area contains two second order ridge segments (Fig. 6.1). In the northern ridge segment, an axial deep to 4500 meters depth is offset relative to the southern robustly magmatic axial volcanic zone by a ~7 km dextral non-transform discontinuity. Dredging east of the Northern Core Complex (NCC) has yielded abundant gabbro and peridotite (Figs. 6.1 and 6.2). For a regional synopsis and geophysical survey, we direct readers to Smith et al. (2014) and Parnell-Turner et al. (2016), respectively. The corrugated surface of the NCC appears to have been cut by a high angle normal fault. This fault drops down approximately 1 km toward the axial valley flow below and the surface bathymetry becomes rough. This fault scarp terminates into a ~1 km wide pair of talus piles in both the north and south. Farther east, a small massif consisting of peridotite, gabbro, diabase and basalt has previously ascribed to the mass-wasted remnants of an incipient detachment fault (Smith, Schouten et al. 2014). However, an unresolved paradox of this model is the absence of a detachment surface "nose" of the original NCC, which would appear to be missing. This structural configuration bears a remarkable similarity to previously mapped OCCs, e.g., Mt. Hudson (Mid-Cayman Rise). In the case of Mt. Hudson, asymmetric spreading caused migration of the OCC toward the axial volcanic ridge (AVR) and ultimately led to rifting and OCC termination (Cheadle, John et al. 2012).

6.4 Methods

6.4.1 Samples

Gabbroic rocks from the 16˚30'N region (MAR), were sampled by dredge during the R/V Knorr Cruise KNR210-05 in 2013 (Smith, Schouten et al. 2014); sample locations are found in Figs. 6.1. and 6.2. Fifteen samples were chosen for analysis to reflect a broad spatial distribution both along and across axis; a total of four yielded zircon. Western dredges D60-27 and D49-13 appear to sample the fault scarp of the NCC, whereas D67-01 and D53-12 were collected nearer the present-day ridge axis, approximately 6 km east of the western dredges. Relatively evolved, oxide gabbros were chosen because of the high probability of them containing zircon, based on previous studies elsewhere (e.g., Atlantis Massif, Grimes et al. (2008)). However, samples of oxide gabbro from this study area yielded no zircon, whereas less fractionated gabbro and troctolite did (Table 1). Samples D49-13, D53-12, and D67-01 are equigranular gabbros; D60-27 is a mylonitic troctolite. Sample photographs are available in the Supplementary Materials (Fig. 6.S1).

6.4.2 Sample Preparation

One-kilogram samples were crushed using standard techniques (hammer and shatter box) and sieved at 250 μm mesh. Care was taken to ensure that no cross-contamination between samples occurred. All crushing equipment was blown with compressed air and washed with deionized water and ethanol between samples. Each crushed sample was washed of rock flour in a water bath, separated using a Frantz magnetic separator at 0.5A, and density separated using methylene iodide (>3.3 $g \cdot cm^{-3}$). Heavy mineral fractions were sorted and handpicked under binocular microscope yielding seven to ten zircon grains per sample. Selected grains were mounted in epoxy, polished, and imaged by cathode luminescence (CL). Prior to SIMS analysis, samples were washed using the technique of Grimes et al. (2009). Figure S6.2 shows CL images highlighting the morphology and internal structure of zircon grains analyzed in this study.

6.4.3 Analytical methods, Data Reduction

A total of four samples returned sufficient zircon for dating and trace element analysis, with each sample yielding a minimum of seven grains. Data were reduced using SQUID 2.51 following Ludwig (2009). Measurements with high common ^{204}Pb (>30%) were discarded from the data set. ^{230}Th-corrected $^{206}Pb/^{238}U$ data are shown in Table 6.2 and plotted in Figure 6.S4 by sample. All reported $^{206}Pb/^{238}U$ dates are weighted means with 2σ uncertainties as standard error of the mean. Detailed analytical procedures can be found in Supplementary Materials.

6.5 Results

6.5.1 U–Pb zircon geochronology

Corrected for ^{230}Th, $^{206}Pb/^{238}U$ weighted mean ages from the four samples range from 1.11 to 1.22 Ma (Fig. 6.2; Table 6.2). Weighted mean ^{230}Th corrected $^{206}Pb/^{238}U$ ages along the

southern transect (D49-13 and D53-12), separated by 6 km E-W, are 1.18 ± 0.074 Ma (2σ) and 1.22 ± 0.027 Ma, respectively, with a combined age of 1.22 ± 0.027 Ma (MSWD of 1.11, n=16). Samples across the northern transect are 1.11 ± 0.083 Ma (D60-27) and 1.14 ± 0.083 Ma (D67-01), also separated by 6 km parallel to spreading (Fig. 6.2). Combined, the northern pair yields an age of 1.14 ± 0.035 Ma (MSWD of 2.1, n=13) and southern pair yields 1.21 ± 0.036 Ma (MSWD of 1.8, n=19). Thus, southern samples appear slightly older than, though still within calculated 2σ uncertainties of, those to the north.

6.5.2 Trace element chemistry and Ti-in-zircon thermometry

Individual zircon grains were also analyzed for trace element abundances of Y, Gd, Yb, Hf, U, and Th. Trace element data are given in Tables 1 and 3. Trace element variation diagrams (Fig. 6.S3) are shown to better discern geochemical relationships between samples. Northern (D60-27 and D67-01) and Southern (D49-13 and D53-12) pairs show similar geochemical characteristics in U versus Ti, Hf versus Ti, and Th/U versus Hf space. Although both northern and southern pairs are each separated by ~6 km E-W, geochemical similarities suggest that they are in fact genetically related. Calculated solidus temperatures from Ti-in-zircon geothermometry to elucidate the thermal history of individual samples following Ferry and Watson (2007) (Table 3). For the southern pair, D53-12 Ti-in-zircon temperatures range from 753–873°C, (median 845°C) whereas D49-13 temperatures are 801–850°C (median 835°C). For the northern pair, D60-27 and D67-01 temperatures are 892–941°C (902°C median) and 800–1015°C (median 898°C), respectively. Thus, northern and southern pairs yield Ti-in-zircon derived temperatures within uncertainty of one another, emphasizing their cogenetic relationships.

6.6 Discussion

6.6.1 Age Distributions: Actual versus Expected

All samples have ^{230}Th corrected ^{206}Pb/^{238}U dates within error of one another regardless of geographic position relative to the present-day ridge axis: an unexpected result. Westernmost samples D60-27 and D49-13 were collected 17 and 18 km, respectively, from the ridge axis, which given their age of ~1.15 Ma corresponds to a spreading rate of ~15 km•Ma^{-1}. However, gabbroic rocks are emplaced at depth and not at the sea floor; samples therefore must have travelled an additional distance before surface denudation. Assuming an inverted spoon-shaped fault geometry approaching a dip of 60° at depth and an 800°C isotherm at 7 km depth as determined for other MAR OCCs (Grimes, John et al. 2008), we calculate net a displacement rate of 20 ± 0.5 km•Ma^{-1}, suggesting ~80% asymmetric spreading westward during detachment faulting based on plate motion models (DeMets, Gordon et al. 2010). In contrast, samples D53-12 and D67-01 were collected 6 km nearer the ridge axis, and yield ages of 1.22 ± 0.027 Ma and 1.14 ± 0.055 Ma, respectively. These dates are older than one would estimate based on their proximity to the ridge

axis. Given the predicted spreading rate of 20 ± 0.5 $km \cdot Ma^{-1}$, these samples should be ~350 ka younger than those to the west and should yield easily resolved dates of ~0.8 Ma.

6.6.2 Tectonic Model

To account for the contemporaneous U-Pb zircon ages and sample distribution, one must consider the effects not only of detachment behavior, but also rifting, diking/magmatism, and mass wasting. In our preferred model, asymmetric spreading of the detachment fault caused eastward migration of the OCC towards and over the then active ridge axis. Rifting, possibly induced by an ephemeral pulse of magmatism to the south, truncated the NCC and generated ridge-parallel normal faults which cross-cut the NCC, dropping the hanging wall into the axial rift valley. Diking and intrusion during continued rifting further separated the OCC nose from the remaining body, leading to the present configuration (Fig. 6.3). This is required to generate the observed offset in U-Pb ages, and is consistent with dredging results where fresh glassy pillow basalts were collected from dredges 62 and 69 between the gabbro outcrops(Fig. 6.1). Relief generated by rifting promoted mass wasting from the fault scarp, carrying talus into the rift valley, consistent with the age and distribution of our samples. Figure 6.4C shows the three dimensional bathymetry, where one can clearly see a debris field that looks quite similar to the apron morphology at 13°20'N described by Escartin et al. (2017). Thus, the observed topography is a function of rifting dynamics, active magma emplacement, lava eruption and subsequent mass wasting, which will invariably convolute magnetic anomaly picks.

Magnetic evidence supporting this model is found in Parnell-Turner et al. (2016) where the authors analyzed magnetic data from the region; Figure 6.2 shows magnetic anomaly profiles with the author's interpreted magnetic chron labels. Two of our samples D60 and D67, fall along their Profile 2 and directly over their anomaly 2 pick (Fig. 4a, Parnell-Turner et al. (2016)). Anomaly 2 corresponds to an age of ~1.85 Ma, while our samples are approximately 1.15 Ma. These anomaly picks rely on a 580˚C isotherm; the zircon data corresponds to a temperature of ~ 800˚C, therefore the magnetic chron should be slightly younger than the zircon dates (see John et al. (2004), Schoolmeesters et al. (2012)). However, the reported magnetic age is ~700ka older! Samples D53 and D49 roughly correspond to profile 3 in Figure 4A of Parnell-Turner et al. (2016). D53 (1.221 ± 0.027Ma) is located approximately at the anomaly 2 (~1.85Ma) pick which again shows a difference of ~600ka from previous interpretations. Lastly, we direct the reader to their Figure 5c, where Line 3 shows the actual magnetic data compared to the author's model. The magnetic model has major difficulties fitting anomaly 2, west of the ridge axis. We interpret such discrepancies as incorrect chron picks due to the convoluted nature of magnetics in the region, since our zircon data place hard constraints on gabbroic crustal ages. Our model explains the challenging magnetics data presented by Parnell-Turner et al. (2016), as well as the age-distance issues implied from all four zircon-bearing samples that yielded identical ages within error. We postulate that their Anomaly 2 (lines 1-3) is in fact C1n.1n (~1.0Ma), which is reasonable given zircons record a higher closure temperature (~800˚C) than the magnetic Curie temperature of

580°C (Haggerty 1978). This corresponds to a ~200 ka difference, consistent with a cooling rate of >800°C·Ma^{-1} (John, Foster et al. 2004).

6.7 Global Context

A global review of OCCs reveals a morphological continuum at various tectonic stages. Building on the model of MacLeod et al. (2009), we propose additional steps to the life cycle for oceanic core complexes. Upon detachment initiation and asymmetric spreading, the OCC will migrate toward the immediate ridge axis, eventually overlying the locus of volcanism (Fig. 6.5, stages 1 through 3). At this point, the AVR may remain stationary, delivering magma to the OCC footwall, generating incipient faulting and promoting the formation of hydrothermal vents as observed presently at Mt. Dent along the Cayman Rise (stage 4). Over time this configuration will terminate OCC displacement, as rifting and diking split the detachment surface and truncate the nose of the OCC (stage 5, Mt Hudson, Cayman Rise). At this point, the AVR may step outward toward the OCC hanging wall, leading to the scenario found at 16°30'N MAR (Stage 6A). Alternatively, the AVR may remain stationary within the truncated OCC, leading to partitioning of the OCC nose from the main body onto the conjugate plate (stage 6B, 5°S MAR (Reston, Weinrebe et al. 2002)). The two outcomes during stage 6 (stationary versus outwardly-stepped AVR) are likely a function of melt supply and ridge dynamics. OCC termination appears to be promoted by proximity to robust magmatism (16°30'N and 5°S MAR, Mt. Dent). We speculate that continuous lateral melt delivery will result in a stationary AVR, whereas anemic melt transport will cause the AVR to step outward. However, we note that both occurrences of Stage 6B conjugate plate partitioning observed to date (5°S MAR and Table Mountain, SWIR) are located at or near transform fault inside corner highs; thus, plate dynamics may ultimately dictate OCC termination in certain cases. We show four archetypical OCCs (Fig. 6.4) in various stages of our revised life cycle. In Panel A, active rifting has cross-cut, but not yet dismembered, Mount Dent after the OCC overstepped the AVR causing lateral dike propagation and rifting along NW-SE trending faults (stage 4). Panel B illustrates a stage 5 locality, Mount Hudson (Mid-Cayman Rise), where truncation by lateral dike propagation and rifting has generated a truncated nose morphology: a probable analog to 16°30'N MAR in the not too distant past. Panel C highlights the 16°N OCC studied here, where rifting has truncated the OCC and separated the nose, followed by an inward AVR jump. The final possibility, continued spreading, (stage 6B), is exemplified by the Table Mountain (Discovery F.Z., SWIR) and 5°S MAR where two halves of the OCC have been partitioned onto conjugate plates (Reston, Weinrebe et al. 2002). Interestingly, some OCCs have managed to avoid truncation including Kane Megamullion, 13°20'N (MAR) and 14°40'N (MAR), however we note that so long as the OCC remains in the vicinity of the ridge axis, rifting remains possible.

6.8 Acknowledgements

Urann acknowledges funding from the Student Research Fund at MIT for travel to complete sample prep and analytical work, and continuing support from MIT-WHOI Joint Program. John and Cheadle were supported by NSF Grant # 1636703. Dick received support from NSF Grants #1637130 and #1657983. We thank Tim Reston, Ross Parnell-Turner, and Deborah Smith for thoughtful discussions which broadened our thinking and improved the manuscript.

6.8 Figures

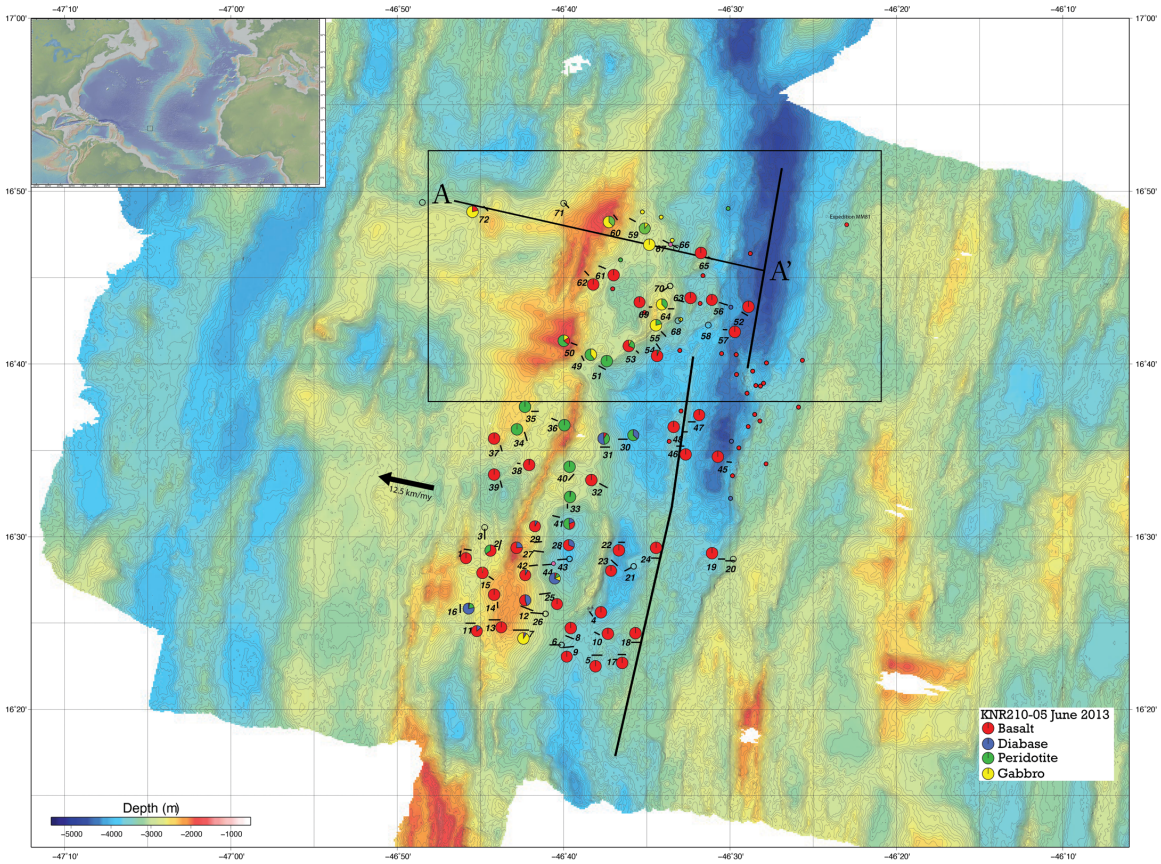

Figure 6.1. Regional bathymetric map. Bathymetric map showing individual dredge tracks (black solid lines) and observed rock types in weight percent on KNR210-05 cruise (2013). Small colored dots indicate dredges conducted on previous expeditions by R/V Boris Petrov and R/V Jean Charcot (Cannat et al., 1992). Thick black line denotes ridge axis from Smith et al. (2014). Black box denotes inset of Fig. 2.

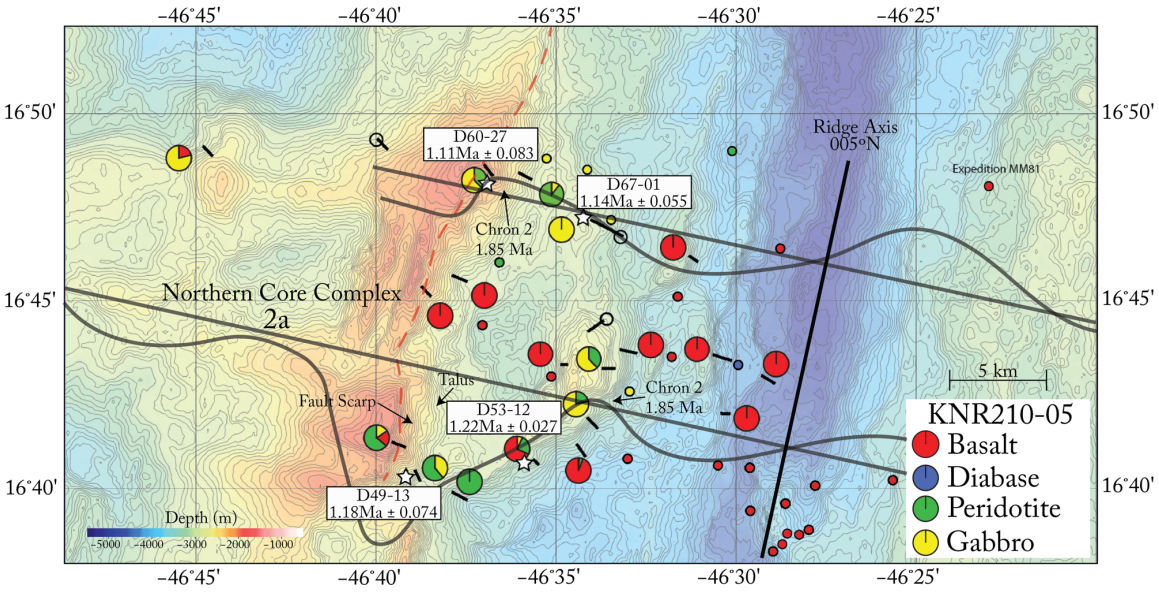

Figure 6.2. Inset from Fig. 1, with identical symbols. Red dashed line denotes interpreted fault. Gray semi-transparent lines delimit ship tracks (straight) and magnetic anomaly data from Parnell-Turner et al.(2016). Ages for the four samples dated in this study are given adjacent to the dredge from which they were collected.

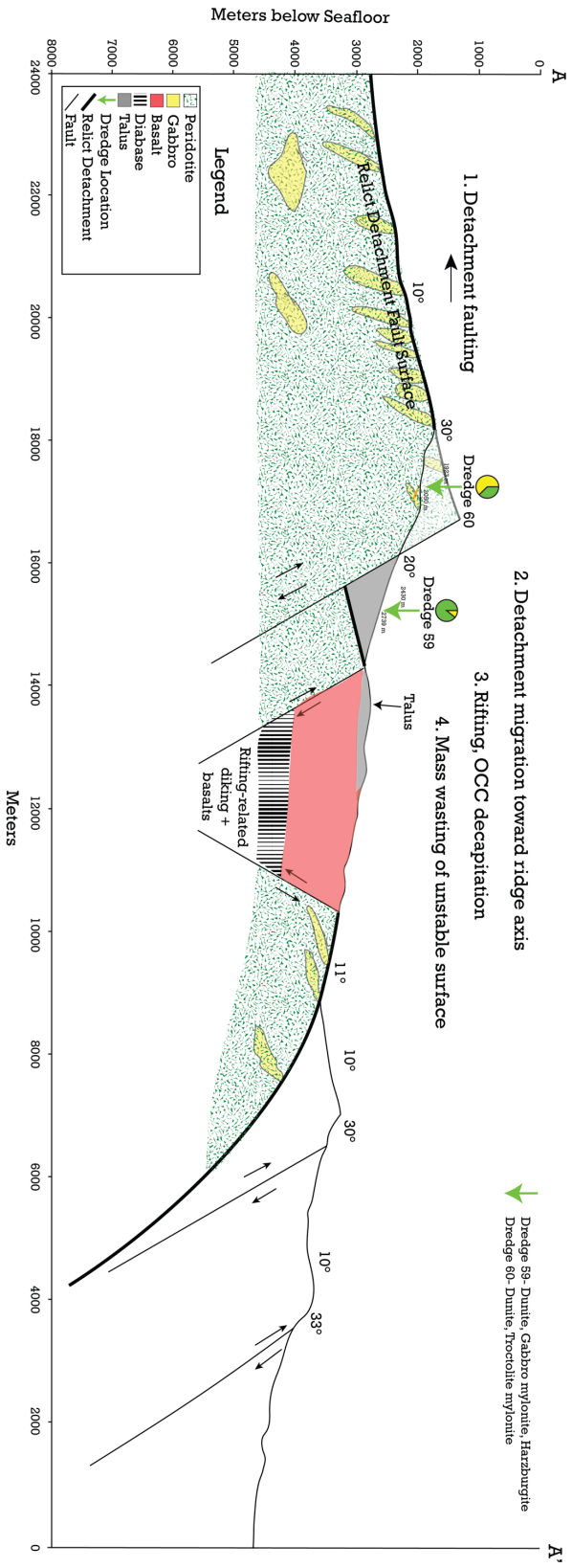

Figure 6.3. Structural interpretation of cross section A-A' (Fig. 1). No vertical exaggeration.

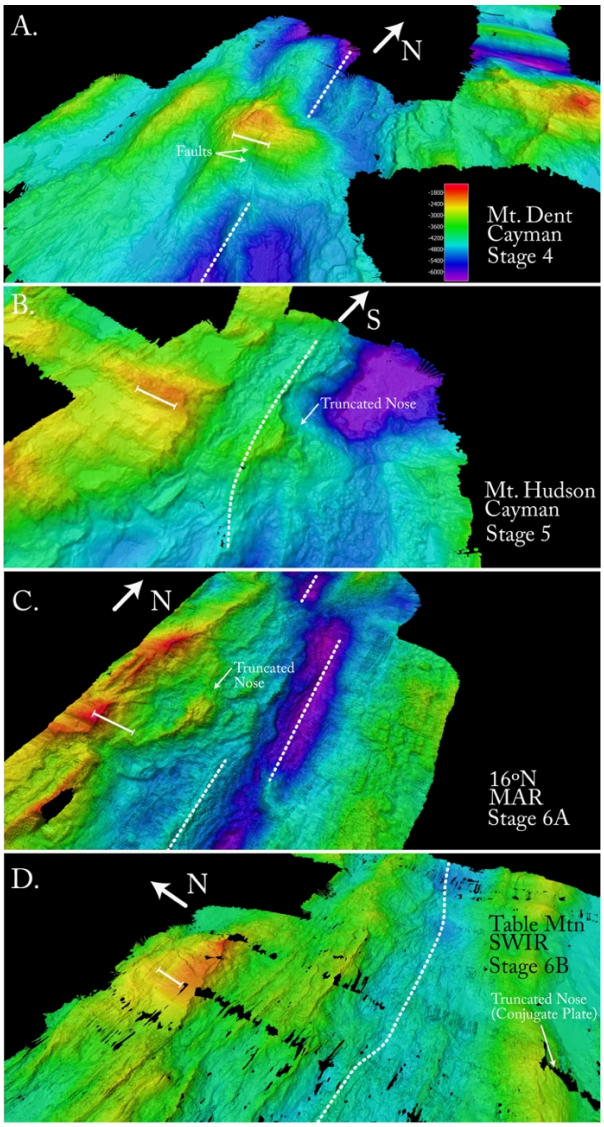

Figure 6.4. Bathymetry exhibiting various stages of OCC stages. White bars denote 50 km scale bar, dashed white lines approximate ridge axis. **A**. Stage 4. Initial OCC rifting observed at Mount Dent, Cayman Rise. NW-SE trending faults cross-cut, but do not yet dismember, OCC surface. Note the OCC has overstepped the AVR (pale blue) causing lateral dike propagation, rifting, and eventual truncation of the OCC. **B**. Stage 5. Continued rifting has caused decapitation of OCC, which now displays a "truncated nose" morphology. Mount Hudson, Mid-Cayman Rise. **C**. Stage 6a. OCC nose has been truncated and AVR has jumped inward toward the conjugate rift valley wall. 16°N NCC, MAR. **D**. Stage 6b. A stationary AVR underlying the relict OCC has partitioned the OCC nose onto the conjugate plate. Table Mountain, SWIR.

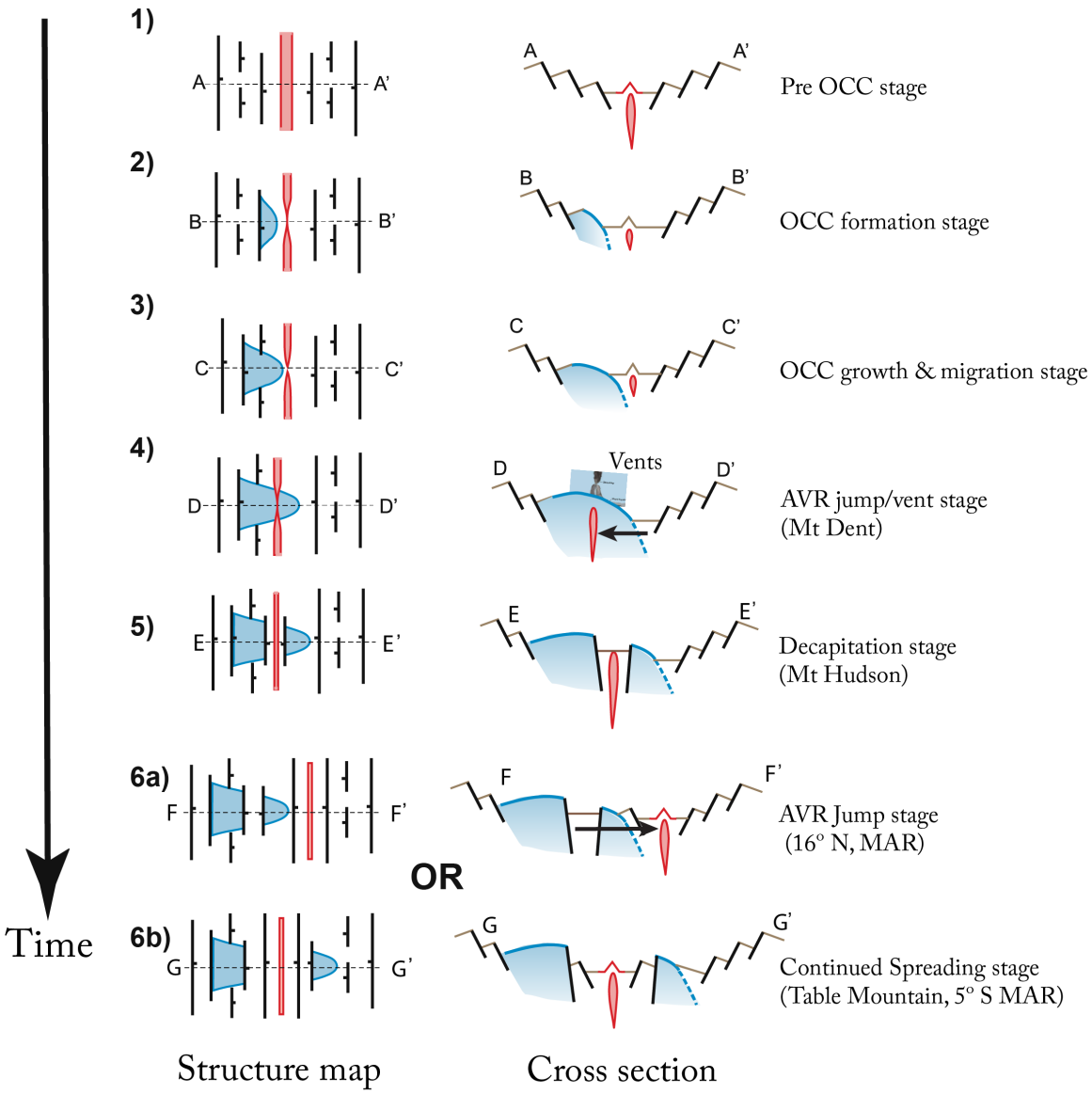

Figure 6.5. Revised life cycle of an oceanic core complex, after Macleod et al. (2009). Corresponding examples provided in Fig. 5.

6.10 Tables

Sample number	Rock type	Latitude	Longitude	Grain size	Texture	Alteration intensity (percent)	Number of grains analyzed	Age (Ma)	2σ	Mean T (°C)	Range T (°C)	Comments
D67-01	gabbro	16°47.155'N	46°34.117'N	fine/coarse	equigranular	0	9	1.14	0.083	905	800-1016	Two domains, one course and one fine grained
D49-13	gabbroic dike in serp. peridotite	16°40.506'N	46°38.957'N	coarse	equigranular	98	10	1.18	0.074	830	801-850	4 cm gabbro vein in harzburgite
D53-12	gabbro	16°40.801'N	46°35.702'N	coarse	equigranular	30	7	1.22	0.027	832	753-873	
D60-27	troctolite	16°48.620'N	46°37.057'N	fine/coarse	protomylonitic	90	8	1.11	0.083	908	892-940	Gradational, protomylonite to ultramylonite

Table 6.1. Sample description, dredge location, rock type, textural descriptions, and number of zircon grains analyzed for samples in this study.

	Concentrations			Atomic Ratio		Atomic Ratio		Atomic Ratio		207Pb Corrected Ages		230Th Corrected Ages (errors 2 sigma, abs)		
Sample Grain	U (µg/g)	Th (µg/g)	206Pb (µg/g)	238U/206Pb	Abs Error (%)	207Pb/206Pb	Abs Error (%)	207Pb corrected 206Pb/238U	Abs Error (%)	206Pb/238 U	2σ	206Pb/238U (Ma)	2σ	Weighted Average Age (Ma), 2σ
D49-13-10.1*	27	21	0.0028	5016	3.2	0.356	22	0.00012	5.2	0.78	0.1	0.86	0.13	
D49-13-5.1*	24	17	0.0026	4560	5.1	0.369	21	0.00013	5.6	0.83	0.1	0.92	0.15	
D49-13-1.1	31	23	0.0037	5117	7.2	0.265	24	0.00014	4.2	0.91	0.1	0.99	0.12	
D49-13-6.1	25	19	0.0033	5450	7.3	0.181	32	0.00015	3.7	0.98	0.1	1.06	0.11	
D49-13-4.1	28	20	0.0038	5576	6.6	0.134	34	0.00016	2.9	1.03	0.09	1.11	0.09	
D49-13-8.1	21	16	0.0030	4621	11.8	0.224	27	0.00017	4.9	1.08	0.2	1.16	0.17	
D49-13-9.1	54	40	0.0081	4906	3.7	0.154	22	0.00018	2.0	1.13	0.07	1.21	0.07	
D49-13-3.1	26	19	0.0041	4423	11.3	0.193	27	0.00018	4.5	1.19	0.2	1.27	0.17	
D49-13-2.1	29	21	0.0045	3987	4.0	0.256	22	0.00018	3.3	1.19	0.1	1.27	0.12	1.181±0.074
D49-13-7.1	39	25	0.0065	4325	5.4	0.174	22	0.00019	2.5	1.25	0.10	1.33	0.10	MSWD = 1.08
D53-12-4.3*	126	118	0.0168	5697	5.7	0.137	20	0.00016	2.2	1.00	0.07	1.08	0.07	
D53-12-7.1	166	152	0.0253	5614	3.4	0.050	24	0.00018	1.2	1.14	0.04	1.22	0.04	
D53-12-1.2	914	2137	0.1397	5486	2.4	0.065	10	0.00018	0.8	1.15	0.03	1.17	0.03	
D53-12-3.2	265	335	0.0404	5430	3.2	0.073	16	0.00018	1.1	1.15	0.04	1.21	0.04	
D53-12-6.1	241	346	0.0374	5279	2.9	0.082	16	0.00018	1.1	1.17	0.04	1.22	0.04	
D53-12-4.4	106	93	0.0170	5107	3.4	0.086	22	0.00019	1.4	1.20	0.05	1.27	0.05	
D53-12-5.3	771	1977	0.1250	5250	2.3	0.054	10	0.00019	0.8	1.22	0.03	1.23	0.03	
D53-12-2.2	65	83	0.0107	4989	5.3	0.087	26	0.00019	1.9	1.22	0.07	1.29	0.07	1.221±0.027
D53-12-8.1	131	343	0.0225	4631	2.3	0.108	18	0.00020	1.1	1.28	0.05	1.29	0.05	MSWD = 1.14
D60-27-7.2*	15	14	0.0009	3673	9.3	0.622	22	0.00007	20.5	0.48	0.3	0.55	0.30	
D60-27-3.2*	22	22	0.0018	5006	9.7	0.456	22	0.00010	8.8	0.62	0.2	0.69	0.17	
D60-27-6.2*	17	15	0.0016	3366	5.7	0.541	23	0.00011	13.5	0.72	0.3	0.79	0.30	
D60-27-4.2	17	16	0.0020	5079	6.6	0.299	27	0.00013	5.2	0.86	0.1	0.94	0.14	
D60-27-9.1	44	45	0.0054	5329	5.7	0.240	20	0.00014	3.1	0.91	0.09	0.98	0.09	
D60-27-11.1	67	81	0.0097	5000	4.6	0.171	19	0.00017	2.1	1.08	0.07	1.15	0.07	
D60-27-12.1	21	14	0.0031	3595	20.1	0.348	19	0.00017	7.7	1.11	0.3	1.19	0.27	
D60-27-2.2	31	38	0.0046	3993	7.1	0.289	20	0.00017	4.0	1.12	0.1	1.18	0.14	1.112±0.083
D60-27-5.2	52	60	0.0079	4901	5.9	0.145	24	0.00018	2.5	1.20	0.09	1.22	0.09	MSWD = 1.10
D67-01-7.3*	45	42	0.0051	6408	6.7	0.166	28	0.00013	3.0	0.85	0.08	0.93	0.08	
D67-01-3.2*	61	50	0.0075	5706	7.9	0.187	20	0.00014	3.1	0.93	0.09	1.01	0.09	
D67-01-2.2	240	172	0.0316	6075	2.0	0.101	15	0.00015	0.9	0.99	0.03	1.07	0.03	
D67-01-9.1	354	310	0.0488	6039	3.4	0.071	16	0.00016	1.2	1.03	0.04	1.11	0.04	
D67-01-5.2	211	196	0.0293	5966	1.9	0.077	19	0.00016	0.9	1.04	0.03	1.11	0.03	
D67-01-1.2	150	122	0.0211	5676	2.4	0.103	19	0.00016	1.1	1.05	0.04	1.13	0.04	
D67-01-8.2	256	139	0.0369	6062	2.7	0.034	23	0.00017	0.9	1.08	0.03	1.17	0.03	
D67-01-4.2	156	87	0.0233	5544	2.3	0.073	20	0.00017	1.0	1.10	0.03	1.21	0.03	1.140±0.055
D67-01-7.4	143	228	0.0228	5228	3.0	0.070	21	0.00019	1.1	1.20	0.04	1.25	0.04	MSWD = 3.3

* Omitted due to high common Pb

Table 6.2. Individual zircon analyses U, Th, Pb concentrations, atomic ratios, ^{230}Th corrected ages and MSWD values for each subset.

Sample Grain	Ti (ppm)	Fe (ppm)	Y (ppm)	Gd (ppm)	Yb (ppm)
D67-01_3.1	51	0.034	998	34	230
D67-01_7.1	66	0.063	931	31	207
D67-01_7.2	97	0.068	3509	123	690
D67-01_2.1	41	0.037	884	19	227
D67-01_8.1	17	0.070	655	10	250
D67-01_6.1	53	0.069	886	27	204
D67-01_1.1	20	0.073	618	10	223
D67-01_5.1	40	0.039	1554	33	435
D67-01_4.1	41	0.055	1051	31	256
D67 Median					
D60-27_7.1	40	3.505	1346	31	508
D60-27_5.1	57	16.402	2312	31	918
D60-27_4.1	44	152.643	1593	38	564
D60-27_2.1	41	0.980	2300	40	846
D60-27_8.1	47	0.073	1429	28	529
D60-27_3.1	50	0.063	1879	41	659
D60-27_6.1	40	0.040	1442	34	523
D60-27_1.1	39	0.260	765	14	319
D60 Median					
D53-12_2.1	11	0.584	638	8	266
D53-12_4.1	31	0.486	1443	35	428
D53-12_5.1	26	0.483	2058	46	532
D53-12_3.1	33	0.664	1772	49	379
D53-12_1.1	27	0.455	3628	123	953
D53-12_4.2	20	0.116	680	10	247
D53-12_5.2	22	0.141	1805	55	416
D53 Median					
D49-13-1.1	23	0.18	3417	94	972
D49-13-2.1	24	0.10	3045	78	887
D49-13-3.1	27	0.30	3080	80	901
D49-13-4.1	25	0.16	2924	80	825
D49-13-5.1	25	0.06	2867	78	805
D49-13-6.1	24	0.13	2980	79	842
D49-13-7.1	19	0.09	3215	68	983
D49-13-8.1	21	0.39	2691	70	782
D49-13-9.1	17	0.15	4319	112	1232
D49-13-10.1	25	0.88	2752	72	798
D49 Median					

Ti in zircon temperatures calculated using SiO2 and TiO2 activities of 0.7 and 0.7, respectively.

Table 6.3. Number of zircon grains analyzed per sample, age, and Ti-in-zircon thermometry results including both the mean temperature and temperature range from Ferry and Watson (2007) using SiO_2 and Ti activities of 0.7.

Sample Grain	Hf (ppm)	U (ppm)	Th (ppm)	Kelvin	°C	1σ
D67-01_3.1	10059	57	49	1199	926	43
D67-01_7.1	9766	47	41	1234	961	45
D67-01_7.2	8962	145	227	1289	1016	48
D67-01_2.1	11427	94	73	1171	898	42
D67-01_8.1	9148	232	123	1073	800	36
D67-01_6.1	10003	70	65	1204	931	43
D67-01_1.1	8160	173	133	1091	818	37
D67-01_5.1	10366	203	177	1168	895	41
D67-01_4.1	11283	160	90	1170	897	42
D67 Median					898	
D60-27_7.1	9875	18	18	1167	894	41
D60-27_5.1	9114	48	47	1213	940	44
D60-27_4.1	10362	21	20	1180	907	42
D60-27_2.1	9910	42	61	1170	897	42
D60-27_8.1	9162	19	17	1188	915	42
D60-27_3.1	9271	21	22	1197	924	43
D60-27_6.1	9712	19	18	1168	895	41
D60-27_1.1	10202	11	8	1165	892	41
D60 Median					902	
D53-12_2.1	12032	76	87	1026	753	34
D53-12_4.1	13070	120	119	1136	863	40
D53-12_5.1	11463	448	992	1118	845	39
D53-12_3.1	10428	305	394	1146	873	40
D53-12_1.1	12785	974	2440	1123	850	39
D53-12_4.2	15470	144	124	1089	816	37
D53-12_5.2	11757	253	608	1100	827	38
D53 Median					845	
D49-13-1.1	11058	32	24	1115	842	39
D49-13-2.1	10822	30	22	1112	839	38
D49-13-3.1	10451	28	21	1103	830	38
D49-13-4.1	10769	29	21	1109	836	38
D49-13-5.1	10860	25	19	1111	838	38
D49-13-6.1	11204	27	20	1093	820	38
D49-13-7.1	11846	43	28	1074	801	37
D49-13-8.1	11051	23	18	1123	850	39
D49-13-9.1	12362	59	45	1107	834	38
D49-13-10.1	10741	28	22	1081	808	37
D49 Median					835	

Table 6.3. (cont.)

Chapter 7

Conclusions and future directions

Instead of summarizing the above findings, here I discuss future research directions that may be of interest to the community.

From Chapter 2, I showed that the halogen content of mantle peridotites may reflect interaction with fluids and silicate melts, and placed new constraints on the F and Cl content of the mantle. Looking forward, more comprehensive assessments must include samples from various P-T conditions across broad geographic extents, to garner a more representative sampling of the upper mantle. Chapter 2 focused on spinel peridotites (i.e. equilibrated at pressures less than 2 GPa), however an evaluation of garnet peridotites would be crucial to understanding the volatile content of the entire mantle above the 410 km transition zone (where garnet peridotite is the dominant lithology) and would be useful in understanding volatile systematics in ocean island basalts (thought to be sourced from garnet bearing lithologies). Furthermore, although I made several inferences as to substitution mechanisms for F in pyroxenes, Fourier-transform infrared spectroscopy is needed to ascertain the exact substitution mechanism observed.

In Chapter 3, I established the volatile abundances of eclogitized oceanic crust, showing that the vast majority (95%) of F is retained by the slab through eclogitization, whereas >95% of Cl is expelled by the time the slab equilibrates at eclogites-facies conditions. I also demonstrated that the Cl content as measured by bulk rock analyses may be significantly higher than by in situ methods, suggesting that the majority of Cl in eclogite is hosted in fluid inclusions. Further, the F/Nd and Cl/K ratios of subducted eclogite are virtually identical to the mantle, suggesting that ocean island basalts enriched in these ratios must either reflect an additional source lithology (e.g., serpentinite) or a fractionation process during melting, perhaps in the garnet field. To expand on this study, several questions remain. Fluorine and Nd bulk partition coefficients are nearly identical in the spinel field, yet could be significantly different in the garnet field, as is the case with H_2O and Ce. Should this be the case, F/Nd enrichments might simply be a function of garnet field melting, negating the need (from the halogen ratio perspective) for an exotic lithology, such as serpentinite. This possibility requires further inquiry. What is the volume proportion of fluid inclusions in bulk eclogite, and how does the chemical composition of fluid inclusions change with continued subduction? How does volatile partitioning change for UHP coesite-bearing eclogites? During breakdown of amphibole (~3 GPa) and phengite (~10 GPa), are volatiles partitioned into a fluid phase, or redistributed into nominally anhydrous phases? A combination of X-ray microtomography, further sampling and experimental studies may provide answers to these and other questions.

Chapter 4 showed that the H_2O content of primitive arc magmas (4–10 wt.%) may be far higher than values inferred from olivine-hosted melt inclusions, and through fractional crystallization increase to nearly 20 wt.% at 1 GPa. This is a significant finding, yet further work is required to substantiate this. One test would be to sample a well-documented layered intrusion (e.g., the Mesoproterozoic Kiglapait of Labrador) where a nominal liquid line of descent during crystal fractionation may be followed in clinopyroxene-bearing lithologies. Agreement between volatile abundances and trace elements would provide compelling evidence that the H_2O content of the liquids was preserved in the minerals, augmenting the contribution made here. Furthermore, the question of H_2O redistribution during diffusive equilibration in slow cooling cumulates arises when discussing the meaning of measured H_2O abundances. Experimental constraints would be useful here. Currently, our understanding of H_2O partitioning between pyroxenes is based on supra-solidus experiments (typically >1100°C) yet cumulates may spend millions of years at sub-solidus conditions prior to sampling. Thus, a series of isobaric experiments at various sub-solidus temperature conditions (e.g., temperature steps from 1100°C down to 500°C) are needed to evaluate sub-solidus equilibration of cumulate rocks.

Chapter 5 documented a parcel of arc mantle that has been recycled into the sub-ridge aesthenosphere and exposed at the 16°N region of the Mid-Atlantic Ridge. Although an exciting finding, the results left more questions than answers. First, in which paleo-arc might this peridotite have been melted? What is the Hf isotopic composition of the Cpx? We would expect extremely radiogenic values, in line with the ReLish component of Salters et al. (2011). How widespread are these peridotites, and what influence might they have on sub-ridge melting dynamics? Intuitively, highly depleted peridotite would not contribute as much melt as fertile sub-ridge peridotite. In this case, does mantle fertility dictate (in part) the crustal architecture observed at mid-ocean ridges globally? Finally, to what extent do other lithologies contribute to melting in regions where anomalously refractory peridotite is observed? Many of these questions will require future expeditions to explore slow and ultra-slow spreading ridges, particularly the South Atlantic, where bathymetry and sampling is sparse (e.g. Fig. 1 of Warren 2016). Our finding that the upper mantle may be more depleted than previously thought requires a reckoning with current paradigms of plate tectonics and the utility of basalts in inferring mantle compositions, which frankly has been a long time coming.

Chapter 6 documented the disparity between geophysical crustal ages and those derived from zircon U-Pb geochronology, presenting a revised life cycle for oceanic core complexes. We were able to show that magnetics data may be obfuscated by mass wasting and tectonics, and thus must be scrutinized in light of tectonic settings from which the data was garnered. Our age models for our samples were inferred based on assumed fault geometries and isotherms. These are good estimates, yet the depth to which ductile shear zones permeate the mantle is not well constrained, nor is the shape (concave down or listric) of the detachment fault at depth. The marked spreading

asymmetry we observed at 16ºN has been observed elsewhere (e.g. Atlantis Massif, Atlantis Bank), yet is often overlooked in geophysical studies where oceanic core complexes are observed.

The future of marine geology is bright; limitations are only imposed when we forego opportunities to expand knowledge for sake of expediency. The most difficult problems will furnish the most important insights, and from there all else follows.

Citations

Abers, G. A. and B. R. Hacker (2016). "A MATLAB toolbox and E xcel workbook for calculating the densities, seismic wave speeds, and major element composition of minerals and rocks at pressure and temperature." Geochemistry, Geophysics, Geosystems **17**(2): 616-624.

Adam, J. and T. Green (2006). "Trace element partitioning between mica-and amphibole-bearing garnet lherzolite and hydrous basanitic melt: 1. Experimental results and the investigation of controls on partitioning behaviour." Contributions to Mineralogy and Petrology **152**(1): 1-17.

Alletti, M., D. R. Baker, B. Scaillet, A. Aiuppa, R. Moretti and L. Ottolini (2009). "Chlorine partitioning between a basaltic melt and H2O–CO2 fluids at Mount Etna." Chemical Geology **263**(1-4): 37-50.

Alonso Perez, R. (2007). The role of garnet in the evolution of hydrous, calc-alkaline magmas: An experimental study at 0.8-1.5 GPa, ETH Zurich.

Alonso-Perez, R., O. Müntener and P. Ulmer (2009). "Igneous garnet and amphibole fractionation in the roots of island arcs: experimental constraints on andesitic liquids." Contributions to Mineralogy and Petrology **157**(4): 541-558.

Anders, E. and N. Grevesse (1989). "Abundances of the elements: Meteoritic and solar." Geochimica et Cosmochimica acta **53**(1): 197-214.

Anderson, A. (1974). "Chlorine, sulfur, and water in magmas and oceans." Geological Society of America Bulletin **85**(9): 1485-1492.

Anderson, D. L. (2007). New theory of the Earth, Cambridge University Press.

Arndt, N. T. and S. L. Goldstein (1989). "An open boundary between lower continental crust and mantle: its role in crust formation and crustal recycling." Tectonophysics **161**(3-4): 201-212.

Aubaud, C., M. M. Hirschmann, A. C. Withers and R. L. Hervig (2008). "Hydrogen partitioning between melt, clinopyroxene, and garnet at 3 GPa in a hydrous MORB with 6 wt.% H 2 O." Contributions to Mineralogy and Petrology **156**(5): 607-625.

Bach, W., C. J. Garrido, H. Paulick, J. Harvey and M. Rosner (2004). "Seawater-peridotite interactions: First insights from ODP Leg 209, MAR 15 N." Geochemistry, Geophysics, Geosystems **5**(9).

Baines, A. G., M. J. Cheadle, B. E. John, C. B. Grimes, J. J. Schwartz and J. L. Wooden (2009). "SHRIMP Pb/U zircon ages constrain gabbroic crustal accretion at Atlantis Bank on the ultraslow-spreading Southwest Indian Ridge." Earth and Planetary Science Letters **287**(3-4): 540-550.

Baines, A. G., M. J. Cheadle, B. E. John and J. J. Schwartz (2008). "The rate of oceanic detachment faulting at Atlantis Bank, SW Indian Ridge." Earth and Planetary Science Letters **273**(1-2): 105-114.

Barth, A. P. and J. L. Wooden (2010). "Coupled elemental and isotopic analyses of polygenetic zircons from granitic rocks by ion microprobe, with implications for melt evolution and the sources of granitic magmas." Chemical Geology **277**(1-2): 149-159.

Behn, M. D. and P. B. Kelemen (2006). "Stability of arc lower crust: Insights from the Talkeetna arc section, south central Alaska, and the seismic structure of modern arcs." Journal of Geophysical Research: Solid Earth **111**(B11).

Bénard, A., K. Koga, N. Shimizu, M. Kendrick, D. Ionov, O. Nebel and R. J. Arculus (2017). "Chlorine and fluorine partition coefficients and abundances in sub-arc mantle xenoliths

(Kamchatka, Russia): implications for melt generation and volatile recycling processes in subduction zones." Geochimica et Cosmochimica Acta **199**: 324-350.
Berndt, J., C. Liebske, F. Holtz, M. Freise, M. Nowak, D. Ziegenbein, W. Hurkuck and J. r. Koepke (2002). "A combined rapid-quench and H2-membrane setup for internally heated pressure vessels: Description and application for water solubility in basaltic melts." American Mineralogist **87**(11-12): 1717-1726.
Bernini, D., M. Wiedenbeck, D. Dolejš and H. Keppler (2013). "Partitioning of halogens between mantle minerals and aqueous fluids: implications for the fluid flow regime in subduction zones." Contributions to Mineralogy and Petrology **165**(1): 117-128.
Beyer, C., S. Klemme, T. Grützner, T. Ireland, C. Magee and D. Frost (2016). "Fluorine partitioning between eclogitic garnet, clinopyroxene, and melt at upper mantle conditions." Chemical Geology **437**: 88-97.
Beyer, C., S. Klemme, M. Wiedenbeck, A. Stracke and C. Vollmer (2012). "Fluorine in nominally fluorine-free mantle minerals: Experimental partitioning of F between olivine, orthopyroxene and silicate melts with implications for magmatic processes." Earth and Planetary Science Letters **337**: 1-9.
Bizimis, M. and A. H. Peslier (2015). "Water in Hawaiian garnet pyroxenites: Implications for water heterogeneity in the mantle." Chemical Geology **397**: 61-75.
Bizimis, M., V. J. M. Salters and E. Bonatti (2000). "Trace and REE content of clinopyroxenes from supra-subduction zone peridotites. Implications for melting and enrichment processes in island arcs." Chemical Geology **165**(1-2): 67-85.
Black, L. P., S. L. Kamo, C. M. Allen, D. W. Davis, J. N. Aleinikoff, J. W. Valley, R. Mundil, I. H. Campbell, R. J. Korsch and I. S. Williams (2004). "Improved 206Pb/238U microprobe geochronology by the monitoring of a trace-element-related matrix effect; SHRIMP, ID–TIMS, ELA–ICP–MS and oxygen isotope documentation for a series of zircon standards." Chemical Geology **205**(1-2): 115-140.
Bloch, E., M. Ibañez-Mejia, K. Murray, J. Vervoort and O. Müntener (2017). "Recent crustal foundering in the Northern Volcanic Zone of the Andean arc: Petrological insights from the roots of a modern subduction zone." Earth and Planetary Science Letters **476**: 47-58.
Bonadiman, C., Y. Hao, M. Coltorti, L. Dallai, B. Faccini, Y. Huang and Q. Xia (2009). "Water contents of pyroxenes in intraplate lithospheric mantle." European Journal of Mineralogy **21**(3): 637-647.
Bonatti, E., A. Peyve, P. Kepezhinskas, N. Kurentsova, M. Seyler, S. Skolotnev and G. Udintsev (1992). "Upper mantle heterogeneity below the Mid-Atlantic Ridge, 0°–15° N." Journal of Geophysical Research: Solid Earth **97**(B4): 4461-4476.
Bonifacie, M., V. Busigny, C. Mével, P. Philippot, P. Agrinier, N. Jendrzejewski, M. Scambelluri and M. Javoy (2008). "Chlorine isotopic composition in seafloor serpentinites and high-pressure metaperidotites. Insights into oceanic serpentinization and subduction processes." Geochimica et Cosmochimica Acta **72**(1): 126-139.
Bouilhol, P., O. Jagoutz, J. M. Hanchar and F. O. Dudas (2013). "Dating the India–Eurasia collision through arc magmatic records." Earth and Planetary Science Letters **366**: 163-175.
Bouvier, A.-S., E. Deloule and N. Métrich (2010). "Fluid inputs to magma sources of St. Vincent and Grenada (Lesser Antilles): new insights from trace elements in olivine-hosted melt inclusions." Journal of petrology **51**(8): 1597-1615.

Bouvier, A.-S., N. Metrich and E. Deloule (2008). "Slab-derived fluids in the magma sources of St. Vincent (Lesser Antilles Arc): volatile and light element imprints." Journal of Petrology **49**(8): 1427-1448.
Bown, J. W. and R. S. White (1994). "Variation with Spreading Rate of Oceanic Crustal Thickness and Geochemistry." Earth and Planetary Science Letters **121**(3-4): 435-449.
Brenan, J. M., F. J. Ryerson and H. F. Shaw (1998). "The role of aqueous fluids in the slab-to-mantle transfer of boron, beryllium, and lithium during subduction: experiments and models." Geochimica et Cosmochimica Acta **62**(19-20): 3337-3347.
Bromiley, D. W. and S. C. Kohn (2007). "Comparisons between fluoride and hydroxide incorporation in nominally anhydrous and fluorine-free mantle minerals." Geochimica et Cosmochimica Acta **71**.
Brunelli, D., A. Cipriani and E. Bonatti (2018). "Thermal effects of pyroxenites on mantle melting below mid-ocean ridges." Nature Geoscience **11**(7): 520-+.
Bucholz, C. E., G. A. Gaetani, M. D. Behn and N. Shimizu (2013). "Post-entrapment modification of volatiles and oxygen fugacity in olivine-hosted melt inclusions." Earth and Planetary Science Letters **374**: 145-155.
Buck, W. R., L. L. Lavier and A. N. Poliakov (2005). "Modes of faulting at mid-ocean ridges." Nature **434**(7034): 719-723.
Burg, J., J. Bodinier, S. Chaudhry, S. Hussain and H. Dawood (1998). "Infra-arc mantle-crust transition and intra-arc mantle diapirs in the Kohistan Complex (Pakistani Himalaya): petro-structural evidence." Terra Nova-Oxford **10**(2): 74-80.
Burg, J. P., O. Jagoutz, H. Dawood and S. S. Hussain (2006). "Precollision tilt of crustal blocks in rifted island arcs: structural evidence from the Kohistan Arc." Tectonics **25**(5).
Burton, K. W., B. Cenki-Tok, F. Mokadem, J. Harvey, A. Gannoun, O. Alard and I. J. Parkinson (2012). "Unradiogenic lead in Earth's upper mantle." Nature Geoscience **5**(8): 570-573.
Byerly, B. L. and J. C. Lassiter (2014). "Isotopically ultradepleted domains in the convecting upper mantle: Implications for MORB petrogenesis." Geology **42**(3): 203-206.
Cabral, R. A., M. G. Jackson, K. T. Koga, E. F. Rose-Koga, E. H. Hauri, M. J. Whitehouse, A. A. Price, J. M. Day, N. Shimizu and K. A. Kelley (2014). "Volatile cycling of H2O, CO 2, F, and C l in the HIMU mantle: A new window provided by melt inclusions from oceanic hot spot lavas at M angaia, C ook I slands." Geochemistry, Geophysics, Geosystems **15**(11): 4445-4467.
Cannat, M., D. Bideau and H. Bougault (1992). "Serpentinized peridotites and gabbros in the Mid-Atlantic Ridge axial valley at 15 37′ N and 16 52′ N." Earth and Planetary Science Letters **109**(1-2): 87-106.
Cannat, M., D. Bideau and H. Bougault (1992). "Serpentinized Peridotites and Gabbros in the Mid-Atlantic Ridge Axial Valley at 15-Degrees-37'n and 16-Degrees-52'n." Earth and Planetary Science Letters **109**(1-2): 87-106.
Cannat, M., Y. Lagabrielle, H. Bougault, J. Casey, N. deCoutures, L. Dmitriev and Y. Fouquet (1997). "Ultramafic and gabbroic exposures at the Mid-Atlantic Ridge: geological mapping in the 15 degrees N region." Tectonophysics **279**(1-4): 193-213.
Cannat, M., C. Mevel, M. Maia, C. Deplus, C. Durand, P. Gente, P. Agrinier, A. Belarouchi, G. Dubuisson and E. Humler (1995). "Thin crust, ultramafic exposures, and rugged faulting patterns at the Mid-Atlantic Ridge (22–24 N)." Geology **23**(1): 49-52.

Caricchi, L., T. E. Sheldrake and J. Blundy (2018). "Modulation of magmatic processes by CO2 flushing." Earth and Planetary Science Letters **491**: 160-171.
Carmichael, I. S. (2002). "The andesite aqueduct: perspectives on the evolution of intermediate magmatism in west-central (105–99 W) Mexico." Contributions to Mineralogy and Petrology **143**(6): 641-663.
Casey, J., Y. Gao, R. Benavidez and C. Dragoi (2010). The Lowest delta7Li Yet Recorded in MORB Glasses: The Connection with Oceanic Core Complex Formation, Refractory Rutile-bearing Eclogitic Mantle Sources and Melt Supply. AGU Fall Meeting Abstracts.
Cawthorn, G. R. and M. J. O'Hara (1976). "Amphibole fractionation in calc-alkaline magma genesis." American Journal of Science **276**(3): 309-329.
Cheadle, M., B. John, C. German and N. Kusznir (2012). The death throes of ocean core complexes: Examples from the Mid-Cayman Spreading Centre. AGU Fall Meeting Abstracts.
Cherniak, D. J. and Y. Liang (2012). "Ti diffusion in natural pyroxene." Geochimica et Cosmochimica Acta **98**: 31-47.
Chin, E. J., V. Soustelle, G. Hirth, A. E. Saal, S. C. Kruckenberg and J. M. Eiler (2016). "Microstructural and geochemical constraints on the evolution of deep arc lithosphere." Geochemistry, Geophysics, Geosystems **17**(7): 2497-2521.
Choi, S. H., J. W. Shervais and S. B. Mukasa (2008). "Supra-subduction and abyssal mantle peridotites of the Coast Range ophiolite, California." Contributions to Mineralogy and Petrology **156**(5): 551-576.
Coble, M. A., S. D. Burgess and E. W. Klemetti (2017). "New zircon (U-Th)/He and U/Pb eruption age for the Rockland tephra, western USA." Quaternary Science Reviews **172**: 109-117.
D'Errico, M. E., J. M. Warren and M. Godard (2016). "Evidence for chemically heterogeneous Arctic mantle beneath the Gakkel Ridge." Geochimica Et Cosmochimica Acta **174**: 291-312.
Dalou, C., K. T. Koga, M. Le Voyer and N. Shimizu (2014). "Contrasting partition behavior of F and Cl during hydrous mantle melting: implications for Cl/F signature in arc magmas." Progress in Earth and Planetary Science **1**(1): 26.
Dalou, C., K. T. Koga, N. Shimizu, J. Boulon and J.-L. Devidal (2012). "Experimental determination of F and Cl partitioning between lherzolite and basaltic melt." Contributions to Mineralogy and Petrology **163**(4): 591-609.
Dalou, C. and B. O. Mysen (2015). "The effect of H2O on F and Cl solubility and solution mechanisms of in aluminosilicate melts at high pressure and high temperature." American Mineralogist **100**(2-3): 633-643.
Dalton, C. A., C. H. Langmuir and A. Gale (2014). "Geophysical and Geochemical Evidence for Deep Temperature Variations Beneath Mid-Ocean Ridges." Science **344**(6179): 80-83.
Debret, B., K. T. Koga, C. Nicollet, M. Andreani and S. Schwartz (2014). "F, Cl and S input via serpentinite in subduction zones: implications for the nature of the fluid released at depth." Terra Nova **26**(2): 96-101.
DeMets, C., R. G. Gordon and D. F. Argus (2010). "Geologically current plate motions." Geophysical Journal International **181**(1): 1-80.
Demouchy, S., A. Ishikawa, A. Tommasi, O. Alard and S. Keshav (2015). "Characterization of hydration in the mantle lithosphere: Peridotite xenoliths from the Ontong Java Plateau as an example." Lithos **212**: 189-201.
Demouchy, S., S. D. Jacobsen, F. Gaillard and C. R. Stern (2006). "Rapid magma ascent recorded by water diffusion profiles in mantle olivine." Geology **34**(6): 429-432.

Dick, H. and R. Fisher (1984). Mineralogic studies of the residues of mantle melting: abyssal and alpine-type peridotites. Developments in Petrology, Elsevier. **11:** 295-308.
Dick, H. J., J. Lin and H. Schouten (2003). "An ultraslow-spreading class of ocean ridge." Nature **426**(6965): 405-412.
Dick, H. J. and J. H. Natland (1996). Late-stage melt evolution and transport in the shallow mantle beneath the East Pacific Rise. Ocean Drilling Program Scientific Results, Texas A&M University, College Station TX.
Dick, H. J. B. and T. Bullen (1984). "Chromian Spinel as a Petrogenetic Indicator in Abyssal and Alpine-Type Peridotites and Spatially Associated Lavas." Contributions to Mineralogy and Petrology **86**(1): 54-76.
Dick, H. J. B., J. Lin and H. Schouten (2003). "An ultraslow-spreading class of ocean ridge." Nature **426**(6965): 405-412.
Dick, H. J. B. and H. Y. Zhou (2015). "Ocean rises are products of variable mantle composition, temperature and focused melting." Nature Geoscience **8**(1): 68-74.
Dingwell, D. B. (1989). "Effect of fluorine on the viscosity of diopside liquid." American Mineralogist **74**(3-4): 333-338.
Dixon, J. E., T. H. Dixon, D. Bell and R. Malservisi (2004). "Lateral variation in upper mantle viscosity: role of water." Earth and Planetary Science Letters **222**(2): 451-467.
Dobson, P. F., H. Skogby and G. R. Rossman (1995). "Water in boninite glass and coexisting orthopyroxene: concentration and partitioning." Contributions to Mineralogy and Petrology **118**(4): 414-419.
Dodge, F., J. Lockwood and L. Calk (1988). "Fragments of the mantle and crust from beneath the Sierra Nevada batholith: Xenoliths in a volcanic pipe near Big Creek, California." Geological Society of America Bulletin **100**(6): 938-947.
Dosso, L., H. Bougault and J. L. Joron (1993). "Geochemical Morphology of the North Mid-Atlantic Ridge, 10-Degrees-24-Degrees-N - Trace Element-Isotope Complementarity." Earth and Planetary Science Letters **120**(3-4): 443-462.
Dosso, L., H. Bougault, C. Langmuir, C. Bollinger, O. Bonnier and J. Etoubleau (1999). "The age and distribution of mantle heterogeneity along the Mid-Atlantic Ridge (31-41 degrees N)." Earth and Planetary Science Letters **170**(3): 269-286.
Ducea, M. N. and J. B. Saleeby (1996). "Buoyancy sources for a large, unrooted mountain range, the Sierra Nevada, California: Evidence from xenolith thermobarometry." Journal of Geophysical Research: Solid Earth **101**(B4): 8229-8244.
Dyment, J., J. Arkani-Hamed and A. Ghods (1997). "Contribution of serpentinized ultramafics to marine magnetic anomalies at slow and intermediate spreading centres: insights from the shape of the anomalies." Geophysical Journal International **129**(3): 691-701.
Escartín, J. and J. Canales (2011). "Detachments in oceanic lithosphere: Deformation, magmatism, fluid flow, and ecosystems." Eos, Transactions American Geophysical Union **92**(4): 31-31.
Escartín, J., C. Mével, C. J. MacLeod and A. McCaig (2003). "Constraints on deformation conditions and the origin of oceanic detachments: The Mid-Atlantic Ridge core complex at 15 45′ N." Geochemistry, Geophysics, Geosystems **4**(8).
Escartín, J., C. Mevel, S. Petersen, D. Bonnemains, M. Cannat, M. Andreani, N. Augustin, A. Bezos, V. Chavagnac and Y. Choi (2017). "Tectonic structure, evolution, and the nature of

oceanic core complexes and their detachment fault zones (13 20′ N and 13 30′ N, Mid Atlantic Ridge)." Geochemistry, Geophysics, Geosystems **18**(4): 1451-1482.
Fabbrizio, A., R. Stalder, K. Hametner, D. Günther and K. Marquardt (2013). "Experimental partitioning of halogens and other trace elements between olivine, pyroxenes, amphibole and aqueous fluid at 2 GPa and 900–1,300 C." Contributions to Mineralogy and Petrology **166**(2): 639-653.
Falus, G., A. Tommasi, J. Ingrin and C. Szabó (2008). "Deformation and seismic anisotropy of the lithospheric mantle in the southeastern Carpathians inferred from the study of mantle xenoliths." Earth and Planetary Science Letters **272**(1-2): 50-64.
Ferriss, E., T. Plank and D. Walker (2016). "Site-specific hydrogen diffusion rates during clinopyroxene dehydration." Contributions to Mineralogy and Petrology **171**(6): 55.
Ferry, J. and E. Watson (2007). "New thermodynamic models and revised calibrations for the Ti-in-zircon and Zr-in-rutile thermometers." Contributions to Mineralogy and Petrology **154**(4): 429-437.
Gaetani, G. A. (2004). "The influence of melt structure on trace element partitioning near the peridotite solidus." Contributions to Mineralogy and Petrology **147**(5): 511-527.
Gaetani, G. A. and T. L. Grove (1998). "The influence of water on melting of mantle peridotite." Contributions to Mineralogy and Petrology **131**(4): 323-346.
Gaetani, G. A., J. A. O'Leary, N. Shimizu, C. E. Bucholz and M. Newville (2012). "Rapid reequilibration of H2O and oxygen fugacity in olivine-hosted melt inclusions." Geology **40**(10): 915-918.
Gale, A., C. A. Dalton, C. H. Langmuir, Y. Su and J. G. Schilling (2013). "The mean composition of ocean ridge basalts." Geochemistry, Geophysics, Geosystems **14**(3): 489-518.
Gao, C. G., H. J. B. Dick, Y. Liu and H. Y. Zhou (2016). "Melt extraction and mantle source at a Southwest Indian Ridge Dragon Bone amagmatic segment on the Marion Rise." Lithos **246**: 48-60.
Gavrilenko, M., M. Krawczynski, P. Ruprecht, W. Li and J. G. Catalano (2019). "The quench control of water estimates in convergent margin magmas." American Mineralogist **104**(7): 936-948.
Gibson, S. A., E. E. Rooks, J. A. Day, C. M. Petrone and P. T. Leat (2020). "The role of sub-continental mantle as both "sink" and "source" in deep Earth volatile cycles." Geochimica et Cosmochimica Acta.
Giovanardi, T., T. Morishita, A. Zanetti, M. Mazzucchelli and R. Vannucci (2013). "Igneous sapphirine as a product of melt-peridotite interactions in the Finero Phlogopite-Peridotite Massif, Western Italian Alps." European Journal of Mineralogy **25**(1): 17-31.
Grant, K., J. Ingrin, J. P. Lorand and P. Dumas (2007). "Water partitioning between mantle minerals from peridotite xenoliths." Contributions to Mineralogy and Petrology **154**(1): 15-34.
Grimes, C. B., M. J. Cheadle, B. E. John, P. W. Reiners and J. L. Wooden (2011). "Cooling rates and the depth of detachment faulting at oceanic core complexes: Evidence from zircon Pb/U and (U-Th)/He ages." Geochemistry, Geophysics, Geosystems **12**(3).
Grimes, C. B., B. E. John, M. J. Cheadle, F. K. Mazdab, J. L. Wooden, S. Swapp and J. J. Schwartz (2009). "On the occurrence, trace element geochemistry, and crystallization history of zircon from in situ ocean lithosphere." Contributions to Mineralogy and Petrology **158**(6): 757.
Grimes, C. B., B. E. John, M. J. Cheadle and J. L. Wooden (2008). "Protracted construction of gabbroic crust at a slow spreading ridge: Constraints from 206Pb/238U zircon ages from

Atlantis Massif and IODP Hole U1309D (30 N, MAR)." Geochemistry, Geophysics, Geosystems **9**(8).
Grove, T. L., M. B. Baker, R. C. Price, S. W. Parman, L. T. Elkins-Tanton, N. Chatterjee and O. Müntener (2005). "Magnesian andesite and dacite lavas from Mt. Shasta, northern California: products of fractional crystallization of H 2 O-rich mantle melts." Contributions to Mineralogy and Petrology **148**(5): 542-565.
Grove, T. L., N. Chatterjee, S. W. Parman and E. Médard (2006). "The influence of H2O on mantle wedge melting." Earth and Planetary Science Letters **249**(1-2): 74-89.
Grove, T. L., L. T. Elkins-Tanton, S. W. Parman, N. Chatterjee, O. Müntener and G. A. Gaetani (2003). "Fractional crystallization and mantle-melting controls on calc-alkaline differentiation trends." Contributions to Mineralogy and Petrology **145**(5): 515-533.
Guggino, S. (2012). Fluorine partitioning between nominally anhydrous minerals (olivine, clinopyroxene, and plagioclase) and silicate melt using secondary ion mass spectrometry and newly synthesized basaltic fluorine microanalytical glass standards, Arizona State University.
Guggino, S. and R. Hervig (2012). "Fluorine partitioning between nominally anhydrous minerals (cpx, ol, plag) and silicate melt." AGUFM **2012**: V31D-2828.
Haggerty, S. E. (1978). "Mineralogical contraints on Curie isotherms in deep crustal magnetic anomalies." Geophysical Research Letters **5**(2): 105-108.
Hamelin, C., A. Bezos, L. Dosso, J. Escartin, M. Cannat and C. Mevel (2013). "Atypically depleted upper mantle component revealed by Hf isotopes at Lucky Strike segment." Chemical Geology **341**: 128-139.
Hamilton, D., C. W. Burnham and E. Osborn (1964). "The solubility of water and effects of oxygen fugacity and water content on crystallization in mafic magmas." Journal of Petrology **5**(1): 21-39.
Harvey, J., A. Gannoun, K. W. Burton, N. W. Rogers, O. Alard and I. J. Parkinson (2006). "Ancient melt extraction from the oceanic upper mantle revealed by Re-Os isotopes in abyssal peridotites from the Mid-Atlantic ridge." Earth and Planetary Science Letters **244**(3-4): 606-621.
Hauri, E., J. Wang, J. E. Dixon, P. L. King, C. Mandeville and S. Newman (2002). "SIMS analysis of volatiles in silicate glasses: 1. Calibration, matrix effects and comparisons with FTIR." Chemical Geology **183**(1-4): 99-114.
Hauri, E. H. (2002). "Osmium isotopes and mantle convection." Philosophical Transactions of the Royal Society of London Series a-Mathematical Physical and Engineering Sciences **360**(1800): 2371-2382.
Hauri, E. H., G. A. Gaetani and T. H. Green (2006). "Partitioning of water during melting of the Earth's upper mantle at H2O-undersaturated conditions." Earth and Planetary Science Letters **248**(3-4): 715-734.
Hedenquist, J. W., A. Arribas and T. J. Reynolds (1998). "Evolution of an intrusion-centered hydrothermal system; Far Southeast-Lepanto porphyry and epithermal Cu-Au deposits, Philippines." Economic Geology **93**(4): 373-404.
Hellebrand, E., J. E. Snow, P. Hoppe and A. W. Hofmann (2002). "Garnet-field melting and late-stage refertilization in 'residual' abyssal peridotites from the Central Indian Ridge." Journal of Petrology **43**(12): 2305-2338.

Henrick, S., V. Dobrosavljevic, H. Dick and V. Salters (2014). Geochemistry of Basalts from the Asymmetric Spreading Ridge Segment at 16.5°N on the Mid-Atlantic Ridge. AGU Fall Meeting Abstracts.
Henrick, S. R. A. (2016). Insights on the Development of Oceanic Core Complexes Through the Geochemistry of Basalts at 16.5°N on the Mid-Atlantic Ridge. Master of Science, Florida State University.
Hirth, G. and D. L. Kohlstedt (1995). "Experimental Constraints on the Dynamics of the Partially Molten Upper-Mantle .2. Deformation in the Dislocation Creep Regime." Journal of Geophysical Research-Solid Earth **100**(B8): 15441-15449.
Hirth, G. and D. L. Kohlstedt (1996). "Water in the oceanic upper mantle: implications for rheology, melt extraction and the evolution of the lithosphere." Earth and Planetary Science Letters **144**(1-2): 93-108.
Humphreys, E. R. and Y. Niu (2009). "On the composition of ocean island basalts (OIB): The effects of lithospheric thickness variation and mantle metasomatism." Lithos **112**(1-2): 118-136.
Ireland, T. R. and I. S. Williams (2003). "Considerations in zircon geochronology by SIMS." Reviews in mineralogy and geochemistry **53**(1): 215-241.
Ishimaru, S., S. Arai, Y. Ishida, M. Shirasaka and V. M. Okrugin (2007). "Melting and multi-stage metasomatism in the mantle wedge beneath a frontal arc inferred from highly depleted peridotite xenoliths from the Avacha volcano, Southern Kamchatka." Journal of Petrology **48**(2): 395-433.
Jackson, S. E. (2008). "LAMTRACE data reduction software for LA-ICP-MS." Mineralogical Association of Canada Short Course Series **40**: 305-307.
Jagoutz, O. and M. D. Behn (2013). "Foundering of lower island-arc crust as an explanation for the origin of the continental Moho." Nature **504**(7478): 131-134.
Jagoutz, O., P. Bouilhol, U. Schaltegger and O. Müntener (2019). "The isotopic evolution of the Kohistan Ladakh arc from subduction initiation to continent arc collision." Geological Society, London, Special Publications **483**(1): 165-182.
Jagoutz, O., O. Müntener, J.-P. Burg, P. Ulmer and E. Jagoutz (2006). "Lower continental crust formation through focused flow in km-scale melt conduits: The zoned ultramafic bodies of the Chilas Complex in the Kohistan island arc (NW Pakistan)." Earth and Planetary Science Letters **242**(3-4): 320-342.
Jagoutz, O., O. Müntener, M. W. Schmidt and J.-P. Burg (2011). "The roles of flux-and decompression melting and their respective fractionation lines for continental crust formation: Evidence from the Kohistan arc." Earth and Planetary Science Letters **303**(1-2): 25-36.
Jagoutz, O., O. Muntener, M. W. Schmidt and J. P. Burg (2011). "The roles of flux- and decompression melting and their respective fractionation lines for continental crust formation: Evidence from the Kohistan arc." Earth and Planetary Science Letters **303**(1-2): 25-36.
Jagoutz, O., O. Müntener, P. Ulmer, T. Pettke, J.-P. Burg, H. Dawood and S. Hussain (2007). "Petrology and mineral chemistry of lower crustal intrusions: the Chilas Complex, Kohistan (NW Pakistan)." Journal of Petrology **48**(10): 1895-1953.
Jagoutz, O. and M. W. Schmidt (2012). "The formation and bulk composition of modern juvenile continental crust: The Kohistan arc." Chemical Geology **298**: 79-96.
Jagoutz, O. and M. W. Schmidt (2013). "The composition of the foundered complement to the continental crust and a re-evaluation of fluxes in arcs." Earth and Planetary Science Letters **371**: 177-190.

Jagoutz, O. E. (2010). "Construction of the granitoid crust of an island arc. Part II: a quantitative petrogenetic model." Contributions to Mineralogy and Petrology **160**(3): 359-381.
Janney, P. E., A. P. Le Roex and R. W. Carlson (2005). "Hafnium isotope and trace element constraints on the nature of mantle heterogeneity beneath the central Southwest Indian Ridge (13 degrees E to 47 degrees E)." Journal of Petrology **46**(12): 2427-2464.
Jean, M. M., J. W. Shervais, S. H. Choi and S. B. Mukasa (2010). "Melt extraction and melt refertilization in mantle peridotite of the Coast Range ophiolite: an LA-ICP-MS study." Contributions to Mineralogy and Petrology **159**(1): 113-136.
Jenner, F. E. and H. S. C. O'Neill (2012). "Analysis of 60 elements in 616 ocean floor basaltic glasses." Geochemistry, Geophysics, Geosystems **13**(2).
John, B. E. and M. J. Cheadle (2010). "Deformation and alteration associated with oceanic and continental detachment fault systems: Are they similar." Diversity of Hydrothermal Systems on Slow Spreading Ocean Ridges, Geophys. Monogr. Ser **188**: 175-205.
John, B. E., M. J. Cheadle, J. S. Gee, C. B. Grimes, A. Morris and N. Pressling (2009). Data report: Spatial and temporal evolution of slow spread oceanic crust—Graphic sections of core recovered from IODP Hole U1309D, Atlantis Massif, 30 N, MAR (including Pb/U zircon geochronology and magnetic remanence data). Proceedings of the Integrated Ocean Drilling Program.
John, B. E., D. A. Foster, J. M. Murphy, M. J. Cheadle, A. G. Baines, C. M. Fanning and P. Copeland (2004). "Determining the cooling history of in situ lower oceanic crust—Atlantis Bank, SW Indian Ridge." Earth and Planetary Science Letters **222**(1): 145-160.
John, T., M. Scambelluri, M. Frische, J. D. Barnes and W. Bach (2011). "Dehydration of subducting serpentinite: implications for halogen mobility in subduction zones and the deep halogen cycle." Earth and Planetary Science Letters **308**(1-2): 65-76.
Karato, S.-i. (2003). "Mapping water content in upper mantle." Geophysical Monograph-American Geophysical Union **138**: 135-152.
Kay, R. W. and S. Mahlburg-Kay (1991). "Creation and destruction of lower continental crust." Geologische Rundschau **80**(2): 259-278.
Kelemen, P. B., E. Kikawa, D. J. Miller and S. S. Party (2007). Leg 209 summary: Processes in a 20-km-thick conductive boundary layer beneath the Mid-Atlantic Ridge, 14–16 N. Proc. Ocean Drill. Program, Sci. Results.
Kendrick, M., C. Hémond, V. Kamenetsky, L. Danyushevsky, C. W. Devey, T. Rodemann, M. Jackson and M. Perfit (2017). "Seawater cycled throughout Earth's mantle in partially serpentinized lithosphere." Nature Geoscience **10**(3): 222-228.
Kendrick, M. A., M. G. Jackson, A. J. Kent, E. H. Hauri, P. J. Wallace and J. Woodhead (2014). "Contrasting behaviours of CO2, S, H2O and halogens (F, Cl, Br, and I) in enriched-mantle melts from Pitcairn and Society seamounts." Chemical Geology **370**: 69-81.
Khan, M. A., R. J. Stern, R. F. Gribble and B. F. Windley (1997). "Geochemical and isotopic constraints on subduction polarity, magma sources, and palaeogeography of the Kohistan intra-oceanic arc, northern Pakistan Himalaya." Journal of the Geological Society **154**(6): 935-946.
Khitarov, N., A. Kadik and E. Lebedev (1968). "Solubility of water in a basalt melt." Geokhimia **7**: 763-772.
Klemm, L. M., T. Pettke and C. A. Heinrich (2008). "Fluid and source magma evolution of the Questa porphyry Mo deposit, New Mexico, USA." Mineralium Deposita **43**(5): 533.

Konzett, J. and D. J. Frost (2009). "The high P–T stability of hydroxyl-apatite in natural and simplified MORB—an experimental study to 15 GPa with implications for transport and storage of phosphorus and halogens in subduction zones." Journal of Petrology **50**(11): 2043-2062.
Krawczynski, M. J., T. L. Grove and H. Behrens (2012). "Amphibole stability in primitive arc magmas: effects of temperature, H 2 O content, and oxygen fugacity." Contributions to Mineralogy and Petrology **164**(2): 317-339.
Kumamoto, K. M., J. M. Warren and E. H. Hauri (2017). "New SIMS reference materials for measuring water in upper mantle minerals." American Mineralogist **102**(3): 537-547.
le Roux, P. J., S. B. Shirey, E. H. Hauri, M. R. Perfit and J. F. Bender (2006). "The effects of variable sources, processes and contaminants on the composition of northern EPR MORB (8–10 N and 12–14 N): Evidence from volatiles (H2O, CO2, S) and halogens (F, Cl)." Earth and Planetary Science Letters **251**(3-4): 209-231.
Le Roux, V., H. J. B. Dick and N. Shimizu (2014). "Tracking flux melting and melt percolation in supra-subduction peridotites (Josephine ophiolite, USA)." Contributions to Mineralogy and Petrology **168**(4).
Le Voyer, M., E. Cottrell, K. A. Kelley, M. Brounce and E. H. Hauri (2015). "The effect of primary versus secondary processes on the volatile content of MORB glasses: An example from the equatorial Mid-Atlantic Ridge (5° N–3° S)." Journal of Geophysical Research: Solid Earth **120**(1): 125-144.
Le Voyer, M., E. Rose-Koga, N. Shimizu, T. Grove and P. Schiano (2010). "Two contrasting H2O-rich components in primary melt inclusions from Mount Shasta." Journal of Petrology **51**(7): 1571-1595.
Lee, C.-T. A. (2005). "Trace element evidence for hydrous metasomatism at the base of the North American lithosphere and possible association with Laramide low-angle subduction." The Journal of Geology **113**(6): 673-685.
Lee, C.-T. A. (2006). "Laser ablation ICP-MS: data reduction." Available from www. cinty lee. org/s/ LASERABLATION ICP. pdf.
Lee, C.-T. A. and M. Tang (2020). "How to make porphyry copper deposits." Earth and Planetary Science Letters **529**: 115868.
Lee, C. T. A. (2003). "Compositional variation of density and seismic velocities in natural peridotites at STP conditions: Implications for seismic imaging of compositional heterogeneities in the upper mantle." Journal of Geophysical Research-Solid Earth **108**(B9).
Li, H.-Y., R.-X. Chen, Y.-F. Zheng and Z. Hu (2018). "Water in garnet pyroxenite from the Sulu orogen: Implications for crust-mantle interaction in continental subduction zone." Chemical Geology **478**: 18-38.
Li, P., Q.-K. Xia, L. Dallai, E. Bonatti, D. Brunelli, A. Cipriani and M. Ligi (2020). "High H 2 O Content in Pyroxenes of Residual Mantle Peridotites at a Mid Atlantic Ridge Segment." Scientific Reports **10**(1): 1-11.
Li, Z. X. A., C. T. A. Lee, A. H. Peslier, A. Lenardic and S. J. Mackwell (2008). "Water contents in mantle xenoliths from the Colorado Plateau and vicinity: Implications for the mantle rheology and hydration-induced thinning of continental lithosphere." Journal of Geophysical Research: Solid Earth **113**(B9).
Liang, Y. and B. D. Liu (2016). "Simple models for disequilibrium fractional melting and batch melting with application to REE fractionation in abyssal peridotites." Geochimica Et Cosmochimica Acta **173**: 181-197.

Lissenberg, C. J., M. Rioux, N. Shimizu, S. A. Bowring and C. Mével (2009). "Zircon dating of oceanic crustal accretion." Science **323**(5917): 1048-1050.
Lloyd, A. S., E. Ferriss, P. Ruprecht, E. H. Hauri, B. R. Jicha and T. Plank (2016). "An assessment of clinopyroxene as a recorder of magmatic water and magma ascent rate." Journal of Petrology **57**(10): 1865-1886.
Ludwig, K. R. and B. G. Center (2009). "A user's manual." Barkeley Geochonology Center: Berkeley, CA, USA: 100.
Luffi, P., J. B. Saleeby, C. T. A. Lee and M. N. Ducea (2009). "Lithospheric mantle duplex beneath the central Mojave Desert revealed by xenoliths from Dish Hill, California." Journal of Geophysical Research: Solid Earth **114**(B3).
MacLeod, C. J., R. Searle, B. Murton, J. Casey, C. Mallows, S. Unsworth, K. Achenbach and M. Harris (2009). "Life cycle of oceanic core complexes." Earth and Planetary Science Letters **287**(3-4): 333-344.
Mallick, S., H. J. B. Dick, A. Sachi-Kocher and V. J. M. Salters (2014). "Isotope and trace element insights into heterogeneity of subridge mantle." Geochemistry Geophysics Geosystems **15**(6): 2438-2453.
Marschall, H. R. (2005). Lithium, beryllium and boron in high-pressure metamorphic rocks from Syros (Greece).
Marschall, H. R., R. Altherr, K. Gméling and Z. Kasztovszky (2009). "Lithium, boron and chlorine as tracers for metasomatism in high-pressure metamorphic rocks: a case study from Syros (Greece)." Mineralogy and Petrology **95**(3-4): 291.
Marschall, H. R., R. Altherr, T. Ludwig, A. Kalt, K. Gméling and Z. Kasztovszky (2006). "Partitioning and budget of Li, Be and B in high-pressure metamorphic rocks." Geochimica et Cosmochimica Acta **70**(18): 4750-4769.
Marshall, E. W., J. C. Lassiter and J. D. Barnes (2018). "On the (mis) behavior of water in the mantle: Controls on nominally anhydrous mineral water content in mantle peridotites." Earth and Planetary Science Letters **499**: 219-229.
McDade, P., J. D. Blundy and B. J. Wood (2003). "Trace element partitioning on the Tinaquillo Lherzolite solidus at 1.5 GPa." Physics of the Earth and Planetary Interiors **139**(1-2): 129-147.
Mckenzie, D. and M. J. Bickle (1988). "The Volume and Composition of Melt Generated by Extension of the Lithosphere." Journal of Petrology **29**(3): 625-679.
Michael, P. (1995). "Regionally distinctive sources of depleted MORB: Evidence from trace elements and H2O." Earth and Planetary Science Letters **131**(3-4): 301-320.
Michael, P. J. and J.-G. Schilling (1989). "Chlorine in mid-ocean ridge magmas: evidence for assimilation of seawater-influenced components." Geochimica et Cosmochimica Acta **53**(12): 3131-3143.
Mitchell, A. L., G. A. Gaetani, J. A. O'leary and E. H. Hauri (2017). "H 2 O solubility in basalt at upper mantle conditions." Contributions to Mineralogy and Petrology **172**(10): 85.
Morgan, J. P. (2001). "Thermodynamics of pressure release melting of a veined plum pudding mantle." Geochemistry Geophysics Geosystems **2**.
Mosenfelder, J. L. and G. R. Rossman (2013). "Analysis of hydrogen and fluorine in pyroxenes: I. Orthopyroxene." American Mineralogist **98**(5-6): 1026-1041.
Mosenfelder, J. L. and G. R. Rossman (2013). "Analysis of hydrogen and fluorine in pyroxenes: II. Clinopyroxene." American Mineralogist **98**(5-6): 1042-1054.

Müntener, O., P. B. Kelemen and T. L. Grove (2001). "The role of H 2 O during crystallization of primitive arc magmas under uppermost mantle conditions and genesis of igneous pyroxenites: an experimental study." Contributions to Mineralogy and Petrology **141**(6): 643-658.
Müntener, O. and P. Ulmer (2006). "Experimentally derived high-pressure cumulates from hydrous arc magmas and consequences for the seismic velocity structure of lower arc crust." Geophysical Research Letters **33**(21).
Müntener, O. and P. Ulmer (2018). "Arc crust formation and differentiation constrained by experimental petrology." American Journal of Science **318**(1): 64-89.
Mysen, B. (2007). "Partitioning of calcium, magnesium, and transition metals between olivine and melt governed by the structure of the silicate melt at ambient pressure." American Mineralogist **92**(5-6): 844-862.
Mysen, B. O. (2007). "The solution behavior of H2O in peralkaline aluminosilicate melts at high pressure with implications for properties of hydrous melts." Geochimica et Cosmochimica Acta **71**(7): 1820-1834.
Mysen, B. O. and G. D. Cody (2004). "Solubility and solution mechanism of H2O in alkali silicate melts and glasses at high pressure and temperature." Geochimica et Cosmochimica Acta **68**(24): 5113-5126.
Navon, O. and E. Stolper (1987). "Geochemical Consequences of Melt Percolation - the Upper Mantle as a Chromatographic Column." Journal of Geology **95**(3): 285-307.
Newman, S. and J. B. Lowenstern (2002). "VolatileCalc: a silicate melt–H2O–CO2 solution model written in Visual Basic for excel." Computers & Geosciences **28**(5): 597-604.
Niu, Y. L. and R. Hekinian (1997). "Spreading-rate dependence of the extent of mantle melting beneath ocean ridges." Nature **385**(6614): 326-329.
Niu, Y. L. and M. J. O'Hara (2008). "Global correlations of ocean ridge basalt chemistry with axial depth: A new perspective." Journal of Petrology **49**(4): 633-664.
O'Leary, J. A., G. A. Gaetani and E. H. Hauri (2010). "The effect of tetrahedral Al3+ on the partitioning of water between clinopyroxene and silicate melt." Earth and Planetary Science Letters **297**(1-2): 111-120.
Parnell-Turner, R., H. Schouten and D. K. Smith (2016). "Tectonic structure of the Mid-Atlantic Ridge near 16°30′N." Geochemistry, Geophysics, Geosystems **17**(10): 3993-4010.
Pearce, N. J., W. T. Perkins, J. A. Westgate, M. P. Gorton, S. E. Jackson, C. R. Neal and S. P. Chenery (1997). "A compilation of new and published major and trace element data for NIST SRM 610 and NIST SRM 612 glass reference materials." Geostandards newsletter **21**(1): 115-144.
Pertermann, M. and M. M. Hirschmann (2003). "Partial melting experiments on a MORB-like pyroxenite between 2 and 3 GPa: Constraints on the presence of pyroxenite in basalt source regions from solidus location and melting rate." Journal of Geophysical Research-Solid Earth **108**(B2).
Peslier, A. H. (2010). "A review of water contents of nominally anhydrous natural minerals in the mantles of Earth, Mars and the Moon." Journal of Volcanology and Geothermal Research **197**(1-4): 239-258.
Peslier, A. H. and J. F. Luhr (2006). "Hydrogen loss from olivines in mantle xenoliths from Simcoe (USA) and Mexico: Mafic alkalic magma ascent rates and water budget of the sub-continental lithosphere." Earth and Planetary Science Letters **242**(3-4): 302-319.

Philippot, P., P. Agrinier and M. Scambelluri (1998). "Chlorine cycling during subduction of altered oceanic crust." Earth and Planetary Science Letters **161**(1-4): 33-44.
Plank, T., K. A. Kelley, M. M. Zimmer, E. H. Hauri and P. J. Wallace (2013). "Why do mafic arc magmas contain~ 4 wt% water on average?" Earth and Planetary Science Letters **364**: 168-179.
Portnyagin, M., K. Hoernle, P. Plechov, N. Mironov and S. Khubunaya (2007). "Constraints on mantle melting and composition and nature of slab components in volcanic arcs from volatiles (H2O, S, Cl, F) and trace elements in melt inclusions from the Kamchatka Arc." Earth and Planetary Science Letters **255**(1-2): 53-69.
Pouchou, J. and F. Pichoir (1984). "A new model for quantitative x-ray microanalysis. I.--application to the analysis of homogeneous samples." Rech. Aerosp.(3): 167-192.
Pouchou, J. and F. Pichoir (1985). PAP'j (rZ) procedure for improved quantitative microanalysis. Pp. 104À106 in: Microbeam Analysis (JT Armstrong, editor), San Francisco Press, San Francisco, California, USA.
Presnall, D. C., G. H. Gudfinnsson and M. J. Walter (2002). "Generation of mid-ocean ridge basalts at pressures from 1 to 7 GPa." Geochimica Et Cosmochimica Acta **66**(12): 2073-2090.
Reid, I. and H. R. Jackson (1981). "Oceanic Spreading Rate and Crustal Thickness." Marine Geophysical Researches **5**(2): 165-172.
Reston, T. J., W. Weinrebe, I. Grevemeyer, E. R. Flueh, N. Mitchell, L. Kirstein, C. Kopp and H. Kopp (2002). "A rifted inside corner massif on the Mid-Atlantic Ridge at 5 S." Earth and Planetary Science Letters **200**(3-4): 255-269.
Richards, J. (2003). "Tectono-magmatic precursors for porphyry Cu-(Mo-Au) deposit formation." Economic Geology **98**(8): 1515-1533.
Rioux, M., M. J. Cheadle, B. E. John and S. A. Bowring (2016). "The temporal and spatial distribution of magmatism during lower crustal accretion at an ultraslow-spreading ridge: High-precision U–Pb zircon dating of ODP Holes 735B and 1105A, Atlantis Bank, Southwest Indian Ridge." Earth and Planetary Science Letters **449**: 395-406.
Ritsema, J. and R. M. Allen (2003). "The elusive mantle plume." Earth and Planetary Science Letters **207**(1-4): 1-12.
Roden, M. F. (1981). "Origin of coexisting minette and ultramafic breccia, Navajo volcanic field." Contributions to Mineralogy and Petrology **77**(2): 195-206.
Rose-Koga, E., K. Koga, M. Moreira, I. Vlastélic, M. Jackson, M. J. Whitehouse, N. Shimizu and N. Habib (2017). "Geochemical systematics of Pb isotopes, fluorine, and sulfur in melt inclusions from São Miguel, Azores." Chemical Geology **458**: 22-37.
Rose-Koga, E., N. Shimizu, J. Devidal, K. Koga and M. Le Voyer (2008). "Investigation of F, S, and Cl standards by ion probe and electron microprobe." AGUFM **2008**: V31B-2145.
Rose-Koga, E. F., K. T. Koga, M. Hamada, T. Hélouis, M. J. Whitehouse and N. Shimizu (2014). "Volatile (F and Cl) concentrations in Iwate olivine-hosted melt inclusions indicating low-temperature subduction." Earth, Planets and Space **66**(1): 81.
Rose-Koga, E. F., K. T. Koga, P. Schiano, M. Le Voyer, N. Shimizu, M. J. Whitehouse and R. Clocchiatti (2012). "Mantle source heterogeneity for South Tyrrhenian magmas revealed by Pb isotopes and halogen contents of olivine-hosted melt inclusions." Chemical Geology **334**: 266-279.

Saal, A. E., E. H. Hauri, C. H. Langmuir and M. R. Perfit (2002). "Vapour undersaturation in primitive mid-ocean-ridge basalt and the volatile content of Earth's upper mantle." Nature **419**(6906): 451-455.
Sadofsky, S. J., M. Portnyagin, K. Hoernle and P. van den Bogaard (2008). "Subduction cycling of volatiles and trace elements through the Central American volcanic arc: evidence from melt inclusions." Contributions to Mineralogy and Petrology **155**(4): 433-456.
Salters, V. J. and A. Stracke (2004). "Composition of the depleted mantle." Geochemistry, Geophysics, Geosystems **5**(5).
Salters, V. J. M., S. Mallick, S. R. Hart, C. E. Langmuir and A. Stracke (2011). "Domains of depleted mantle: New evidence from hafnium and neodymium isotopes (vol 12, Q08001, 2011)." Geochemistry Geophysics Geosystems **12**.
Sauter, D., M. Cannat, S. Roumejon, M. Andreani, D. Birot, A. Bronner, D. Brunelli, J. Carlut, A. Delacour, V. Guyader, C. J. MacLeod, G. Manatschal, V. Mendel, B. Menez, V. Pasini, E. Ruellan and R. Searle (2013). "Continuous exhumation of mantle-derived rocks at the Southwest Indian Ridge for 11 million years." Nature Geoscience **6**(4): 314-320.
Sautter, V., O. Jaoul and F. Abel (1988). "Aluminum diffusion in diopside using the27Al (p, γ) 28Si nuclear reaction: preliminary results." Earth and Planetary Science Letters **89**(1): 109-114.
Scambelluri, M., O. Müntener, L. Ottolini, T. T. Pettke and R. Vannucci (2004). "The fate of B, Cl and Li in the subducted oceanic mantle and in the antigorite breakdown fluids." Earth and Planetary Science Letters **222**(1): 217-234.
Schaeffer, A. J. and S. Lebedev (2013). "Global shear speed structure of the upper mantle and transition zone." Geophysical Journal International **194**(1): 417-449.
Schaffer, L. A., A. H. Peslier, A. D. Brandon, M. Bizimis, R. Gibler, M. Norman and J. Harvey (2019). "Effects of melting, subduction-related metasomatism, and sub-solidus equilibration on the distribution of water contents in the mantle beneath the Rio Grande Rift." Geochimica et Cosmochimica Acta **266**: 351-381.
Schaltegger, U., G. Zeilinger, M. Frank and J. P. Burg (2002). "Multiple mantle sources during island arc magmatism: U–Pb and Hf isotopic evidence from the Kohistan arc complex, Pakistan." Terra Nova **14**(6): 461-468.
Schärer, U. (1984). "The effect of initial230Th disequilibrium on young UPb ages: the Makalu case, Himalaya." Earth and planetary science letters **67**(2): 191-204.
Schoolmeesters, N., M. J. Cheadle, B. E. John, P. W. Reiners, J. Gee and C. B. Grimes (2012). "The cooling history and the depth of detachment faulting at the Atlantis Massif oceanic core complex." Geochemistry, Geophysics, Geosystems **13**(10).
Schroeder, T., B. John and B. R. Frost (2002). "Geologic implications of seawater circulation through peridotite exposed at slow-spreading mid-ocean ridges." Geology **30**(4): 367-370.
Schwartz, J. J., B. E. John, M. J. Cheadle, E. A. Miranda, C. B. Grimes, J. L. Wooden and H. J. Dick (2005). "Dating the growth of oceanic crust at a slow-spreading ridge." Science **310**(5748): 654-657.
Selverstone, J. and Z. D. Sharp (2011). "Chlorine isotope evidence for multicomponent mantle metasomatism in the Ivrea Zone." Earth and Planetary Science Letters **310**(3-4): 429-440.
Seyler, M., J. P. Lorand, H. J. B. Dick and M. Drouin (2007). "Pervasive melt percolation reactions in ultra-depleted refractory harzburgites at the Mid-Atlantic Ridge, 15 degrees 20 ' N: ODP Hole 1274A." Contributions to Mineralogy and Petrology **153**(3): 303-319.

Seyler, M., J. P. Lorand, M. J. Toplis and G. Godard (2004). "Asthenospheric metasomatism beneath the mid-ocean ridge: Evidence from depleted abyssal peridotites." Geology **32**(4): 301-304.
Shaw, A. M., M. D. Behn, S. E. Humphris, R. A. Sohn and P. M. Gregg (2010). "Deep pooling of low degree melts and volatile fluxes at the 85 E segment of the Gakkel Ridge: evidence from olivine-hosted melt inclusions and glasses." Earth and Planetary Science Letters **289**(3-4): 311-322.
Shervais, J. (1978). "Ultramafic and mafic layers in the Alpine-type lherzolite massif at Balmuccia, NW Italy."
Shimizu, K., A. E. Saal, C. E. Myers, A. N. Nagle, E. H. Hauri, D. W. Forsyth, V. S. Kamenetsky and Y. Niu (2016). "Two-component mantle melting-mixing model for the generation of mid-ocean ridge basalts: implications for the volatile content of the Pacific upper mantle." Geochimica et Cosmochimica Acta **176**: 44-80.
Silantyev, S., N. Bortnikov, K. Shatagin, V. Bel'tenev, N. Kononkova, Y. V. Bychkova and E. Krasnova (2016). "Petrogenetic conditions at 18–20 N MAR: interaction between hydrothermal and magmatic systems." Petrology **24**(4): 336-366.
Silantyev, S., N. Bortnikov, K. Shatagin, Y. V. Bychkova, E. Krasnova and V. Bel'tenev (2015). "Peridotite-basalt association at MAR between 19° 42′ and 19° 59′ N: Evaluation of petrogenetic conditions and material balance during hydrothermal transformation of the oceanic crust." Petrology **23**(1): 1-21.
Simon, N. S. C., E. R. Neumann, C. Bonadiman, M. Coltorti, G. Delpech, M. Gregoire and E. Widom (2008). "Ultra-refractory domains in the oceanic mantle lithosphere sampled as mantle xenoliths at ocean islands." Journal of Petrology **49**(6): 1223-1251.
Sisson, T. and T. Grove (1993). "Experimental investigations of the role of H 2 O in calc-alkaline differentiation and subduction zone magmatism." Contributions to mineralogy and petrology **113**(2): 143-166.
Sisson, T. and G. Layne (1993). "H2O in basalt and basaltic andesite glass inclusions from four subduction-related volcanoes." Earth and Planetary Science Letters **117**(3-4): 619-635.
Smith, D. K., J. Escartín, H. Schouten and J. R. Cann (2008). "Fault rotation and core complex formation: Significant processes in seafloor formation at slow-spreading mid-ocean ridges (Mid-Atlantic Ridge, 13–15 N)." Geochemistry, Geophysics, Geosystems **9**(3).
Smith, D. K., H. Schouten, H. J. Dick, J. R. Cann, V. Salters, H. R. Marschall, F. Ji, D. Yoerger, A. Sanfilippo and R. Parnell-Turner (2014). "Development and evolution of detachment faulting along 50 km of the Mid-Atlantic Ridge near 16.5° N." Geochemistry, Geophysics, Geosystems **15**(12): 4692-4711.
Smith, D. K., H. Schouten, H. J. B. Dick, J. R. Cann, V. Salters, H. R. Marschall, F. W. Ji, D. Yoerger, A. Sanfilippo, R. Parnell-Turner, C. Palmiotto, A. Zheleznov, H. L. Bai, W. Junkin, B. Urann, S. Dick, M. Sulanowska, P. Lemmond and S. Curry (2014). "Development and evolution of detachment faulting along 50 km of the Mid-Atlantic Ridge near 16.5 degrees N." Geochemistry Geophysics Geosystems **15**(12): 4692-4711.
Spilliaert, N., N. Métrich and P. Allard (2006). "S–Cl–F degassing pattern of water-rich alkali basalt: modelling and relationship with eruption styles on Mount Etna volcano." Earth and Planetary Science Letters **248**(3-4): 772-786.
Stacey, J. t. and J. Kramers (1975). "Approximation of terrestrial lead isotope evolution by a two-stage model." Earth and planetary science letters **26**(2): 207-221.

Stracke, A., F. Genske, J. Berndt and J. M. Koornneef (2019). "Ubiquitous ultra-depleted domains in Earth's mantle." Nature Geoscience **12**(10): 851-855.
Straub, S. M. and G. D. Layne (2003). "The systematics of chlorine, fluorine, and water in Izu arc front volcanic rocks: implications for volatile recycling in subduction zones." Geochimica et Cosmochimica Acta **67**(21): 4179-4203.
Sun, C. G. and Y. Liang (2012). "Distribution of REE between clinopyroxene and basaltic melt along a mantle adiabat: effects of major element composition, water, and temperature." Contributions to Mineralogy and Petrology **163**(5): 807-823.
Tahirkheli, R. A. K. and M. Q. Jan (1979). "Geology of Kohistan, Karakorum Himalaya, northern Pakistan." Special issue of the Geological Bulletin of the University of Peshawar, Pakistan **11**(1): 1-30.
Tucholke, B. E., J. Lin and M. C. Kleinrock (1998). "Megamullions and mullion structure defining oceanic metamorphic core complexes on the Mid-Atlantic Ridge." Journal of Geophysical Research: Solid Earth **103**(B5): 9857-9866.
Ulmer, P., R. Kaegi and O. Müntener (2018). "Experimentally derived intermediate to silica-rich arc magmas by fractional and equilibrium crystallization at 1· 0 GPa: An evaluation of phase relationships, compositions, liquid lines of descent and oxygen fugacity." Journal of Petrology **59**(1): 11-58.
Umino, S., K. Kitamura, K. Kanayama, A. Tamura, N. Sakamoto, O. Ishizuka and S. Arai (2015). "Thermal and chemical evolution of the subarc mantle revealed by spinel-hosted melt inclusions in boninite from the Ogasawara (Bonin) Archipelago, Japan." Geology **43**(2): 151-154.
Urann, B., V. Le Roux, K. Hammond, H. Marschall, C.-T. Lee and B. Monteleone (2017). "Fluorine and chlorine in mantle minerals and the halogen budget of the Earth's mantle." Contributions to Mineralogy and Petrology **172**(7): 51.
Urann, B. M., V. Le Roux, T. John, G. M. Beaudoin and J. D. Barnes (2020). "The distribution and abundance of halogens in eclogites: An in situ SIMS perspective of the Raspas Complex (Ecuador)." American Mineralogist: Journal of Earth and Planetary Materials **105**(3): 307-318.
Van den Bleeken, G. and K. T. Koga (2015). "Experimentally determined distribution of fluorine and chlorine upon hydrous slab melting, and implications for F–Cl cycling through subduction zones." Geochimica et Cosmochimica Acta **171**: 353-373.
Wang, D., M. Mookherjee, Y. Xu and S.-i. Karato (2006). "The effect of water on the electrical conductivity of olivine." Nature **443**(7114): 977-980.
Wanless, V., M. Behn, A. Shaw and T. Plank (2014). "Variations in melting dynamics and mantle compositions along the Eastern Volcanic Zone of the Gakkel Ridge: insights from olivine-hosted melt inclusions." Contributions to Mineralogy and Petrology **167**(5): 1005.
Wanless, V., A. Shaw, M. Behn, S. Soule, J. Escartín and C. Hamelin (2015). "Magmatic plumbing at Lucky Strike volcano based on olivine-hosted melt inclusion compositions." Geochemistry, Geophysics, Geosystems **16**(1): 126-147.
Wanless, V. D. and A. M. Shaw (2012). "Lower crustal crystallization and melt evolution at mid-ocean ridges." Nature Geoscience **5**(9): 651-655.
Warren, J. M. (2016). "Global variations in abyssal peridotite compositions." Lithos **248**: 193-219.
Warren, J. M. and E. H. Hauri (2014). "Pyroxenes as tracers of mantle water variations." Journal of Geophysical Research: Solid Earth **119**(3): 1851-1881.

Warren, J. M., N. Shimizu, C. Sakaguchi, H. J. B. Dick and E. Nakamura (2009). "An assessment of upper mantle heterogeneity based on abyssal peridotite isotopic compositions." Journal of Geophysical Research-Solid Earth **114**.
Wasylenki, L. E., M. B. Baker, A. J. R. Kent and E. M. Stolper (2003). "Near-solidus melting of the shallow upper mantle: Partial melting experiments on depleted peridotite." Journal of Petrology **44**(7): 1163-1191.
Williams, C. M. (2007). Oceanic lithosphere magnetization: Marine magnetic investigations of crustal accretion and tectonic processes in mid-ocean ridge environments, WOODS HOLE OCEANOGRAPHIC INSTITUTION MA.
Wilson, S. C., B. J. Murton and R. N. Taylor (2013). "Mantle composition controls the development of an Oceanic Core Complex." Geochemistry Geophysics Geosystems **14**(4): 979-995.
Workman, R. K. and S. R. Hart (2005). "Major and trace element composition of the depleted MORB mantle (DMM)." Earth and Planetary Science Letters **231**(1-2): 53-72.
Wu, J. and K. T. Koga (2013). "Fluorine partitioning between hydrous minerals and aqueous fluid at 1 GPa and 770–947 C: a new constraint on slab flux." Geochimica et Cosmochimica Acta **119**: 77-92.
Zanetti, A., M. Mazzucchelli, G. Rivalenti and R. Vannucci (1999). "The Finero phlogopite-peridotite massif: an example of subduction-related metasomatism." Contributions to Mineralogy and Petrology **134**(2-3): 107-122.
Zhou, H. Y. and H. J. B. Dick (2013). "Thin crust as evidence for depleted mantle supporting the Marion Rise." Nature **494**(7436): 195-200.

9. Supplementary Material

S.2 Supplementary material accompanying Chapter 2

S.2.1 Sample Preparation Procedure For F-Cl Analyses

Our study involved utilizing both glass thin sections and individual grains mounted in indium. We noticed no difference in data quality in one versus the other, and an identical cleaning process was taken for each sample regardless of the mounting medium. Prior to analysis, thin sections were re-polished by hand with 0.25 μm colloidal silica on a velvet pad. Samples were rinsed, then cleaned again on a velvet pad with de-ionized water to remove any remnant polishing compound. Thin sections were then ultra-sonicated in de-ionized water. Sample surfaces were wiped with medical grade sterilized cotton swabs soaked in water and ethanol, alternating between the two until each surface had been wiped three times with each solvent. Samples were wiped dry and immediately placed in a vacuum chamber where they remained until gold coating. In order to reduce the surface discharge, samples were gold-coated to a thickness of 160nm. After that, the samples were placed in the SIMS air lock chamber to pump down for about 12 hours, typically overnight. Although the overnight pump-down procedure improved the quality of our analyses, pump-down times longer than 12 hours did not improve the quality further. It should be noted that compressed air was avoided when drying samples since some compressed air contains trace amounts of fluorine. Individual grains obtained from hand samples were first mounted in epoxy for initial polishing. Each epoxy mount was polished using 200-grit sandpaper, then 400, 800, 5μm, 1μm, and finally 0.25μm colloidal silica. Grains were then removed from their epoxy mount and pressed into indium to avoid potential volatile input from epoxy degassing during analysis. Mounted samples were not ultra-sonicated to avoid grains falling out of their pressed indium. Once pressed mounts were imaged, the above cleaning, gold-coating, and storage procedure was implemented to prepare samples for analysis.

S.2.2 Technical Developments and Analytical Settings for F-Cl Measurement

The challenge in developing a technical protocol for measuring low concentrations (< 1 ppm) of F and Cl in mantle minerals is two-fold. First, some minerals (olivine and pyroxenes) have very low amounts of F and Cl to be ionized. Second, halogens may be present in the sample chamber, which can increase the analysis background and overestimate the halogen content of the sample. The ability to quantify one's background during sample measurement is of the upmost importance, and we caution that not all literature data stands up to rigorous scrutiny regarding sample contamination and background interference.

To minimize the ionization and transmission of the proportion of F and Cl that does not belong to the sample, a strong primary Cs^+ beam of 5.0–7.5nA was used to sputter through the sample surface. In addition, a 30 x 30 μm^2 raster and a 400 μm field aperture were used, which only allowed transmission of ions from the innermost 3.8 μm diameter of the beam crater. Electron gun tuning was critical to reduce surface F and Cl desorption to a minimum. Deflectors, quadrupole lens, ion coil, were re-tuned at each measurement to keep the path of sputtered ions as straight as possible. Secondary magnet mass calibration was done before each measurement, and

mass resolving power was > 6000 (m/dm at 10 % peak height). We measured $^{19}F/^{30}Si$ and $^{35}Cl/^{30}Si$ ratios in glass standards D51-3, D52-5, 519-4-1, 46D, 1649-3, 1654-3, to produce a calibration curve for each session (a typical session is one week). As our analytical procedures improved, F and Cl values in Herasil®® and Synthetic Forsterite decreased until we attained reproducibility for the most recent sessions. Over the course of one year, we also noticed that Herasil®® was systematically associated with lower F and higher Cl concentration compared to Synthetic Forsterite, given us confidence that we observed a real difference in concentrations for those two samples. For all measurement sessions, we assume that Herasil®® contains no F, Synthetic Forsterite contains no Cl, and that F concentrations in Herasil®® and Cl concentrations in Synthetic Forsterite represent our maximum background for F and Cl, respectively, for each session. Although this approach results in large error bars at low concentrations, it is the most conservative approach when no low concentration standards exist. In addition, if any surface contamination remained after our thorough preparation, it should be taken into account by our conservative background error, as the standards and mounts containing Herasil®® and Synthetic Forsterite were cleaned and stored in similar conditions as samples. In Figure 1c and 1d, we illustrate a typical week of measurements. The first day would be dedicated to standard measurements and tuning the instrument to reach the lowest possible F and Cl values in Herasil®® and Synthetic Forsterite, at which point measurements on samples could begin. Herasil® and Synthetic Forsterite were measured again later during the week to check for reproducibility. The average F content in Herasil®® and the average Cl content in Synthetic Forsterite after the machine was tuned to optimal settings would represent our maximum background for that session. Synthetic Forsterite and Herasil®® measured F and Cl concentrations for each analytical session are available in Table 1. Calibration curve 2σ error was no more than 5% for Cl and 10% for F throughout all sessions, implying complete homogeneity of reference materials within error.

S.2.3 Analytical Settings for B, Be, Li Measurements and Major Elements

Li, Be, and B measurements were made at the Institut für Geowissenschaften, Universität Heidelberg using a Cameca IMS 3f ion microprobe with a 10kV/20nA $^{16}O^-$ primary beam as outlined in Marschall et al. (2006). Compositions of mineral phases in Finero samples were determined using a Cameca SX 51 electron microprobe equipped with five wavelength-dispersive spectrometers (Institut für Geowissenschaften, Universität Heidelberg). Operating conditions were 20 nA beam current and 15 kV acceleration voltage. Details on counting times, crystals, standards and detection limits are given in Marschall (2005). PAP correction was applied to the raw data (Pouchou and Pichoir 1984, Pouchou and Pichoir 1985).

Composition of mineral phases in Mid-Atlantic Ridge sample KNR210-05 D41-24 were completed using a JEOL JXA-8200 electron microprobe at the Massachusetts Institute of Technology. A 10nA beam current and 15kV accelerating potential were used for all analyses. Beam diameter was 1 micron. Calibration standards were synthetic diopside-jadeite (DJ35) for cpx, synthetic aluminous orthopyroxene (alp7) for Opx, and natural Marjalotti olivine (marj) for olivine. Data reduction was done using CITZAF software. The counting times used for the phase analyses range was 40s on peak, and 20s on background.

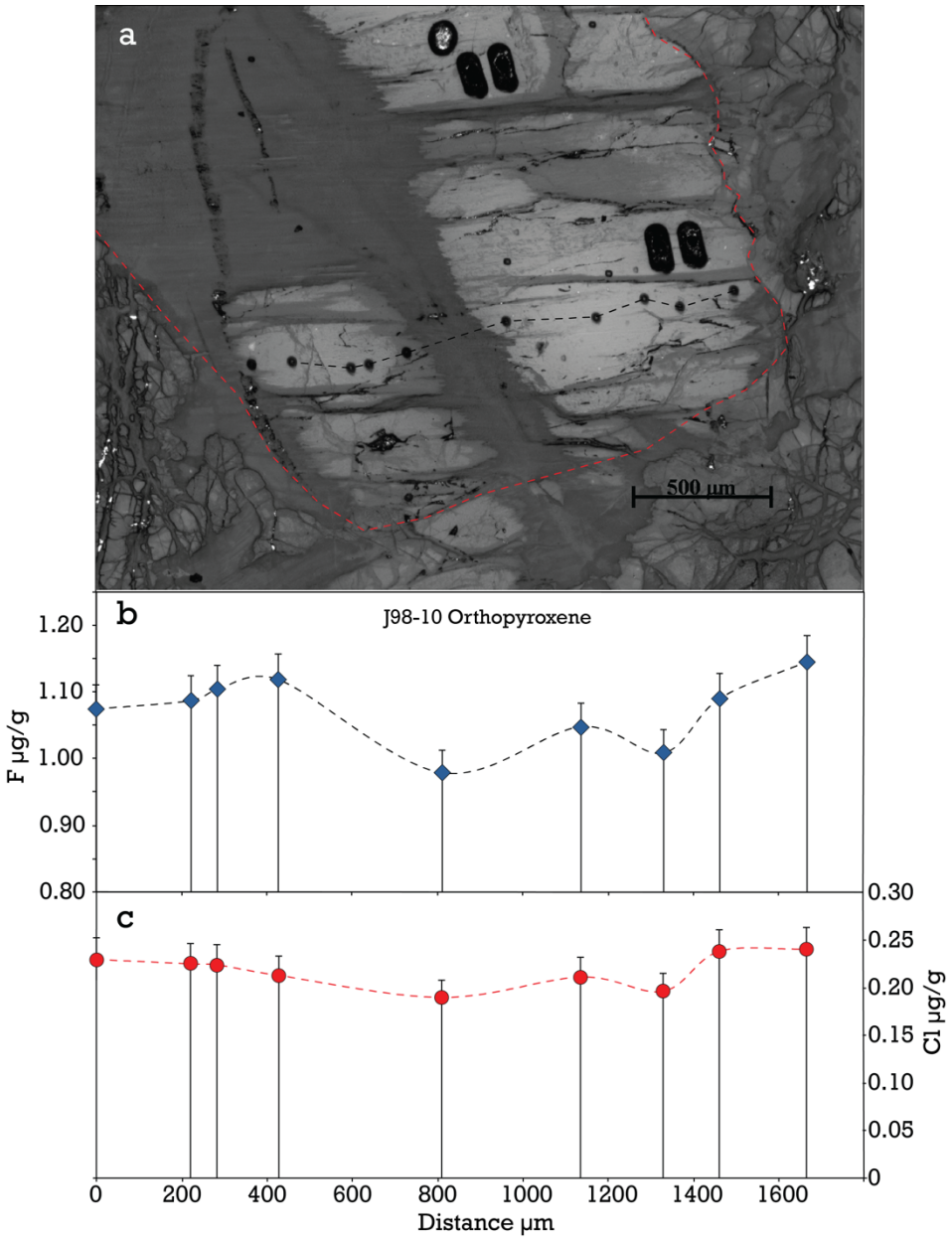

Fig. 2.S1 F and Cl profile across J98-10 orthopyroxene. Positive error bars are internal errors propagated with calibration curve errors. Negative error bars are internal errors propagated with calibration curve errors and maximum background errors monitored by Cl measurements in Synthetic Forsterite and F measurements in Herasil® glass. Individual measurements are reported in Table 3.

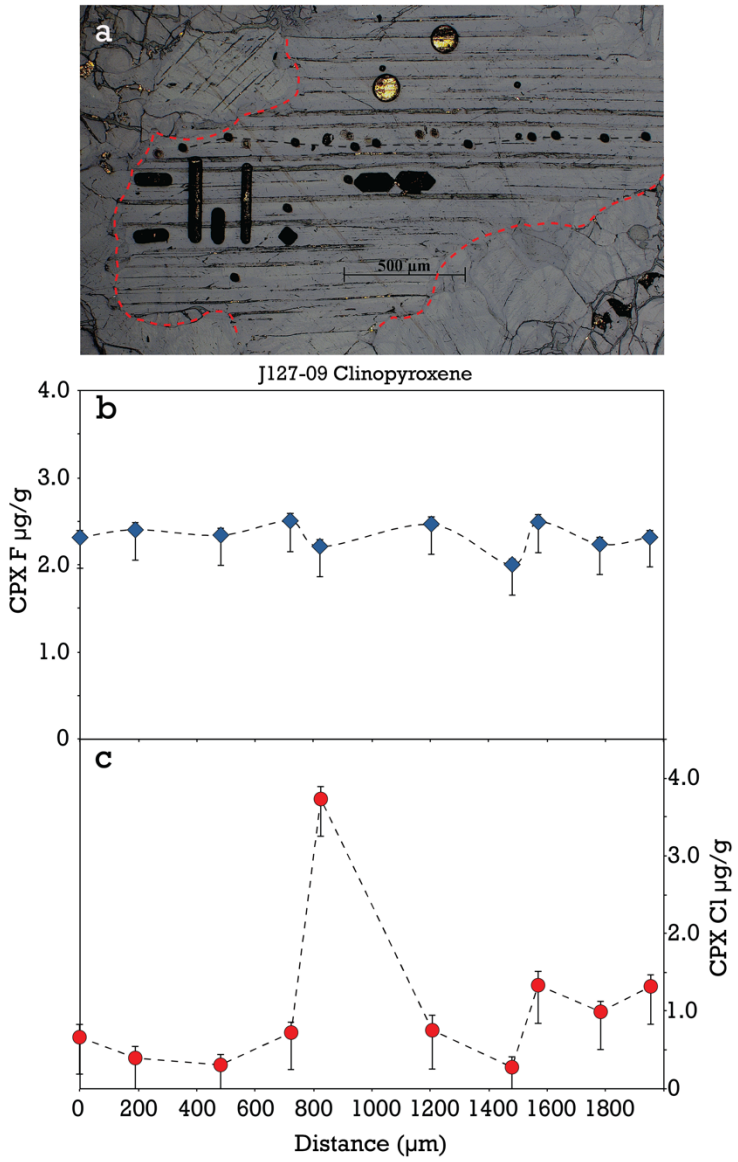

Fig. 2.S2 a. Reflected light photomicrograph of clinopyroxene in J127-09, with grain boundary outlined with red dashed line and SIMS profile denoted with black dashed line. **b.** J127-09 clinopyroxene F concentration profile, showing little to no intra-grain variation. **c.** Cl concentration profile in J127-09 clinopyroxene, showing how the presence of micro-cracks can lead to overestimation of the Cl content of mantle minerals. Positive error bars are internal errors propagated with calibration curve errors. Negative error bars are internal errors propagated with calibration curve errors and maximum background errors monitored by Cl measurements in Synthetic Forsterite and F measurements in Herasil®® glass. Individual measurements are reported in Table 3.

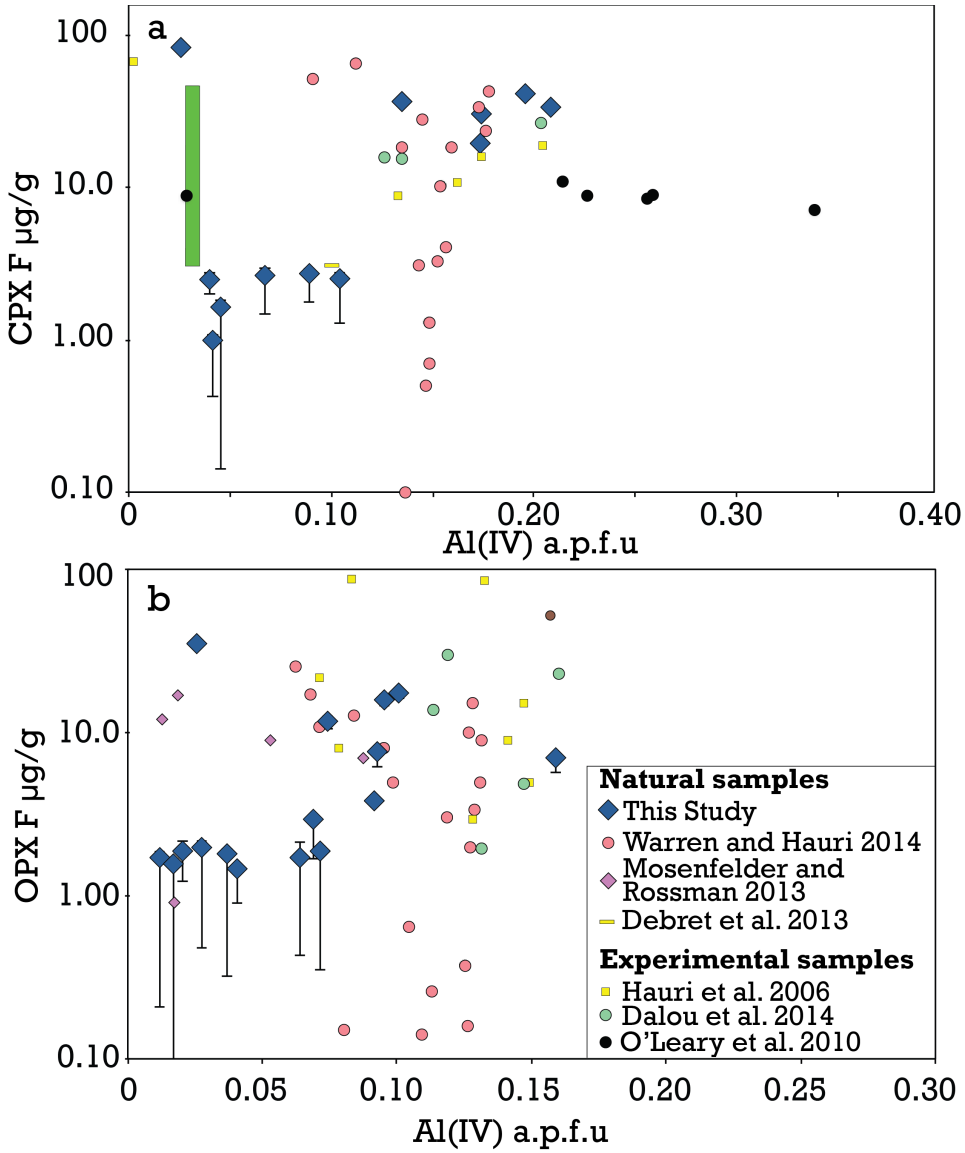

Figure 2.S3 a. Clinopyroxene Al(IV) in atoms per formula unit, plotted against F in µg/g for all samples in this study, as well as literature data (experiments and natural samples). Green bar indicates range of Fin1b profile measurements. **b.** Orthopyroxene Al(IV) in a.p.f.u. plotted against F in µg/g for all samples in this study and available literature (experiments and natural samples). Individual sample measurements can be found in Tables 2 and 4.

S.3 Supplementary material accompanying Chapter 3

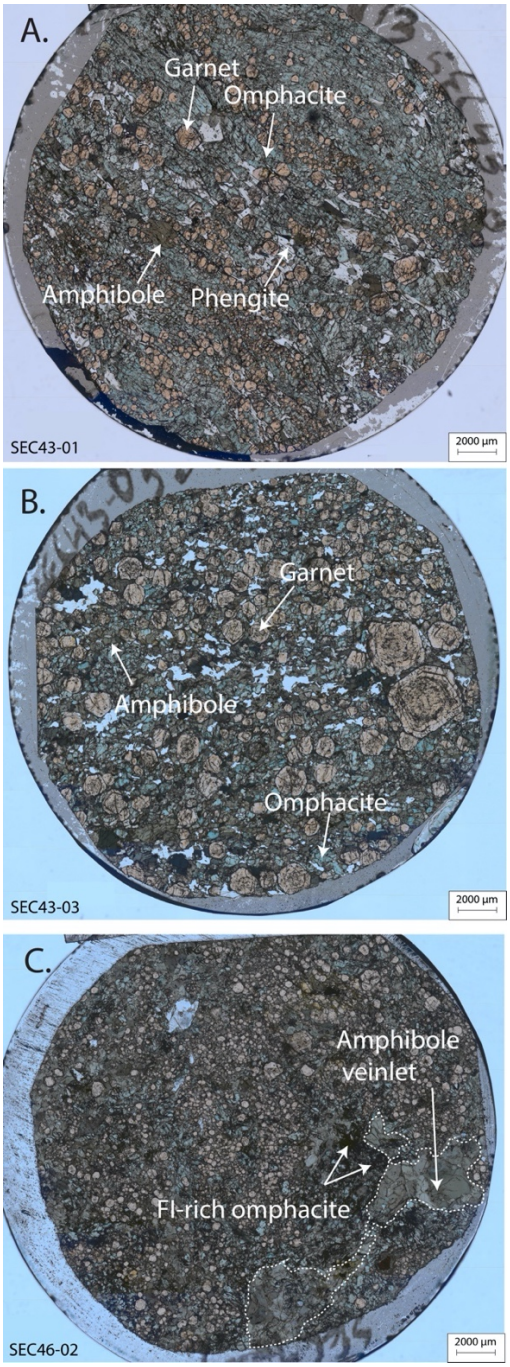

Figure 3.S1. Representative full-section photomicrographs of Raspas samples analyzed in this study. A. Prograde assemblage in SEC43-01 contains garnet porphyroblasts within a matrix of omphacite and lesser quartz and phengite with minor apatite and rutile. The sample shows no evidence for retrogression. B. SEC43-03 megacrystic garnet showing sector zoning with minor quartz. C. Amphibole veinlet in sample SEC46-02, outlined in white dashed line. Adjacent omphacite shows abundant fluid inclusions (dark patches).

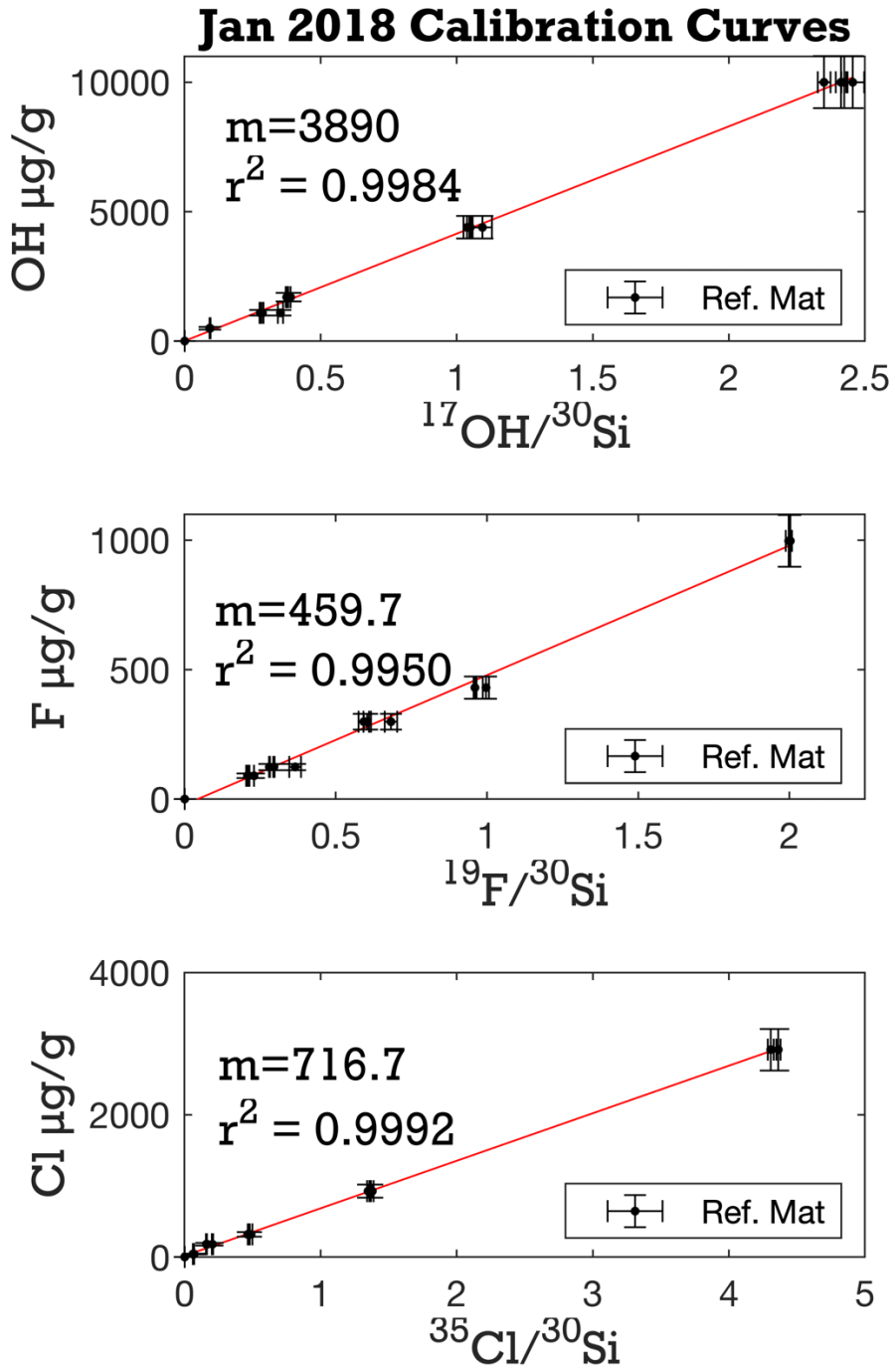

Figure 3.S2. Representative calibration slope used in this study. Calibration slope confidence intervals were calculated with a non-linear bootstrapping technique using 5,000 iterations.

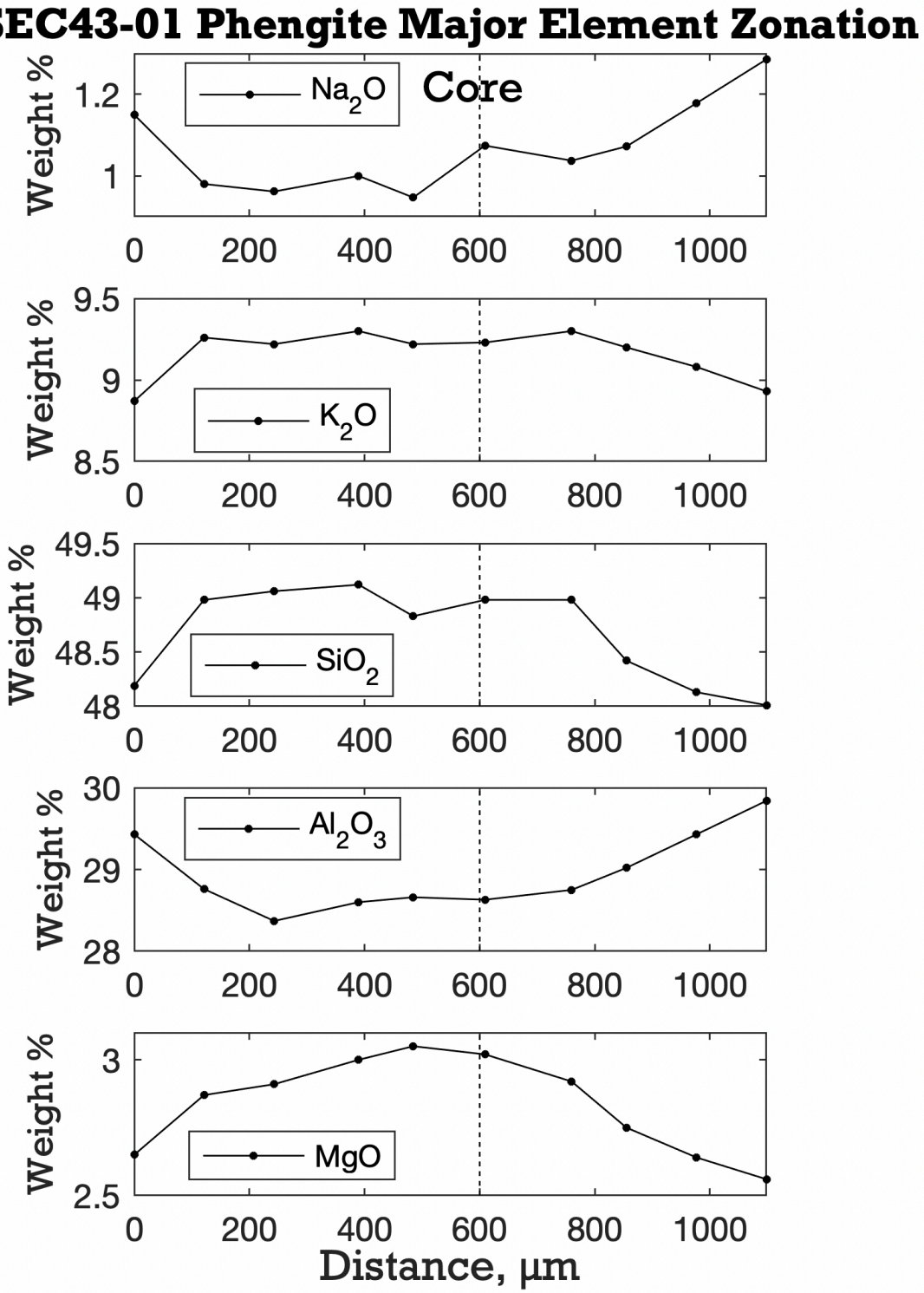

Figure 3.S3. SEC43-01 phengite EMP profile from rim to rim shows Na_2O and Al_2O_3 increases from core to rim, while K_2O, SiO_2, and MgO all decrease toward the grain boundary.

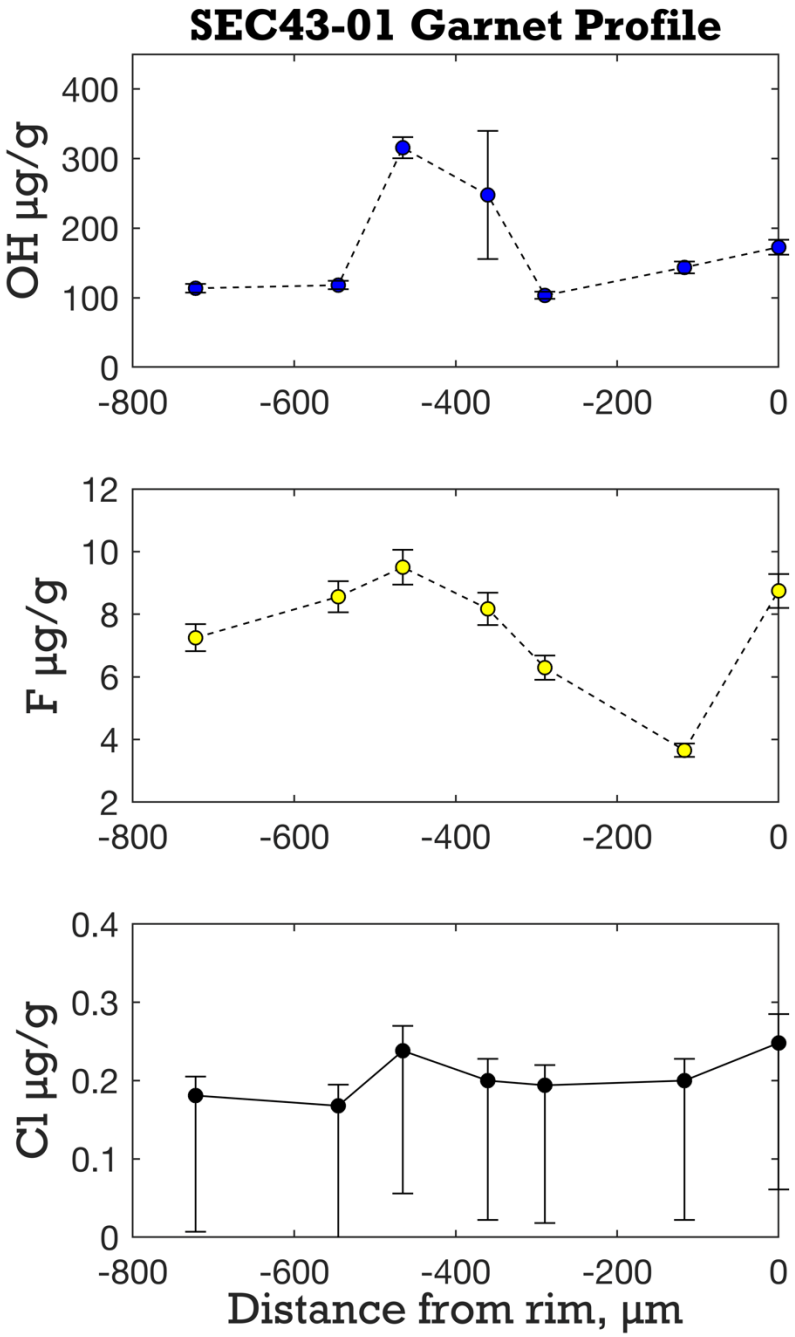

Figure 3.S4. SEC43-01 garnet core to rim transect. Zero values represent rim, 750 µm spot location is the garnet core. Overall, OH and F show intragrain variability likely related to partitioning and re-equilibration during garnet growth. The combination of internal and propagated calibration slope uncertainty corresponds to the positive error bar on our analyses. The negative error bars are larger for Cl because they incorporate the conservative uncertainty on the maximum background.

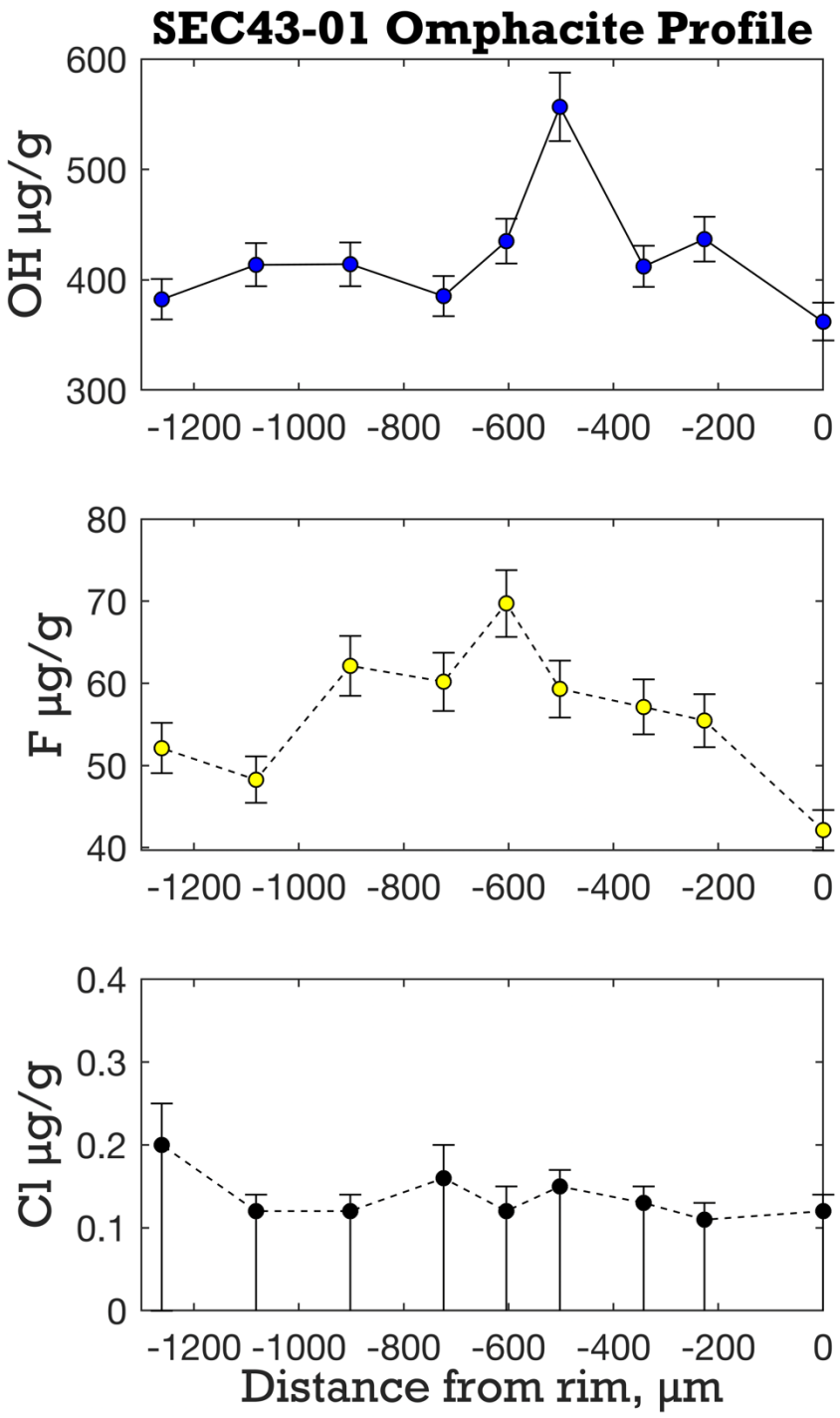

Figure 3.S5. SEC43-01 omphacite core (~1300 µm) to rim (zero µm) profile for OH, F, and Cl. Significant variations occur on length scales of <100 µm, with apparent rim depletions in F and OH.

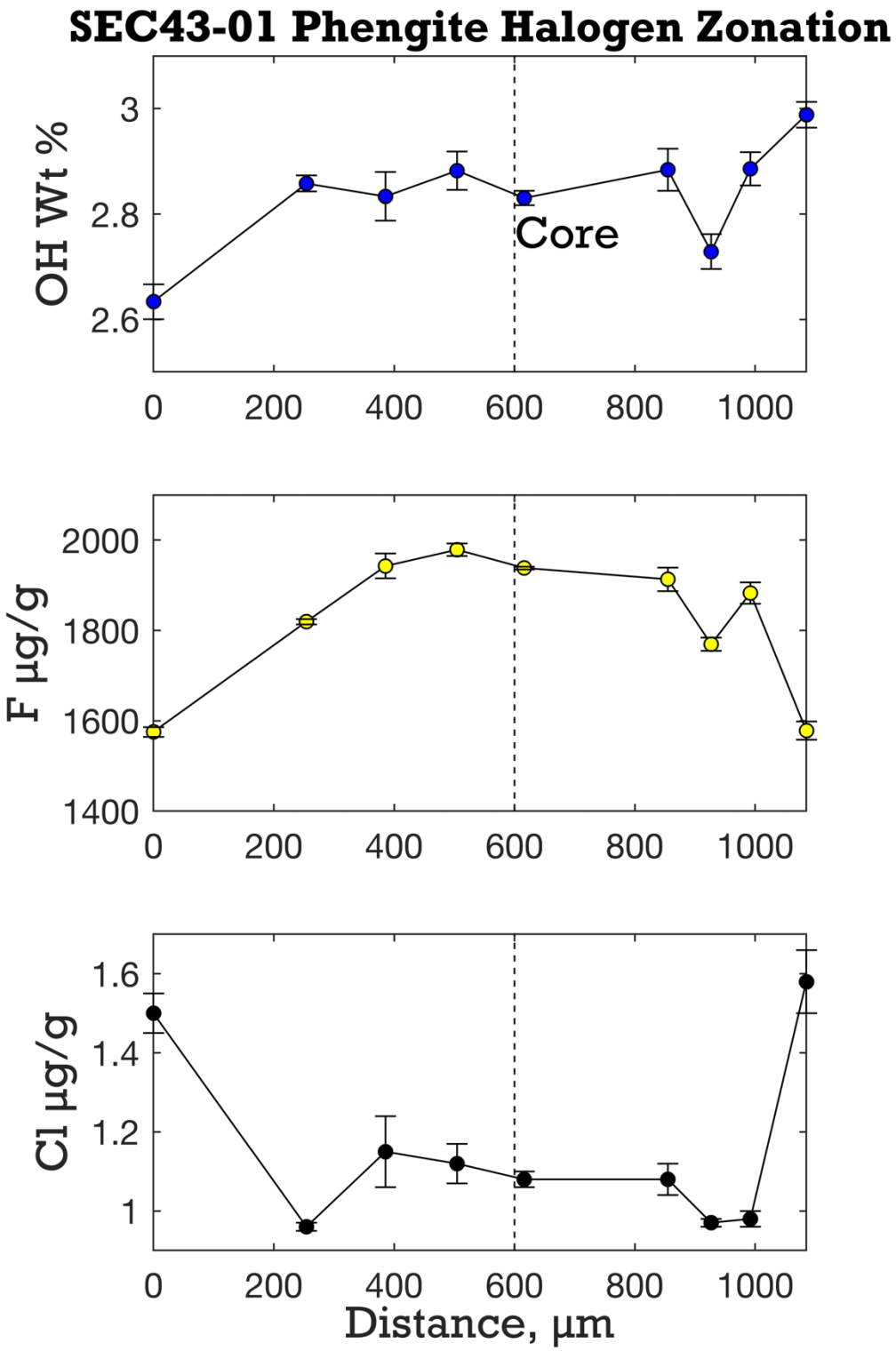

Figure 3.S6. SEC43-01 phengite rim-to-rim transect. F shows depletions toward the grain boundaries, while Cl shows rim enrichments of approximately 40%.

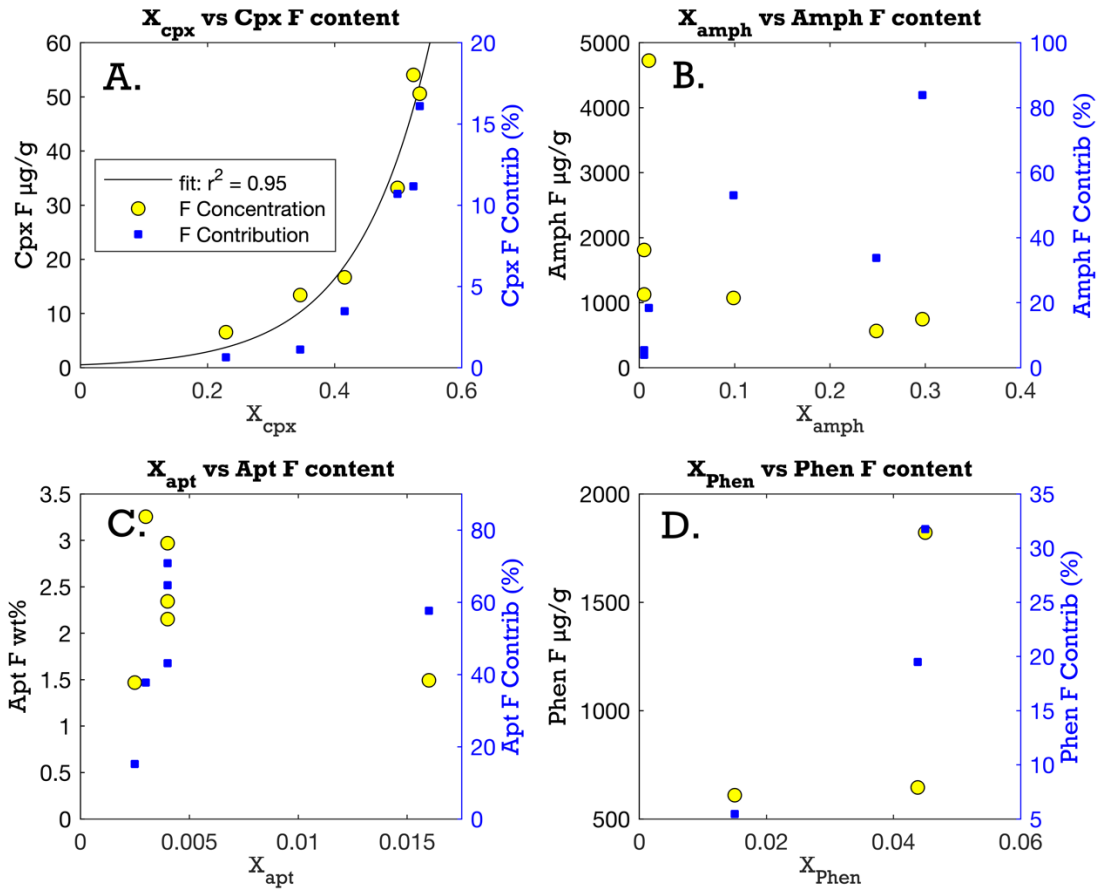

Figure 3.S7. Fluorine concentrations (black y-axis, yellow dots) and contributions to the bulk-rock (blue y-axis, blue dots) plotted against modal proportion of each phase for A. omphacite, B. amphibole, C. apatite, and D. phengite.

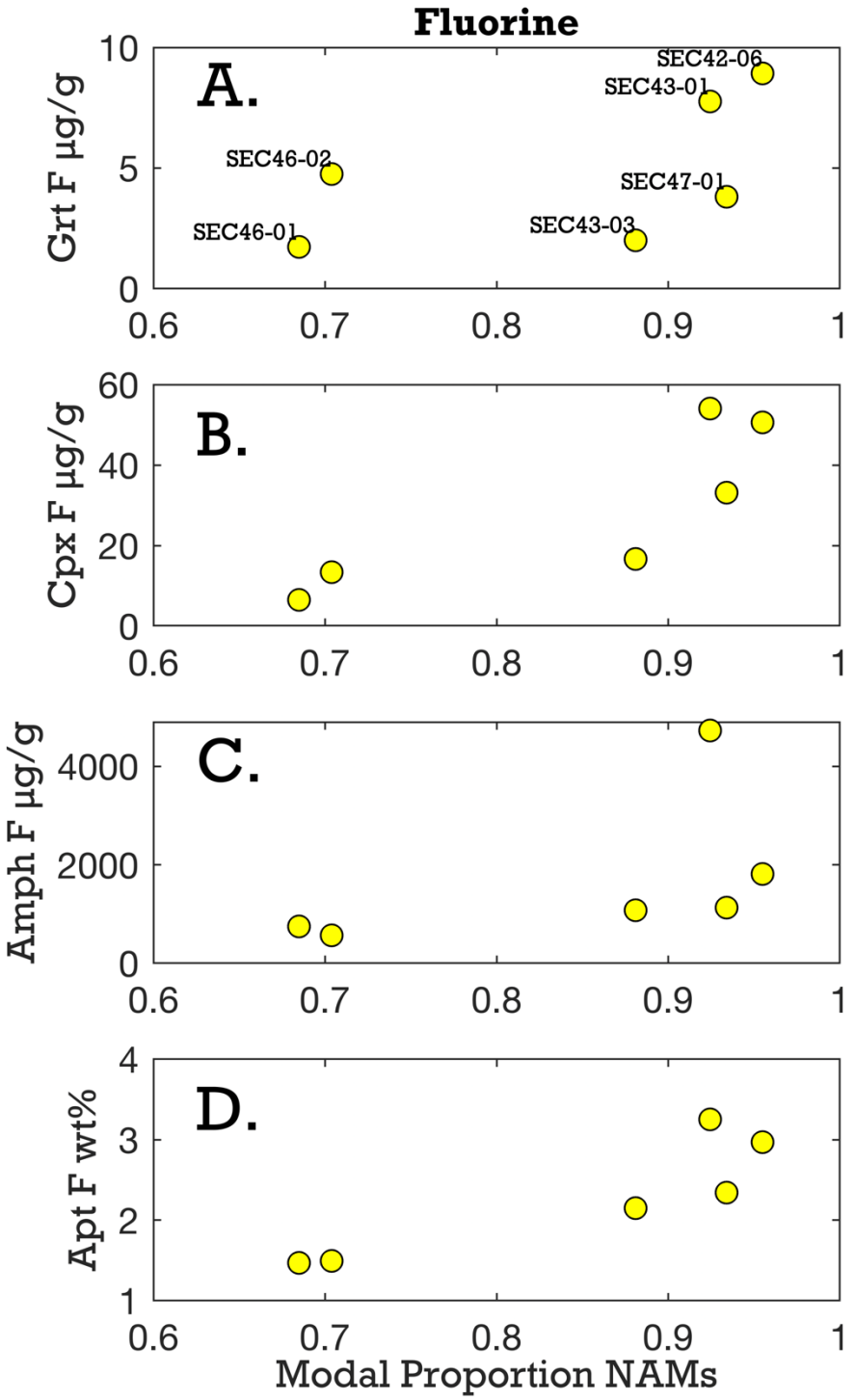

Figure 3.S8. Fluorine and chlorine concentrations in each phase as a function of the modal proportion of nominally anhydrous minerals (omphacite plus garnet). As the modal proportion of NAMs increases, so does the halogen concentration in most phases.

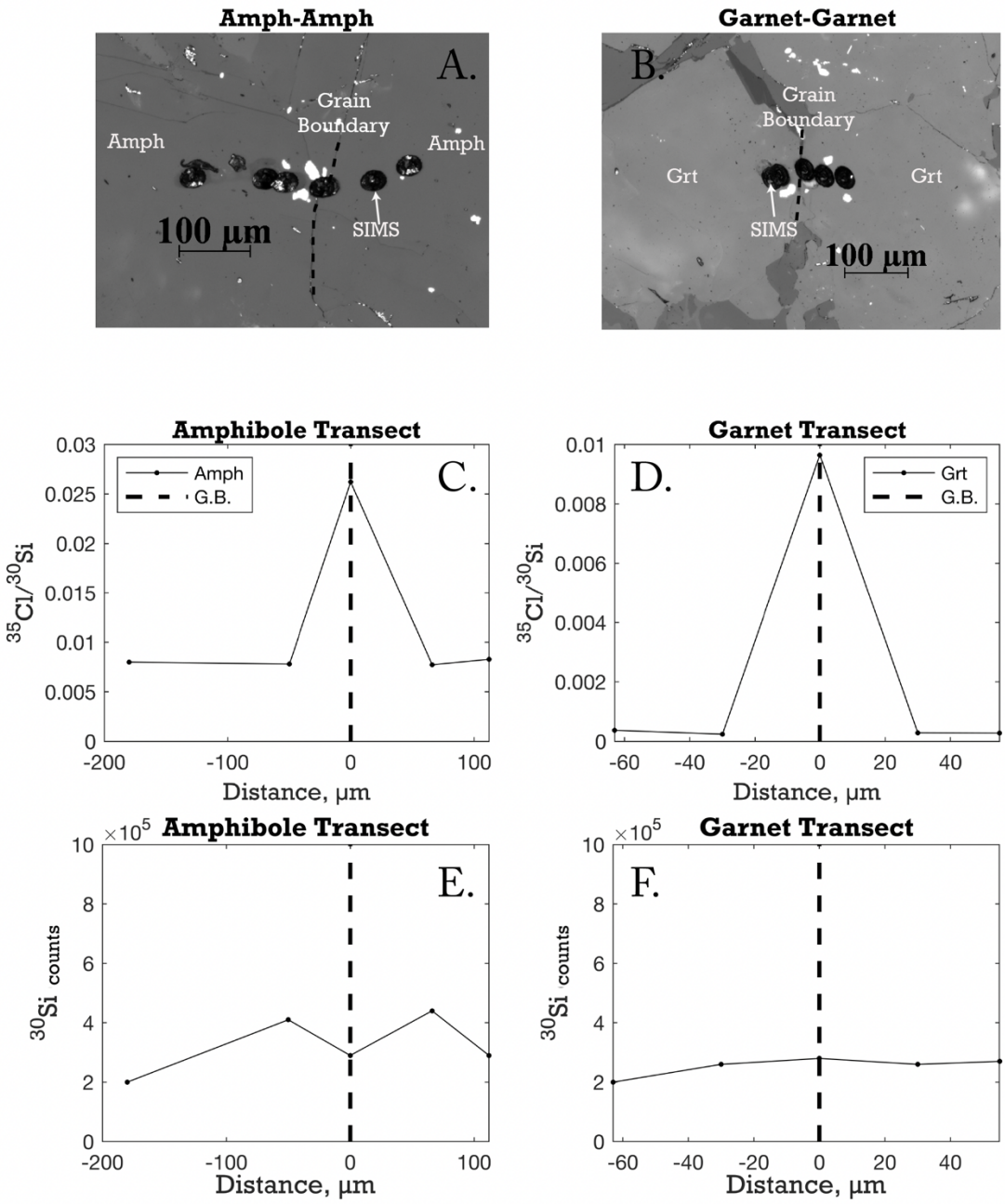

Figure 3.S9. Grain boundary transects using SIMS across amphibole (A.) and garnet (B.). While there are likely unaccounted for matrix effects with this approach, both measurements on the grain boundary qualitatively show pronounced spikes in Cl/Si ratios at near-constant constant Si counts, indicating Cl enrichment within the grain boundary (C. and D.). Also shown are raw ^{30}Si counts for comparison (panels E and F).

Chapter 3 Supplementary Tables

Table S1. Garnet major element compositions (EMPA)

			wt.%	wt.%	wt.%	wt.%
	Tot. Dist (μm)	Dist to grain boundary (μm)	Cr2O3	Al2O3	CaO	MnO
Line 1 SEC42-06_grt_profile	0	-1346	0.04	21.96	8.76	0.62
Line 2 SEC42-06_grt_profile	144	-1202	0.02	22.07	7.48	0.52
Line 3 SEC42-06_grt_profile	316	-1030	0.07	21.92	7.68	0.36
Line 4 SEC42-06_grt_profile	440	-907	0.05	21.81	8.22	0.44
Line 5 SEC42-06_grt_profile	580	-766	0.04	21.48	8.54	0.35
Line 6 SEC42-06_grt_profile	724	-622	0.07	21.50	8.56	0.77
Line 7 SEC42-06_grt_profile	904	-442	0.05	21.58	8.90	0.80
Line 8 SEC42-06_grt_profile	1001	-345	0.10	21.53	8.89	0.54
Line 9 SEC42-06_grt_profile	1195	-151	0.13	21.15	9.04	0.72
Line 10 SEC42-06_grt_profile	1346	0	0.03	22.07	8.02	0.49
SEC42-06 Average			0.06	21.71	8.41	0.56
Line 1 43-01_grt_grt->phen	0	-555	0.03	21.84	8.81	0.91
Line 2 43-01_grt_grt->phen	62	-493	0.14	21.96	8.74	0.81
Line 3 43-01_grt_grt->phen	124	-431	0.09	22.02	8.42	0.71
Line 4 43-01_grt_grt->phen	185	-370	0.06	21.92	7.77	0.60
Line 5 43-01_grt_grt->phen	247	-308	0.08	22.02	7.54	0.61
Line 6 43-01_grt_grt->phen	308	-247	0.04	22.00	6.93	0.59
Line 7 43-01_grt_grt->phen	370	-185	0.07	22.21	7.18	0.49
Line 8 43-01_grt_grt->phen	431	-124	0.02	22.49	7.74	0.44
Line 9 43-01_grt_grt->phen	493	-62	0.02	22.50	7.95	0.49
Line 10 43-01_grt_grt->phen	555	0	0.02	22.79	8.53	0.52
Line 1 43-01_grt_grt->cpx1	0	-451	0.04	22.07	8.79	0.79
Line 2 43-01_grt_grt->cpx1	49	-402	0.06	22.13	8.60	0.68
Line 3 43-01_grt_grt->cpx1	97	-353	0.06	22.15	8.16	0.62
Line 4 43-01_grt_grt->cpx1	150	-301	0.09	22.25	8.58	0.59
Line 5 43-01_grt_grt->cpx1	200	-251	0.02	22.10	7.25	0.55
Line 6 43-01_grt_grt->cpx1	250	-201	0.02	22.01	7.06	0.45
Line 7 43-01_grt_grt->cpx1	299	-152	0.07	22.29	6.80	0.35
Line 8 43-01_grt_grt->cpx1	329	-122	0.05	22.34	6.84	0.37
Line 9 43-01_grt_grt->cpx1	401	-50	0.04	22.44	7.43	0.47
Line 10 43-01_grt_grt->cpx1	451	0	0.04	22.27	8.06	0.53
Sec43-01 Average			0.05	22.19	7.86	0.58

Table S1. (cont.)

	wt.% Na2O	wt.% TiO2	wt.% SiO2	wt.% K2O	wt.% FeO	wt.% MgO	wt.% Total
Line 1 SEC42-06_grt_profile	0.00	0.07	38.00	0.00	25.30	4.23	98.98
Line 2 SEC42-06_grt_profile	0.02	0.03	37.75	0.00	26.38	4.58	98.86
Line 3 SEC42-06_grt_profile	0.00	0.09	37.54	0.00	26.60	4.39	98.65
Line 4 SEC42-06_grt_profile	0.03	0.12	37.29	0.00	26.56	4.20	98.72
Line 5 SEC42-06_grt_profile	0.00	0.15	36.81	0.00	26.95	3.56	97.87
Line 6 SEC42-06_grt_profile	0.00	0.10	36.54	0.00	26.74	3.32	97.61
Line 7 SEC42-06_grt_profile	0.00	0.07	36.82	0.00	25.48	4.04	97.73
Line 8 SEC42-06_grt_profile	0.06	0.07	36.85	0.00	25.25	4.39	97.67
Line 9 SEC42-06_grt_profile	0.00	0.10	36.09	0.00	26.14	3.54	96.91
Line 10 SEC42-06_grt_profile	0.00	0.03	38.43	0.00	26.23	4.78	100.08
SEC42-06 Average	0.01	0.08	37.21	0.00	26.16	4.10	98.31
Line 1 43-01_grt_grt->phen	0.04	0.11	38.30	0.00	26.11	3.90	100.06
Line 2 43-01_grt_grt->phen	0.04	0.10	38.05	0.01	25.88	4.27	100.00
Line 3 43-01_grt_grt->phen	0.02	0.02	38.19	0.00	25.92	4.30	99.68
Line 4 43-01_grt_grt->phen	0.00	0.08	38.23	0.00	26.48	4.56	99.70
Line 5 43-01_grt_grt->phen	0.05	0.07	38.29	0.01	26.76	4.83	100.26
Line 6 43-01_grt_grt->phen	0.12	0.05	38.53	0.01	26.71	5.03	100.01
Line 7 43-01_grt_grt->phen	0.00	0.01	38.50	0.00	26.45	5.11	100.02
Line 8 43-01_grt_grt->phen	0.01	0.01	38.70	0.00	25.45	5.26	100.13
Line 9 43-01_grt_grt->phen	0.00	0.01	38.81	0.00	25.51	5.17	100.47
Line 10 43-01_grt_grt->phen	0.06	0.02	39.07	0.04	24.75	4.97	100.77
Line 1 43-01_grt_grt->cpx1	0.05	0.11	38.28	0.00	25.64	3.97	99.74
Line 2 43-01_grt_grt->cpx1	0.00	0.10	38.41	0.00	25.69	4.40	100.06
Line 3 43-01_grt_grt->cpx1	0.00	0.09	38.53	0.00	25.93	4.47	100.01
Line 4 43-01_grt_grt->cpx1	0.00	0.03	38.22	0.00	25.56	4.48	99.80
Line 5 43-01_grt_grt->cpx1	0.00	0.05	38.33	0.00	27.12	4.69	100.12
Line 6 43-01_grt_grt->cpx1	0.00	0.06	37.57	0.01	27.23	4.64	99.04
Line 7 43-01_grt_grt->cpx1	0.04	0.05	38.46	0.01	27.26	5.01	100.34
Line 8 43-01_grt_grt->cpx1	0.00	0.05	38.53	0.00	26.86	5.15	100.19
Line 9 43-01_grt_grt->cpx1	0.00	0.05	38.84	0.00	24.89	5.69	99.85
Line 10 43-01_grt_grt->cpx1	0.00	0.02	38.48	0.00	25.30	4.86	99.57
Sec43-01 Average	0.02	0.05	38.42	0.01	26.08	4.74	99.99

Table S1. (cont.)

	a.p.f.u. Cr	a.p.f.u. Al	a.p.f.u. Ca	a.p.f.u. Mn	a.p.f.u. Na	a.p.f.u. Ti	a.p.f.u. Si
Line 1 SEC42-06_grt_profile	0.0024	2.039	0.739	0.0413	0	0.0044	2.993
Line 2 SEC42-06_grt_profile	0.0014	2.054	0.633	0.035	0.003	0.0018	2.981
Line 3 SEC42-06_grt_profile	0.0043	2.048	0.652	0.0243	0	0.0054	2.976
Line 4 SEC42-06_grt_profile	0.0032	2.042	0.7	0.0298	0.0049	0.0069	2.962
Line 5 SEC42-06_grt_profile	0.0027	2.037	0.736	0.0237	0	0.0088	2.961
Line 6 SEC42-06_grt_profile	0.0047	2.048	0.741	0.0528	0	0.0064	2.953
Line 7 SEC42-06_grt_profile	0.0031	2.042	0.765	0.0541	0	0.0041	2.956
Line 8 SEC42-06_grt_profile	0.006	2.034	0.764	0.0364	0.009	0.004	2.955
Line 9 SEC42-06_grt_profile	0.0082	2.031	0.789	0.0495	0	0.0063	2.94
Line 10 SEC42-06_grt_profile	0.002	2.026	0.669	0.0325	0.0004	0.0015	2.994
SEC42-06 Average	0.00	2.04	0.72	0.04	0.00	0.00	2.97
Line 1 43-01_grt_grt->phen	0.0018	2.015	0.738	0.0603	0.0067	0.0067	2.998
Line 2 43-01_grt_grt->phen	0.0086	2.026	0.733	0.0538	0.0057	0.0059	2.978
Line 3 43-01_grt_grt->phen	0.0054	2.034	0.707	0.0469	0.003	0.0011	2.992
Line 4 43-01_grt_grt->phen	0.0038	2.024	0.652	0.0399	0	0.0044	2.995
Line 5 43-01_grt_grt->phen	0.0048	2.024	0.63	0.0403	0.0077	0.0043	2.985
Line 6 43-01_grt_grt->phen	0.0026	2.021	0.578	0.0387	0.018	0.0027	3.003
Line 7 43-01_grt_grt->phen	0.0041	2.037	0.599	0.0323	0.0007	0.0004	2.996
Line 8 43-01_grt_grt->phen	0.0014	2.053	0.642	0.0289	0.0022	0.0005	2.996
Line 9 43-01_grt_grt->phen	0.0015	2.047	0.658	0.0324	0.0004	0.0004	2.996
Line 10 43-01_grt_grt->phen	0.0009	2.063	0.702	0.034	0.0096	0.0011	3
Line 1 43-01_grt_grt->cpx1	0.0023	2.037	0.737	0.0523	0.007	0.0068	2.997
Line 2 43-01_grt_grt->cpx1	0.0035	2.033	0.718	0.0447	0	0.0056	2.993
Line 3 43-01_grt_grt->cpx1	0.0036	2.034	0.681	0.0411	0	0.0051	3.001
Line 4 43-01_grt_grt->cpx1	0.0055	2.048	0.718	0.039	0	0.0019	2.984
Line 5 43-01_grt_grt->cpx1	0.0014	2.033	0.606	0.0366	0	0.0031	2.991
Line 6 43-01_grt_grt->cpx1	0.0012	2.051	0.598	0.0302	0	0.0033	2.97
Line 7 43-01_grt_grt->cpx1	0.0043	2.042	0.567	0.0228	0.0055	0.0031	2.989
Line 8 43-01_grt_grt->cpx1	0.0033	2.046	0.569	0.0243	0	0.0027	2.993
Line 9 43-01_grt_grt->cpx1	0.0024	2.046	0.616	0.0305	0	0.0028	3.005
Line 10 43-01_grt_grt->cpx1	0.0026	2.047	0.673	0.035	0	0.0014	3
Sec43-01 Average	0.00	2.04	0.66	0.04	0.00	0.00	2.99

Table S1. (cont.)

	a.p.f.u. K	a.p.f.u. Fe	a.p.f.u. Mg	a.p.f.u. Total
Line 1 SEC42-06_grt_profile	0.0001	1.667	0.497	7.9833
Line 2 SEC42-06_grt_profile	0	1.742	0.539	7.9903
Line 3 SEC42-06_grt_profile	0	1.763	0.518	7.9911
Line 4 SEC42-06_grt_profile	0	1.765	0.497	8.0108
Line 5 SEC42-06_grt_profile	0	1.813	0.426	8.0082
Line 6 SEC42-06_grt_profile	0	1.807	0.4	8.0129
Line 7 SEC42-06_grt_profile	0	1.71	0.484	8.0183
Line 8 SEC42-06_grt_profile	0	1.693	0.525	8.0264
Line 9 SEC42-06_grt_profile	0.0003	1.781	0.43	8.0353
Line 10 SEC42-06_grt_profile	0.0001	1.709	0.555	7.9896
SEC42-06 Average	0.00	1.75	0.49	8.01
Line 1 43-01_grt_grt->phen	0	1.709	0.455	7.9906
Line 2 43-01_grt_grt->phen	0.0013	1.693	0.498	8.0033
Line 3 43-01_grt_grt->phen	0	1.698	0.502	7.9894
Line 4 43-01_grt_grt->phen	0	1.735	0.533	7.9872
Line 5 43-01_grt_grt->phen	0.0008	1.745	0.561	8.0029
Line 6 43-01_grt_grt->phen	0.0014	1.741	0.585	7.9915
Line 7 43-01_grt_grt->phen	0.0004	1.721	0.593	7.984
Line 8 43-01_grt_grt->phen	0.0004	1.648	0.607	7.9795
Line 9 43-01_grt_grt->phen	0.0001	1.647	0.595	7.9778
Line 10 43-01_grt_grt->phen	0.0038	1.589	0.569	7.9725
Line 1 43-01_grt_grt->cpx1	0	1.679	0.463	7.9814
Line 2 43-01_grt_grt->cpx1	0	1.674	0.511	7.9829
Line 3 43-01_grt_grt->cpx1	0	1.689	0.519	7.9738
Line 4 43-01_grt_grt->cpx1	0	1.669	0.522	7.9875
Line 5 43-01_grt_grt->cpx1	0	1.77	0.545	7.9861
Line 6 43-01_grt_grt->cpx1	0.0008	1.8	0.546	8.0005
Line 7 43-01_grt_grt->cpx1	0.001	1.772	0.58	7.9868
Line 8 43-01_grt_grt->cpx1	0	1.745	0.596	7.9794
Line 9 43-01_grt_grt->cpx1	0.0003	1.61	0.656	7.969
Line 10 43-01_grt_grt->cpx1	0.0004	1.65	0.565	7.9745
Sec43-01 Average	0.00	1.70	0.55	7.99

Table S1. (cont.)

	X Almandine	X Pyrope	X Grossular	X Spessartine	Fe/(Fe+Mg)
Line 1 SEC42-06_grt_profile	0.57	0.17	0.25	0.01	0.77
Line 2 SEC42-06_grt_profile	0.59	0.18	0.21	0.01	0.76
Line 3 SEC42-06_grt_profile	0.60	0.18	0.22	0.01	0.77
Line 4 SEC42-06_grt_profile	0.59	0.17	0.23	0.01	0.78
Line 5 SEC42-06_grt_profile	0.60	0.14	0.25	0.01	0.81
Line 6 SEC42-06_grt_profile	0.60	0.13	0.25	0.02	0.82
Line 7 SEC42-06_grt_profile	0.57	0.16	0.25	0.02	0.78
Line 8 SEC42-06_grt_profile	0.56	0.17	0.25	0.01	0.76
Line 9 SEC42-06_grt_profile	0.58	0.14	0.26	0.02	0.81
Line 10 SEC42-06_grt_profile	0.58	0.19	0.23	0.01	0.75
SEC42-06 Average	0.58	0.16	0.24	0.01	0.78
Line 1 43-01_grt_grt->phen	0.58	0.15	0.25	0.02	0.79
Line 2 43-01_grt_grt->phen	0.57	0.17	0.25	0.02	0.77
Line 3 43-01_grt_grt->phen	0.57	0.17	0.24	0.02	0.77
Line 4 43-01_grt_grt->phen	0.59	0.18	0.22	0.01	0.76
Line 5 43-01_grt_grt->phen	0.59	0.19	0.21	0.01	0.76
Line 6 43-01_grt_grt->phen	0.59	0.20	0.20	0.01	0.75
Line 7 43-01_grt_grt->phen	0.58	0.20	0.20	0.01	0.74
Line 8 43-01_grt_grt->phen	0.56	0.21	0.22	0.01	0.73
Line 9 43-01_grt_grt->phen	0.56	0.20	0.22	0.01	0.73
Line 10 43-01_grt_grt->phen	0.55	0.20	0.24	0.01	0.74
Line 1 43-01_grt_grt->cpx1	0.57	0.16	0.25	0.02	0.78
Line 2 43-01_grt_grt->cpx1	0.57	0.17	0.24	0.02	0.77
Line 3 43-01_grt_grt->cpx1	0.58	0.18	0.23	0.01	0.76
Line 4 43-01_grt_grt->cpx1	0.57	0.18	0.24	0.01	0.76
Line 5 43-01_grt_grt->cpx1	0.60	0.18	0.20	0.01	0.76
Line 6 43-01_grt_grt->cpx1	0.61	0.18	0.20	0.01	0.77
Line 7 43-01_grt_grt->cpx1	0.60	0.20	0.19	0.01	0.75
Line 8 43-01_grt_grt->cpx1	0.59	0.20	0.19	0.01	0.75
Line 9 43-01_grt_grt->cpx1	0.55	0.23	0.21	0.01	0.71
Line 10 43-01_grt_grt->cpx1	0.56	0.19	0.23	0.01	0.74
Sec43-01 Average	0.58	0.19	0.22	0.01	0.76

Table S1. (cont.)

			wt.%	wt.%	wt.%	wt.%
	Tot. Dist (μm)	Dist to grain boundary (μm)	Cr2O3	Al2O3	CaO	MnO
Line 1 SEC43-03_Grt1	0	-502	0.00	22.21	9.32	1.13
Line 2 SEC43-03_GRT1	36	-465	0.00	22.14	9.95	1.17
Line 3 SEC43-03 GRT1	72	-430	0.00	21.99	9.97	1.28
Line 4 SEC43-03 GRT1	107	-395	0.00	21.76	10.41	1.30
Line 5 SEC43-03 GRT1	143	-358	0.00	21.86	10.28	1.33
Line 6 SEC43-03 GRT1	179	-323	0.00	21.87	10.71	1.67
Line 7 SEC43-03 GRT1	215	-287	0.00	21.48	10.98	2.43
Line 8 SEC43-03 GRT1	251	-251	0.00	21.04	10.15	2.12
Line 9 SEC43-03 GRT1	288	-214	0.02	22.36	11.27	2.24
Line 10 SEC43-03 GRT1	326	-176	0.00	21.64	11.42	1.62
Line 11 SEC43-03 GRT1	362	-140	0.06	21.54	9.80	0.75
Line 12 SEC43-03 GRT1	397	-105	0.00	21.41	10.31	0.72
Line 13 SEC43-03 GRT1	434	-68	0.00	23.15	10.49	0.58
Line 14 SEC43-03 GRT1	450	-52	0.00	21.88	10.47	0.64
Line 15 SEC43-03 GRT1	502	0	0.00	21.60	7.47	0.79
Line 1 SEC43-03_Grt2	0	-1245	0.04	22.12	10.35	2.17
Line 2 SEC43-03_Grt2	64	-1181	0.00	22.16	10.21	1.55
Line 3 SEC43-03_Grt2	126	-1119	0.00	22.44	9.46	1.11
Line 4 SEC43-03_Grt2	190	-1055	0.00	22.08	10.12	0.86
Line 5 SEC43-03_Grt2	254	-991	0.00	22.03	10.06	0.77
Line 6 SEC43-03_Grt2	330	-915	0.00	21.89	10.22	0.73
Line 7 SEC43-03_Grt2	383	-862	0.00	21.94	9.55	0.71
Line 8 SEC43-03_Grt2	447	-798	0.00	22.17	10.23	0.68
Line 9 SEC43-03_Grt2	523	-722	0.00	22.26	9.92	0.68
Line 10 SEC43-03_Grt2	596	-649	0.00	22.05	10.29	0.69
Line 11 SEC43-03_Grt2	659	-586	0.00	22.20	9.88	0.66
Line 12 SEC43-03_Grt2	741	-504	0.01	22.31	9.25	0.73
Line 13 SEC43-03_Grt2	794	-451	0.00	22.40	10.21	0.68
Line 14 SEC43-03_Grt2	864	-381	0.02	22.20	10.17	0.65
Line 15 SEC43-03_Grt2	924	-321	0.01	22.35	10.14	0.59
Line 16 SEC43-03_Grt2	988	-257	0.07	22.17	9.90	0.65
Line 17 SEC43-03_Grt2	1052	-193	0.01	22.53	10.11	0.44
Line 18 SEC43-03_Grt2	1116	-130	0.00	22.52	7.04	0.58
Line 19 SEC43-03_Grt2	1176	-70	0.03	22.64	7.06	0.62
Line 20 SEC43-03_Grt2	1245	0	0.02	22.32	8.09	0.60
SEC43-03 Average			0.01	22.08	9.86	1.03

Table S1. (cont.)

	wt.% Na2O	wt.% TiO2	wt.% SiO2	wt.% K2O	wt.% FeO	wt.% MgO	wt.% Total
Line 1 SEC43-03_Grt1	0.01	0.07	38.46	0.01	24.72	4.96	100.90
Line 2 SEC43-03_GRT1	0.05	0.12	38.44	0.00	24.18	4.82	100.87
Line 3 SEC43-03 GRT1	0.01	0.15	38.23	0.00	24.09	4.75	100.46
Line 4 SEC43-03 GRT1	0.04	0.64	38.00	0.00	23.27	4.55	99.97
Line 5 SEC43-03 GRT1	0.05	0.16	38.27	0.00	23.72	4.65	100.32
Line 6 SEC43-03 GRT1	0.08	0.19	38.18	0.00	23.33	4.27	100.30
Line 7 SEC43-03 GRT1	0.05	0.12	37.65	0.00	24.00	3.32	100.03
Line 8 SEC43-03 GRT1	0.00	0.16	37.00	0.01	23.78	4.06	98.31
Line 9 SEC43-03 GRT1	0.03	0.11	38.89	0.00	24.06	2.63	101.60
Line 10 SEC43-03 GRT1	0.02	0.10	37.50	0.00	23.91	3.62	99.84
Line 11 SEC43-03 GRT1	0.06	0.06	37.66	0.00	24.43	4.92	99.28
Line 12 SEC43-03 GRT1	0.02	0.05	37.40	0.00	24.36	4.80	99.07
Line 13 SEC43-03 GRT1	0.03	0.06	39.77	0.00	24.04	4.38	102.51
Line 14 SEC43-03 GRT1	0.07	0.01	37.66	0.00	23.43	5.09	99.26
Line 15 SEC43-03 GRT1	0.03	0.03	37.02	0.00	26.40	5.37	98.71
Line 1 SEC43-03_Grt2	0.06	0.17	38.53	0.00	23.64	4.15	101.23
Line 2 SEC43-03_Grt2	0.00	0.20	38.54	0.00	23.98	4.51	101.15
Line 3 SEC43-03_Grt2	0.00	0.05	38.35	0.00	24.66	4.81	100.88
Line 4 SEC43-03_Grt2	0.01	0.09	38.23	0.01	24.46	4.73	100.59
Line 5 SEC43-03_Grt2	0.00	0.14	38.33	0.00	24.57	4.83	100.73
Line 6 SEC43-03_Grt2	0.02	0.14	38.46	0.00	24.13	4.82	100.40
Line 7 SEC43-03_Grt2	0.05	0.12	38.54	0.00	24.84	5.05	100.80
Line 8 SEC43-03_Grt2	0.02	0.16	38.61	0.00	24.37	4.74	100.99
Line 9 SEC43-03_Grt2	0.00	0.13	38.64	0.00	24.43	4.87	100.94
Line 10 SEC43-03_Grt2	0.01	0.19	38.51	0.00	24.23	4.70	100.68
Line 11 SEC43-03_Grt2	0.02	0.12	38.54	0.00	24.70	4.87	100.98
Line 12 SEC43-03_Grt2	0.00	0.07	38.42	0.00	25.49	4.89	101.16
Line 13 SEC43-03_Grt2	0.00	0.03	38.65	0.00	24.43	4.64	101.04
Line 14 SEC43-03_Grt2	0.00	0.06	38.36	0.01	24.88	4.78	101.13
Line 15 SEC43-03_Grt2	0.00	0.02	38.43	0.00	24.30	4.87	100.71
Line 16 SEC43-03_Grt2	0.00	0.00	38.42	0.01	24.61	4.84	100.67
Line 17 SEC43-03_Grt2	0.00	0.02	38.41	0.00	24.54	4.72	100.77
Line 18 SEC43-03_Grt2	0.00	0.02	38.23	0.00	26.45	5.97	100.81
Line 19 SEC43-03_Grt2	0.00	0.00	38.45	0.00	26.27	5.85	100.91
Line 20 SEC43-03_Grt2	0.00	0.00	38.32	0.00	25.84	5.63	100.82
SEC43-03 Average	0.02	0.11	38.26	0.00	24.47	4.70	100.54

Table S1. (cont.)

	a.p.f.u.	a.p.f.u.	a.p.f.u.	a.p.f.u.	a.p.f.u.	a.p.f.u.	a.p.f.u.
	Cr	Al	Ca	Mn	Na	Ti	Si
Line 1 SEC43-03_Grt1	0	2.022	0.772	0.0742	0.0014	0.0042	2.971
Line 2 SEC43-03_GRT1	0	2.016	0.824	0.0766	0.0072	0.0071	2.97
Line 3 SEC43-03 GRT1	0	2.012	0.829	0.0841	0.0014	0.0085	2.968
Line 4 SEC43-03 GRT1	0	1.999	0.869	0.086	0.0061	0.0377	2.961
Line 5 SEC43-03 GRT1	0.0002	2.002	0.856	0.088	0.0076	0.0092	2.975
Line 6 SEC43-03 GRT1	0	2.007	0.893	0.11	0.0119	0.011	2.972
Line 7 SEC43-03 GRT1	0	1.995	0.927	0.162	0.0074	0.0073	2.965
Line 8 SEC43-03 GRT1	0	1.983	0.87	0.144	0	0.0093	2.959
Line 9 SEC43-03 GRT1	0.0011	2.033	0.931	0.146	0.0043	0.0062	3.001
Line 10 SEC43-03 GRT1	0	2.008	0.963	0.108	0.0037	0.006	2.952
Line 11 SEC43-03 GRT1	0.0037	1.997	0.826	0.0502	0.0084	0.0036	2.963
Line 12 SEC43-03 GRT1	0	1.994	0.873	0.048	0.0026	0.0032	2.953
Line 13 SEC43-03 GRT1	0	2.06	0.849	0.0373	0.0045	0.0035	3.003
Line 14 SEC43-03 GRT1	0	2.022	0.88	0.0427	0.0105	0.0008	2.953
Line 15 SEC43-03 GRT1	0	2.022	0.635	0.0529	0.0045	0.002	2.941
Line 1 SEC43-03_Grt2	0.0022	2.013	0.856	0.142	0.009	0.0098	2.975
Line 2 SEC43-03_Grt2	0.0002	2.014	0.843	0.101	0	0.0116	2.972
Line 3 SEC43-03_Grt2	0	2.044	0.783	0.0724	0	0.0031	2.963
Line 4 SEC43-03_Grt2	0	2.019	0.841	0.0564	0.0018	0.0052	2.965
Line 5 SEC43-03_Grt2	0	2.01	0.834	0.0506	0	0.008	2.968
Line 6 SEC43-03_Grt2	0	2	0.849	0.0477	0.0036	0.0079	2.982
Line 7 SEC43-03_Grt2	0	1.999	0.791	0.0467	0.0068	0.007	2.98
Line 8 SEC43-03_Grt2	0	2.015	0.845	0.0445	0.0036	0.0094	2.976
Line 9 SEC43-03_Grt2	0	2.021	0.819	0.0446	0.0004	0.0076	2.977
Line 10 SEC43-03_Grt2	0	2.01	0.852	0.0454	0.0021	0.0111	2.978
Line 11 SEC43-03_Grt2	0	2.018	0.817	0.0429	0.0025	0.007	2.973
Line 12 SEC43-03_Grt2	0.0005	2.029	0.765	0.0474	0	0.0041	2.964
Line 13 SEC43-03_Grt2	0	2.033	0.843	0.0441	0	0.002	2.977
Line 14 SEC43-03_Grt2	0.001	2.02	0.841	0.0424	0	0.0036	2.961
Line 15 SEC43-03_Grt2	0.0006	2.035	0.839	0.0387	0	0.0013	2.968
Line 16 SEC43-03_Grt2	0.0045	2.022	0.821	0.0428	0	0.0001	2.973
Line 17 SEC43-03_Grt2	0.0004	2.05	0.837	0.0287	0	0.001	2.965
Line 18 SEC43-03_Grt2	0	2.05	0.583	0.0378	0	0.0013	2.952
Line 19 SEC43-03_Grt2	0.0016	2.057	0.583	0.0404	0	0	2.963
Line 20 SEC43-03_Grt2	0.0013	2.033	0.67	0.0392	0	0	2.961
SEC43-03 Average	0.00	2.02	0.82	0.07	0.00	0.01	2.97

Table S1. (cont.)

	a.p.f.u.	a.p.f.u.	a.p.f.u.	a.p.f.u.
	K	Fe	Mg	Total
Line 1 SEC43-03_Grt1	0.001	1.597	0.572	8.0148
Line 2 SEC43-03_GRT1	0	1.563	0.555	8.019
Line 3 SEC43-03 GRT1	0	1.564	0.55	8.017
Line 4 SEC43-03 GRT1	0	1.517	0.529	8.0048
Line 5 SEC43-03 GRT1	0	1.542	0.539	8.019
Line 6 SEC43-03 GRT1	0	1.519	0.495	8.0189
Line 7 SEC43-03 GRT1	0	1.581	0.389	8.0337
Line 8 SEC43-03 GRT1	0.0007	1.59	0.484	8.0401
Line 9 SEC43-03 GRT1	0	1.553	0.302	7.9777
Line 10 SEC43-03 GRT1	0.0002	1.574	0.425	8.0399
Line 11 SEC43-03 GRT1	0	1.607	0.578	8.0369
Line 12 SEC43-03 GRT1	0	1.609	0.565	8.0478
Line 13 SEC43-03 GRT1	0.0002	1.518	0.492	7.9676
Line 14 SEC43-03 GRT1	0	1.537	0.595	8.041
Line 15 SEC43-03 GRT1	0	1.754	0.636	8.0474
Line 1 SEC43-03_Grt2	0	1.527	0.478	8.012
Line 2 SEC43-03_Grt2	0	1.547	0.518	8.0068
Line 3 SEC43-03_Grt2	0.0001	1.593	0.554	8.0126
Line 4 SEC43-03_Grt2	0.0012	1.587	0.547	8.0237
Line 5 SEC43-03_Grt2	0.0003	1.591	0.558	8.0199
Line 6 SEC43-03_Grt2	0	1.565	0.557	8.0122
Line 7 SEC43-03_Grt2	0	1.606	0.582	8.0185
Line 8 SEC43-03_Grt2	0.0004	1.571	0.545	8.0099
Line 9 SEC43-03_Grt2	0	1.575	0.56	8.0047
Line 10 SEC43-03_Grt2	0	1.567	0.542	8.0076
Line 11 SEC43-03_Grt2	0	1.593	0.56	8.0134
Line 12 SEC43-03_Grt2	0	1.645	0.563	8.018
Line 13 SEC43-03_Grt2	0	1.574	0.533	8.0061
Line 14 SEC43-03_Grt2	0.0011	1.606	0.55	8.0261
Line 15 SEC43-03_Grt2	0	1.57	0.561	8.0136
Line 16 SEC43-03_Grt2	0.0005	1.593	0.558	8.0149
Line 17 SEC43-03_Grt2	0	1.584	0.543	8.0091
Line 18 SEC43-03_Grt2	0	1.709	0.688	8.0211
Line 19 SEC43-03_Grt2	0	1.693	0.672	8.01
Line 20 SEC43-03_Grt2	0	1.67	0.649	8.0236
SEC43-03 Average	0.00	1.59	0.54	8.02

Table S1. (cont.)

	X Almandine	X Pyrope	X Grossular	X Spessartine	Fe/(Fe+Mg)
Line 1 SEC43-03_Grt1	0.53	0.19	0.26	0.02	0.74
Line 2 SEC43-03_GRT1	0.52	0.18	0.27	0.03	0.74
Line 3 SEC43-03 GRT1	0.52	0.18	0.27	0.03	0.74
Line 4 SEC43-03 GRT1	0.51	0.18	0.29	0.03	0.74
Line 5 SEC43-03 GRT1	0.51	0.18	0.28	0.03	0.74
Line 6 SEC43-03 GRT1	0.50	0.16	0.30	0.04	0.75
Line 7 SEC43-03 GRT1	0.52	0.13	0.30	0.05	0.80
Line 8 SEC43-03 GRT1	0.51	0.16	0.28	0.05	0.77
Line 9 SEC43-03 GRT1	0.53	0.10	0.32	0.05	0.84
Line 10 SEC43-03 GRT1	0.51	0.14	0.31	0.04	0.79
Line 11 SEC43-03 GRT1	0.52	0.19	0.27	0.02	0.74
Line 12 SEC43-03 GRT1	0.52	0.18	0.28	0.02	0.74
Line 13 SEC43-03 GRT1	0.52	0.17	0.29	0.01	0.76
Line 14 SEC43-03 GRT1	0.50	0.19	0.29	0.01	0.72
Line 15 SEC43-03 GRT1	0.57	0.21	0.21	0.02	0.73
Line 1 SEC43-03_Grt2	0.51	0.16	0.29	0.05	0.76
Line 2 SEC43-03_Grt2	0.51	0.17	0.28	0.03	0.75
Line 3 SEC43-03_Grt2	0.53	0.18	0.26	0.02	0.74
Line 4 SEC43-03_Grt2	0.52	0.18	0.28	0.02	0.74
Line 5 SEC43-03_Grt2	0.52	0.18	0.27	0.02	0.74
Line 6 SEC43-03_Grt2	0.52	0.18	0.28	0.02	0.74
Line 7 SEC43-03_Grt2	0.53	0.19	0.26	0.02	0.73
Line 8 SEC43-03_Grt2	0.52	0.18	0.28	0.01	0.74
Line 9 SEC43-03_Grt2	0.53	0.19	0.27	0.01	0.74
Line 10 SEC43-03_Grt2	0.52	0.18	0.28	0.02	0.74
Line 11 SEC43-03_Grt2	0.53	0.19	0.27	0.01	0.74
Line 12 SEC43-03_Grt2	0.54	0.19	0.25	0.02	0.75
Line 13 SEC43-03_Grt2	0.53	0.18	0.28	0.01	0.75
Line 14 SEC43-03_Grt2	0.53	0.18	0.28	0.01	0.74
Line 15 SEC43-03_Grt2	0.52	0.19	0.28	0.01	0.74
Line 16 SEC43-03_Grt2	0.53	0.19	0.27	0.01	0.74
Line 17 SEC43-03_Grt2	0.53	0.18	0.28	0.01	0.74
Line 18 SEC43-03_Grt2	0.57	0.23	0.19	0.01	0.71
Line 19 SEC43-03_Grt2	0.57	0.22	0.20	0.01	0.72
Line 20 SEC43-03_Grt2	0.55	0.21	0.22	0.01	0.72
SEC43-03 Average	0.53	0.18	0.27	0.02	0.75

Table S1. (cont.)

			wt.%	wt.%	wt.%	wt.%
	Tot. Dist (μm)	Dist to grain boundary (μm)	Cr2O3	Al2O3	CaO	MnO
Line 1 SEC46-01_grt1	0	-557	0.02	22.26	7.96	1.83
Line 2 SEC46-01_grt1	20	-537	0.00	22.19	7.76	2.73
Line 3 SEC46-01_grt1	66	-491	0.00	22.57	7.84	1.61
Line 4 SEC46-01_grt1	87	-470	0.00	22.30	7.59	1.46
Line 5 SEC46-01_grt1	116	-441	0.01	22.19	7.76	1.43
Line 6 SEC46-01_grt1	145	-412	0.00	22.33	8.18	1.29
Line 7 SEC46-01_grt1	174	-384	0.00	22.28	8.09	1.19
Line 8 SEC46-01_grt1	203	-355	0.00	22.37	8.09	1.09
Line 9 SEC46-01_grt1	236	-321	0.01	22.45	7.95	1.01
Line 10 SEC46-01_grt1	260	-297	0.00	22.50	7.63	1.03
Line 11 SEC46-01_grt1	284	-273	0.01	22.52	8.22	0.98
Line 12 SEC46-01_grt1	335	-222	0.03	22.72	7.75	0.91
Line 13 SEC46-01_grt1	349	-208	0.00	22.47	7.13	0.97
Line 14 SEC46-01_grt1	373	-185	0.03	22.69	7.72	0.91
Line 15 SEC46-01_grt1	405	-152	0.03	22.67	8.04	0.74
Line 16 SEC46-01_grt1	439	-118	0.00	22.51	9.40	0.68
Line 17 SEC46-01_grt1	468	-89	0.00	22.54	8.72	0.64
Line 18 SEC46-01_grt1	473	-85	0.00	22.64	8.53	0.59
Line 19 SEC46-01_grt1	514	-43	0.00	22.68	7.61	0.58
Line 20 SEC46-01_grt1	557	0	0.00	22.66	8.96	0.49
Line 1 SEC46-1_grt3	0	**-227.6**	0.0305	22.35	6.92	1.69
Line 2 SEC46-01_grt3	25.7	**-201.9**	0.1208	22.48	6.84	1.32
Line 3 SEC46-01_grt3	51.2	**-176.4**	0.0217	22.52	6.94	0.9555
Line 4 SEC46-01_grt3	76.9	**-150.7**	0.0428	22.45	7.02	0.9969
Line 5 SEC46-01_grt3	102.6	**-125.0**	0.0214	22.45	9.63	0.6204
Line 6 SEC46-01_grt3	128.1	**-99.5**	0.0876	22.5	10.08	0.5765
Line 7 SEC46-01_grt3	153.8	**-73.8**	0.0264	22.75	8.93	0.5603
Line 8 SEC46-01_grt3	179.5	**-48.1**	0.057	22.68	8.23	0.5325
Line 9 SEC46-01_grt3	205.0	**-22.6**	0.038	22.69	7.82	0.5725
Line 10 SEC46-01_grt3	227.6	**0.0**	0.0466	22.57	9.88	0.5333
Line 1 SEC46-01_grt2	0	**-279.6**	0.0224	22.45	7.21	0.5875
Line 2 SEC46-01_grt2	20.4	**-259.2**	0.0191	22.38	7.02	0.5871
Line 3 SEC46-01_grt2	39.8	**-239.8**	0.0479	22.39	7.25	0.7083
Line 4 SEC46-01_grt2	60.2	**-219.4**	0.0163	22.61	7.1	0.7309
Line 5 SEC46-01_grt2	80.6	**-199.0**	0.0185	22.43	7.14	0.6994
Line 6 SEC46-01_grt2	101.0	**-178.6**	0.0246	22.45	7.57	0.5824
Line 7 SEC46-01_grt2	120.4	**-159.2**	0.038	22.5	7.77	0.533
Line 8 SEC46-01_grt2	140.8	**-138.8**	0.0453	22.51	8.06	0.5967
Line 9 SEC46-01_grt2	161.0	**-118.6**	0.0487	22.51	8.35	0.4907
Line 10 SEC46-01_grt2	181.4	**-98.2**	0.0619	22.49	7.29	0.5534
Line 11 SEC46-01_grt2	201.8	**-77.8**	0.0328	22.4	10.53	0.5186
Line 12 SEC46-01_grt2	221.2	**-58.4**	0	22.78	9.5	0.5296
Line 13 SEC46-01_grt2	239.5	**-40.1**	0.0203	22.62	8.96	0.5501
Line 14 SEC46-01_grt2	264.1	**-15.5**	0.0336	22.57	8.34	0.5595
Line 15 SEC46-01_grt2	279.6	**0.0**	0.0392	22.51	8.62	0.522
SEC46-01 Average			0.02	22.50	8.09	0.87

Table S1. (cont.)

	wt.%	wt.%	wt.%	wt.%	wt.%	wt.%	wt.%
	Na2O	TiO2	SiO2	K2O	FeO	MgO	Total
Line 1 SEC46-01_grt1	0.02	0.17	38.59	0.00	24.07	5.67	100.59
Line 2 SEC46-01_grt1	0.00	0.21	38.59	0.00	23.95	5.52	100.95
Line 3 SEC46-01_grt1	0.04	0.21	38.75	0.00	24.37	5.83	101.22
Line 4 SEC46-01_grt1	0.03	0.19	38.67	0.00	24.59	5.95	100.78
Line 5 SEC46-01_grt1	0.05	0.15	38.64	0.00	24.50	5.95	100.69
Line 6 SEC46-01_grt1	0.00	0.16	38.70	0.00	24.25	5.74	100.66
Line 7 SEC46-01_grt1	0.00	0.15	38.31	0.00	24.25	5.90	100.17
Line 8 SEC46-01_grt1	0.02	0.12	38.42	0.00	24.49	5.95	100.55
Line 9 SEC46-01_grt1	0.04	0.08	38.72	0.00	24.57	5.97	100.81
Line 10 SEC46-01_grt1	0.08	0.08	38.54	0.00	24.85	6.12	100.82
Line 11 SEC46-01_grt1	0.04	0.05	38.51	0.00	24.45	5.91	100.69
Line 12 SEC46-01_grt1	0.00	0.04	38.75	0.00	24.73	6.08	101.01
Line 13 SEC46-01_grt1	0.02	0.03	38.53	0.00	25.15	6.38	100.68
Line 14 SEC46-01_grt1	0.03	0.04	38.21	0.00	24.76	6.18	100.58
Line 15 SEC46-01_grt1	0.01	0.02	38.42	0.00	24.70	6.00	100.63
Line 16 SEC46-01_grt1	0.01	0.04	38.42	0.00	23.67	5.57	100.29
Line 17 SEC46-01_grt1	0.00	0.05	38.64	0.00	24.32	5.87	100.78
Line 18 SEC46-01_grt1	0.00	0.05	38.37	0.00	24.45	5.90	100.54
Line 19 SEC46-01_grt1	0.00	0.04	38.38	0.00	25.00	6.15	100.44
Line 20 SEC46-01_grt1	0.04	0.00	38.36	0.00	23.69	5.70	99.90
Line 1 SEC46-1_grt3	0.0048	0.0552	37.97	0	25.41	5.87	100.3005
Line 2 SEC46-01_grt3	0.0024	0.0412	38.1	0	25.66	6.17	100.7343
Line 3 SEC46-01_grt3	0	0.0322	38.04	0	25.85	6.19	100.5493
Line 4 SEC46-01_grt3	0.0407	0.0136	38.1	0	25.49	6.28	100.4339
Line 5 SEC46-01_grt3	0.0378	0.0228	38.13	0	23.69	5.48	100.0824
Line 6 SEC46-01_grt3	0.0024	0.0444	38.75	0	23.67	5.44	101.1508
Line 7 SEC46-01_grt3	0.0426	0.0199	39	0	24.57	5.81	101.7091
Line 8 SEC46-01_grt3	0	0.0085	38.93	0	25.03	5.97	101.4379
Line 9 SEC46-01_grt3	0.0499	0.0073	38.66	0	25.19	6.22	101.2477
Line 10 SEC46-01_grt3	0.0165	0	38.51	0	23.7	5.53	100.7863
Line 1 SEC46-01_grt2	0.0309	0.0142	38.56	0.0015	25.16	6.55	100.5864
Line 2 SEC46-01_grt2	0.0571	0.0333	38.62	0	25.18	6.51	100.4065
Line 3 SEC46-01_grt2	0.0476	0.0503	38.46	0	25.07	6.44	100.4641
Line 4 SEC46-01_grt2	0.0572	0.0294	38.44	0	25.21	6.52	100.7137
Line 5 SEC46-01_grt2	0.0262	0.0435	38.38	0	25.18	6.54	100.4576
Line 6 SEC46-01_grt2	0.0285	0.0312	38.54	0	24.93	6.22	100.3766
Line 7 SEC46-01_grt2	0.0594	0.0277	38.65	0	24.92	6.34	100.8381
Line 8 SEC46-01_grt2	0.0475	0.0617	38.52	0	24.86	6.19	100.8912
Line 9 SEC46-01_grt2	0.0639	0.0397	38.74	0	24.44	6.13	100.813
Line 10 SEC46-01_grt2	0.0309	0.039	38.87	0	25.23	6.46	101.0251
Line 11 SEC46-01_grt2	0.0188	0.0376	38.83	0.006	22.9	5.36	100.6337
Line 12 SEC46-01_grt2	0.1128	0.0694	39.19	0	23.55	5.61	101.3417
Line 13 SEC46-01_grt2	0.0686	0.0267	38.7	0	24.27	5.88	101.0956
Line 14 SEC46-01_grt2	0.0735	0.0107	38.66	0.0042	24.72	5.88	100.8514
Line 15 SEC46-01_grt2	0.0831	0.0533	38.67	0	24.55	5.74	100.7875
SEC46-01 Average	0.03	0.06	38.55	0.00	24.61	5.99	100.72

Table S1. (cont.)

	a.p.f.u.	a.p.f.u.	a.p.f.u.	a.p.f.u.	a.p.f.u.	a.p.f.u.	a.p.f.u.
	Cr	Al	Ca	Mn	Na	Ti	Si
Line 1 SEC46-01_grt1	0.0014	2.025	0.658	0.12	0.0032	0.0097	2.978
Line 2 SEC46-01_grt1	0	2.017	0.641	0.178	0	0.0121	2.976
Line 3 SEC46-01_grt1	0	2.039	0.643	0.105	0.0057	0.012	2.97
Line 4 SEC46-01_grt1	0	2.023	0.626	0.095	0.0039	0.0112	2.977
Line 5 SEC46-01_grt1	0.0007	2.016	0.641	0.093	0.0082	0.0089	2.978
Line 6 SEC46-01_grt1	0	2.027	0.675	0.084	0.0007	0.0095	2.98
Line 7 SEC46-01_grt1	0	2.033	0.672	0.0783	0	0.0085	2.966
Line 8 SEC46-01_grt1	0	2.034	0.669	0.0709	0.0029	0.0072	2.964
Line 9 SEC46-01_grt1	0.0007	2.034	0.654	0.0657	0.0064	0.0049	2.976
Line 10 SEC46-01_grt1	0	2.04	0.629	0.0669	0.0114	0.0045	2.965
Line 11 SEC46-01_grt1	0.0007	2.044	0.678	0.064	0.006	0.003	2.965
Line 12 SEC46-01_grt1	0.0017	2.052	0.637	0.0588	0.0004	0.0026	2.969
Line 13 SEC46-01_grt1	0	2.039	0.588	0.0632	0.0036	0.0018	2.967
Line 14 SEC46-01_grt1	0.0021	2.062	0.638	0.0593	0.005	0.0026	2.946
Line 15 SEC46-01_grt1	0.0016	2.058	0.663	0.0483	0.0018	0.0014	2.958
Line 16 SEC46-01_grt1	0	2.048	0.778	0.0442	0.0011	0.0024	2.966
Line 17 SEC46-01_grt1	0	2.041	0.718	0.0416	0	0.0027	2.969
Line 18 SEC46-01_grt1	0.0002	2.056	0.704	0.0387	0	0.003	2.957
Line 19 SEC46-01_grt1	0	2.061	0.629	0.0378	0	0.0024	2.959
Line 20 SEC46-01_grt1	0	2.066	0.743	0.0323	0.0057	0.0001	2.967
Line 1 SEC46-1_grt3	0.0019	2.047	0.576	0.111	0.0007	0.0032	2.95
Line 2 SEC46-01_grt3	0.0074	2.048	0.567	0.086	0.0004	0.0024	2.945
Line 3 SEC46-01_grt3	0.0013	2.054	0.575	0.0626	0	0.0019	2.944
Line 4 SEC46-01_grt3	0.0026	2.048	0.583	0.0654	0.0061	0.0008	2.949
Line 5 SEC46-01_grt3	0.0013	2.05	0.8	0.0407	0.0057	0.0013	2.954
Line 6 SEC46-01_grt3	0.0053	2.032	0.827	0.0374	0.0004	0.0026	2.969
Line 7 SEC46-01_grt3	0.0016	2.042	0.729	0.0361	0.0063	0.0011	2.97
Line 8 SEC46-01_grt3	0.0034	2.042	0.673	0.0344	0	0.0005	2.973
Line 9 SEC46-01_grt3	0.0023	2.048	0.641	0.0371	0.0074	0.0004	2.96
Line 10 SEC46-01_grt3	0.0028	2.045	0.814	0.0347	0.0025	0	2.961
Line 1 SEC46-01_grt2	0.0014	2.037	0.594	0.0383	0.0046	0.0008	2.968
Line 2 SEC46-01_grt2	0.0012	2.033	0.58	0.0383	0.0085	0.0019	2.976
Line 3 SEC46-01_grt2	0.0029	2.035	0.599	0.0463	0.0071	0.0029	2.966
Line 4 SEC46-01_grt2	0.001	2.05	0.585	0.0476	0.0085	0.0017	2.957
Line 5 SEC46-01_grt2	0.0011	2.039	0.59	0.0457	0.0039	0.0025	2.96
Line 6 SEC46-01_grt2	0.0015	2.041	0.625	0.038	0.0043	0.0018	2.972
Line 7 SEC46-01_grt2	0.0023	2.036	0.639	0.0347	0.0088	0.0016	2.968
Line 8 SEC46-01_grt2	0.0028	2.038	0.663	0.0388	0.0071	0.0036	2.959
Line 9 SEC46-01_grt2	0.003	2.036	0.686	0.0319	0.0095	0.0023	2.973
Line 10 SEC46-01_grt2	0.0037	2.03	0.598	0.0359	0.0046	0.0022	2.977
Line 11 SEC46-01_grt2	0.002	2.028	0.866	0.0337	0.0028	0.0022	2.982
Line 12 SEC46-01_grt2	0	2.045	0.775	0.0342	0.0167	0.004	2.985
Line 13 SEC46-01_grt2	0.0012	2.042	0.736	0.0357	0.0102	0.0015	2.965
Line 14 SEC46-01_grt2	0.002	2.043	0.686	0.0364	0.011	0.0006	2.97
Line 15 SEC46-01_grt2	0.0024	2.039	0.71	0.034	0.0124	0.0031	2.972
SEC46-01 Average	0.00	2.04	0.67	0.06	0.00	0.00	2.97

Table S1. (cont.)

	a.p.f.u.	a.p.f.u.	a.p.f.u.	a.p.f.u.
	K	Fe	Mg	Total
Line 1 SEC46-01_grt1	0	1.554	0.652	8.0013
Line 2 SEC46-01_grt1	0	1.545	0.634	8.0031
Line 3 SEC46-01_grt1	0	1.562	0.666	8.0028
Line 4 SEC46-01_grt1	0	1.583	0.683	8.0021
Line 5 SEC46-01_grt1	0	1.579	0.684	8.0089
Line 6 SEC46-01_grt1	0	1.562	0.659	7.9973
Line 7 SEC46-01_grt1	0	1.57	0.681	8.0089
Line 8 SEC46-01_grt1	0	1.58	0.684	8.012
Line 9 SEC46-01_grt1	0	1.58	0.684	8.0057
Line 10 SEC46-01_grt1	0	1.599	0.702	8.0178
Line 11 SEC46-01_grt1	0	1.574	0.678	8.0127
Line 12 SEC46-01_grt1	0	1.585	0.695	8.0015
Line 13 SEC46-01_grt1	0	1.619	0.732	8.0136
Line 14 SEC46-01_grt1	0	1.597	0.711	8.0231
Line 15 SEC46-01_grt1	0	1.591	0.688	8.0111
Line 16 SEC46-01_grt1	0.0001	1.528	0.641	8.0089
Line 17 SEC46-01_grt1	0	1.563	0.672	8.0073
Line 18 SEC46-01_grt1	0	1.576	0.677	8.0119
Line 19 SEC46-01_grt1	0	1.612	0.707	8.0083
Line 20 SEC46-01_grt1	0.0002	1.532	0.657	8.0033
Line 1 SEC46-1_grt3	0	1.651	0.68	8.0209
Line 2 SEC46-01_grt3	0	1.658	0.711	8.0252
Line 3 SEC46-01_grt3	0	1.673	0.714	8.0258
Line 4 SEC46-01_grt3	0	1.65	0.724	8.0289
Line 5 SEC46-01_grt3	0	1.535	0.633	8.021
Line 6 SEC46-01_grt3	0	1.516	0.621	8.0107
Line 7 SEC46-01_grt3	0	1.565	0.66	8.0112
Line 8 SEC46-01_grt3	0	1.598	0.68	8.0043
Line 9 SEC46-01_grt3	0	1.613	0.71	8.0192
Line 10 SEC46-01_grt3	0	1.524	0.633	8.017
Line 1 SEC46-01_grt2	0.0001	1.619	0.752	8.0153
Line 2 SEC46-01_grt2	0	1.623	0.747	8.0089
Line 3 SEC46-01_grt2	0	1.617	0.74	8.0162
Line 4 SEC46-01_grt2	0	1.621	0.748	8.0198
Line 5 SEC46-01_grt2	0	1.624	0.752	8.0183
Line 6 SEC46-01_grt2	0	1.608	0.715	8.0066
Line 7 SEC46-01_grt2	0	1.6	0.726	8.0164
Line 8 SEC46-01_grt2	0	1.597	0.709	8.0183
Line 9 SEC46-01_grt2	0	1.569	0.701	8.0118
Line 10 SEC46-01_grt2	0	1.616	0.738	8.0055
Line 11 SEC46-01_grt2	0.0006	1.471	0.613	8.0013
Line 12 SEC46-01_grt2	0	1.5	0.637	7.997
Line 13 SEC46-01_grt2	0	1.555	0.671	8.0176
Line 14 SEC46-01_grt2	0.0004	1.588	0.674	8.0114
Line 15 SEC46-01_grt2	0	1.578	0.658	8.0089
SEC46-01 Average	0.00	1.58	0.69	8.01

Table S1. (cont.)

	X Almandine	X Pyrope	X Grossular	X Spessartine	Fe/(Fe+Mg)
Line 1 SEC46-01_grt1	0.52	0.22	0.22	0.04	0.70
Line 2 SEC46-01_grt1	0.52	0.21	0.21	0.06	0.71
Line 3 SEC46-01_grt1	0.52	0.22	0.22	0.04	0.70
Line 4 SEC46-01_grt1	0.53	0.23	0.21	0.03	0.70
Line 5 SEC46-01_grt1	0.53	0.23	0.21	0.03	0.70
Line 6 SEC46-01_grt1	0.52	0.22	0.23	0.03	0.70
Line 7 SEC46-01_grt1	0.52	0.23	0.22	0.03	0.70
Line 8 SEC46-01_grt1	0.53	0.23	0.22	0.02	0.70
Line 9 SEC46-01_grt1	0.53	0.23	0.22	0.02	0.70
Line 10 SEC46-01_grt1	0.53	0.23	0.21	0.02	0.69
Line 11 SEC46-01_grt1	0.53	0.23	0.23	0.02	0.70
Line 12 SEC46-01_grt1	0.53	0.23	0.21	0.02	0.70
Line 13 SEC46-01_grt1	0.54	0.24	0.20	0.02	0.69
Line 14 SEC46-01_grt1	0.53	0.24	0.21	0.02	0.69
Line 15 SEC46-01_grt1	0.53	0.23	0.22	0.02	0.70
Line 16 SEC46-01_grt1	0.51	0.21	0.26	0.01	0.70
Line 17 SEC46-01_grt1	0.52	0.22	0.24	0.01	0.70
Line 18 SEC46-01_grt1	0.53	0.23	0.24	0.01	0.70
Line 19 SEC46-01_grt1	0.54	0.24	0.21	0.01	0.70
Line 20 SEC46-01_grt1	0.52	0.22	0.25	0.01	0.70
Line 1 SEC46-1_grt3	0.55	0.23	0.19	0.04	0.71
Line 2 SEC46-01_grt3	0.55	0.24	0.19	0.03	0.70
Line 3 SEC46-01_grt3	0.55	0.24	0.19	0.02	0.70
Line 4 SEC46-01_grt3	0.55	0.24	0.19	0.02	0.70
Line 5 SEC46-01_grt3	0.51	0.21	0.27	0.01	0.71
Line 6 SEC46-01_grt3	0.51	0.21	0.28	0.01	0.71
Line 7 SEC46-01_grt3	0.52	0.22	0.24	0.01	0.70
Line 8 SEC46-01_grt3	0.54	0.23	0.23	0.01	0.70
Line 9 SEC46-01_grt3	0.54	0.24	0.21	0.01	0.69
Line 10 SEC46-01_grt3	0.51	0.21	0.27	0.01	0.71
Line 1 SEC46-01_grt2	0.54	0.25	0.20	0.01	0.68
Line 2 SEC46-01_grt2	0.54	0.25	0.19	0.01	0.68
Line 3 SEC46-01_grt2	0.54	0.25	0.20	0.02	0.69
Line 4 SEC46-01_grt2	0.54	0.25	0.19	0.02	0.68
Line 5 SEC46-01_grt2	0.54	0.25	0.20	0.02	0.68
Line 6 SEC46-01_grt2	0.54	0.24	0.21	0.01	0.69
Line 7 SEC46-01_grt2	0.53	0.24	0.21	0.01	0.69
Line 8 SEC46-01_grt2	0.53	0.24	0.22	0.01	0.69
Line 9 SEC46-01_grt2	0.53	0.23	0.23	0.01	0.69
Line 10 SEC46-01_grt2	0.54	0.25	0.20	0.01	0.69
Line 11 SEC46-01_grt2	0.49	0.21	0.29	0.01	0.71
Line 12 SEC46-01_grt2	0.51	0.22	0.26	0.01	0.70
Line 13 SEC46-01_grt2	0.52	0.22	0.25	0.01	0.70
Line 14 SEC46-01_grt2	0.53	0.23	0.23	0.01	0.70
Line 15 SEC46-01_grt2	0.53	0.22	0.24	0.01	0.71
SEC46-01 Average	0.53	0.23	0.22	0.02	0.70

Table S1. (cont.)

	Tot. Dist (μm)	Dist to grain boundary (μm)	wt.% Cr2O3	wt.% Al2O3	wt.% CaO	wt.% MnO
Line 1 SEC46-02_grt1	0	-216	0.03	22.16	10.31	0.71
Line 2 SEC46-02_grt1	54	-162	0.02	22.29	10.56	0.65
Line 3 SEC46-02_grt1	108	-108	0.05	22.39	10.48	0.67
Line 4 SEC46-02_grt1	163	-53	0.02	22.60	9.58	0.57
Line 5 SEC46-02_grt1	216	0	0.00	22.44	8.17	0.65
Line 1 SEC46-02_grt2	0	-222	0.01	22.44	11.06	0.62
Line 2 SEC46-02_grt2	23	-198	0.06	22.47	10.01	0.58
Line 3 SEC46-02_grt2	48	-174	0.00	22.56	10.55	0.60
Line 4 SEC46-02_grt2	72	-150	0.01	22.43	10.37	0.60
Line 5 SEC46-02_grt2	95	-127	0.03	22.33	9.73	0.70
Line 6 SEC46-02_grt2	122	-100	0.03	22.48	9.50	0.66
Line 7 SEC46-02_grt2	146	-76	0.01	22.53	9.86	0.63
Line 8 SEC46-02_grt2	171	-51	0.02	22.60	9.72	0.56
Line 9 SEC46-02_grt2	194	-28	0.01	22.39	9.73	0.59
Line 10 SEC46-02_grt2	222	0	0.06	22.63	8.32	0.59
SEC46-02 Average			0.02	22.45	9.86	0.62
Line 1 SEC47-01_grt1	0	-146	0.00	22.07	9.78	1.01
Line 2 SEC47-01_grt1	37	-109	0.05	22.28	9.43	0.59
Line 3 SEC47-01_grt1	73	-73	0.03	22.25	8.06	0.55
Line 4 SEC47-01_grt1	110	-36	0.03	22.38	7.59	0.64
Line 5 SEC47-01_grt1	146	0	0.04	22.35	8.89	0.64
Line 1 SEC47-01_grt2	0	-112	0.01	22.17	9.72	0.64
Line 2 SEC47-01_grt2	28	-84	0.04	22.18	9.46	0.70
Line 3 SEC47-01_grt2	56	-56	0.05	22.05	9.26	0.44
Line 4 SEC47-01_grt2	84	-28	0.02	22.42	8.13	0.41
Line 5 SEC47-01_grt2	112	0	0.04	22.52	7.99	0.58
Line 1 SEC47-01_grt3	0	-160	0.10	22.08	9.78	0.77
Line 2 SEC47-01_grt3	48	-112	0.16	22.10	9.75	0.63
Line 3 SEC47-01_grt3	86	-74	0.09	22.10	8.86	0.66
Line 4 SEC47-01_grt3	123	-36	0.03	22.40	7.98	0.57
Line 5 SEC47-01_grt3	160	0	0.02	22.47	8.11	0.62
SEC47-01 Average			0.05	22.25	8.85	0.63

Table S1. (cont.)

	wt.% Na2O	wt.% TiO2	wt.% SiO2	wt.% K2O	wt.% FeO	wt.% MgO	wt.% Total
Line 1 SEC46-02_grt1	0.06	0.13	38.48	0.00	24.07	4.87	100.82
Line 2 SEC46-02_grt1	0.04	0.14	38.77	0.00	23.51	5.04	101.03
Line 3 SEC46-02_grt1	0.05	0.09	38.42	0.00	23.82	4.88	100.85
Line 4 SEC46-02_grt1	0.04	0.11	38.78	0.00	24.21	5.41	101.31
Line 5 SEC46-02_grt1	0.05	0.06	38.69	0.00	25.31	5.70	101.07
Line 1 SEC46-02_grt2	0.03	0.07	38.73	0.00	22.83	4.96	100.73
Line 2 SEC46-02_grt2	0.06	0.05	38.68	0.00	24.89	4.66	101.45
Line 3 SEC46-02_grt2	0.09	0.04	38.54	0.00	23.75	4.94	101.07
Line 4 SEC46-02_grt2	0.00	0.04	38.51	0.00	24.63	4.57	101.16
Line 5 SEC46-02_grt2	0.03	0.01	38.31	0.00	26.11	4.21	101.47
Line 6 SEC46-02_grt2	0.06	0.10	38.84	0.00	24.54	5.40	101.62
Line 7 SEC46-02_grt2	0.01	0.13	38.69	0.00	24.00	5.49	101.36
Line 8 SEC46-02_grt2	0.05	0.12	38.80	0.00	24.15	5.30	101.31
Line 9 SEC46-02_grt2	0.01	0.10	38.64	0.00	24.83	4.95	101.24
Line 10 SEC46-02_grt2	0.04	0.02	38.98	0.00	24.64	5.98	101.26
SEC46-02 Average	0.04	0.08	38.66	0.00	24.35	5.09	101.18
Line 1 SEC47-01_grt1	0.08	0.12	38.40	0.00	25.80	4.20	101.46
Line 2 SEC47-01_grt1	0.06	0.15	38.37	0.00	26.22	4.58	101.73
Line 3 SEC47-01_grt1	0.00	0.12	38.55	0.00	26.99	5.00	101.56
Line 4 SEC47-01_grt1	0.00	0.11	38.43	0.00	27.12	5.18	101.48
Line 5 SEC47-01_grt1	0.00	0.07	38.63	0.00	26.42	4.64	101.67
Line 1 SEC47-01_grt2	0.09	0.14	38.41	0.00	26.12	4.26	101.55
Line 2 SEC47-01_grt2	0.00	0.13	38.42	0.00	26.10	4.49	101.52
Line 3 SEC47-01_grt2	0.07	0.15	38.40	0.00	26.85	4.39	101.66
Line 4 SEC47-01_grt2	0.07	0.08	38.47	0.00	27.12	4.85	101.57
Line 5 SEC47-01_grt2	0.07	0.07	38.50	0.00	26.35	5.25	101.37
Line 1 SEC47-01_grt3	0.05	0.09	38.39	0.00	26.06	4.13	101.44
Line 2 SEC47-01_grt3	0.06	0.12	38.50	0.00	25.85	4.48	101.66
Line 3 SEC47-01_grt3	0.01	0.16	38.25	0.00	26.91	4.35	101.40
Line 4 SEC47-01_grt3	0.01	0.11	38.39	0.00	27.23	4.80	101.52
Line 5 SEC47-01_grt3	0.04	0.07	38.75	0.00	25.83	5.59	101.50
SEC47-01 Average	0.04	0.11	38.46	0.00	26.46	4.68	101.54

Table S1. (cont.)

	a.p.f.u. Cr	a.p.f.u. Al	a.p.f.u. Ca	a.p.f.u. Mn	a.p.f.u. Na	a.p.f.u. Ti	a.p.f.u. Si
Line 1 SEC46-02_grt1	0.0018	2.016	0.853	0.0464	0.0093	0.0077	2.97
Line 2 SEC46-02_grt1	0.0013	2.017	0.869	0.0424	0.0067	0.0084	2.977
Line 3 SEC46-02_grt1	0.0028	2.034	0.866	0.0436	0.0078	0.0054	2.962
Line 4 SEC46-02_grt1	0.0011	2.039	0.785	0.0367	0.0056	0.0062	2.968
Line 5 SEC46-02_grt1	0	2.032	0.672	0.0425	0.0068	0.0037	2.973
Line 1 SEC46-02_grt2	0.0005	2.033	0.911	0.0401	0.0039	0.0038	2.977
Line 2 SEC46-02_grt2	0.0034	2.034	0.824	0.0374	0.0089	0.0028	2.97
Line 3 SEC46-02_grt2	0.0003	2.044	0.868	0.039	0.0127	0.0022	2.961
Line 4 SEC46-02_grt2	0.0008	2.037	0.856	0.039	0	0.0021	2.967
Line 5 SEC46-02_grt2	0.002	2.033	0.806	0.0457	0.0051	0.0008	2.96
Line 6 SEC46-02_grt2	0.0016	2.025	0.778	0.043	0.0095	0.0059	2.969
Line 7 SEC46-02_grt2	0.0007	2.033	0.808	0.0405	0.0021	0.0078	2.961
Line 8 SEC46-02_grt2	0.001	2.039	0.797	0.0363	0.007	0.0067	2.97
Line 9 SEC46-02_grt2	0.0004	2.029	0.801	0.0381	0.0018	0.0055	2.971
Line 10 SEC46-02_grt2	0.0034	2.038	0.681	0.038	0.006	0.0012	2.979
SEC46-02 Average	0.00	2.03	0.81	0.04	0.01	0.00	2.97
Line 1 SEC47-01_grt1	0	2.011	0.81	0.0662	0.0116	0.0069	2.968
Line 2 SEC47-01_grt1	0.0032	2.022	0.778	0.0384	0.009	0.0087	2.955
Line 3 SEC47-01_grt1	0.0021	2.02	0.665	0.0361	0	0.0068	2.969
Line 4 SEC47-01_grt1	0.0021	2.033	0.626	0.0416	0	0.0065	2.962
Line 5 SEC47-01_grt1	0.0022	2.026	0.733	0.0418	0	0.0038	2.971
Line 1 SEC47-01_grt2	0.0004	2.017	0.804	0.0417	0.013	0.0083	2.965
Line 2 SEC47-01_grt2	0.0022	2.017	0.782	0.0457	0.0004	0.0075	2.964
Line 3 SEC47-01_grt2	0.0031	2.007	0.766	0.0286	0.0098	0.009	2.965
Line 4 SEC47-01_grt2	0.0013	2.036	0.671	0.0268	0.0101	0.0045	2.964
Line 5 SEC47-01_grt2	0.0027	2.043	0.659	0.0376	0.0097	0.0042	2.962
Line 1 SEC47-01_grt3	0.006	2.013	0.81	0.0502	0.0069	0.0052	2.968
Line 2 SEC47-01_grt3	0.01	2.007	0.804	0.041	0.009	0.0071	2.966
Line 3 SEC47-01_grt3	0.0058	2.017	0.735	0.0434	0.0022	0.0091	2.962
Line 4 SEC47-01_grt3	0.0017	2.037	0.66	0.0373	0.0022	0.0063	2.962
Line 5 SEC47-01_grt3	0.0014	2.03	0.666	0.0404	0.0053	0.0038	2.971
SEC47-01 Average	0.00	2.02	0.73	0.04	0.01	0.01	2.96

Table S1. (cont.)

	a.p.f.u. K	a.p.f.u. Fe	a.p.f.u. Mg	a.p.f.u. Total
Line 1 SEC46-02_grt1	0	1.554	0.56	8.0182
Line 2 SEC46-02_grt1	0	1.51	0.576	8.0078
Line 3 SEC46-02_grt1	0	1.536	0.561	8.0186
Line 4 SEC46-02_grt1	0	1.55	0.617	8.0086
Line 5 SEC46-02_grt1	0	1.626	0.653	8.009
Line 1 SEC46-02_grt2	0	1.467	0.568	8.0043
Line 2 SEC46-02_grt2	0	1.599	0.534	8.0135
Line 3 SEC46-02_grt2	0	1.527	0.566	8.0202
Line 4 SEC46-02_grt2	0	1.587	0.524	8.0129
Line 5 SEC46-02_grt2	0	1.687	0.485	8.0246
Line 6 SEC46-02_grt2	0	1.569	0.615	8.016
Line 7 SEC46-02_grt2	0	1.536	0.626	8.0152
Line 8 SEC46-02_grt2	0	1.546	0.604	8.007
Line 9 SEC46-02_grt2	0	1.596	0.567	8.0098
Line 10 SEC46-02_grt2	0	1.575	0.681	8.0026
SEC46-02 Average	0.00	1.56	0.58	8.01
Line 1 SEC47-01_grt1	0	1.668	0.484	8.0258
Line 2 SEC47-01_grt1	0.0001	1.689	0.526	8.0294
Line 3 SEC47-01_grt1	0	1.739	0.574	8.012
Line 4 SEC47-01_grt1	0	1.748	0.595	8.0142
Line 5 SEC47-01_grt1	0	1.7	0.532	8.0098
Line 1 SEC47-01_grt2	0	1.686	0.49	8.0254
Line 2 SEC47-01_grt2	0	1.684	0.516	8.0188
Line 3 SEC47-01_grt2	0	1.733	0.505	8.0265
Line 4 SEC47-01_grt2	0	1.748	0.556	8.0177
Line 5 SEC47-01_grt2	0	1.696	0.602	8.0162
Line 1 SEC47-01_grt3	0	1.685	0.476	8.0203
Line 2 SEC47-01_grt3	0	1.665	0.514	8.0231
Line 3 SEC47-01_grt3	0	1.743	0.502	8.0195
Line 4 SEC47-01_grt3	0	1.757	0.552	8.0155
Line 5 SEC47-01_grt3	0	1.656	0.639	8.0129
SEC47-01 Average	0.00	1.71	0.54	8.02

Table S1. (cont.)

	X Almandine	X Pyrope	X Grossular	X Spessartine	Fe/(Fe+Mg)
Line 1 SEC46-02_grt1	0.52	0.19	0.28	0.02	0.74
Line 2 SEC46-02_grt1	0.50	0.19	0.29	0.01	0.72
Line 3 SEC46-02_grt1	0.51	0.19	0.29	0.01	0.73
Line 4 SEC46-02_grt1	0.52	0.21	0.26	0.01	0.72
Line 5 SEC46-02_grt1	0.54	0.22	0.22	0.01	0.71
Line 1 SEC46-02_grt2	0.49	0.19	0.31	0.01	0.72
Line 2 SEC46-02_grt2	0.53	0.18	0.28	0.01	0.75
Line 3 SEC46-02_grt2	0.51	0.19	0.29	0.01	0.73
Line 4 SEC46-02_grt2	0.53	0.17	0.28	0.01	0.75
Line 5 SEC46-02_grt2	0.56	0.16	0.27	0.02	0.78
Line 6 SEC46-02_grt2	0.52	0.20	0.26	0.01	0.72
Line 7 SEC46-02_grt2	0.51	0.21	0.27	0.01	0.71
Line 8 SEC46-02_grt2	0.52	0.20	0.27	0.01	0.72
Line 9 SEC46-02_grt2	0.53	0.19	0.27	0.01	0.74
Line 10 SEC46-02_grt2	0.53	0.23	0.23	0.01	0.70
SEC46-02 Average	0.52	0.19	0.27	0.01	0.73
Line 1 SEC47-01_grt1	0.55	0.16	0.27	0.02	0.78
Line 2 SEC47-01_grt1	0.56	0.17	0.26	0.01	0.76
Line 3 SEC47-01_grt1	0.58	0.19	0.22	0.01	0.75
Line 4 SEC47-01_grt1	0.58	0.20	0.21	0.01	0.75
Line 5 SEC47-01_grt1	0.57	0.18	0.24	0.01	0.76
Line 1 SEC47-01_grt2	0.56	0.16	0.27	0.01	0.77
Line 2 SEC47-01_grt2	0.56	0.17	0.26	0.02	0.77
Line 3 SEC47-01_grt2	0.57	0.17	0.25	0.01	0.77
Line 4 SEC47-01_grt2	0.58	0.19	0.22	0.01	0.76
Line 5 SEC47-01_grt2	0.57	0.20	0.22	0.01	0.74
Line 1 SEC47-01_grt3	0.56	0.16	0.27	0.02	0.78
Line 2 SEC47-01_grt3	0.55	0.17	0.27	0.01	0.76
Line 3 SEC47-01_grt3	0.58	0.17	0.24	0.01	0.78
Line 4 SEC47-01_grt3	0.58	0.18	0.22	0.01	0.76
Line 5 SEC47-01_grt3	0.55	0.21	0.22	0.01	0.72
SEC47-01 Average	0.57	0.18	0.24	0.01	0.76

Table S2. Omphacite major element compositions (EMPA)

			wt. %	wt. %	wt. %
	Tot. Dist (μm)	Dist to grain boundary (μm)	TiO2	SiO2	K2O
Line 1 SEC42-06_cpx1	0	-314	0.17	54.41	0.01
Line 2 SEC42-06_cpx1	32	-282	0.16	54.26	0.00
Line 3 SEC42-06_cpx1	64	-250	0.17	54.47	0.00
Line 4 SEC42-06_cpx1	108	-206	0.20	54.46	0.00
Line 5 SEC42-06_cpx1	153	-161	0.17	54.36	0.00
Line 6 SEC42-06_cpx1	185	-129	0.16	54.77	0.00
Line 7 SEC42-06_cpx1	224	-89	0.12	54.63	0.00
Line 8 SEC42-06_cpx1	254	-60	0.14	54.56	0.00
Line 9 SEC42-06_cpx1	293	-21	0.13	54.78	0.01
Line 10 SEC42-06_cpx1	314	0	0.13	54.83	0.00
Line 1 SEC42-06_cpx2_core->rim	0	-692	0.17	54.73	0.00
Line 2 SEC42-06_cpx2_core->rim	157	-535	0.14	54.55	0.00
Line 3 SEC42-06_cpx2_core->rim	443	-249	0.19	54.61	0.00
Line 4 SEC42-06_cpx2_core->rim	565	-127	0.18	54.15	0.00
Line 5 SEC42-06_cpx2_core->rim	692	0	0.15	54.66	0.00
SEC42-06 Average			0.16	54.55	0.00
Line 1 43-01_Cpx1	0	-1944	0.12	54.95	0.00
Line 2 43-01_Cpx1	211	-1734	0.15	54.82	0.00
Line 3 43-01_Cpx1	442	-1502	0.13	54.97	0.00
Line 4 43-01_Cpx1	647	-1298	0.16	54.87	0.00
Line 5 43-01_Cpx1	862	-1082	0.12	54.82	0.00
Line 6 43-01_Cpx1	1078	-866	0.11	55.44	0.00
Line 7 43-01_Cpx1	1293	-651	0.13	55.36	0.00
Line 8 43-01_Cpx1	1532	-412	0.10	55.35	0.00
Line 9 43-01_Cpx1	1738	-207	0.14	55.43	0.00
Line 10 43-01_Cpx1	1944	0	0.14	55.32	0.00
SEC43-01 Average			0.13	55.13	0.00
Line 1 SEC43-03_omph1	0	-210	0.21	54.26	0.00
Line 2 SEC43-03_omph1	23	-187	0.20	54.38	0.00
Line 3 SEC43-03_omph1	47	-164	0.17	54.41	0.00
Line 4 SEC43-03_omph1	70	-141	0.21	54.35	0.00
Line 5 SEC43-03_omph1	94	-117	0.21	54.36	0.00
Line 6 SEC43-03_omph1	117	-94	0.19	54.22	0.00
ne 7 SEC43-03_omph1 pit @8	138	-73	0.24	54.20	0.00
Line 8 SEC43-03_omph1	164	-47	0.19	54.21	0.00
Line 9 SEC43-03_omph1	187	-24	0.21	54.10	0.00
Line 10 SEC43-03_omph1	210	0	0.20	53.95	0.00
SEC43-03 Average			0.20	54.24	0.00

Table S2. (cont.)

	wt. %	wt. %	wt. %	wt. %	wt. %	wt. %	wt. %
	MnO	Na2O	Cr2O3	Al2O3	CaO	FeO	MgO
Line 1 SEC42-06_cpx1	0.05	6.17	0.05	10.07	13.56	6.70	8.14
Line 2 SEC42-06_cpx1	0.04	6.56	0.07	9.99	13.49	6.66	8.10
Line 3 SEC42-06_cpx1	0.04	6.33	0.04	10.06	13.66	6.73	8.13
Line 4 SEC42-06_cpx1	0.04	6.56	0.05	10.27	13.48	6.63	7.97
Line 5 SEC42-06_cpx1	0.02	6.37	0.07	9.90	13.54	6.65	8.09
Line 6 SEC42-06_cpx1	0.02	6.35	0.06	10.07	13.40	6.88	8.03
Line 7 SEC42-06_cpx1	0.05	6.42	0.06	10.26	13.32	6.86	8.07
Line 8 SEC42-06_cpx1	0.02	6.68	0.02	10.42	13.15	6.70	7.95
Line 9 SEC42-06_cpx1	0.04	6.34	0.02	9.87	13.64	6.89	8.19
Line 10 SEC42-06_cpx1	0.02	6.11	0.03	9.98	13.46	6.95	8.22
Line 1 SEC42-06_cpx2_core->rim	0.02	6.74	0.00	9.74	13.82	6.65	8.19
Line 2 SEC42-06_cpx2_core->rim	0.00	6.29	0.03	10.05	13.67	6.74	8.01
Line 3 SEC42-06_cpx2_core->rim	0.03	6.57	0.01	10.20	13.75	6.69	7.96
Line 4 SEC42-06_cpx2_core->rim	0.03	6.55	0.03	10.17	13.68	6.79	8.06
Line 5 SEC42-06_cpx2_core->rim	0.02	6.51	0.06	10.20	13.51	6.81	7.93
SEC42-06 Average	0.03	6.44	0.04	10.08	13.54	6.76	8.07
Line 1 43-01_Cpx1	0.02	6.13	0.05	10.37	13.99	4.98	8.89
Line 2 43-01_Cpx1	0.02	6.09	0.12	10.22	14.16	5.04	8.73
Line 3 43-01_Cpx1	0.01	5.94	0.09	10.04	14.39	4.92	9.26
Line 4 43-01_Cpx1	0.01	5.90	0.06	10.09	14.41	5.10	8.89
Line 5 43-01_Cpx1	0.01	6.23	0.04	10.14	14.22	5.02	8.88
Line 6 43-01_Cpx1	0.00	6.22	0.06	10.02	14.41	4.88	8.89
Line 7 43-01_Cpx1	0.03	6.29	0.06	10.06	14.40	4.88	8.87
Line 8 43-01_Cpx1	0.01	6.15	0.07	9.85	14.35	4.98	8.90
Line 9 43-01_Cpx1	0.01	6.07	0.06	10.19	14.18	4.97	8.57
Line 10 43-01_Cpx1	0.01	6.20	0.07	10.28	14.28	5.04	8.61
SEC43-01 Average	0.01	6.12	0.07	10.13	14.28	4.98	8.85
Line 1 SEC43-03_omph1	0.03	6.19	0.00	10.38	13.85	6.15	8.37
Line 2 SEC43-03_omph1	0.03	6.21	0.03	10.42	13.82	6.18	8.43
Line 3 SEC43-03_omph1	0.02	6.27	0.02	10.41	13.94	6.22	8.48
Line 4 SEC43-03_omph1	0.04	6.08	0.02	10.46	13.96	6.18	8.43
Line 5 SEC43-03_omph1	0.02	5.94	0.04	10.35	13.95	6.23	8.52
Line 6 SEC43-03_omph1	0.03	6.29	0.06	10.30	13.94	6.17	8.41
ne 7 SEC43-03_omph1 pit @8	0.03	6.04	0.03	10.46	13.93	6.27	8.53
Line 8 SEC43-03_omph1	0.01	6.24	0.03	10.47	14.09	6.23	8.56
Line 9 SEC43-03_omph1	0.05	6.18	0.02	10.33	14.00	6.31	8.49
Line 10 SEC43-03_omph1	0.03	6.59	0.03	10.33	13.87	6.66	8.35
SEC43-03 Average	0.03	6.20	0.03	10.39	13.94	6.26	8.46

Table S2. (cont.)

	wt. %	a.p.f.u.	a.p.f.u.	a.p.f.u.	a.p.f.u.	a.p.f.u.	a.p.f.u.
	Total	Ti	Si	K	Mn	Na	Cr
Line 1 SEC42-06_cpx1	99.33	0.0046	1.976	0.0007	0.0016	0.434	0.0014
Line 2 SEC42-06_cpx1	99.33	0.0044	1.973	0.0001	0.0013	0.462	0.0019
Line 3 SEC42-06_cpx1	99.63	0.0046	1.974	0	0.0013	0.445	0.001
Line 4 SEC42-06_cpx1	99.66	0.0055	1.972	0	0.0011	0.46	0.0016
Line 5 SEC42-06_cpx1	99.17	0.0047	1.978	0.0001	0.0007	0.45	0.002
Line 6 SEC42-06_cpx1	99.74	0.0045	1.981	0	0.0007	0.445	0.0016
Line 7 SEC42-06_cpx1	99.79	0.0033	1.975	0	0.0014	0.45	0.0018
Line 8 SEC42-06_cpx1	99.63	0.0037	1.974	0	0.0007	0.469	0.0004
Line 9 SEC42-06_cpx1	99.92	0.0036	1.98	0.0003	0.0013	0.444	0.0007
Line 10 SEC42-06_cpx1	99.74	0.0035	1.982	0.0001	0.0006	0.428	0.0009
Line 1 SEC42-06_cpx2_core->rim	100.07	0.0047	1.977	0	0.0007	0.472	0.0001
Line 2 SEC42-06_cpx2_core->rim	99.47	0.0037	1.978	0	0	0.442	0.0007
Line 3 SEC42-06_cpx2_core->rim	100.01	0.0052	1.972	0	0.0009	0.46	0.0004
Line 4 SEC42-06_cpx2_core->rim	99.64	0.005	1.965	0	0.001	0.461	0.0008
Line 5 SEC42-06_cpx2_core->rim	99.86	0.0041	1.976	0.0001	0.0007	0.456	0.0018
SEC42-06 Average	99.67	0.00	1.98	0.00	0.00	0.45	0.00
Line 1 43-01_Cpx1	99.50	0.0033	1.976	0	0.0005	0.428	0.0015
Line 2 43-01_Cpx1	99.34	0.004	1.977	0	0.0005	0.426	0.0033
Line 3 43-01_Cpx1	99.74	0.0034	1.974	0	0.0003	0.414	0.0024
Line 4 43-01_Cpx1	99.50	0.0044	1.976	0	0.0004	0.412	0.0018
Line 5 43-01_Cpx1	99.49	0.0034	1.975	0	0.0004	0.435	0.0012
Line 6 43-01_Cpx1	100.03	0.0031	1.984	0	0	0.431	0.0016
Line 7 43-01_Cpx1	100.07	0.0034	1.982	0	0.0008	0.436	0.0017
Line 8 43-01_Cpx1	99.77	0.0027	1.987	0	0.0003	0.428	0.0021
Line 9 43-01_Cpx1	99.61	0.0037	1.99	0	0.0002	0.422	0.0016
Line 10 43-01_Cpx1	99.95	0.0038	1.982	0	0.0003	0.43	0.0021
SEC43-01 Average	99.70	0.00	1.98	0.00	0.00	0.43	0.00
Line 1 SEC43-03_omph1	99.45	0.0059	1.965	0.0001	0.0009	0.434	0.0001
Line 2 SEC43-03_omph1	99.70	0.0053	1.964	0	0.001	0.435	0.0008
Line 3 SEC43-03_omph1	99.94	0.0045	1.962	0	0.0008	0.438	0.0004
Line 4 SEC43-03_omph1	99.74	0.0058	1.963	0.0002	0.0013	0.425	0.0007
Line 5 SEC43-03_omph1	99.62	0.0056	1.965	0	0.0007	0.416	0.001
Line 6 SEC43-03_omph1	99.61	0.0051	1.963	0	0.0011	0.441	0.0017
ne 7 SEC43-03_omph1 pit @8	99.73	0.0065	1.958	0	0.001	0.423	0.0009
Line 8 SEC43-03_omph1	100.03	0.0051	1.955	0	0.0004	0.436	0.0009
Line 9 SEC43-03_omph1	99.69	0.0057	1.958	0	0.0014	0.434	0.0006
Line 10 SEC43-03_omph1	100.01	0.0056	1.953	0	0.0008	0.462	0.0009
SEC43-03 Average	99.75	0.01	1.96	0.00	0.00	0.43	0.00

Table S2. (cont.)

	a.p.f.u. Al	a.p.f.u. Ca	a.p.f.u. Fe	a.p.f.u. Fe3+	a.p.f.u. Mg	a.p.f.u. Total
Line 1 SEC42-06_cpx1	0.431	0.527	0.203	0	0.441	4.0203
Line 2 SEC42-06_cpx1	0.428	0.526	0.203	0	0.439	4.0388
Line 3 SEC42-06_cpx1	0.43	0.53	0.204	0	0.439	4.029
Line 4 SEC42-06_cpx1	0.438	0.523	0.201	0	0.43	4.0322
Line 5 SEC42-06_cpx1	0.425	0.528	0.202	0	0.439	4.0296
Line 6 SEC42-06_cpx1	0.429	0.519	0.208	0	0.433	4.0219
Line 7 SEC42-06_cpx1	0.437	0.516	0.207	0	0.435	4.0266
Line 8 SEC42-06_cpx1	0.444	0.51	0.203	0	0.429	4.0339
Line 9 SEC42-06_cpx1	0.42	0.528	0.208	0	0.441	4.027
Line 10 SEC42-06_cpx1	0.425	0.521	0.21	0	0.443	4.0142
Line 1 SEC42-06_cpx2_core->rim	0.415	0.535	0.201	0	0.441	4.0466
Line 2 SEC42-06_cpx2_core->rim	0.43	0.531	0.205	0	0.433	4.0235
Line 3 SEC42-06_cpx2_core->rim	0.434	0.532	0.202	0	0.429	4.0356
Line 4 SEC42-06_cpx2_core->rim	0.435	0.532	0.206	0	0.436	4.0419
Line 5 SEC42-06_cpx2_core->rim	0.435	0.523	0.206	0	0.427	4.0297
SEC42-06 Average	0.43	0.53	0.20	0.00	0.44	4.03
Line 1 43-01_Cpx1	0.439	0.539	0.15	0	0.476	4.0134
Line 2 43-01_Cpx1	0.435	0.547	0.152	0	0.469	4.0138
Line 3 43-01_Cpx1	0.425	0.554	0.148	0	0.495	4.0161
Line 4 43-01_Cpx1	0.428	0.556	0.154	0	0.477	4.0096
Line 5 43-01_Cpx1	0.431	0.549	0.151	0	0.477	4.023
Line 6 43-01_Cpx1	0.423	0.553	0.146	0	0.474	4.0157
Line 7 43-01_Cpx1	0.425	0.552	0.146	0	0.473	4.0199
Line 8 43-01_Cpx1	0.417	0.552	0.15	0	0.476	4.0152
Line 9 43-01_Cpx1	0.431	0.545	0.149	0	0.459	4.0016
Line 10 43-01_Cpx1	0.434	0.548	0.151	0	0.46	4.0113
SEC43-01 Average	0.43	0.55	0.15	0.00	0.47	4.01
Line 1 SEC43-03_omph1	0.443	0.538	0.186		0.452	4.0251
Line 2 SEC43-03_omph1	0.444	0.535	0.187		0.454	4.0262
Line 3 SEC43-03_omph1	0.442	0.539	0.188		0.456	4.0308
Line 4 SEC43-03_omph1	0.445	0.54	0.187		0.454	4.0221
Line 5 SEC43-03_omph1	0.441	0.54	0.188		0.459	4.0163
Line 6 SEC43-03_omph1	0.439	0.541	0.187		0.454	4.0329
ne 7 SEC43-03_omph1 pit @8	0.445	0.539	0.189		0.459	4.0215
Line 8 SEC43-03_omph1	0.445	0.545	0.188		0.46	4.0354
Line 9 SEC43-03_omph1	0.441	0.543	0.191		0.458	4.0328
Line 10 SEC43-03_omph1	0.441	0.538	0.202		0.45	4.0533
SEC43-03 Average	0.44	0.54	0.19	#DIV/0!	0.46	4.03

Table S2. (cont.)

	XWo = Ca/Ca+Mg+FeT	XEn = Mg/Ca+Mg+FeT	XFs = FeT/Ca+Mg+FeT	Mg/(Mg+Fe)
Line 1 SEC42-06_cpx1	45.00	37.66	17.34	0.68
Line 2 SEC42-06_cpx1	45.03	37.59	17.38	0.68
Line 3 SEC42-06_cpx1	45.18	37.43	17.39	0.68
Line 4 SEC42-06_cpx1	45.32	37.26	17.42	0.68
Line 5 SEC42-06_cpx1	45.17	37.55	17.28	0.68
Line 6 SEC42-06_cpx1	44.74	37.33	17.93	0.68
Line 7 SEC42-06_cpx1	44.56	37.56	17.88	0.68
Line 8 SEC42-06_cpx1	44.66	37.57	17.78	0.68
Line 9 SEC42-06_cpx1	44.86	37.47	17.67	0.68
Line 10 SEC42-06_cpx1	44.38	37.73	17.89	0.68
Line 1 SEC42-06_cpx2_core->rim	45.45	37.47	17.08	0.69
Line 2 SEC42-06_cpx2_core->rim	45.42	37.04	17.54	0.68
Line 3 SEC42-06_cpx2_core->rim	45.74	36.89	17.37	0.68
Line 4 SEC42-06_cpx2_core->rim	45.32	37.14	17.55	0.68
Line 5 SEC42-06_cpx2_core->rim	45.24	36.94	17.82	0.67
SEC42-06 Average	45.07	37.37	17.55	0.68
Line 1 43-01_Cpx1	46.27	40.86	12.88	0.76
Line 2 43-01_Cpx1	46.83	40.15	13.01	0.76
Line 3 43-01_Cpx1	46.28	41.35	12.36	0.77
Line 4 43-01_Cpx1	46.84	40.19	12.97	0.76
Line 5 43-01_Cpx1	46.64	40.53	12.83	0.76
Line 6 43-01_Cpx1	47.14	40.41	12.45	0.76
Line 7 43-01_Cpx1	47.14	40.39	12.47	0.76
Line 8 43-01_Cpx1	46.86	40.41	12.73	0.76
Line 9 43-01_Cpx1	47.27	39.81	12.92	0.75
Line 10 43-01_Cpx1	47.28	39.69	13.03	0.75
SEC43-01 Average	46.86	40.38	12.77	0.76
Line 1 SEC43-03_omph1	45.75	38.44	15.82	0.71
Line 2 SEC43-03_omph1	45.49	38.61	15.90	0.71
Line 3 SEC43-03_omph1	45.56	38.55	15.89	0.71
Line 4 SEC43-03_omph1	45.72	38.44	15.83	0.71
Line 5 SEC43-03_omph1	45.49	38.67	15.84	0.71
Line 6 SEC43-03_omph1	45.77	38.41	15.82	0.71
ne 7 SEC43-03_omph1 pit @8	45.41	38.67	15.92	0.71
Line 8 SEC43-03_omph1	45.68	38.56	15.76	0.71
Line 9 SEC43-03_omph1	45.55	38.42	16.02	0.71
Line 10 SEC43-03_omph1	45.21	37.82	16.97	0.69
SEC43-03 Average	45.56	38.46	15.98	0.71

Table S2. (cont.)

	Tot. Dist (μm)	Dist to grain boundary (μm)	wt. % TiO2	wt. % SiO2	wt. % K2O
Line 1 SEC46-01_omph1	0	-364	0.25	54.11	0.01
Line 2 SEC46-01_omph1	25	-339	0.18	54.07	0.00
Line 3 SEC46-01_omph1	50	-313	0.16	53.95	0.01
Line 4 SEC46-01_omph1	76	-288	0.36	49.19	0.19
Line 5 SEC46-01_omph1	101	-262	0.13	54.04	0.00
Line 6 SEC46-01_omph1	126	-238	0.14	53.89	0.00
Line 7 SEC46-01_omph1	147	-217	0.15	54.79	0.00
Line 8 SEC46-01_omph1	194	-170	0.20	53.91	0.01
Line 9 SEC46-01_omph1	212	-152	0.35	53.85	0.00
Line 10 SEC46-01_omph1	238	-126	0.14	53.79	0.00
Line 11 SEC46-01_omph1	263	-101	0.11	54.20	0.00
Line 12 SEC46-01_omph1	289	-75	0.14	54.06	0.00
Line 13 SEC46-01_omph1	314	-50	0.13	54.18	0.00
Line 14 SEC46-01_omph1	340	-24	0.14	54.28	0.00
Line 15 SEC46-01_omph1	364	0	0.16	54.24	0.00
Line 1 SEC46-01_omph2	0	-310	0.12	53.56	0.00
Line 2 SEC46-01_omph2	78	-232	0.15	53.03	0.01
Line 3 SEC46-01_omph2	155	-155	0.12	53.60	0.00
Line 4 SEC46-01_omph2	233	-77	0.17	53.48	0.01
SEC46-01 Average			0.17	53.70	0.01
Line 1 SEC46-02_omph1	0	-175	0.14	54.47	0.00
Line 2 SEC46-02_omph1	19	-156	0.11	54.37	0.01
Line 3 SEC46-02_omph1	39	-136	0.10	54.30	0.01
Line 4 SEC46-02_omph1	59	-116	0.13	54.26	0.01
Line 5 SEC46-02_omph1	78	-97	0.12	54.09	0.00
Line 6 SEC46-02_omph1	98	-77	0.12	54.26	0.00
Line 7 SEC46-02_omph1	117	-58	0.09	54.29	0.01
Line 8 SEC46-02_omph1	136	-39	0.12	54.35	0.01
Line 9 SEC46-02_omph1	156	-19	0.08	54.63	0.00
Line 10 SEC46-02_omph1	175	0	0.10	54.29	0.01
Line 1 SEC46-02_omph2	0	-238	0.09	54.32	0.00
Line 2 SEC46-02_omph2	59	-178	0.09	54.23	0.00
Line 3 SEC46-02_omph2	119	-119	0.13	54.29	0.00
Line 4 SEC46-02_omph2	178	-59	0.11	54.36	0.00
Line 5 SEC46-02_omph2	238	0	0.12	54.08	0.00
SEC46-02 Average			0.11	54.31	0.00

Table S2. (cont.)

	wt. %	wt. %	wt. %	wt. %	wt. %	wt. %	wt. %
	MnO	Na2O	Cr2O3	Al2O3	CaO	FeO	MgO
Line 1 SEC46-01_omph1	0.04	4.17	0.03	7.54	17.63	4.48	11.20
Line 2 SEC46-01_omph1	0.03	4.39	0.00	8.13	17.04	4.49	10.79
Line 3 SEC46-01_omph1	0.01	4.18	0.01	7.95	17.26	4.55	10.94
Line 4 SEC46-01_omph1	0.01	2.58	0.00	9.97	11.09	8.72	14.83
Line 5 SEC46-01_omph1	0.01	4.45	0.01	7.99	17.21	4.62	10.83
Line 6 SEC46-01_omph1	0.00	4.14	0.02	7.56	17.51	4.58	11.11
Line 7 SEC46-01_omph1	0.02	4.19	0.01	8.31	17.21	4.57	10.50
Line 8 SEC46-01_omph1	0.02	4.18	0.02	7.47	17.65	4.60	11.18
Line 9 SEC46-01_omph1	0.03	4.08	0.02	7.56	17.66	4.56	11.21
Line 10 SEC46-01_omph1	0.01	4.04	0.04	7.34	17.75	4.64	11.33
Line 11 SEC46-01_omph1	0.04	4.28	0.10	7.48	17.28	4.53	11.05
Line 12 SEC46-01_omph1	0.03	4.24	0.10	7.66	17.34	4.62	11.08
Line 13 SEC46-01_omph1	0.03	4.02	0.06	7.35	17.59	4.62	11.20
Line 14 SEC46-01_omph1	0.03	4.34	0.06	7.71	17.48	4.53	11.13
Line 15 SEC46-01_omph1	0.03	4.12	0.07	7.46	17.40	4.65	11.24
Line 1 SEC46-01_omph2	0.03	4.01	0.07	7.72	17.46	4.71	10.95
Line 2 SEC46-01_omph2	0.03	4.17	0.08	7.84	17.52	4.70	10.99
Line 3 SEC46-01_omph2	0.03	3.99	0.05	7.40	17.72	4.74	11.15
Line 4 SEC46-01_omph2	0.03	4.12	0.09	7.53	17.54	4.65	11.10
SEC46-01 Average	0.02	4.09	0.04	7.79	17.12	4.82	11.25
Line 1 SEC46-02_omph1	0.03	5.90	0.04	9.31	14.79	5.20	9.25
Line 2 SEC46-02_omph1	0.01	5.79	0.04	9.33	14.91	5.23	9.26
Line 3 SEC46-02_omph1	0.02	5.69	0.00	9.49	14.80	5.26	9.13
Line 4 SEC46-02_omph1	0.02	5.90	0.02	9.27	14.98	5.36	9.24
Line 5 SEC46-02_omph1	0.01	5.65	0.04	9.28	14.97	5.39	9.09
Line 6 SEC46-02_omph1	0.02	5.78	0.02	9.20	14.89	5.39	9.29
Line 7 SEC46-02_omph1	0.02	5.95	0.02	9.23	14.77	5.22	9.31
Line 8 SEC46-02_omph1	0.02	5.54	0.03	9.35	14.82	5.17	9.17
Line 9 SEC46-02_omph1	0.02	6.03	0.05	9.65	14.57	5.08	9.24
Line 10 SEC46-02_omph1	0.01	5.61	0.03	9.28	14.87	5.28	9.40
Line 1 SEC46-02_omph2	0.01	5.50	0.02	9.09	15.03	5.40	9.37
Line 2 SEC46-02_omph2	0.01	5.69	0.04	9.25	14.95	5.38	9.34
Line 3 SEC46-02_omph2	0.01	5.71	0.04	9.15	14.93	5.39	9.16
Line 4 SEC46-02_omph2	0.02	5.59	0.00	9.13	15.07	5.41	9.21
Line 5 SEC46-02_omph2	0.02	5.55	0.04	9.22	14.92	5.39	9.28
SEC46-02 Average	0.02	5.73	0.03	9.28	14.88	5.30	9.25

Table S2. (cont.)

	wt. %	a.p.f.u.	a.p.f.u.	a.p.f.u.	a.p.f.u.	a.p.f.u.	a.p.f.u.
	Total	Ti	Si	K	Mn	Na	Cr
Line 1 SEC46-01_omph1	99.46	0.0067	1.963	0.0003	0.0014	0.294	0.0009
Line 2 SEC46-01_omph1	99.12	0.0049	1.964	0	0.0011	0.309	0
Line 3 SEC46-01_omph1	99.02	0.0044	1.963	0.0003	0.0002	0.295	0.0004
Line 4 SEC46-01_omph1	96.95	0.0102	1.839	0.0092	0.0004	0.187	0
Line 5 SEC46-01_omph1	99.29	0.0035	1.963	0	0.0003	0.314	0.0002
Line 6 SEC46-01_omph1	98.96	0.0039	1.965	0.0001	0.0001	0.293	0.0006
Line 7 SEC46-01_omph1	99.75	0.0041	1.974	0	0.0007	0.293	0.0002
Line 8 SEC46-01_omph1	99.24	0.0054	1.962	0.0002	0.0008	0.295	0.0007
Line 9 SEC46-01_omph1	99.32	0.0095	1.958	0	0.001	0.287	0.0005
Line 10 SEC46-01_omph1	99.08	0.0039	1.962	0.0001	0.0004	0.286	0.0011
Line 11 SEC46-01_omph1	99.08	0.0031	1.972	0	0.0014	0.302	0.0029
Line 12 SEC46-01_omph1	99.27	0.004	1.965	0	0.0009	0.298	0.0028
Line 13 SEC46-01_omph1	99.19	0.0036	1.971	0	0.001	0.284	0.0019
Line 14 SEC46-01_omph1	99.70	0.0038	1.964	0	0.0008	0.304	0.0018
Line 15 SEC46-01_omph1	99.37	0.0045	1.969	0	0.0009	0.29	0.0019
Line 1 SEC46-01_omph2	98.63	0.0034	1.961	0.0002	0.0008	0.284	0.0019
Line 2 SEC46-01_omph2	98.52	0.0041	1.947	0.0003	0.0008	0.297	0.0025
Line 3 SEC46-01_omph2	98.80	0.0034	1.961	0	0.0008	0.283	0.0013
Line 4 SEC46-01_omph2	98.71	0.0046	1.958	0.0003	0.0008	0.292	0.0025
SEC46-01 Average	99.02	0.00	1.96	0.00	0.00	0.29	0.00
Line 1 SEC46-02_omph1	99.12	0.0037	1.976	0.0001	0.0008	0.415	0.001
Line 2 SEC46-02_omph1	99.06	0.0029	1.974	0.0004	0.0004	0.408	0.0011
Line 3 SEC46-02_omph1	98.80	0.0028	1.975	0.0004	0.0005	0.401	0.0001
Line 4 SEC46-02_omph1	99.19	0.0036	1.971	0.0005	0.0006	0.415	0.0007
Line 5 SEC46-02_omph1	98.63	0.0032	1.974	0.0002	0.0002	0.4	0.0011
Line 6 SEC46-02_omph1	98.98	0.0033	1.974	0.0002	0.0007	0.408	0.0006
Line 7 SEC46-02_omph1	98.91	0.0025	1.975	0.0004	0.0006	0.42	0.0006
Line 8 SEC46-02_omph1	98.59	0.0033	1.98	0.0004	0.0008	0.392	0.001
Line 9 SEC46-02_omph1	99.35	0.0022	1.974	0	0.0006	0.423	0.0015
Line 10 SEC46-02_omph1	98.88	0.0028	1.974	0.0004	0.0004	0.396	0.0009
Line 1 SEC46-02_omph2	98.84	0.0025	1.978	0	0.0004	0.389	0.0006
Line 2 SEC46-02_omph2	98.98	0.0025	1.973	0	0.0004	0.401	0.0011
Line 3 SEC46-02_omph2	98.82	0.0035	1.978	0.0001	0.0003	0.404	0.0013
Line 4 SEC46-02_omph2	98.90	0.003	1.978	0	0.0008	0.394	0
Line 5 SEC46-02_omph2	98.62	0.0032	1.974	0	0.0006	0.393	0.0012
SEC46-02 Average	98.91	0.00	1.98	0.00	0.00	0.40	0.00

Table S2. (cont.)

	a.p.f.u. Al	a.p.f.u. Ca	a.p.f.u. Fe	a.p.f.u. Fe3+	a.p.f.u. Mg	a.p.f.u. Total
Line 1 SEC46-01_omph1	0.322	0.685	0.136		0.606	4.0154
Line 2 SEC46-01_omph1	0.348	0.663	0.136		0.584	4.01
Line 3 SEC46-01_omph1	0.341	0.673	0.139		0.594	4.0104
Line 4 SEC46-01_omph1	0.439	0.444	0.273		0.827	4.0289
Line 5 SEC46-01_omph1	0.342	0.67	0.14		0.586	4.0191
Line 6 SEC46-01_omph1	0.325	0.684	0.14		0.604	4.0158
Line 7 SEC46-01_omph1	0.353	0.665	0.138		0.564	3.9921
Line 8 SEC46-01_omph1	0.321	0.688	0.14		0.606	4.0192
Line 9 SEC46-01_omph1	0.324	0.688	0.139		0.607	4.0141
Line 10 SEC46-01_omph1	0.316	0.693	0.141		0.616	4.0196
Line 11 SEC46-01_omph1	0.321	0.674	0.138		0.6	4.0145
Line 12 SEC46-01_omph1	0.328	0.675	0.141		0.6	4.0148
Line 13 SEC46-01_omph1	0.315	0.686	0.14		0.607	4.0096
Line 14 SEC46-01_omph1	0.329	0.678	0.137		0.6	4.0185
Line 15 SEC46-01_omph1	0.319	0.677	0.141		0.608	4.0114
Line 1 SEC46-01_omph2	0.333	0.685	0.144		0.598	4.0113
Line 2 SEC46-01_omph2	0.339	0.689	0.144		0.602	4.0258
Line 3 SEC46-01_omph2	0.319	0.695	0.145		0.608	4.0166
Line 4 SEC46-01_omph2	0.325	0.688	0.142		0.606	4.0193
SEC46-01 Average	0.33	0.67	0.15	#DIV/0!	0.61	4.02
Line 1 SEC46-02_omph1	0.398	0.575	0.158		0.5	4.0277
Line 2 SEC46-02_omph1	0.4	0.58	0.159		0.501	4.0268
Line 3 SEC46-02_omph1	0.407	0.577	0.16		0.495	4.0189
Line 4 SEC46-02_omph1	0.397	0.583	0.163		0.5	4.0345
Line 5 SEC46-02_omph1	0.399	0.585	0.165		0.495	4.0228
Line 6 SEC46-02_omph1	0.395	0.58	0.164		0.504	4.0299
Line 7 SEC46-02_omph1	0.396	0.576	0.159		0.505	4.0352
Line 8 SEC46-02_omph1	0.401	0.579	0.158		0.498	4.0135
Line 9 SEC46-02_omph1	0.411	0.564	0.154		0.498	4.0283
Line 10 SEC46-02_omph1	0.398	0.58	0.161		0.509	4.0225
Line 1 SEC46-02_omph2	0.39	0.586	0.165		0.508	4.0195
Line 2 SEC46-02_omph2	0.396	0.583	0.164		0.506	4.0271
Line 3 SEC46-02_omph2	0.393	0.583	0.164		0.497	4.0243
Line 4 SEC46-02_omph2	0.392	0.588	0.165		0.5	4.0209
Line 5 SEC46-02_omph2	0.397	0.583	0.165		0.505	4.022
SEC46-02 Average	0.40	0.58	0.16	#DIV/0!	0.50	4.02

Table S2. (cont.)

	XWo = Ca/Ca+Mg+FeT	XEn = Mg/Ca+Mg+FeT	XFs = FeT/Ca+Mg+FeT	Mg/(Mg+Fe)
Line 1 SEC46-01_omph1	48.00	42.47	9.53	0.82
Line 2 SEC46-01_omph1	47.94	42.23	9.83	0.81
Line 3 SEC46-01_omph1	47.87	42.25	9.89	0.81
Line 4 SEC46-01_omph1	28.76	53.56	17.68	0.75
Line 5 SEC46-01_omph1	47.99	41.98	10.03	0.81
Line 6 SEC46-01_omph1	47.90	42.30	9.80	0.81
Line 7 SEC46-01_omph1	48.65	41.26	10.10	0.80
Line 8 SEC46-01_omph1	47.98	42.26	9.76	0.81
Line 9 SEC46-01_omph1	47.98	42.33	9.69	0.81
Line 10 SEC46-01_omph1	47.79	42.48	9.72	0.81
Line 11 SEC46-01_omph1	47.73	42.49	9.77	0.81
Line 12 SEC46-01_omph1	47.67	42.37	9.96	0.81
Line 13 SEC46-01_omph1	47.87	42.36	9.77	0.81
Line 14 SEC46-01_omph1	47.92	42.40	9.68	0.81
Line 15 SEC46-01_omph1	47.48	42.64	9.89	0.81
Line 1 SEC46-01_omph2	48.00	41.91	10.09	0.81
Line 2 SEC46-01_omph2	48.01	41.95	10.03	0.81
Line 3 SEC46-01_omph2	48.00	41.99	10.01	0.81
Line 4 SEC46-01_omph2	47.91	42.20	9.89	0.81
SEC46-01 Average	46.92	42.81	10.27	0.81
Line 1 SEC46-02_omph1	46.63	40.55	12.81	0.76
Line 2 SEC46-02_omph1	46.77	40.40	12.82	0.76
Line 3 SEC46-02_omph1	46.83	40.18	12.99	0.76
Line 4 SEC46-02_omph1	46.79	40.13	13.08	0.75
Line 5 SEC46-02_omph1	46.99	39.76	13.25	0.75
Line 6 SEC46-02_omph1	46.47	40.38	13.14	0.75
Line 7 SEC46-02_omph1	46.45	40.73	12.82	0.76
Line 8 SEC46-02_omph1	46.88	40.32	12.79	0.76
Line 9 SEC46-02_omph1	46.38	40.95	12.66	0.76
Line 10 SEC46-02_omph1	46.40	40.72	12.88	0.76
Line 1 SEC46-02_omph2	46.54	40.35	13.11	0.75
Line 2 SEC46-02_omph2	46.53	40.38	13.09	0.76
Line 3 SEC46-02_omph2	46.86	39.95	13.18	0.75
Line 4 SEC46-02_omph2	46.93	39.90	13.17	0.75
Line 5 SEC46-02_omph2	46.53	40.30	13.17	0.75
SEC46-02 Average	46.67	40.33	13.00	0.76

Table S2. (cont.)

	Tot. Dist (μm)	Dist to grain boundary (μm)	wt. % TiO2	wt. % SiO2	wt. % K2O
Line 1 SEC47-01_omph1	0	-327	0.11	54.54	0.00
Line 2 SEC47-01_omph1	82	-245	0.11	54.24	0.00
Line 3 SEC47-01_omph1	164	-163	0.09	54.44	0.00
Line 4 SEC47-01_omph1	245	-82	0.11	54.33	0.00
Line 5 SEC47-01_omph1	327	0	0.13	54.35	0.00
Line 1 SEC47-01_omph2	0	-96	0.10	54.53	0.00
Line 2 SEC47-01_omph2	24	-72	0.09	54.31	0.00
Line 3 SEC47-01_omph2	49	-47	0.12	54.42	0.00
Line 4 SEC47-01_omph2	73	-23	0.10	54.08	0.01
Line 5 SEC47-01_omph2	96	0	0.12	54.38	0.01
SEC47-01 Average			0.11	54.36	0.00

Table S2. (cont.)

	wt. %	wt. %	wt. %	wt. %	wt. %	wt. %	wt. %
	MnO	Na2O	Cr2O3	Al2O3	CaO	FeO	MgO
Line 1 SEC47-01_omph1	0.04	6.15	0.01	9.09	14.29	6.03	8.73
Line 2 SEC47-01_omph1	0.03	6.03	0.03	9.30	14.15	5.90	8.61
Line 3 SEC47-01_omph1	0.02	6.05	0.06	9.22	14.34	6.04	8.76
Line 4 SEC47-01_omph1	0.01	6.34	0.06	9.64	13.90	6.33	8.39
Line 5 SEC47-01_omph1	0.03	6.38	0.02	9.81	13.96	6.51	8.27
Line 1 SEC47-01_omph2	0.00	6.24	0.03	9.50	13.73	5.95	8.65
Line 2 SEC47-01_omph2	0.00	6.02	0.01	9.41	13.77	5.89	8.57
Line 3 SEC47-01_omph2	0.01	6.20	0.02	9.57	13.82	5.95	8.53
Line 4 SEC47-01_omph2	0.01	6.03	0.03	9.62	13.75	6.19	8.43
Line 5 SEC47-01_omph2	0.01	6.03	0.03	9.80	13.75	6.17	8.22
SEC47-01 Average	0.02	6.15	0.03	9.50	13.95	6.10	8.52

Table S2. (cont.)

	wt. %	a.p.f.u.	a.p.f.u.	a.p.f.u.	a.p.f.u.	a.p.f.u.	a.p.f.u.
	Total	Ti	Si	K	Mn	Na	Cr
Line 1 SEC47-01_omph1	98.99	0.0029	1.987	0	0.0011	0.435	0.0004
Line 2 SEC47-01_omph1	98.41	0.0031	1.985	0	0.0011	0.428	0.0008
Line 3 SEC47-01_omph1	99.02	0.0024	1.983	0	0.0007	0.427	0.0016
Line 4 SEC47-01_omph1	99.12	0.0031	1.978	0.0001	0.0004	0.447	0.0017
Line 5 SEC47-01_omph1	99.45	0.0035	1.974	0	0.0008	0.449	0.0005
Line 1 SEC47-01_omph2	98.74	0.0027	1.987	0.0002	0.0001	0.441	0.0008
Line 2 SEC47-01_omph2	98.08	0.0024	1.991	0.0002	0.0001	0.428	0.0004
Line 3 SEC47-01_omph2	98.64	0.0032	1.985	0	0.0004	0.439	0.0006
Line 4 SEC47-01_omph2	98.26	0.0028	1.982	0.0004	0.0005	0.428	0.001
Line 5 SEC47-01_omph2	98.52	0.0032	1.986	0.0005	0.0003	0.427	0.0009
SEC47-01 Average	98.72	0.00	1.98	0.00	0.00	0.43	0.00

Table S2. (cont.)

	a.p.f.u. Al	a.p.f.u. Ca	a.p.f.u. Fe	a.p.f.u. Fe3+	a.p.f.u. Mg	a.p.f.u. Total
Line 1 SEC47-01_omph1	0.39	0.558	0.184		0.474	4.0325
Line 2 SEC47-01_omph1	0.401	0.555	0.181		0.47	4.0251
Line 3 SEC47-01_omph1	0.396	0.56	0.184		0.475	4.0297
Line 4 SEC47-01_omph1	0.414	0.542	0.193		0.455	4.0344
Line 5 SEC47-01_omph1	0.42	0.543	0.198		0.448	4.0368
Line 1 SEC47-01_omph2	0.408	0.536	0.181		0.47	4.0268
Line 2 SEC47-01_omph2	0.406	0.541	0.181		0.468	4.0182
Line 3 SEC47-01_omph2	0.412	0.54	0.182		0.464	4.0262
Line 4 SEC47-01_omph2	0.416	0.54	0.19		0.461	4.0217
Line 5 SEC47-01_omph2	0.422	0.538	0.189		0.448	4.015
SEC47-01 Average	0.41	0.55	0.19	#DIV/0!	0.46	4.03

Table S2. (cont.)

	XWo = Ca/Ca+Mg+FeT	XEn = Mg/Ca+Mg+FeT	XFs = FeT/Ca+Mg+FeT	Mg/(Mg+Fe)
Line 1 SEC47-01_omph1	45.89	38.98	15.13	0.72
Line 2 SEC47-01_omph1	46.02	38.97	15.01	0.72
Line 3 SEC47-01_omph1	45.94	38.97	15.09	0.72
Line 4 SEC47-01_omph1	45.55	38.24	16.22	0.70
Line 5 SEC47-01_omph1	45.67	37.68	16.65	0.69
Line 1 SEC47-01_omph2	45.16	39.60	15.25	0.72
Line 2 SEC47-01_omph2	45.46	39.33	15.21	0.72
Line 3 SEC47-01_omph2	45.53	39.12	15.35	0.72
Line 4 SEC47-01_omph2	45.34	38.71	15.95	0.71
Line 5 SEC47-01_omph2	45.79	38.13	16.09	0.70
SEC47-01 Average	45.63	38.77	15.59	0.71

Table S3. Phengite major element compositions (EMPA).

			Wt. %	Wt. %	Wt. %	Wt. %
	Tot. Dist (μm)	Dist to grain boundary (μm)	TiO2	F	Cl	MnO
Line 1 SEC42-06_Phen1	0	-123	1.04	0.00	0.00	0.00
Line 2 SEC42-06_Phen1	31	-92	0.97	0.00	0.00	0.00
Line 3 SEC42-06_Phen1	61	-62	1.05	0.00	0.01	0.00
Line 4 SEC42-06_Phen1	91	-32	0.99	0.00	0.01	0.00
Line 5 SEC42-06_Phen1	123	0	0.92	0.00	0.01	0.00
SEC42-06 Average			0.99	0.00	0.01	0.00
Line 1 43-01_Phen1	0	-1098	0.92	0.00	0.01	0.01
Line 2 43-01_Phen1	121	-977	0.76	0.06	0.01	0.01
Line 3 43-01_Phen1	243	-855	0.74	0.02	0.00	0.00
Line 4 43-01_Phen1	390	-708	0.78	0.02	0.00	0.02
Line 5 43-01_Phen1	485	-613	0.68	0.07	0.01	0.00
Line 6 43-01_Phen1	609	-489	0.62	0.01	0.01	0.01
Line 7 43-01_Phen1	760	-338	0.81	0.00	0.01	0.01
Line 8 43-01_Phen1	855	-243	0.90	0.00	0.01	0.00
Line 9 43-01_Phen1	977	-121	0.96	0.04	0.00	0.00
Line 10 43-01_Phen1	1098	0	0.88	0.00	0.01	0.00
SEC43-01 Average			0.80	0.02	0.01	0.01
Line 1 SEC47-01 phen1	0	-1108	0.75	0.05	0.00	0.00
Line 2 sec47-01 phen1	277	-831	0.73	0.00	0.00	0.00
Line 3 sec47-01 phen1	553	-555	0.69	0.04	0.00	0.01
Line 4 sec47-01 phen1	863	-244	0.75	0.00	0.00	0.00
Line 5 sec47-01 phen1	1108	0	0.69	0.00	0.00	0.00
Line 1 SEC47-01 phen2	0	-305	0.64	0.00	0.00	0.00
Line 2 SEC47-01 phen2	29	-275	0.58	0.00	0.00	0.01
Line 3 SEC47-01 phen2	68	-237	0.62	0.00	0.00	0.00
Line 4 SEC47-01 phen2	101	-204	0.63	0.00	0.00	0.01
Line 5 SEC47-01 phen2	136	-169	0.53	0.00	0.00	0.00
Line 6 SEC47-01 phen2	169	-135	0.57	0.00	0.00	0.01
Line 7 SEC47-01 phen2	203	-102	0.59	0.00	0.00	0.00
Line 8 SEC47-01 phen2	237	-68	0.58	0.00	0.00	0.00
Line 9 SEC47-01 phen2	270	-34	0.53	0.00	0.00	0.02
Line 10 SEC47-01 phen2	305	0	0.63	0.00	0.00	0.00
SEC47-01 Average			0.63	0.01	0.00	0.00

Table S3. (cont.)

	Wt. %	Wt. %	Wt. %	Wt. %	Wt. %	Wt. %
T	Na2O	Cr2O3	SiO2	K2O	FeO	MgO
Line 1 SEC42-06_Phen1	1.27	0.00	47.68	8.89	2.60	2.45
Line 2 SEC42-06_Phen1	1.08	0.03	47.59	8.87	2.54	2.44
Line 3 SEC42-06_Phen1	1.23	0.05	47.54	8.95	2.53	2.39
Line 4 SEC42-06_Phen1	1.18	0.02	47.87	8.87	2.50	2.47
Line 5 SEC42-06_Phen1	1.43	0.03	47.98	8.77	2.51	2.40
SEC42-06 Average	1.24	0.03	47.73	8.87	2.54	2.43
Line 1 43-01_Phen1	1.15	0.06	48.19	8.87	1.72	2.65
Line 2 43-01_Phen1	0.98	0.07	48.98	9.26	1.86	2.87
Line 3 43-01_Phen1	0.96	0.05	49.06	9.22	1.87	2.91
Line 4 43-01_Phen1	1.00	0.07	49.12	9.30	1.98	3.00
Line 5 43-01_Phen1	0.95	0.11	48.83	9.22	1.87	3.05
Line 6 43-01_Phen1	1.07	0.08	48.98	9.23	1.87	3.02
Line 7 43-01_Phen1	1.04	0.04	48.98	9.30	1.99	2.92
Line 8 43-01_Phen1	1.07	0.06	48.42	9.20	1.89	2.75
Line 9 43-01_Phen1	1.18	0.05	48.13	9.08	1.90	2.64
Line 10 43-01_Phen1	1.29	0.02	48.01	8.93	1.77	2.56
SEC43-01 Average	1.07	0.06	48.67	9.16	1.87	2.84
Line 1 SEC47-01 phen1	1.20	0.06	48.42	9.09	2.32	2.83
Line 2 sec47-01 phen1	1.06	0.05	48.4	9.18	2.36	2.92
Line 3 sec47-01 phen1	1.01	0.03	48.77	9.13	2.28	2.85
Line 4 sec47-01 phen1	1.12	0.01	48.76	9.15	2.36	2.76
Line 5 sec47-01 phen1	1.09	0.07	48.66	9.21	2.24	2.73
Line 1 SEC47-01 phen2	1.14	0.07	48.3	9.18	2.37	2.92
Line 2 SEC47-01 phen2	0.97	0.06	49.13	9.28	2.42	3.05
Line 3 SEC47-01 phen2	1.03	0.05	48.94	9.34	2.46	3.11
Line 4 SEC47-01 phen2	1.04	0.04	49.08	9.32	2.31	3.01
Line 5 SEC47-01 phen2	1.00	0.03	48.98	9.13	2.47	3.36
Line 6 SEC47-01 phen2	0.94	0.06	49.15	9.41	2.47	3.04
Line 7 SEC47-01 phen2	0.89	0.06	49.15	9.38	2.43	3.05
Line 8 SEC47-01 phen2	0.94	0.06	49.23	9.47	2.53	2.98
Line 9 SEC47-01 phen2	1.02	0.07	48.15	8.98	3.94	2.74
Line 10 SEC47-01 phen2	1.05	0.06	48.01	9.01	2.65	2.44
SEC47-01 Average	1.03	0.05	48.74	9.22	2.51	2.92

Table S3. (cont.)

	Wt. %	Wt. %	Wt. %			
T	Al2O3	CaO	Total	H2O (100 minus sum)	F µg/g	Cl µg/g
Line 1 SEC42-06_Phen1	29.31	0.01	93.26	6.74	-	-
Line 2 SEC42-06_Phen1	29.35	0.00	92.88	7.12	-	-
Line 3 SEC42-06_Phen1	29.45	0.00	93.19	6.81	-	-
Line 4 SEC42-06_Phen1	29.56	0.00	93.47	6.53	-	82
Line 5 SEC42-06_Phen1	29.42	0.02	93.49	6.51	-	106
SEC42-06 Average	29.42	0.01	93.26	6.74		
					-	-
Line 1 43-01_Phen1	29.43	0.01	93.02	6.98	-	71
Line 2 43-01_Phen1	28.76	0.00	93.61	6.39	648	-
Line 3 43-01_Phen1	28.37	0.00	93.20	6.80	-	-
Line 4 43-01_Phen1	28.60	0.00	93.90	6.10	-	-
Line 5 43-01_Phen1	28.66	0.00	93.45	6.55	668	102
Line 6 43-01_Phen1	28.63	0.00	93.53	6.47	-	125
Line 7 43-01_Phen1	28.75	0.01	93.84	6.16	-	63
Line 8 43-01_Phen1	29.02	0.00	93.33	6.67	-	114
Line 9 43-01_Phen1	29.43	0.00	93.41	6.59	-	-
Line 10 43-01_Phen1	29.84	0.00	93.30	6.70	-	71
SEC43-01 Average	28.95	0.00	93.46			
Line 1 SEC47-01 phen1	29.1	0	93.86	6.14	519	-
Line 2 sec47-01 phen1	28.9	0	93.58	6.42	-	-
Line 3 sec47-01 phen1	29.0	0.0054	93.78	6.22	434	-
Line 4 sec47-01 phen1	29.3	0.0107	94.25	5.75	-	-
Line 5 sec47-01 phen1	29.3	0	93.96	6.04	-	-
Line 1 SEC47-01 phen2	28.5	0	93.15	6.85	-	-
Line 2 SEC47-01 phen2	28.2	0.0061	93.67	6.33	-	-
Line 3 SEC47-01 phen2	28.1	0	93.59	6.41	-	-
Line 4 SEC47-01 phen2	28.4	0.0097	93.84	6.16	-	-
Line 5 SEC47-01 phen2	27.9	0.0286	93.44	6.56	-	-
Line 6 SEC47-01 phen2	28.3	0	93.91	6.09	-	-
Line 7 SEC47-01 phen2	28.3	0	93.81	6.19	-	-
Line 8 SEC47-01 phen2	28.1	0	93.89	6.11	-	-
Line 9 SEC47-01 phen2	28.3	0.04	93.82	6.18	-	-
Line 10 SEC47-01 phen2	29.8	0.0097	93.64	6.36	-	-
SEC47-01 Average	28.62	0.01	93.75			

Table S4. Amphibole major element compositions with endmember species

	Cumulative Dist µm	Dist to grain boundary (µm)	TiO2	F	Cl	MnO
Line 1 SEC42-06_amph1	0	-370	0.69	0.18	0.00	0.08
Line 2 SEC42-06_amph1	112	-258	0.72	0.14	0.00	0.06
Line 3 SEC42-06_amph1	172	-197	0.60	0.12	0.01	0.04
Line 4 SEC42-06_amph1	173	-196	0.64	0.13	0.01	0.05
Line 5 SEC42-06_amph1	180	-190	0.65	0.17	0.01	0.07
Line 6 SEC42-06_amph1	218	-151	0.67	0.09	0.01	0.07
Line 7 SEC42-06_amph1	264	-106	0.71	0.10	0.01	0.04
Line 8 SEC42-06_amph1	312	-58	0.71	0.11	0.01	0.06
Line 9 SEC42-06_amph1	339	-31	0.67	0.11	-	0.06
Line 10 SEC42-06_amph1	370	0	0.33	0.10	0.00	0.04
SEC42-06 Average			0.64	0.12	0.01	0.06
Line 1 43-01_Amph1	0	-456	0.59	0.28	-	0.04
Line 2 43-01_Amph1	51	-405	0.60	0.23	0.00	0.05
Line 3 43-01_Amph1	102	-354	0.68	0.20	-	0.04
Line 4 43-01_Amph1	152	-304	0.66	0.13	0.00	0.04
Line 5 43-01_Amph1	203	-253	0.65	0.09	-	0.05
Line 6 43-01_Amph1	253	-202	0.69	0.18	-	0.05
Line 7 43-01_Amph1	304	-152	0.69	0.11	-	0.03
Line 8 43-01_Amph1	355	-101	0.67	0.20	0.00	0.05
Line 9 43-01_Amph1	405	-51	0.59	0.13	0.01	0.05
Line 10 43-01_Amph1	456	0	0.61	0.13	0.00	0.04
SEC43-01 Average			0.64	0.17	0.00	0.04
Line 1 SEC43-03_amph1	0	-640	0.58	0.12	-	0.02
Line 2 SEC43-03_amph1	35	-605	0.69	0.08	-	0.03
Line 3 SEC43-03_amph1	91	-549	0.70	0.06	-	0.02
Line 4 SEC43-03_amph1	137	-503	0.74	0.04	-	0.06
Line 5 SEC43-03_amph1	182	-458	0.61	0.08	-	0.06
Line 6 SEC43-03_amph1	227	-412	0.69	0.11	-	0.02
Line 7 SEC43-03_amph1	272	-367	0.72	0.08	-	0.05
Line 8 SEC43-03_amph1	320	-320	0.63	0.16	-	0.01
Line 9 SEC43-03_amph1	366	-274	0.75	0.05	-	0.03
Line 10 SEC43-03_amph1	411	-229	0.72	0.16	-	0.03
Line 11 SEC43-03_amph1	466	-174	0.64	0.01	0.00	0.06
Line 12 SEC43-03_amph1	506	-134	0.71	0.02	0.01	0.03
Line 13 SEC43-03_amph1	551	-89	0.69	0.09	0.00	0.05
Line 14 SEC43-03_amph1	596	-43	0.64	0.05	0.01	0.05
Line 15 SEC43-03_amph1	640	0	0.50	0.06	0.00	0.07
SEC43-03 Average			0.67	0.08	0.00	0.04

Table S4. (cont.)

	Weight %					
	Na2O	Cr2O3	SiO2	K2O	FeO	MgO
Line 1 SEC42-06_amph1	4.13	0.04	44.17	0.70	13.73	10.06
Line 2 SEC42-06_amph1	3.94	0.03	45.16	0.69	13.30	10.79
Line 3 SEC42-06_amph1	4.28	0.03	44.28	0.61	12.70	10.30
Line 4 SEC42-06_amph1	4.10	0.00	43.52	0.60	12.21	10.23
Line 5 SEC42-06_amph1	4.17	0.03	44.58	0.63	13.22	10.38
Line 6 SEC42-06_amph1	4.16	0.02	44.94	0.65	13.11	10.68
Line 7 SEC42-06_amph1	4.33	0.04	44.57	0.67	13.06	10.34
Line 8 SEC42-06_amph1	4.15	0.02	44.64	0.67	12.95	10.28
Line 9 SEC42-06_amph1	4.33	0.04	45.05	0.63	13.08	10.40
Line 10 SEC42-06_amph1	4.24	0.05	47.93	0.34	12.82	11.43
SEC42-06 Average	4.18	0.03	44.88	0.62	13.02	10.49
Line 1 43-01_Amph1	3.98	0.01	45.32	0.63	11.29	10.86
Line 2 43-01_Amph1	4.06	0.05	44.60	0.64	11.33	11.24
Line 3 43-01_Amph1	4.10	0.02	44.66	0.71	11.39	11.11
Line 4 43-01_Amph1	4.13	0.06	44.62	0.69	11.23	11.12
Line 5 43-01_Amph1	4.03	0.04	44.58	0.72	11.00	11.13
Line 6 43-01_Amph1	4.10	0.04	44.24	0.72	10.95	11.12
Line 7 43-01_Amph1	4.06	0.05	44.39	0.69	10.85	11.16
Line 8 43-01_Amph1	4.26	0.00	44.55	0.71	11.09	11.20
Line 9 43-01_Amph1	4.17	0.01	44.51	0.63	11.03	11.38
Line 10 43-01_Amph1	4.44	0.04	44.48	0.60	11.06	11.53
SEC43-01 Average	4.13	0.03	44.60	0.67	11.12	11.19
Line 1 SEC43-03_amph1	4.39	0.02	45.88	0.28	10.94	12.49
Line 2 SEC43-03_amph1	4.27	-	45.01	0.28	11.5	12.06
Line 3 SEC43-03_amph1	4.47	0.03	45.33	0.31	11.39	11.86
Line 4 SEC43-03_amph1	4.34	0.02	45.28	0.31	11.16	12.03
Line 5 SEC43-03_amph1	3.61	0.03	46.67	0.31	11.42	12.72
Line 6 SEC43-03_amph1	4.27	0.01	44.97	0.34	11.48	12.07
Line 7 SEC43-03_amph1	4.52	0.00	45.18	0.37	11.3	12.09
Line 8 SEC43-03_amph1	4.32	0.01	44.76	0.36	11.64	11.7
Line 9 SEC43-03_amph1	4.38	-	44.97	0.36	11.79	12.08
Line 10 SEC43-03_amph1	4.46	0.00	44.75	0.34	11.71	11.91
Line 11 SEC43-03_amph1	4.35	0.00	43.87	0.37	12.21	11.54
Line 12 SEC43-03_amph1	4.42	0.01	44.49	0.34	12.04	11.58
Line 13 SEC43-03_amph1	4.24	0.03	44.25	0.34	12.44	11.42
Line 14 SEC43-03_amph1	4.46	0.03	44.14	0.30	12.37	11.57
Line 15 SEC43-03_amph1	4.43	0.05	41.03	0.41	13.04	10.42
SEC43-03 Average	4.33	0.02	44.71	0.33	11.76	11.84

Table S4. (cont.)

	Al2O3	CaO	Total	H2O	Ti	F
Line 1 SEC42-06_amph1	14.82	8.72	97.33	2.67	0.076	0.086
Line 2 SEC42-06_amph1	13.69	8.96	97.48	2.52	0.079	0.066
Line 3 SEC42-06_amph1	14.36	8.43	95.75	4.25	0.067	0.054
Line 4 SEC42-06_amph1	14.20	8.20	93.89	6.11	0.073	0.061
Line 5 SEC42-06_amph1	14.55	8.62	97.09	2.91	0.072	0.079
Line 6 SEC42-06_amph1	14.39	8.55	97.34	2.66	0.074	0.040
Line 7 SEC42-06_amph1	15.03	8.51	97.41	2.59	0.078	0.047
Line 8 SEC42-06_amph1	14.99	8.40	96.99	3.01	0.078	0.049
Line 9 SEC42-06_amph1	14.43	8.34	97.14	2.86	0.074	0.051
Line 10 SEC42-06_amph1	11.94	8.19	97.43	2.57	0.037	0.044
SEC42-06 Average	14.24	8.49	96.78	3.22	0.071	0.058
Line 1 43-01_Amph1	15.39	8.89	97.28	2.72	0.065	0.131
Line 2 43-01_Amph1	15.18	8.66	96.64	3.36	0.066	0.108
Line 3 43-01_Amph1	15.56	8.77	97.24	2.76	0.074	0.090
Line 4 43-01_Amph1	15.55	8.63	96.87	3.13	0.072	0.060
Line 5 43-01_Amph1	15.50	8.66	96.44	3.56	0.072	0.040
Line 6 43-01_Amph1	15.53	8.67	96.30	3.70	0.077	0.086
Line 7 43-01_Amph1	15.53	8.78	96.34	3.66	0.077	0.049
Line 8 43-01_Amph1	15.36	8.66	96.77	3.23	0.074	0.094
Line 9 43-01_Amph1	15.02	8.68	96.20	3.80	0.065	0.060
Line 10 43-01_Amph1	14.80	8.74	96.47	3.53	0.067	0.060
SEC43-01 Average	15.34	8.71	96.65	3.35	0.071	0.078
Line 1 SEC43-03_amph1	14.29	8.61	97.61	2.39	0.063	0.054
Line 2 SEC43-03_amph1	15.4	8.64	97.96	2.04	0.075	0.035
Line 3 SEC43-03_amph1	15.22	8.41	97.80	2.20	0.076	0.027
Line 4 SEC43-03_amph1	15.22	8.46	97.65	2.35	0.080	0.020
Line 5 SEC43-03_amph1	13.12	9.15	97.78	2.22	0.066	0.035
Line 6 SEC43-03_amph1	15.31	8.49	97.76	2.24	0.075	0.049
Line 7 SEC43-03_amph1	15.21	8.49	97.99	2.01	0.078	0.035
Line 8 SEC43-03_amph1	15.67	8.64	97.90	2.10	0.069	0.072
Line 9 SEC43-03_amph1	15.2	8.47	98.08	1.92	0.082	0.025
Line 10 SEC43-03_amph1	15.49	8.52	98.09	1.91	0.079	0.073
Line 11 SEC43-03_amph1	15.81	8.6	97.46	2.54	0.070	0.006
Line 12 SEC43-03_amph1	15.51	8.64	97.80	2.20	0.078	0.010
Line 13 SEC43-03_amph1	15.79	8.54	97.88	2.12	0.075	0.042
Line 14 SEC43-03_amph1	15.49	8.56	97.66	2.34	0.070	0.022
Line 15 SEC43-03_amph1	18.08	9.18	97.28	2.72	0.056	0.027
SEC43-03 Average	15.39	8.63	97.78	2.22	0.073	0.035

Table S4. (cont.)

Atoms per formula unit

	Cl	Mn	Na	Cr	Si	K
Line 1 SEC42-06_amph1	0.001	0.010	1.180	0.005	6.513	0.132
Line 2 SEC42-06_amph1	0.001	0.007	1.121	0.003	6.626	0.129
Line 3 SEC42-06_amph1	0.004	0.005	1.236	0.003	6.593	0.115
Line 4 SEC42-06_amph1	0.002	0.006	1.205	0.000	6.596	0.117
Line 5 SEC42-06_amph1	0.004	0.009	1.192	0.004	6.565	0.118
Line 6 SEC42-06_amph1	0.002	0.008	1.184	0.003	6.587	0.122
Line 7 SEC42-06_amph1	0.002	0.005	1.230	0.005	6.532	0.126
Line 8 SEC42-06_amph1	0.002	0.008	1.182	0.003	6.560	0.126
Line 9 SEC42-06_amph1	0.000	0.007	1.233	0.005	6.612	0.118
Line 10 SEC42-06_amph1	0.001	0.005	1.194	0.006	6.957	0.064
SEC42-06 Average	0.002	0.007	1.196	0.004	6.614	0.117
Line 1 43-01_Amph1	0.000	0.005	1.120	0.002	6.588	0.116
Line 2 43-01_Amph1	0.001	0.006	1.155	0.006	6.538	0.119
Line 3 43-01_Amph1	0.000	0.005	1.157	0.002	6.508	0.132
Line 4 43-01_Amph1	0.001	0.005	1.170	0.007	6.517	0.129
Line 5 43-01_Amph1	0.000	0.006	1.144	0.004	6.528	0.134
Line 6 43-01_Amph1	0.000	0.006	1.167	0.005	6.500	0.135
Line 7 43-01_Amph1	0.000	0.004	1.154	0.006	6.509	0.129
Line 8 43-01_Amph1	0.001	0.007	1.208	0.001	6.521	0.133
Line 9 43-01_Amph1	0.002	0.007	1.190	0.001	6.544	0.118
Line 10 43-01_Amph1	0.000	0.006	1.265	0.005	6.532	0.112
SEC43-01 Average	0.000	0.006	1.173	0.004	6.529	0.126
Line 1 SEC43-03_amph1	0.000	0.002	1.229	0.002	6.622	0.052
Line 2 SEC43-03_amph1	0.000	0.004	1.194	0.000	6.491	0.052
Line 3 SEC43-03_amph1	0.000	0.003	1.250	0.003	6.540	0.058
Line 4 SEC43-03_amph1	0.000	0.007	1.215	0.002	6.534	0.056
Line 5 SEC43-03_amph1	0.000	0.007	1.009	0.004	6.728	0.057
Line 6 SEC43-03_amph1	0.000	0.003	1.196	0.002	6.500	0.062
Line 7 SEC43-03_amph1	0.000	0.006	1.264	0.000	6.513	0.067
Line 8 SEC43-03_amph1	0.000	0.002	1.211	0.001	6.473	0.067
Line 9 SEC43-03_amph1	0.000	0.003	1.226	0.000	6.489	0.066
Line 10 SEC43-03_amph1	0.000	0.004	1.249	0.000	6.464	0.062
Line 11 SEC43-03_amph1	0.000	0.008	1.230	0.000	6.395	0.069
Line 12 SEC43-03_amph1	0.001	0.004	1.244	0.001	6.451	0.062
Line 13 SEC43-03_amph1	0.001	0.007	1.193	0.003	6.424	0.064
Line 14 SEC43-03_amph1	0.001	0.006	1.258	0.004	6.426	0.056
Line 15 SEC43-03_amph1	0.001	0.009	1.269	0.006	6.060	0.078
SEC43-03 Average	0.000	0.005	1.216	0.002	6.474	0.062

Table S4. (cont.)

	Fe	Mg	Al	Ca	Total	Subgroup of (OH,F,Cl)
Line 1 SEC42-06_amph1	1.693	2.212	2.577	1.377	15.86	
Line 2 SEC42-06_amph1	1.632	2.359	2.368	1.409	15.80	
Line 3 SEC42-06_amph1	1.582	2.287	2.521	1.345	15.81	
Line 4 SEC42-06_amph1	1.547	2.311	2.536	1.331	15.79	
Line 5 SEC42-06_amph1	1.628	2.278	2.526	1.360	15.83	
Line 6 SEC42-06_amph1	1.607	2.334	2.486	1.342	15.79	
Line 7 SEC42-06_amph1	1.601	2.259	2.596	1.337	15.82	
Line 8 SEC42-06_amph1	1.592	2.252	2.595	1.322	15.77	
Line 9 SEC42-06_amph1	1.605	2.275	2.497	1.312	15.79	
Line 10 SEC42-06_amph1	1.556	2.473	2.044	1.274	15.66	
SEC42-06 Average	1.604	2.304	2.475	1.341	15.79	Na-Ca
Line 1 43-01_Amph1	1.373	2.354	2.637	1.385	15.77	
Line 2 43-01_Amph1	1.389	2.456	2.623	1.361	15.83	
Line 3 43-01_Amph1	1.388	2.414	2.674	1.370	15.82	
Line 4 43-01_Amph1	1.371	2.420	2.677	1.350	15.78	
Line 5 43-01_Amph1	1.347	2.430	2.676	1.359	15.74	
Line 6 43-01_Amph1	1.345	2.435	2.691	1.365	15.81	
Line 7 43-01_Amph1	1.330	2.438	2.684	1.380	15.76	
Line 8 43-01_Amph1	1.357	2.443	2.650	1.358	15.85	
Line 9 43-01_Amph1	1.356	2.494	2.602	1.368	15.81	
Line 10 43-01_Amph1	1.358	2.524	2.561	1.376	15.87	
SEC43-01 Average	1.361	2.441	2.648	1.367	15.80	Na-Ca
Line 1 SEC43-03_amph1	1.320	2.687	2.430	1.332	15.7929	
Line 2 SEC43-03_amph1	1.386	2.594	2.617	1.335	15.7826	
Line 3 SEC43-03_amph1	1.374	2.550	2.589	1.300	15.7695	
Line 4 SEC43-03_amph1	1.347	2.588	2.589	1.308	15.746	
Line 5 SEC43-03_amph1	1.377	2.733	2.229	1.413	15.6579	
Line 6 SEC43-03_amph1	1.387	2.600	2.608	1.316	15.7979	
Line 7 SEC43-03_amph1	1.362	2.597	2.585	1.312	15.8183	
Line 8 SEC43-03_amph1	1.408	2.523	2.671	1.339	15.8351	
Line 9 SEC43-03_amph1	1.423	2.599	2.586	1.309	15.8074	
Line 10 SEC43-03_amph1	1.414	2.566	2.638	1.319	15.8678	
Line 11 SEC43-03_amph1	1.489	2.507	2.716	1.343	15.8325	
Line 12 SEC43-03_amph1	1.460	2.504	2.651	1.342	15.809	
Line 13 SEC43-03_amph1	1.510	2.472	2.702	1.328	15.8198	
Line 14 SEC43-03_amph1	1.506	2.511	2.658	1.336	15.8534	
Line 15 SEC43-03_amph1	1.610	2.295	3.147	1.453	16.0102	
SEC43-03 Average	1.425	2.555	2.628	1.339	15.81	Na-Ca

Table S4. (cont.)

Calculated using Locock 2014 Workbook

	Species	Formula
Line 1 SEC42-06_amph1		
Line 2 SEC42-06_amph1		
Line 3 SEC42-06_amph1		
Line 4 SEC42-06_amph1		
Line 5 SEC42-06_amph1		
Line 6 SEC42-06_amph1		
Line 7 SEC42-06_amph1		
Line 8 SEC42-06_amph1		
Line 9 SEC42-06_amph1		
Line 10 SEC42-06_amph1		
SEC42-06 Average	katophorite	(Na0.584K0.116)Σ0.7 (Ca1.338Na0.609Fe0.045Mn0.007)Σ1.999 (Mg2.3Fe3+i1.463Al1.07Fe2+0.092Ti0.071Cr0.004)Σ5 (Si6.602Al1.398)Σ8 O22 ((OH)1.941F0.059Cl0.002)Σ2.001
Line 1 43-01_Amph1		
Line 2 43-01_Amph1		
Line 3 43-01_Amph1		
Line 4 43-01_Amph1		
Line 5 43-01_Amph1		
Line 6 43-01_Amph1		
Line 7 43-01_Amph1		
Line 8 43-01_Amph1		
Line 9 43-01_Amph1		
Line 10 43-01_Amph1		
SEC43-01 Average	katophorite	(Na0.575K0.126)Σ0.701 (Ca1.365Na0.596Fe0.034Mn0.006)Σ2.001 (Mg2.437Fe3+i1.257Al1.162Ti0.071Fe2+0.069Cr0.004)Σ5 (Si6.519Al1.481)Σ8 O22 ((OH)1.922F0.078)Σ2
Line 1 SEC43-03_amph1		
Line 2 SEC43-03_amph1		
Line 3 SEC43-03_amph1		
Line 4 SEC43-03_amph1		
Line 5 SEC43-03_amph1		
Line 6 SEC43-03_amph1		
Line 7 SEC43-03_amph1		
Line 8 SEC43-03_amph1		
Line 9 SEC43-03_amph1		
Line 10 SEC43-03_amph1		
Line 11 SEC43-03_amph1		
Line 12 SEC43-03_amph1		
Line 13 SEC43-03_amph1		
Line 14 SEC43-03_amph1		
Line 15 SEC43-03_amph1		
SEC43-03 Average	katophorite	(Na0.651K0.062)Σ0.713 (Ca1.333Na0.559Fe0.102Mn0.005)Σ1.999 (Mg2.545Fe3+i1.129Al1.064Fe2+0.188Ti0.072Cr0.002)Σ5 (Si6.448Al1.552)Σ8 O22 ((OH)1.964F0.035)Σ1.999

Table S4. (cont.)

	Cumulative Dist µm	Dist to grain boundary (µm)	TiO2	F	Cl	MnO
Line 1 SEC46-01_amph3	0	-324	0.52	0.01	0.01	0.05
Line 2 SEC46-01_amph3	35	-290	0.49	0.00	0.01	0.02
Line 3 SEC46-01_amph3	62	-263	0.50	-	0.01	0.03
Line 4 SEC46-01_amph3	120	-205	0.48	-	-	0.03
Line 5 SEC46-01_amph3	151	-173	0.46	-	-	0.05
Line 6 SEC46-01_amph3	193	-131	0.45	-	-	0.04
Line 7 SEC46-01_amph3	221	-103	0.44	-	-	0.07
Line 8 SEC46-01_amph3	256	-69	0.45	-	-	0.04
Line 9 SEC46-01_amph3	290	-35	0.49	0.01	-	0.05
Line 10 SEC46-01_amph3	324	0	0.41	-	-	0.03
Line 1 SEC46-01_amph1	0	-224	0.49	-	-	0.03
Line 2 SEC46-01_amph1	24	-200	0.52	-	-	0.03
Line 3 SEC46-01_amph1	50	-174	0.47	-	-	0.03
Line 4 SEC46-01_amph1	74	-150	0.47	0.03	-	0.03
Line 5 SEC46-01_amph1	100	-124	0.49	0.01	-	0.05
Line 6 SEC46-01_amph1	124	-100	0.50	0.19	0.01	0.01
Line 7 SEC46-01_amph1	149	-75	0.51	0.04	0.01	0.00
Line 8 SEC46-01_amph1	174	-50	0.51	0.04	0.01	0.02
Line 9 SEC46-01_amph1	193	-32	0.51	0.14	0.01	0.02
Line 10 SEC46-01_amph1	224	0	0.39	0.10	0.01	0.03
SEC46-01 Average			0.48	0.03	0.00	0.03
Line 1 SEC46-02_Amph2	0	-436	0.47	0.04	0.01	0.05
Line 2 SEC46-02_Amph2	109	-327	0.46	0.02	0.00	0.02
Line 3 SEC46-02_Amph2	218	-218	0.44	0.01	0.01	-
Line 4 SEC46-02_Amph2	327	-109	0.46	0.02	0.00	0.00
Line 5 SEC46-02_Amph2	436	0	0.44	0.07	0.01	0.03
Line 1 SEC46-02_amph3	0	-608	0.47	-	-	0.03
Line 2 SEC46-02_amph3	153	-455	0.43	0.05	0.00	0.05
Line 3 SEC46-02_amph3	304	-304	0.45	0.00	0.00	0.02
Line 4 SEC46-02_amph3	456	-152	0.46	0.07	-	0.03
Line 5 SEC46-02_amph3	608	0	0.43	0.00	0.00	0.05
SEC46-02 Average			0.45	0.03	0.00	0.03
Line 1 SEC47-01 Amph1	0	-128	0.29	0.18	0.01	0.09
Line 2 SEC47-01 Amph1	32	-95	0.30	0.22	0.00	0.09
Line 3 SEC47-01 Amph1	64	-64	0.26	0.22	0.00	0.10
Line 4 SEC47-01 Amph1	96	-32	0.22	0.27	0.00	0.09
Line 5 SEC47-01 Amph1	128	0	0.31	0.27	0.00	0.10
SEC47-01 Average			0.28	0.23	0.00	0.09

Table S4. (cont.)

	Weight %					
	Na2O	Cr2O3	SiO2	K2O	FeO	MgO
Line 1 SEC46-01_amph3	3.1	0.04	46.85	0.41	8.68	14.99
Line 2 SEC46-01_amph3	2.94	0.06	46.66	0.39	8.55	15.07
Line 3 SEC46-01_amph3	2.91	0.05	46.66	0.41	8.63	15.15
Line 4 SEC46-01_amph3	3.05	0.08	46.4	0.38	8.66	15.05
Line 5 SEC46-01_amph3	3.03	0.03	47.08	0.41	8.42	15.49
Line 6 SEC46-01_amph3	3.05	0.10	48.24	0.38	8.45	15.47
Line 7 SEC46-01_amph3	2.89	0.07	48.35	0.38	8.44	15.32
Line 8 SEC46-01_amph3	2.91	0.08	48.07	0.39	8.54	15.05
Line 9 SEC46-01_amph3	2.95	0.12	47.97	0.37	8.58	15.09
Line 10 SEC46-01_amph3	2.73	0.12	48.5	0.33	8.58	15.25
Line 1 SEC46-01_amph1	2.72	0.08	47.49	0.38	8.6	15.47
Line 2 SEC46-01_amph1	2.91	0.06	47.54	0.38	8.57	15.3
Line 3 SEC46-01_amph1	2.89	0.09	47.69	0.41	8.67	15.32
Line 4 SEC46-01_amph1	2.76	0.08	47.6	0.37	8.63	15.49
Line 5 SEC46-01_amph1	2.88	0.08	47.34	0.40	8.73	15.22
Line 6 SEC46-01_amph1	2.93	0.03	48.08	0.41	8.71	15.36
Line 7 SEC46-01_amph1	2.84	0.07	48.13	0.41	8.57	15.18
Line 8 SEC46-01_amph1	2.9	0.04	47.83	0.39	8.66	15.33
Line 9 SEC46-01_amph1	2.76	0.05	48.51	0.40	8.55	14.92
Line 10 SEC46-01_amph1	2.79	0.04	48.69	0.34	8.11	15.72
SEC46-01 Average	2.90	0.07	47.68	0.39	8.57	15.26
Line 1 SEC46-02_Amph2	3.35	0.05	47.63	0.36	10.15	13.55
Line 2 SEC46-02_Amph2	3.09	0.07	47.06	0.32	10.19	13.61
Line 3 SEC46-02_Amph2	3.31	0.03	47.4	0.34	10.2	13.73
Line 4 SEC46-02_Amph2	3.09	0.04	47.34	0.34	10.24	13.55
Line 5 SEC46-02_Amph2	3.15	0.08	47.39	0.33	10.07	13.5
Line 1 SEC46-02_amph3	3.26	0.04	47.15	0.36	10.48	13.58
Line 2 SEC46-02_amph3	3.33	0.03	47.02	0.35	10.37	13.47
Line 3 SEC46-02_amph3	3.25	0.01	46.76	0.35	10.6	13.23
Line 4 SEC46-02_amph3	3.22	0.04	46.95	0.39	10.34	13.23
Line 5 SEC46-02_amph3	3.34	0.03	47.38	0.35	10.63	13.24
SEC46-02 Average	3.24	0.04	47.21	0.35	10.33	13.47
Line 1 SEC47-01 Amph1	4.21	0.04	48.45	0.28	14.01	11.21
Line 2 SEC47-01 Amph1	4.04	0.06	48.49	0.24	13.35	11.63
Line 3 SEC47-01 Amph1	3.92	0.07	49.3	0.22	13.33	12.28
Line 4 SEC47-01 Amph1	4.21	0.06	49.11	0.28	13.64	11.59
Line 5 SEC47-01 Amph1	4.35	0.07	48.84	0.25	13.52	11.49
SEC47-01 Average	4.15	0.06	48.84	0.25	13.57	11.64

Table S4. (cont.)

	Al2O3	CaO	Total	H2O	Ti	F
Line 1 SEC46-01_amph3	11.48	9.9	96.03	3.97	0.057	0.005
Line 2 SEC46-01_amph3	11.46	9.99	95.66	4.34	0.054	0.002
Line 3 SEC46-01_amph3	11.34	9.93	95.62	4.38	0.055	0.000
Line 4 SEC46-01_amph3	11.32	9.86	95.31	4.69	0.053	0.000
Line 5 SEC46-01_amph3	11.15	9.92	96.04	3.96	0.050	0.000
Line 6 SEC46-01_amph3	11.08	9.95	97.22	2.78	0.049	0.000
Line 7 SEC46-01_amph3	11.06	9.95	96.97	3.03	0.048	0.000
Line 8 SEC46-01_amph3	11.26	10.03	96.83	3.17	0.049	0.000
Line 9 SEC46-01_amph3	11.63	10.04	97.31	2.69	0.053	0.005
Line 10 SEC46-01_amph3	10.73	10.33	97.01	2.99	0.044	0.000
Line 1 SEC46-01_amph1	11.38	10.02	96.66	3.34	0.053	0.000
Line 2 SEC46-01_amph1	11.4	10	96.70	3.30	0.056	0.000
Line 3 SEC46-01_amph1	11.29	10.03	96.89	3.11	0.051	0.000
Line 4 SEC46-01_amph1	11.1	10.01	96.58	3.42	0.051	0.016
Line 5 SEC46-01_amph1	11.5	10.04	96.74	3.26	0.053	0.005
Line 6 SEC46-01_amph1	11.43	10.06	97.72	2.28	0.053	0.086
Line 7 SEC46-01_amph1	11.47	10	97.25	2.75	0.055	0.020
Line 8 SEC46-01_amph1	11.52	10.09	97.34	2.66	0.055	0.018
Line 9 SEC46-01_amph1	11.65	10.05	97.57	2.43	0.054	0.065
Line 10 SEC46-01_amph1	10.63	10.11	96.96	3.04	0.042	0.048
SEC46-01 Average	11.29	10.02	96.72	3.28	0.052	0.013
Line 1 SEC46-02_Amph2	12.11	9.72	97.48	2.52	0.051	0.018
Line 2 SEC46-02_Amph2	11.86	9.88	96.59	3.41	0.050	0.010
Line 3 SEC46-02_Amph2	12.22	9.88	97.56	2.44	0.048	0.005
Line 4 SEC46-02_Amph2	11.98	9.89	96.96	3.04	0.050	0.007
Line 5 SEC46-02_Amph2	12.09	9.92	97.08	2.92	0.048	0.032
Line 1 SEC46-02_amph3	12.04	9.96	97.36	2.64	0.051	0.000
Line 2 SEC46-02_amph3	12.21	9.83	97.15	2.85	0.047	0.022
Line 3 SEC46-02_amph3	12.52	9.89	97.09	2.91	0.049	0.002
Line 4 SEC46-02_amph3	12.57	9.78	97.07	2.93	0.050	0.030
Line 5 SEC46-02_amph3	12.33	9.63	97.41	2.59	0.046	0.000
SEC46-02 Average	12.19	9.84	97.17	2.83	0.049	0.013
Line 1 SEC47-01 Amph1	11.1	7.46	97.33	2.67	0.032	0.082
Line 2 SEC47-01 Amph1	10.89	7.91	97.22	2.78	0.033	0.102
Line 3 SEC47-01 Amph1	10.1	7.91	97.71	2.29	0.028	0.103
Line 4 SEC47-01 Amph1	10.9	7.49	97.86	2.14	0.024	0.122
Line 5 SEC47-01 Amph1	10.67	7.33	97.19	2.81	0.034	0.125
SEC47-01 Average	10.73	7.62	97.46	2.54	0.030	0.107

Table S4. (cont.)

	Atoms per formula unit					
	Cl	Mn	Na	Cr	Si	K
Line 1 SEC46-01_amph3	0.002	0.007	0.872	0.004	6.805	0.075
Line 2 SEC46-01_amph3	0.002	0.003	0.830	0.007	6.799	0.073
Line 3 SEC46-01_amph3	0.003	0.003	0.822	0.006	6.804	0.076
Line 4 SEC46-01_amph3	0.000	0.004	0.866	0.009	6.793	0.072
Line 5 SEC46-01_amph3	0.000	0.006	0.851	0.004	6.827	0.076
Line 6 SEC46-01_amph3	0.000	0.005	0.845	0.012	6.897	0.069
Line 7 SEC46-01_amph3	0.000	0.008	0.801	0.008	6.922	0.069
Line 8 SEC46-01_amph3	0.000	0.004	0.809	0.010	6.899	0.072
Line 9 SEC46-01_amph3	0.000	0.006	0.817	0.014	6.855	0.067
Line 10 SEC46-01_amph3	0.000	0.004	0.758	0.014	6.946	0.060
Line 1 SEC46-01_amph1	0.000	0.004	0.759	0.010	6.834	0.069
Line 2 SEC46-01_amph1	0.000	0.003	0.812	0.006	6.839	0.069
Line 3 SEC46-01_amph1	0.000	0.003	0.806	0.011	6.853	0.075
Line 4 SEC46-01_amph1	0.000	0.004	0.772	0.009	6.860	0.069
Line 5 SEC46-01_amph1	0.000	0.006	0.805	0.010	6.818	0.073
Line 6 SEC46-01_amph1	0.003	0.001	0.811	0.004	6.859	0.075
Line 7 SEC46-01_amph1	0.003	0.001	0.786	0.008	6.879	0.075
Line 8 SEC46-01_amph1	0.003	0.002	0.805	0.004	6.840	0.072
Line 9 SEC46-01_amph1	0.002	0.002	0.762	0.006	6.906	0.073
Line 10 SEC46-01_amph1	0.002	0.003	0.773	0.005	6.964	0.062
SEC46-01 Average	0.001	0.004	0.808	0.008	6.860	0.071
Line 1 SEC46-02_Amph2	0.002	0.007	0.933	0.006	6.844	0.066
Line 2 SEC46-02_Amph2	0.001	0.003	0.870	0.008	6.830	0.060
Line 3 SEC46-02_Amph2	0.002	0.000	0.923	0.003	6.809	0.062
Line 4 SEC46-02_Amph2	0.001	0.000	0.866	0.004	6.840	0.064
Line 5 SEC46-02_Amph2	0.002	0.004	0.881	0.009	6.839	0.061
Line 1 SEC46-02_amph3	0.000	0.003	0.913	0.005	6.802	0.066
Line 2 SEC46-02_amph3	0.000	0.006	0.933	0.004	6.798	0.065
Line 3 SEC46-02_amph3	0.001	0.003	0.911	0.001	6.767	0.065
Line 4 SEC46-02_amph3	0.000	0.003	0.904	0.005	6.787	0.071
Line 5 SEC46-02_amph3	0.001	0.006	0.934	0.004	6.824	0.065
SEC46-02 Average	0.001	0.003	0.907	0.005	6.814	0.064
Line 1 SEC47-01 Amph1	0.002	0.012	1.191	0.005	7.063	0.052
Line 2 SEC47-01 Amph1	0.000	0.011	1.141	0.006	7.064	0.045
Line 3 SEC47-01 Amph1	0.000	0.012	1.101	0.008	7.137	0.041
Line 4 SEC47-01 Amph1	0.001	0.011	1.180	0.007	7.107	0.052
Line 5 SEC47-01 Amph1	0.000	0.012	1.228	0.008	7.117	0.046
SEC47-01 Average	0.001	0.012	1.168	0.007	7.098	0.047

Table S4. (cont.)

	Fe	Mg	Al	Ca	Total	Subgroup of (OH,F,Cl)
Line 1 SEC46-01_amph3	1.054	3.246	1.966	1.541	15.6339	
Line 2 SEC46-01_amph3	1.042	3.274	1.968	1.560	15.615	
Line 3 SEC46-01_amph3	1.052	3.294	1.949	1.552	15.6156	
Line 4 SEC46-01_amph3	1.061	3.285	1.953	1.546	15.6414	
Line 5 SEC46-01_amph3	1.022	3.349	1.905	1.542	15.632	
Line 6 SEC46-01_amph3	1.010	3.296	1.866	1.524	15.5724	
Line 7 SEC46-01_amph3	1.011	3.270	1.866	1.527	15.5293	
Line 8 SEC46-01_amph3	1.025	3.220	1.904	1.543	15.5351	
Line 9 SEC46-01_amph3	1.026	3.215	1.959	1.537	15.5538	
Line 10 SEC46-01_amph3	1.027	3.255	1.811	1.586	15.5051	
Line 1 SEC46-01_amph1	1.035	3.318	1.931	1.544	15.5565	
Line 2 SEC46-01_amph1	1.032	3.280	1.934	1.542	15.5739	
Line 3 SEC46-01_amph1	1.042	3.281	1.912	1.544	15.5778	
Line 4 SEC46-01_amph1	1.040	3.328	1.885	1.546	15.5792	
Line 5 SEC46-01_amph1	1.051	3.268	1.953	1.549	15.5909	
Line 6 SEC46-01_amph1	1.039	3.266	1.922	1.538	15.6565	
Line 7 SEC46-01_amph1	1.024	3.234	1.933	1.531	15.5491	
Line 8 SEC46-01_amph1	1.036	3.268	1.942	1.546	15.5912	
Line 9 SEC46-01_amph1	1.018	3.166	1.955	1.534	15.5427	
Line 10 SEC46-01_amph1	0.970	3.352	1.792	1.549	15.5611	
SEC46-01 Average	1.031	3.273	1.915	1.544	15.58	Ca
Line 1 SEC46-02_Amph2	1.219	2.903	2.052	1.496	15.5946	
Line 2 SEC46-02_Amph2	1.237	2.944	2.030	1.536	15.5786	
Line 3 SEC46-02_Amph2	1.225	2.940	2.070	1.520	15.6061	
Line 4 SEC46-02_Amph2	1.238	2.918	2.041	1.531	15.561	
Line 5 SEC46-02_Amph2	1.216	2.904	2.056	1.534	15.5848	
Line 1 SEC46-02_amph3	1.264	2.921	2.047	1.539	15.6105	
Line 2 SEC46-02_amph3	1.253	2.902	2.081	1.522	15.6328	
Line 3 SEC46-02_amph3	1.284	2.855	2.136	1.534	15.6075	
Line 4 SEC46-02_amph3	1.250	2.851	2.142	1.514	15.6076	
Line 5 SEC46-02_amph3	1.280	2.842	2.094	1.486	15.5812	
SEC46-02 Average	1.247	2.898	2.075	1.521	15.60	Ca
Line 1 SEC47-01 Amph1	1.707	2.435	1.907	1.166	15.6531	
Line 2 SEC47-01 Amph1	1.627	2.527	1.870	1.234	15.6607	
Line 3 SEC47-01 Amph1	1.613	2.651	1.724	1.226	15.6435	
Line 4 SEC47-01 Amph1	1.650	2.501	1.859	1.161	15.6742	
Line 5 SEC47-01 Amph1	1.648	2.496	1.833	1.144	15.6905	
SEC47-01 Average	1.649	2.522	1.839	1.186	15.66	Na-Ca

Table S4. (cont.)

Calculated using Locock 2014 Workbook

	Species	Formula
Line 1 SEC46-01_amph3		
Line 2 SEC46-01_amph3		
Line 3 SEC46-01_amph3		
Line 4 SEC46-01_amph3		
Line 5 SEC46-01_amph3		
Line 6 SEC46-01_amph3		
Line 7 SEC46-01_amph3		
Line 8 SEC46-01_amph3		
Line 9 SEC46-01_amph3		
Line 10 SEC46-01_amph3		
Line 1 SEC46-01_amph1		
Line 2 SEC46-01_amph1		
Line 3 SEC46-01_amph1		
Line 4 SEC46-01_amph1		
Line 5 SEC46-01_amph1		
Line 6 SEC46-01_amph1		
Line 7 SEC46-01_amph1		
Line 8 SEC46-01_amph1		
Line 9 SEC46-01_amph1		
Line 10 SEC46-01_amph1		
SEC46-01 Average	pargasite	(Na0.439K0.071)Σ0.51 (Ca1.538Na0.366Fe0.091Mn0.004)Σ1.999 (Mg3.261Fe3+0.769Al0.743Fe2+0.167Ti0.052Cr0.008)Σ5 (Si6.835Al1.165)Σ8 O22 ((OH)1.986F0.013Cl0.001)Σ2
Line 1 SEC46-02_Amph2		
Line 2 SEC46-02_Amph2		
Line 3 SEC46-02_Amph2		
Line 4 SEC46-02_Amph2		
Line 5 SEC46-02_Amph2		
Line 1 SEC46-02_amph3		
Line 2 SEC46-02_amph3		
Line 3 SEC46-02_amph3		
Line 4 SEC46-02_amph3		
Line 5 SEC46-02_amph3		
SEC46-02 Average	pargasite	(Na0.483K0.064)Σ0.547 (Ca1.518Na0.422Fe0.057Mn0.003)Σ2 (Mg2.892Fe3+1.081Al0.868Fe2+0.106Ti0.049Cr0.005)Σ5.001 (Si6.798Al1.202)Σ8 O22 ((OH)1.987F0.013Cl0.001)Σ2.001
Line 1 SEC47-01 Amph1		
Line 2 SEC47-01 Amph1		
Line 3 SEC47-01 Amph1		
Line 4 SEC47-01 Amph1		
Line 5 SEC47-01 Amph1		
SEC47-01 Average	winchite	(Na0.449K0.047)Σ0.496 (Ca1.182Na0.714Fe0.092Mn0.012)Σ2 (Mg2.512Fe3+1.369Al0.901Fe2+0.181Ti0.03Cr0.007)Σ5 (Si7.07Al0.93)Σ8 O22 ((OH)1.893F0.106Cl0.001)Σ2

Table S5. Apatite major element compositions.

Supplementary Table 5. Apatite Compositions (EMPA)

			Weight %									
	# grains	# measurements	P2O5	1 s.d. (%)	F	1 s.d. (%)	CaO	1 s.d. (%)	Cl	1 s.d. (%)	Total	OH
SEC 42-06	5	23	40.94	0.8%	2.97	7.7%	53.94	0.8%	0.051	16%	97.89	2.11
SEC 43-01	5	27	41.62	1.5%	3.25	3.2%	53.52	1.1%	0.041	75%	98.44	1.56
SEC 43-03	3	10	41.93	0.6%	2.15	4.4%	52.46	1.2%	0.019	54%	96.56	3.44
SEC46-01	3	9	42.02	0.6%	1.47	5.6%	52.19	0.5%	0.020	14%	95.70	4.30
SEC46-02	3	9	42.00	0.5%	1.49	6.6%	52.39	0.3%	0.030	13%	95.91	4.09
SEC47-01	3	9	41.92	0.7%	2.34	5.7%	51.64	0.3%	0.029	18%	95.93	4.07

Table S6. Titanite major element composition (EPMA)

Supplementary Table 6. Titanite major elem

Comment	No.	TiO2	F	K2O	Cl	Na2O
Line 1 SEC46-02_titanite	46	36.97	0	0.012	0.0092	0.012
Line 2 SEC46-02_titanite	47	36.78	0	0.014	0.0124	0.021
Line 3 SEC46-02_titanite	48	36.48	0	0.014	0.0038	0.097
Line 4 SEC46-02_titanite	49	36.96	0	0.012	0.0065	0.044
Line 5 SEC46-02_titanite	50	36.91	0	0.015	0.0086	0.025
Average		36.82	0	0.013	0.0081	0.040

Supplementary Table 6. Titani Weight %

Comment	Cr2O3	SiO2	CaO	MnO	MgO	Al2O3	FeO	Total
Line 1 SEC46-02_titanite	0.11	29.65	28.38	0.0454	0.01	1.84	0.20	97.24
Line 2 SEC46-02_titanite	0.10	29.91	28.23	0.0285	0.00	1.85	0.22	97.17
Line 3 SEC46-02_titanite	0.08	29.83	28.3	0.0310	0.00	2.07	0.20	97.11
Line 4 SEC46-02_titanite	0.07	29.89	28.26	0.0060	0.00	1.79	0.21	97.25
Line 5 SEC46-02_titanite	0.07	29.73	28.18	0.0320	0.00	1.78	0.28	97.03
Average	0.09	29.802	28.27	0.0286	0.00	1.87	0.22	97.16

Table S7. Halogen intra-grain profiles (SIMS)

Supplementary Table 7. Halogen intra-grain profiles (SIMS)

SEC43-01													
Garnet	SEC43-01_grt_1@44	SEC43-01_grt_0707@50	SEC43-01_grt_3@46	SEC43-01_grt_06@49	SEC43-01_grt_04@47	SEC43-01_grt_5@48	SEC43-01_grt_2@45				Grain Mean	Grain S.D. (%)
OH µg/g	114	118	316	248	104	144	173				174	46%
OH Error % (2SE Int+Calib)	5.4%	5.0%	4.8%	37.1%	5.1%	5.8%	6.2%					
F µg/g	7.25	8.56	9.51	8.17	6.29	3.66	8.74				7.45	26%
F Error % (2SE Int+Calib)	6.0%	5.8%	5.9%	6.3%	6.2%	5.9%	6.1%					
S µg/g	-	0.04	0.06	0.05	0.05	0.07	-					
C Error % (2SE Int+Calib)	-	13.8%	17.7%	17.1%	12.9%	16.0%	-					
Cl µg/g	0.18	0.17	0.24	0.20	0.19	0.20	0.25				0.20	14%
Cl Error % (2SE Int+Calib)	13.0%	16.1%	13.4%	13.8%	13.5%	13.8%	14.8%					
Distance (µm)	722	546	465	360	290	117	0					
	Core						Rim					
Omphacite	SEC43-01_omph_3@70	SEC43-01_omph_3@72	SEC43-01_omph_5@74	SEC43-01_omph_7@76	SEC43-01_omph_3@77	SEC43-01_omph_9@78	SEC43-01_omph_6@75	SEC43-01_omph_4@73	SEC43-01_omph_2@71			
OH µg/g	362	437	412	557	435	385	414	414	383		422	13%
OH Error % (2SE Int+Calib)	4.7%	4.6%	4.6%	5.6%	4.7%	4.7%	4.8%	4.7%	4.8%			
F µg/g	42.1	55.5	57.1	59.3	69.7	60.2	62.1	48.3	52.1		56.3	14%
F Error % (2SE Int+Calib)	5.8%	5.8%	5.8%	5.8%	5.8%	5.9%	5.9%	5.8%	5.9%			
S µg/g	0.03	0.03	-	0.03	0.02	-	0.04	-	-			
C Error % (2SE Int+Calib)	13.4%	16.0%	-	17.4%	13.7%	-	12.2%	-	-			
Cl µg/g	0.12	0.11	0.13	0.15	-	-	0.12	0.12	-		0.13	11%
Cl Error % (2SE Int+Calib)	16.2%	15.1%	12.2%	14.7%	-	-	13.8%	13.5%	-			
Distance (µm)	0	227	343	502	604	724	902	1082	1262			
	Rim								Core			
Phengite	SEC43-01_phen_3@52	SEC43-01_phen_3@53	SEC43-01_phen_5@55	SEC43-01_phen_6@54	SEC43-01_phen_3@51	SEC43-01_phen_9@63	SEC43-01_phen_8@62	SEC43-01_phen_2@61	SEC43-01_phen_6@60			
OH µg/g	26335	28580	28337	28820	28304	28840	27286	28857	29884	28360	4%	
OH Error % (2SE Int+Calib)	4.6%	4.5%	4.7%	4.6%	4.5%	4.7%	4.6%	4.6%	4.6%			
F µg/g	1575	1819	1943	1979	1938	1913	1769	1883	1578	1822	8%	
F Error % (2SE Int+Calib)	5.8%	5.8%	6.0%	5.9%	5.8%	5.9%	5.9%	5.9%	5.9%			
S µg/g	0.90	0.53	0.42	0.43	0.45	0.58	0.52	0.50	0.51			
C Error % (2SE Int+Calib)	7.4%	7.4%	10.0%	6.9%	8.3%	6.7%	8.1%	7.0%	6.7%			
Cl µg/g	1.50	0.96	1.15	1.12	1.08	1.08	0.97	0.98	1.58	1.16	20%	
Cl Error % (2SE Int+Calib)	12.5%	12.1%	13.9%	12.6%	12.2%	12.6%	12.2%	12.2%	12.8%			
Distance (µm)	0	254	386	505	616	855	927	992	1086			
Rim, to grt grain boundary					Core			Rim, to omphacite grain boundary				

Table S8. Inter-mineral partition coefficients

Supplementary Table 8. Intermineral partition coefficients						
	Cpx			Grt		
Sample	F (µg/g)	Cl (µg/g)	OH (µg/g)	F (µg/g)	Cl (µg/g)	OH (µg/g)
SEC 42-06	50.6	0.18	**651**	8.92	0.17	**113**
SEC 43-01	54.1	0.13	433	7.76	0.18	125
SEC 43-03	16.7	0.08	**773**	2.01	0.10	**201**
SEC46-01	6.53	0.11	**446**	1.73	0.11	**85**
SEC46-02	13.5	1.17	770	4.76	0.11	60
SEC47-01	33.2	0.07	**445**	3.81	0.08	80
Mean						
1SD						
Literature						
Debret et al. 2016						
Gala.1	11.07	117		3.89	64	
QE29d.4	17.05	71.85		18.61	9.4	
Gala.4	6.13	110.4		4.5	14.9	
QE29d.3				8.2	53	
Hughes et al. 2018						
DC58G						
DC50B						
DC58L						
Page et al. 2016						
TUR12						
TUR14A						
TUR23						
TUR30						
TUR31						
TUR32						
TUR33						

Table S8. (cont.)

Supplementary Table 8. Intermineral partition												
	Phen				Amph				Apatite			
Sample	F (µg/g)	Cl (µg/g)	OH (µg/g)	F/Cl	F (µg/g)	Cl (µg/g)	OH (µg/g)	F/Cl	F (µg/g)	Cl (µg/g)	OH (µg/g)	F/Cl
SEC 42-06	610	2.13	**22452**	**286**	1812	82.7	18682	22	**29700**	**510**	**18800**	**58**
SEC 43-01	1822	1.16	28360	**1571**	4727	11.6	20187	407	32541	410	15560	**79**
SEC 43-03					1073	0.64	**17952**	1676	**21510**	**192**	**32819**	**112**
SEC46-01					747	10.3	**17292**	72	**14689**	**197**	**41670**	**75**
SEC46-02					563	11.8	23449	48	14933	304	40213	**49**
SEC47-01	645	1.22	**26410**	**529**	1127	15.5	**15747**	73	**23422**	**288**	**39719**	**81**
Mean												
1SD												
Literature												
Debret et al. 2016												
Gala.1												
QE29d.4	326.5	40.25		8.1								
Gala.4												
QE29d.3	428	65		6.6								
Hughes et al. 2018												
DC58G	1880	1.56		1205					9260	80		116
DC50B	1333	66.75		20					29480	38		776
DC58L	190	43.2		4.4					17680	76.5		231
Page et al. 2016												
TUR12					218	46		4.7	30600	-		
TUR14A	503	77		6.5	335	97		3.5	30590	130		235
TUR23									32790	163		201
TUR30	572	21		27	390	18		21.7	29560	60		493
TUR31									35070	108		325
TUR32					256	46		5.6	31800	113		281
TUR33	372	69		5.4	84	87		1.0	28770	253		114

Supplementary Table 8. Intermineral partition												
	Intermineral Partition Coefficients (cpx-grt)			Intermineral Partition Coefficients (cpx-amph)			Intermineral Partition Coefficients (grt-amph)			Intermineral Partition Coefficients (amph-phen)		
Sample	DF Cpx-Grt	DCl Cpx-Grt	DOH Cpx-Grt	DF Cpx-Amph	DCl Cpx-Amph	DOH Cpx-Amph	DF Grt-Amph	DCl Grt-Amph	DOH Grt-Amph	D F Amph-Phen	DCl Amph-Phen	D OH Amph-Phen
SEC 42-06	5.7		5.74	0.028		0.035	0.005		0.006	3.0	38.8	
SEC 43-01	7.0		3.47	0.011		0.021	0.002		0.006	2.6	10.0	
SEC 43-03	8.3		3.84	0.016		0.043	0.002		0.011			
SEC46-01	3.8		5.24	0.009		0.026	0.002		0.005			
SEC46-02	2.8		12.8	0.024		0.033	0.008		0.003			
SEC47-01	8.7		5.58	0.029		0.028	0.003		0.005	1.7	12.7	
Mean	6.0		6.1	0.0195		0.0310	0.0038		0.0060	2.44	20.5	
1SD	2.4		3.4	0.0088		0.0076	0.0026		0.0029	0.63	15.9	
	40%		56%	45%		25%	69%		48%	26%	78%	
Literature												
Debret et al. 2016												
Gala.1	2.8											
QE29d.4	0.9											
Gala.4	1.4											
QE29d.3												
Hughes et al. 2018												
DC58G												
DC50B												
DC58L												
Page et al. 2016												
TUR12												
TUR14A										0.67	1.26	
TUR23												
TUR30										0.68	0.86	
TUR31												
TUR32												
TUR33										0.23	1.26	

Table S8. (cont.)

Supplementary Table 8. Intermineral partition												
	Intermineral Partition Coefficients (Cpx-Apt)			Intermineral Partition Coefficients (Amph-Apt)			Intermineral Partition Coefficients (Cpx-Phen)			Intermineral Partition Coefficients (Phen-Apt)		
Sample	DF Cpx-Apt	DCl Cpx-Apt	DOH Cpx-Apt	DF Amph-Apt	DCl Amph-Apt	DOH Amph-Apt	DF Cpx/Phen	DCl Cpx/Phen	DOH Cpx/Phen	DF Phen/Apt	DCl Phen/Apt	DOH Phen/Apt
SEC 42-06	0.0017		0.0346	0.0610	0.1621	0.9937	0.0829	0.0845	0.0290	0.0205	0.0042	1.1942
SEC 43-01	0.0017		0.0278	0.1453	0.0283	1.2974	0.0297	0.1121	0.0153	0.0560	0.0028	1.8227
SEC 43-03	0.0008		0.0236	0.0499	0.0033	0.5470						
SEC46-01	0.0004		0.0107	0.0509	0.0526	0.4150						
SEC46-02	0.0009		0.0191	0.0377	0.0387	0.5831						
SEC47-01	0.0014		0.0112	0.0481	0.0536	0.3965	0.0514	0.0574	0.0168	0.0275	0.0042	0.6649
Mean	0.0012		0.0212	0.0655	0.0565	0.7054	0.0547	0.0847	0.0204	0.0347	0.0037	1.2273
1SD	0.0005		0.0094	0.0398	0.0550	0.3615	0.0268	0.0273	0.0075	0.0188	0.0008	0.5796
	45%		44%	61%	97%	51%	49%	32%	37%	54%	21%	47%
Literature												
Debret et al. 2016												
Gala.1												
QE29d.4												
Gala.4												
QE29d.3												
Hughes et al. 2018												
DC58G										0.203	0.020	
DC50B										0.045	1.757	
DC58L										0.011	0.565	
Page et al. 2016												
TUR12				0.0071								
TUR14A				0.0110	0.7462					0.016	0.592	
TUR23												
TUR30				0.0132	0.3000					0.019	0.350	
TUR31												
TUR32				0.0081	0.4071							
TUR33				0.0029	0.3439					0.013	0.273	

Table S9. Pyrohydrolysis raw data and reference material replicates

Supplementary Table 9. Pyrohydrolysis raw data and reference material replicates

		Uncorrected for Yield					Corrected for Yield					
	Analysis #	F (µg/g)	Cl (µg/g)		F (µg/g)	Cl (µg/g)	F (µg/g)	Cl (µg/g)		F (µg/g)	Cl (µg/g)	Yield Corrected to Batch #
SEC42-6	2	99.74	10.00	Average	**91.94**	**8.85**	**130.98**	**13.13**	Average	**114.56**	**11.04**	**1**
SEC42-6'	3	84.72	8.35	Std. Dev.	7.53	1.00	**102.35**	**10.09**	Std. Dev.	14.77	1.81	2
	4	91.34	8.20	Stdev%	8%	11%	**110.35**	**9.90**	Stdev%	12.89%	16%	2
SEC43-1	2	163.91	9.27	Average	**108.51**	**7.05**	**215.24**	**12.17**	Average	**136.83**	**8.85**	**1**
SEC43-1'	3	77.69	6.40	Std. Dev.	48.08	1.97	**93.86**	**7.73**	Std. Dev.	68.01	2.93	2
	4	83.92	5.49	Stdev%	44%	28%	**101.39**	**6.64**	Stdev%	49.71%	33.12%	2
SEC43-3	2	151.98	6.73	Average	**152.25**	**5.37**	**199.58**	**8.84**	Average	**189.25**	**6.73**	**1**
SEC43-3'	3	148.65	5.44	Std. Dev.	3.74	1.40	**179.58**	**6.57**	Std. Dev.	10.02	2.04	2
	4	156.12	3.94	Stdev%	2%	26%	**188.61**	**4.76**	Stdev%	5.3%	30.4%	2
SEC46-1	2	192.26	11.03	Average	**154.37**	**9.06**	**252.47**	**14.49**	Average	**193.23**	**11.34**	**1**
SEC46-1'	3	128.56	7.56	Std. Dev.	33.52	1.78	**155.31**	**9.14**	Std. Dev.	51.97	2.80	2
	4	142.30	8.59	Stdev%	22%	20%	**171.91**	**10.38**	Stdev%	26.9%	24.7%	2
SEC46-2	2	162.16	15.16	Average	**160.25**	**16.06**	**212.95**	**19.90**	Average	**199.28**	**19.94**	**1**
SEC46-2'	3	156.39	16.95	Std. Dev.	3.35	0.90	**188.93**	**20.47**	Std. Dev.	12.35	0.52	2
	4	162.22	16.09	Stdev%	2%	6%	**195.98**	**19.44**	Stdev%	6%	3%	2
SEC47-1	2	113.07	7.62	Average	**111.60**	**7.10**	**148.48**	**10.01**	Average	**138.78**	**8.84**	**1**
SEC47-1'	3	108.15	7.03	Std. Dev.	3.00	0.49	**130.65**	**8.49**	Std. Dev.	9.02	1.04	2
	4	113.58	6.65	Stdev%	3%	7%	**137.22**	**8.03**	Stdev%	6%	12%	2

*apostrophe (') indicates a duplicated sample

Standards			
	F ppm	**Cl ppm**	
JB-2-1	76.65	268.22	pyrohydrolysis group (SEC42-6, 43-1, 43-3, 46-1, 46-2, 47-1)
JB-2-2	73.70	215.25	
JB-2-3	74.67	233.68	
Batch 1 Mean	**75.01**	**239.05**	
Batch 1 Std	**1.50**	**26.89**	
Yield Batch 1	**76.1%**	**85.1%**	
Yield Std (%)	2.0%	11.3%	
JB-2-9	80.64	191.80	hydrolysis, duplicate group (SEC42-6', 43-1', 43-3', 46-1', 46-2', 47-1')
JB-2-11	82.04	208.73	
JB-2-12	81.93	241.47	
Batch 2 Mean	**81.53**	**214.00**	
Batch 2 Std	**0.78**	**25.25**	
Yield Batch 2	**82.8%**	**76.2%**	
Yield Std (%)	1.0%	11.8%	
Average (all)	78.27	226.53	
Std. Dev. (all)	3.73	27.07	
JB-2**	98.50	281.00	
Yield (min)*	75%	68%	
Yield (max)*	83%	95%	
Yield (average)	79%	81%	
STD ALL (average)	4%	5%	

igneous.html) reports the F and Cl concentration of JB-2 as 98.5ppm and 281ppm, respectively.

	Uncorrected for Yield				Corrected for Yield by Batch							
			1SD Pos (yield uncert)				1SD		1SD Propogated		1SD Propogated	
Sample	F (µg/g)	Cl (µg/g)	F (%)	Cl (%)	F (µg/g)	Cl (µg/g)	F (µg/g)	Cl (µg/g)	F %	Cl %	F (µg/g)	Cl (µg/g)
SEC42-06	**91.94**	**8.85**	22.5%	23.0%	**114.56**	**11.04**	14.77	1.81	13.05%	19.91%	14.95	2.20
SEC43-01	**108.51**	**7.05**	49.0%	34.4%	**136.83**	**8.85**	68.01	2.93	49.75%	34.98%	68.07	3.09
SEC43-03	**152.25**	**5.37**	21.1%	32.8%	**189.25**	**6.73**	10.02	2.04	5.66%	32.39%	10.71	2.18
SEC46-01	**154.37**	**9.06**	30.2%	28.1%	**193.23**	**11.34**	51.97	2.80	26.91%	27.38%	52.00	3.10
SEC46-02	**160.25**	**16.06**	21.1%	20.8%	**199.28**	**19.94**	12.35	0.52	6.27%	12.08%	12.49	2.41
SEC47-01	**111.60**	**7.10**	21.1%	21.2%	**138.78**	**8.84**	9.02	1.04	6.57%	16.65%	9.11	1.47
SEC50-01												

S.4 Supplementary material accompanying Chapter 4

Detailed sample description

Southern Plutonic Complex (SPC): SPC contains a series of garnet pyroxenite, garnet gabbro, garnet diorite and diorite thought to be derived from primitive hydrous melts generated by flux melting in the mantle wedge(Jagoutz, Muntener et al. 2011) (Supplementary Figure 1). The duration of SPC magmatism is thought to be prolonged, beginning at c. 120 Ma(Bouilhol, Jagoutz et al. 2013) though perhaps as early as 150 Ma(Jagoutz, Bouilhol et al. 2019), with cessation ~80 Ma with the exception of volumetrically minor diking(Jagoutz, Bouilhol et al. 2019). The main magmatic mineral phases are pyroxene, garnet, plagioclase, pargasitic amphibole and minor oxides. Garnet pyroxenites KK5 and KK8 display equigranular textures, with approximately coequal amounts of clinopyroxene and garnet. In KK5, pargasitic amphibole occurs in coequal amounts to garnet and clinopyroxene, whereas KK8 contains significantly less amphibole (<5 vol.%). Minor Fe-Ti oxides are omnipresent. Garnet diorite P05-5A is more complex and contains sausseritized plagioclase, garnet, clinopyroxene, pargasitic amphibole, quartz, epidote, and oxides. Quartz-epidote and quartz-amphibole symplectites are common. SPC samples are thought to be related by a similar liquid line of descent, namely that of a hydrous parental magma, each a crystal fractionation product at different stages of differentiation. This interpretation is corroborated by field evidence; however, complications arise due to the prolonged nature of magmatic activity. Deviations from experimentally derived cumulates, particularly the juxtaposition of pyroxene-garnet hornblendites and garnet hornblende gabbros, suggest that multiple batches of magma (likely with different compositions and H_2O contents) were involved in SPC genesis(Müntener and Ulmer 2018). Trace element modeling illustrates this difference. Multiply saturated liquids (Cpx-Grt-Amph) that crystallized KK5 (most primitive garnet-pyroxenite) would, upon further fractionation, be too depleted in heavy rare earth elements due to garnet precipitation to then produce the REE concentrations observed in KK8 and P05-5A. Thus, when discussing SPC parental magma water abundances, care was taken to discuss ranges, as a single magma is unlikely to have formed all three samples sequentially.

Chilas: The Chilas Complex is dominated by gabbronorites (95%), thought to have been derived from a nominally dry parental magma during intra-arc extension-related intrusion ~85 Ma(Khan, Stern et al. 1997, Burg, Bodinier et al. 1998, Schaltegger, Zeilinger et al. 2002, Burg, Jagoutz et al. 2006, Jagoutz, Müntener et al. 2006, Jagoutz, Müntener et al. 2007, Jagoutz, Muntener et al. 2011, Jagoutz, Bouilhol et al. 2019). For a comprehensive field, petrologic, and geochemical description, we refer the reader to Jagoutz et al.(Jagoutz, Müntener et al. 2007). The main mineral phases are clinopyroxene, orthopyroxene, plagioclase, olivine and lesser magnesio-hornblende which often occurs as mantles on pyroxene. For this study, three samples (C66, C48, C7) were analyzed, all of which have been previously described. The samples share a common liquid line of descent, with C66, an olivine gabbronorite, the most primitive. C48 and C7 are progressively more evolved, as inferred from major and trace element characteristics.

Electron microprobe

All mineral phases were analyzed using JEOL JXA-8200 electron microprobe (EMP) at the

Massachusetts Institute of Technology. A 1 nA beam current and 15 kV accelerating potential were used for all analyses except apatite, which utilized a 10 nA beam current. Beam diameter was <1 μm for Cpx, garnet and Opx and 10 μm for amphibole. Data reduction was done using CITZAF software (Armstrong 1995). The counting times used for phase analysis was 40 s on peak, and 20s on background. With respect to halogen abundances in amphibole, detection limits based on counting statistics were ~470 μg/g for F and ~60 μg/g for Cl.

LA-ICP-MS (KK5 and KK8 analyzed at Lausanne)
The constituent minerals in polished thin sections were analyzed with a Geolas 200M 193 nm ArF excimer laser coupled with an Elan 6100 DRC quadrupole ICP-MS (LA- ICP-MS) at the University of Lausanne. The performance of the LA-ICP-MS was tested with SRM 612 glass from NIST in order to improve the sensibility (Mg >10000 cps and La >60000 cps) and to minimize doubly charged ions (Ba/Ba2+ <3 %) and oxide production rates (Th/ThO <0.5 %). The laser system allows optimization of the beam size for analysis (20 to 100 micrometers), adjusted via an aperture in the beam path, with a frequency of 10 hz and energy of 140 mJ (equivalent to c. 10 J/cm2 on-sample fluence). Helium was used as the cell gas. The acquisition times for background and ablation interval were ~60s and 10-25 seconds, respectively. Dwell times per isotope ranged from 10 to 20 ms, and peak-hopping mode was employed. Absolute trace and REE element concentrations were then determined using CaO (determined by Electron Microprobe) as internal standard and SRM 612 glass from NIST as external standard. The average element abundances in SRM 612 were taken from Pearce et al(Pearce, Perkins et al. 1997). The data reduction and calculation employed the Lamtrace software(Jackson 2008).

LA-ICP-MS (P05-5A analyzed at WHOI)
Minerals of interest (garnet and clinopyroxene) were analyzed in polished thick section (150μm thickness) utilizing an ASI RESOlution excimer laser (193 nm) fed to a Thermo Scientific iCAP Q quadrupole ICP-MS. Analyses were performed with a 5 Hz rep rate and 2 J/cm^2 fluence on 100μm spots. Total dwell time was 120 seconds with 30 seconds of background on both the front and back end of each analysis. Gas flow was 5 ml/min (N_2), 500 ml/min (He) and 1 L/min (Ar). NIST-612, BCR-2G, BIR-1G and BHVO-2G were used as reference materials to generate a calibration slope for each isotope of interest. Data was reduced using the software package of Cin-Ty Lee (Rice University)(Lee 2006).

Secondary ion mass spectrometry
SIMS analyses were conducted at the Northeast National Ion Microprobe facility at Woods Hole Oceanographic Institution on a Cameca 1280. A detailed sample protocol may be found in Urann et al.(2020); here we discuss additional protocols built on that work. Calibration slopes (m) were obtained by plotting measured isotope ratios (x) against known reference material concentrations (y) of the form $y = mx$ for each element of interest. Sample unknowns were then calculated by multiplying measured ratios by m. Calibration slope uncertainties were assessed utilizing a bootstrapping technique (5000 iterations) to derive 95% confidence intervals. Water and F measurements where the internal precision (2 standard error over 5 counting cycles) was greater than 15% were screened and excluded from the data set; these low precision measurements were associated with elevated C (not reported) and Cl concentrations and are

likely the result of analyses conducted on micro-fractures. After screening, analytical uncertainties (internal precision: typically 2SE ~2 % OH, <2% F, <7% Cl) were combined with calibration slope uncertainties (accuracy: typical uncertainty 4% OH, 2.5% F, <9% Cl, 95% confidence intervals) to yield no more than 8%, 6% and 16% total uncertainty (2SE, 95% confidence intervals) for OH, F and Cl measurements, respectively. Cpx and Opx volatile standards of Kumamoto et al.(Kumamoto, Warren et al. 2017) were utilized for water, F and P. Since mineral-specific calibrations are not well constrained and/or not available for volatiles in garnet and amphibole, nor for C, S and Cl in pyroxenes, we used a basaltic glass calibration. Continuous measurements of ALV519-4-1 were used throughout the session to monitor instrument drift, which was found to be negligible. The OH, F, and Cl concentrations of Suprasil and Herasil® 102, both optical-quality glasses, along with Synthetic Forsterite, were measured regularly in each session. There are no published values for the OH, F, and Cl content of Suprasil, Herasil® 102 and Synthetic Forsterite, but those samples are believed to have very low OH, F, and Cl concentrations (less than 0.1 μg/g), respectively (E. Hauri, *pers. comm.*). To quantify our maximum backgrounds, we assume that Suprasil contains no OH, Herasil® contains no F, and Synthetic Forsterite contains no Cl. Background OH, F, and Cl values were less than 3 μg/g, 0.15 μg/g, and 0.09 μg/g, respectively, for all sessions. Individual mineral analyses were not corrected for background when background values were less than propagated 2SE uncertainty; otherwise, measurements are corrected to remove backgrounds. We recommend that the measured OH contents of Suprasil 102 be conservatively multiplied by 1.85 for Opx background and multiplied by 1.95 for Cpx background, reflecting the average difference in Si content between the pyroxene and glasses (Le Roux et al. 2020, submitted). For example, if the Suprasil background is ~5 ppm, it means that the real background is ~9 ppm for an Opx and ~10 ppm for a Cpx. Cl measurement uncertainties on omphacite, garnet, and phengite are near parity with Synthetic Forsterite Cl values. We therefore subtracted our background Cl values from measured values for all values presented in tables.

Volatile flux model

To calculate the water carrying capacity of the delaminate, we use a simple bimineralic assemblage of 50% Cpx and 50% garnet calculated for KK samples (~1000 μg/g H_2O) and P05 (~2000 μg/g H_2O) to provide a range of values (Supplementary Table 4). To arrive at a water flux in kg/yr, we multiply the delaminate flux (6.4-8.1 km^3/yr) by a crustal density of 2900kg/m^3, multiplied by our delaminate water content of 1000–2000 μg/g.

Crystallization model

We use an equilibrium crystallization model with mineral-melt partition coefficients mineral modal abundances (10/60/30 Cpx/Plag/Opx) after Jagoutz et al.(Jagoutz, Müntener et al. 2007). We use a starting melt composition in equilibrium with the most primitive olivine gabbronorite (C66), whose Cpx show no Sr or Eu anomalies and thus preceded plagioclase fractionation. For Figure 4, we show H_2O concentrations plotted against Nd. Typically, Ce is used when discussing H2O, however this is only appliable in mantle systems (i.e. modal abundances for olivine/Opx/Cpx of ~70/25/5) where the bulk partition coefficients are quite similar. Here we chose Nd because it has the lowest bulk partition coefficient (0.0315) of the REEs in the assemblage (0.0315 to 0.1494). We note that this is still nearly an order of magnitude larger than

the calculated bulk D for H_2O of 0.0038, however for illustrative purposes the use of Nd does not appreciably alter our findings.

Whereas Jagoutz's in situ model incorporates the use of an interstitial liquid, our model is also able to reproduce trace element abundances, albeit at a higher degree of crystallization than the in situ model. For example, for C48 in-situ crystallization modeling yields ~60% crystallization with 2-7% interstitial liquid from a starting composition in equilibrium with C66 olivine gabbronorite; our equilibrium model yields ~80% crystallization with no interstitial liquid. We note that no significant mineral rim zonation was observed, which may suggest equilibration with interstial melt. Quantifying the amount of interstitial melt is notoriously difficult, and typically inferred based on scatter among data from single samples. Qualitatively then, Chilas gabbronorites record water enrichments with increasing degrees of crystallization, in agreement with observed trace element abundances.

Fractionation correction

Chilas gabbronorites are thought to have undergone crystallization prior to the onset of plagioclase formation of between 30 and 50%, having crystalized olivine and clinopyroxene in an approximate 70:30 proportion. Thus, we back calculated the composition of the initial melt based on a fractional crystallization model, using partition coefficients for olivine and clinopyroxene of 0.00126 and 0.0126, respectively. The former was taken from experiment B330 of Hauri et al.(Hauri, Gaetani et al. 2006) which was conducted at 1.2 GPa and 1200°C. The latter was calculated based on the average $Al_{(IV)}$ and Ca content of clinopyroxenes from olivine websterites (C03-43,C03-44,C03-45) from Jagoutz et al.(Jagoutz, Müntener et al. 2007) and the parameterization of O'Leary et al.(O'Leary, Gaetani et al. 2010). Nd and F $D_{cpx\text{-}melt}$ were 0.187 and 0.042; the former from Jagoutz et al.(Jagoutz, Müntener et al. 2007) and the latter by multiplying the above Cpx H_2O partition coefficient by our empirically determined value of 1.934 due to the robust relationship between H_2O and F in Kohistan Cpx.

Two methods were used for SPC. First, a correction was made for fractionation of SPC garnet pyroxenites, assuming 35-60% fractionation of ultramafics (olivine + pyroxene, using modes and partition coefficients from above) before the onset of amphibole saturation based on experimental studies (Müntener and Ulmer 2018, Ulmer, Kaegi et al. 2018). Second, we utilize the quantitative petrogenetic model of Jagoutz(Jagoutz 2010) to evaluate a range of initial melt H_2O abundances. We assume that H_2O in each lithology's bulk composition is the difference of the oxide sum from 100 and track the evolution of the melt H_2O content. To generate Figure 5, the Cpx Mg# of each sample was used to calculate the equilibrium melt Mg#, and thus the SiO_2 content of the liquid with which it is in equilibrium.

Inter-mineral partitioning of volatiles

Cpx-Opx: To evaluate whether our samples are in equilibrium with respect to H_2O abundances, we plotted coexisting Cpx and Opx H_2O concentrations along with literature data (Supplementary Figure 3). Experimental studies yield a $D_{Cpx/Opx}$ of 1.3, whereas natural peridotites extend to higher values (~2.4 on average)(Warren and Hauri 2014). Chilas samples C48 and C7 yield $D_{Cpx/Opx}$ values of 6.0 and 10.4, respectively. These values are higher than peridotites, yet similar to crystallization products (pyroxenites) measured by Warren and Hauri with a mean $D_{Cpx/Opx}$ of 4.6 ± 1.5 and values up to 25. We speculate that intrinsic differences (e.g.

composition, oxygen fugacity) between restites and cumulates are the likely cause of the discrepancy. The most glaring explanation is the difference in mineralogy, particularly the aluminous phase, in existing experimental partitioning data sets (i.e. Hauri et al. (2006)) experiments contained no plagioclase) compared to Chilas gabbronorites studied here, where plagioclase constitutes at least 40% (modally) of all samples. As a result, plagioclase incorporates Al and leaves coexisting orthopyroxene and clinopyroxene less aluminous. Since H_2O partition coefficients between pyroxene and melt are a function (in part) of the tetrahedrally and octahedrally coordinated Al in pyroxene, the partition coefficients in gabbronorites will be quite different. In practice, lower H_2O $D_{opx\text{-}melt}$ for the gabbronorite phase assemblage will lead to significantly higher H_2O $D_{Cpx\text{-}Opx}$. For example, the peridotites of Warren and Hauri (2014) yield, on average, calculated $D_{Cpx\text{-}melt}$ and $D_{Opx\text{-}melt}$ of 0.0168 and 0.0154, respectively. Chilas samples yield 0.0107 and 0.0055, respectively. In this example, for a plagioclase-bearing assemblage (Chilas), $D_{Cpx\text{-}melt}$ is ~35% lower than a plagioclase-free assemblage. Similarly, $D_{Opx\text{-}melt}$ is ~64% lower in gabbronorites compared to plagioclase-free experimental assemblages. With the introduction of modally-significant aluminous phases, (e.g. plagioclase, amphibole, micas) relative partitioning between phases may be affected. Recently, some workers proposed that the discrepancy between natural and experimental samples was the result of sub-solidus equilibration(Schaffer, Peslier et al. 2019, Gibson, Rooks et al. 2020). As discussed in the text, Ti distribution between Cpx and Opx is not consistent with significant redistribution. In addition, pyroxene exsolution is observed in gabbronorites, which suggests that diffusion rates were low with respect to cooling rates (Jagoutz, Müntener et al. 2007).

Cpx-Grt: We also consider the equilibrium distribution of H_2O between Cpx and garnet ($D_{Cpx/Grt}$), which we plot in Supplementary Figure 4. Experimental data broadly define $D_{Cpx/Grt}$ of 3 to 14. KK garnet pyroxenites plot well within this experimentally bound range, whereas garnet diorite P05-5A falls out of the experimental range. A number of factors may contribute to this. First, P05-5A contains a more complex mineral assemblage than typical experiments upon which $D_{Cpx/Grt}$ is based, and includes paragonite, epidote, and amphibole (and sympectites, see sample description). Furthermore, H_2O partition coefficients between garnet and melt are known to vary by nearly an order of magnitude (Aubaud, Hirschmann et al. 2008), and correlate positively with garnet TiO_2 content. We note that in Kohistan samples, garnet H_2O content is positively correlated with pyrope content and shows a negative relationship with almandine fraction. Importantly, $D_{Cpx\text{-}Grt}$ for water covaries positively with garnet almandine content and negatively with pyrope content, indicative of crystal-chemical controls on H_2O distribution.

Figures

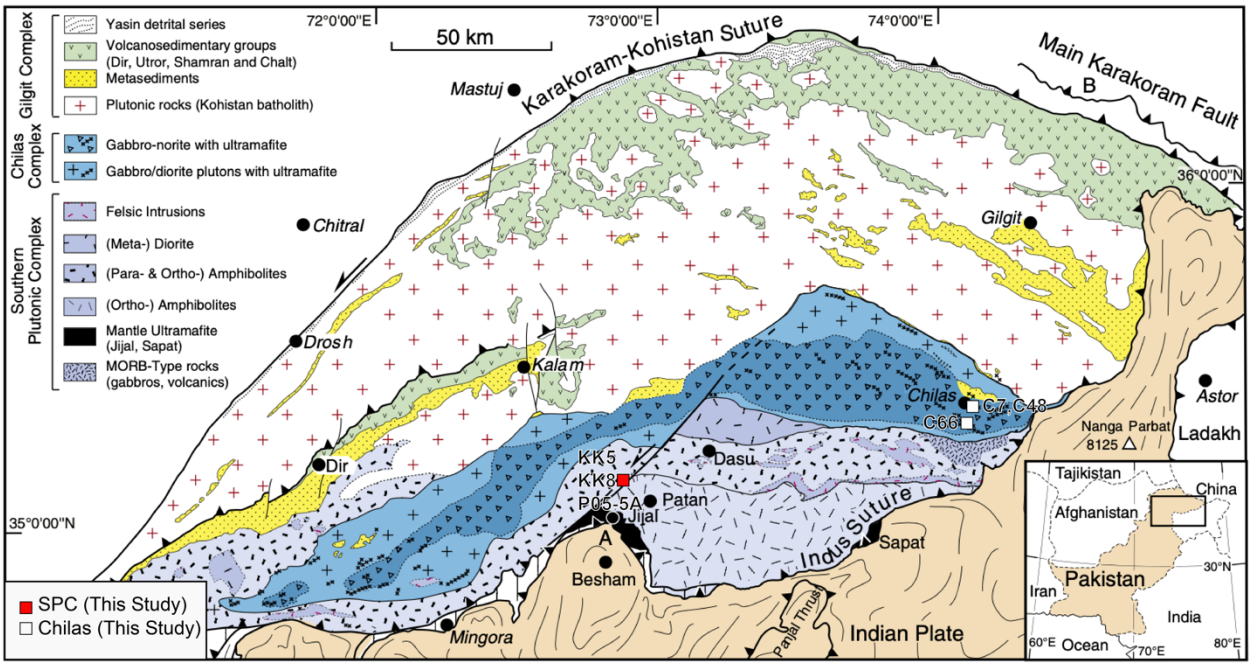

Figure 4.S1. Geologic map of Kohistan region, after Jagoutz and Schmidt (2012). Localities sampled in this study labeled. Samples KK5 and KK8 were collected approximately 1 km apart.

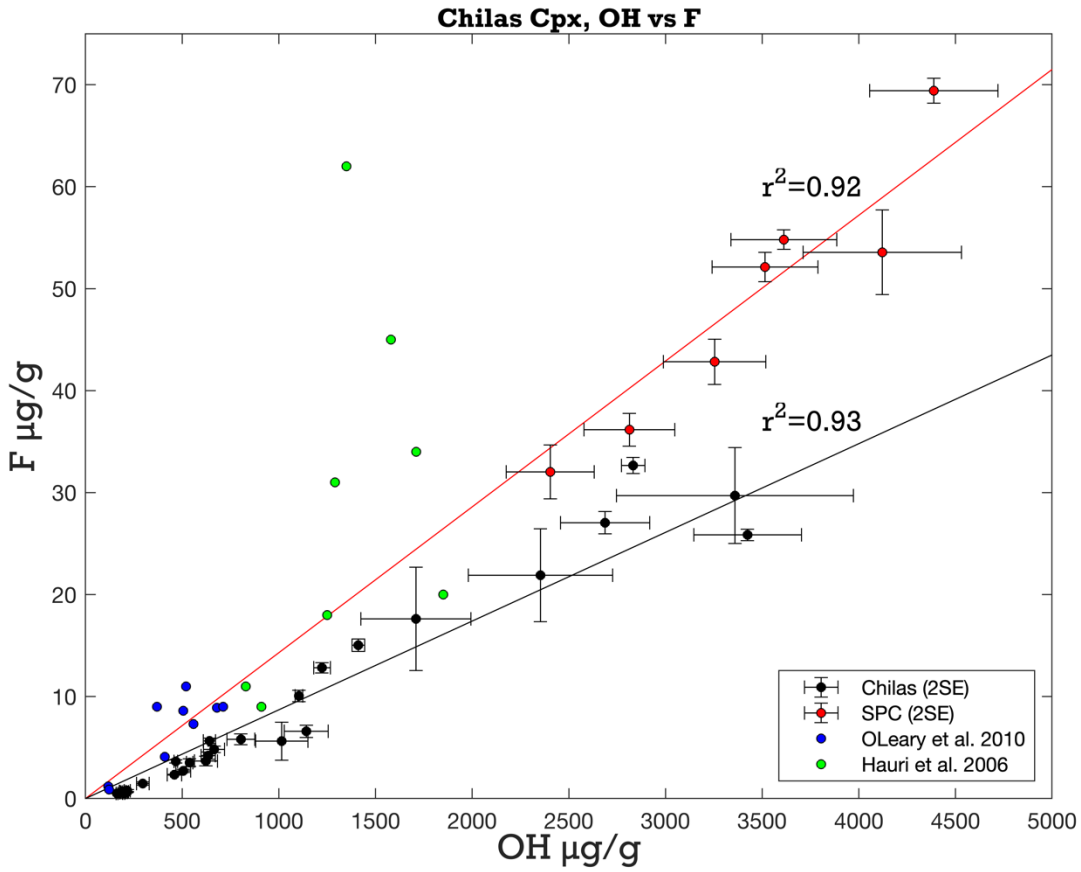

Fig. 4.S2. OH plotted against F for Kohistan samples, includes experimental values from O'Leary et al. (2010) and Hauri et al (2006). Slopes for Chilas and SPC are 0.0087 and 0.0143, respectively, with an origin of zero.

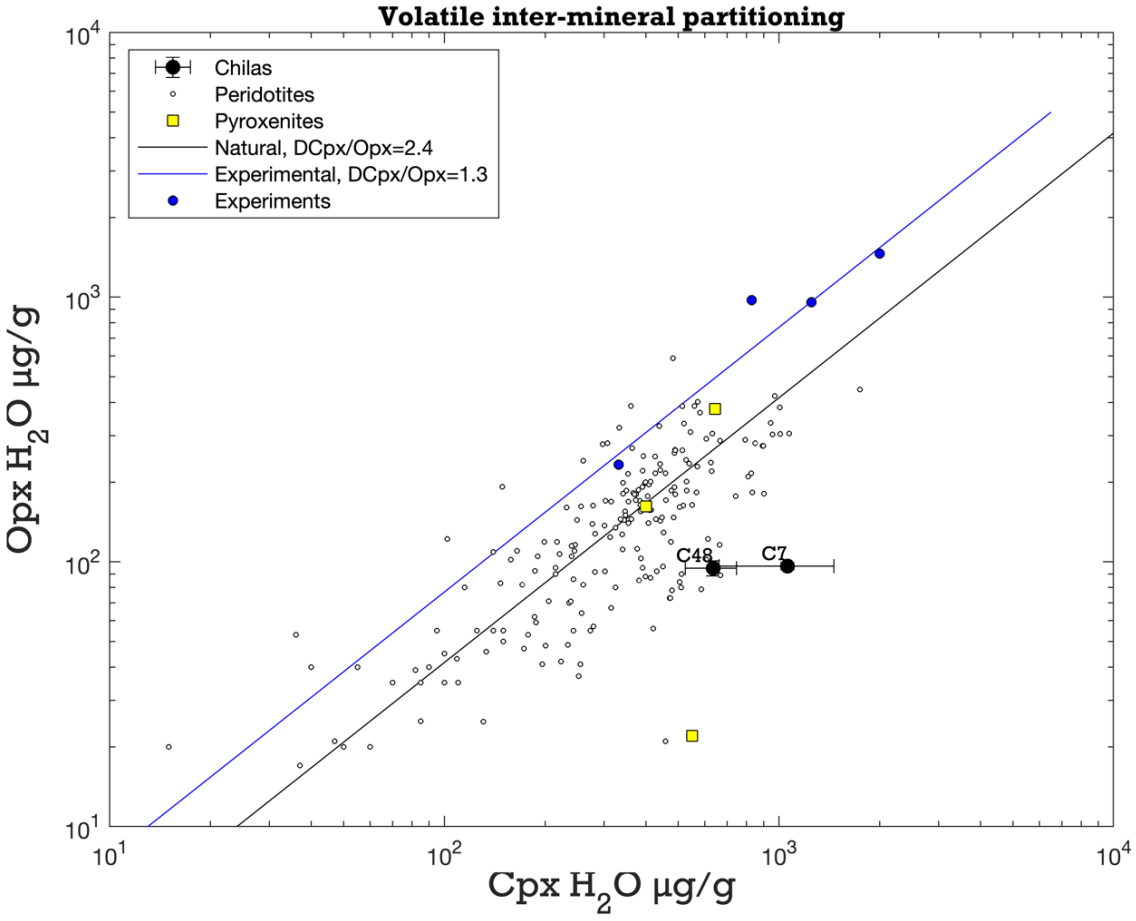

Fig. 4.S3. Inter-mineral partitioning of OH between Cpx and Opx. Data from literature (Hauri, Gaetani et al. 2006, Wang, Mookherjee et al. 2006, Grant, Ingrin et al. 2007, Falus, Tommasi et al. 2008, Li, Lee et al. 2008, Bonadiman, Hao et al. 2009, Peslier 2010, Warren and Hauri 2014, Bizimis and Peslier 2015, Demouchy, Ishikawa et al. 2015, Kumamoto, Warren et al. 2017, Marshall, Lassiter et al. 2018, Gibson, Rooks et al. 2020, Li, Xia et al. 2020).

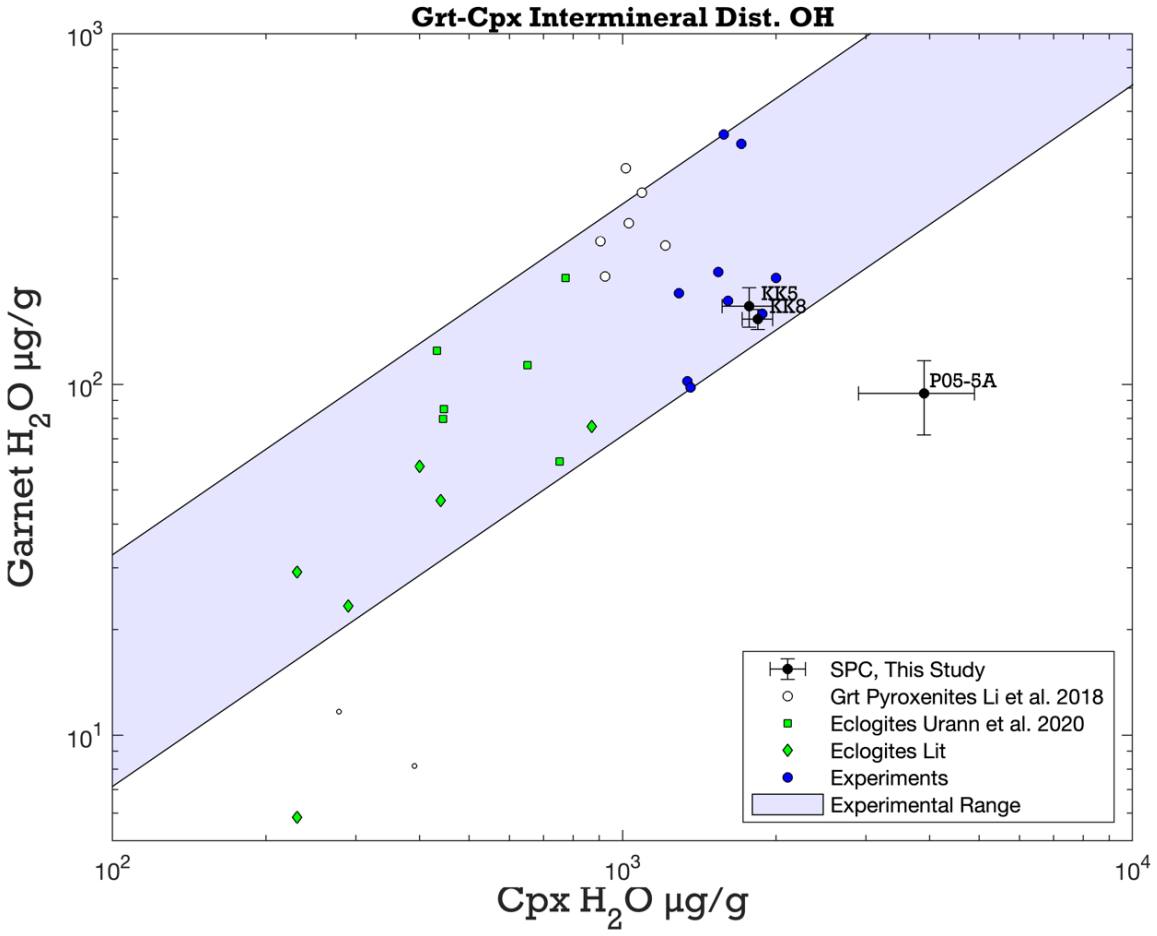

Fig. 4.S4. Inter-mineral partitioning of OH between Cpx and garnet. Experimental data from the literature (Hauri, Gaetani et al. 2006, Aubaud, Hirschmann et al. 2008, Peslier 2010). Garnet pyroxenites from Li et al. (2018).

Chapter 4 Supplementary Tables

Table S1. Individual spot volatile (SIMS) and major element (EMPA) analyses.

| | | |

Table S1. (cont.)

| | | |

Table S1. (cont.)

| | | |

Table S1. (cont.)

| | | |

Table S2. Trace element analyses calculated H_2O partition coefficients, and calculated equilibrium melts.

Sample	Detail	Li7(LR)	Ca43(LR)	Sc45(LR)	Ti49(LR)	V51(LR)	Cr53(LR)	Mn55(LR)	Co59(LR)	Ni60(LR)	Cu65(LR)	Zn66(LR)
P05-5A	Cpx2 all mean	6.34	142529	45.3	4150	816	30.6	311	37.0	47.9	14.1	184
	Cpx2 core mean	5.47	143376	46.2	4260	768	28.5	309	38.7	48.8	2.67	186
	Cpx2 rim mean	7.20	141682	44.4	4039	864	32.7	313	35.3	47.0	25.5	182
	Grt2 all mean	0.440	58349	68.9	493	244	22.9	3869	67.2	2.78	20.1	188
	Grt2 core mean	0.413	52345	72.0	552	262	25.4	4027	68.7	3.09	1.31	196
	Grt2 rim mean	0.468	64352	65.9	433	227	20.3	3710	65.6	2.48	38.9	180
KK8	cpx mean	3.51	163190	93.5	2946	765	61.6	80.2	41.1	89.5		64.3
	Grt Mean		53603	173	246	188	41.6	2899	59.8	3.21		47.4
KK5	Cpx mean	2.83	151516	46.1	3599	555	412	508	34.0	75.8		43.2
	Garnet mean	0.820	53603	134	402	167	593	3890	65.9	5.02		45.5
Calculated Cpx-Melt Partition Coefficient	KK5 Dcpx-melt											
	KK8 Dcpx-melt											
	P05-5A Dcpx-melt											
Calculated Equilibrium Melt Composition	KK5 melt (µg/g)											
	KK8 melt (µg/g)											
	P05-5A melt (µg/g)											

N.B. Trace element data for Chilas samples C66, C48, and C7 are available in Jagoutz et al. 2007

Table S2. (cont.)

μg/g

Sample	Detail	Ga71(LR)	Ge72(LR)	Rb85(LR)	Sr88(LR)	Y89(LR)	Zr90(LR)	Nb93(LR)	Mo95(LR)	Sn118(LR)	Sb121(LR)	Cs133(LR)
P05-5A	Cpx2 all mean	28.4			15.6	0.402				0.829	0.019	
	Cpx2 core mean	30.6			18.2	0.606				0.835	0.021	
	Cpx2 rim mean	26.3		0.019	12.9	0.198				0.823	0.018	
	Grt2 all mean	13.5			0.068	18.6				0.053	0.032	
	Grt2 core mean	15.3		0.013	0.059	14.7				0.059	0.033	
	Grt2 rim mean	11.8			0.078	22.6				0.046	0.031	
KK8	cpx mean			0.030	33.9	4.17	8.35	0.001				0.007
	Grt Mean				0.028	46.2	1.20					
KK5	Cpx mean			0.019	27.9	2.75	2.93	0.008				0.003
	Garnet mean			0.025	0.029	32.8	1.16	0.016				0.025
Calculated Cpx-Melt Partition Coefficient	KK5 Dcpx-melt											
	KK8 Dcpx-melt											
	P05-5A Dcpx-melt											
Calculated Equilibrium Melt Composition	KK5 melt (μg/g)											
	KK8 melt (μg/g)											
	P05-5A melt (μg/g)											

Table S2. (cont.)

Sample	Detail	Ba137(LR)	La139(LR)	Ce140(LR)	Pr141(LR)	Nd146(LR)	Sm149(LR)	Eu151(LR)	Gd160(LR)	Tb159(LR)	Dy161(LR)	Ho165(LR)
P05-5A	Cpx2 all mean	4.60	0.007	0.126	0.088	0.974	0.599	0.173	0.421	0.039	0.180	0.020
	Cpx2 core mean	4.75	0.009	0.188	0.132	1.74	0.867	0.289	0.686	0.063	0.245	0.028
	Cpx2 rim mean	4.44	0.004	0.033	0.021	0.211	0.199	0.056	0.156	0.016	0.082	0.010
	Grt2 all mean			0.010	0.010	0.341	1.12	0.951	2.97	0.531	3.53	0.709
	Grt2 core mean			0.010	0.008	0.353	1.26	1.03	3.01	0.486	2.92	0.527
	Grt2 rim mean				0.013	0.329	0.976	0.869	2.93	0.575	4.14	0.891
KK8	cpx mean	0.284	0.523	2.30	0.542	4.17	1.63	0.807	1.61	0.248	1.24	0.198
	Grt Mean				0.009	0.109	0.371	0.384	1.60	0.548	5.78	1.82
KK5	Cpx mean	0.061	0.243	1.12	0.264	1.80	0.983	0.492	1.05	0.177	0.798	0.120
	Garnet mean	0.000	0.000	0.009	0.024	0.098	0.341	0.364	1.49	0.494	4.54	1.28
Calculated Cpx-Melt Partition Coefficient	KK5 Dcpx-melt		0.112	0.195	0.310	0.451	0.707	0.792	0.846	0.863	0.841	0.790
	KK8 Dcpx-melt		0.082	0.138	0.213	0.300	0.447	0.490	0.514	0.515	0.493	0.456
	P05-5A Dcpx-melt		0.118	0.218	0.360	0.540	0.870	0.978	1.04	1.05	1.01	0.938
Calculated Equilibrium Melt Composition	KK5 melt (µg/g)		2.17	5.72	0.852	3.99	1.39	0.621	1.24	0.205	0.948	0.152
	KK8 melt (µg/g)		6.39	16.7	2.55	13.9	3.66	1.65	3.13	0.481	2.52	0.433
	P05-5A melt (µg/g)		0.063	0.581	0.244	1.80	0.689	0.177	0.404	0.037	0.177	0.022

Table S2. (cont.)

Sample	Detail	Er167(LR)	Tm169(LR)	Yb173(LR)	Lu175(LR)	Notes
P05-5A	Cpx2 all mean	0.037	0.004	0.028	0.004	
	Cpx2 core mean	0.046	0.005	0.033	0.005	
	Cpx2 rim mean	0.018	0.003	0.017	0.003	
	Grt2 all mean	1.87	0.259	1.79	0.256	
	Grt2 core mean	1.28	0.175	1.21	0.162	
	Grt2 rim mean	2.47	0.344	2.37	0.351	
KK8	cpx mean	0.382	0.040	0.204	0.020	
	Grt Mean	6.54	1.12	9.08	1.43	
KK5	Cpx mean	0.241	0.022	0.130	0.010	
	Garnet mean	4.45	0.726	5.93	0.959	
Calculated Cpx-Melt Partition Coefficient	KK5 Dcpx-melt	0.723	0.649	0.577	0.511	Calculated using Sun and Liang (2012)
	KK8 Dcpx-melt	0.412	0.365	0.322	0.283	Calculated using Sun and Liang (2012)
	P05-5A Dcpx-melt	0.841	0.741	0.645	0.560	Calculated using Sun and Liang (2012)
Calculated Equilibrium Melt Composition	KK5 melt (µg/g)	0.333	0.034	0.225	0.019	
	KK8 melt (µg/g)	0.928	0.109	0.635	0.071	
	P05-5A melt (µg/g)	0.044	0.005	0.043	0.007	

Table S3. Equilibrium crystallization model for Chilas.

Equilibrium Crystallization

Partition Coefficients								
Element	Olivine	CPX	Plag	OPX	Melt	Spinel		*D*
Nd		0.187	0.021	0.0007				0.0315
H2O		0.01568	0.00018	0.0071				0.0038
Hauri et al., Exp. B330		Si	Ca					
Dunite C174 (Jagoutz et al. 2007)		1.897	0.978					

Source	*C66 Equilibrium Melt*		
Composition (F=0)		PrimMant	source/CI
Nd	8.02	1.354	5.92422
H2O	12100	250	48.4

	Olivine	CPX	Plag	OPX	Melt	Spinel	Sum
Mode %		0.100	0.600	0.300	0.000	0.000	1.0

	Melt (µg/g) from Cpx				
	Nd	Nd 2SE		H2O	H2O 2SE
C7	62.3963	6.67		109500	40900
C48	38.8	8.18		63800	9600
C66	8.02			12100	900

Table S3. (cont.)

Melt Fraction	1.00	0.90	0.80	0.70	0.60	0.50	0.40	0.30	0.25	0.23	0.20	0.15	0.14
RESULTS:	*Liquid*	µg/g											
% Crystallized	*0.00*	*0.10*	*0.20*	*0.30*	*0.40*	*0.50*	*0.60*	*0.70*	*0.75*	*0.78*	*0.80*	*0.85*	*0.86*
Nd	8.02	8.88	9.95	11.3	13.1	15.6	19.1	24.9	29.3	32.2	35.6	45.4	48.0
H2O	12100	13439	15111	17258	20116	24108	30079	39979	47855	53084	59595	78968	84459

Table S3. (cont.)

Melt Fraction	0.13	0.12	0.10	0.09	0.08	0.07	0.06	0.05	0.04	0.03	0.02
RESULTS:											
% Crystallized	*0.87*	*0.88*	*0.90*	*0.91*	*0.92*	*0.93*	*0.94*	*0.95*	*0.96*	*0.97*	*0.98*
Nd	51.0	54.3	62.5	67.6	73.6	80.8	89.5	100	114	132	158
H2O	90771	98102	117003	129475	144923	164558	190346	225719	277241	359239	510113

Table S4. Delamination flux model

Supplementary Table 4: Volatile Flux Model

	km^3/yr	Source:					
Subduction flux:	19	Jagoutz et al. 2013					
Delamination Flux Range	6.4-8.1	Jagoutz et al. 2013					
		SPC Mineral Mean					
	Material Flux (km3/yr)	Cpx H2O (μg/g)	Grt H2O (μg/g)	Amph H2O (μg/g)	Bulk Rock H2O (μg/g)	Water Flux kg/yr	Uncertainty (1SD)
Delamination Hydrous Mean (Cpx/Grt/Amph)	7.3	2504	138	18888	5071	1.06622E+11	22.2%
Delamination Hydrous High (Cpx/Grt/Amph)	8.1	3900	94	20875	5392	1.26661E+11	
Delamination Hydrous Low (Cpx/Grt/Amph)	6.4	1806	160	19151	4452	8.26E+10	
Delamination Anhydrous Mean (Cpx/Grt)	7.3	2504	138		1321	2.78E+10	49.7%
Delamination Anhydrous High (Cpx/Grt)	8.1	3900	94		1997	4.69E+10	
Delamination Anhydrous Low (Cpx/Grt)	6.4	1806	160		983	1.82E+10	

S.5 Supplementary material accompanying Chapter 5

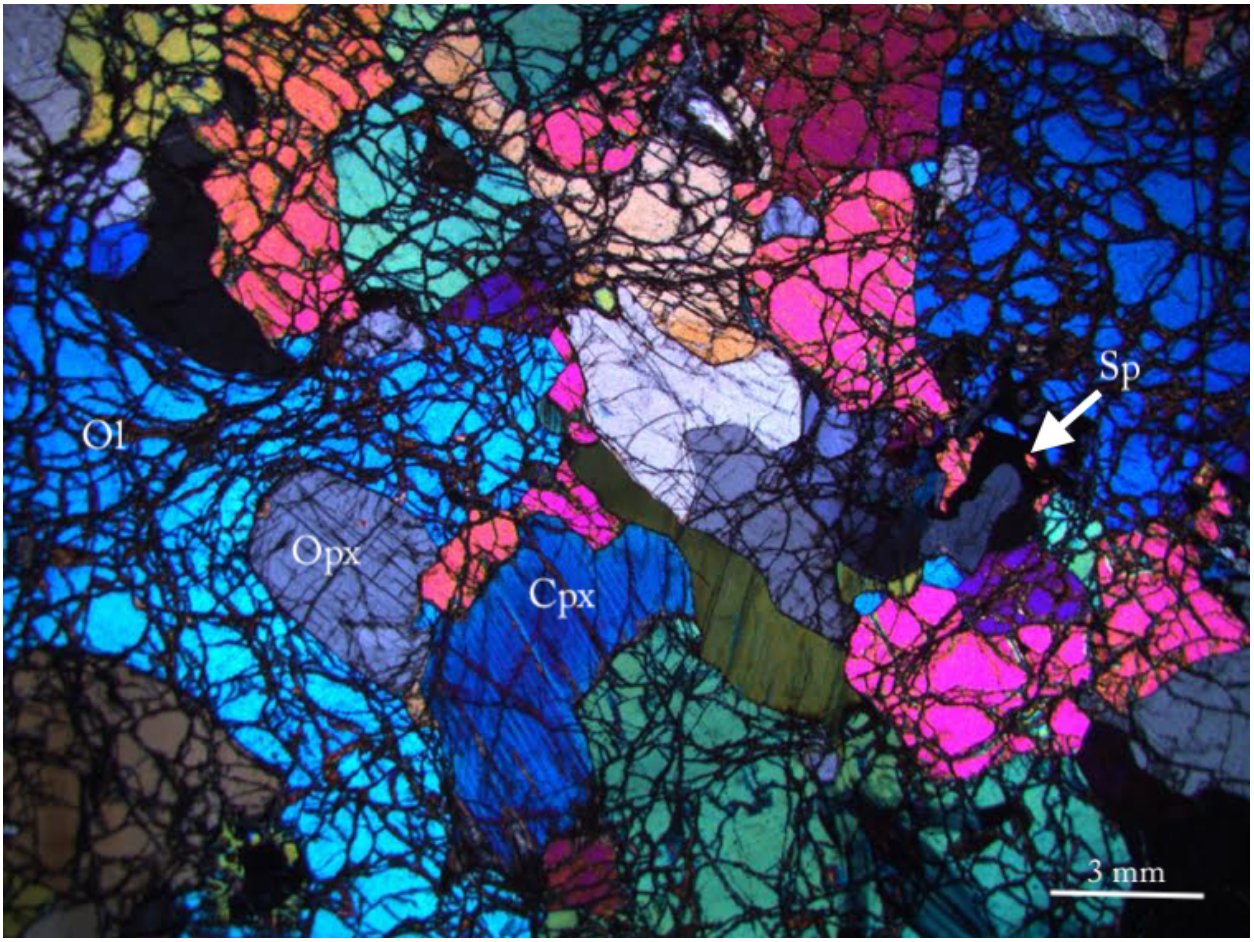

Figure 5.S1. Protogranular harzburgite under crossed nicols. Textures are consistent with primary Cpx, not exsolved from Opx. Field of view is 2.5 cm. Ol, Sp, Cpx, Opx are olivine, spinel, clinopyroxene, and orthopyroxene, respectively.

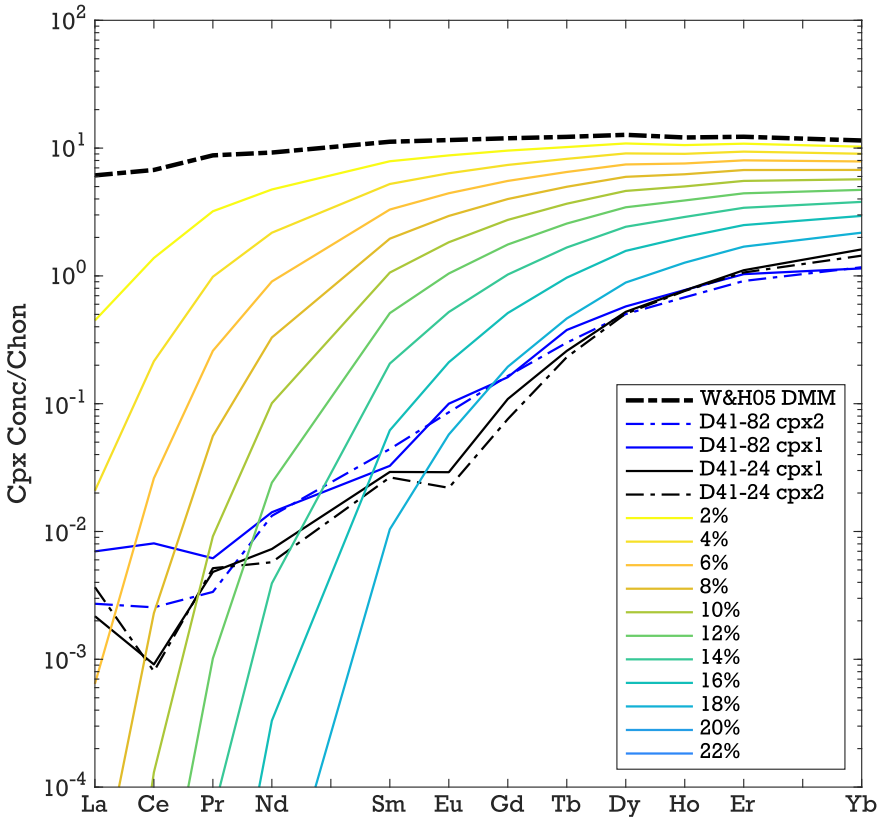

Figure 5.S2. Spider diagram of REE with anhydrous fractional melting model of spinel-bearing peridotite utilizing MatLab script of Warren (2016) and references therein, modified using anhydrous melting modes of Wasylenki et al. (2003). Partition coefficients from Sun and Liang (2012). Note that anhydrous melting is unable to replicate observed REE abundances before Cpx exhaustion. Shown are the median values of five measurements per grain for the samples in this study, normalized to chondrite values of Anders and Grevesse (1989). Thick black dashed line indicates depleted MORB mantle (DMM) values suggested by Workman and Hart (2005).

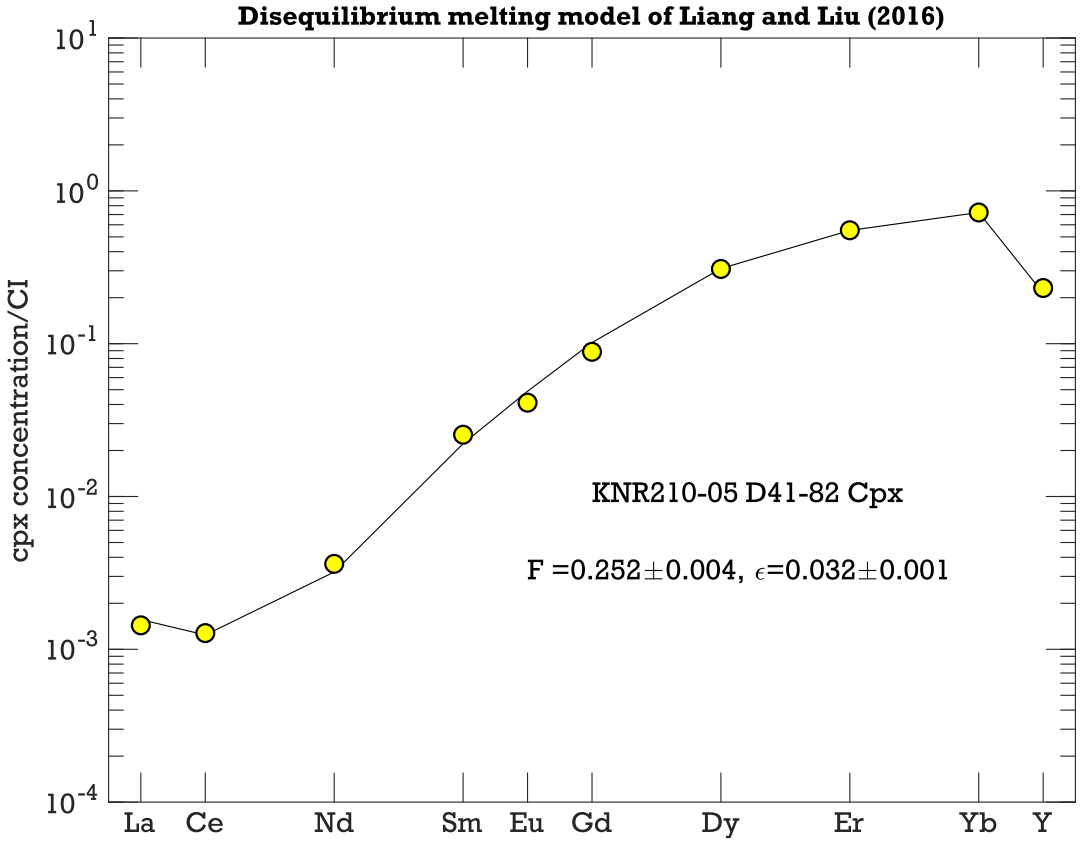

Figure 5.S3. REE + Y fractional disequilibrium melting model of Liang and Liu(2016), modified to incorporate hydrous melting parameters with starting mineral modal abundances of Workman and Hart (2005) DMM. Partition coefficients are from Sun and Liang (2012), with hydrous melting modes of Bizimis et al. (2000). Values are normalized to chondrite values of Anders and Grevesse (1989).

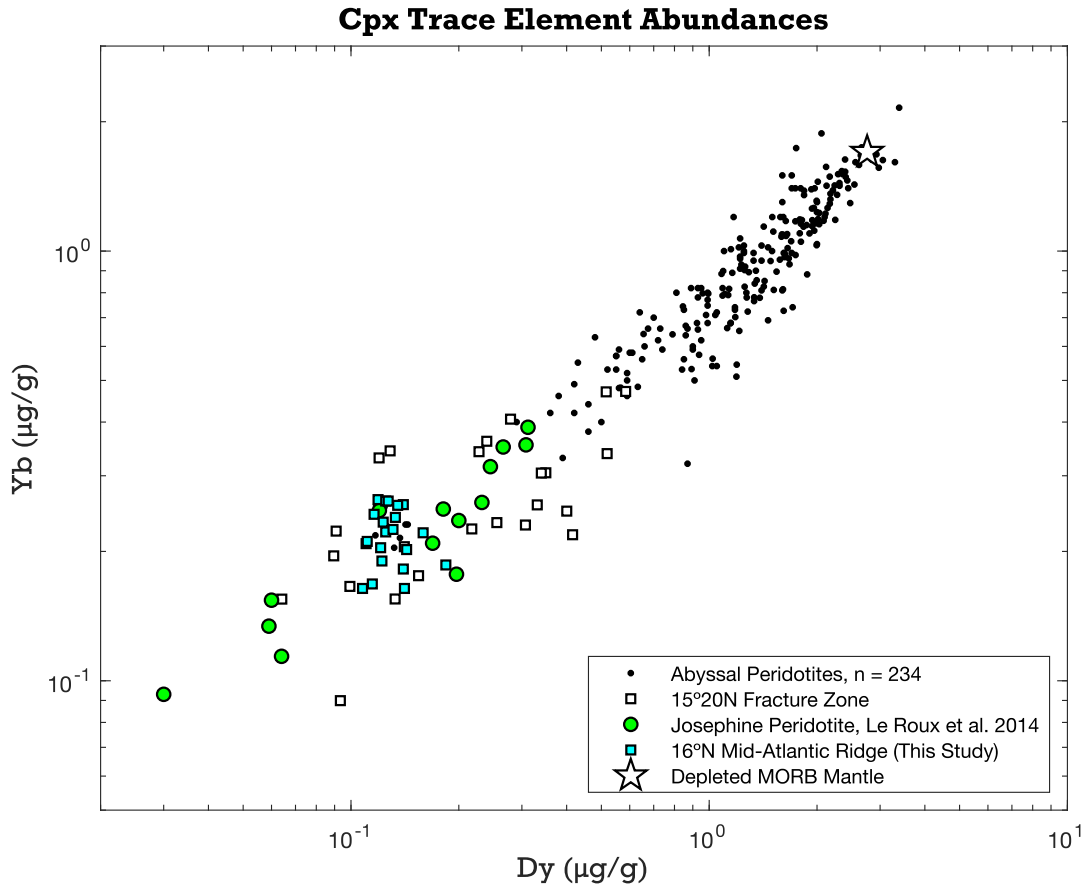

Figure 5.S4. Clinopyroxene Yb vs. Dy abundances in log-log space, illustrating the highly depleted nature of mantle both in the 16°N and 15°20'N Fracture Zone regions compared to the abyssal peridotite compilation of Warren (2016). Also plotted is data from an SSZ environment, the Josephine peridotite, for comparison. Josephine peridotite data from Le Roux et al. (2014).

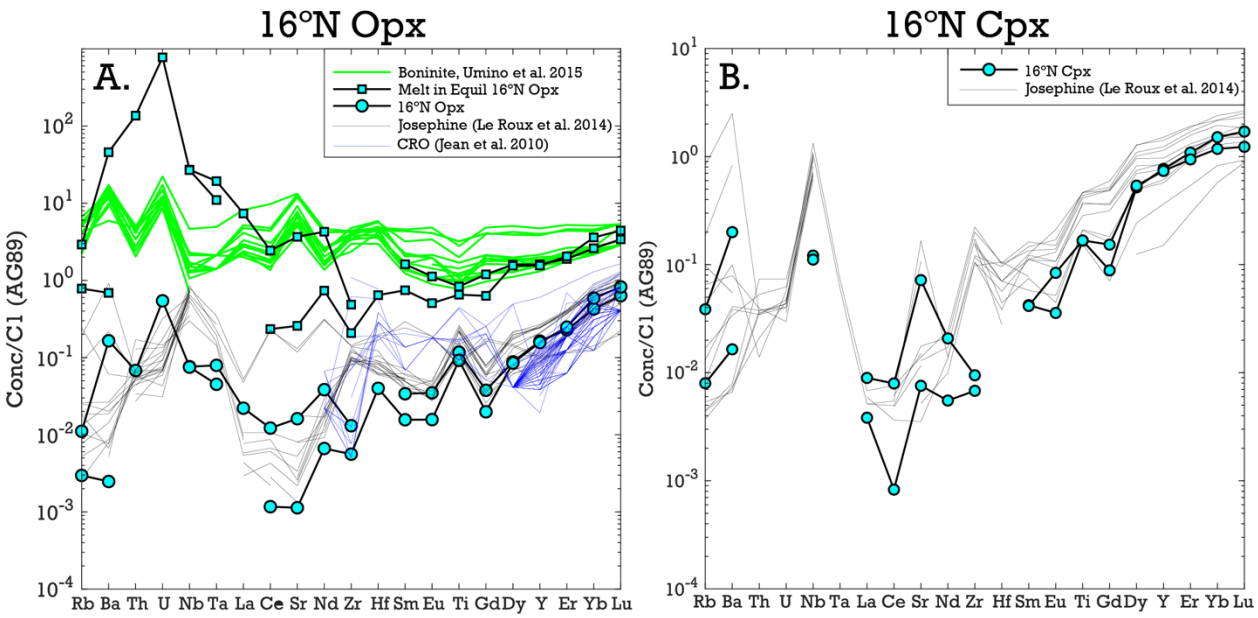

Figure 5.S5. A. Calculated melts in equilibrium with 16°N Opx (blue squares) as well as 16°N Opx trace element concentrations (blue circles) normalized to chondritic values of Anders and Grevesse (1989). Calculated melts show extreme fluid immobile element depletion and fluid mobile element enrichments, consistent with flux melting and interaction with boninitic-like melts. B. 16°N Cpx. Thin lines are literature data from the Josephine peridotite and Coast Range Ophiolite (CRO) peridotites (Jean, Shervais et al. 2010, Le Roux, Dick et al. 2014). Boninite data from Unimo et al. (2015). Opx-melt partition coefficients from the literature(McDade, Blundy et al. 2003, Adam and Green 2006).

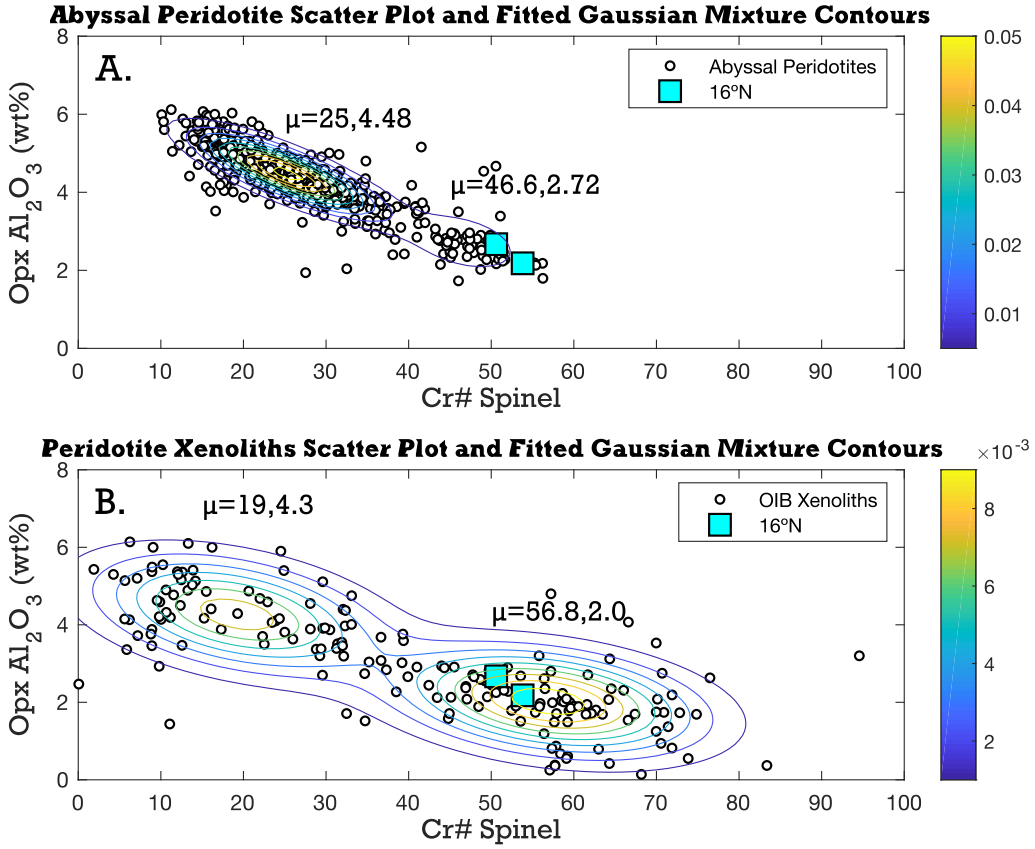

Figure 5.S6. Probability density contours of Opx Al_2O_3 content and spinel Cr# from A. mid-ocean ridge peridotites (MORP) from Warren et al. (2016) and B. ocean island basalt hosted peridotite xenoliths from Simon et al. created using MATLAB Statistics toolbox. Probability contours are color-coded, while mixing calculations suggest two populations with mean values (μ) listed in each figure. We note that abyssal peridotite data show a heavy sampling bias toward fracture zones (~75% of samples) compared to the stochastic sampling of ocean island basalt xenoliths

Chapter 5 Supplementary Tables

Table S1. Major element (EMPA) analyses of individual phases

Olivine														
Sample ID	Dredge Location		wt %											
	Latitude (°)	Longitude (°	CaO	SiO2	MnO	FeO	MgO	TiO2	Al2O3	NiO	Total	Mg#	No. Meas.	
D53-02	16.679	-46.594	0.06	41.11	0.12	8.03	50.61	0.01	0.01	0.33	100.28	91.8	6	
D33-02 Ol A	16.531	-46.663	0.09	40.13	0.11	8.50	49.55	0.00	0.11	0.32	98.83	91.7	6	
D33-02 Ol B	16.531	-46.663	0.06	40.75	0.15	8.63	50.64	0.00	0.01	0.40	100.64	91.3	5	
D33-02 Ol C	16.531	-46.663	0.08	40.64	0.13	8.50	50.72	0.00	0.01	0.40	100.48	91.4	5	
D33-02 Ol D	16.531	-46.663	0.04	40.63	0.14	8.64	49.95	0.02	0.01	0.36	99.80	91.2	5	
D41-24 Ol A	16.521	-46.675	0.08	40.29	0.12	8.80	50.65	0.00	0.00	0.37	100.30	91.1	6	
D41-24 Ol B	16.521	-46.675	0.07	40.24	0.12	8.76	50.64	0.00	0.00	0.38	100.22	91.1	6	
D41-24 Ol C	16.521	-46.675	0.08	40.32	0.14	8.70	50.41	0.00	0.00	0.38	100.03	91.2	6	
D41-82 Ol A	16.521	-46.675	0.03	40.31	0.13	7.86	51.48	0.00	0.00	0.41	100.2	92.1	6	
D41-82 Ol B	16.521	-46.675	0.03	40.06	0.11	7.94	51.00	0.00	0.02	0.41	99.57	92.0	6	
D41-82 Ol C	16.521	-46.675	0.03	40.18	0.12	7.90	51.24	0.00	0.01	0.41	99.90	92.0	6	
D27-16	16.487	-46.692	0.12	38.10	0.15	8.72	50.90	0.06	0.12	0.43	98.60	91.2	6	
D51-03	16.664	-46.629	0.08	38.34	0.10	8.50	50.58	0.00	0.00	0.41	98.01	91.4	5	
D49-02 Ol A	16.673	-46.648	0.09	40.54	0.10	8.77	50.77	0.00	0.00	0.39	100.67	91.2	5	
D49-02 Ol B	16.673	-46.648	0.10	41.10	0.11	8.83	49.61	0.00	0.02	0.40	100.15	90.9	5	
D34-04	16.599	-46.705	0.05	40.69	0.09	8.00	51.02	0.00	0	0.40	100.25	91.9	5	

Table S1. (cont.)

Spinel	Dredge Location		wt %															
Sample ID	Lat	Long	SiO2	TiO2	Al2O3	Cr2O3	FeO	MnO	MgO	CaO	NiO	ZnO	Total	Mg#	Cr#	No. Meas.
D02-23	16.493	-46.731	0.0	0.00	35.4	31.6	15.8	0.07	16.6	0.00	0.00	0.00	99.39	71.0	37.4	6
D33-04	16.531	-46.663	0.0	0.08	25.9	44.2	13.9	0.17	15.6	0.00	0.02	0.05	100.00	69.7	53.4	6
D34-04	16.599	-46.705	0.0	0.01	28.7	40.3	13.9	0.18	16.0	0.01	0.03	0.03	99.30	71.1	48.5	6
D35-05	16.622	-46.696	0.0	0.00	31.7	36.2	14.5	0.14	16.8	0.00	0.04	0.01	99.34	73.0	43.4	6
D36-01	16.614	-46.676	0.0	0.15	29.8	38.2	15.9	0.25	16.1	0.01	0.13	0.18	100.65	68.5	46.0	6
D40-02	16.558	-46.660	0.0	0.08	22.9	42.6	22.4	0.27	12.4	0.00	0.08	0.12	100.89	57.2	55.6	6
D40-05	16.558	-46.660	0.3	0.00	21.6	50.2	14.2	0.29	13.6	0.00	0.07	0.17	100.48	62.3	61.0	6
D41-04	16.521	-46.675	0.0	0.00	20.3	51.5	14.6	0.23	14.2	0.00	0.01	0.02	100.76	64.9	63.0	6
D41-24	16.521	-46.675	0.0	0.01	28.2	42.6	15.6	0.24	14.7	0.00	0.09	0.14	101.52	65.9	50.6	16
D41-82	16.521	-46.675	0.01	0.03	23.7	41.1	21.5	0.28	13.9	0.01	0.18	0.11	100.81	63.1	53.8	12
D42-01	16.474	-46.697	0.0	0.05	18.9	49.4	19.5	0.33	12.3	0.00	0.03	0.09	100.61	57.8	63.7	6
D42-01	16.474	-46.697	0.0	0.02	35.7	35.0	14.2	0.19	16.0	0.00	0.17	0.08	101.37	68.2	39.7	6
D49-07	16.673	-46.648	0.0	0.00	28.4	41.0	14.6	0.23	16.4	0.00	0.12	0.06	100.89	72.0	49.2	6
D49-05	16.673	-46.648	0.0	0.07	19.9	49.3	19.4	0.34	11.9	0.01	0.08	0.17	101.26	55.7	62.5	6
D49-02	16.673	-46.648	0.0	0.01	29.7	39.5	15.1	0.19	16.1	0.01	0.16	0.11	100.90	64.9	47.1	13
D49-01	16.673	-46.648	0.0	0.14	31.3	37.5	15.8	0.19	15.5	0.00	0.11	0.09	100.70	63.6	44.5	10
D50-03	16.686	-46.657	0.0	0.03	34.0	34.2	14.6	0.20	17.1	0.00	0.11	0.04	100.33	73.1	40.3	6
D51-03	16.664	-46.629	0.0	0.07	34.8	34.7	14.4	0.18	16.6	0.01	0.15	0.13	101.08	67.2	40.1	15
D51-02	16.664	-46.629	0.0	0.05	32.8	36.4	13.7	0.21	17.3	0.01	0.16	0.09	100.67	74.3	42.7	6
D51-01	16.664	-46.629	0.1	0.08	32.8	34.6	13.3	0.19	17.0	0.01	0.17	0.08	98.39	74.0	41.4	6
D53-02	16.679	-46.594	0.0	0.03	29.7	40.6	12.7	0.21	17.3	0.00	0.15	0.09	100.72	75.0	47.9	6
D54-23	16.684	-46.573	0.0	0.04	30.3	38.1	15.1	0.23	16.4	0.00	0.14	0.11	100.59	71.8	45.7	6
D55-02	16.696	-46.568	0.0	0.03	30.1	39.1	14.6	0.23	16.4	0.00	0.11	0.13	100.72	71.5	46.5	6
D55-06	16.696	-46.568	0.0	0.03	30.3	38.5	14.8	0.20	16.1	0.00	0.11	0.14	100.24	70.5	46.1	6
D55-08	16.696	-46.568	0.0	0.04	29.8	37.9	15.0	0.18	16.2	0.00	0.12	0.12	99.21	71.4	46.1	6
D60-18	16.808	-46.616	0.0	0.48	28.0	34.1	25.2	0.28	12.0	0.00	0.16	0.17	100.33	54.1	45.0	6
Pyroxenes	Dredge Location		wt %													
Sample ID	Latitude (°)	Longitude (°	TiO2	SiO2	K2O	MnO	Na2O	Cr2O3	Al2O3	CaO	FeO	MgO	Total	Mg#	No. Meas.	
D41-24 Cpx1	16.521	-46.675	0.01	52.8	0.00	0.11	0.02	1.37	3.41	18.1	3.43	21.14	100.38	91.7	10	
D41-24 Cpx2	16.521	-46.675	0.00	52.9	0.01	0.12	0.01	1.41	3.54	18.5	3.43	20.79	100.74	91.6	10	
D41-24 Opx1	16.521	-46.675	0.00	55.8	0.00	0.14	0.00	0.91	2.59	2.30	5.69	32.36	99.78	91.0	10	
D41-24 Opx2	16.521	-46.675	0.02	55.7	0.00	0.14	0.01	0.98	2.76	2.52	5.63	32.03	99.82	91.0	10	
D41-82 Cpx1	16.521	-46.675	0.03	52.9	0.00	0.09	0.18	1.17	2.94	21.6	2.79	18.61	100.30	92.2	10	
D41-82 Cpx2	16.521	-46.675	0.01	52.9	0.00	0.08	0.14	1.26	2.89	21.8	2.86	18.48	100.41	92.0	10	
D41-82 Opx1	16.521	-46.675	0.01	56.1	0.00	0.14	0.02	0.83	2.22	2.58	5.37	32.61	99.87	91.6	10	
D41-82 Opx2	16.521	-46.675	0.02	56.2	0.00	0.11	0.02	0.71	2.13	2.05	5.39	33.21	99.86	91.6	10	

Table S2. Trace element analyses of orthopyroxene and clinopyroxene

µg/g

Element	D41-82_CPX1-01	D41-82_CPX1-02	D41-82_CPX1-03	D41-82_CPX1-04	D41-82_CPX1-05
Li7	4.1	4.1	4.4	3.7	3.6
Be9	<0.0121	<0.0185	0.0	<0.0235	0.0
Mg25	113788	112984	113934	111404	114069
Mg26	18.6	18.6	18.6	18.6	18.6
Ca43	152161	147221	136818	150680	139920
Sc45	41.8	39.9	35.9	46.2	40.9
Ti49	124.5	78.9	67.8	90.2	78.7
V51	28.7	26.8	25.4	29.1	28.0
Cr53	8121	8347	7829	8802	7978
Mn55	637.9	621.6	604.4	729.3	695.9
Co59	25.1	25.7	25.3	26.9	25.6
Ni60	418.3	424.7	438.9	431.8	430.9
Cu65	4.2	4.4	4.1	3.9	4.3
Zn66	16.4	16.1	18.6	17.5	16.6
Ga71	2.1	2.1	2.0	2.1	2.0
Ge72	1.1	1.1	1.1	1.2	1.1
Rb85	0.1	0.1	0.2	0.1	0.0
Sr88	1.9	0.8	1.0	0.8	0.2
Y89	1.343	1.204	1.040	1.298	1.223
Zr90	0.4	0.1	0.0	0.0	0.0
Nb93	0.1	0.0	0.0	0.0	0.0
Cs133	0.0	0.0	0.0	0.0	0.0
Ba137	8.8	0.6	0.6	0.4	0.3
La139	0.036	0.004	<0.00061	0.001	0.002
Ce140	0.115	0.010	0.004	0.005	0.001
Pr141	0.015	0.001	<0.00051	0.001	<0.00048
Nd146	0.066	0.018	0.006	<0.0045	0.003
Sm149	0.021	<0.0048	0.005	<0.0043	<0.0052
Eu151	0.011	0.008	0.002	0.006	0.005
Gd157	0.048	0.030	0.032	0.033	0.024
Tb159	0.015	0.014	0.010	0.014	0.014
Dy161	0.184	0.140	0.108	0.159	0.125
Ho165	0.049	0.046	0.034	0.043	0.042
Er167	0.205	0.161	0.129	0.182	0.164
Tm169	0.031	0.028	0.024	0.029	0.028
Yb173	0.186	0.182	0.164	0.221	0.222
Lu175	0.033	0.032	0.025	0.033	0.032
Hf178	0.018	0.005	<0.0035	<0.0044	0.003
Ta181	0.005	<0.00118	<0.00083	<0.00110	<0.00103
Pb208	0.034	0.011	0.019	0.035	0.011
Th232	0.007	<0.00208	<0.00171	<0.00236	<0.00229

Table S2. (cont.)

µg/g

Element		D41-82_CPX2-01	D41-82_CPX2-02	D41-82_CPX2-03	D41-82_CPX2-04	D41-82_CPX2-05
Li7		3.3	4.0	3.1	2.6	2.2
Be9		<0.0169	<0.0097	<0.0097	0.0	0.0
Mg25		111581	112697	114540	113545	114439
Mg26		18.5	18.5	18.5	18.5	18.5
Ca43		134557	116934	116694	132342	123796
Sc45		38.4	35.0	34.3	38.6	36.0
Ti49		75.8	63.7	62.1	69.7	65.1
V51		25.8	23.5	24.8	26.4	25.7
Cr53		7481	7029	7421	7819	7770
Mn55		622.3	634.2	707.6	709.5	723.5
Co59		25.2	26.8	28.5	27.1	27.3
Ni60		420.5	422.5	440.6	438.0	427.7
Cu65		3.7	3.7	4.3	4.0	4.8
Zn66		16.4	18.3	17.6	17.1	17.3
Ga71		1.9	1.9	1.9	2.0	1.9
Ge72		1.0	1.0	1.1	1.2	1.1
Rb85		0.2	0.1	0.1	0.0	0.0
Sr88		1.0	0.7	0.3	0.1	0.0
Y89		1.2	1.0	1.0	1.2	1.1
Zr90		0.1	0.0	0.0	0.0	0.0
Nb93		0.0	0.0	0.0	0.0	0.0
Cs133		0.0	0.0	0.0	0.0	<0.00079
Ba137		1.2	0.6	0.2	0.1	0.0
La139		0.0	0.0	0.0	0.0	<0.00056
Ce140		0.0	0.0	0.0	0.0	0.0
Pr141		0.0	0.0	<0.00030	0.0	0.0
Nd146		0.0	0.0	<0.0030	<0.0031	0.0
Sm149		0.0	0.0	<0.0036	0.0	<0.0040
Eu151		0.005	0.003	0.003	0.006	0.005
Gd157		0.037	0.026	0.032	0.035	0.023
Tb159		0.012	0.010	0.010	0.014	0.011
Dy161		0.143	0.141	0.115	0.122	0.121
Ho165		0.040	0.034	0.037	0.047	0.038
Er167		0.145	0.126	0.123	0.151	0.156
Tm169		0.025	0.023	0.025	0.024	0.026
Yb173		0.202	0.164	0.168	0.190	0.204
Lu175		0.030	0.029	0.028	0.031	0.031
Hf178		<0.0039	<0.0023	<0.0026	<0.0033	<0.0039
Ta181		<0.00098	<0.00080	0.0	<0.00085	0.0
Pb208		0.0	0.0	0.0	0.0	0.0
Th232		<0.0022	<0.00212	<0.00116	<0.00163	<0.00184

Table S2. (cont.)

µg/g

Element		D41-82_OPX1-01	D41-82_OPX1-02	D41-82_OPX1-03	D41-82_OPX1-04	D41-82_OPX1-05
Li7		2.6	1.8	1.6	1.6	1.6
Be9		<0.0132	0.0	0.0	0.0	0.0
Mg25		194421	205834	197464	205020	197122
Mg26		32.6	32.6	32.6	32.6	32.6
Ca43		16141	16950	16688	16600	15946
Sc45		24.1	26.2	25.7	24.7	25.2
Ti49		59.4	50.3	50.3	49.7	47.5
V51		11.9	12.1	11.3	11.2	11.3
Cr53		5076	5589	5464	5698	5367
Mn55		1027.1	1054.8	1042.5	1052.4	1031.8
Co59		57.5	60.1	59.6	61.2	58.8
Ni60		775.5	796.1	813.0	832.6	788.8
Cu65		5.8	6.1	5.4	5.5	5.7
Zn66		43.4	44.1	43.1	44.7	43.4
Ga71		1.8	2.1	1.9	1.9	1.8
Ge72		1.2	1.2	1.2	1.3	1.2
Rb85		0.0	<0.0069	<0.0067	0.0	0.0
Sr88		0.5	0.0	0.0	0.2	0.1
Y89		0.251	0.239	0.224	0.213	0.225
Zr90		0.1	0.1	0.0	0.0	0.0
Nb93		0.0	0.0	0.0	0.0	0.0
Cs133		0.0	<0.00121	<0.00091	0.0	<0.00075
Ba137		0.9	0.1	0.1	0.2	0.1
La139		0.0	0.0	<0.00065	<0.00049	<0.00051
Ce140		0.0	0.0	0.0	0.0	0.0
Pr141		0.0	<0.00059	<0.00027	0.0	<0.00039
Nd146		0.0	<0.0045	<0.0042	<0.0037	<0.00170
Sm149		<0.0043	<0.0056	<0.0040	<0.0044	<0.0040
Eu151		<0.00121	0.0	<0.00130	0.0	<0.00144
Gd157		0.0	<0.0051	<0.0053	<0.0040	0.0
Tb159		0.0	<0.00140	0.0	0.0	0.0
Dy161		0.0	0.0	0.0	0.0	0.0
Ho165		0.0	0.0	0.0	0.0	0.0
Er167		0.0	0.0	0.0	0.0	0.0
Tm169		0.0	0.0	0.0	0.0	0.0
Yb173		0.1	0.1	0.1	0.1	0.1
Lu175		0.0	0.0	0.0	0.0	0.0
Hf178		<0.0048	<0.0036	<0.0029	<0.0036	<0.0034
Ta181		<0.00165	<0.00124	<0.00102	<0.00098	<0.00145
Pb208		0.0	<0.0054	0.0	0.0	0.0
Th232		<0.0023	0.0	<0.00210	<0.00202	<0.00210

Table S2. (cont.)

µg/g

Element		D41-82_OPX2-01	D41-82_OPX2-02	D41-82_OPX2-03	D41-82_OPX2-04	D41-82_OPX2-05
Li7		0.9	1.1	1.1	1.0	1.0
Be9		<0.0207	0.0	<0.0119	<0.00	0.0
Mg25		206512	210130	212669	207374	201527
Mg26		33.2	33.2	33.2	33.2	33.2
Ca43		15449	15873	16558	15526	16876
Sc45		24.6	24.3	23.8	26.7	24.9
Ti49		57.6	50.0	47.5	51.8	47.6
V51		16.2	16.5	16.5	16.9	16.4
Cr53		5100	5360	5474	5215	5108
Mn55		1061.8	1073.0	1085.6	1079.7	1069.8
Co59		59.2	60.5	60.3	59.0	59.6
Ni60		799.9	833.4	838.8	805.3	806.0
Cu65		9.3	9.4	9.8	9.2	9.5
Zn66		43.7	43.5	44.6	42.0	42.0
Ga71		1.7	1.7	1.8	1.9	1.7
Ge72		1.2	1.2	1.2	1.2	1.2
Rb85		0.0	<0.0075	0.0	<0.0081	<0.0080
Sr88		0.3	0.0	0.0	0.0	0.0
Y89		0.3	0.3	0.3	0.3	0.3
Zr90		0.1	0.0	0.0	0.0	0.0
Nb93		0.0	0.0	0.0	0.0	0.0
Cs133		<0.00111	<0.00115	<0.00099	<0.00140	<0.00110
Ba137		1.9	<0.046	0.0	0.1	0.0
La139		0.0	<0.00060	<0.00071	0.0	0.0
Ce140		0.0	0.0	<0.00052	<0.00097	<0.00061
Pr141		0.0	<0.00063	<0.00038	<0.00078	<0.00071
Nd146		0.0	<0.0039	<0.0038	<0.0018	<0.0034
Sm149		0.0	<0.0041	0.0	<0.0050	<0.0076
Eu151		0.0	<0.00115	0.0	<0.00140	0.0
Gd157		0.0	<0.0049	<0.0053	<0.0058	0.0
Tb159		0.0	0.0	0.0	<0.00107	0.0
Dy161		0.0	0.0	0.0	0.0	0.0
Ho165		0.0	0.0	0.0	0.0	0.0
Er167		0.0	0.0	0.0	0.0	0.0
Tm169		0.0	0.0	0.0	0.0	0.0
Yb173		0.1	0.1	0.1	0.1	0.1
Lu175		0.0	0.0	0.0	0.0	0.0
Hf178		<0.0037	<0.0046	<0.0033	<0.0037	<0.0039
Ta181		0.0	<0.00118	<0.00102	<0.00111	0.0
Pb208		<0.0035	<0.0038	0.0	<0.0043	<0.0053
Th232		<0.0018	<0.0026	<0.0022	<0.0021	<0.0022

Table S2. (cont.)

µg/g

Element		D41-24_CPX1-01	D41-24_CPX1-02	D41-24_CPX1-03	D41-24_CPX1-04	D41-24_CPX1-05
Li7		1.364	1.276	1.803	1.879	1.612
Be9		<0.0188	<0.0132	<0.0182	<0.00	<0.0122
Mg25		129692	127244	132308	129315	128075
Mg26		21.14	21.14	21.14	21.14	21.14
Ca43		150344	142641	141822	144200	145996
Sc45		48.7	46.05	45.32	46.05	46.86
Ti49		77.94	72.12	72.94	72.35	74.06
V51		219.62	202.81	203.12	203.86	213.61
Cr53		10414	9759	10143	9856	10177
Mn55		852.95	909.02	935.61	922.3	914.97
Co59		35.82	36	36.46	35.87	36.36
Ni60		544.32	520.63	543.13	531.47	546.47
Cu65		3.29	3.95	3.34	3.14	3.44
Zn66		27.37	23.99	24.43	23.36	23.41
Ga71		2.78	2.71	2.76	2.83	2.89
Ge72		1.33	1.25	1.36	1.35	1.38
Rb85		0.0271	0.0126	0.0217	0.0119	0.0148
Sr88		0.0944	0.0254	0.0798	0.0667	0.0692
Y89		1.296	1.178	1.199	1.203	1.229
Zr90		0.0225	0.0251	0.0334	0.0211	0.0315
Nb93		0.0344	0.0292	0.0314	0.0308	0.0266
Cs133		0.00142	<0.00115	0.00274	0.00219	0.00111
Ba137		0.1052	0.056	0.0464	0.0513	0.0122
La139		<0.00073	<0.00051	<0.00029	<0.00026	<0.00061
Ce140		<0.00055	<0.00063	0.00034	<0.00039	<0.00070
Pr141		0.00032	<0.00039	<0.00086	<0.00043	<0.00057
Nd146		<0.00	<0.0030	<0.0038	<0.0034	<0.0032
Sm149		<0.0040	<0.0046	<0.0051	<0.0036	<0.0043
Eu151		0.00173	<0.00	0.00264	<0.00153	<0.00120
Gd157		0.0247	0.0164	0.0133	0.0214	0.0265
Tb159		0.0079	0.009	0.0114	0.0094	0.0113
Dy161		0.119	0.125	0.127	0.14	0.135
Ho165		0.0428	0.038	0.0431	0.0461	0.0381
Er167		0.191	0.18	0.168	0.176	0.176
Tm169		0.0347	0.0278	0.034	0.0297	0.0364
Yb173		0.264	0.262	0.262	0.257	0.256
Lu175		0.0439	0.0487	0.0391	0.0395	0.047
Hf178		<0.0024	<0.0024	<0.0029	<0.0026	<0.0031
Ta181		<0.00133	<0.00120	<0.00105	<0.00095	<0.00130
Pb208		<0.0039	<0.0035	0.0047	<0.0033	0.0048
Th232		<0.00248	<0.0028	<0.00270	<0.00224	<0.00193

Table S2. (cont.)

µg/g

Element		D41-24_CPX2-01	D41-24_CPX2-02	D41-24_CPX2-03	D41-24_CPX2-04	D41-24_CPX2-05
Li7		1.55	1.784	1.533	1.754	1.762
Be9		<0.00	<0.0112	<0.0157	<0.0166	<0.0090
Mg25		124407	124031	127946	125782	125179
Mg26		20.79	20.79	20.79	20.79	20.79
Ca43		140470	139307	144322	138898	144071
Sc45		45.35	45.21	46.6	44.4	46.89
Ti49		70.94	69.69	73.04	70	73.27
V51		198.34	197.08	210.49	199.54	207.16
Cr53		9419	9404	10005	9544	9828
Mn55		867.87	877.3	897.97	866.67	868.99
Co59		34.31	34.08	35.66	34.16	34.65
Ni60		504.38	506.38	528.15	500.61	520.66
Cu65		2.95	4.65	4.6	3.14	4.86
Zn66		23.24	22.53	22.75	22.45	22.7
Ga71		2.66	2.64	2.74	2.64	2.66
Ge72		1.22	1.2	1.28	1.14	1.24
Rb85		<0.0067	<0.0059	0.0112	0.0169	0.0293
Sr88		0.0168	0.0399	0.0291	0.0301	0.139
Y89		1.17	1.155	1.215	1.134	1.213
Zr90		0.0313	0.0233	0.027	0.0272	0.0259
Nb93		0.0288	0.0275	0.0307	0.0304	0.0284
Cs133		<0.00089	<0.00093	<0.00101	<0.00071	<0.00088
Ba137		0.007	0.0052	0.0157	0.026	0.0601
La139		0.00104	0.00086	0.00076	0.00058	0.00119
Ce140		<0.00	<0.00052	<0.00045	<0.00033	0.00074
Pr141		<0.00064	<0.00047	0.00031	<0.00039	<0.00046
Nd146		<0.0028	0.0026	<0.0029	<0.00107	0.0023
Sm149		<0.0038	0.0104	<0.0039	0.0033	0.0049
Eu151		0.00185	<0.00110	0.00123	0.00208	<0.00117
Gd157		0.0103	0.0149	0.0149	0.0167	0.0144
Tb159		0.0084	0.0074	0.0101	0.00791	0.0126
Dy161		0.116	0.123	0.111	0.131	0.133
Ho165		0.0402	0.0449	0.0424	0.0368	0.0441
Er167		0.175	0.173	0.169	0.1606	0.159
Tm169		0.0317	0.032	0.0379	0.0278	0.0305
Yb173		0.244	0.234	0.211	0.225	0.24
Lu175		0.0408	0.0392	0.0383	0.0382	0.039
Hf178		<0.0036	<0.00203	<0.0037	<0.0028	<0.0028
Ta181		<0.00071	<0.00078	<0.00109	<0.00081	<0.00080
Pb208		<0.0043	0.0038	<0.0033	<0.0032	0.006
Th232		<0.00244	0.00198	<0.0028	<0.00146	<0.00169

Table S2. (cont.)

µg/g

Element		D41-24_OPX1-01	D41-24_OPX1-02	D41-24_OPX1-03	D41-24_OPX1-04	D41-24_OPX1-05
Li7		0.301	0.28	0.249	0.348	0.195
Be9		<0.01	0.0156	<0.0150	0.0047	<0.0097
Mg25		193681	193482	203694	199544	189087
Mg26		32.36	32.36	32.36	32.36	32.36
Ca43		16549	16383	16875	16726	15294
Sc45		29.42	29.57	30.3	30.91	30.55
Ti49		40.57	40.03	41.5	42.04	39.56
V51		117.35	119.27	126.89	122.89	119.99
Cr53		6259	6237	6657	6207	5916
Mn55		1051.01	1049.28	1111.43	1088.15	1056.65
Co59		60.81	61.35	63.9	61.39	59.02
Ni60		810.32	813.07	846.76	808.93	775.79
Cu65		4.53	5.36	5.09	4.71	4.98
Zn66		47.93	47.13	48.2	48.2	45.56
Ga71		2.143	2.131	2.269	2.255	2.101
Ge72		1.26	1.27	1.22	1.28	1.21
Rb85		<0.0068	<0.0062	0.0058	<0.0059	0.0067
Sr88		<0.00217	<0.00220	0.0026	<0.00205	<0.00177
Y89		0.248	0.25	0.255	0.246	0.236
Zr90		0.0403	0.0187	0.0265	0.0302	0.0231
Nb93		0.018	0.0202	0.0169	0.0194	0.0184
Cs133		<0.00099	<0.00085	<0.00073	<0.00088	<0.00082
Ba137		0.0037	0.0084	<0.0027	<0.0043	<0.0039
La139		<0.00084	<0.00048	<0.00023	<0.00037	<0.00047
Ce140		0.00012	<0.00041	0.00046	<0.00047	<0.00049
Pr141		<0.00069	<0.00053	<0.00049	<0.00034	<0.00028
Nd146		<0.0030	<0.0033	0.0019	<0.0034	<0.00174
Sm149		<0.0053	<0.0031	<0.0032	<0.0046	<0.0024
Eu151		<0.00115	<0.00124	<0.00104	<0.00129	<0.00106
Gd157		<0.0073	<0.0040	<0.0047	0.0035	<0.0039
Tb159		0.00086	0.00119	<0.00067	0.00094	0.0012
Dy161		0.0255	0.0203	0.021	0.0157	0.0137
Ho165		0.0084	0.01	0.00723	0.00681	0.00611
Er167		0.0359	0.0389	0.0486	0.0301	0.0367
Tm169		0.0125	0.0086	0.0093	0.0103	0.0095
Yb173		0.099	0.088	0.093	0.109	0.095
Lu175		0.0184	0.0214	0.0218	0.0217	0.0181
Hf178		0.0045	<0.0028	0.0038	<0.00150	<0.0025
Ta181		<0.00093	<0.00100	<0.00119	0.00076	<0.00107
Pb208		<0.0035	0.0031	<0.0031	0.0028	<0.0036
Th232		<0.00209	<0.00229	<0.00171	<0.00190	<0.00190

Table S2. (cont.)

µg/g

Element			D41-24_OPX2-01	D41-24_OPX2-02	D41-24_OPX2-03	D41-24_OPX2-04
Li7			0.334	0.385	0.461	0.294
Be9			<0.00	<0.0158	<0.0265	<0.0166
Mg25			195933	191205	197681	193339
Mg26			32.03	32.03	32.03	32.03
Ca43			15178	16197	16474	16251
Sc45			27.81	29.3	28.89	29.94
Ti49			38.51	39.31	39.81	39.29
V51			115.9	119.4	121.18	121.61
Cr53			6110	6182	6318	6365
Mn55			1031.45	1054.5	1053.84	1074.37
Co59			60.32	61.67	63.07	62.51
Ni60			807.11	820.36	815.95	834.37
Cu65			4.56	5.11	6.28	6.13
Zn66			48.33	48.41	46.9	48.89
Ga71			2.143	2.194	2.2	2.24
Ge72			1.26	1.28	1.22	1.22
Rb85			0.008	<0.0078	<0.0077	<0.0078
Sr88			0.0128	0.0192	0.0114	0.0045
Y89			0.229	0.249	0.242	0.246
Zr90			0.0126	0.0181	0.0176	0.0183
Nb93			0.0181	0.0198	0.0187	0.0198
Cs133			<0.00127	<0.00104	<0.00108	<0.00126
Ba137			0.0071	<0.01	<0.0048	<0.0052
La139			<0.00069	<0.00060	<0.00088	<0.00063
Ce140			<0.00056	<0.00062	0.00153	0.00071
Pr141			<0.00058	<0.00073	0.00045	<0.00068
Nd146			0.0041	<0.0028	<0.0047	<0.0036
Sm149			<0.0085	<0.0055	0.0023	<0.0041
Eu151			<0.00169	0.00087	<0.00129	<0.00
Gd157			<0.0051	0.0043	<0.0062	<0.0060
Tb159			0.00074	0.00151	0.00106	0.0014
Dy161			0.023	0.0169	0.0294	0.0207
Ho165			0.0078	0.0067	0.0088	0.0077
Er167			0.0414	0.0312	0.0445	0.0417
Tm169			0.0081	0.0079	0.0109	0.0116
Yb173			0.096	0.087	0.081	0.113
Lu175			0.0186	0.0181	0.0198	0.0196
Hf178			<0.0025	<0.0040	<0.0055	<0.0036
Ta181			<0.00175	<0.00	0.00052	<0.00144
Pb208			0.0047	0.0049	<0.0033	<0.0038
Th232			<0.0026	<0.0033	<0.0026	<0.00201

Table S2. (cont.)

µg/g

Element	D41-24_OPX2-05
Li7	0.366
Be9	<0.0104
Mg25	197084
Mg26	32.03
Ca43	16432
Sc45	29.76
Ti49	40.12
V51	123.43
Cr53	6282
Mn55	1071.94
Co59	62.04
Ni60	826.57
Cu65	5.46
Zn66	48.54
Ga71	2.21
Ge72	1.19
Rb85	<0.0061
Sr88	0.0025
Y89	0.248
Zr90	0.0154
Nb93	0.0156
Cs133	<0.00073
Ba137	0.004
La139	<0.00055
Ce140	<0.00023
Pr141	<0.00021
Nd146	<0.0037
Sm149	<0.0057
Eu151	0.00089
Gd157	<0.0042
Tb159	0.00125
Dy161	0.0203
Ho165	0.0085
Er167	0.044
Tm169	0.0076
Yb173	0.097
Lu175	0.0222
Hf178	<0.0032
Ta181	<0.00070
Pb208	<0.0025
Th232	<0.00212

Table S3. Reference Materials

Element	BHVO-2#01	BHVO-2#02	BHVO-2#03	BHVO-2#04	BHVO-2#05
Li7	4.36	4.47	4.40	4.31	4.45
Be9	1.32	1.39	1.22	1.25	1.32
Mg25	42707	43177	43359	42294	43899
Mg26	7.13	7.13	7.13	7.13	7.13
Ca43	81084	82809	80718	80481	82904
Sc45	33.2	33.2	33.1	32.1	33.5
Ti49	16246	16440	16284	16113	16455
V51	313	307	306	303	313
Cr53	291	298	291	290	294
Mn55	1307	1319	1328	1307	1330
Co59	44.6	43.7	43.8	43.7	44.0
Ni60	115	117	117	115	116
Cu65	129	126	126	127	125
Zn66	98.9	103	102	106	101
Ga71	22.0	22.0	22.2	21.8	22.0
Ge72	1.57	1.53	1.65	1.70	1.64
Rb85	8.98	9.38	9.17	9.33	9.12
Sr88	388	405	393	398	394
Y89	25.8	26.5	26.1	25.5	26.0
Zr90	167	175	170	167	170
Nb93	18.0	18.9	18.1	18.2	18.3
Cs133	0.1	0.1	0.1	0.1	0.1
Ba137	128.3	133.8	131.8	130.5	128.1
La139	15.1	15.7	15.0	15.0	15.1
Ce140	36.4	39.5	37.2	37.4	37.1
Pr141	5.3	5.5	5.2	5.3	5.3
Nd146	24.4	25.4	24.0	24.2	24.3
Sm149	6.0	6.3	6.0	6.0	6.2
Eu151	2.1	2.1	2.1	2.0	2.1
Gd157	6.2	6.3	6.1	6.0	6.2
Tb159	0.9	0.9	0.9	0.9	0.9
Dy161	5.2	5.5	5.2	5.1	5.2
Ho165	1.0	1.0	1.0	0.9	1.0
Er167	2.5	2.7	2.6	2.5	2.6
Tm169	0.3	0.4	0.3	0.3	0.3
Yb173	2.0	2.1	2.0	1.9	2.0
Lu175	0.3	0.3	0.3	0.3	0.3
Hf178	4.3	4.5	4.3	4.2	4.3
Ta181	1.2	1.2	1.1	1.1	1.1
Pb208	1.7	1.8	1.6	1.7	1.7
Th232	1.2	1.3	1.2	1.2	1.2

Table S3. (cont.)

Element	BHVO-2#06	BHVO-2#02	BHVO-2#03	BHVO-2#04	BHVO-2#05
Li7	4.42	4.45	4.42	4.28	4.38
Be9	1.34	1.23	1.44	1.32	1.17
Mg25	42783	43414	43369	41837	42813
Mg26	7.13	7.13	7.13	7.13	7.13
Ca43	81448	81034	82690	80901	81089
Sc45	33.2	33.2	32.7	32.7	33.6
Ti49	16318	16399	16324	16049	16393
V51	309	309	306	308	308
Cr53	295	294	293	293	289
Mn55	1311	1322	1330	1292	1308
Co59	44.2	44.2	43.8	43.8	44.1
Ni60	116	116	117	115	115
Cu65	128	129	129	121	128
Zn66	100	105	99.94	99.45	99.16
Ga71	22.1	22.1	22.2	21.7	21.8
Ge72	1.51	1.56	1.72	1.54	1.53
Rb85	9.18	9.35	9.19	8.94	9.19
Sr88	397	398	397	390	401
Y89	26.3	26.37	25.89	25.25	26.63
Zr90	172	170	171	166	176
Nb93	18.4	18.16	18.55	18.15	18.56
Cs133	0.1	0.1028	0.0984	0.096	0.1031
Ba137	132.6	131.31	131.71	128.55	133.81
La139	15.5	15.34	15.1	14.93	15.59
Ce140	38.1	37.63	37.5	37.58	37.87
Pr141	5.4	5.38	5.35	5.25	5.46
Nd146	25.0	24.72	24.14	24.38	25.01
Sm149	6.1	6.04	6.18	6.1	6.14
Eu151	2.1	2.059	2.055	2.09	2.14
Gd157	6.3	6.17	6.15	6.13	6.22
Tb159	0.9	0.929	0.912	0.903	0.953
Dy161	5.4	5.18	5.4	5.22	5.59
Ho165	1.0	0.975	0.989	0.967	1.013
Er167	2.6	2.543	2.555	2.601	2.56
Tm169	0.3	0.335	0.349	0.332	0.357
Yb173	2.1	2.05	1.99	1.93	2.12
Lu175	0.3	0.275	0.279	0.282	0.298
Hf178	4.5	4.35	4.25	4.31	4.46
Ta181	1.2	1.143	1.115	1.199	1.19
Pb208	1.8	1.741	1.651	1.683	1.72
Th232	1.3	1.22	1.201	1.239	1.241

Table S3. (cont.)

Element	BHVO-2#06	Mean	RSD (%)			BIR-1#01
Li7	4.49	4.4	1.5			3.0
Be9	1.34	1.3	6.1			0.1
Mg25	43793	43040.5	1.5			59105.0
Mg26	7.13	7.1	0.0			9.4
Ca43	81740	81536.2	1.1			96046.4
Sc45	32.9	33.0	1.3			42.5
Ti49	16398	16311	0.8			5800.8
V51	309	308	0.9			324.8
Cr53	296	293	0.9			401.3
Mn55	1335	1317	1.0			1368.9
Co59	44.1	44.0	0.6			52.9
Ni60	117	116.0	0.7			171.0
Cu65	130	127.1	1.9			121.9
Zn66	106	102.0	2.7			70.8
Ga71	22.3	22.0	0.9			15.8
Ge72	1.66	1.60	4.7			1.5
Rb85	9.38	9.20	1.6			0.2
Sr88	397	396	1.2			110.7
Y89	26.14	26.0	1.6			14.3
Zr90	169	170	1.8			13.5
Nb93	18.17	18.3	1.5			0.6
Cs133	0.1012	0.1	2.7			0.0
Ba137	130.67	131.0	1.5			10.3
La139	15.17	15.2	1.8			0.6
Ce140	37.48	37.6	2.0			1.9
Pr141	5.35	5.4	1.7			0.4
Nd146	24.37	24.5	1.8			2.4
Sm149	6.05	6.1	1.5			1.0
Eu151	2.02	2.1	1.7			0.5
Gd157	6.15	6.2	1.3			1.6
Tb159	0.914	0.9	2.0			0.3
Dy161	5.11	5.3	3.1			2.3
Ho165	0.966	1.0	2.3			0.5
Er167	2.54	2.6	2.5			1.6
Tm169	0.333	0.3	2.5			0.2
Yb173	2	2.0	3.3			1.6
Lu175	0.267	0.3	3.4			0.2
Hf178	4.26	4.3	2.5			0.6
Ta181	1.11	1.2	3.3			0.0
Pb208	1.71	1.7	3.0			3.0
Th232	1.201	1.2	2.6			0.0

Table S3. (cont.)

Element	BIR-1#02	BIR-1#03	BIR-1#04	BIR-1#05	BIR-1#06
Li7	2.9	2.9	2.9	3.1	3.0
Be9	0.1	0.1	0.1	0.1	0.1
Mg25	56727.4	57999.9	57966.2	58234.6	58159.4
Mg26	9.4	9.4	9.4	9.4	9.4
Ca43	92981.7	94522.6	94592.4	96686.4	95747.5
Sc45	41.7	42.8	43.7	44.3	43.7
Ti49	5632.7	5787.5	5801.0	5924.7	5810.6
V51	309.8	319.0	309.9	317.0	315.3
Cr53	388.7	402.5	402.0	404.2	394.8
Mn55	1344.3	1372.1	1326.7	1339.7	1309.0
Co59	51.5	52.3	51.6	52.6	52.7
Ni60	166.5	170.2	166.8	168.5	166.0
Cu65	118.7	121.3	120.9	124.5	120.9
Zn66	70.5	73.6	69.0	74.7	68.7
Ga71	15.3	16.3	16.0	16.0	15.6
Ge72	1.4	1.6	1.4	1.3	1.3
Rb85	0.2	0.2	0.2	0.3	0.2
Sr88	106.8	108.2	110.2	112.4	110.1
Y89	13.6	14.3	14.7	15.4	15.0
Zr90	12.9	13.4	13.7	14.4	13.7
Nb93	0.5	0.5	0.5	0.5	0.5
Cs133	0.0	0.0	0.0	0.0	0.0
Ba137	7.9	6.6	6.5	7.2	6.5
La139	0.6	0.5	0.6	0.6	0.6
Ce140	1.8	1.8	1.8	2.0	1.9
Pr141	0.4	0.4	0.4	0.4	0.4
Nd146	2.3	2.2	2.3	2.4	2.3
Sm149	1.0	1.0	1.0	1.2	1.1
Eu151	0.5	0.5	0.5	0.5	0.6
Gd157	1.6	1.6	1.8	1.8	1.8
Tb159	0.3	0.3	0.3	0.4	0.3
Dy161	2.2	2.3	2.5	2.5	2.6
Ho165	0.5	0.5	0.5	0.6	0.5
Er167	1.5	1.5	1.6	1.7	1.7
Tm169	0.2	0.2	0.2	0.3	0.2
Yb173	1.5	1.6	1.7	1.7	1.6
Lu175	0.2	0.2	0.2	0.2	0.2
Hf178	0.5	0.5	0.5	0.5	0.5
Ta181	0.0	0.0	0.0	0.0	0.0
Pb208	2.8	3.2	3.1	3.4	3.2
Th232	0.0	0.0	0.0	0.0	0.0

Table S3. (cont.)

Element	BIR-1#02	BIR-1#03	BIR-1#04	BIR-1#05	BIR-1#06	Mean
Li7	2.95	3.05	3.07	3.11	2.89	3.0
Be9	0.156	0.116	0.057	0.117	0.138	0.1
Mg25	54689.38	58469.63	56609.72	57510.8	57125.45	57509
Mg26	9.4	9.4	9.4	9.4	9.4	9.4
Ca43	93185.53	96984.88	93531.55	95941.91	90088.02	94574
Sc45	42.5	42.56	41.88	42.35	40.6	42.6
Ti49	5782.94	5813.49	5667.7	5708.86	5512.86	5749
V51	318.35	322.73	314.82	319.32	312.48	317
Cr53	404.02	409.22	399.22	397.58	384.15	399
Mn55	1358.89	1387.89	1364.75	1355.05	1332.3	1351
Co59	52.6	52.99	52.23	52.01	51.32	52.2
Ni60	169.22	174.07	167.49	168.93	164.37	168.5
Cu65	121.67	126.48	124.6	125.53	123	122.7
Zn66	72.75	75.34	74.79	76.76	69.59	72.4
Ga71	15.92	16.02	15.39	15.82	15.51	15.8
Ge72	1.33	1.6	1.43	1.4	1.38	1.42
Rb85	0.21	0.251	0.28	0.269	0.193	0.23
Sr88	108.13	111.76	109.16	110.75	103.93	109
Y89	14.37	14.28	14.17	14.28	13.5	14.4
Zr90	13.34	14	14.14	13.87	12.65	13.6
Nb93	0.526	0.545	0.528	0.531	0.505	0.53
Cs133	0.0063	0.0071	0.00538	0.0058	0.00545	0.01
Ba137	6.73	7.02	7.06	7.24	5.96	7.18
La139	0.638	0.591	0.619	0.609	0.547	0.60
Ce140	1.974	2.04	1.981	1.981	1.75	1.91
Pr141	0.363	0.4	0.39	0.363	0.346	0.37
Nd146	2.44	2.4	2.261	2.37	2.18	2.32
Sm149	1.059	1.172	1.047	1.093	1.021	1.07
Eu151	0.511	0.567	0.535	0.543	0.487	0.53
Gd157	1.774	1.823	1.71	1.701	1.618	1.71
Tb159	0.345	0.354	0.339	0.333	0.314	0.34
Dy161	2.4	2.55	2.46	2.42	2.18	2.40
Ho165	0.519	0.562	0.518	0.533	0.478	0.53
Er167	1.629	1.671	1.628	1.553	1.449	1.59
Tm169	0.26	0.252	0.237	0.248	0.225	0.24
Yb173	1.72	1.64	1.65	1.67	1.42	1.61
Lu175	0.242	0.252	0.235	0.233	0.215	0.23
Hf178	0.489	0.519	0.563	0.54	0.515	0.52
Ta181	0.0335	0.0422	0.0377	0.0392	0.0333	0.04
Pb208	3.16	3.36	3.33	3.34	2.85	3.15
Th232	0.0358	0.0301	0.0368	0.0311	0.0242	0.03

Table S3. (cont.)

Element	RSD (%)	ref*	Mean/ref
Li7	2.9	3.2	0.93
Be9	27.0	0.12	0.88
Mg25	2.1		
Mg26	0.0		
Ca43	2.2		
Sc45	2.4		
Ti49	1.9	5600	1.03
V51	1.5	319	0.99
Cr53	1.8	391	1.02
Mn55	1.7	1363.12	0.99
Co59	1.1	52	1.00
Ni60	1.6	166	1.01
Cu65	1.9	119	1.03
Zn66	3.9	72	1.01
Ga71	2.0	15.3	1.03
Ge72	8.3	1.4	1.01
Rb85	14.7	0.2	1.13
Sr88	2.2	109	1.00
Y89	3.8	15.6	0.92
Zr90	3.8	14	0.97
Nb93	3.2	0.55	0.97
Cs133	24.5	0.007	0.82
Ba137	15.9	7.14	1.01
La139	5.4	0.615	0.98
Ce140	5.0	1.92	0.99
Pr141	5.0	0.37	1.00
Nd146	3.6	2.38	0.97
Sm149	5.2	1.12	0.96
Eu151	4.1	0.53	1.00
Gd157	5.4	1.87	0.92
Tb159	5.4	0.36	0.94
Dy161	5.4	2.51	0.95
Ho165	5.0	0.56	0.94
Er167	5.3	1.66	0.96
Tm169	5.2	0.25	0.96
Yb173	5.9	1.65	0.98
Lu175	4.8	0.25	0.94
Hf178	5.5	0.582	0.89
Ta181	9.1	0.0357	1.02
Pb208	6.3	3.1	1.02
Th232	16.1	0.032	0.94

Table S4. Previously unpublished major and trace element data for 14-17°N MAR peridotites (HJBD) and literature data.

Sample	Lat	Long	Depth	FSR mm/yr	Ridge	Location	Lithology	Type
ABP12	14.911	44.438	3333		MAR	15°20'FZ	Harzburgite	
ABP12	14.911	44.438	3333		MAR	15°20'FZ	Peridotite	
ABP12	14.911	44.438	3333		MAR	15°20'FZ	Peridotite	
ABP12	14.911	44.438	3333		MAR	15°20'FZ	Peridotite	
ABP16	15.617	46.683	3390		MAR	15°20'FZ	Harzburgite	
ABP16	15.617	46.683	3390		MAR	15°20'FZ	Harzburgite	
ABP16	15.617	46.683	3390		MAR	15°20'FZ	Harzburgite	
ABP16	15.617	46.683	3390		MAR	15°20'FZ	Harzburgite	
ABP16	15.617	46.683	3390		MAR	15°20'FZ	Harzburgite	
ABP16	15.617	46.683	3390		MAR	15°20'FZ	Harzburgite	
ABP16	15.617	46.683	3390		MAR	15°20'FZ	Harzburgite	
ABP16	15.617	46.683	3390		MAR	15°20'FZ	Harzburgite	
ABP16	15.617	46.683	3390		MAR	15°20'FZ	Harzburgite	
ABP16	15.617	46.683	3390		MAR	15°20'FZ	Harzburgite	
ABP16	15.617	46.683	3390		MAR	15°20'FZ	Harzburgite	
ABP16	15.617	46.683	3390		MAR	15°20'FZ	Harzburgite	
ABP16	15.617	46.683	3390		MAR	15°20'FZ	Harzburgite	
ABP16	15.617	46.683	3390		MAR	15°20'FZ	Harzburgite	
ABP16	15.617	46.683	3390		MAR	15°20'FZ	Harzburgite	
ABP16	15.617	46.683	3390		MAR	15°20'FZ	Harzburgite	
ABP16	15.617	46.683	3390		MAR	15°20'FZ	Harzburgite	
ABP16	15.617	46.683	3390		MAR	15°20'FZ	Harzburgite	
ABP16	15.617	46.683	3390		MAR	15°20'FZ	Harzburgite	
ABP16	15.617	46.683	3390		MAR	15°20'FZ	Harzburgite	
ABP16	15.617	46.683	3390		MAR	15°20'FZ	Harzburgite	
ABP16	15.617	46.683	3390		MAR	15°20'FZ	Harzburgite	
ABP16	15.617	46.683	3390		MAR	15°20'FZ	Harzburgite	
ABP16	15.617	46.683	3390		MAR	15°20'FZ	Harzburgite	
ABP16	15.617	46.683	3390		MAR	15°20'FZ	Harzburgite	
ABP16	15.617	46.683	3390		MAR	15°20'FZ	Harzburgite	
ABP16	14.808	45.089	3400		MAR	15°20'FZ	Harzburgite	
ABP16	15.083	44.933	3068		MAR	15°20'FZ	Harzburgite	
ABP16	15.083	44.933	3068		MAR	15°20'FZ	Harzburgite	
ABP16	15.083	44.933	3068		MAR	15°20'FZ	Harzburgite	
ABP16	15.083	44.933	3068		MAR	15°20'FZ	Harzburgite	
ABP16	15.083	44.933	3068		MAR	15°20'FZ	Harzburgite	
ABP16	15.083	44.933	3068		MAR	15°20'FZ	Harzburgite	
ABP16	15.083	44.933	3068		MAR	15°20'FZ	Harzburgite	
ABP16	15.082	45.058	2707		MAR	15°20'FZ	Spinel Harzburgite	
ABP16	15.082	45.058	2707		MAR	15°20'FZ	Harzburgite	
ABP16	15.133	45.083	2965		MAR	15°20'FZ	Spinel Harzburgite	
ABP16	15.133	45.083	2965		MAR	15°20'FZ	Spinel Harzburgite	
ABP16	15.063	45.110	2660		MAR	15°20'FZ	Harzburgite	
ABP16	15.099	44.972	2734		MAR	15°20'FZ	Spinel Harzburgite	
ABP16	15.099	44.972	2734		MAR	15°20'FZ	Spinel Harzburgite	
ABP16	15.099	44.972	2734		MAR	15°20'FZ	Spinel Harzburgite	
ABP16	15.099	44.972	2734		MAR	15°20'FZ	Harzburgite	
ABP16	15.099	44.972	2734		MAR	15°20'FZ	Spinel Harzburgite	
ABP16	15.099	44.972	2734		MAR	15°20'FZ	Spinel Harzburgite	
ABP16	15.099	44.972	2734		MAR	15°20'FZ	Spinel Harzburgite	
ABP16	15.099	44.972	2734		MAR	15°20'FZ	Harzburgite	
ABP16	15.099	44.972	2734		MAR	15°20'FZ	Spinel Harzburgite	
ABP16	15.099	44.972	2734		MAR	15°20'FZ	Spinel Harzburgite	
ABP16	15.099	44.972	2734		MAR	15°20'FZ	Spinel Harzburgite	

Table S4. (cont.)

	Mode					Olivine (wt%)						
Sample	OL	OPX	CPX	SP	Plag	SiO2	FeO	MnO	MgO	CaO	NiO	Fo
ABP12												
ABP12												
ABP12												
ABP12												
ABP16												
ABP16												
ABP16						41.7	8.49	0.10	49.87	0.11	0.36	91.3
ABP16												
ABP16												
ABP16												
ABP16						41.4	8.64	0.11	49.88	0.11	0.38	91.1
ABP16						41.6	8.50	0.12	49.57	0.08	0.36	91.2
ABP16												
ABP16												
ABP16						41.8	8.25	0.13	49.51	0.08	0.33	91.4
ABP16												
ABP16												
ABP16												
ABP16												
ABP16												
ABP16												
ABP16												
ABP16												
ABP16												
ABP16												
ABP16												
ABP16												
ABP16						41.8	8.47	0.13	50.31	0.06	0.34	91.4
ABP16						41.6	8.88	0.12	50.23	0.08	0.19	91.0
ABP16						40.9	8.87	0.10	50.83	0.10	0.34	91.1
ABP16												
ABP16												
ABP16												
ABP16												
ABP16												
ABP16						41.5	8.56	0.11	49.07	0.11	0.35	91.1
ABP16	86.5	12.7	0.0	0.7	0.0							
ABP16												
ABP16	86.3	12.1	0.0	1.5	0.0							
ABP16	85.2	14.0	0.0	0.8	0.0							
ABP16												
ABP16	87.5	12.2	0.0	0.3	0.0	40.8	8.32	0.15	50.74	0.07	0.30	91.6
ABP16												
ABP16	88.5	10.6	0.0	0.8	0.0							
ABP16						41.9	8.00	0.12	49.48	0.08	0.35	91.7
ABP16	75.1	24.4	0.0	0.5	0.0							
ABP16	87.3	12.0	0.0	0.7	0.0							
ABP16	79.9	19.7	0.0	0.5	0.0							
ABP16						41.9	7.83	0.13	49.60	0.09	0.39	91.9
ABP16	90.9	8.9	0.0	0.2	0.0							
ABP16												
ABP16												

Table S4. (cont.)

	Orthopyroxene (wt%)									Clinopyroxene (wt%)	
Sample	SiO2	TiO2	Al2O3	Cr2O3	FeO	MnO	MgO	CaO	Na2O	SiO2	TiO2
ABP12	55.2	0.06	3.56	0.82	5.63	0.13	32.9	1.94	0.02		
ABP12											
ABP12	54.5	0.02	2.99	0.86	5.75	0.12	32.9	1.52	0.05	51.5	0.08
ABP12											
ABP16											
ABP16											
ABP16	55.7	0.06	3.26	0.99	5.58	0.12	32.1	1.40	0.04	52.6	0.15
ABP16											
ABP16											
ABP16											
ABP16											
ABP16											
ABP16	56.5	0.07	3.35	1.00	5.72	0.11	32.3	1.66	0.04		
ABP16											
ABP16											
ABP16											
ABP16											
ABP16											
ABP16											
ABP16											
ABP16											
ABP16											
ABP16											
ABP16											
ABP16											
ABP16											
ABP16	56.1	0.05	3.35	0.98	5.62	0.11	31.8	1.81	0.08		
ABP16											
ABP16	56.0	0.02	2.81	0.91	5.61	0.13	31.9	2.90	0.02		
ABP16	56.7	0.03	2.06	0.74	5.45	0.10	33.2	1.72	0.02		
ABP16											
ABP16											
ABP16											
ABP16											
ABP16											
ABP16											
ABP16	56.9	0.04	1.57	0.63	5.63	0.16	33.3	0.98	0.11	54.2	0.07
ABP16											
ABP16											
ABP16											
ABP16											
ABP16											
ABP16											
ABP16											
ABP16											
ABP16	56.4	0.06	2.19	0.72	5.48	0.14	31.4	1.42	0.07	53.8	0.08
ABP16											
ABP16											
ABP16	56.6	0.05	2.75	0.78	5.36	0.14	32.1	1.31	0.04		
ABP16										53.3	0.10
ABP16											
ABP16											
ABP16											

Table S4. (cont.)

Sample	Al2O3	Cr2O3	FeO	MnO	MgO	CaO	Na2O
ABP12							
ABP12							
ABP12	3.17	1.06	2.14	0.08	17.3	23.54	0.13
ABP12							
ABP16							
ABP16							
ABP16	3.61	1.48	2.25	0.09	16.7	22.10	0.61
ABP16							
ABP16							
ABP16						

Table S4. (cont.)

	Clinopyroxene REE, μg/g							
Sample	La	Ce	Nd	Sm	Eu	Dy	Er	Yb
ABP12								
ABP12								
ABP12								
ABP12								
ABP16								
ABP16								
ABP16								
ABP16								
ABP16								
ABP16								
ABP16								
ABP16								
ABP16								
ABP16								
ABP16								
ABP16								
ABP16								
ABP16								
ABP16								
ABP16								
ABP16								
ABP16								
ABP16								
ABP16								
ABP16								
ABP16								
ABP16								
ABP16	0.222	0.583	0.452	0.562	0.146	0.516	0.310	0.470
ABP16								
ABP16	0.225	0.140	0.207	0.211	0.074	0.217	0.198	0.226
ABP16	0.104	0.074	0.196	0.174	0.037	0.133	0.113	0.155
ABP16	0.022	0.152	0.226	0.280	0.066	0.416	0.212	0.219
ABP16	0.500	1.013	0.583	0.442	0.065	0.585	0.247	0.471
ABP16	0.315	0.314	0.166	0.138	0.063	0.141	0.148	0.205
ABP16								
ABP16								
ABP16								
ABP16								
ABP16								
ABP16								
ABP16	0.060	0.254	0.485	0.206	0.158	0.519	0.323	0.338
ABP16	0.038	0.082	0.104	0.053	0.025	0.255	0.209	0.233
ABP16								
ABP16								
ABP16								
ABP16	0.363	0.371	0.430	0.306	0.111	0.350	0.235	0.305
ABP16								
ABP16								
ABP16								
ABP16	0.023	0.049	0.055	0.028	0.032	0.307	0.248	0.230
ABP16	0.046	0.228	0.261	0.206	0.058	0.400	0.231	0.248

Table S4. (cont.)

	Spinel (wt%)								
Sample	SiO2	TiO2	Al2O3	Cr2O3	Fe2O3	FeO	MnO	MgO	NiO
ABP12	0.08	0.10	33.3	35.5	1.52	13.1	0.21	15.53	0.15
ABP12	0.06	0.01	31.3	36.8	1.29	14.3	0.15	14.34	0.12
ABP12	0.05	0.05	29.9	39.5	0.88	14.2	0.21	14.39	0.12
ABP12	0.05	0.03	32.6	36.3	0.86	14.3	0.19	14.59	0.13
ABP16		0.11	29.6	37.5	2.66	13.3		14.95	
ABP16	0.09	0.11	29.1	38.4	3.17	12.9	0.19	15.37	
ABP16		0.22	27.5	39.6	2.58	14.2		14.24	
ABP16		0.12	29.2	38.4	2.48	13.1		15.08	
ABP16		0.08	30.2	34.8	4.63	14.1		14.47	
ABP16		0.05	31.3	37.0	2.55	12.3		16.00	
ABP16		0.09	30.9	36.0	2.55	16.0		13.54	
ABP16		0.06	32.9	35.4	1.97	11.0		16.81	
ABP16		0.12	29.4	38.0	2.46	13.7		14.75	
ABP16		0.09	29.2	38.8	2.21	14.4		14.43	
ABP16		0.03	27.0	42.4	1.94	11.9		15.75	
ABP16		0.09	30.0	38.6	1.65	12.7		15.49	
ABP16		0.10	30.2	37.2	2.64	13.4		15.08	
ABP16		0.11	29.1	38.0	3.11	12.9		15.23	
ABP16		0.07	26.3	40.4	3.38	15.7		13.22	
ABP16		0.10	29.6	38.6	2.36	12.9		15.38	
ABP16		0.19	26.2	41.1	2.71	15.3		13.54	
ABP16		0.15	27.1	37.6	4.47	17.3		12.24	
ABP16		0.06	32.9	33.4	3.12	12.4		15.75	
ABP16	0.06	0.03	37.9	29.6	2.80	13.4	0.17	15.87	0.19
ABP16	0.04	0.07	33.5	35.0	2.70	13.4	0.17	15.62	0.16
ABP16		0.11	28.7	39.2	1.79	13.2		14.89	
ABP16	0.07	0.07	32.4	35.6	1.95	12.0	0.15	15.98	0.17
ABP16		0.06	27.0	42.0	1.72	13.1		14.96	
ABP16									
ABP16									
ABP16									
ABP16									
ABP16									
ABP16									
ABP16									
ABP16	0.11	0.12	19.2	51.5	-0.15	14.8	0.21	13.07	
ABP16									
ABP16	0.05	0.08	19.4	48.6	2.57	17.8	0.28	11.12	0.05
ABP16									
ABP16									
ABP16	0.07	0.13	20.4	48.9	0.95	14.7	0.19	13.16	0.03
ABP16	0.00	0.12	21.8	49.2	1.06	12.4	0.22	15.06	0.06
ABP16									
ABP16									
ABP16	0.12	0.10	22.4	48.5	-0.39	14.1	0.22	13.79	
ABP16									
ABP16									
ABP16									
ABP16									
ABP16									
ABP16									
ABP16									

Table S4. (cont.)

Sample	Mg#	Cr#	Mode Ref	Ol Ref	Opx Ref	Cpx Ref	Spin Ref	Station	Sample #	Notes
ABP12	67.8	41.7	HJBD	HJBD	HJBD	HJBD	HJBD	17	9	
ABP12	64.2	44.1	HJBD	HJBD	HJBD	HJBD	HJBD	17	25	
ABP12	64.3	47.0	HJBD	HJBD	HJBD	HJBD	HJBD	17	29	
ABP12	64.6	42.8	HJBD	HJBD	HJBD	HJBD	HJBD	17	31	
ABP16	66.6	45.9	HJBD	HJBD	HJBD	HJBD	HJBD	56	9	
ABP16	68.0	47.0	HJBD	HJBD	HJBD	HJBD	HJBD	56	10	
ABP16	64.1	49.1	HJBD	HJBD	HJBD	HJBD	HJBD	56	11	
ABP16	67.2	46.9	HJBD	HJBD	HJBD	HJBD	HJBD	56	20	
ABP16	64.6	43.6	HJBD	HJBD	HJBD	HJBD	HJBD	56	20	
ABP16	69.9	44.2	HJBD	HJBD	HJBD	HJBD	HJBD	56	39	
ABP16	60.1	43.8	HJBD	HJBD	HJBD	HJBD	HJBD	56	52	
ABP16	73.2	41.9	HJBD	HJBD	HJBD	HJBD	HJBD	56	58	
ABP16	65.8	46.4	HJBD	HJBD	HJBD	HJBD	HJBD	56	59	
ABP16	64.2	47.1	HJBD	HJBD	HJBD	HJBD	HJBD	56	61	
ABP16	70.2	51.3	HJBD	HJBD	HJBD	HJBD	HJBD	56	62	
ABP16	68.5	46.3	HJBD	HJBD	HJBD	HJBD	HJBD	56	64	
ABP16	66.7	45.2	HJBD	HJBD	HJBD	HJBD	HJBD	56	66	
ABP16	67.7	46.7	HJBD	HJBD	HJBD	HJBD	HJBD	56	67	
ABP16	60.0	50.8	HJBD	HJBD	HJBD	HJBD	HJBD	56	67	
ABP16	68.0	46.7	HJBD	HJBD	HJBD	HJBD	HJBD	56	73	
ABP16	61.2	51.3	HJBD	HJBD	HJBD	HJBD	HJBD	56	74	
ABP16	55.8	48.2	HJBD	HJBD	HJBD	HJBD	HJBD	56	74	
ABP16	69.4	40.5	HJBD	HJBD	HJBD	HJBD	HJBD	56	76	
ABP16	67.8	34.3	HJBD	HJBD	HJBD	HJBD	HJBD	56	76	
ABP16	67.5	41.2	HJBD	HJBD	HJBD	HJBD	HJBD	56	77	
ABP16	66.7	47.8	HJBD	HJBD	HJBD	HJBD	HJBD	56	79	
ABP16	70.3	42.4	HJBD	HJBD	HJBD	HJBD	HJBD	56	80	
ABP16	67.1	51.1	HJBD	HJBD	HJBD	HJBD	HJBD	56	99	
ABP16			HJBD	HJBD	HJBD	HJBD	HJBD	68	19	
ABP16			HJBD	HJBD	HJBD	HJBD	HJBD	71	173	
ABP16			HJBD	HJBD	HJBD	HJBD	HJBD	71	145a	
ABP16			HJBD	HJBD	HJBD	HJBD	HJBD	71	145b	
ABP16			HJBD	HJBD	HJBD	HJBD	HJBD	71	35	
ABP16			HJBD	HJBD	HJBD	HJBD	HJBD	71	176	
ABP16			HJBD	HJBD	HJBD	HJBD	HJBD	71	187	
ABP16	61.1	64.3	HJBD	HJBD	HJBD	HJBD	HJBD	71	175	
ABP16			HJBD	HJBD	HJBD	HJBD	HJBD	73	3	
ABP16	52.6	62.7	HJBD	HJBD	HJBD	HJBD	HJBD	73	42	
ABP16			HJBD	HJBD	HJBD	HJBD	HJBD	75	74	
ABP16			HJBD	HJBD	HJBD	HJBD	HJBD	75	76	
ABP16	61.5	61.6	HJBD	HJBD	HJBD	HJBD	HJBD	76	1	
ABP16	68.4	60.2	HJBD	HJBD	HJBD	HJBD	HJBD	77	1	
ABP16			HJBD	HJBD	HJBD	HJBD	HJBD	77	3	
ABP16			HJBD	HJBD	HJBD	HJBD	HJBD	77	6	
ABP16	63.5	59.3	HJBD	HJBD	HJBD	HJBD	HJBD	77	7	
ABP16			HJBD	HJBD	HJBD	HJBD	HJBD	77	10	
ABP16			HJBD	HJBD	HJBD	HJBD	HJBD	77	19	
ABP16			HJBD	HJBD	HJBD	HJBD	HJBD	77	23	
ABP16			HJBD	HJBD	HJBD	HJBD	HJBD	77	29	
ABP16			HJBD	HJBD	HJBD	HJBD	HJBD	77	31	
ABP16			HJBD	HJBD	HJBD	HJBD	HJBD	77	36	
ABP16			HJBD	HJBD	HJBD	HJBD	HJBD	77	38	

Table S4. (cont.)

Sample	Lat	Long	Depth	FSR mm/yr	Ridge	Location	Lithology	Type
ABP16	15.099	44.972	2734		MAR	15°20'FZ	Spinel Harzburgite	
ABP16	15.099	44.972	2734		MAR	15°20'FZ	Harzburgite	
ABP16	15.099	44.972	2734		MAR	15°20'FZ	Harzburgite	
ABP16	15.099	44.972	2734		MAR	15°20'FZ	Spinel Harzburgite	
ABP16	15.099	44.972	2734		MAR	15°20'FZ	Spinel Harzburgite	
ABP16	15.099	44.972	2734		MAR	15°20'FZ	Harzburgite	
ABP16	15.099	44.972	2734		MAR	15°20'FZ	Spinel Harzburgite	
ABP16	15.099	44.972	2734		MAR	15°20'FZ	Spinel Harzburgite	
ANT9	15.2388	44.7108	4200		MAR	15°20'FZ	Peridotite	
ANT9	15.333				MAR	15°20'FZ	Peridotite	
ANT9	15.1415	44.9093	4600		MAR	15°20'FZ	Harzburgite	
ANT9	15.1415	44.9093	4600		MAR	15°20'FZ	Harzburgite	
ANT9	15.1415	44.9093	4600		MAR	15°20'FZ	Harzburgite	
ANT9	15.0583	44.975	3400		MAR	15°20'FZ	Peridotite	
ANT9	15.333				MAR	15°20'FZ	Peridotite	
ANT9	15.333				MAR	15°20'FZ	Harzburgite	
ANT9	15.333				MAR	15°20'FZ	Peridotite	
ANT9	14.7045	44.8975	2200		MAR	15°20'FZ	Peridotite	
ANT9	15.7343	44.7127	3800		MAR	15°20'FZ	Peridotite	
ANT9	15.1003	44.9645	3200		MAR	15°20'FZ	Harzburgite	
ANT9	15.333				MAR	15°20'FZ	Peridotite	
ANT9	15.8587	46.8465	2650		MAR	15°20'FZ	Peridotite	
ANT9	15.333				MAR	15°20'FZ	Peridotite	
ANT9	15.333				MAR	15°20'FZ	Peridotite	
MM81	15.333				MAR	Rift V Wall	Harzburgite A	
MM81	15.333				MAR	Rift V Wall	Harzburgite B	
STR3	15.333				MAR	15°20'FZ	Harzburgite	
STR3	15.333				MAR	15°20'FZ	Harzburgite	
STR3	15.333				MAR	15°20'FZ	Harzburgite	
STR3	15.333				MAR	15°20'FZ	Harzburgite	
STR3	15.333				MAR	15°20'FZ	Harzburgite	
STR3	15.333				MAR	15°20'FZ	Harzburgite	
SeDr8-7-9	14.751667	44.9683	2752		MAR	S. of 15°20'FZ	Harzburgite	
41K3863-11	14.7533	44.979	3020		MAR	S. of 15°20'FZ	Harzburgite	
41K3869-4-1	14.7533	44.979	3020		MAR	S. of 15°20'FZ	Harzburgite	
SeDr5-1-1	12.975	44.8633	3975		MAR	S. of 15°20'FZ	Harzburgite	
SeDr5-2-12	12.975	44.8633	3975		MAR	S. of 15°20'FZ	Harzburgite	
22L1040	12.973667	44.86033	4150		MAR	S. of 15°20'FZ	Harzburgite	
22L1086-1	12.972	44.8633	4110		MAR	S. of 15°20'FZ	Harzburgite	
26L1419-19	12.97867	44.8985	3491		MAR	S. of 15°20'FZ	Harzburgite	
26L1454-13	12.9938	44.907833	3290.5		MAR	S. of 15°20'FZ	Harzburgite	
26L1454-14	12.9938	44.907833	3290.5		MAR	S. of 15°20'FZ	Harzburgite	
34L64 1	19.7136	45.848	3133		MAR	19°N	Harzburgite	
34L64 2	19.7136	45.848	3133		MAR	19°N	Harzburgite	
34L64 3	19.7136	45.848	3133		MAR	19°N	Harzburgite	
34L64 4	19.7136	45.848	3133		MAR	19°N	Lherzolite	
34L67 1	19.731933	45.85783	3108.5		MAR	19°N	Harzburgite	
34L67 3	19.731933	45.85783	3108.5		MAR	19°N	Harzburgite	
34L67 4	19.731933	45.85783	3108.5		MAR	19°N	Harzburgite	
34L68 4	19.7345	45.85038	3036.5		MAR	19°N	Harzburgite	
34L68 5	19.7345	45.85038	3036.5		MAR	19°N	Harzburgite	
34L125 1	19.921733	46.05788	2716		MAR	19°N	Harzburgite	
34L125 2	19.921733	46.05788	2716		MAR	19°N	Harzburgite	
34L125 3	19.921733	46.05788	2716		MAR	19°N	Harzburgite	
34L127 3	19.9576	46.0523	2368		MAR	19°N	Harzburgite	
34L127 4	19.9576	46.0523	2368		MAR	19°N	Harzburgite	
34L136 1	19.9261	46.03566	2650		MAR	19°N	Harzburgite	
34L137 1	19.98713	46.06631667	2547		MAR	19°N	Harzburgite	
D01-1	13.8198	44.9432	2932		MAR	13°N	Harzburgite	
D01-16	13.8198	44.9432	2932		MAR	13°N	Harzburgite	
D01-4	13.8198	44.9432	2932		MAR	13°N	Harzburgite	

Table S4. (cont.)

	Mode					Olivine (wt%)						
Sample	OL	OPX	CPX	SP	Plag	SiO2	FeO	MnO	MgO	CaO	NiO	Fo
ABP16	79.0	20.9	0.0	0.1	0.0							
ABP16						41.5	8.42	0.12	49.45	0.07	0.34	91.3
ABP16												
ABP16	85.6	13.8	0.0	0.6	0.0							
ABP16	89.2	9.6	0.1	1.0	0.0	40.4	8.55	0.15	51.40	0.10	0.28	91.5
ABP16												
ABP16	79.8	19.5	0.0	0.7	0.0							
ABP16	74.7	24.6	0.0	0.6	0.0							
ANT9												
ANT9												
ANT9						40.7	8.96	0.15	50.03	0.06	0.40	90.9
ANT9						40.7	8.96	0.15	50.03	0.06	0.40	90.9
ANT9						40.6	8.98	0.17	49.89	0.10	0.41	90.8
ANT9												
ANT9												
ANT9						40.6	9.03	0.13	49.89	0.09	0.38	90.8
ANT9						41.3	8.49	0.10	50.76	0.06	0.34	91.4
ANT9												
ANT9												
ANT9						41.1	8.42	0.15	49.91	0.04	0.37	91.4
ANT9						40.8	8.64	0.10	50.82	0.13	0.33	91.3
ANT9												
ANT9												
ANT9												
MM81												
MM81												
STR3												
STR3						40.4	8.67	0.10	50.61	0.03	0.38	91.2
STR3												
STR3												
STR3						42.0	8.62	0.10	48.28	0.06	0.36	90.9
STR3						40.6	8.48	0.10	50.44	0.11	0.40	91.4
SeDr8-7-9						40.6	10.49	0.15	49.08	0.06	0.39	89.2
41K3863-11												
41K3869-4-1												
SeDr5-1-1												
SeDr5-2-12						42.0	8.39	0.14	49.39	0.04	0.36	91.2
22L1040												
22L1086-1												
26L1419-19						41.41	8.97	0.18	50.09	0.07	0.38	90.7
26L1454-13						41.08	8.7	0.16	50.5	0.11	0.39	91
26L1454-14						40.07	8.58	0.14	49.73	0.08	0.32	91
34L64 1												
34L64 2												
34L64 3												
34L64 4												
34L67 1						39.94	10.08	0.2	49.19	0.08	0.42	89.7
34L67 3						39.27	9.84	0.17	49.99	0.04	0.46	90.1
34L67 4						39.67	9.68	0.13	49.62	0.03	0.46	90.1
34L68 4												
34L68 5												
34L125 1												
34L125 2												
34L125 3												
34L127 3												
34L127 4												
34L136 1												
34L137 1												
D01-1												
D01-16												
D01-4												

Table S4. (cont.)

	Orthopyroxene (wt%)									Clinopyroxene (wt%)	
Sample	SiO2	TiO2	Al2O3	Cr2O3	FeO	MnO	MgO	CaO	Na2O	SiO2	TiO2
ABP16											
ABP16	56.3	0.05	1.64	0.45	5.88	0.13	34.3	0.96	0.04	53.9	0.07
ABP16											
ABP16											
ABP16											
ABP16											
ABP16											
ABP16											
ANT9											
ANT9										55.6	0.05
ANT9	55.2	0.00	2.17	0.80	5.40	0.13	32.6	2.22	0.02	56.6	0.02
ANT9	55.2	0.00	2.17	0.80	5.40	0.13	32.6	2.22	0.02	56.6	0.02
ANT9										57.1	0.04
ANT9											
ANT9											
ANT9											
ANT9											
ANT9										56.3	0.04
ANT9											
ANT9										57.2	0.04
ANT9										56.6	0.05
ANT9											
ANT9											
ANT9										56.0	0.03
MM81	55.9	0.01	2.65	0.80	5.25	0.08	33.2	2.10	0.05		
MM81	55.9	0.03	2.53	0.78	5.52	0.13	33.0	1.91	0.05		
STR3	55.2	0.04	3.04	0.73	5.83	0.13	32.6	1.55	0.01		
STR3	55.4	0.01	2.71	0.75	5.60	0.13	33.1	1.66	0.00		
STR3	56.3	0.01	2.35	0.81	5.70	0.11	33.2	2.28	0.00		
STR3	56.3	0.01	2.35	0.81	5.70	0.11	33.2	2.28	0.00		
STR3	56.9	0.02	2.20	0.83	5.44	0.11	34.1	1.62	0.03		
STR3	55.9	0.02	2.73	1.04	5.26	0.12	33.3	1.94	0.02		
SeDr8-7-9											
41K3863-11											
41K3869-4-1											
SeDr5-1-1											
SeDr5-2-12											
22L1040											
22L1086-1											
26L1419-19											
26L1454-13											
26L1454-14											
34L64 1											
34L64 2											
34L64 3											
34L64 4											
34L67 1											
34L67 3											
34L67 4											
34L68 4											
34L68 5											
34L125 1											
34L125 2											
34L125 3											
34L127 3											
34L127 4											
34L136 1											
34L137 1											
D01-1											
D01-16											
D01-4											

Table S4. (cont.)

Sample	Al2O3	Cr2O3	FeO	MnO	MgO	CaO	Na2O
ABP16							
ABP16	1.85	0.89	2.10	0.08	17.7	22.81	0.46
ABP16							
ABP16							
ABP16							
ABP16							
ABP16							
ABP16							
ANT9							
ANT9	3.53	0.91	5.62	0.13	33.0	2.12	0.03
ANT9	2.38	0.88	5.52	0.13	33.3	2.32	0.02
ANT9	2.38	0.88	5.52	0.13	33.3	2.32	0.02
ANT9	1.93	0.89	5.39	0.14	34.4	1.26	0.04
ANT9							
ANT9							
ANT9							
ANT9							
ANT9	2.52	0.91	5.41	0.12	33.3	2.19	0.03
ANT9							
ANT9	1.58	0.74	5.40	0.14	34.0	1.98	0.12
ANT9	2.00	0.78	5.32	0.15	34.1	1.66	0.06
ANT9							
ANT9							
ANT9	2.16	0.83	5.34	0.12	34.4	1.20	0.04
MM81							
MM81							
STR3							
STR3							
STR3							
STR3							
STR3							
STR3							
SeDr8-7-9							
41K3863-11							
41K3869-4-1							
SeDr5-1-1							
SeDr5-2-12							
22L1040							
22L1086-1							
26L1419-19							
26L1454-13							
26L1454-14							
34L64 1							
34L64 2							
34L64 3							
34L64 4							
34L67 1							
34L67 3							
34L67 4							
34L68 4							
34L68 5							
34L125 1							
34L125 2							
34L125 3							
34L127 3							
34L127 4							
34L136 1							
34L137 1							
D01-1							
D01-16							
D01-4							

Table S4. (cont.)

	Clinopyroxene REE, µg/g							
Sample	La	Ce	Nd	Sm	Eu	Dy	Er	Yb
ABP16								
ABP16								
ABP16								
ABP16								
ABP16	0.017	0.019	0.062	0.056	0.050	0.093	0.117	0.090
ABP16								
ABP16								
ABP16								
ANT9								
ANT9								
ANT9	0.044	0.015	0.059	0.080	0.041	0.064	0.145	0.155
ANT9	0.048	0.061	0.191	0.128	0.028	0.091	0.160	0.223
ANT9	0.168	0.056	0.095	0.064	0.119	0.090	0.125	0.195
ANT9								
ANT9								
ANT9	0.062	0.105	0.098	0.098	0.012	0.110	0.151	0.209
ANT9								
ANT9								
ANT9								
ANT9	0.128	0.033	0.118	0.085	0.055	0.340	0.237	0.304
ANT9								
ANT9								
ANT9								
ANT9								
MM81								
MM81								
STR3								
STR3								
STR3	0.408	0.171	0.348	0.099	0.018	0.120	0.228	0.330
STR3	0.182	0.221	0.276	0.674	0.137	0.129	0.211	0.343
STR3	0.022	0.025	0.035	0.060		0.154	0.192	0.176
STR3	0.022	0.013	0.063	0.109	0.012	0.099	0.130	0.166
SeDr8-7-9								
41K3863-11								
41K3869-4-1								
SeDr5-1-1								
SeDr5-2-12								
22L1040								
22L1086-1								
26L1419-19								
26L1454-13								
26L1454-14								
34L64 1								
34L64 2								
34L64 3								
34L64 4								
34L67 1								
34L67 3								
34L67 4								
34L68 4								
34L68 5								
34L125 1								
34L125 2								
34L125 3								
34L127 3								
34L127 4								
34L136 1								
34L137 1								
D01-1								
D01-16								
D01-4								

Table S4. (cont.)

	Spinel (wt%)								
Sample	SiO2	TiO2	Al2O3	Cr2O3	Fe2O3	FeO	MnO	MgO	NiO
ABP16									
ABP16	0.12	0.08	21.9	48.5	-0.52	14.9	0.19	13.15	
ABP16		0.03	15.7	51.3	1.73	20.7		8.67	
ABP16									
ABP16	0.01	0.04	18.7	49.8	3.56	13.9	0.27	13.50	0.09
ABP16	0.03	0.07	23.4	48.0	-0.32	15.4	0.20	13.15	0.06
ABP16									
ABP16									
ANT9		0.04	35.4	33.4	3.17	10.0	0.13	17.91	0.13
ANT9									
ANT9	0.05	0.02	25.9	43.9	1.33	14.1	0.20	14.24	0.11
ANT9	0.05	0.02	25.9	43.9	1.33	14.1	0.20	14.24	0.11
ANT9	0.07	0.06	26.3	44.8	0.79	13.9	0.18	14.59	0.17
ANT9		0.18	27.6	41.3	3.25	11.6	0.19	16.21	0.11
ANT9		0.01	26.0	44.4	1.76	12.2	0.18	15.80	0.09
ANT9	0.12	0.11	24.8	44.6	1.96	15.1	0.17	13.75	0.16
ANT9		0.09	21.8	49.3	1.52	12.6	0.20	14.93	0.04
ANT9									
ANT9		0.06	29.4	39.8	3.30	11.3	0.19	16.56	0.13
ANT9	0.09	0.12	22.9	48.8	0.18	14.0	0.17	14.13	0.14
ANT9		0.15	19.4	51.7	1.54	13.1	0.24	14.40	0.05
ANT9		0.06	25.3	44.0	3.07	12.4	0.19	15.38	0.09
ANT9		0.02	28.4	40.0	3.59	12.7	0.18	15.48	0.10
ANT9									
MM81	0.01	0.07	27.5	41.4	2.77	13.6	0.25	14.80	0.12
MM81									
STR3	0.11	0.08	34.3	33.8	2.84	13.3	0.17	15.73	0.20
STR3	0.12	0.04	28.2	41.8	1.42	14.4	0.18	14.50	0.14
STR3	0.13	0.07	25.9	46.1	0.07	13.5	0.17	14.52	0.14
STR3	0.13	0.07	25.9	46.1	0.07	13.5	0.17	14.52	0.14
STR3	0.13	0.07	26.1	45.4	0.43	12.6	0.18	15.22	0.12
STR3									
SeDr8-7-9	0.06	0.21	26.7	42.6		18.3	0.29	12.18	0.12
41K3863-11	0.12	0.07	25.9	42.2		15.34	0.16	15.20	0.13
41K3869-4-1	0.08	0.03	25.5	42.2		16.7	0.18	14.79	0.12
SeDr5-1-1	0.15	0.05	35.1	31.2		14.5	0.22	15.61	0.00
SeDr5-2-12	0.08	0.02	38.9	28.3		14.59	0.21	16.44	0.00
22L1040	0.07	0.05	32.4	33.8		17.7	0.18	14.59	0.14
22L1086-1	0.08	0.26	22.3	40.4		24.8	0.21	11.14	0.14
26L1419-19	0.09	0.10	34.3	33.8		14.37	0.10	16.11	0.14
26L1454-13	0.08	0.03	33.6	34.2		16.07	0.22	14.88	0.00
26L1454-14	0.10	0.03	33.7	34.4		14.24	0.16	16.26	0.00
34L64 1	0.06	0.12	36.6	30.3		16.27	0.20	14.95	0.28
34L64 2									
34L64 3									
34L64 4	0.05	0.05	34.6	32.3		18.6	0.23	13.58	0.14
34L67 1	0.07	0.08	39.2	25.8		14.86	0.19	17.03	0.28
34L67 3	0.50	0.02	39.2	25.8		16.51	0.16	17.06	0.25
34L67 4	0.24	0.01	40.8	24.4		16.67	0.18	16.85	0.21
34L68 4	0.09	0.04	37.1	27.4		18.6	0.20	13.53	0.38
34L68 5	0.08	0.07	38.1	29.3		15.55	0.10	15.74	0.12
34L125 1									
34L125 2									
34L125 3	0.05	0.16	29.5	35.7		19.84	0.28	13.25	0.19
34L127 3									
34L127 4									
34L136 1									
34L137 1									
D01-1	0.01	0.05	29.13	41.20	1.67	12.88	0.21	15.43	0.12
D01-16	0.02	0.02	30.27	39.81	1.67	12.37	0.22	15.78	0.14
D01-4	0.02	0.10	29.06	40.08	2.08	13.51	0.24	14.77	0.11

Table S4. (cont.)

Sample	Mg#	Cr#	Mode Ref	Ol Ref	Opx Ref	Cpx Ref	Spin Ref	Station	Sample #	Notes
ABP16			HJBD	HJBD	HJBD	HJBD	HJBD	77	39	
ABP16	61.2	59.8	HJBD	HJBD	HJBD	HJBD	HJBD	77	40	
ABP16	42.8	68.7	HJBD	HJBD	HJBD	HJBD	HJBD	77	47	
ABP16			HJBD	HJBD	HJBD	HJBD	HJBD	77	79	
ABP16	63.4	64.1	HJBD	HJBD	HJBD	HJBD	HJBD	77	90	
ABP16	60.3	57.9	HJBD	HJBD	HJBD	HJBD	HJBD	77	146	
ABP16			HJBD	HJBD	HJBD	HJBD	HJBD	77	159	
ABP16			HJBD	HJBD	HJBD	HJBD	HJBD	77	163	
ANT9	76.2	38.8	HJBD	HJBD	HJBD	HJBD	HJBD	8	1	
ANT9			HJBD	HJBD	HJBD	HJBD	HJBD	6	9	Exact latitude unknown
ANT9	64.3	53.1	HJBD	HJBD	HJBD	HJBD	HJBD	10	10	Cpx Core, REE
ANT9	64.3	53.1	HJBD	HJBD	HJBD	HJBD	HJBD	10	10	Cpx Rim, REE
ANT9	65.1	53.3	HJBD	HJBD	HJBD	HJBD	HJBD	10	12	
ANT9	71.4	50.1	HJBD	HJBD	HJBD	HJBD	HJBD	11	113	
ANT9	69.9	53.4	HJBD	HJBD	HJBD	HJBD	HJBD	16	21	Exact latitude unknown
ANT9	61.9	54.7	HJBD	HJBD	HJBD	HJBD	HJBD	21	188	Cpx3b, Exact latitude unknown
ANT9	67.9	60.3	HJBD	HJBD	HJBD	HJBD	HJBD	40	44	Exact latitude unknown
ANT9			HJBD	HJBD	HJBD	HJBD	HJBD	47	4	
ANT9	72.3	47.6	HJBD	HJBD	HJBD	HJBD	HJBD	48	14	
ANT9	64.1	58.8	HJBD	HJBD	HJBD	HJBD	HJBD	49	17	
ANT9	66.3	64.2	HJBD	HJBD	HJBD	HJBD	HJBD	62	64	Exact latitude unknown
ANT9	68.8	53.8	HJBD	HJBD	HJBD	HJBD	HJBD	70	2	
ANT9	68.6	48.6	HJBD	HJBD	HJBD	HJBD	HJBD	71	27	Exact latitude unknown
ANT9			HJBD	HJBD	HJBD	HJBD	HJBD	79	83	Exact latitude unknown
MM81	66.0	50.3	HJBD	HJBD	HJBD	HJBD	HJBD	12	285	Exact latitude unknown
MM81			HJBD	HJBD	HJBD	HJBD	HJBD	12	285	Exact latitude unknown
STR3	67.7	39.8	HJBD	HJBD	HJBD	HJBD	HJBD	22	11	Exact latitude unknown
STR3	64.1	49.8	HJBD	HJBD	HJBD	HJBD	HJBD	22	13	Exact latitude unknown
STR3	65.5	54.4	HJBD	HJBD	HJBD	HJBD	HJBD	24	3	Cpx1, Exact latitude unknown
STR3	65.5	54.4	HJBD	HJBD	HJBD	HJBD	HJBD	24	3	Cpx3, Exact latitude unknown
STR3	68.1	53.9	HJBD	HJBD	HJBD	HJBD	HJBD	33	15	Exact latitude unknown
STR3			HJBD	HJBD	HJBD	HJBD	HJBD	63	27	Exact latitude unknown
SeDr8-7-9	55.2	51.7		Silantyev et al. 2011			Silantyev et al. 2011			
41K3863-11	68.3	52		Silantyev et al. 2011			Silantyev et al. 2011			
41K3869-4-1	66.6	52.6		Silantyev et al. 2011			Silantyev et al. 2011			
SeDr5-1-1	68.6	37.4		Silantyev et al. 2011			Silantyev et al. 2011			
SeDr5-2-12	70.4	33.4		Silantyev et al. 2011			Silantyev et al. 2011			
22L1040	64.4	41.2		Silantyev et al. 2011			Silantyev et al. 2011			
22L1086-1	51.8	54.9		Silantyev et al. 2011			Silantyev et al. 2011			
26L1419-19	69.7	39.8		Silantyev et al. 2011			Silantyev et al. 2011			
26L1454-13	65.0	40.6		Silantyev et al. 2011			Silantyev et al. 2011			
26L1454-14	71.0	40.6		Silantyev et al. 2011			Silantyev et al. 2011			
34L64 1	65.4	35.7		Silantyev et al. 2015			Silantyev et al. 2015			
34L64 2				Silantyev et al. 2015			Silantyev et al. 2015			
34L64 3				Silantyev et al. 2015			Silantyev et al. 2015			
34L64 4	59.8	38.5		Silantyev et al. 2015			Silantyev et al. 2015			
34L67 1	71.5	32.8		Silantyev et al. 2015			Silantyev et al. 2015			
34L67 3	71.1	30.6		Silantyev et al. 2015			Silantyev et al. 2015			
34L67 4	70.5	28.6		Silantyev et al. 2015			Silantyev et al. 2015			
34L68 4	60.2	33.1		Silantyev et al. 2015			Silantyev et al. 2015			
34L68 5	67.4	34.0		Silantyev et al. 2015			Silantyev et al. 2015			
34L125 1				Silantyev et al. 2015			Silantyev et al. 2015			
34L125 2				Silantyev et al. 2015			Silantyev et al. 2015			
34L125 3	59.8	44.8		Silantyev et al. 2015			Silantyev et al. 2015			
34L127 3				Silantyev et al. 2015			Silantyev et al. 2015			
34L127 4				Silantyev et al. 2015			Silantyev et al. 2015			
34L136 1				Silantyev et al. 2015			Silantyev et al. 2015			
34L137 1				Silantyev et al. 2015			Silantyev et al. 2011			
D01-1	59.47	53.86					Unsworth 15°20 Datasheets			
D01-16	68.66	48.96					Unsworth 15°20 Datasheets			
D01-4	64.71	46.14					Unsworth 15°20 Datasheets			

Table S4. (cont.)

Sample	Lat	Long	Depth	FSR mm/yr	Ridge	Location	Lithology	Type
D01-6	13.8198	44.9432	2932		MAR	13°N	Harzburgite	
D01-7	13.8198	44.9432	2932		MAR	13°N	Harzburgite	
D01-8	13.8198	44.9432	2932		MAR	13°N	Harzburgite	
D07-10	13.3007	44.9312	2962		MAR	13°N	Harzburgite	
D07-3	13.3007	44.9312	2962		MAR	13°N	Harzburgite	
D07-6	13.3007	44.9312	2962		MAR	13°N	Harzburgite	
D07-7	13.3007	44.9312	2962		MAR	13°N	Harzburgite	
D09-22.1	13.3192	44.9343	2354		MAR	13°N	Peridotite	
D09-4.1	13.3192	44.9343	2354		MAR	13°N	Mylonite peridotite	
D09-4.2	13.3192	44.9343	2354		MAR	13°N	Mylonite peridotite	
D09-4.3	13.3192	44.9343	2354		MAR	13°N	Mylonite peridotite	
D13-11	13.3188	44.8871	3196		MAR	13°N	Harzburgite	
D13-15	13.3188	44.8871	3196		MAR	13°N	Harzburgite	
D13-15	13.3188	44.8871	3196		MAR	13°N	Harzburgite	
D13-24	13.3188	44.8871	3196		MAR	13°N	Harzburgite/Dunite	
D13-30	13.3188	44.8871	3196		MAR	13°N	Harzburgite	
D13-35	13.3188	44.8871	3196		MAR	13°N	Harzburgite	
D13-4	13.3188	44.8871	3196		MAR	13°N	Harzburgite	
D13-40	13.3188	44.8871	3196		MAR	13°N	Harzburgite	
D13-7	13.3188	44.8871	3196		MAR	13°N	Harzburgite	
D16-1	13.0270	44.8388	4820		MAR	13°N	Harzburgite	
D16-1	13.0270	44.8388	4820		MAR	13°N	Harzburgite	
D16-6	13.0270	44.8388	4820		MAR	13°N	Harzburgite	
D16-8	13.0270	44.8388	4820		MAR	13°N	Harzburgite	
D21-04	13.0185	44.8572	4357		MAR	13°N	Harzburgite	
D21-10	13.0185	44.8572	4357		MAR	13°N	Harzburgite	
D21-2	13.0185	44.8572	4357		MAR	13°N	Harzburgite	
D21-25	13.0185	44.8572	4357		MAR	13°N	Harzburgite	
D21-28	13.0185	44.8572	4357		MAR	13°N	Harzburgite	
D21-3	13.0185	44.8572	4357		MAR	13°N	Harzburgite	
D21-5	13.0185	44.8572	4357		MAR	13°N	Harzburgite	
D28-15	13.8430	44.9378	2768		MAR	13°N	Harzburgite	
D28-22	13.8430	44.9378	2768		MAR	13°N	Harzburgite	
D28-31	13.8430	44.9378	2768		MAR	13°N	Harzburgite	
D28-37	13.8430	44.9378	2768		MAR	13°N	Harzburgite	
D28-6	13.8430	44.9378	2768		MAR	13°N	Harzburgite	
D28-6	13.8430	44.9378	2768		MAR	13°N	Harzburgite	
D28-7	13.8430	44.9378	2768		MAR	13°N	Harzburgite	

Table S4. (cont.)

Sample	Mg#	Cr#	Mode Ref	Ol Ref	Opx Ref	Cpx Ref	Spin Ref	Station	Sample #	Notes
D01-6	63.61	48.00					**Unsworth 15°20 Datasheets**			
D01-7	69.79	40.18					**Unsworth 15°20 Datasheets**			
D01-8	68.22	46.34					**Unsworth 15°20 Datasheets**			
D07-10	66.75	52.01					**Unsworth 15°20 Datasheets**			
D07-3	69.23	40.52					**Unsworth 15°20 Datasheets**			
D07-6	65.67	48.70					**Unsworth 15°20 Datasheets**			
D07-7	69.09	49.00					**Unsworth 15°20 Datasheets**			
D09-22.1	66.25	39.79					**Unsworth 15°20 Datasheets**			
D09-4.1	66.17	50.28					**Unsworth 15°20 Datasheets**			
D09-4.2	65.45	51.54					**Unsworth 15°20 Datasheets**			
D09-4.3	65.29	50.57					**Unsworth 15°20 Datasheets**			
D13-11	61.17	47.90					**Unsworth 15°20 Datasheets**			
D13-15	59.48	51.00					**Unsworth 15°20 Datasheets**			
D13-15	62.17	47.19					**Unsworth 15°20 Datasheets**			
D13-24	60.97	47.16					**Unsworth 15°20 Datasheets**			
D13-30	54.74	49.66					**Unsworth 15°20 Datasheets**			
D13-35	59.51	51.04					**Unsworth 15°20 Datasheets**			
D13-4	55.71	53.54					**Unsworth 15°20 Datasheets**			
D13-40	65.35	43.77					**Unsworth 15°20 Datasheets**			
D13-7	63.24	50.58					**Unsworth 15°20 Datasheets**			
D16-1	65.65	52.03					**Unsworth 15°20 Datasheets**			
D16-1	68.06	39.96					**Unsworth 15°20 Datasheets**			
D16-6	67.42	39.70					**Unsworth 15°20 Datasheets**			
D16-8	59.51	56.61					**Unsworth 15°20 Datasheets**			
D21-04	61.70	50.92					**Unsworth 15°20 Datasheets**			
D21-10	58.72	50.59					**Unsworth 15°20 Datasheets**			
D21-2	63.82	46.62					**Unsworth 15°20 Datasheets**			
D21-25	65.80	48.07					**Unsworth 15°20 Datasheets**			
D21-28	66.92	43.19					**Unsworth 15°20 Datasheets**			
D21-3	56.99	49.14					**Unsworth 15°20 Datasheets**			
D21-5	58.51	49.94					**Unsworth 15°20 Datasheets**			
D28-15	65.97	50.31					**Unsworth 15°20 Datasheets**			
D28-22	63.00	48.05					**Unsworth 15°20 Datasheets**			
D28-31	62.99	52.27					**Unsworth 15°20 Datasheets**			
D28-37	59.12	51.41					**Unsworth 15°20 Datasheets**			
D28-6	63.69	50.74					**Unsworth 15°20 Datasheets**			
D28-6	56.25	50.38					**Unsworth 15°20 Datasheets**			
D28-7	59.92	48.82					**Unsworth 15°20 Datasheets**			

Table S5. Melting model parameters

								Anhydrous Melting							
				Partition Coefficients											
		Bulk Starting Concentration (ug/g)	Olivine	Cpx (Sp)	Cpx (Grt)	Opx	Spinel	Garnet	Cpx-out (Phx), Cox-Sp	Th (ug/g) at Cpx-out	Yb (ug/g) at Cpx-out	Literature Source			
	Yb	0.365	0.014	0.41	1.43	0.09	0.005					Hellebrand et al. 2002 after Suhr et al. 1998 and Blundy et al. 1998			
	Ti	716.3	0.015	0.35	0.71	0.1	0.15					Hellebrand et al. 2002 after Suhr et al. 1998 and Blundy et al. 1998			
	Starting Mineral Modes														
Initial mineral mode (Sp-Bearing)			0.57	0.13		0.21		0.09				Calc after Hellebrand et al. (2002)			
Initial mineral mode (Grt-Bearing)			0.57	0.13		0.28	0.02					Workman and Hart 2005			
Grt to Sp coefficients		-0.444	0.444		0.666	0.333	-1					Rxn of Johnson et al. 1990			
	Melting modes														
Spinel Field Only, W&H05 Min Modes		-0.22	0.71		0.38	0.13		18%	258	0.13		Baker and Stolper 1994			
		-0.347	0.735		0.571	0.041		19%	204	0.11		Wasylenki et al. 2003			
		-0.06	0.67		0.28	0.11		19%	204	0.11		Exp. L62-L63, Kinzler 1997			
		-0.13	0.89		0.13	0.12		14%	546	0.37		Exp. L134-L138, Kinzler 1997			
Garnet Field		0.04		1.05	-0.19		0.11					Walter 1998			
Grt+Cpx Melting								4/21	193	0.143	Grt: Walter 1998, Sp: Kinzler 1997, L134-L138				
								2/22	218	0.147	Grt: Walter 1998, Sp: Baker and Stolper 1994				
								3/21	211	0.143	Grt: Walter 1998, Sp: Wasylenki et al. 2003				
								5/19	227	0.181	Grt: Walter 1998, Sp: Kinzler 1997, L62-L63				

Table S5. (cont.)

| Hydrous Melting | | |

Table S5. (cont.)

Partition Coefficients

Hellebrand, E., et al. (2002). "Garnet-field melting and late-stage refertilization in 'residual' abyssal peridotites from the Central Indian Ridge." Journal of Petrology **43**(12): 2305-2338.

Suhr, G., et al. (1998). "Infiltration of refractory melts into the lowermost oceanic crust: evidence from dunite- and gabbro-hosted clinopyroxenes in the Bay of Islands ophiolite." Contributions to Mineralogy and Petrology **131**(2-3): 136-154.

Blundy, J. D., et al. (1998). "Heavy REE are compatible in clinopyroxene on the spinel lherzolite solidus." Earth and Planetary Science Letters **160**(3-4): 493-504.

McDade, P., et al. (2003). "Trace element partitioning between mantle wedge peridotite and hydrous MgO-rich melt." American Mineralogist **88**(11-12): 1825-1831.

Johnson, K. T. M. (1998). "Experimental determination of partition coefficients for rare earth and high-field-strength elements between clinopyroxene, garnet, and basaltic melt at high pressures." Contributions to Mineralogy and Petrology **133**(1-2): 60-68.

Yao, L., et al. (2012). "A parameterized model for REE distribution between low-Ca pyroxene and basaltic melts with applications to REE partitioning in low-Ca pyroxene along a mantle adiabat and during pyroxenite-derived melt and peridotite interaction." Contributions to Mineralogy and Petrology **164**(2): 261-280

Sun, C., & Liang, Y. (2012). Distribution of REE between clinopyroxene and basaltic melt along a mantle adiabat: effects of major element composition, water, and temperature. *Contributions to Mineralogy and Petrology*, *163*(5), 807-823.

Initial mineral modes

Workman RK, Hart SR (2005) Major and trace element composition of the depleted MORB mantle (DMM). Earth and Planetary Science Letters 231:53–72. doi: 10.1016/j.epsl.2004.12.005

Melting modes

Baker, M. B. and E. M. Stolper (1994). "Determining the Composition of High-Pressure Mantle Melts Using Diamond Aggregates." Geochimica Et Cosmochimica Acta **58**(13): 2811-2827.

Wasylenki LE (2003) Near-solidus Melting of the Shallow Upper Mantle: Partial Melting Experiments on Depleted Peridotite. Journal of Petrology 44:1163–1191. doi: 10.1093/petrology/44.7.1163

Kinzler, R. J. (1997). "Melting of mantle peridotite at pressures approaching the spinel to garnet transition: Application to mid-ocean ridge basalt petrogenesis." Journal of Geophysical Research: Solid Earth **102**(B1): 853-874.

Walter, M. J. (1998). "Melting of garnet peridotite and the origin of komatiite and depleted lithosphere." Journal of Petrology **39**(1): 29-60.

Bizimis, M., et al. (2000). "Trace and REE content of clinopyroxenes from supra-subduction zone peridotites. Implications for melting and enrichment processes in island arcs." Chemical Geology **165**(1-2): 67-85.

Grove, T. L. and C. B. Till (2019). "H 2 O-rich mantle melting near the slab–wedge interface." Contributions to Mineralogy and Petrology **174**(10): 80.

Gaetani, G. A. and T. L. Grove (1998). "The influence of water on melting of mantle peridotite." Contributions to Mineralogy and Petrology **131**(4): 323-346.

Initial bulk rock Yb and Ti abundances

Workman RK, Hart SR (2005) Major and trace element composition of the depleted MORB mantle (DMM). Earth and Planetary Science Letters 231:53–72. doi: 10.1016/j.epsl.2004.12.005

S.6 Supplementary material accompanying Chapter 6

Analytical methods, Data Reduction

Zircons extracted from the samples were mounted in epoxy and polished, imaged in reflected light and CL, and analyzed at the U.S.G.S-Stanford Ion Microprobe Laboratory using the sensitive high-resolution ion microprobe-reverse geometry (SHRIMP-RG). We used a 7.1-7.5 nA O^{2-} defocused primary beam with a mass resolving power (Δm/m) of 6500 at 10% peak height to resolve interferences. The acquisition routine included $^{30}Si^{16}O$, ^{48}Ti, ^{56}Fe, ^{89}Y, ^{155}Gd, $^{172}Gd^{16}O$, $^{90}Zr^{16}O$, $^{180}Hf^{16}O$, ^{204}Pb, background measured 0.05 AMU above the ^{204}Pb peak, ^{206}Pb, ^{207}Pb, ^{208}Pb, ^{238}U, $^{232}Th^{16}O$, and $^{238}U^{16}O$. The goal of these measurements was focused on measuring $^{206}Pb/^{238}U$ ages, with a common Pb correction based on ^{207}Pb. Counting times for each mass were 0.1, 0.1, 0.1, 0.1, 0.1, 0.1, 1, 0.5, 4, 6, 75, 20, 4, 6, 2, 2 seconds, respectively. U/Pb analyses were conducted following the methods of Coble et al. (2017). Calculated zircon ages were standardized relative to Rockland tephra (R33) zircon (419Ma) of Black et al. (2004) throughout the analytical session. Data reduction follows the methods described by Ireland and Williams (2003). We report individual spots as $^{206}Pb/^{238}U$ ages corrected for common Pb using ^{207}Pb and based on a zero-age model Pb composition from Stacey and Kramers (1975), and initial $^{238}U/^{230}Th$ disequilibrium with the method of Schärer (1984). For R33 (Rockland tephra) zircon, we used an initial $^{232}Th/^{238}U$ melt value of 2.99. Trace element concentrations in zircon were calculated relative to Madagascar Green (MAD) zircon from Barth and Wooden (2010).

Trace element chemistry and Ti-in-zircon thermometry

We use an activity coefficient of 0.7 for both SiO_2 and TiO_2. These values were chosen to be conservative in our temperature estimates due to the primitive nature of the samples, as no rutile was observed in thin sections. TiO_2 activity is >0.5 for most systems, with lower values for mafic systems with respect to felsic systems; even if the TiO_2 activity is unknown, the Ti-in-zircon thermometer is thought to underestimate temperatures by at most, 70°C {Hayden:2007gl, Ferry:2007bz}. We further assume negligible sub-solidus diffusional re-equilibration, based on previously inferred rapid cooling rates of > 800°C per Ma of lower oceanic crust {John:2004ig}) Our temperature calculations do not have a material impact on the results of this work, so we do not discuss them further.

Figures

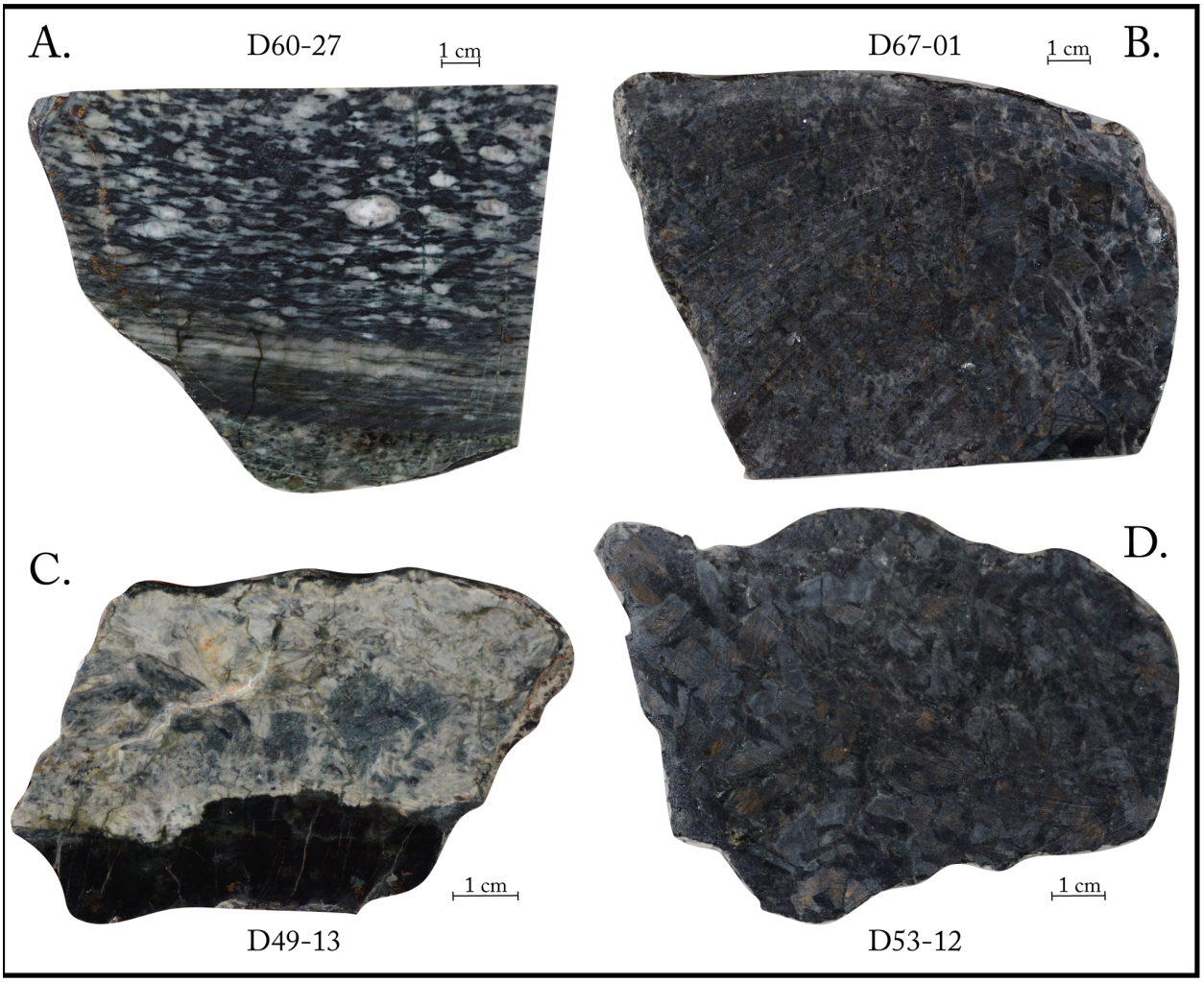

Fig. 6.S1. Samples analyzed in this study. A. Protomylonitic to ultramylonitic troctolite. B. Equigranular oxide bearing gabbro. C. Gabbroic dike in contact with heavily serpentinized harzburgite. Gabbro is heavily altered to talc + tremolite. D. Equigranular oxide bearing gabbro.

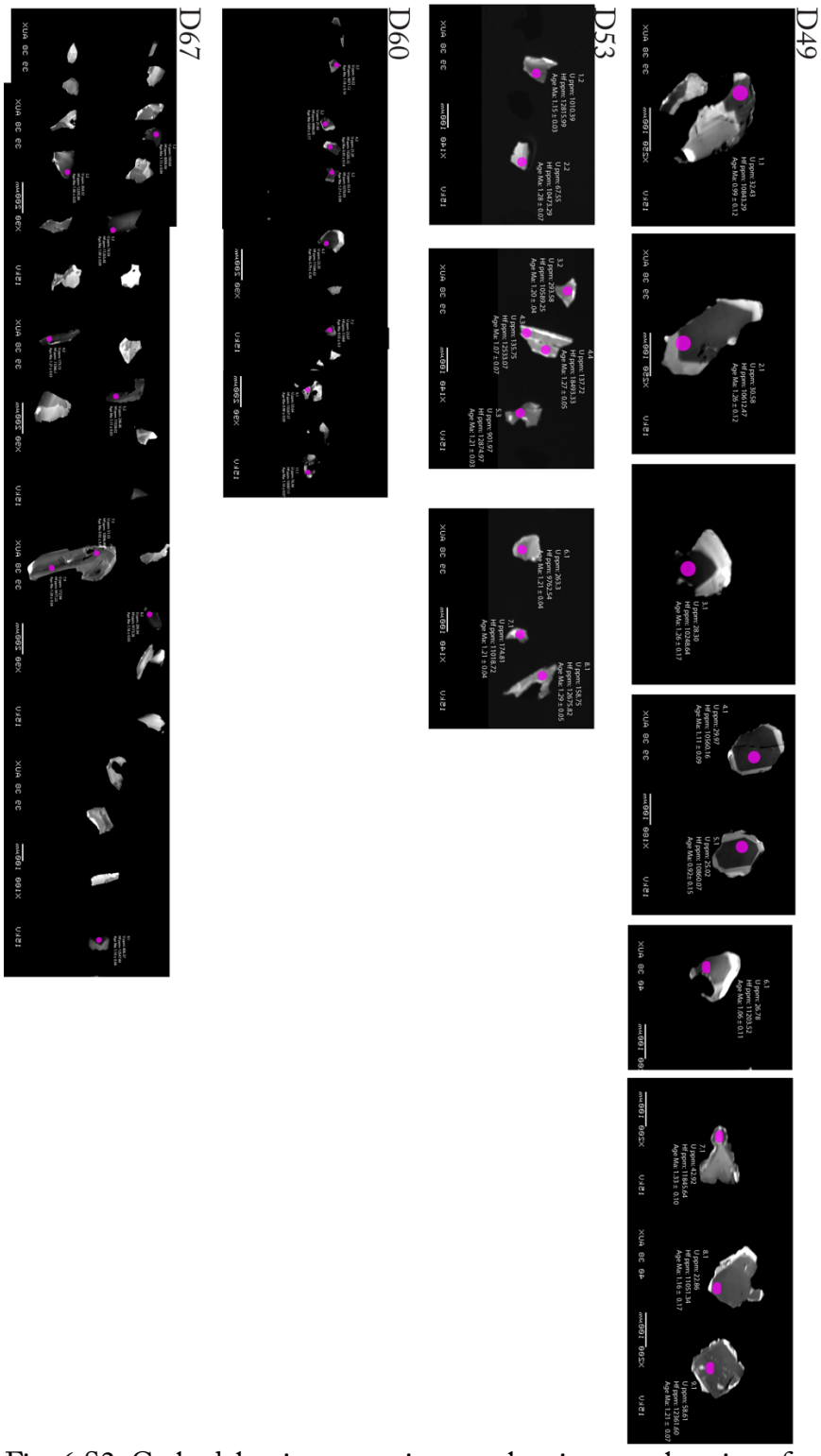

Fig. 6.S2. Cathodeluminescence images showing spot locations for isotopic age and trace element analysis of zircon in samples D60-27, D67-01, D49-13 and D53-12. Numbers correspond to the analyses listed in Table 6.2.

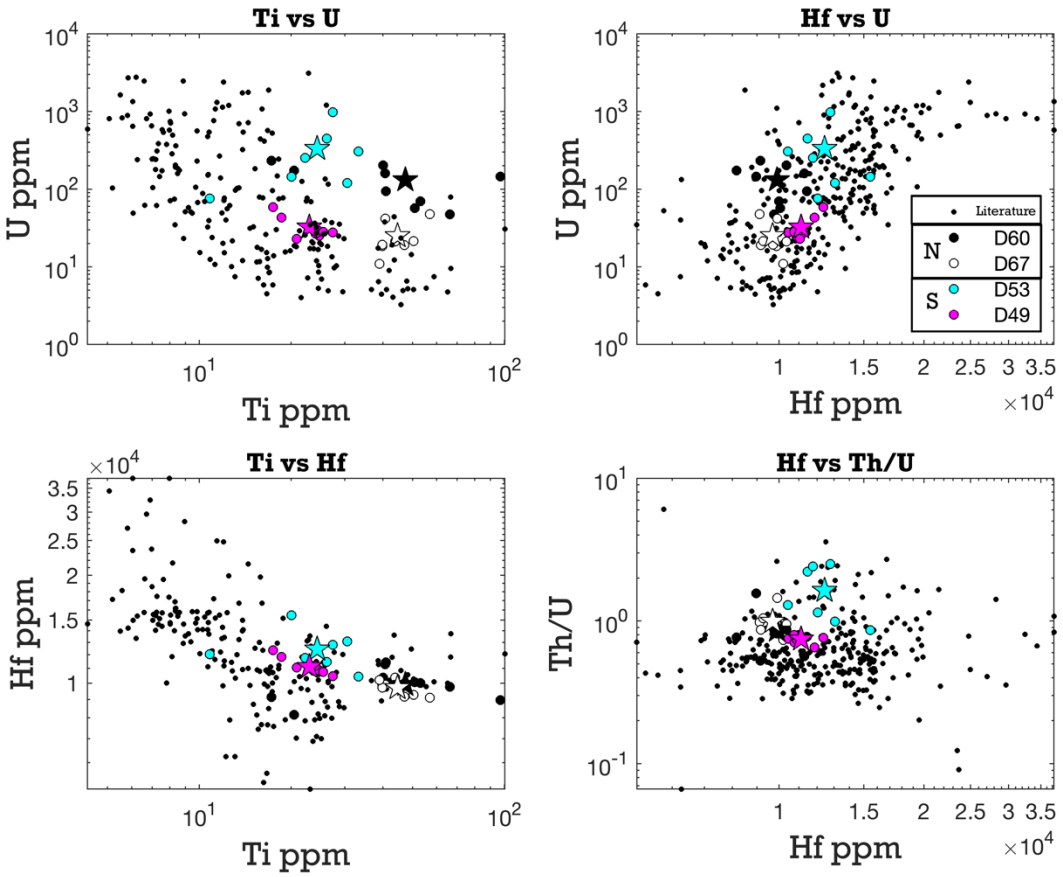

Figure 6.S3. Trace element concentrations and ratios showing genetic similarity of the samples. Individual zircons labeled as circles; stars denote sample means.

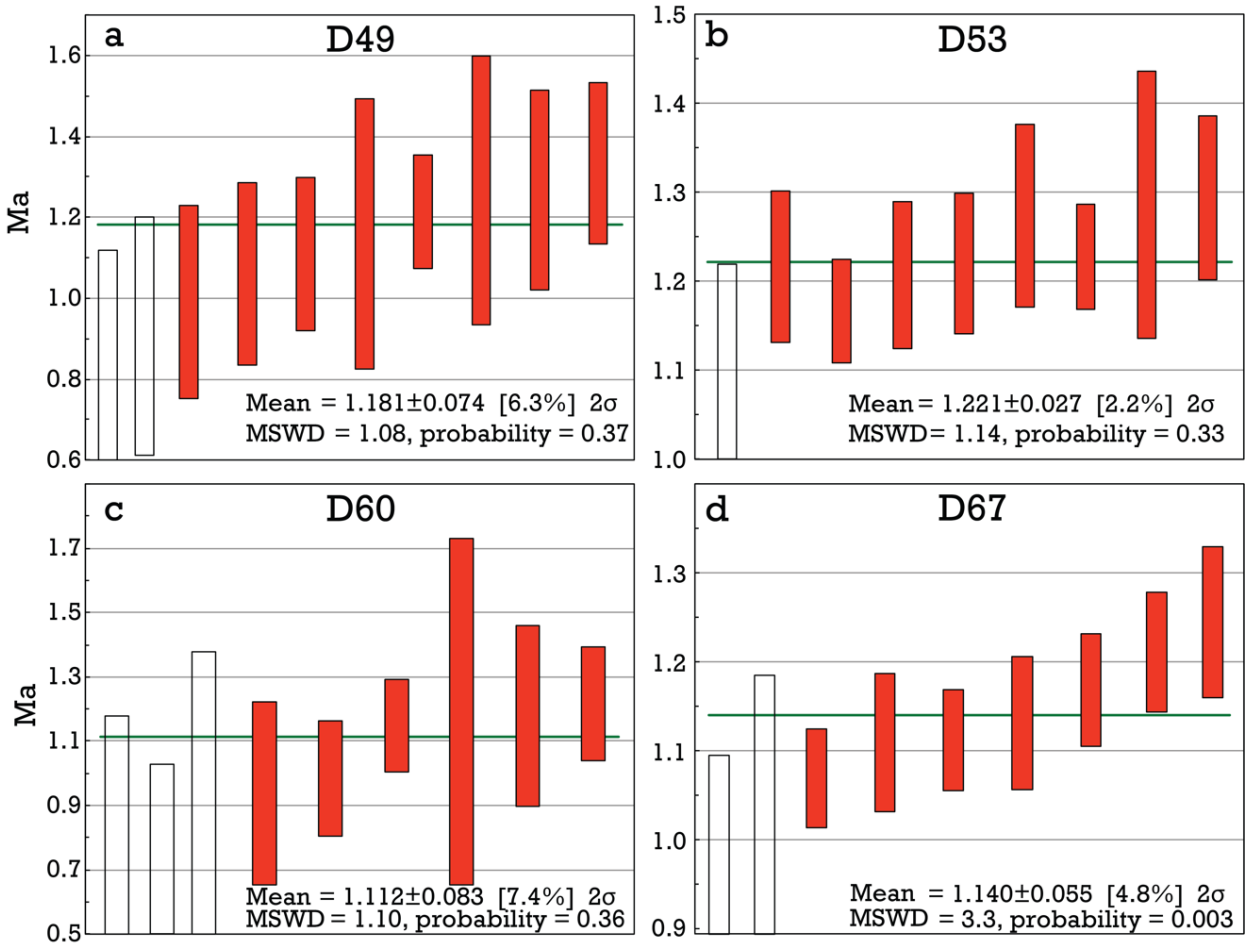

Figure 6.S4. $^{206}Pb/^{238}U$ zircon ages for samples from 16°N Mid-Atlantic ridge used in this study. Ages corrected for ^{230}Th disequilibrium. Spot analyses shown as unfilled bars were rejected when calculating weighted averages on the basis of high common lead (f_{206}>30%). The weighted average age (dark green line) and 95% confidence limit (box height) for each sample are shown graphically.

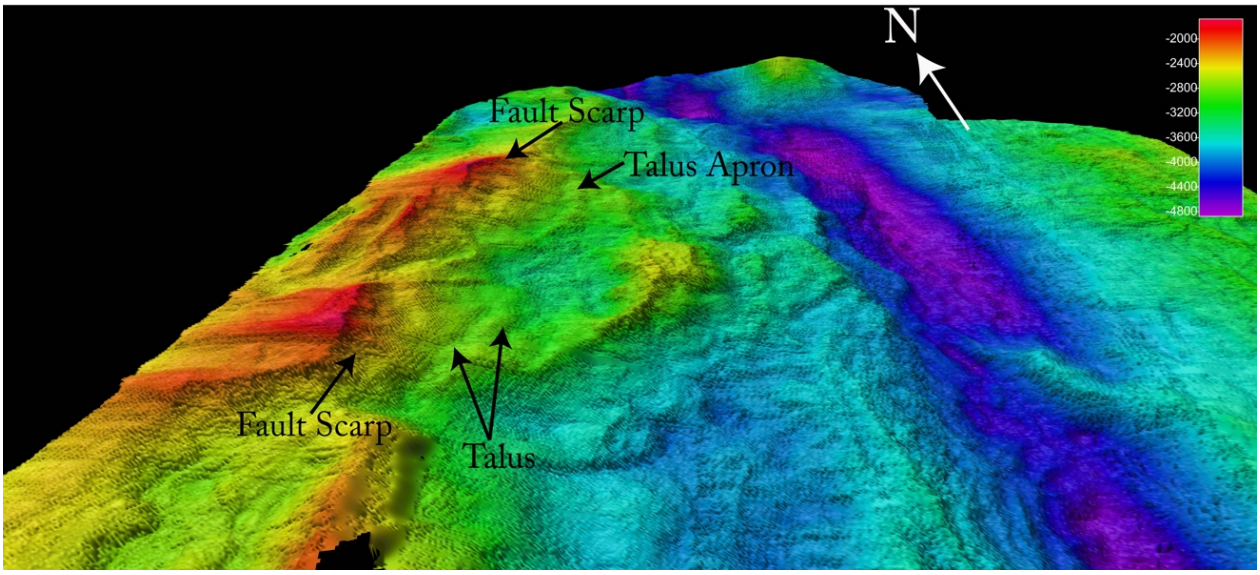

Figure 6.S5. Oblique view due north toward the Northern Core Complex at 16°N MAR. Note the fault scarps at elevation, with mass wasting and erosional features downslope. Also noteworthy are the apparent debris aprons located at both the northern and southern ends of the Northern Core Complex, presumably talus piles.